Proceedings

35th ASPE Annual Meeting
October 20 – October 22, 2020

Virtual Meeting

American Society for
Precision Engineering

230 Washington Ave. Ext., Suite 101 Albany, NY 12203

518-463-8687

Proceedings of

The Thirty-Fifth Annual Meeting of the
American Society for Precision Engineering

October 20–22, 2020
Virtual Meeting

The American Society for Precision Engineering (ASPE) is a multidisciplinary professional and technical society concerned with research and development, design, manufacture and measurement of high accuracy components and systems. ASPE activities encompass relevant aspects of mechanical, electronic, optical and production engineering, physics, chemistry, and computer and materials science. Membership is open to anyone interested in any aspect of precision engineering.

Founded in 1986, ASPE provides a focus for a diverse but important community. Other professional organizations have covered aspects of precision engineering, always as a sideline to their principal goals. ASPE is based on the core of generic concepts necessary to achieve precision in any application; independent of discipline, ASPE intends to be the focus for precision technology – and to represent all facets from research to application.

The Annual Meeting has evolved into an international forum for the exchange of ideas and presentation of research results relating to precision engineering, metrology, controls and system integration. Precision engineers and scientists from private industry, government laboratories, and universities meet to learn about the latest developments and to exchange ideas about the future directions of these technologies.

Preface

This book comprises the proceedings of the 35th ASPE Annual Meeting. The contributions reflect the authors' opinions and are published as presented to ASPE, without change. Their inclusion in this publication does not necessarily constitute endorsement by the ASPE, or its editorial staff.

Individual readers of this book and nonprofit libraries acting for them are permitted to make fair use of the material contained in this book to be used in teaching or research; provided they copy said paper in total, as written by the author. Permission is granted to quote excerpts from the scientific or technical works in this book with proper acknowledgment of the source to include: The author's name, the book name, and the ASPE tag line. Reproduction of figures and tables is likewise permitted from the contents of this book, provided that the same acknowledgment of the same source and content is provided.

Any other type reproduction, systematic copying or multiple reproduction of any material in this book is expressly prohibited except with the written permission of the ASPE editorial staff, addressed to the Society's headquarters.

Organizing and Technical Program Committee

Annual Meeting Chairperson
Dr. Marcin B. Bauza, ZEISS Industrial Quality Solutions

Technical Program Committee Chairpersons
Prof. Michael A. Cullinan, The University of Texas at Austin
Micro-Nano Technologies

Dr. Jonathan D. Ellis, Clerio Vision
Metrology Systems

Dr. Stephen J. Furst, Smart Material Solutions, Inc.
Precision Manufacturing

Prof. Richard K. Leach, University of Nottingham
Characterization

Prof. Chinedum E. Okwudire, University of Michigan
Controls and Mechatronics

Dr. Richard M. Seugling, Lawrence Livermore National Laboratory
Precision Design

Tutorials Chairs
Dr. Vivek G. Badami, Zygo Corporation
Dr. Stephen J. Ludwick, Aerotech, Inc.

Exhibits Session Chairs
Dr. Byron R. Knapp, Professional Instruments Company
Mr. Don L. Martin, Lion Precision

Students and Young Members Chairs
Mr. Luis A. Aguirre, 3M Company
Prof. Stuart T. Smith, University of North Carolina – Charlotte

Scientific Review Committee

Contents

ASPE Lifetime Achievement Award

John S. Taylor
University of North Carolina at Charlotte

The Lifetime Achievement Award was conceived to honor particularly noteworthy contributions to the advancement of the discipline and/or Society over a career of service in precision engineering, and this year, ASPE is pleased to present this very special award to **John S. Taylor** for leadership in advancements in the field of additive manufacturing.

Dr. John S. Taylor is an Adjunct Professor at the Center for Precision Metrology at the University of North Carolina at Charlotte. After 33 years in varied roles in precision engineering, he retired from Lawrence Livermore National Laboratory in 2017 as Group Leader for Precision Systems and Manufacturing. He received his MS and PhD degrees in Mechanical Engineering from Purdue University.

John joined LLNL in 1984 to support the Large Optics Diamond Turning Machine, exploring diamond machinability and tool wear. John served as Optics Group Leader and Program Leader for LLNL's EUV Lithography Program (partnered with Sandia and LBNL), which demonstrated the first EUV scanner for the EUV LLC consortium of chip makers. The EUVL Optics Group designed and constructed the world's first diffraction-limited wide-field EUV lithographic camera, thus establishing the feasibility of lithographic-quality imaging using soft x-rays. The series of four lithographic cameras that were fielded for the Engineering Test Stand and the Micro-Exposure Tool constituted the most accurate optical systems constructed to date (2003), as demonstrated by rigorous measurements of the aligned system wavefront errors at a wavelength of 13.4 nm. Precision engineering principles were essential in guiding the system error budget, which spanned optical design, polishing, coating, mechanical structure, fixturing, assembly, alignment, and full spectrum figure and finish metrology. The most enjoyable aspect of this work was the day-to-day collaboration with world-class engineers and scientists from three national laboratories, chip makers, and industry.

John greatly enjoyed the variety of positions he assumed at LLNL and the breadth and depth of his colleagues. His work in the Chip Science Group on machinability and diamond tool wear on electroless nickel and silicon brought a deterministic understanding to previously non-repeatable processes. He gained hands-on experience with pitch polishing and metrology of Wolter optics for an EUV satellite, which highlighted the synergy of combining optics polishing with CNC machine tools. He led initial production analyses of the optics for the National Ignition Facility, which gave him a keen appreciation of the global optics companies. He served as chief engineer for NIF target fabrication during the transition from the previous craftsman approach to fabrication to a metrology-intensive deterministic production process. During the Laboratory's technology-transfer era, John led industrial projects to improve the determinism of polishing aspheric lithographic optics and on commercializing CNC grinding of optics. With broader rewarding impact, John lead several task forces and review committees to resolve production and quality control issues for LLNL projects. In recent years, John has lectured and mentored students at UNCC, DTU, and other institutions, and continues to support ASPE topical meetings.

John is an enthusiastic charter member of ASPE and served as President (2014 and Director-at-Large. As President, he initiated the Technical Leadership Committees and the series of topical meetings on additive manufacturing, which began a partnership with euspen. Among his most enjoyable professional experiences, John co-chaired many ASPE Topical Meetings: *Achieving Precision in Additive Manufacturing* (2014-present, with Richard Leach, *Precision Engineering and Mechatronics Supporting the Semiconductor Industry* (2012 with Jan van Eijk, *Precision Mechanical Design and Mechatronics for Sub-50nm Semiconductor Equipment* (2008 with Jan van Eijk, and *Metal Platings for Precision Finishing Operations* (1991 with Chris Evans. John chaired the 2016 ASPE Annual Meeting in Portland and received the 2016 ASPE Distinguished Service Award. John has six patents, presented numerous technical papers, and is a member of euspen, ASME, ASTM F-42, OSA, SME, and is a Fellow of SPIE.

ASPE Distinguished Service Award

Luis A. Aguirre

The Distinguished Service Award was conceived to honor noteworthy contributions and service to the Society, and this year, ASPE is pleased to present this award to **Luis A. Aguirre**.

Luis A. Aguirre received a BSEE/ME from the University de San Carlos de Guatemala in 1983, where he also taught as an assistant of the electronics laboratory. For 3 years, he taught electrical circuits and electronic materials and work developing automation systems for several companies as a systems integrator. In 1988, he completed his MSME from Texas A&M University with emphasis on controls for vision-guided robotics and artificial intelligence.

Luis has worked at 3M for the past 32 years developing manufacturing and R&D machines.   During the first 10 years, he worked mainly on robotics, flexible automation and roll to roll converting of flexible electronic and communications components. Over the last 22 years, he largely has been working on the development of many challenging precision systems for development of micro-nano patterning applications. During his career at 3M, some of his technical accomplishments have been: 6 US patents, 2 Inventive Engineering awards, 1 Outstanding Engineering, 4 Inventive contributions, 2 Technical Circle of Excellence Nominations, and received 2 corporate Genesis and the Engineering Innovation grants.

Luis' technical volunteer work has included serving as the President of the IEEE student branch and co-chair of the motion controls technical sub-committee for 7 years at 3M. Also, in the early 2000's, Luis collaborated with the NEMI (The National Electronics Manufacturing Initiative as part of the Final Assembly Technical Team.   From 2010 to 2012, he served on the ASPE Board of Directors as Director-at-Large. In addition, Luis has served as the chair of the 2015 Annual Meeting and the chair of the ASPE nominating committee in 2016. Beginning in 2016, he was the chair of the ASPE Student Challenge where he continues to serve today.

ASPE Distinguished Service Award

Stuart Smith

The Distinguished Service Award was conceived to honor noteworthy contributions and service to the Society, and this year, ASPE is pleased to present this award to **Stuart Smith.**

Stuart Smith has been working in engineering for more than four decades starting in 1977 with a factory maintenance apprenticeship with Miles Redfern Ltd (UK). He is now a Professor of Mechanical Engineering in the Center for Precision Metrology at UNC Charlotte. He leads the instrument development group that has spun out three North Carolina companies Albany Instruments Inc., 2000, Motus Mechanical Inc., 2014 (now Motus Dynamics Inc., 2016) and InsituTec Inc. 2002 specializing in eddy current sensing technologies, mechanism construction kits and fine motion control metrology systems respectively. Throughout the years his main focus has been the development of instrumentation and sensor technologies primarily aimed towards the challenges of atomic scale discrimination and modifications. This work has resulted in 20 patents, over 97 journal publications, and the authorship of three books.

ASPE College of Fellows

Election to the ASPE College of Fellows is a highly prestigious honor that is intended to recognize and honor those exceptional members of the Society who have made outstanding contributions to the art and practice of Precision Engineering through original research, significant innovations, education and outreach, or service to the profession.

The ASPE Constitution defines the **Fellow** membership grade as follows, *"Those eligible as candidates for election to Fellows shall be members who have contributed to the advancement of precision engineering by significant, original research or who have rendered some other special service to its cause. Any member of the Society may nominate another member for the grade of Fellow."*

ELIGIBILTY
Nominees for the ASPE College of Fellows must:

- Be an ASPE member in good standing for a minimum of ten continuous years.
- Have at least 20 years of experience in a technological field relevant to Precision Engineering.
- Have at least a Bachelor's degree in a relevant engineering or technical field, or sufficient engineering practice to provide its equivalent.

ASPE is proud to recognize the following individuals as charter members of the College of Fellows:

Jon Pratt
National Institute of Standards & Technology

Tony L. Schmitz
University of Tennessee - Knoxville

Theo Ruijl
MI-Partners

Alex Slocum
MIT

2020 Scholarships Recipients

Graham J. Siddall ASPE Student Scholarship

The winner of the 2020 Graham J. Siddall ASPE Student Scholarship is **Alper Dumanli**, Oregon State (Burak Sencer, Advisor). This award includes the ASPE Annual Meeting registration fee and 4 tutorial fees.

With a 10-year student endowment, Graham Siddall will recognize a student scholar in the field of precision engineering. This prestigious award is valued at $1,000 and additionally will support the student winner in the form of waived conference and tutorial fees.

Graham Siddall received his BS degree in Production Engineering and Management with First Class honors from the University of Nottingham in England. He received his M.Sc. and Ph.D. degrees in Natural Philosophy (Physics) in 1971 and 1975, respectively, working under the guidance of Professor R.V. Jones at the University of Aberdeen in Scotland.

After working in surface metrology at Rank Taylor Hobson in Leicester, England, Dr. Siddall was awarded a Lindemann Research Fellowship to the United States where he joined the team at Stanford University working on the NASA/Stanford Gyro Relativity Experiment. His work at Stanford focused on developing the metrology techniques and equipment needed to manufacture the very precise spherical quartz rotors used in the cryogenic gyroscopes for the GP-B space mission. Following this, Dr. Siddall joined Hewlett-Packard Labs in Palo Alto, working in the X-ray and E-beam Lithography group, primarily in the area of precision stage design.   He went on to become the Vice President of research, development and engineering at GCA Corporation which marked the beginning of a long and distinguished stint in semiconductor capital equipment. Following GCA, in 1988, Dr. Siddall joined Tencor Instruments in California as Vice President of Technical Marketing and later became its first Chief Operating Officer. Over the next ten years the Company grew tenfold and merged with KLA in 1997, to form KLA-Tencor Corporation, where Dr. Siddall led the multi-billion dollar Wafer Inspection Group as Executive Vice President.   In July 1999, he left KLA to join Credence Systems, a semiconductor test equipment company, as its President and Chief Executive Officer and then later, as Chairman of the Board, before retiring in October 2005.

Following a number of Board positions in the semiconductor and electronics industry, most recently as Chairman of the Board of DCG Systems, Inc., Dr. Siddall has now relocated to the Pacific Northwest and has developed an interest in the area of eye research and the mitigation of eye disease. He is an active member of the University of Washington Medicine Eye Institute Community Action Board and has become an investor in the field of medical instrumentation startups. In 2016 he was awarded an Honorary Doctorate (D.Sc.) by Aberdeen University for his technical, business and philanthropic achievements.

2020 Scholarships Recipients

R.V. Jones ASPE Student Scholarship

The winner of the 2020 R.V. Jones ASPE Student Scholarship is **Xiangyu Guo**, Texas A & M University (ChaBum Lee, Advisor. This award includes the ASPE Annual Meeting registration fee and 4 tutorial fees.

The R. V. Jones Memorial Scholarship recognizes a distinguished student scholar in the field of precision engineering. This prestigious award is valued at $750 and additionally will support the student winner in the form of waived conference and tutorial fees.

This scholarship is named in recognition of Professor R. V. Jones of the University of Aberdeen (Scotland.   Much of his work at Aberdeen involved unusual and novel instrumentation pushed to the ultimate limits of precision. He stood in a tradition of physicists who saw accuracy of measurement and precision engineering as a key to both scientific and technological advances, and therefore a worthy subject for study in its own right. Dr Jones authored the editorial for the very first edition of the Society's Journal. He was the Keynote Speaker at the 1990 Annual Meeting of the ASPE and a recipient of the ASPE's 1990 Distinguished Contributor Award. Professor Jones had a distinguished career and made significant contributions in a number of fields. During World War II he was responsible for Scientific Intelligence in the British armed forces; he was decorated with the CB and CBE and awarded the Medal of Freedom and the Medal for Merit by the President of the United States. A graduate of Wadham College (Oxford, he became Professor of Natural Philosophy at the University of Aberdeen in 1946 where he made important contributions to both education and scientific research. His work in the field of precision instrument design is world renowned and his book 'Instruments and Experiences' is relevant to all precision engineers. His international best seller 'Most Secret War' about his experiences in Scientific Intelligence (published in the US as 'The Wizard War' was the subject of a BBC television series. He passed away in 1997 in Aberdeen, Scotland.

ASPE Student Scholarships

ASPE is proud to award two student scholarships for the 35th Annual Meeting. This year's scholarship recipients are **Heebum Chun**, Texas A & M University (ChaBum Lee, Advisor) and **Ryan Copenhaver**, University of Tennessee, Knoxville (Tony Schmitz, Advisor). The ASPE Student Scholarships include a waiver of the Annual Meeting registration fee and 4 tutorials fees.

ASPE 2020 Sustaining Corporate Sponsors

3M Company
St. Paul, MN 55144
www.mmm.com

Aerotech, Inc.
101 Zeta Drive
Pittsburgh, PA 15238
412-963-7470
www.aerotech.com

Ametek Precitech, Inc.
44 Blackbrook Road
Keene, NH 03431
603-357-2511
www.precitech.com

ASM Pacific Technology Ltd.
20/F, Gateway ts, 8 Cheung Fai Road
Tsing Yi, New Territories
Hong Kong
852-2619 2000
www.asmpacific.com

Carl Zeiss Industrial Metrology
6250 Sycamore Lane North
Maple Grove, MN 55369
763-744-2400
www.zeiss.com/metrology

Chardon Tool
115 Parker Court
Chardon, OH 44024
440-286-6440
www.ChardonTool.com

Cranfield Precision
Division of Fives Landis Ltd.
Woburn House, Adams Close
Kempston, Bedford, MK42 7JE
United Kingdom
44-0-1234-312820
www.cranfieldprecision.com

Lion Precision
7166 4th Street North
Oakdale, MN 55128
651-484-6544
800-250-9297
www.lionprecision.com

Mahr, Inc.
1144 Eddy Street
Providence, RI 02905
401-782-3168
www.mahr.com

Makino
7680 Innovation Way
Mason, OH 45040
513-573-7200
www.makino.com

Moore Nanotechnology Systems, LLC
230 Old Homestead Highway
Swanzey, NH 03446
603-352-3030
www.nanotechsys.com

New Way Air Bearings
50 McDonald Boulevard
Aston, PA 19014
610-494-6700
www.newwayairbearings.com

Physik Instrumente
16 Albert Street
Auburn, MA 01501
508-832-3456
www.pi-usa.us

Specialty Components, Inc.
14 Village Lane
Wallingford, CT 06492
203-284-9112
www.specialtycomponents.com

VDL Enabling Technologies Group USA
3758 Spinnaker Court
Fremont, CA 94538-1706
510-996-4662
www.vdletg.com

ASPE would like to thank our
Sustaining Corporate Sponsors

ASPE 2020 Corporate Sponsors

ABTech
126 Route 12 North
Fitzwilliam, NH 03447
603-585-7106
abtechmfg.com

Parker Hannifin Corporation
1140 Sandy Hill Road
Irwin, PA 15642
724-861-8200
www.parker.com/emn

ADCOLE Corporation
669 Forest Street
Marlborough, MA 01752
508-485-9100
www.adcole.com

Prior Scientific, Inc.
80 Reservoir Park Drive
Rockland, MA 02370
781-878-8442
www.prior.com

Contour Fine Tooling, Inc.
143 Jaffrey Road
Marlborough, NH 03455
603-876-4908
www.contour-diamonds.com

Professional Instruments Company
7800 Powell Road
Hopkins, MN 55343
952-933-3315
www.airbearings.com

Corning, Inc.
Corning, NY 14831
607-974-3842
www.corning.com

University of North Carolina-Charlotte
Center for Precision Metrology
9201 University City Blvd.
Charlotte, NC 28223-0001
704-687-8499
cpm.uncc.edu

K & Y Diamond
2645 Diab
Laurent, Quebec H4S 1E7
Canada
514-333-5606
www.kydiamond.ca

Zygo Corporation
Laurel Brook Road
Middlefield, CT 06455-0448
860-347-8506
Toll-free: (800) ZYGO-NOW
www.zygo.com

ASPE would like to thank our Corporate Sponsors.

ASPE 2020 Annual Meeting Oral Sessions

Session 1
Precision Manufacturing
Tuesday, October 20, 2020, 10:00 AM - 11:35 AM
Session Chair:
Stephen J. Furst (Smart Material Solutions, Inc.)

Session 2
Precision Design
Tuesday, October 20, 2020, 1:00 PM - 2:05 PM
Session Chair:
Richard M. Seugling (Lawrence Livermore National Laboratory)

*No abstract included

Session 3
Controls and Mechatronics
Wednesday, October 21, 2020, 7:30 AM - 9:05 AM
Session Chair:
Chinedum E. Okwudire (University of Michigan)

Session 4
Micro/Nano Technologies
Wednesday, October 21, 2020, 1:30 PM - 3:05 PM
Session Chair:
Michael A. Cullinan (The University of Texas at Austin)

*No abstract included

Session 5
Metrology Systems
Thursday, October 22, 2020, 10:00 AM - 11:40 AM
Session Chair:
Jonathan D. Ellis (Clerio Vision)

Session 6
Measurement Errors & Uncertainty
Thursday, October 22, 2020, 1:00 PM - 2:35 PM
Session Chair:
Richard K. Leach (University of Nottingham)

*No abstract included

*No abstract included

Poster Sessions

Tuesday, October 20, 2020, 12:00 PM - 1:00 PM

Thursday, October 22, 2020, 12:00 PM - 1:00 PM

Controls and Mechatronics

Metrology & Characterization

*No abstract included

Micro and Nano Technologies

Precision Design

*No abstract included

Precision Manufacturing

*No abstract included

Precision Manufacturing

*No abstract included

Technical Papers

A STUDY OF THE MICRO-STRUCTURE OF DIAMOND TURNED SURFACES AND THE GENERATION DIFFRACTION COLOR

Takeshi Hashimoto[1,2], Jeffery W. Roblee[1], Jiwang Yan[2]
[1]AMETEK Precitech Inc.
Keene NH, USA
[2] Keio University, Department of Mechanical Engineering, Faculty of Science and Technology, Yokohama, Japan

INTRODUCTION

Diamond turning is one of the most popular processes for fabricating optical components. Ultraprecision diamond turning has progressed rapidly in recent years. Surfaces can now be generated with finishes well below 1 nm Sa consistently on Nickel Phosphorus. However, even though the measured surface finish by scanning interferometry is acceptable for visible wavelength optics, the surface can still cause significant diffraction of white light. These "rainbow colors" or "tool marks" are readily visible with a stereomicroscope and a high intensity light. For many applications, these surface structures lead to unacceptable optical performance despite the excellent surface finish.

MOTIVATION

Currently, the most common and fastest inspection method of surface quality for small cell phone mold is a cosmetic inspection using a stereo microscope with a high intensity Halogen light. However, this method provides little information that can be used to improve the surface quality. The motivation of this study is to understand the micro-structures that cause diffraction on diamond turned surfaces and seek to develop a process to improve the surface finish itself. Several Nickel Phosphorus plated surfaces were diamond turned with different tool radii, tool types and cutting conditions to understand the diffraction color. Cutting conditions for eliminating diffraction color are also examined as well as discussion of tool mark issues.

LIGHT SCATTERING FROM DIAMOND TURNED SURFACES

Perfectly smooth surfaces only reflect light specularly. If there are surface irregularities, light is scattered in directions other than the specular one.
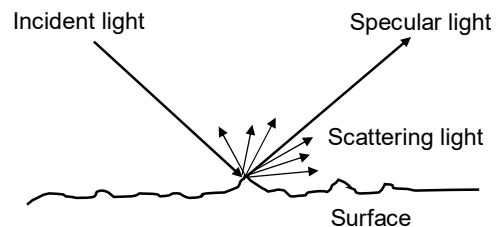
Figure 1. Light scattering from surface

Light scattering is also divided into two categories: i) Angular Scattering from Periodic Surface Features, ii) Angular Scattering from Non-Periodic Surface Features. Diamond turned surfaces made by an ultra-precision machine tool usually contain a precise periodic pattern. So, it is categorized as type i. The scattering from periodic patterns can be expressed by the principle of the light diffraction theory. The relationship between the incident angle and diffractive angle of the light with wavelength can be described by:

$$\sin \theta_m = \sin \theta_i + \mathrm{m}\frac{\lambda}{d} \qquad (1)$$

Where θ_m is the diffracted light angle from surface normal, θ_i is incident light angle, m is the order of diffraction. For microrough surfaces, only the first diffracted order (m=1), needs to be considered. λ is wavelength of the incident light. Visible light contains wavelengths between 380nm and 740nm and d is the periodic pitch, which is equivalent to the feed per revolution of the diamond turning process.
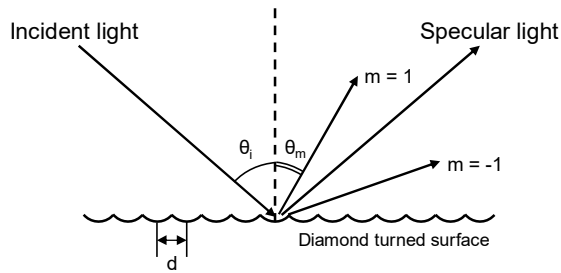
Figure 2. Light scattering from diamond turned surface

It is clear from equation (1) that the angle into which wavelength of light is diffracted or scattered depends only on the lateral spacing between the pattern, not surface finish dependent. Based on this principle, less than minimum wavelength of light around 300nm feed per revolution is selected, diffraction on the diamond turned surface goes away in theory.

EXPERIMENTAL SETUP
Part Cutting
To verify the diffraction color appearances with different roughness surfaces, nickel plated samples were machined with the same feed per revolution using four different tool radii (30µm, 90µm, 500µm and 2500µm). Machining experiments were performed on an ultra-precision diamond turning lathe (Nanoform X, AMETEK Precitech Inc). 12.7mm diameter flats were machined with 2µm feed per revolution at 1500rpm spindle rotation speed. Machine setup for this experimental testing is showed below.
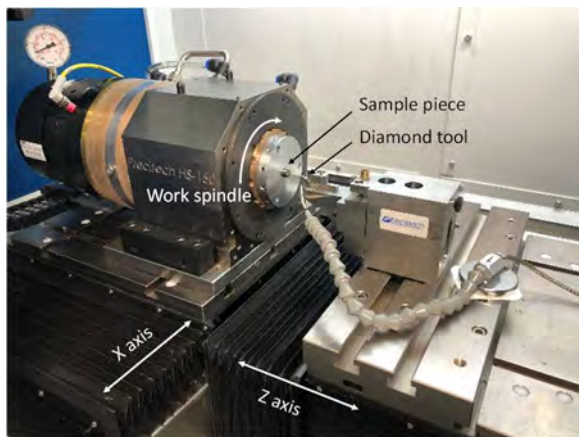
Figure 3. Experimental setup

Visual Inspection
The visual inspection of the surface was done by stereo microscope with a 20x objective setup. A 100W high intensity light was set up 65 mm away from the sample surface with an incidence angle of 45 degrees.
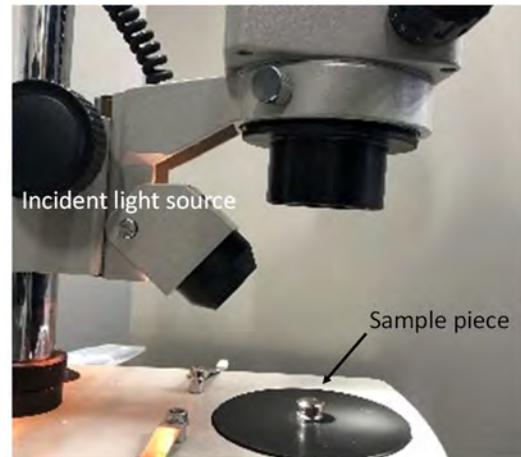
Figure 4. Visual inspection setup

Surface finish Measurement
The surfaces of these samples were measured on an Atomic Force Microscopy (AFM5100N, Hitachi High-Tech Corporation). The measurement area was 20µm x 20µm, with a data spacing equivalent to a lateral resolution of 40nm. All of the measured data were analyzed by software from Digital Surf (Mountain Map 7).
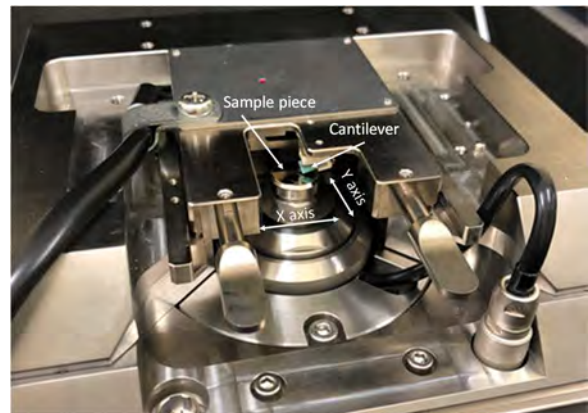
Figure 5. Measurement setup

RESULTS AND DISCUSSION
Visual inspection of the surface
Visual inspection of the surfaces with high intensity light clearly shows diffraction rainbow color (Figure.6). In terms of the diffraction color

intensity, surfaces that were generated by 30μm and 90μm radius tool had relatively high intensity. Surfaces that were generated by 500μm and 2500μm radius tool has lower intensity but almost the same level.
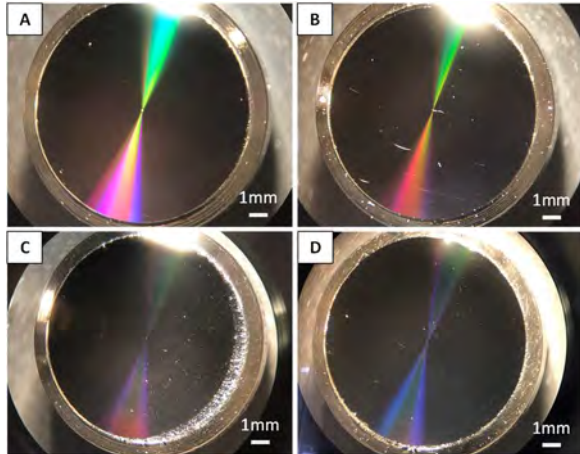
Figure 6. Visual inspection results from different tool radii. A. 30μm, B. 90μm, C. 500μm, D. 2500μm

Surface finish
The 2μm periodic structure and rms finish of each surface shown below. These are profiles that were extracted from the AFM measurements.
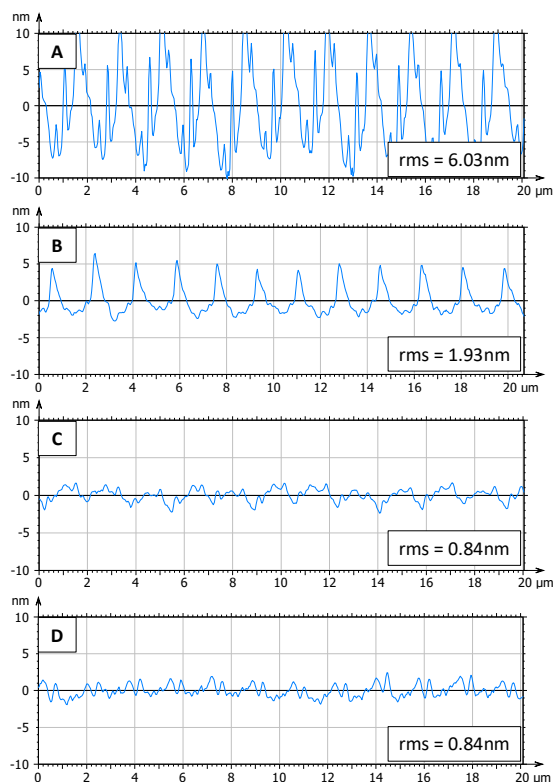
Figure 7. Profiles of AFM measurements from different tool radii. A. 30μm, B. 90μm, C. 500μm, D. 2500μm

Total integrated scatter
Total Integrated Scatter (TIS) is the ratio of scattered power without specular reflected light in one hemisphere to the specular reflected power. This ratio explains how much scatter and diffraction happen from a surface. The surface finishes in this study are much smaller than visible wavelengths. Therefore, TIS is given by the approximation below:

$$TIS \cong (4\pi\delta cos\theta_0/\lambda)^2 \qquad (2)$$

Where δ is rms surface finish, θ_0 is the angle of incidence light, λ is the wavelength of light. From this equation, TIS is the function of square of RMS finish. Measured RMS results can be applied into this equation to calculate TIS from each surface.

To calculate TIS in this case, the average TIS value between 380nm and 740nm wavelengths of light was used. AFM measurement results are applied to calculate them. Incident angle is fixed at 45 degrees. Relationship between tool radius and surface finish RMS and TIS are in Figure.8 below.
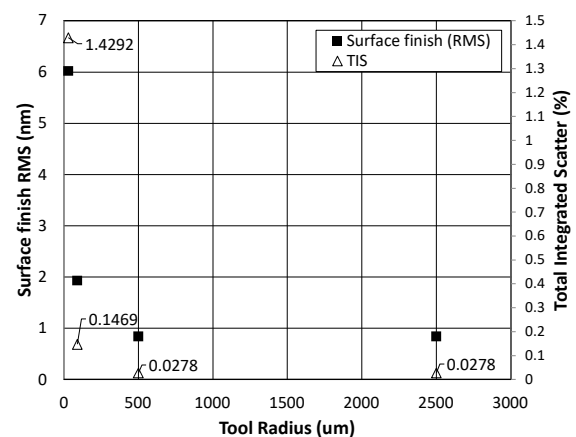
Figure 8. Surface finish RMS and TIS vs Tool Radius

Even though the scattering is only 0.03% with less than 1nm RMS finish by AFM measurement, the surface still shows diffraction color clearly with the current inspection method. This tells us that a

surface finish less than 1nm RMS is still not enough and how important the feed per revolution is. To eliminate diffraction color completely using only a diamond turning process, the feed per revolution must be reduced until the diffraction angle of the light is outside the observable range. This implies a feed of less than 300nm.

EXPERIMENTAL VERIFICATION OF NO COLOR CUTTING
Experimental testing
Experimental cuts were made on 12.7mm diameter nickel plated flat samples using the same machine setup as before. In the case shown below, a 30µm radius tool was used with a feed of 150nm/rev at 1500rpm spindle rotation speed.

Visual inspection
Visual inspection of the surface was done with the same setup as previous testing. This time, there is no evidence of diffraction rainbow color.
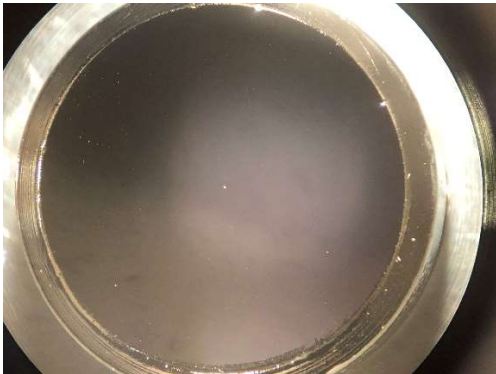
Figure 9. Visual inspection of a No Color surface

Surface finish
The surface was again measured by an AFM. The extracted profile from the areal measurement is shown below. The surface finish is 0.356nm rms and the Total Integrated Scatter (TIS) calculated from eq (2) is 0.005%, which is 10 times smaller than 2µm feed per revolution cut with a 500µm tool radius. A Power Spectral Density analysis of the profile shows a peak at 147nm, which is equivalent to the feed per revolution of the diamond tool.
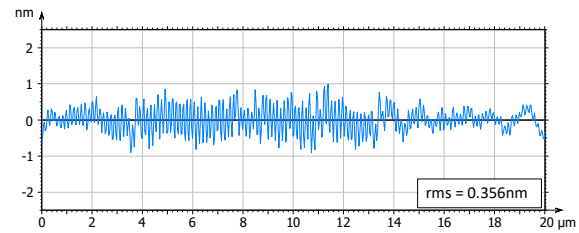
Figure 10. Surface profile from a no color surface
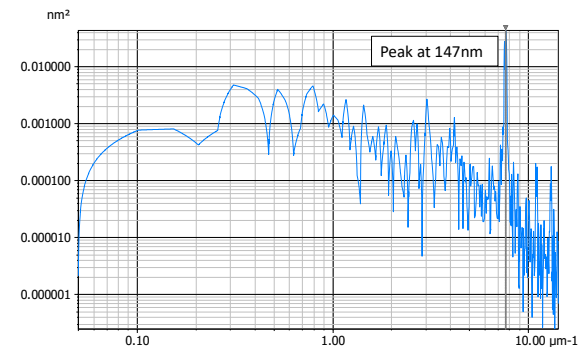
Figure 11. PSD analysis of the surface profile

FUTURE WORK
Sometimes white lines show up on the surface when cutting a no diffraction color surface, which is often called a "tool mark" in the industry. The causes and mechanisms of "tool marks" must be identified in order to bring them under control.

SUMMARY
The diffraction color problem on diamond turned surfaces was considered from diffraction theory and light scattering using Atomic Force Microscopy measurements. This simple theory explains the diffraction color appearance based on the incident light angle and pattern pitch on the surface. High lateral resolution data can accurately characterize the surface and Total Integrated Scattering (TIS) can be used to estimate the diffraction color problem.

REFERENCES
[1] F. Träger, Springer handbook of lasers and optics, in Springer Handbook of Lasers and Optics (2012)
[2] A. F. Purdie, "Applied optics and optical engineering, volµme VII," Opt. Laser Technol. (1980)
[3] E. L. Church and J. M. Zavada, "Residual surface roughness of diamond-turned optics," Appl. Opt. 14(8), 1788 (1975)

TOOL POINT RECEPTANCE VARIATION WITH SPINDLE-HOLDER-TOOL SELECTION

Tony Schmitz[1,2]
[1]Mechanical, Aerospace, and Biomedical Engineering
University of Tennessee, Knoxville
Knoxville, TN 37996, USA
[2]Energy and Transportation Science Division
Oak Ridge National Laboratory
Oak Ridge, TN 37830, USA

INTRODUCTION[1]

Modal analysis is applied to measure and model the structural dynamics of complex systems [1]. Because an important consideration in milling is the vibration behavior of the cutting tool during material removal, modal techniques are used to study machine-spindle-holder-tool combinations [2]. Important parameters for predicting milling vibration behavior, which can be stable (i.e., exhibits forced vibration only) or unstable (i.e., exhibits either self-excited or period-n bifurcations [3]), are the workpiece material, tool geometry, machining parameters, and structural dynamics [2, 4]. The workpiece material and tool geometry collectively define the relationship between the commanded chip geometry and the cutting force required to shear away the chip. This relationship may be parameterized in the form of a mechanistic cutting force model or the force may be predicted from the material's constitutive model using finite element analysis. The structural dynamics depend on the machine, spindle, holder, and tool combination, including the tool's extension length from the holder.

Because the tool point receptance (or frequency response function, FRF) is required to select stable machining parameters, identifying it for arbitrary machine-spindle-holder-tool assemblies is required. This may be achieved through modal testing techniques, such as impact testing where an instrumented hammer is used to apply the impulsive force input and a linear transducer (typically an accelerometer) is used to measure the corresponding response output. The receptance is the complex, frequency domain ratio of the output to the input. To reduce measurement time, Schmitz et al. derived receptance coupling substructure analysis (RCSA) for tool point FRF prediction [5-9].

This paper describes a case study of tool point receptances for 72 combinations obtained using three CNC machine tools, two holders, two collets, and six carbide rods. Measurement and prediction are completed for each combination. The measurements are performed using impact testing. Predictions are completed using RCSA, where models of the tool and holder are coupled to a measurement of spindle, again obtained by impact testing using a standard artifact. It is demonstrated that the tool point receptance depends not only on the tool and holder geometries, but also on the spindle receptances and the interactions between them. Effects of the tool point receptances on machining stability are presented.

RCSA

RCSA analytically couples receptance models for the holder and tool to a receptance measurement for the machine-spindle. The required steps are described in the following paragraphs. To begin, consider the tool and holder modeling.

The direct receptances for the free-free beam shown in Fig. 1 due to externally applied harmonic forces $f_1(t)$ and $f_2(t)$, applied at coordinates $x_1(t)$ and $x_2(t)$, and moments $m_1(t)$ and $m_2(t)$, applied at $\theta_1(t)$ and $\theta_2(t)$, are provided in Eq. 1. The corresponding cross receptances are shown in Eq. 2. (Note that the coordinates are

listed to consider f or m individually, unlike Eq. 3 which combines the effects). These receptances are used to represent the tool and holder sections prior to coupling.

$$\begin{matrix} x_1 = h_{11}f_1 & x_1 = l_{11}m_1 & x_2 = h_{22}f_2 & x_2 = l_{22}m_2 \\ \theta_1 = n_{11}f_1 & \theta_1 = p_{11}m_1 & \theta_2 = n_{22}f_2 & \theta_2 = p_{22}m_2 \end{matrix} \tag{1}$$

$$\begin{matrix} x_1 = h_{12}f_2 & x_1 = l_{12}m_2 & x_2 = h_{21}f_1 & x_2 = l_{21}m_1 \\ \theta_1 = n_{12}f_2 & \theta_1 = p_{12}m_2 & \theta_2 = n_{21}f_1 & \theta_2 = p_{21}m_1 \end{matrix} \tag{2}$$
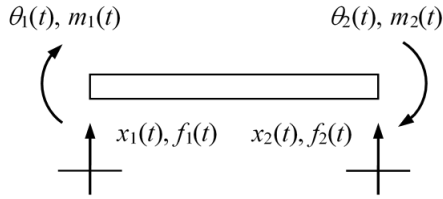
FIGURE 1. Free-free beam coordinates.

Equations 1 and 2 can be written in matrix form and compactly represented using the notation shown in Eq. 3.

$$\begin{Bmatrix} x_1 \\ \theta_1 \end{Bmatrix} = \begin{bmatrix} h_{11} & l_{11} \\ n_{11} & p_{11} \end{bmatrix} \begin{Bmatrix} f_1 \\ m_1 \end{Bmatrix} \text{ or } \{u_1\} = [R_{11}]\{q_1\}$$
$$\begin{Bmatrix} x_2 \\ \theta_2 \end{Bmatrix} = \begin{bmatrix} h_{22} & l_{22} \\ n_{22} & p_{22} \end{bmatrix} \begin{Bmatrix} f_2 \\ m_2 \end{Bmatrix} \text{ or } \{u_2\} = [R_{22}]\{q_2\} \tag{3}$$

In Eq. 3, R_{ij} is the generalized receptance matrix that describes both translational and rotational component behavior. The individual entries in these matrices include contributions from both the rigid body and flexural modes. In this study, the frequency dependent entries were calculated using the Timoshenko beam model, which includes the effects of rotary inertia and shear. It was implemented using finite elements [8], where each four degree-of-freedom (rotation and displacement at each end) free-free beam section was modeled using appropriate mass and stiffness matrices.

These receptances can be used to couple components at their end points in order to predict assembly dynamics. For example, a free-free beam with diameter d_1 can be coupled to a second free-free beam with larger diameter d_2 to synthesize the receptances for a stepped shaft (see Fig 2). The assembly flexural receptances, shown in Eq. 4 (the upper case variables denote assembly coordinates, forces, moments, and

receptances), are determined by first writing the component displacements/rotations; see Eq. 5.
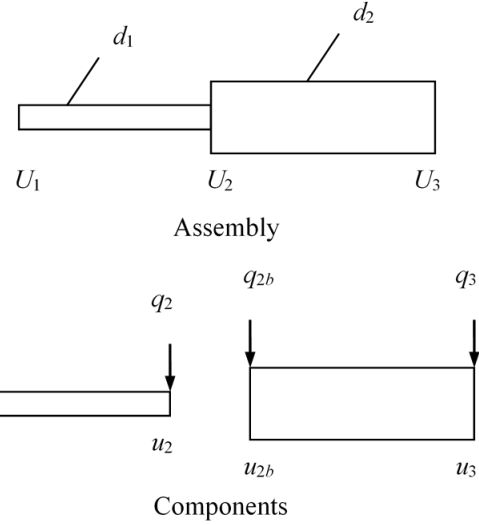
FIGURE 2. Stepped shaft assembly (top) and components (bottom). Diameters d_1 and d_2 are identified in the assembly schematic.

$$\begin{Bmatrix} U_1 \\ U_2 \\ U_3 \end{Bmatrix} = \begin{bmatrix} G_{11} & G_{12} & G_{13} \\ G_{21} & G_{22} & G_{23} \\ G_{31} & G_{32} & G_{33} \end{bmatrix} \begin{Bmatrix} Q_1 \\ Q_2 \\ Q_3 \end{Bmatrix} \text{ where } U_i = \begin{Bmatrix} X_i \\ \Theta_i \end{Bmatrix},$$
$$G_{ij} = \begin{bmatrix} H_{ij} & L_{ij} \\ N_{ij} & P_{ij} \end{bmatrix}, \text{ and } Q_i = \begin{Bmatrix} F_i \\ M_i \end{Bmatrix} \tag{4}$$

$$\begin{matrix} u_1 = R_{11}q_1 + R_{12}q_2 & u_2 = R_{21}q_1 + R_{22}q_2 \\ u_{2b} = R_{2b2b}q_{2b} + R_{2b3}q_3 & u_3 = R_{32b}q_{2b} + R_{33}q_3 \end{matrix} \tag{5}$$

For this stepped shaft example, a rigid connection is applied at the interface. The corresponding compatibility conditions are:

$$u_2 - u_{2b} = 0 \text{ and } u_i = U_i, \tag{6}$$

where i = 1 to 3 and the latter expression specifies that the component and assembly coordinates are defined at the same spatial positions. The equilibrium conditions vary with the external force/moment location. To determine the first column of the assembly receptance matrix in Eq. 4, Q_1 is applied to coordinate U_1. In this case, the equilibrium conditions are:

$$q_2 + q_{2b} = 0, q_1 = Q_1, \text{ and } q_3 = 0. \tag{7}$$

Substitution of the component displacements/ rotations and equilibrium conditions into the compatibility conditions yields q_2; see Eq. 8. The

expression for G_{11} is then given by Eq. 9. The other two first column receptances are determined in a similar manner. To find the receptances in the second and third columns, Q_2 must be applied to U_2 and Q_3 to U_3, respectively.

$$q_2 = -(R_{22} + R_{2b2b})^{-1}R_{21}Q_1 \qquad (8)$$

$$G_{11} = \frac{U_1}{Q_1} = \frac{u_1}{Q_1} = \frac{R_{11}q_1 + R_{12}q_2}{Q_1}$$

$$G_{11} = R_{11} - R_{12}(R_{22} + R_{2b2b})^{-1}R_{21} = \begin{bmatrix} H_{11} & L_{11} \\ N_{11} & P_{11} \end{bmatrix} \qquad (9)$$

In the case of finite stiffness and non-zero damping at the contact interface between components, the compatibility conditions can be modified to reflect the new coordinate displacement/rotation relationships. The Eq. 6 compatibility condition for the flexible-damped connection is now rewritten as:

$$K(u_2 - u_{2b}) = -q_{2b} \qquad (10)$$

where the complex stiffness matrix is defined in Eq. 11 for a viscous damping model. In this matrix, the stiffness (k) and damping terms (c) are defined by their subscripts. The k_{xf} term, for example, describes the stiffness that relates force to displacement, while the stiffness $k_{\theta m}$ relates rotation to moment.

$$K = \begin{bmatrix} k_{xf} + i\omega c_{xf} & k_{\theta f} + i\omega c_{\theta f} \\ k_{xm} + i\omega c_{xm} & k_{\theta m} + i\omega c_{\theta m} \end{bmatrix} \qquad (11)$$

Using the Eq. 10 compatibility condition, the assembly receptance from Eq. 9 is modified to be:

$$G_{11} = R_{11} - R_{12}(R_{22} + R_{2b2b} + K^{-1})^{-1}R_{21}. \qquad (12)$$

For tool point receptance predictions, coordinates 1 and 2 in Eq. 12 are defined by the two ends of the holder-tool model, while coordinate 2b is associated with the machine-spindle. To experimentally identify the R_{2b2b} receptances, a standard artifact with the appropriate spindle-holder connection (e.g., CAT-40 or HSK-63A) is inserted in the spindle under test. The four direct receptances at the free end of the artifact are determined from a single displacement-to-force measurement as described in [9]. The machine-spindle receptances are then determined from the machine-spindle-artifact receptances using the inverse RCSA approach detailed in [8]. In this method, the assembly receptances are

measured and then the free-free portion of the artifact beyond the holder flange is extracted to isolate the machine-spindle receptances; see Fig. 3.
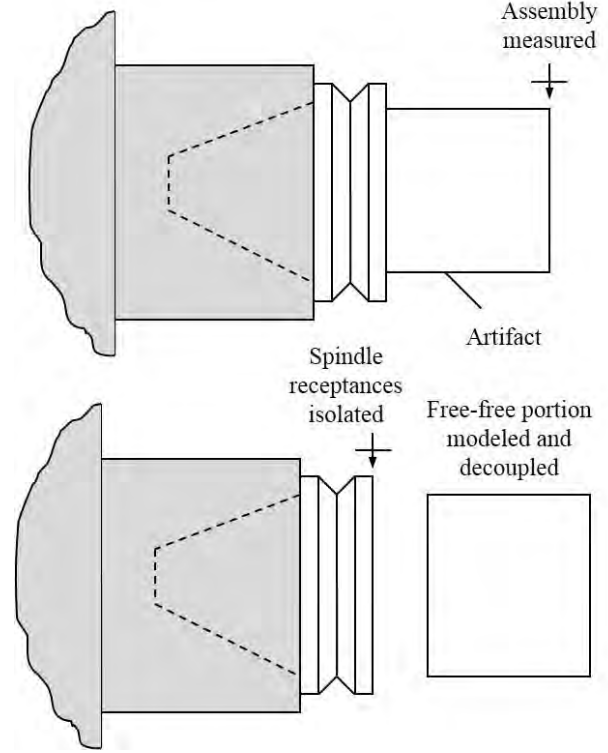
FIGURE 3. Machine-spindle receptances are determined using inverse RCSA.
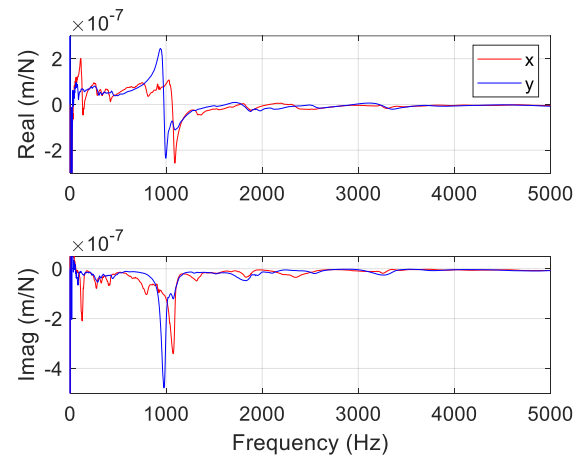
FIGURE 4. Haas TM1P machine-spindle receptances for the x and y directions.

RESULTS AND DISCUSSION

The RCSA approach was used to predict the tool point receptances for 72 machine-spindle-holder-tool combinations. This included three CNC machining centers: Haas TM1P, Haas VF5XT, and Makino a51nx; two collet holders: Parlec C40-32ER 312 and Parlec C40-32ER 412; two collets: ER32 12.7 mm and ER32 19.05 mm; and six carbide rods: 12.7 mm diameter, 77.01 mm long, 12.7 mm diameter, 102.62 mm long, 12.7 mm diameter, 127.36 mm long, 12.7 mm diameter, 152.72 mm long, 19.05 mm diameter, 76.24 mm long, 19.05 mm diameter, 153.26 mm long.
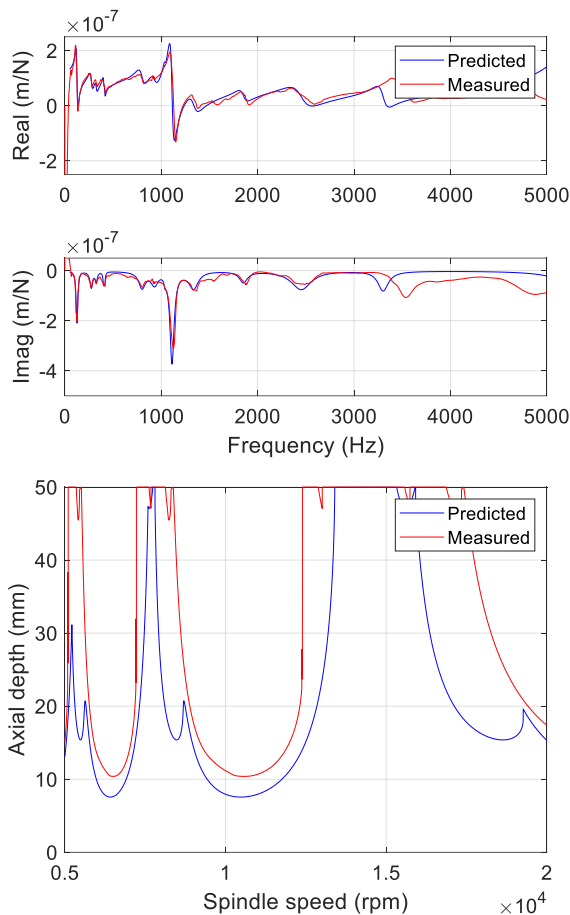
FIGURE 5. Haas TM1P: Parlec C40-32ER 312 holder with a 12.7 mm diameter, 77.01 mm long, 37 mm stickout carbide rod. (Top) Tool tip x receptances. (Bottom) Stability maps.

The first step was to determine the machine-spindle receptances for each of the three CNC machining centers using inverse RCSA. The artifact measurement the Haas TM1P (CAT-40 spindle-holder connection) is displayed in Fig. 4. Multiple vibration modes appear in the 5000 Hz

measurement bandwidth. The measurements were completed using a PCB 086C03 modal hammer, PCB 352C23 low-mass accelerometer, and MLI's MetalMax TXF software. The portion of the cylindrical steel artifact beyond the flange was then extracted to isolate the machine-spindle receptances (see Fig. 3).

Tool tip measurements and predictions in the x direction for the Parlec C40-32ER 312 holder with a 12.7 mm diameter, 77.01 mm long, 37 mm stickout carbide rod are displayed in Figs. 5-7 for the three CNC machining centers. The associated stability maps are also included for 25% radial immersion down milling, 6061-T6 aluminum workpiece material, four teeth, and x direction feed. These are included to demonstrate the dramatic difference in stability behavior with changes in tool tip receptance from one machine to the next.
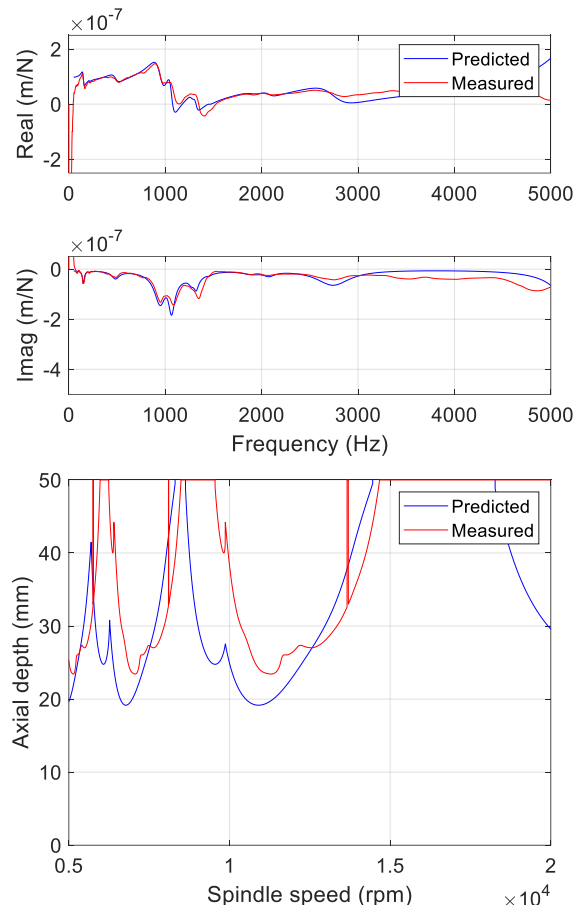
FIGURE 6. Haas VF5XT: Parlec C40-32ER 312 holder with a 12.7 mm diameter, 77.01 mm long, 37 mm stickout carbide rod. (Top) Tool tip x receptances. (Bottom) Stability maps.
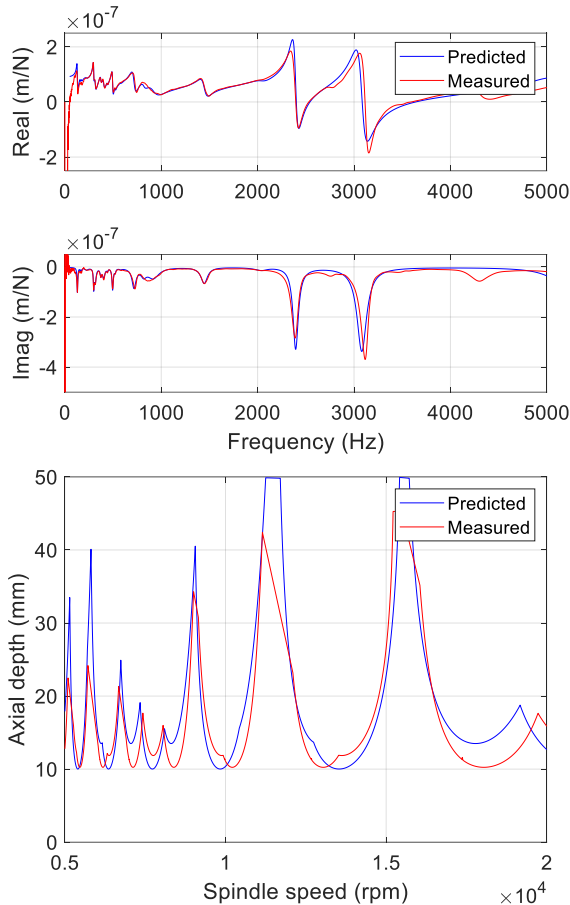
FIGURE 7. Makino a51nx: Parlec C40-32ER 312 holder with a 12.7 mm diameter, 77.01 mm long, 37 mm stickout carbide rod. (Top) Tool tip x receptances. (Bottom) Stability maps.

Figures 5-7 demonstrate a case where the tool length is short/stiff and the tool tip receptances therefore display multiple spindle-related modes. Figures 8-10, on the other hand, present the case where the tool length-to-diameter ratio is higher (so its stiffness is lower) and the tool's first bending mode dominates the tool tip receptance. Here, the y direction measurements and predictions for the Parlec C40-32ER 312 with a 19.05 mm diameter, 153.26 mm long, 113 mm stickout carbide rod are shown. It is interesting to note that the Makino a51nx result still includes interaction with spindle modes since there are spindle natural frequencies near the tool's first bending mode natural frequency.

CONCLUSIONS
This paper reported tool point receptance measurements and predictions for 72 machine-spindle-holder-tool combinations arranged using three CNC machine tools, two holders, two

collets, and six carbide rods. The predictions were completed using receptance coupling substructure analysis (RCSA). The dependence of milling stability behavior on tool point receptance was demonstrated and it was seen that the same tooling inserted in a different spindle affects the milling performance.

FIGURE 8. Haas TM1P: Parlec C40-32ER 312 holder with a 19.05 mm diameter, 153.26 mm long, 113 mm stickout carbide rod. (Top) Tool tip y receptances. (Bottom) Stability maps.
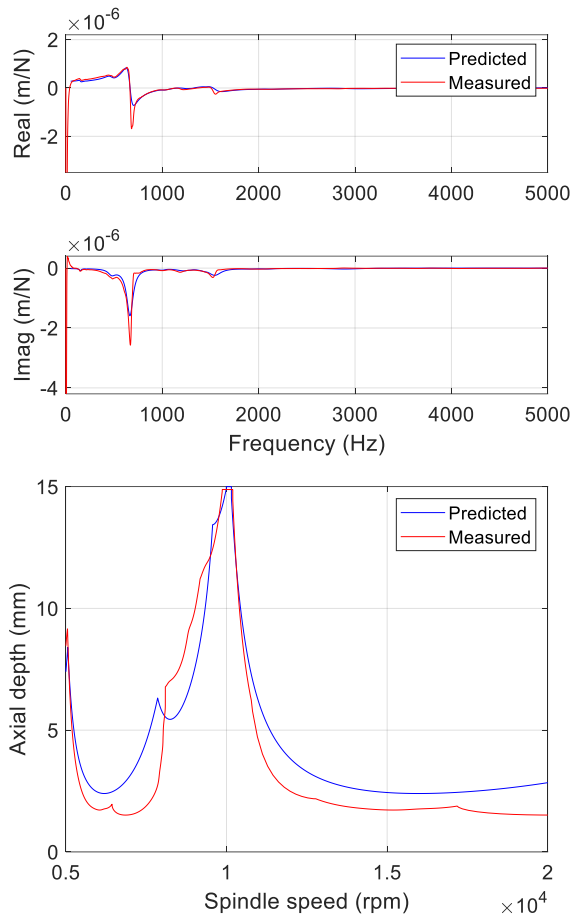
FIGURE 9. Haas VF5XT: Parlec C40-32ER 312 holder with a 19.05 mm diameter, 153.26 mm long, 113 mm stickout carbide rod. (Top) Tool tip y receptances. (Bottom) Stability maps.

REFERENCES

[1] Ewins, D.J., 1984. Modal testing: Theory and practice (Vol. 15). Letchworth: Research Studies Press.

[2] Schmitz, T.L. and Smith, K.S., 2019. Machining dynamics: Frequency response to improved productivity, 2nd Ed. Springer, New York.

[3] Honeycutt, A. and Schmitz, T., 2018. Milling bifurcations: A review of literature and experiment. Journal of Manufacturing Science and Engineering, 140(12), 120801.

[4] Altıntaş, Y., 2000. Manufacturing automation. Cambridge University Press, New York.

[5] Schmitz, T.L. and Donaldson, R.R., 2000. Predicting high-speed machining dynamics by substructure analysis. CIRP Annals-Manufacturing Technology, 49(1), pp. 303-308.

[6] Schmitz, T.L., Davies, M.A. and Kennedy, M.D., 2001. Tool point frequency response

prediction for high-speed machining by RCSA. Journal of Manufacturing Science and Engineering, 123(4), pp. 700-707.
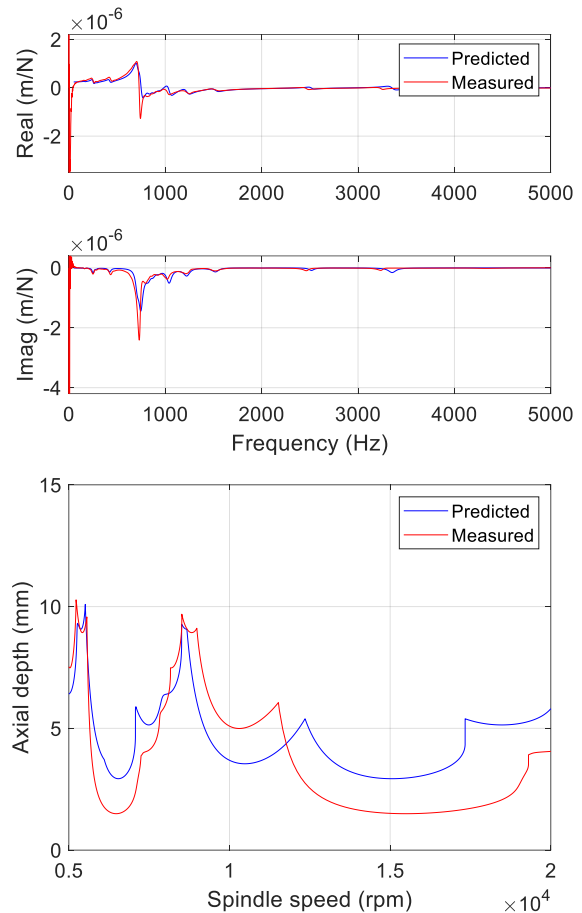
FIGURE 10. Makino a51nx: Parlec C40-32ER 312 holder with a 19.05 mm diameter, 153.26 mm long, 113 mm stickout carbide rod. (Top) Tool tip y receptances. (Bottom) Stability maps.

[7] Schmitz, T.L., Davies, M.A., Medicus, K. and Snyder, J., 2001. Improving high-speed machining material removal rates by rapid dynamic analysis. CIRP Annals-Manufacturing Technology, 50(1), pp. 263-268.

[8] Schmitz, T.L. and Duncan, G.S., 2005. Three-component receptance coupling substructure analysis for tool point dynamics prediction. Journal of Manufacturing Science and Engineering, 127(4), pp. 781-790.

[9] Kumar, U.V. and Schmitz, T.L., 2012. Spindle dynamics identification for receptance coupling substructure analysis. Precision Engineering, 36(3), pp. 435-443.

MODELING AND SIMULATION OF MODULATED TOOL PATH (MTP) TURNING STABILITY

Ryan W. Copenhaver[1,2] and Tony L. Schmitz[1,2]
[1]Mechanical, Aerospace, and Biomedical Engineering
University of Tennessee, Knoxville
Knoxville, TN 37996, USA
[2]Energy and Transportation Science Division
Oak Ridge National Laboratory
Oak Ridge, TN 37830, USA

ABSTRACT
A time domain simulation for predicting stability during modulated tool path turning (MTP) is presented. Stability maps for MTP parameter pairs (oscillation magnitude and frequency) at selected chip widths are provided, where stability is determined using a periodic sampling-based metric. An AISI 1026 steel tube turning setup is used to complete MTP stability tests. It includes in-process measurements of cutting force, tool displacement, tool velocity, and a once-per-revolution signal. Predicted and measured signals are compared to verify simulation accuracy, including tests with and without MTP that demonstrate a change in stability for the same spindle speed and chip width.

INTRODUCTION
Conventional turning operations often exhibit uninterrupted cutting. This tends to produce a continuous chip that can wrap and collect near the cutting edge when machining ductile metals. The local buildup of this continuous chip can result in workpiece scratching, tool damage, machinist injury, and increased cycle time to clear the chips. Conventional chip management may use engineered rake face geometries [1] or high-pressure coolant directed at the rake face-chip interface [2], for example. Modulated tool path (MTP) turning offers an alternative approach, where discrete chips are formed by repeatedly interrupting the continuous chip formation using the machine axes to superimpose low frequency tool oscillations on the nominal tool feed motion. Prior MTP efforts have demonstrated broken chip length control. Stability behavior for MTP turning was also reported [3]. In this paper, a time domain simulation for MTP turning is described. This simulation is then used, together with a stability metric based on periodic sampling, to develop process stability maps. These stability maps are verified experimentally and compared to continuous turning (no MTP) performance.
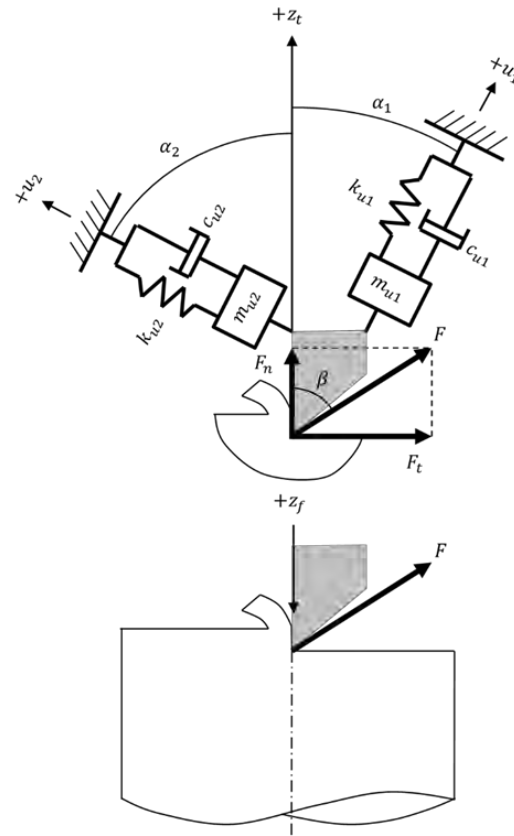
FIGURE 1. (Top) Flexible tool MTP turning dynamics model. The tangential, F_t, normal, F_n, and resultant force, F, components are identified, as well as the modal parameters that represent the structural dynamics in two orthogonal directions, u_1 and u_2. The MTP feed motion, z_f, and tool vibration, z_t, are also identified. (Bottom) Model orientation for the tube turning tests completed in this study.

METHODOLOGY
In order to model the cutting force and tool vibration during MTP turning, a time domain simulation was developed. In each time step of the simulation, the instantaneous chip thickness is calculated by considering the current and previous surfaces. The

cutting force is then calculated using this chip thickness, the chip width, and cutting force model. Once the force is known, the second-order differential equations of motion for the flexible cutter are solved by numerical integration [4-5]. The corresponding tool displacement is then used together with the commanded MTP motion to calculate the chip thickness in the next time step.

For numerical integration using the semi-implicit Euler method, the requirement is that the time step is small enough to avoid numerical instability. For this study, the time step was selected to be 50 times smaller than the smallest vibration period for the structural dynamics. Given the time step, the simulation time vector and corresponding MTP feed motion, z_f, are described; see Fig. 1. The time vector, t, is defined from zero to the maximum simulation time in equal increments, dt. The MTP feed motion is then specified by Eq. 1:

$$z_f = \left(\frac{\Omega}{60} f_r\right) t + RAF \cdot f_r \cdot \sin\left(\frac{\Omega}{60} 2\pi \cdot OPR \cdot t\right), \quad (1)$$

where Ω is the spindle speed (rpm), f_r is the feed per revolution, RAF is the ratio of the MTP motion amplitude to the feed per revolution, and OPR is the number of sinusoidal MTP oscillations per revolution of the rotating part.
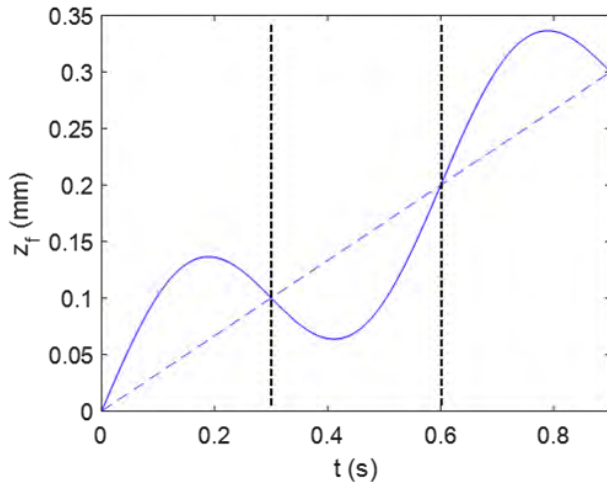
FIGURE 2. MTP feed motion for three spindle revolutions. The spindle speed is 200 rpm, the feed per revolution is 0.1 mm, and the RAF and OPR values are 0.8 and 0.5. The dashed, positive slope line identifies the constant feed, while the solid line shows its sum with the sinusoidal MTP contribution. The vertical dotted lines denote each revolution.

Figure 2 displays the MTP feed motion for a spindle speed of 200 rpm, a feed per revolution of 0.1 mm, and RAF and OPR values of 0.8 and 0.5, respectively.

In the figure, the dashed line denotes the constant feed advance of the tool into the part, while the solid line shows the superposition of the MTP oscillation onto the constant feed. The vertical dotted lines identify each revolution; three revolutions are plotted.

As noted, the first task in each simulation iteration is to calculate the instantaneous chip thickness. Fig. 3 aids in the calculation description by displaying the Fig. 2 data parsed by revolution. The revolution numbers are included on the right-hand side of the figure. The nominal chip thickness is the difference between the current tool position and the maximum value of all previous revolutions. Fig. 3 shows the chip thickness for revolution 2 as the hatched areas. The chip thickness is zero when the revolution 2 oscillation dips below the revolution 1 oscillation. The $+z_f$ direction is positive into the part, so "below" here means away from the part and no cutting occurs.

Figure 4 displays the chip thickness for revolution 3. Note that the instantaneous chip thickness is the difference between revolutions 3 and 1 for the time period between 0.0645 s and 0.2355 s and the difference between revolutions 3 and 2 for all other times. The corresponding chip thickness profile for the two revolutions is shown in Fig. 5. The two revolutions are segmented by the vertical dotted line. Because the OPR is 0.5 for this example, the chip thickness profile in Fig. 5 repeats every two revolutions in the absence of tool vibrations. MTP turning therefore exhibits periodic excitation, unlike traditional turning where the chip thickness and force are nominally constant.
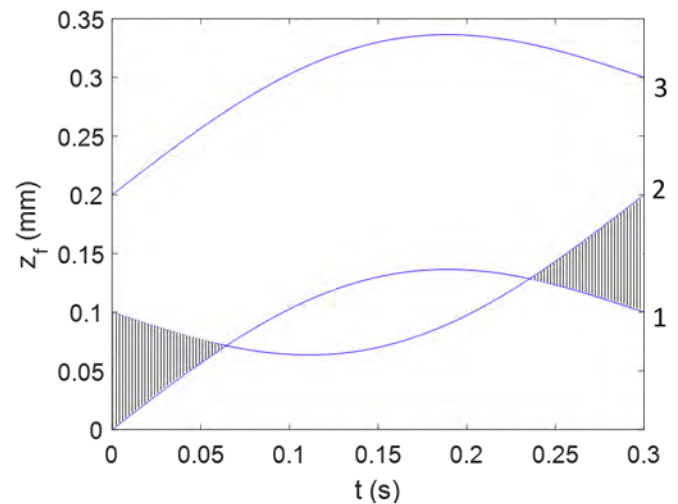
FIGURE 3. Chip thickness calculation for revolution 2. The nonzero chip thickness zones are denoted by the hatched areas.
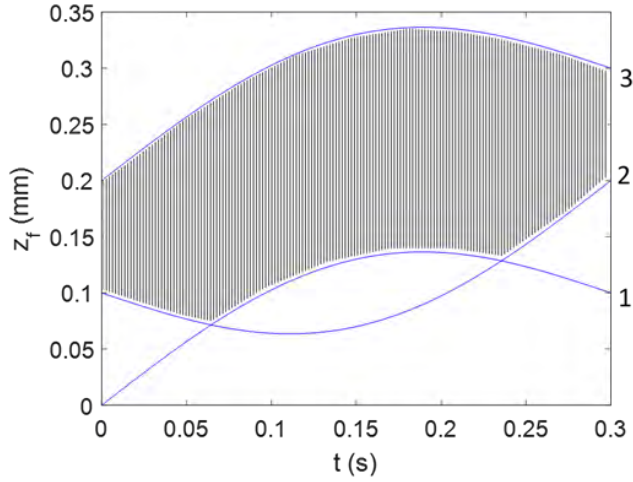
FIGURE 4. Chip thickness calculation for revolution 3. The instantaneous chip thickness is the difference between the current MTP motion and the maximum of all prior revolutions at the same rotation angle.

FIGURE 5. Instantaneous chip thickness for revolutions 2 and 3 considering the MTP motion only.

Figures 3 and 4 demonstrate the strategy for calculating the instantaneous chip thickness, h. Mathematically, this can be expressed as:

$$h = z_{f,n} - \max\{z_{f,n-1}, z_{f,n-2}, \dots\},\qquad(2)$$

where n is the current revolution. To include the tool dynamics, which are excited by the periodic forcing function displayed in Fig. 5, Eq. 2 must be augmented to include the effect of the tool displacement. If z_t is the tool displacement in the surface normal direction and it is considered positive out of the cut (see Fig. 1), then a positive tool displacement for the current revolution decreases the chip thickness. A positive tool displacement in a previous revolution, on the other hand, indicates that material that was intended to be removed was left behind. Therefore, a positive tool displacement for the maximum previous revolution yields a larger instantaneous chip thickness in the current revolution. Eq. 2 is updated to include the tool motion:

$$h = (z_{f,n} - z_{t,n}) - \max\{(z_{f,n-1} - z_{t,n-1}), (z_{f,n-2} - z_{t,n-2}), \dots\}\qquad(3)$$

Returning to Fig. 5, the chip thickness is now calculated from Eq. 3 as shown in Eq. 4.

$$h = (z_{f,2} - z_{t,2}) - (z_{f,1} - z_{t,1}) = z_{f,2} - z_{f,1} - z_{t,2} + z_{t,1}\qquad(4)$$

Equation 4 shows the effect of the tool vibrations directly. A positive $z_{t,2}$ reduces the current chip thickness, while a positive $z_{t,1}$ increases the current chip thickness. The final consideration is that Eqs. 2-4 can yield negative values, e.g., during the interval from 0.0645 s and 0.2355 s in Fig. 3. When $h < 0$, this indicates that no cutting occurs and the chip thickness is set equal to zero. This nonlinearly is incorporated in the numerical simulation.

Given the chip thickness, the cutting force is $F = K_s bh$, where K_s is the specific cutting force coefficient and b is the chip width. The resultant force is related to the tangential and normal direction force components through the force angle, β.

$$F_t = F \sin\beta = (K_s \sin\beta)bh = k_t bh\qquad(5)$$

$$F_n = F \cos\beta = (K_s \cos\beta)bh = k_n bh\qquad(6)$$

The resultant force is projected into the two mode directions to determine the corresponding displacements u_1 and u_2.

$$F_{u1} = F \cos(\beta - \alpha_1)\quad(7)\quad F_{u2} = F \cos(\beta + \alpha_2)\quad(8)$$

$$\begin{aligned}\ddot{u}_1 &= \frac{F_{u1} - c_{u1}\dot{u}_1 - k_{u1}u_1}{m_{u1}}\\ \dot{u}_1 &= \dot{u}_1 + \ddot{u}_1 dt\\ u_1 &= u_1 + \dot{u}_1 dt\end{aligned}\qquad(9)$$

$$\begin{aligned}\ddot{u}_2 &= \frac{F_{u2} - c_{u2}\dot{u}_2 - k_{u2}u_2}{m_{u2}}\\ \dot{u}_2 &= \dot{u}_2 + \ddot{u}_2 dt\\ u_2 &= u_2 + \dot{u}_2 dt\end{aligned}\qquad(10)$$

The semi-implicit Euler integration procedure used to determine the current tool displacement components in the u_1 and u_2 directions proceeds according to Eqs. 9 and 10. In these two equations, m, c, and k are the modal mass, damping, and stiffness values, respectively, and the over-dots indicate time derivatives. Once u_1 and u_2 are known, they are projected into the surface normal direction to determine the new tool displacement.

$$z_t = u_1 \cos \alpha_1 + u_2 \cos \alpha_2 \qquad (11)$$

To establish the MTP turning stability, periodic sampling was implemented [6], where the process signals are sampled at the forcing period. The discretized sampling period, SP, is defined in Eq. 12, where SR is the number of steps per revolution; see Eq. 13. If the process is stable, the sampled points repeat. If it is unstable, they do not repeat.

$$SP = \frac{SR}{OPR} \qquad (12) \qquad\qquad SR = \frac{60}{dt \cdot \Omega} \qquad (13)$$

To automatically differentiate between stable (periodic) and unstable (secondary Hopf) conditions, the metric, M, was applied to the sampled points:

$$M = \frac{\sum_{i=2}^{N} |z_{ts}(i) - z_{ts}(i-1)|}{N} \qquad (14)$$

where z_{ts} is the vector of once-per-MTP period sampled z_t displacements and N is the length of the z_{ts} vector [7]. For stable cuts, the M value is ideally zero (within the limits of numerical precision). For unstable cuts, however, $M > 0$. The use of this metric enables multiple simulations to be completed over a range of RAF and OPR values and a stability map to be automatically produced by plotting a single contour at an arbitrarily small M value.

RESULTS AND DISCUSSION

Turning experiments were completed on a Haas TL-1 CNC lathe. The tubular workpiece material was AISI 1026 steel. To keep a consistent surface speed, the workpieces were machined to have a mean diameter of 70 mm with varying wall thicknesses. Type C, 80° parallelogram carbide inserts with a zero rake angle, 7° relief angle, and a flat rake face were used. All experiments were conducted at a mean cutting speed of 122 m/min (556 rpm) with a nominal feed per revolution of 0.102 mm. Stability was controlled by varying the tube wall thickness (chip width) and RAF and OPR values.

Dynamic cutting forces were measured using a three-axis dynamometer (Kistler 9257B) mounted to the cross slide. A notch-type flexure was mounted to the

dynamometer. This flexure carried the carbide insert and acted as the cutting tool. A laser vibrometer (Polytec OFV-534/OFV-5000) was used to measure the feed direction, z_f, velocity of the cutting tool and a capacitance probe (Lion Precision C-18-13-2.0) was used to measure tool displacement, z_t. A laser tachometer was used to determine the actual spindle speed for periodic sampling at the MTP forcing frequency; see Fig. 6. The normal direction is aligned with the spindle axis, while the tangential direction is tangent to the cut surface (vertical). The tool's frequency response function was measured using impact testing. Modal fitting was completed to extract the modal mass, m, viscous damping, c, and stiffness, k, values for the simulation.
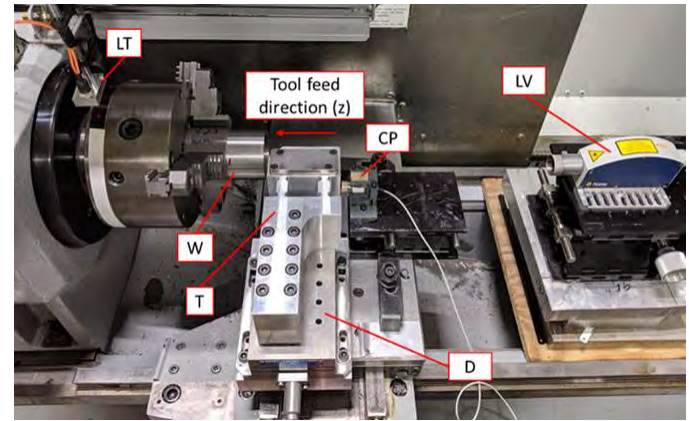
FIGURE 6. Photograph of tube turning setup including workpiece (W), dynamometer (D), flexure-based cutting tool (T), laser tachometer (LT), laser vibrometer (LV), and capacitance probe (CP).
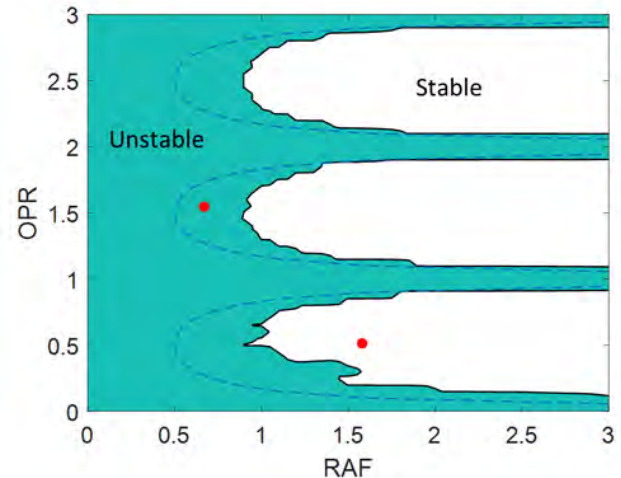
FIGURE 7. Stability map for b = 4.5 mm. Only selected {RAF, OPR} pairs are stable for this chip width. Test points are denoted by dots.

The force model coefficients were identified from continuous (stable) cutting tests, where the force components in the normal and tangential directions were measured by the dynamometer for known chip thickness and width values. This process was repeated for decreasing chip thickness values until a continuous chip was no longer formed. The best fits to the measured forces are provided in Eqs. 14-15 (units are N/mm^2).

$$k_n = -3355h^{0.81} + 2520 \qquad (14)$$

$$k_t = -3490h^{0.22} + 4795 \qquad (15)$$
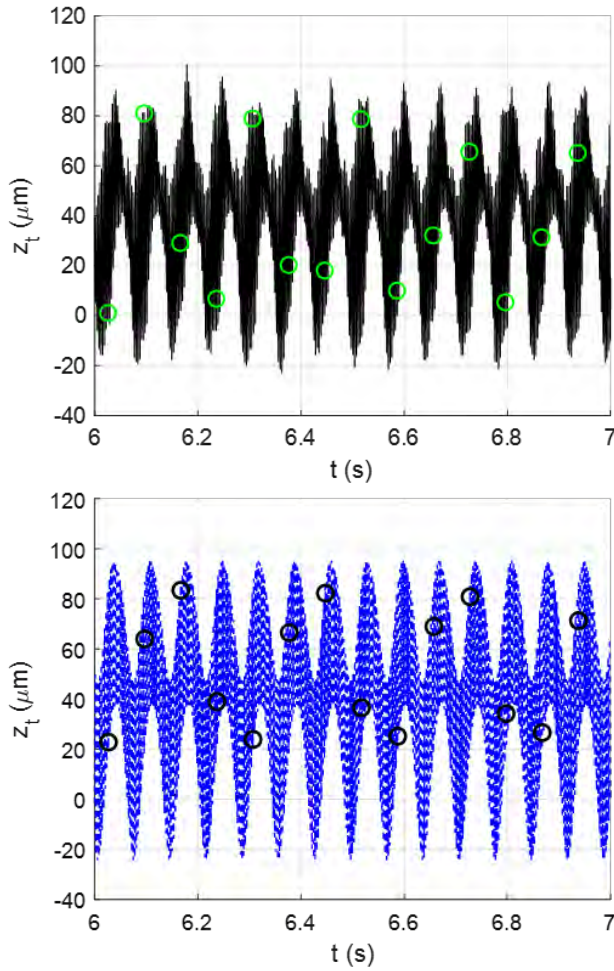
FIGURE 8. Measured (top) and predicted (bottom) tool displacement for b = 4.5 mm, RAF = 0.65, and OPR = 1.54. The result is unstable (chatter).

Time domain simulations were completed on a grid of {RAF, OPR} pairs from 0 to 3 in steps of 0.05 for individual chip width values. The M value was computed for each pair and recorded. A stability map was then produced by plotting a single contour (solid

line) at M = 1 μm. Additionally, the analytical chip breaking limit [7] was superimposed on each stability map (dashed line); see Fig. 7. To verify the stability predictions, cutting tests were performed. Figure 8 displays the predicted and simulated tool motion with periodic samples (circles). The cut is unstable for the {0.65, 1.54} pair, even though discontinuous chips were produced. With MTP parameters of {1.60, 0.50}, however, the cut is now stable; see Fig. 9. Cutting was unstable for no MTP conditions at b = 4.5 mm.
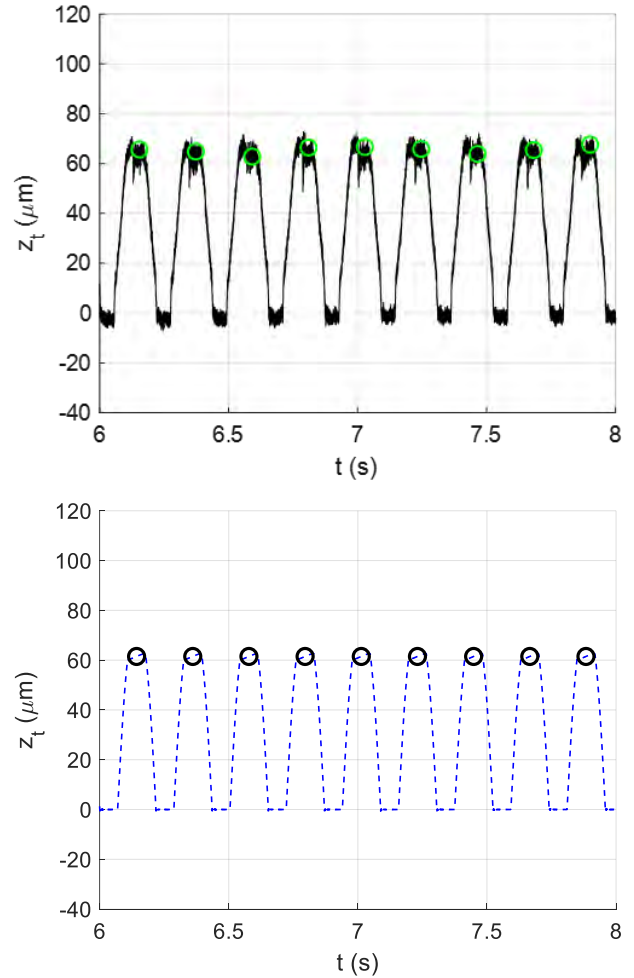
FIGURE 9. Measured (top) and predicted (bottom) tool displacement for b = 4.5 mm, RAF = 1.60, and OPR = 0.50. The result is stable.

CONCLUSIONS
A time domain simulation with periodic sampling for automated stability identification was implemented to produce stability maps for modulated tool path (MTP) turning. It was shown that either stable or unstable behavior can be obtained for the same spindle speed-chip width combination by varying only the MTP parameters. Predictions agreed with experiments.

REFERENCES
[1] Jawahir IS. On the controllability of chip breaking cycles and modes of chip breaking in metal machining. CIRP Annals 1990;39/1: 47-51.
[2] Rahman M, Kumar AS, Choudhury MR. Identification of effective zones for high pressure coolant in milling. CIRP Annals 2000;49/1: 47-52.
[3] Copenhaver R, Smith S, Schmitz T. Stability analysis of modulated tool path turning. CIRP Annals 2018;67/1: 49-52.
[4] Schmitz T, Smith S. Mechanical Vibrations: Modeling and Measurement. New York: Springer; 2012.
[5] Schmitz T, Smith S. Machining Dynamics: Frequency Response to Improved Productivity. 2nd ed. New York: Springer; 2019.
[6] Honeycutt A, Schmitz, T. A new metric for automated stability identification in time domain milling simulation. Journal of Manufacturing Science and Engineering 2016;138/7: 074501.
[7] Mann JB, Guo Y, Saldana, C, Compton WD, Chandrasekar, S. Enhancing material removal processes using modulation-assisted machining. Tribology International 2011;44: 1225-1235.

AN INVESTIGATION OF MAGNETIC FIELD ASSISTED MASS POLISHING FOR PRECISION MANUFACTURING OF OPTICAL FREEFORM SURFACES

C.F. Cheung *, C.J. Wang, Y. M. Loh, L. T. Ho
State Key Laboratory of Ultra-precision Machining Technology
Department of Industrial and Systems Engineering
The Hong Kong Polytechnic University, Hung Hom, Kowloon, Hong Kong

INTRODUCTIONS

Freeform surfaces have been widely used in various industrial applications, such as imaging, illumination, aerospace, biomedical engineering, green energy, etc. [1,2] The polishing process usually takes most of the time during the manufacturing process of precision freeform surfaces, which imposes a lot of challenges for meeting the increasing market demand. Hence, several kinds of mass finishing processes were developed to implement mass finishing of freeform surfaces, such as vibratory finishing, centrifugal barrel finishing, rotary barrel finishing, centrifugal disc finishing and spindle finishing [3]. However, those mass finishing methods cannot achieve high surface form accuracy and nanometric surface finish.

The magnetic field-assisted polishing method has been used for polishing various kinds of surfaces for decades due to its high adaptability to curved surfaces [4]. Shinmura et al. [5] conducted research on the finishing of roller surface based on magnetic field assisted finishing for the first time, and the surface roughness was reduced from 0.45 µm to 0.04 µm. Yamaguchi et al. [6-8] further developed this technology and used a rotational magnetic field for the finishing of internal surfaces. Jain, et al. [9] and Chang, et al. [10] also conducted magnetic field assisted polishing of roller surface, and the polished surface roughness was smaller than 0.1 µm. However, most of the current applications of magnetic field-assisted polishing only polish one workpiece in one setup which makes the polishing process time-consuming. Hence, this paper presents the development of a magnetic field assisted mass polishing (MAMP) process, which not only implements mass polishing for precision manufacturing, but also be able to obtain nanometric surface roughness for a batch of optical freeform surfaces.

Magnetic field assisted mass polishing (MAMP)

Figure 1 shows the working principle and the design of a prototype of MAMP system [11]. A magnetic field is set up outside the annular chamber of MAMP process to drive the magnetic brush to impinge on and remove materials from the workpiece mounted inside the chamber. The magnetic brush is generated by the magnetic abrasives under the effect of the magnetic field. The permanent magnet pairs are mounted on a rotary table, and the rotary table is driven by one servo motor, resulting in the generation of the rotating magnetic field, leading to the rotation of the magnetic brush accordingly. Bonded magnetic abrasives and loose magnetic abrasives could be used for rough polishing and fine polishing. The bonded magnetic abrasive is the ferromagnetic particle bonded with different kinds of polishing abrasives, while the loose magnetic abrasive is the ferromagnetic particle mixing with the polishing abrasive.

Experiments

In this study, an experimental prototype has been built up as shown in Fig. 1(a). Two pairs of N52 Neodymium permanent magnet (size: 25.4mm×25.4mm×50.8 mm) were mounted on the rotary table as shown in Fig. 1(c). Two magnetic brush can be generated as shown in Fig. 1(d). The workpiece with a cylindrical surface is designed for the polishing test in this study, and detail dimension of the workpiece has been shown in Fig. 2(a). Six workpieces can be polished simultaneously according to the fixture design in Fig. 1(e). Moreover, the number of the workpiece can be further increased through changing the design of the fixture. The target surface is clamped facing the outer wall of the chamber. Two kinds of magnetic abrasives were adopted for the rough polishing and fine polishing, which are bonded magnetic abrasive and loose abrasive, respectively. Table 1 shows the three groups of polishing conditions.
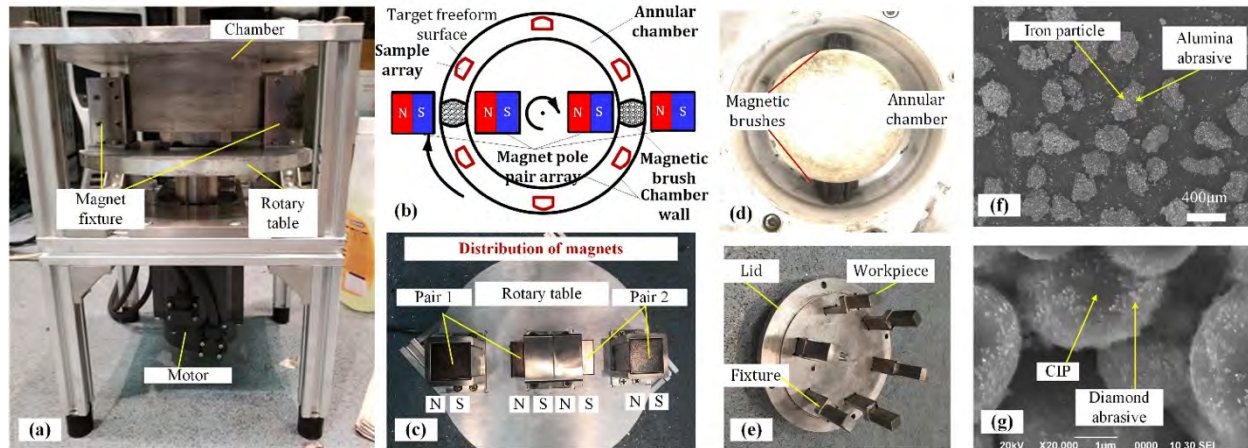
FIGURE 1. Principle and design of a MAMP system. (a) Snapshot of the MAMP device, (b) schematic diagram of the MAMP method, (c) distribution of the permanent magnet pairs, (d) generated two magnetic brushes under the effect of the magnetic field, (e) demonstration of workpiece clamping, (f) SEM photo of the bonded magnetic abrasive for rough polishing, and (g) SEM photo of the loose magnetic abrasive for fine polishing.

TABLE 1. Polishing conditions

Conditions	Group 1	Group 2	Group 3
Workpiece type	Cylindrical surface	Freeform surface	Cylindrical surface
Workpiece material	304 stainless steel	304 stainless steel	304 stainless steel
Average initial surface arithmetic roughness (Ra)	455.4 nm	261 nm	74nm
Rotation speed	1500 rpm	1500 rpm	1500 rpm
Magnetic abrasive for rough polishing	Bonded type magnetic abrasive	Boded type magnetic abrasive	N/A
Magnetic abrasive for fine polishing	Loose type magnetic abrasive. Weight percentage of the polishing slurry is 23.3%.	Loose type magnetic abrasive. Weight percentage of the polishing slurry is 23.3%.	Loose type magnetic abrasive. Weight percentage of the polishing slurry varies from 0, 10%, 20%, 30%, 40% and 50%
Polishing time	30 min rough polishing and 20 min fine polishing	30 min rough polishing and 20 min fine polishing	20 min fine polishing
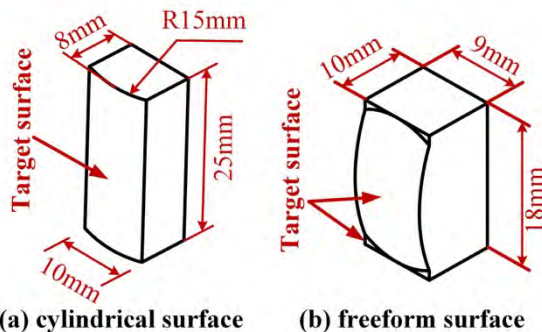
FIGURE 2. Sample design for the polishing test. (a) Cylindrical surface, and (b) freeform surface.

The bonded magnetic abrasive is iron particle (i.e. 100−200 μm, 80 wt.%) bonding with alumina abrasive (i.e. ~2 μm in average, 20 wt.%), as shown in Fig. 1(f). The loose magnetic abrasive is a mixture of carbonyl iron powder (CIP) and nanometer scale alumina abrasive (~150 nm) as shown in Fig. 1(g).

Three groups of polishing experiments were conducted in this study. The first one is the rough polishing and fine polishing of the cylindrical surface. Polishing test was then conducted on the freeform surface as shown in Fig. 2(b), which is a compound surface including one aspheric surface and 4 flat surfaces. An investigation on the effect of the polishing

abrasive concentration was conducted during the fine polishing process. The percentage of the solid in the polishing slurry used in this experiment is 19~22%.

The surface roughness before and after polishing was measured on ZYGO NEXVIEW 3D optical profilometer. And the surface profile was measured on Talysurf PGI1240. The micro surface topography before and after polishing was also measured on Hitachi Electron Microscope TM3000.

RESULTS AND DISCUSSIONS

Figure 3 shows the snapshots of the cylindrical samples before polishing, after rough polishing and fine polishing, respectively. It can be seen that the surface finish of the workpiece has been largely improved after polishing, and mirror-like surface was obtained after fine polishing. According to the results from Zygo interferometer showed in Fig. 4, the surface roughness was reduced to Sa 49.8 nm after rough polishing, and further reduced to Sa 13.8nm after fine polishing.

Before polishing

After rough polishing

After fine polishing

FIGURE 4. Surface roughness measurement of the surface before and after polishing

In order to observe the change of micro-scale topography of the surface before and after polishing, the photos taken under the scan electron microscope (SEM) were also provided in Fig. 5. Two photos with different magnifications were presented for each stage. These results indicate that the initial rough surface has been successfully smoothened after rough polishing and fine polishing.

Before polishing

After rough polishing

After fine polishing

FIGURE 3. Snapshots of the cylindrical surface at three different stages.
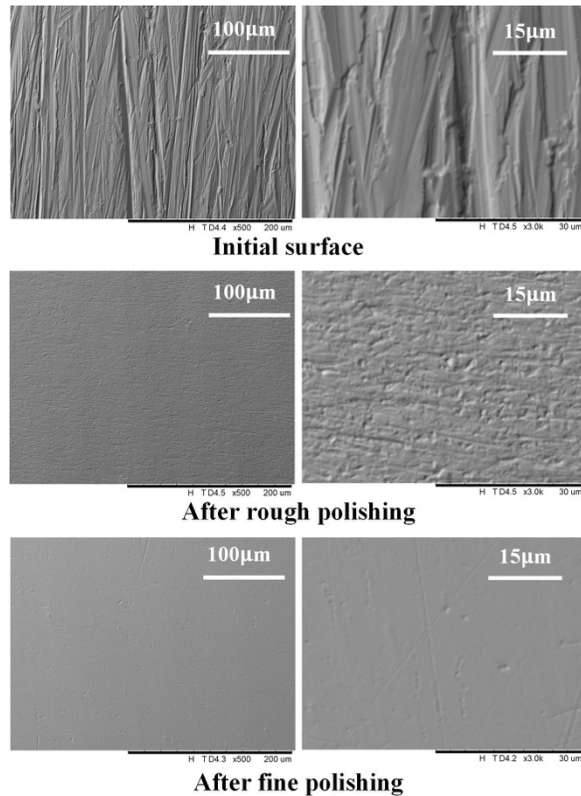
FIGURE 5. SEM measurement results of the surface before and after polishing

Polishing performance test of MAMP on free form surface, which is a compound surface was also conducted. Figure 6 shows the surface before and after polishing. Mirror-like freeform surface was also obtained after MAMP. The surface roughness was reduced from Ra 261nm to Ra 15nm ， which proves the feasibility of MAMP for freeform surface.
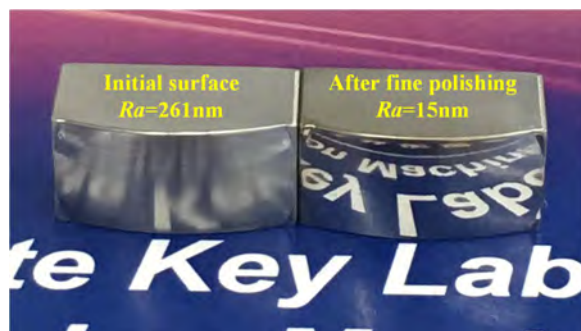
FIGURE 6. Snapshots of the freeform surface before and after MAMP

CONCLUSIONS

In this paper, a novel magnetic field-assisted mass polishing (MAMP) method is presented to implement mass finishing technology for precision manufacturing optical freeform surfaces with nanometric surface finish. A prototype MAMP system has been designed and built. A series of experiments were also carried out to demonstrate the technical feasibility of this novel mass finishing process. The results show that the MAMP process are effective for mass polishing a number of optical freeform workpiece concurrently with nanometric surface finish. The success of this research work will provide a novel and high efficient precision manufacturing technology for optical freeform surfaces.

FUTURE PLAN

The MAMP process is a newly developed process for the mass finishing of freeform surface targeting on implementing nanometric surface roughness. In order to make this process more robust and stable, further investigations on various aspects are still undergoing, such as the optimal concentration of the polishing slurry, multi-scale material removal mechanism, optimal clamping orientation for samples with different geometry, etc.

ACKNOWLEDGEMENTS

REFERENCES

[1] Fang FZ, Zhang XD, Weckenmann A, Zhang GX, Evans C (2013) Manufacturing and measurement of freeform optics. CIRP Annals-Manufacturing Technology 62(2):823-46.
[2] Cheung CF, Wang C, Ho LT, Chen J. Curvature-adaptive multi-jet polishing of freeform surfaces. CIRP Annals. 2018 Jan 1;67(1):357-60.
[3] Hashimoto F, and Johnson SP. (2015) Modeling of vibratory finishing machines.

CIRP Annals-Manufacturing Technology 64(1): 345-348.

[4] Hashimoto F, Yamaguchi H, Krajnik P, Wegener K, Chaudhari R, Hoffmeister HW, and Kuster F (2016) Abrasive fine-finishing technology. CIRP Annals-Manufacturing Technology 65(2): 597-620.

[5] Shinmura T, Takazawa K, Hatano E, Matsunaga M, and Matsuo T (1990) Study on magnetic abrasive finishing. CIRP Annals-Manufacturing Technology 39(1): 325-328.

[6] Yamaguchi H, and Shinmura T (2000) Study of an internal magnetic abrasive finishing using a pole rotation system: Discussion of the characteristic abrasive behavior. Precision Engineering 24(3): 237-244.

[7] Yamaguchi H, Kang J, Hashimoto F (2011) Metastable austenitic stainless steel tool for magnetic abrasive finishing. CIRP Annals-Manufacturing Technology 60(1):339-42.

[8] Yamaguchi H, Nteziyaremye V, Stein M, and Li W (2015) Hybrid tool with both fixed-abrasive and loose-abrasive phases. CIRP Annals-Manufacturing Technology 64(1): 337-340.

[9] Jain VK, Kumar P, Behera PK, Jayswal SC (2001) Effect of working gap and circumferential speed on the performance of magnetic abrasive finishing process. Wear 250(1-12):384-90.

[10] Chang GW, Yan BH, Hsu RT. (2002) Study on cylindrical magnetic abrasive finishing using unbonded magnetic abrasives. International Journal of Machine Tools and Manufacture 42(5):575-83.

[11] Wang C, Cheung CF, Ho LT, Yung KL, Kong L. (2020) A novel magnetic field-assisted mass polishing of freeform surfaces. Journal of Materials Processing Technology. 279:116552.

BALANCED DESIGN EFFORT FOR CONTAMINATION CONTROL IN PRECISION SEMICONDUCTOR MEASUREMENT EQUIPMENT

Ir. E.G. Hijkoop[1], Dr.Ir. K. Verbaan[1], BSc MPhil B. Martens[1], Ir. M.H.M. Kouters[1]
[1]Development and Engineering
NTS-Group
Eindhoven, Noord-Brabant, Netherlands

INTRODUCTION

This paper presents a machine design approach with focus on design-for-cleanliness for atmospheric precision cleanroom measurement equipment. Nowadays, cleanliness requirements are becoming more strict for both particle and outgassing contamination, which increases design efforts substantially, leading to high development cost for this class of equipment. This paper presents a method to comply with these requirements and gives an overview of the field of design for cleanliness for atmospheric machines.

Technically, the background of this work is a typical optical inspection tool in which particles on the substrate surface lead to measurement errors. Typical measurement times are long – several days – which increases the chance on gathering particles on the surface of the substrate. In addition, specific outgassing components in the downstream air, such as silicones, cause irreversible damage to the sensitive optics. An overview of the system is shown in Figure 1.
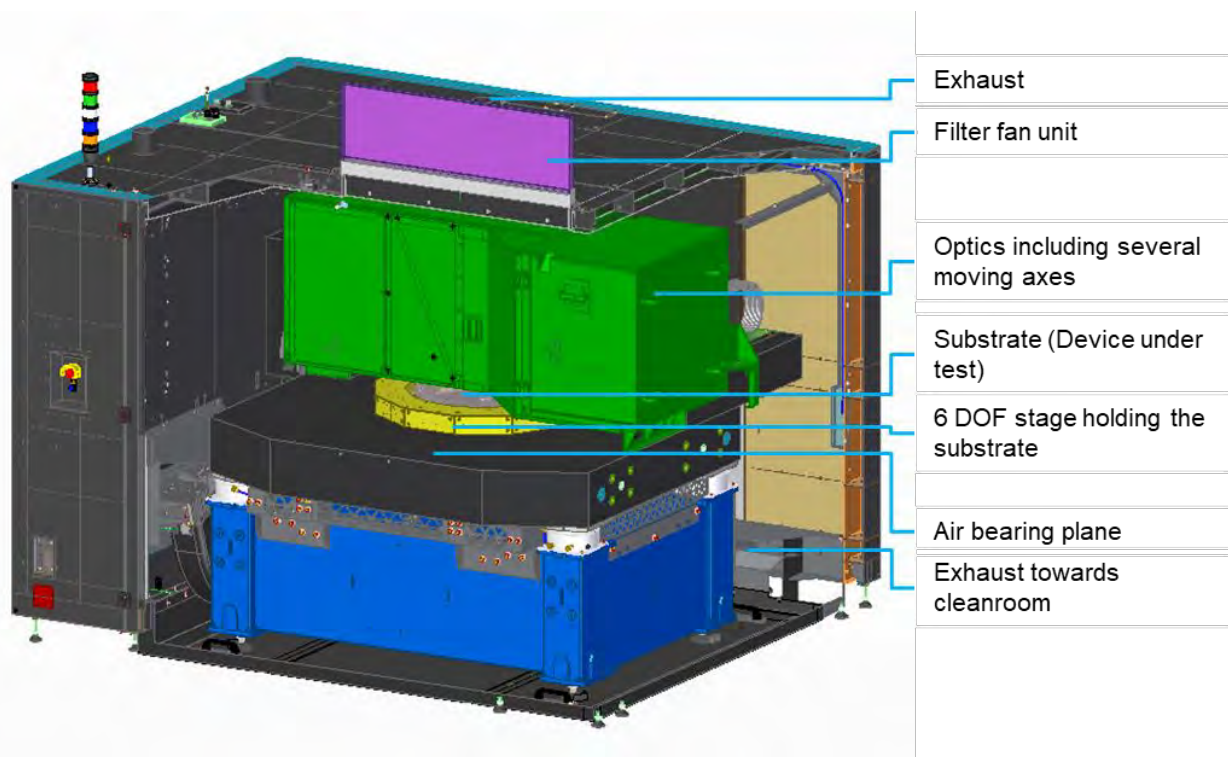
Figure 1: Overview of the system.

CLEANLINESS-ZONE STRATEGY

This paper elaborates on these two topics – particle and outgassing contamination – and presents a way in which a machine is designed with these requirements.

First, a cleanliness-zone strategy is chosen by focusing on the most critical volumes, thereby permitting other volumes to be less clean. In this particular case, the volumes direct above and below the substrate are considered to be critical.

Second, two main cleanliness contributors are identified to achieve the required contamination control within the clean-zone: airborne particles and molecular outgassing. Each contributor requires a different approach in which theory, experience and pragmatism need to be balanced to satisfy constraints on cost and timing. Therefore both the airborne particles around the substrate and outgassing of non-volatile organic contaminants are modelled and verified.

Particles

Particles can be divided in two groups: airborne particles and particle deposition. The dividers between the two groups depend on the particle size and density in combination with the air flow velocity. For critical areas the Stokes' law[1] is used to determine the force exerted on the particle by the upward laminar flow and by making it equal to the gravitational force acting on the particle. For other areas the assumption is that particles <10 µm stay airborne as the local air flow is relatively high.

A high level of airborne particles in the process room is problematic because over time the airborne particles will deposit on the substrate and the air bearing surface. Those particles will be blown off that surface again by the stage's air bearings and might end up on the substrate. Secondly, the main air flow blows out into a ISO:6 cleanroom risking the contamination of other processes in the cleanroom.

The airborne particles are counteracted by filtering the incoming ISO:6 cleanroom air using a filter fan unit containing a U16 filter to ISO:1 [2] air and limiting the amount of added particles to the air. This is achieved in the mechanical design by placing the contaminating machine parts, such as linear guides, downstream and away from the substrate as shown in Figure 2. In addition to this the contaminating machine parts are equipped with covers and an exhaust, ensuring a inward air flow trapping the produced particles inside the covers. Turbulent flows result in unpredictable particle deposition and removal, and must therefore be avoided. This is modelled in detail using computational fluid dynamics (CFD) analyses.
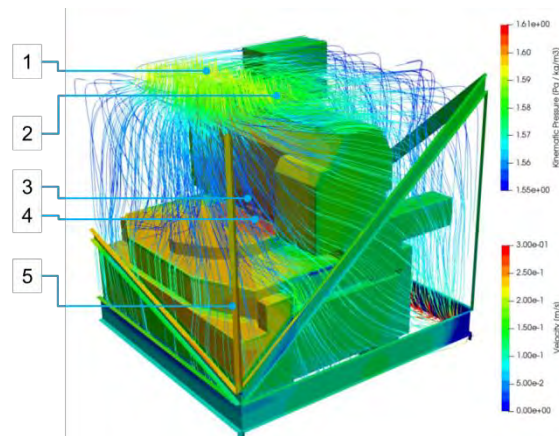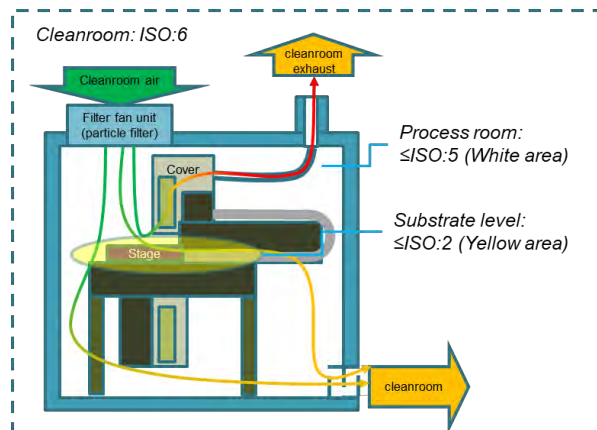
Figure 2: Concept air flow design including zone definition (left), detailed design (right).

Secondly, the particle deposition on the critical locations can be counteracted by designing covers and guiding air flow correctly. In the design shown in Figure 3 the covers (hardware particle barrier) catch the bigger particles (≥10 µm) before they reach the substrate top plane.

For the smaller particles the minimum required upward flow is estimated using Stokes' law and the small particles are kept inside the cover as well. In our case the resulting minimum required upward air flow is 0.023 m/s.
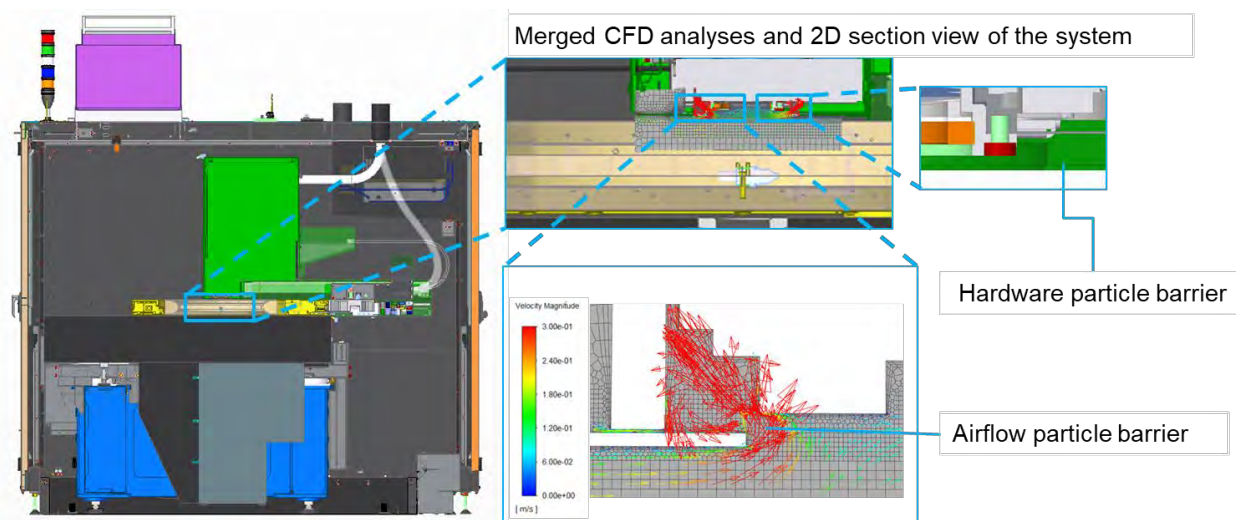
Figure 3: Air flow design above the substrate into the optical cover.

Molecular outgassing

The main hazard to the optical components is contamination by molecular outgassing of the machine. The design approach regarding this contaminant is that at first the contribution of the components to the outgassing of non-volatile organic compounds is modelled based on the ideal gas law. A major difficulty is that big uncertainties are present in available outgassing material data [3], [4]. Input parameters for the model are difficult to estimate, which makes the outcome prone to large variations. Rest gas analyses (RGA) measurements are performed on critical components and coatings to estimate their contribution. This way of working allows to remove the big contributors from the design. It would be costly, time-consuming and not always possible to test the outgassing for all components used in the system. Therefore, the pragmatic choice is made to add air-extraction of the contaminated air on the most critical areas, like motors and greased linear guides.

MEASUREMENTS

Verification measurements are performed on the air flow, airborne particles and TOC non-volatiles (Molar mass >120 g/mol or a boiling point >150 °C).

Flow measurements are performed to verify the direction and velocity of the air flow. A small size custom-built flow sensor is developed and verified as no commercially available miniature sensor which measures at low air flows is available. This flow sensor works on the principle of heating up a central sphere and measuring the temperature in the orthogonally placed NTCs as shown in Figure 4. The air flow direction and velocities are measured at various locations in the system and show that the predicted flow directions match in all cases. The measured flow velocities resemble the predicted flow velocities in larger sections (Table 1) within approximately 30%. But the measurements are not unambiguous in smaller passages such as the one shown Figure 3. This discrepancy is caused by the different self-heating that occurs at low flow velocities in a confined space, compared to the large air volume of the calibration wind tunnel. In addition, it was difficult to place the two relevant NTCs in line with the air flow, due to a difficult to reach measurement location. Differences between the simplified CFD model and the hardware adds to the deviations. This is visible for position 5 (shown in Figure 2), as the granite slab and frame below have less restrictions in reality than was modelled.
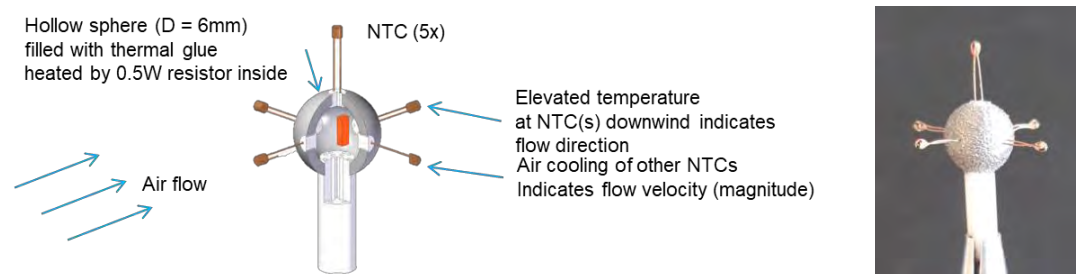
Figure 4: Flow sensor design and working principle (left), Built prototype (right).

Position	Description	Measured velocity (m/s)	CFD model prediction (m/s)	Measured velocity, linearly corrected for flow input difference with CFD (v_measured/2.8)	Deviation from CFD (%)
1	Input flow from FFU	0.5	0.20	0.18	-10%
2	Above optical cover	0.5	0.15	0.18	+20%
3	Flow into optical cover above substrate	No result	0.30	N/A	N/A
4	Main backflow over the substrate	0.75	0.20	0.27	+35%
5	Corners granite	0.7	0.10	0.25	+150%

Table 1: Air flow estimation from the CFD compared to the measured air flow. The position numbers correspond to the number is Figure 2.

The airborne particles are measured at the substrate level and at the exhaust to the cleanroom during throughput testing of the system. During this test all 18 axes move in a certain sequence. The sampling device is a Lighthouse 3016 handheld particle counter. For the measurements above the substrate the isokinetic sample probe is elongated with a 6 feet tubing. In

Figure 5 the measurement results of the topside of the substrate is shown. A walking average of 1 m^3 is calculated from the raw particle counter data and shows contamination at the beginning. This contamination is caused by opening and closing the doors, moving the build-in hoist and positioning the particle counter into the system. After a recovering period of approximately 1 hour no particles are detected anymore. This shows that the air above the substrate is clean and resembles the expectations.
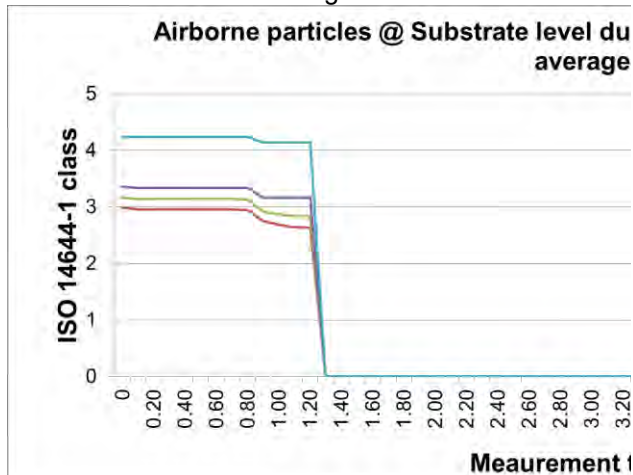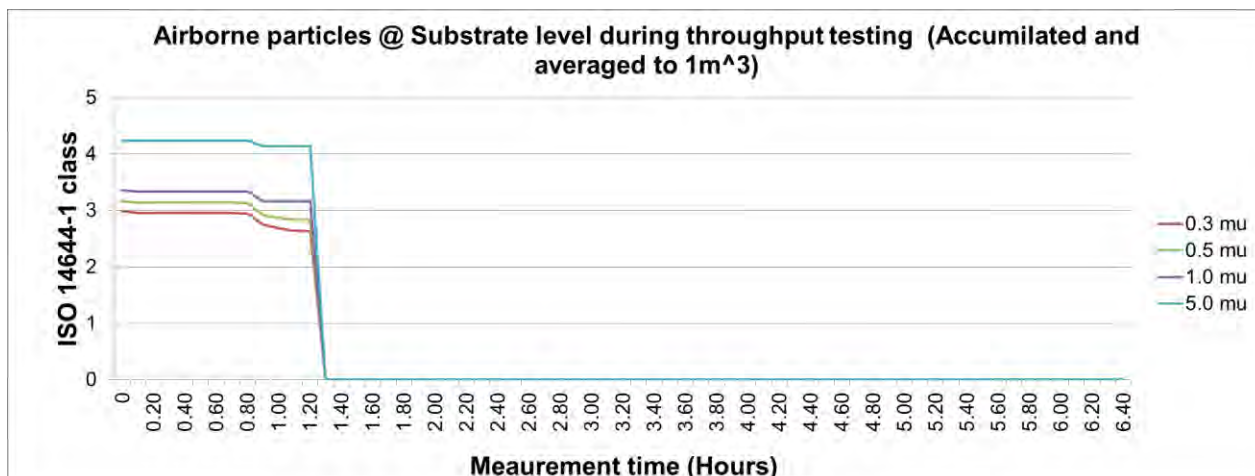
Figure 5: Airborne particle measurement at substrate level.

Next the particle counter is positioned on the floor inside the system, just before the cleanroom exhaust. Figure 6 shows the resulting airborne quality of just worse than ISO:4. Interestingly, the ISO class is dominated by the larger particle sizes. This is caused by the fact that if only one 5 µm particle is measured, this results in a significant higher ISO class than when one 0.3 µm particle is measured. Furthermore we can conclude that the system output air will not become much cleaner than ISO 4 as the 0.3 µm particles will be dominant. If needed this could only be achieved by making design changes to cable-guides, exhaust tubing and the substrate handling.
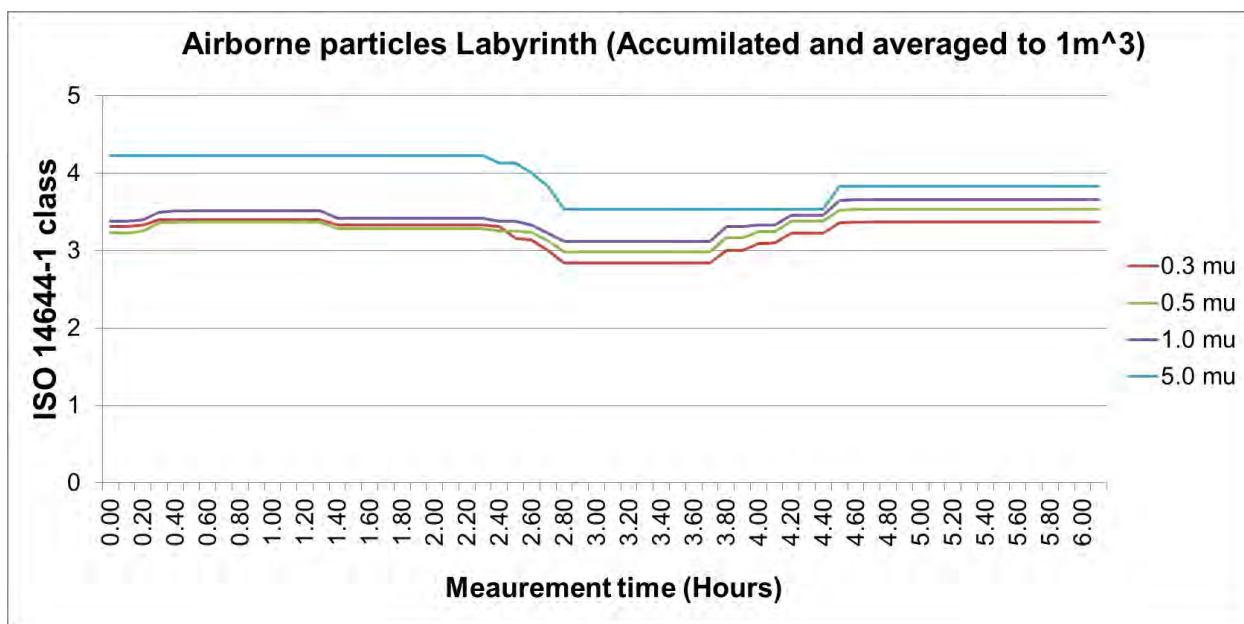
Figure 6: Airborne particle measurement at the exit labyrinth.

To finalize, the system air out flow is TENAX sampled and the absorption tubes are developed with a GC-MS setup (gas chromatography – mass spectroscopy). Because the system dilutes the outgassing components by the air flow and the materials were selected according the RGA tests, the system complies with a factor of 3 with respect to the requirement of 50 ng/L. Improvements are possible by baking-out several components, choosing different cabling and selecting different components based on their outgassing behavior.

CONCLUSION

In this design-example it is shown that by following the zone strategy, the contamination

requirements of a system are met. The steps taken are: First determine the critical zones in the system. Then focus the cleanliness effort on those areas. In this example by focusing on materials, air flow and covers. Finally making pragmatic tradeoffs for identified risks, like adding exhausts to linear guides.

This approach can be used for a wide range of systems and lowers the total design effort without compromising the needed contamination control.

FUTURE WORK

To achieve higher order outgassing contamination control with correct predictions there is still work to do in making material outgassing data widely available including the measurement specifications.

As seen in the air flow measurements, the flow direction can be modelled correctly and the air flow velocity can be measured in open spaces.

However the flow velocities in confined spaces needs improvement.

REFERENCES

[1] Stokes, G. G. On the effect of internal friction of fluids on the motion of pendulums". Transactions of the Cambridge Philosophical Society. 9, part ii: 8–106. The formula for terminal velocity (V)appears on p. [52], equation (127): 1851

[2] ISO 14644-1:2015 Cleanrooms and associated controlled environments — Part 1: Classification of air cleanliness by particle concentration

[3] Powers C. Outgassing Data for Selecting Spacecraft Materials Online (https://outgassing.nasa.gov/), NASA: 2018

[4] David Garton, Vacuum Technology and Vacuum Design Handbook for Accelerator Technicians. Australian Nuclear Science and Technology Organisation, ISBN number: 192126814X: 2011

DESIGN OF AN ULTRAFAST OSCILLATING BLADE MICROTOME BASED ON VIBRATION CANCELLATION

Xinlei Fu[1], Jialong Chen[1], Jiarui Yang[2], Shuaibin Chang[3], David A. Boas[2,3], and Shih-Chi Chen[1,*]
[1]Department of Mechanical and Automation Engineering
The Chinese University of Hong Kong
Shatin, N.T., Hong Kong SAR, China
[2]Department of Biomedical Engineering
Boston University, Boston, MA 02215, USA
[3]Department of Electrical and Computer Engineering
Boston University, Boston, MA 02215, USA
[*]Email: scchen@mae.cuhk.edu.hk

In this paper, we present the modeling, design and characterization of an ultrafast oscillating blade microtome that can stably operate at programmable speeds up to 260 Hz for sectioning soft tissues with high precision. To demonstrate the performance, the microtome is applied for sectioning dorsolateral prefrontal cortex of a human brain with reconstructed 2D and 3D images. The microtome is designed based on the principle of vibration cancellation and compliant mechanisms, which effectively suppress error blade motions in the undesired directions. The new microtome enables the precise sectioning of various soft tissues, including tissues processed by optical clearing or expansion microscopy protocols, which may find important applications in the fields of 3D imaging and biophotonics.

INTRODUCTION
Precision tissue sectioning is one of the enabling steps in 3D whole organ imaging due to the immense size of an organ, e.g., brain, and the limited imaging depths of advanced microscopy methods, such as confocal or two-photon excitation (TPE) microscopy [1,2]. Although the tissue clearing technique [3] has largely eliminated the scattering problems in tissues, the imaging depth is still constrained by the working distance of an objective lens, which is typically on the scale of 10s to 100s of microns for high numerical aperture (NA) objectives. On the other hand, expansion microscopy [4] enables super-resolution imaging via regular fluorescent microscopes by synthesizing a swellable polymer network within a biological specimen for expansion over a factor of 10. Yet, the expanded specimen becomes softened which prevents effective sectioning via conventional microtomes. The development of these new imaging and material processing techniques necessitate the development of a new class of microtome to slice soft tissues or organs into thin sections for microscopic imaging, followed by volume image reconstruction of the entire organ.

One common approach to enhance the cutting results is to harden the tissues, for example, by embedding the tissues with paraffin wax or freezing the tissues to cryogenic temperature for processing. However, these protocols are not suitable for processing living tissues nor to be combined with tissue clearing or expansion microscopy. To address the issue, i.e., sectioning soft tissues at suitable temperatures $(4 - 20\ ^{0}C)$ without chemicals, we propose to harden the (living) tissues by exploiting their intrinsic viscoelastic properties, i.e., tissue stiffness increases with increasing cutting frequency [5]. This calls for an oscillating blade microtome of high operation frequency. Although oscillating blade microtomes have been around for more than three decades [6], their performance is still limited by the low operation frequency, i.e., < 80 Hz, and the associated parasitic blade motions at higher frequencies (i.e., > 60 Hz). According to fracture mechanics, optimal sectioning results can be achieved by minimizing the global deformation in tissues and locally maximizing the stress concentration [7]. This can be achieved by locally stiffening the tissues with a fast oscillating blade. Our analytical study [5] shows that when the blade frequency goes beyond 200 Hz, the sectioning results can be effectively improved.

Yet, this goal can only be realized when the parasitic blade motions, i.e., motions transverse to the blade oscillation direction, are suppressed to within 1 micron. A microtome that meets this requirement can address critical issues in many emerging imaging and biological applications, such as super-resolution imaging via expansion microscopy and tissue optical clearing, or the combination of them.

DESIGN
The new microtome is designed based on the compliant mechanism, where monolithic flexible beams function as mechanical bearings to generate precise and repeatable motions of an oscillating blade. When a vibrating blade microtome is in operation, as illustrated in Fig. 1, the sample is fed to the blade in a direction, i.e., cutting direction, transverse to the oscillating direction of the blade. To achieve high sectioning quality, the blade should be operated at high frequency (> 200 Hz) in the cutting plane, i.e., x-y plane, where parasitic motions perpendicular to the cutting plane need to be suppressed. Due to the size and intrinsic mass of the microtome as well as the fact that the excitation source, e.g. unbalanced dynamic forces, in flexures increases quadratically with frequency, it is extremely challenging to design a mechanism that can operate smoothly beyond 200 Hz. We address this issue by exploiting the concept of vibration cancellation, i.e., to cancel out the excitation source of the parasitic motions by adopting a multi-symmetry design.
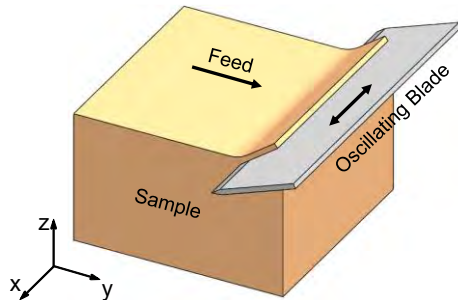
FIGURE 1. Sectioning a soft material via an oscillating blade, where the blade oscillates in the x direction; and the sample is fed to the oscillating blade in the y direction.

Figure 2 presents the design of the ultrafast microtome, where a double symmetry configuration, i.e., symmetry about the *x* and *y* axes, is adopted. The symmetric design means two synchronized microtome units need to operate in parallel, where the blades oscillate in

opposite directions. This arrangement effectively cancels out vibrations during high speed operations and doubles the throughput of tissue sectioning. As shown in Fig 2A and 2D, the blade holder is supported by two sets of parallel beams to confine the blade motion in the *x*-axis. By adjusting the length and aspect ratio of the beams, the in-plane and out-of-plane stiffness of the mechanism can be optimized. The blade motion is generated by two opposing voice-coil motors (VCMs), which are selected based on their high force density and precision. One way to increase the resonance frequency is to remove the redundant mass on the mechanism and to use materials of high stiffness and low density. Considering cost and flexing capability, the monolithic mechanism is made from a 1" thick aluminum 7075 plate. To ensure the VCMs can generate sufficient oscillation amplitudes in the target operation frequency (i.e., 5 - 260 Hz), we design the resonance frequency of the mechanism to 200 Hz. Based on this constraint, the supporting beams are designed to be 1 mm thick, 85 mm long and distanced by 45 mm.

A

B

C
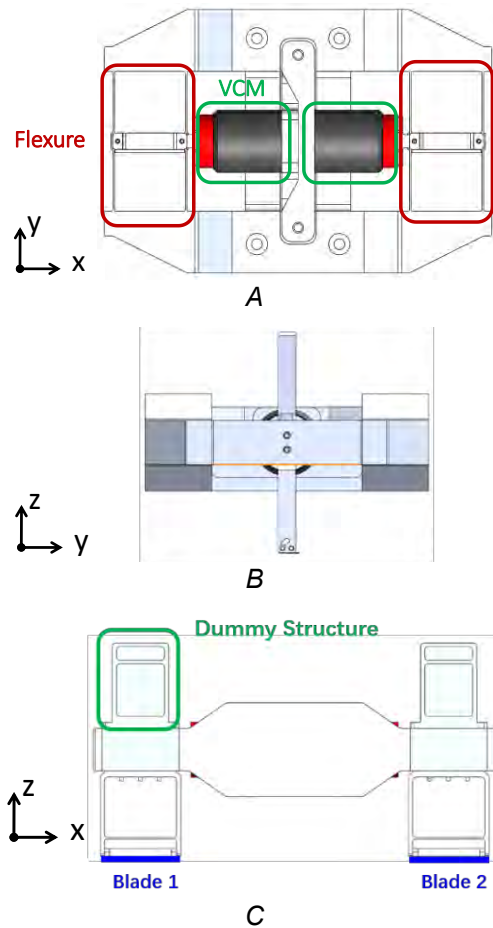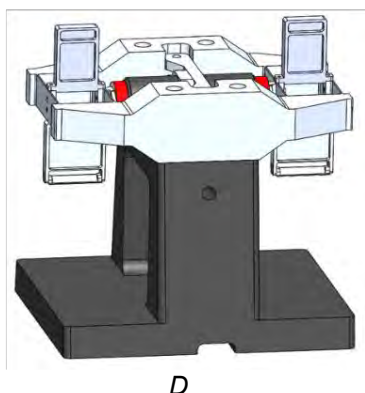
FIGURE 2. Design concept of the flexure-based ultrafast microtome. A. top view; B. side view; C. front view; and D. isometric view.

A shown in Fig. 2B and 2C, the blade holders extend 50 mm downward from the mechanism to position the moving blades close to the sample, which is immersed in the water tank. This unavoidably lowers the mechanism's center of mass, exerting torques to the blade holders and causing them to wobble about the *y*-axis. To address this issue, dummy structures are added to the top of the blade holders to bring the center of mass to the mechanism plane, where the forces of the VCMs are applied to. This arrangement effectively eliminates the unwanted torques generated in dynamic operations. Figure 2D shows the CAD model of the ultrafast microtome, which is installed on a custom-made cast iron base to absorb disturbance forces. Our modeling result predicts the parasitic motions can be controlled within 1 μm with an oscillation amplitude of 200 μm at 260 Hz.

During assembly, it is important to ensure all critical components, e.g., VCMs, are well aligned to achieve the predicted performance. On the other hand, fabrication errors may compromise the symmetry design, e.g., dimensions of the beams as well as the mass of the dummy structures and blade holders. These issues can be addressed by careful characterization and post assembly adjustments.

CHARACTERIZATION

In this section, we present the characterization of the ultrafast microtome using six capacitive probes (Lion Precision, C8/CPL290). Figure 3 shows the metrology setup, where cap probes B1 - B3 measure motions of the blade holders and dummy structure in the *x*-axis; and cap probes C1 - C3 measure parasitic motions in the *z*-axis and

θ_y-axis. A vibration controller (LDS Dactron COMET) sets the displacement in channel B1 to constant over the entire frequency testing range (i.e., 0 – 260 Hz); and the rest of the cap probes are measured in reference to cap probe B1.
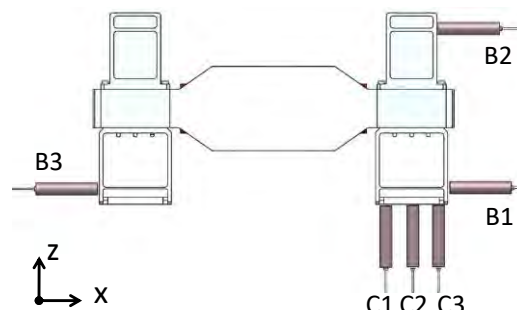
FIGURE 3. Metrology setup for the ultrafast microtome, where six capacitance probes are used to measure the oscillating amplitude (B1 - B3) and parasitic motions (C1 - C3).

Figure 4 presets the measured displacements in all six channels from 5 – 260 Hz. Figure 4A compares the motions and phases of the blade holders (B1 & B3) and dummy structure (B2), where an oscillation amplitude of 200 μm is achieved throughout the entire frequency range. From the results, we can confirm the two blade holders achieve synchronized motions in opposite directions, which cancels out most dynamic forces generated during the resonance. The small deviations between channels B1 and B3 indicate that there is still little unbalanced dynamic forces, which has been absorbed by the base. The amplitude difference between channels B1 and B2 is ~1%, which contributes to the parasitic blade motions measured in channels C1-C3.

A
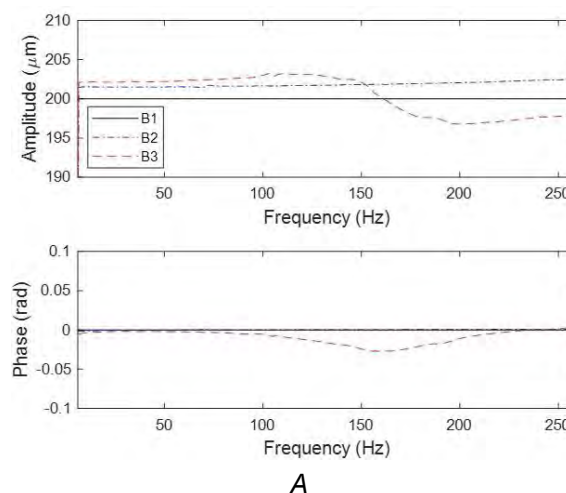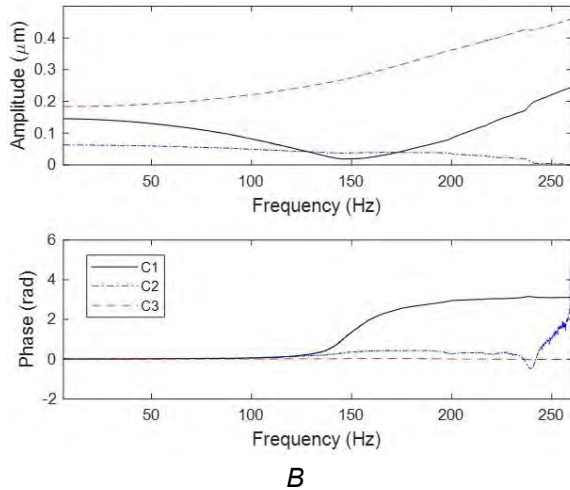
FIGURE 4. A. Measured blade oscillation amplitude; and B. parasitic motions.

Figure 4B presents the measured parasitic blade motions and phases (C1 - C3), where the maximum error motion is 0.45 µm at 260 Hz. From the results, we can also confirm the parasitic motions increase quadratically with frequency as predicted by the model. The parasitic motions at the center of the blade (C2) are much smaller than those measured at the blade edges (C1 & C3), which indicates the dominant error motion is rotation about the *y*-axis, induced by the misalignment between the center of mass and the VCM axis. These parasitic motions can be further minimized by fine tuning the dummy structure and alignment. Overall, the double symmetry microtome design has demonstrated excellent vibration cancellation capability with a wide frequency tuning range (i.e., 5 - 260 Hz) and an oscillation amplitude of ~200 µm, achieving the design goals. Table 1 summarizes the performance of the ultrafast microtome.

TABLE 1. Specifications of the microtome

Feed rate	0 – 10 mm/s
Oscillation frequency	5 – 260 Hz
Oscillation amplitude	0 – 0.2 mm
Sectioning thickness	10 – 500 µm
Blade size	< 60 mm
Parasitic motion	< 500 nm

SECTIONING & IMAGING RESULTS
The ultrafast microtome is installed both at the Chinese University of Hong Kong and Boston University (BU), where the BU team, led by Dr. David Boas integrates the ultrafast microtome to a custom-built optical coherence tomography imaging system for automatic sectioning and 3D reconstruction of a human brain.
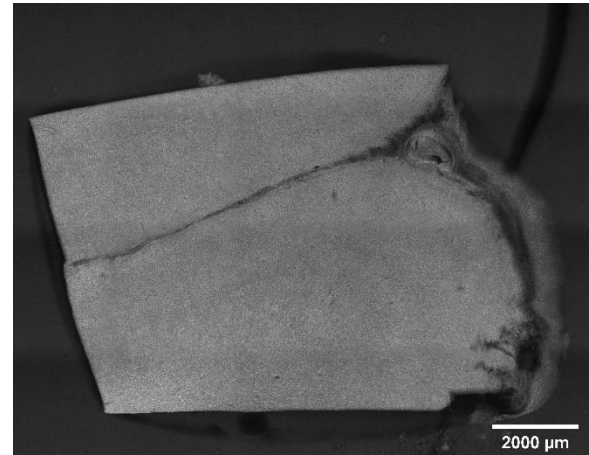
A

B

FIGURE 5. Dorsolateral prefrontal cortex of a human brain sectioned by the ultrafast microtome. A. average intensity projection of the volume OCT; and B. reconstructed sample surface based on a surface finding algorithm.

Figure 5A presents the preliminary sectioning and imaging results of dorsolateral prefrontal cortex of a human brain at BU based on the ultrafast microtome and the OCT system, where each slice is 150 µm thick. Figure 5B shows the reconstructed sample surface generated by a custom-developed surface finding algorithm, where the standard deviation of the brain slice surface index is below 10, suggesting high tissue sectioning quality based on the empirical criterion. Figure 6 presents an autofluorescence image of a stitched human brain slice via a TPE microscope. These results confirm the precision and practicality of the new ultrafast microtome.
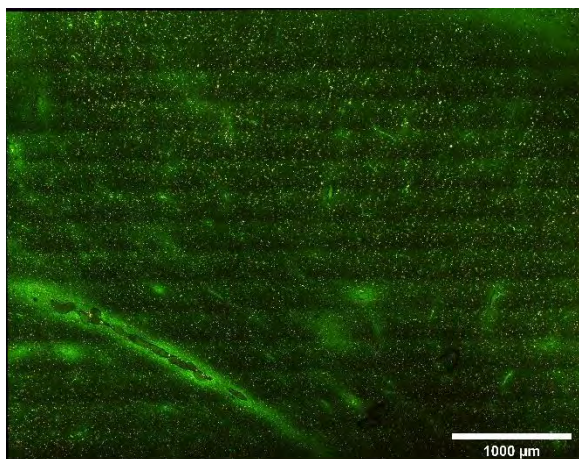
FIGURE 6. Autofluorescence image of a stitched human brain slice using a commercial TPE microscope.

In the last experiment, we test whether the microtome can section expanded hydrogels, i.e., materials for expansion microscopy. Before sectioning, the hydrogel is expanded 10 times and embedded in 1% agarose. The microtome is equipped with a 60 mm sapphire blade; and the sectioning is performed at 250 Hz with an oscillation amplitude of 175 μm. The gel block is fed to the microtome at 0.2 mm/s. The sectioning results are presented in Fig. 7, where one may find a thin section of gel is removed, leaving a high-quality flat surface for follow-up imaging sequence. This confirms the ultrafast microtome can be used for processing ultra-soft tissues.
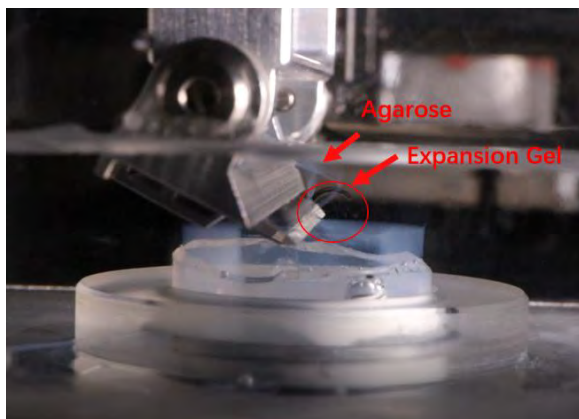
FIGURE 7. Sectioning a block of expanded hydrogel embedded in agarose (12 × 12 × 12 mm³) for expansion microscopy applications.

CONCLUSION
We have presented the design and characterization of an ultrafast oscillating blade microtome based on vibration cancellation and compliant mechanism. The new microtome achieves a wide frequency tuning range from 5 – 260 Hz and an oscillation amplitude of 200 μm. The characterization results show that parasitic motions are suppressed to within 0.5 μm throughput the entire operation range, enabling the new microtome to process ultra-soft materials, e.g., expanded hydrogels, for the first time. The predicted performance has been validated by sectioning and imaging experiments on human brain tissues and gel sectioning experiments. The new microtome may find important applications in 3D organ imaging when combined with tissue clearing and expansion microscopy techniques

REFERENCES
[1] Pawley J. Handbook of Biological Confocal Microscopy. New York, NY: Springer; 2010.
[2] Svoboda K, Yasuda R. Principles of Two-Photon Excitation Microscopy and Its Applications to Neuroscience. Neuron. 2006; 50(6): 823-839.
[3] Ueda H, Ertürk A, Chung K, Gradinaru V, Chédotal A, Tomancak P et al. Tissue Clearing and Its Applications in Neuroscience. Nature Reviews Neuroscience. 2020; 21(2): 61-79.
[4] Chen F, Tillberg P, Boyden E. Expansion Microscopy. Science. 2015; 347(6221): 543-548.
[5] Wang J, Li C, Chen S. Sectioning Soft Materials with an Oscillating Blade. Precision Engineering. 2019; 56: 96-100.
[6] Abdelaal H, Kim H, Wagstaff R, Sawahata R, Southern P, Skinner P. Comparison of Vibratome and Compresstome Sectioning of Fresh Primate Lymphoid and Genital Tissues for in situ MHC-tetramer and Immunofluorescence Staining. Biological Procedures Online. 2015; 17(1): 2.
[7] Reyssat E, Tallinen T, Le Merrer M, Mahadevan L. Slicing Softly with Shear. Physical Review Letters. 2012; 109: 244301.

OPTOMECHANICAL SPHERICAL MANIPULATOR WITH AN ADJUSTABLE CENTER OF ROTATION

Koen J. Smelt[1], Jan J. de Jong[1,2], Coen A. Blok[1], and Dannis M. Brouwer[2]

[1]DEMCON
Enschede, The Netherlands

[2]Precision Engineering
University of Twente
Enschede, The Netherlands

INTRODUCTION

Compound lens testing with a Fizeau interferometer requires a spherical motion to align the mechanical axis of the return optic with the transmitted laser beam (Figure 1). However, the location of the exit pupil differs between lens types, from somewhere inside the lens for entocentric lenses up to infinity for telecentric lenses. This therefore requires a corresponding adjustment of the remote center of rotation (RCR) of the alignment stage. Typical goniometer stages have a fixed RCR and require two additional translational stages for this alignment procedure, leading to an unintuitive and time-ineffective adjustment. In fact, for the desired motion only three degrees of freedom (DOFs) is needed, while conventional stages will require at least 4 DOF. To accommodate the alignment of different lens types, this paper presents a 3-DOF spherical manipulator, whose RCR can be adjusted from close to the end-effector up to a rotation about infinity i.e. pure translation.

Besides optical kinematic mounts, such a spherical mechanism with an adjustable RCR could be used in other disciplines. For example in keyhole surgery, peg-in-the-hole assembly, or non-contact scanning of spherical objects.

In this paper we present a kinematic optomechanical mount for testing of different lenses in a Fizeau interferometer. First the
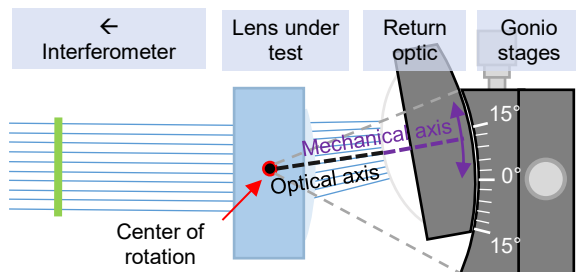
FIGURE 1. Fizeau interferometer lens testing requires a spherical motion of the return optic to align the mechanical and optical axes.

requirements, concepts and final design of the mechanism is presented, followed by an evaluation based on FEM and measurements of a 3D printed prototype.

DESIGN
Requirements

In Table 1. a list of requirements for the current application can be found. The main requirements concern the accuracy of rotation. The quality of lens testing will suffer when the RCR location differs too much from the optical center of the lens or if the motion is no longer pure spherical. Additionally, the stiffness of support should be sufficiently high to withstand the actuator forces and gravity and to prevent deflections in unwanted directions. Although the rotation round the mechanical axis (Figure 1) has no direct influence on the lens testing, it might result in unwanted parasitic motion in other directions and should be prevented as much as possible.

Conceptual design

We distinguish three main procedures to achieve such an adjustable spherical motion. In the first approach the motion is constrained by three rods whose axis intersect at the RCR. This leads to a spatial trapezoidal type mechanism whose base width is varied (parallel approach). The second type consist of stacking for two rotations about perpendicularly intersecting axes (serial approach). The third approach synchronizes the translation of a 2-DOF rotation and a 2-DOF

TABLE 1. List of requirements for the design.

Description	Value	Unit
Range of motion	±3	°
Lateral motion	±2	mm
Min. distance to RCR	45	mm
Max. distance to RCR	∞	~
Accuracy of spherical motion	5	μm
Accuracy of RCR location	15	%
Support stiffness (bending)	12	Nm/rad
Support stiffness (torsion)	0.2	Nm/rad
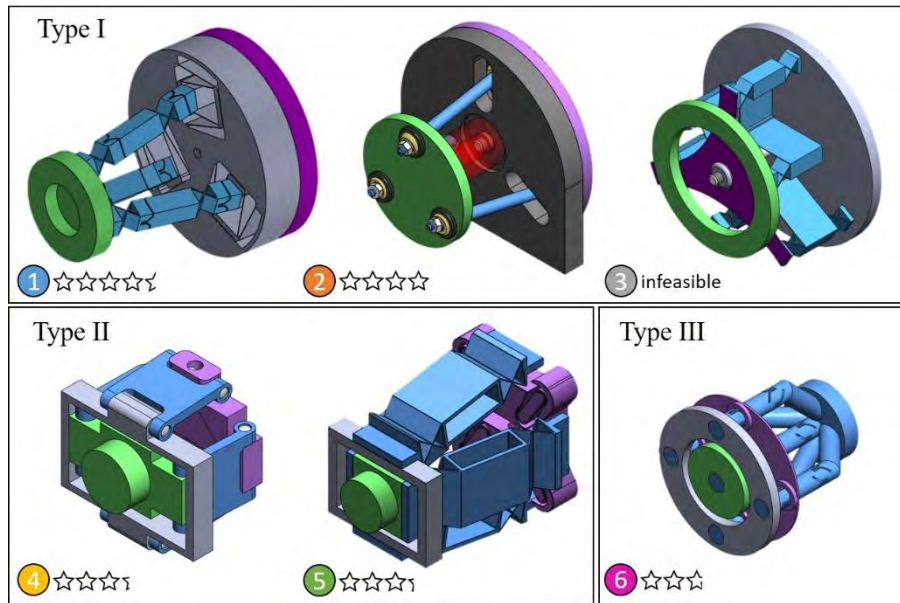
FIGURE 2. Six different concepts. With the end-effector (green), legs (blue), fixed world (grey) and the mechanism to change orientation of the legs (purple).

translation stage to obtain the desired 3-DOF motion (hybrid approach). In all these motion some form of synchronization between the different DOF is required.

Based on these three motion types, 6 designs were proposed (Figure 2), some based on conventional joint while other used flexure joints. Finally concept 1 was chosen because of simplicity and because the spherical motion is purely flexure mechanism based. Such flexure based mechanism are known for their high repeatability and low hysteresis making them ideally suited for high-precision motion applications [1].
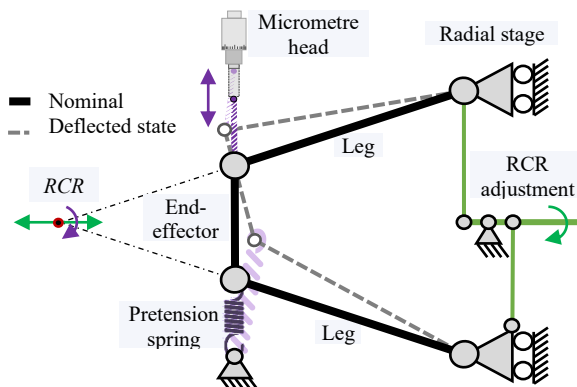
FIGURE 3. The working principle of the isosceles trapezoid mechanism with an adjustable remote center of rotation (RCR). By pulling the end-effector towards the micrometer head, the end-effector is deflected about the RCR. Varying the base width results in a changing RCR location.

Figure 3 shows the working principle of the chosen concept. The legs act as two force members such that the overall motion is constrained to the common intersection point of these legs. By adjusting the width of the base this intersection point changes, leading to a different RCR.

Detailed design

In Figure 4, the 3D printed functional model is shown. Each leg consist of two newly designed 2-DOF flexure joints. The base attachment point of the legs are placed on parallel flexure stage to allow for a changing base width. By changing the base width the RCR shifts from near the end-effector to infinity if the legs are parallel. To synchronize the individual legs a spiral slotted disc is attached at the back. The spherical motion itself is actuated by a micrometer (Figure 3). In this section some of these design elements are highlighted whereas the following section is devoted to the novel high stiffness legs.

As Figure 3 shows, the RCR is located at the intersection of the three legs of the mechanism. In order to shift the RCR closer or further away from the end-effector, the joints at the base are radially shifted in or outward from $22\,\text{mm}$ to $33\,\text{mm}$. The range of motion of the joints becomes $\pm 11°$. Together with the desired travel of the end-effector of $\pm 2\,\text{mm}$, the joints in the legs must be able to tilt $\pm 15°$ in the main direction (R_y). Perpendicular to this tilting motion the joints in the legs should be able to rotate $\pm 2.5°$ in (R_x) direction, to allow for spherical movement.

As shown in Figure 4, three radial stages are present in the base to allow the radial movement of the legs. To prevent parasitic motion and save space, a compound parallel guide is used. By using two sets of antagonistic parallel leaf springs, connected at an intermediate body, the parasitic motion of the first set is compensated by the second. In addition, space is saved by slightly angling the parallel leaf springs.

These radial stages are actuated by a 'pin-in-slot' mechanism located at the backside of the base. This disk with spiral shaped slots rotates concentric with the z-axis using a shoulder bolt. The 'pins' are attached to the radial stages and protrude through the spiralling slots. To eliminate backlash in these slots, countersunk screws are used in combination with chamfered edges of the spirals. In order to keep the faces in contact, the disk is pre-tensioned by a spring over the shoulder bolt. This also results in helpful self-locking after adjustment of the RCR distance.

Large range of motion flexure joints

A new type of compliant cardan flexure is developed to function as the legs of the mechanism. The compliances in the legs are concentrated into two flexure hinges with intersecting centers of rotation, as shown in Figure 5. Since the support stiffness benefits from a lumped instead of distributed compliance [2] a small leaf spring hinge (SLSH) and cartwheel hinge (CH) are combined. The CH is responsible for the large deflection in R_y-direction of $\pm 15°$, while the SLSH can cope with smaller rotation of $\pm 2.5°$ in R_x- direction. It is important that the rotation centres intersect, so that the location of the RCR of the spherical mechanism is the same
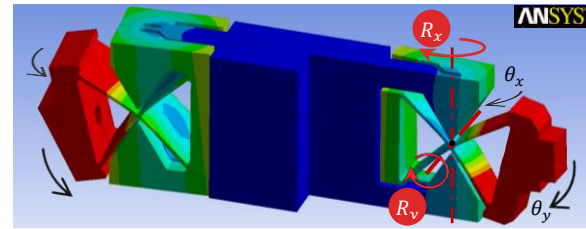
FIGURE 5. Simulated deformation plot of one of the legs in deflected state, with partial section view. This 3D printed part uses two novel flexure based cardan joints.

for tip and tilting motions. By integrating of the SLSH into the support of the CH a compact cardan joint design is obtained. Furthermore, the maximal allowable range of motion is physically limited by rigid parts of the joints in order to prevent the flexure from exceeding the yield stress.

To produce these flexures, 3D printing is the best suited production method due to the presence of some undercuts. Other techniques like wire-EDM cutting are feasible but require assembly from multiple parts. The geometry of the cardan joints in the legs is optimized using the mechanical properties of the PLA plastic, which is used in the functional model. The range of motion was optimized for the highest axial stiffness.

For analysing stiffness and range of motion two methods are used: The first method uses analytical approximations to predict the stiffness and maximal deflection of the joint using equations known from literature for the cartwheel and small leaf flexure joint [3]. These equations are used for calculating initial lengths. With a finite element model in ANSYS, a more detailed
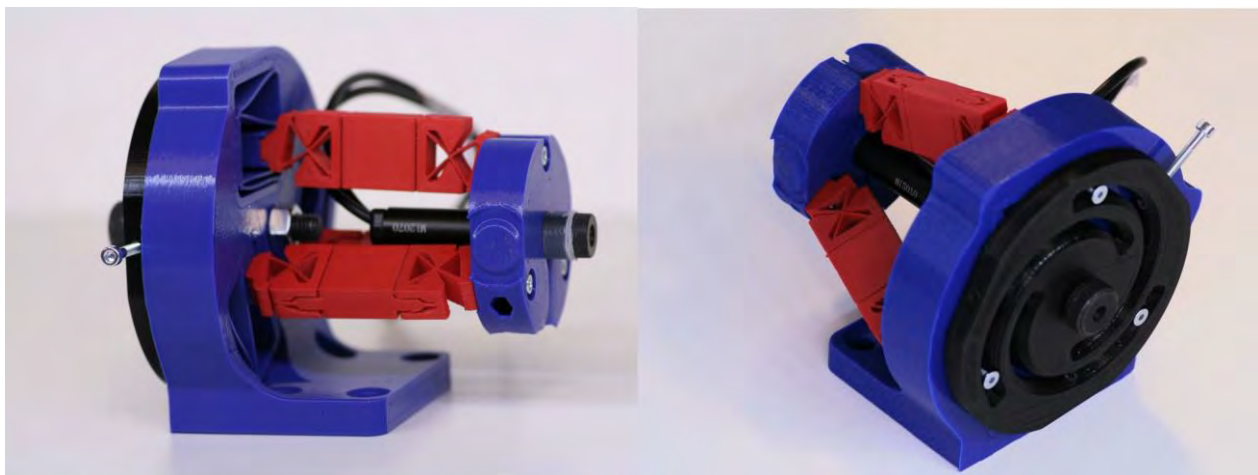
FIGURE 4. A 3D printed functional model of the spherical mechanism with adjustable remote center of rotation in the translating (left) and the pivoting (right) configurations. The legs are red, the spiral guide is black and the base and end-effector are blue.
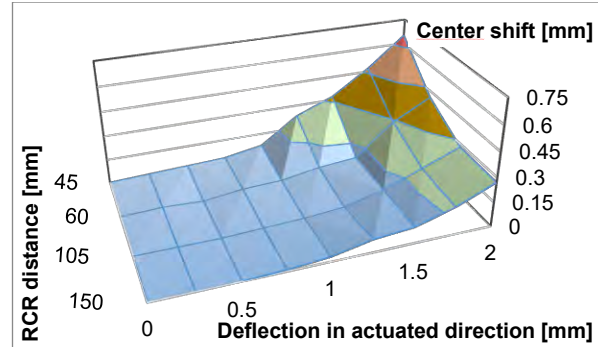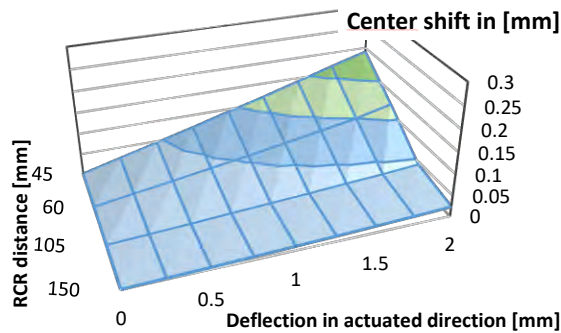
FIGURE 6. Left: Estimated lateral center shift of the RCR, using the PRBM model. Right: Experimentally determined lateral center shift of RCR of the functional 3d printed model.

design of the joint as a whole was optimized. It was found that the printed legs were able to reach the desired range of motion without failing. Other influences on maximal yield strength of the material are print temperature, layer height, infill percentage, porosity, and extrusion width [4].

EVALUATION

The mechanism is designed for spherical motion around a specified RCR. Ideally, the end-effector stays perfectly oriented towards this point for all motion. However, for this mechanism this is only true at in the initial position due to a kinematic change of the intersection point of the legs (Figure 3). This causes more rotation of the end-effector for a given translation, resulting in a different RCR. This phenomenon is called centre shift.

This centre shift was measured on the prototype by placing a camera sensor at location of the desired RCR. On the end-effector a laser pointer is mounted to illuminate the sensor at the RCR. In the ideal case, the camera sensor does not move during deflection. In practice, it does. Therefore, the change in spot location is taken as a measure for the centre shift. In Figure 6, the centre shift computed by a kinematic model and measurements on 3D printed prototype are shown.

As expected, the centre shift increases with larger deflections and a shorter distance towards the RCR. From the experimental validation, it could be determined that the centre shift increased more than expected for deflections larger than 1.0 mm. This is attributed to the finite support stiffness of the mechanism. Since the actuation force is applied at the end-effector and not in-line with the centre of compliance, an additional angular error is introduced, causing a 'diving' motion of end-effector. The additional centre shift was found to be within the limits of the current application

CONCLUSION

In this paper we proposed a 3-DOF flexure based mechanism with an adjustable center of rotation to align a lens in a Fizeau interferometer. The mechanism consist of three flexure-based legs that connect to the end-effector in a trapezoidal manner. Each leg consists of two novel flexure-based joints that comprise of a cartwheel hinge and a short leaf spring hinge with intersecting axes. This compact design combines a relative high support stiffness with large range of motion in one direction. These legs are placed on synchronized parallel flexure guides to accommodate the radial movement of the base connection points for the RCR adjustment. The evaluation of a 3D printed prototype showed that the angular error of the end-effector is well below 0.1° for deflections smaller than 1.0 mm. Although for larger deflections the angular error was increased up to 0.8° due to center shift, the desired accuracy of the Fizeau interferometer application has been demonstrated.

REFERENCES

[1] M. Naves, M. Nijenhuis, W.B.J. Hakvoort, and D.M. Brouwer. Flexure-based 60 degrees stroke actuator suspension for a high torque iron core motor. Precision Engineering, vol 63, 2020

[2] L. L. Howell and A. A. Midha. Method for the Design of Compliant Mechanisms With Small-Length Flexural Pivots. ASME. J. Mech. Des. March 1994; 116(1): 280–290.

[3] J. Wu, S. Cai, J. Cui, and J. Tan, "A generalized analytical compliance model for cartwheel flexure hinges," Review of Scientific Instruments, vol. 86, 2015.

[4] B. Wittbrodt and J. Pearce, "The effects of pla color on material properties of 3-d printed components," Additive Manufacturing, vol. 8, 10 2015.

EFFICIENT MODELING FOR THE DESIGN OF A
LARGE-STROKE FULLY FLEXURE-BASED 6-DOF HEXAPOD

Marijn Nijenhuis, Mark Naves, Wouter B.J. Hakvoort, Dannis M. Brouwer
Precision Engineering
Faculty of Engineering Technology
University of Twente
Enschede, Overijssel, The Netherlands

INTRODUCTION

This paper discusses new stiffness modeling developments that support the design phase of precision machinery. The recently developed T-Flex hexapod robot, a fully flexure-based 6-DOF parallel manipulator, has been the instigator for this work and serves as the case study [1]. The 6RSS hexapod consists of joints that are entirely flexure based: it has twelve spherical flexure joints and six revolute flexure joints, which suspend six iron-core torque motors [2,3]. The use of large-stroke flexure joints enables a large range of motion of ±50 mm (simultaneous translations) and ±15 degrees (rotations), without friction and play. This way, a positioning repeatability of less than 100 nm has been achieved, as confirmed by measurements on the first prototype [1].

The design optimization of the hexapod and all flexure joints requires numerous iterations and heavily depends on the modeling efficiency. Modeling the system is challenging due to the large number of flexible components that make up the assembled system. For example, the twelve spherical joints already consist of 144 individual flexures. Moreover, accurate modeling requires that the nonlinear stiffness characteristics of the flexures at the large strokes are taken into account. Earlier work in literature on the compliance analysis of arbitrary mechanism topologies seems limited to 2-D or linear theory [10,11].

In this paper, we present new modeling techniques for the efficient simulation of large elastic structures, such as the flexure-based hexapod. These techniques are based on a recently developed analytical formulation of the nonlinear 3-D leaf spring stiffness [4]. It has been implemented as a new beam element in flexible multibody software [5]. This element is tailored to the modeling of the support stiffness of leaf springs. A very coarse discretization, namely of only one such element per leaf spring, is already sufficiently accurate for the practical deflections of up to 15% of the length. This greatly reduces the memory usage and the computation time, enabling the modeling and optimization of large elastic structures on desktop hardware.

The contribution of this paper is a modeling strategy based on the nonlinear compliance matrix that corresponds with the leaf spring stiffness formulation. This compliance matrix can be used for the direct evaluation of the compliance of large assemblies of leaf springs. It can be readily implemented in numerical computing software, does not require dedicated static analysis software, and is available for download [6]. This modeling strategy further reduces the computational effort. It facilitates the design optimization of flexure mechanisms, for which a large number of simulations is generally required.
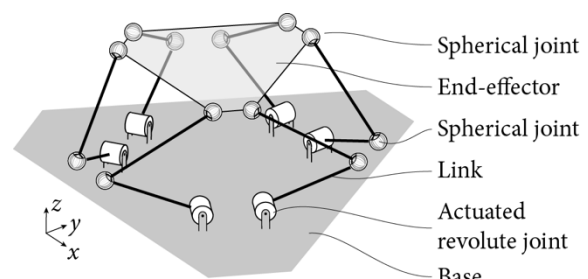
FIGURE 1. Schematic overview of the T-Flex.

T-FLEX: FULLY FLEXURE-BASED HEXAPOD

The T-Flex hexapod is a parallel manipulator with six degrees of freedom and 6RSS layout (Figure 1) [1]. The six parallel chains each contain an actuated revolute joint at the base and two passive spherical joints connected via two links. All joints are fully flexure-based and optimized for high support stiffness at large strokes [2,3]. This means that the hexapod can operate with low
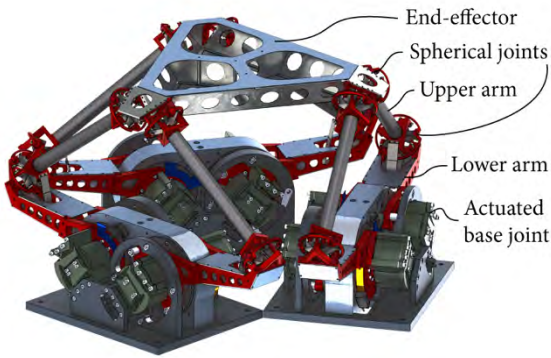
FIGURE 2 (above). Rendering of hexapod.
FIGURE 3 (right). Photograph of first prototype.
The end-effector and spherical joints are
preliminary versions made of PLA plastic.
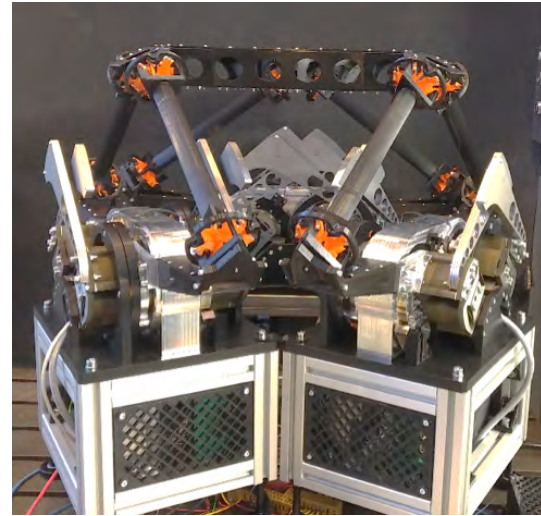
hysteresis, a high positioning repeatability (100 nm), and a large workspace (100x100x100 mm^3) relative to the mechanism's build volume (0.25 m^3). Figure 2 provides a rendering of the design. Figure 3 provides a photo of the first prototype.

LEAF SPRING STIFFNESS MODELING

The third-order stiffness formulation provides an accurate parametric description of the nonlinear static characteristics of a single leaf spring, such as error (parasitic) motion and support stiffness decrease [4,5]. This mathematical model captures the effects of in-plane and out-of-plane bending, shear, extension, torsion, warping and Wagner torque, including the geometrically nonlinear interactions in 3D. The model has been developed with the assumptions that practical leaf springs have

- a width that is the same order of magnitude as the length;
- a thickness that is two orders smaller;
- loads that are at least an order smaller than the critical buckling load.

These assumptions seem valid for a large class of leaf springs encountered in practice, especially for those in lateral loading conditions. The model has high accuracy for transverse displacements up to 15% of the leaf spring length, as verified by means of nonlinear plate elements in ANSYS.

Since the model is based on a beam formulation, a clear benefit appears when it is implemented as a numerical element; the implementation in the flexible multibody software SPACAR [7] can be used to model systems with a large number of leaf springs. Since only one such element per leaf spring is needed, this approach offers the computational efficiency of beam elements at the accuracy of a mesh of plate elements.

The computation time with a model of a single spherical joint, containing six folded leaf springs or twelve regular leaf springs, is reduced by a factor of 3 to 3.4 seconds, compared to a standard beam element model, for a simulation of the support stiffness decrease throughout the joint workspace [5].

For the T-Flex, the number of elements required in a conventional nonlinear FEM analysis with a sufficiently fine mesh is a problem on desktop hardware. The twelve spherical joints each already contain 12 leaf springs. With the new element, the models and the memory data structures, which typically scale with the square of the number of degrees of freedom, remain relatively small, enabling simulation on desktop hardware of the full system, without the need for prior simplification, such as kinematic assumptions and symmetry conditions. A simulation of the support stiffness decrease throughout the workspace at 10 steps can be performed in 171 seconds on desktop hardware. Thus, the modeling approach opens up the use of nonlinear static analysis of large flexure-based systems [5].
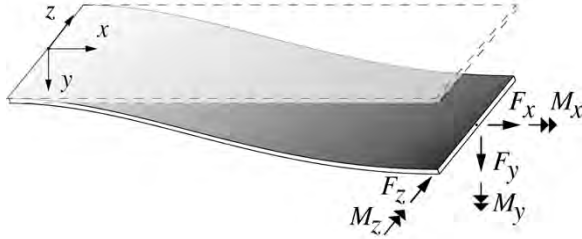
FIGURE 4. Fixed-free leaf spring loaded by forces and moments at the free end. The resulting displacements and rotations are measured at the same location.

NONLINEAR COMPLIANCE MATRIX OF A LEAF SPRING

In the previous section, the use of a recently-developed beam element in dedicated multibody software was discussed. In this section, we present an alternative way of efficiently modeling systems with a large number of flexible components, without the need for specific software. It is based on a new derivation of the compliance matrix that corresponds with the nonlinear leaf spring stiffness formulation [5]. This compliance matrix is the explicit relationship between the forces and moments applied at the free end of a fixed-free leaf spring (Figure 4), and the resulting displacements and rotations:

$$\begin{bmatrix} du_x \\ du_y \\ du_z \\ d\varphi_x \\ d\varphi_y \\ d\varphi_z \end{bmatrix} = C_{\text{leaf}} \begin{bmatrix} dF_x \\ dF_y \\ dF_z \\ dM_x \\ dM_y \\ dM_z \end{bmatrix} \quad \text{or} \quad d\boldsymbol{u} = C_{\text{leaf}} d\boldsymbol{F}$$

Here, vector $d\boldsymbol{u}$ represents small increments in the displacements and rotations, and $d\boldsymbol{F}$ represents small increments in the forces and moments at the free end. Since compliance matrix C_{leaf} is based on the nonlinear leaf spring stiffness formulation, it takes into account changes in the compliance due to the deformation of the leaf spring. This means that C_{leaf} is still a function of the *principal motion*, i.e. the intended deformation, of the leaf spring. This deformation is associated with the directions of low stiffness and used, by design, to create the intended motion of the flexure-based system. For a leaf spring, it is given by the three degrees of freedom $\varphi_x, u_y, \varphi_z$, which are due to bending out-of-plane and torsion. The compliance matrix reflects this and is given as

$$d\boldsymbol{u} = (C_0 + C_{\text{def}}(\varphi_x, u_y, \varphi_z))d\boldsymbol{F}$$

where C_0 is the standard compliance matrix based on linear analysis in the undeformed state. Matrix C_{def} is new and accounts for the geometrical nonlinearities due to the deformed state. Full expressions are provided for download in Ref. 6.

COMPLIANCE OF LARGE ASSEMBLIES OF FLEXIBLE ELEMENTS

The nonlinear compliance matrix of the previous section can be used for the efficient evaluation of the compliance of mechanisms containing a large number of leaf springs. The evaluation is a two-step process that leverages the kinematic constraint-based design procedure commonly applied to flexure mechanisms [8].

First, the principal motion is determined in a kinematic or static analysis, depending on the preferred software tools. The intended motion of the entire mechanism is determined as a function of its intended degrees of freedom. This includes the principal motion, i.e. the deformation in directions of low stiffness, of all leaf springs. This step is usually already part of the design process of the mechanism. It can be carried out with linear FEM, pseudo-rigid body models, multibody software, etc. For the hexapod, it means performing an inverse kinematic analysis that describes what all joint angles are, given a prescribed 6-DOF motion of the end-effector. From the joint angles, the principal motion of each leaf spring in the system can be calculated. Parasitic (error) motion of the leaf springs can also be determined in this step if of interest.

Second, the compliance is evaluated at a desired location on the full mechanism, in its neutral or its deformed state. A compliance model of the full mechanism can be constructed based on scaled copies of the leaf spring compliance matrix C_{leaf} to account for all leaf springs and all rigid interconnections. The principal motion of the mechanism, determined in the first step, is now the input that describes the deformed state and determines the contribution of the nonlinear compliance C_{def} to the total system compliance.

This approach works because flexure mechanisms commonly have well-defined, designed and cheaply-computed kinematic behavior. By design, loads in supporting directions produce only small motion deviations; they can be considered as small perturbations with respect to the principal motion. For this reason, only the principal motion needs to be

taken into account for an accurate prediction of the nonlinear compliance effects in all directions.

Creating a compliance model for a system of multiple leaf springs

When multiple leaf springs are connected in series, i.e. they form one chain from ground to end-effector, the compliance at the end-effector is the sum of the compliance of all components. The relative position, orientation and deformation of all individual components does need to be taken into account. It can be based on the principal motion determined in the first step of the previous section. The folded leaf spring in Figure 5 serves as an example for the approach. It consists of two identical leaf springs connected in series and at an angle.
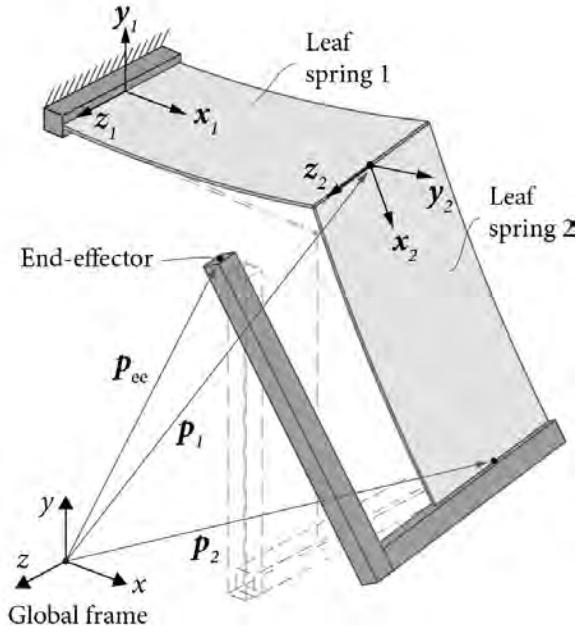
FIGURE 5. Deformed folded leaf spring as an example of the construction of a nonlinear compliance matrix at the end-effector, based on the contributions of the individual leaf springs.

The total compliance is evaluated at the end-effector location, given by vector $\boldsymbol{p}_{\text{ee}}$, and aligned with the global coordinate frame. The contribution of the first leaf spring is given by

$$C_1 = Q_1^T C_{\text{leaf}} Q_1$$

Matrix $\boldsymbol{Q}_1$ is 6×6 and performs a coordinate transformation [9] on $\boldsymbol{C}_{\text{leaf}}$ to account for the position and orientation of the first leaf spring with respect to the global frame. It is given by

$$Q_1 = \begin{bmatrix} R_1 & 0 \\ R_1 S_1 & R_1 \end{bmatrix}$$

Here, $\boldsymbol{R}_1$ is the 3×3 rotation matrix that describes the rotation of the three orthogonal vectors $\boldsymbol{x}_1, \boldsymbol{y}_1, \boldsymbol{z}_1$ that are attached to the centroid of the cross-section of leaf spring 1 at the left side (the fixed end). The rotation is described with respect to the global frame, such that

$$[\boldsymbol{x}_1 \quad \boldsymbol{y}_1 \quad \boldsymbol{z}_1] = \boldsymbol{R}_1^T$$

Matrix $\boldsymbol{S}_1$ in $\boldsymbol{Q}_1$ is the 3×3 skew-symmetric matrix

$$S_1 = \begin{bmatrix} 0 & -r_1(3) & r_1(2) \\ r_1(3) & 0 & -r_1(1) \\ -r_1(2) & r_1(1) & 0 \end{bmatrix}$$

that corresponds with vector $\boldsymbol{r}_1$, which points from the right side (the free end) of leaf spring 1 to the end-effector:

$$r_1 = p_{\text{ee}} - p_1 = [r_1(1) \quad r_1(2) \quad r_1(3)]^T$$

Whenever the end-effector location and the right side of the leaf spring do not coincide, i.e. when $\boldsymbol{r}_1$ is nonzero, it is as if there is a rigid connection between the two points.

The contribution of leaf spring 2, given by $\boldsymbol{C}_2$, can be constructed following the same steps. The total compliance at the end-effector then becomes $\boldsymbol{C}_1 + \boldsymbol{C}_2$ since the two leaf springs are connected in series.

Note that the position of both leaf spring ends ($\boldsymbol{p}_1$ and $\boldsymbol{p}_2$), the position of the end-effector ($\boldsymbol{p}_{\text{ee}}$), the orientation of the left side of leaf spring 2 ($\boldsymbol{x}_2, \boldsymbol{y}_2, \boldsymbol{z}_2$), and the unscaled compliance matrix ($\boldsymbol{C}_{\text{leaf}}$) all depend on the principal motion of the full system, i.e. on the intended deformation of the folded leaf spring in the directions of low stiffness.

This example illustrated the case of two leaf spring connected in series. When instead components are connected in parallel to an end-effector, i.e. when each component forms a separate force path from ground to end-effector, the stiffness of the individual components can be summed to obtain the total stiffness at the end-effector. The stiffness matrix is the inverse of the compliance matrix and easily obtained in a numerical evaluation. The effective compliance $\boldsymbol{C}_{\text{par}}$ at an end-effector due to two parallel-stacked

flexible components, with compliances C_3 and C_4, is given by

$$C_{\mathrm{par}} = (C_3^{-1} + C_4^{-1})^{-1}$$

One of the benefits of this direct compliance matrix approach is that it can be automated algorithmically. Also, because the compliance of each flexible component is transformed directly to the end-effector, the size of the matrices involved does not exceed 6×6, regardless of the number of components. Since the compliance matrix is an explicit closed-form nonlinear function of the principal motion, it can be evaluated quickly, without the need for iterative solving. Further, since the mathematical steps only involve standard linear algebra, it can be implemented in a wide variety of software tools.

For the simulation of the T-Flex, this approach is useful because it requires very little memory compared to more common finite element analysis, which is generally unusable for this type of mechanism. The efficiency of the particular implementation then determines the computation time. The approach is currently limited to exactly-constrained flexure mechanisms; the effects due to internal loads in overconstrained designs are not accounted for.

CONCLUSION

We have presented new modeling techniques for the efficient static analysis of flexure mechanisms with a large number of flexible components. The techniques are based on a 3-D nonlinear leaf spring stiffness formulation. With a dedicated beam element in multibody software and a direct compliance matrix evaluation approach, the nonlinear analysis and optimization of large and complex flexure mechanisms, such as the T-Flex hexapod, becomes possible.

REFERENCES

[1]   Naves M, Hakvoort WBJ, Nijenhuis M, Brouwer DM. T-Flex: A large range of motion fully flexure-based 6-DOF hexapod. Proceedings of the 20th international conference of the european society for precision engineering and nanotechnology; 2020 Jun 8-12; Geneva, Switzerland.

[2]   Naves M, Aarts RGKM, Brouwer DM. Large stroke high off-axis stiffness three degree of freedom spherical flexure joint. Precision Engineering. 2019; 56; 422-431.

[3]   Naves M, Nijenhuis M, Hakvoort WBJ, Brouwer DM. Flexure-based 60 degrees stroke actuator suspension for a high torque iron core motor. Precision Engineering. 2019; 63; 105-114.

[4]   Nijenhuis M, Meijaard JP, Brouwer DM. A spatial closed-form nonlinear stiffness model for sheet flexures based on a mixed variational principle including third-order effects. Precision Engineering. In press 2020.

[5]   Nijenhuis M. Spatial flexure mechanism analysis [dissertation]. Enschede, The Netherlands: University of Twente; 2020.

[6]   Mathematical expressions: nonlinear compliance matrix [internet]. Nijenhuis M [cited 2020 Aug 7]. http://marijnnijenhuis.nl/compliance

[7]   Jonker JB, Meijaard JP. SPACAR – Computer Program for Dynamic Analysis of Flexible Spatial Mechanisms and Manipulators. In: Schiehlen W, editor. Multibody Systems Handbook. Berlin: Springer-Verlag; 1990. p. 123-143.

[8]   Soemers HMJR. Design Principles for precision mechanisms. Enschede, The Netherlands: T-pointpress; 2010.

[9]   Grootens ME. Synthesis and Optimization of Large Stroke Flexure Hinges [MSc thesis]. Enschede, The Netherlands: University of Twente; 2014.

[10]   Su H, Shi H, Yu J. A Symbolic Formulation for Analytical Compliance Analysis and Synthesis of Flexure Mechanisms. Journal of Mechanical Design. 2012;134(5).

[11]   Kim CJ, Moon Y, Kota S. A Building Block Approach to the Conceptual Synthesis of Compliant Mechanisms Utilizing Compliance and Stiffness Ellipsoids. Journal of Mechanical Design. 2008;130(2).

DECOUPLED, OPEN-LOOP, MULTI-DOF ROTATION OF A SPHERICAL PERMANENT MAGNETIC DIPOLE ACTUATOR

Tyler T. Hamer[1], Joshua Chabot[2], and David L. Trumper[1]
[1]Department of Mechanical Engineering
Massachusetts Institute of Technology
Cambridge, MA, USA
[2]MIT Lincoln Laboratory
Lexington, MA, USA

INTRODUCTION

A spacecraft's attitude control system (ACS), which rotates the spacecraft in 3 degrees of freedom (DoFs), typically consists of multiple actuators such as reaction wheels, control moment gyroscopes (CMGs) and/or thrusters. SWaP (Size, Weight, and Power), torque generation, momentum storage, pointing stability, and reliability are all considered in choosing the actuators for an ACS. Reaction wheels have low torque generation and momentum storage whereas more efficient CMGs have large footprints due to their gimbal structures. The common use of PWM control for thrusters and mechanical bearings in reaction wheels and CMGs, introduces pointing jitter. Lastly, thrusters consume finite onboard propellant, resulting in limited mission duration.

Reaction spheres rotate a spacecraft about an arbitrary axis with an equal-and-opposite torque about their rotation axis when accelerated about that axis, similar to reaction wheels, or with an equal-and-opposite gyroscopic torque when their rotation axis is reoriented, similar to CMGs. Thus, reaction spheres operated as CMGs are potentially high efficiency torque generation choices for an ACS. Also, reaction spheres are often magnetically levitated, eliminating the need for both gimbal structures and mechanical bearings. Therefore, reaction spheres potentially have higher momentum storage, pointing accuracy, and reliability for lower SWaP too.

While NASA first proposed reaction spheres over a half century ago, limitations with previous designs have kept the technology from commercialization [1, 2]. Recently, reaction spheres with a dipole permanent magnet as the rotor have appeared promising due to their mechanical simplicity and simple modeling despite their inherent underactuation [3, 4]. Torque cannot be generated about the rotor's magnetization axis. In particular, Figure 1 depicts a bench-level prototype for a reaction
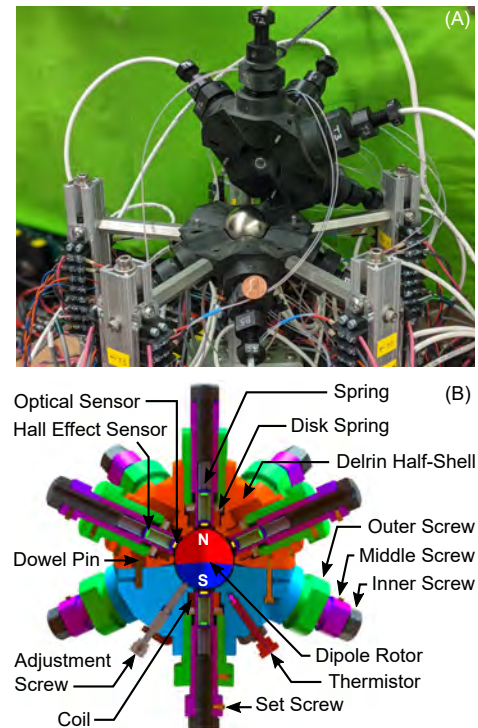
FIGURE 1. A permanent magnetic dipole reaction sphere (a) fully-wired and-assembled, bench-level prototype with (b) label cross section [5–7].

sphere with a dipole permanent magnet as the rotor that was designed and fabricated. After modeling the reaction sphere and demonstrating closed-loop vertical suspension of its dipole rotor [5], commutation laws, which decouple the rotor's dynamics, and multi-DoF-translation and-orientation sensing were implemented [6]. Afterwards, angular velocity estimation and decoupled, closed-loop, multi-DoF suspension of the rotor were demonstrated [7]. Building on the work from [5–7], this paper presents open-loop rotation of the rotor about the stator's X-,Y-, and Z-axes despite the prototype's underactuation while closed-loop multi-DoF suspension is maintained.

COIL-HALL EFFECT SENSOR CROSSTALK

A radial array of $b = 12$ equidistant Hall effect sensors measures the magnetic flux density normal to their surfaces from which the rotor's orientation is estimated [6] and in turn the rotor's angular velocity [7]. Each Hall effect sensor is coaxially aligned with one of $b = 12$ coils, offset $10.2\,\mu m$ from the coil's center so the measured magnetic flux density consists of (1) the rotor's magnetic flux density, (2) the surrounding coil's magnetic flux density known as self-crosstalk, and (3) the non-surrounding coils' magnetic flux densities known as mutual-crosstalk. Since each coil is practically a solenoid, self-crosstalk can be simply predicted as a solenoid's magnetic flux density along the axis of that solenoid and calibrated out. Mutual-crosstalk is more difficult to calculate however and calibrating out self-crosstalk is $b = 12$ operations while calibrating out all crosstalk is $b^2 = 144$ operations. Thus to avoid unnecessary complexity, both self- and mutual-crosstalk are measured to determine if just self-crosstalk or all crosstalk needs to be calibrated out.

To measure both types of crosstalk, the rotor is removed from the prototype and the ath coil's current I_{c_a} is varied sinusoidally with an amplitude of $0.75\,A$ over 90 frequencies from $1\,Hz$ to $1\,kHz$. For self-crosstalk, the magnetic flux density B_{H_a} measured by the ath Hall effect sensor, the Hall effect sensor the actuated coil surrounds, is compared to I_{c_a}. To calibrate out self-crosstalk, the actuated coil's predicted magnetic flux density $\hat{B}_{c_a}$ along that Hall effect sensor's axis, and hence that coil's axis n_{c_a}, is subtracted from B_{H_a}. Figure 3 depicts the self-crosstalk frequency response for each Hall-effect sensor and its surrounding coil before and after $(\hat{B}_{c_a} \cdot n_{c_a})$ is subtracted. For mutual-crosstalk, the magnetic flux density B_{H_1} measured by the 1st Hall effect sensor, the Hall effect sensor whose axis is along the positive Z-axis $(n_{c_1} = n_z)$ as shown in Figure 2, is compared to I_{c_a}. Figure 4 depicts the 1st Hall effect sensor's mutual-crosstalk frequency response before and after $(\hat{B}_{c_1} \cdot n_{c_1})$ is subtracted.

Calibrating out self-crosstalk reduces the magnitude of the self-crosstalk frequency response by over an order of magnitude from $650\,\mu T/A$ to a range of $3.3\,\mu T/A - 41\,\mu T/A$ at the suspension loop's crossover frequency $\omega_c = 60\,Hz$. Given each coil's power amplifier supplies at most $1.7\,A$, the maximum magnetic flux density each Hall effect sensor measures from its surrounding coil decreases from $1.1\,mT$ to a range of $5.7\,\mu T - 69\,\mu T$, both drastically less than the $120\,mT$ maximum each Hall effect sensors measures when the rotor's magnetiza-
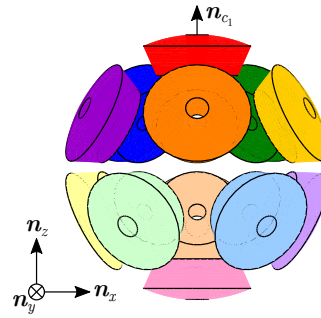
FIGURE 2. Legend for Figures 3 and 4. Coil's color corresponds to the coil which current is applied. Diametrically-opposed coils are different tints of the same color with darker coils having a +Z-position and lighter coils having a –Z-position.

tion axis aligns with that Hall effect sensor's axis. The range of magnitudes for the post-calibration self-crosstalk frequency responses reflects how accurately the self-crosstalk between each Hall effect sensor and its surrounding coil is calibrated out. The more accurate the calibration, the lower magnitude is.

Also, the magnitude of the 1st Hall effect sensor's mutual-crosstalk frequency response decreases as the distance between each coil and the 1st Hall effect sensor increases as expected. After calibration, the 1st Hall effect sensor's self-crosstalk frequency response is similar in magnitude to the 1st Hall effect sensor's mutual-crosstalk frequency responses with the closest non-surrounding coils, the 5 coils whose axis have a positive Z-component. Thus calibrating out the mutual-crosstalk for any of the coils, especially the farther away coils, yields diminishing returns, failing to justify the additional complexity.

ROTATION FREQUENCY RESPONSE

To evaluate decoupled, open-loop rotation of the rotor about the stator's X-, Y-, and Z-axes (n_x, n_y, n_z) in the frequency domain, the control current for rotation about each of those axes is varied sinusoidally with an amplitude of $0.75\,A$ from $1\,Hz$ to $1\,kHz$ while the suspension control loops keeps the rotor centered within the stator. Proper commutation of the coils has 2 effects: (1) Proper commutation constantly reorients the rotor such that the rotor's magnetization axis is orthogonal to the control current's rotation axis, enabling rotation about any axis in 3 dimensions even though torque cannot be generated about the rotor's magnetization axis. (2) Proper commutation decouples the rotor's (plant's) translational and rotational DoF, roughly reducing the rotational plant dynamics to that of a free mass:

$$P_{\omega_a \omega_a}(s) = \frac{\Omega_a}{I_{\omega_a}} \approx \frac{K_T}{Js}, \qquad (1)$$
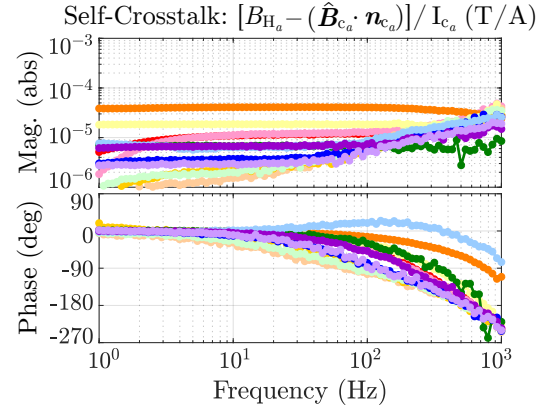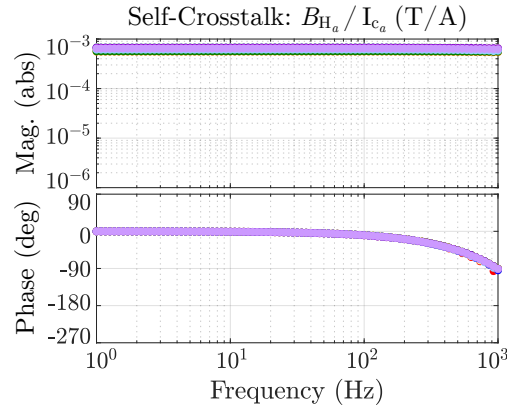
FIGURE 3. Frequency response for self-crosstalk, the magnetic flux density each Hall effect sensor measures when its surrounding coil is excited, (left) before and (right) after self-crosstalk is calibrated out. Legend provided in Figure 2.
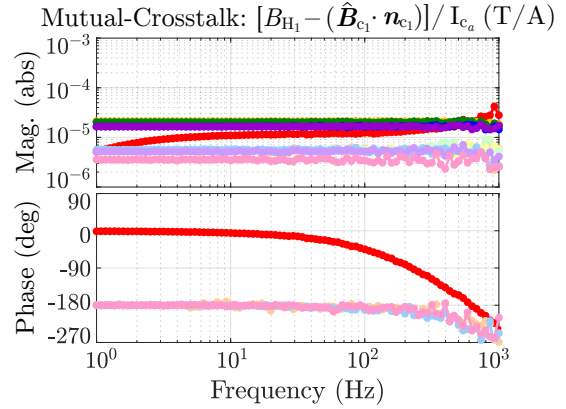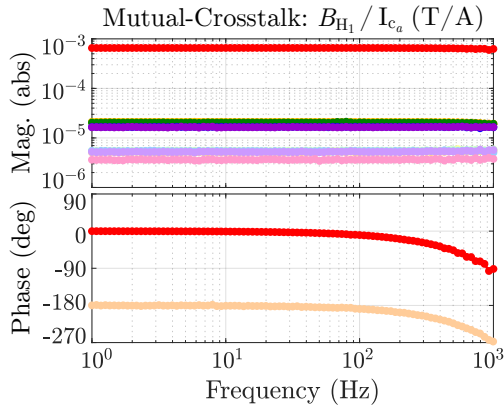
FIGURE 4. 1st Hall effect sensor's frequency response for mutual-crosstalk, the magnetic flux density the 1st Hall effect sensor measures when its non-surrounding coils are excited, (left) before and (right) after self-crosstalk is calibrated out. Legend provided in Figure 2.

where $P_{\omega_a \omega_a}(s)$ is the open-loop rotational plant transfer function given by the ratio of rotor's angular velocity Ω_a about the ath axis to the control current I_{ω_a} applied for rotation about the ath axis. $J = 31.4\,\mathrm{mg/m^2}$ is the rotor's moment of inertia about any axis as the rotor is a sphere and K_T is the single-coil torque constant. K_T is predicted to be 22.6 mN·m/A, double the value calculated in [5] due to a missing factor of 2 in analytic expression in [5].

The measured rotational plant frequency responses before and after calibrating out self-crosstalk depicted as bode plots in Figure 5 respectively, is a composite of frequency responses measured once the rotor's magnetization axis is orthogonal to each control current's rotation axis, rather than the instantaneous frequency responses. A composite of frequency responses is measured as the torque commutation law immediately reorients the rotor such that the rotor's magnetization axis is orthogonal to the control current's rotation axis. At low frequencies, the on-diagonal frequency re-

sponses are 2-3 orders greater in magnitude than the off-diagonal frequency responses, validating the torque commutation law decouples the rotor's rotational DoF. Additionally at low frequencies, the on-diagonal responses are well modeled by Equation (1), verifying the rotor is reoriented and then rotated as a free mass about any axis in 3 dimensions, despite the rotor's underactuation.

At high frequencies, every rotational frequency response increases at a rate of 1 order of magnitude per decade due to the coil-Hall effect sensor crosstalk. Since physically the rotor is a free mass, changes in both the rotor's angular velocity and magnetic flux density due to coil excitation decrease as the excitation frequency increases in accordance with Equation (1), whereas the crosstalk remains flat as shown in Figures 3 and 4. Thus at high frequencies, the component of the measured magnetic flux densities at the excitation frequency is dominated by crosstalk. Correspondingly, the frequency at which crosstalk begins to dominate in-
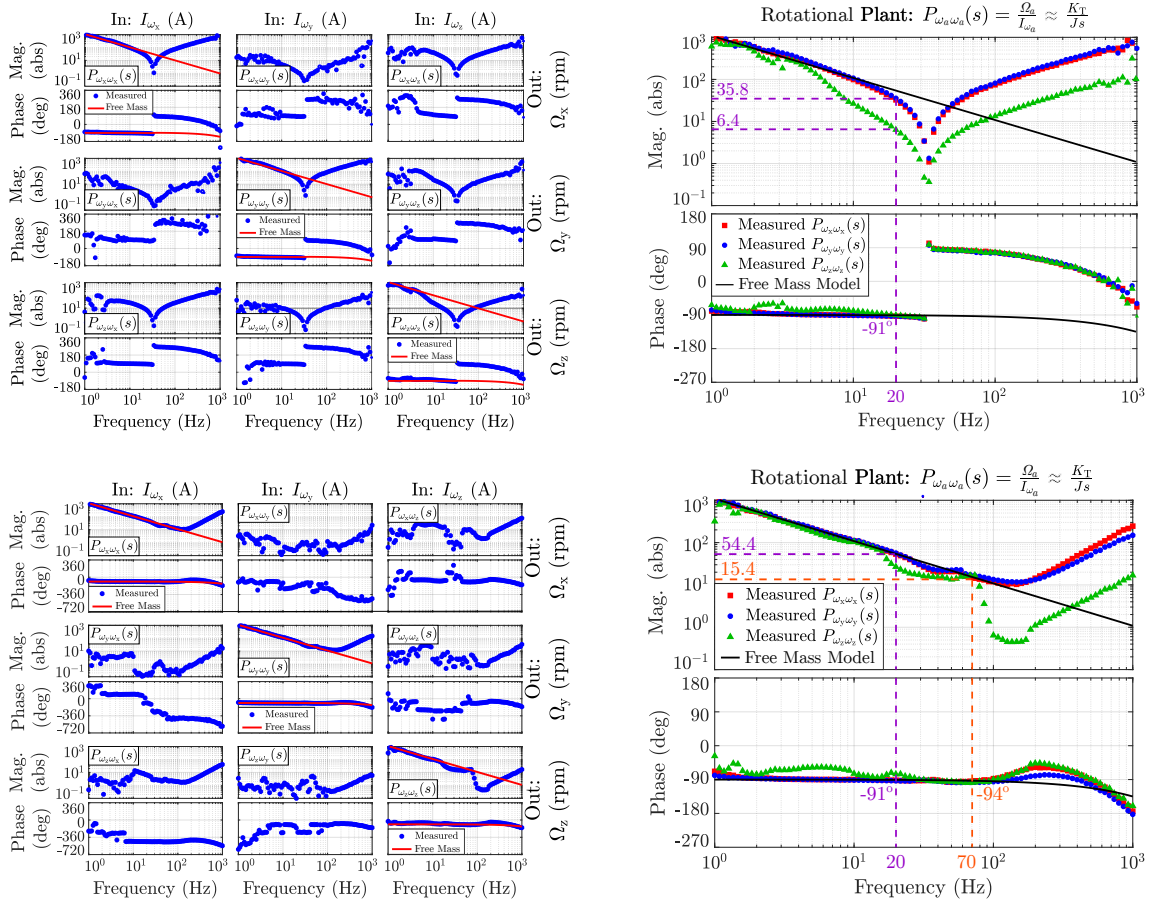
FIGURE 5. Composite of rotational plant frequency responses (top row) before and (bottom row) after self-crosstalk is calibrated out. (left column) The 3×3 multi-input multi-output (MIMO) frequency response matrix's columns and (right column) the on-diagonal frequency responses are measured once the rotor's magnetization axis is orthogonal to the control current's rotation axis.

creases when self-crosstalk is calibrated out. After a least squares fit of the magnetic flux densities measured by the Hall effect sensors to determine the rotor's orientation, the change in the rotor's orientation is differentiated to estimate the rotor's angular velocity. This differentiation tilts the crosstalk frequency responses from flat to increasing at a rate of 1 order of magnitude per decade so the rotational plant frequency response increases at that rate too.

Lastly, the magnitude dip in the Z-axis's on-diagonal response is a frequency-dependent nonlinearity corresponding to a decrease in K_{T} for rotation about the Z-axis. Since gravity points along the Z-axis, the rotor's most energy efficient orientation to offset gravity occurs when the rotor's magnetization axis is along the Z-axis. Thus while the torque commutation law attempts to reorient the rotor such that the rotor's magnetization axis is orthogonal to the Z-axis when commanded to rotate about the Z-axis, the force commutation law attempts to realign the rotor's magnetization axis with the Z-axis. At

frequencies where crosstalk is significant, the force commutation law prevents the torque commutation law from fully orienting the rotor such the rotor's magnetization axis is orthogonal to the Z-axis, resulting in a lower K_{T} and in turn a lower magnitude in the frequency response.

ROTATION TIME RESPONSE
To evaluate decoupled, open-loop rotation of the rotor about the stator's X-, Y-, and Z-axes (n_x, n_y, n_z) in the time domain, the control current for rotation about each of those axes is stepped to 0.75 A and back and then to –0.75 A and back to generate 1280 rpm trapezoidal angular velocity profiles while the suspension control loops keeps the rotor centered within the stator. Again, proper commutation reorients the rotor so rotation about the desired axis is controllable and decouples the rotor's dynamics. Figure 6 shows these time responses for open-loop rotation of the rotor about the stator's X-, Y-, and Z-axes in terms of the rotor's angular velocity and the orbit of the rotor's magnetization axis. Figure 7 sep-
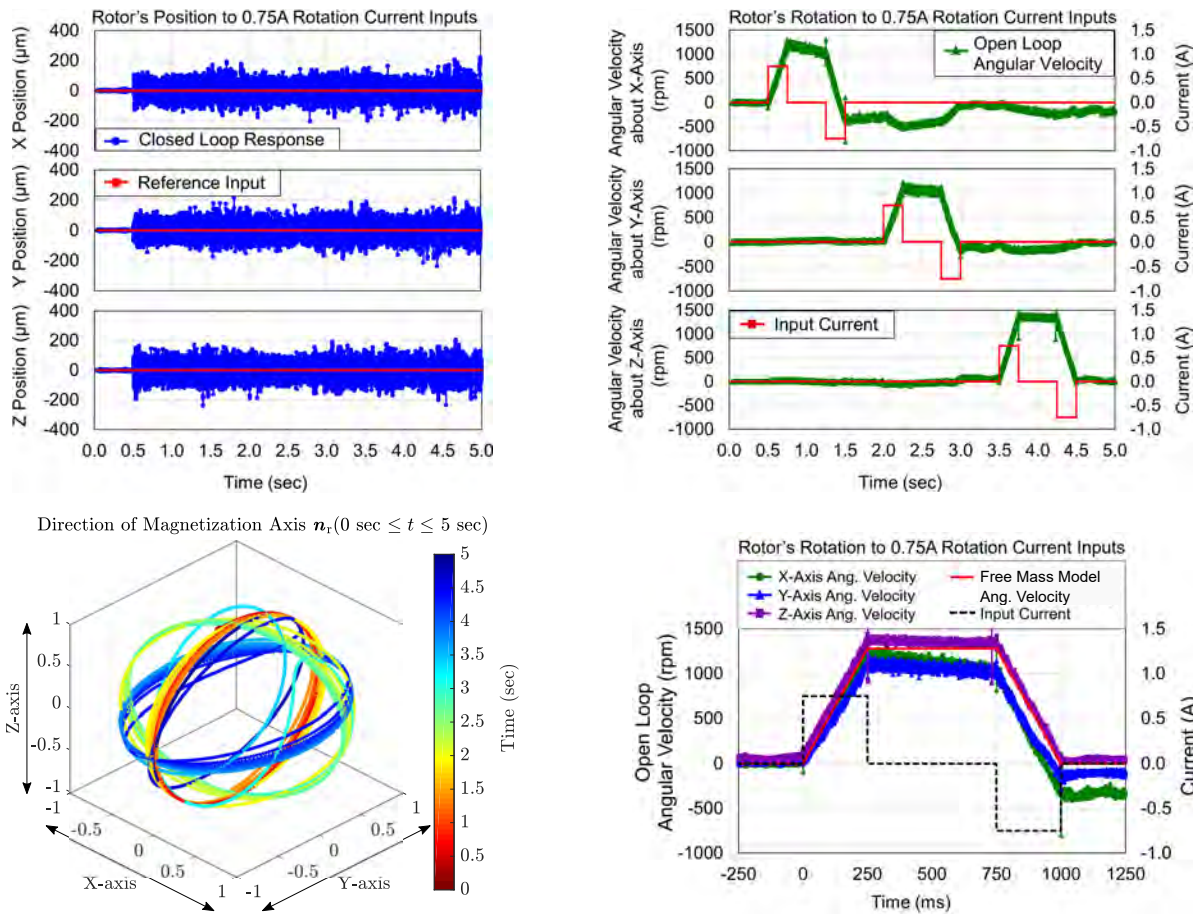
FIGURE 6. Time response of (upper-left) the rotor's 3D position, (upper right) 3D angular velocity, and (lower left) magnetization axis's direction $\boldsymbol{n}_{\mathrm{r}}$ for $\pm$ 0.75 A rotation current steps applied to generate trapezoidal angular velocity profiles. (lower right) Angular velocity time responses are overlaid against the modeled time response of a spherical free mass.

arates the orbit of the rotor's magnetization axis for rotation about each axis. Additionally, Figure 6 compares the angular velocity time responses against the open-loop time response of a free mass (Equation (1)) and shows the cross-coupled, closed-loop time response of the 3 translational DoFs.

The rotor successfully rotates about the stator's X-, Y-, and Z-axes axes despite the rotor's underactuation. During each trapezoidal angular velocity profile's ramp up, the rotor's angular velocity about each axis increases by $1120 - 1370$ rpm in 250 ms versus a predicted 1280 rpm, corresponding to a measured K_T of $19.1 - 22.4$ mN·m/A, within $0.73 - 15\%$ of the predicted K_T of 22.6 mN·m/A. Additionally, the rotor's angular velocity drifts $14.9 - 169$ rpm over 500 ms during each trapezoidal angular velocity profile's constant part and the rotor's average rotation axis $E[\boldsymbol{n}_\omega(t)]$ is within $1.6° - 25.6°$ of the desired rotation axis over the entire trapezoidal angular velocity profile. Both drift and the rotation axis's misalignment can be reduced with feedback.

Finally, rotation about each axis produces only minor rotations about the other axes and deviations in the rotor's position, supporting all the rotor's DoF are decoupled. However, once the rotor begins to rotate, noise in the rotor's position increases as the performance of the optical sensors used for translation feedback degrades as previously seen [7].

CONCLUSION
Compared to reaction wheels, CMGs, and thrusters, reaction spheres are options for ACSs with potentially lower SWaP (Size, Wight, and Power) and potentially higher torque generation, momentum storage, pointing accuracy, and reliability. This paper continues the work from [5–7] on a reaction sphere with a dipole permanent magnet as the rotor. In particular, crosstalk between the reaction sphere's coils and Hall effect sensors was examined and decoupled, open-loop rotation of the bench-level prototype's rotor about the stator's X-, Y-, and Z-axes while the rotor is simultaneously closed-loop, multi-DoF suspended was presented.

Direction of Magnetization Axis $\boldsymbol{n}_\mathrm{r}(0.5\ \mathrm{sec} \leq t \leq 1.5\ \mathrm{sec})$

Direction of Magnetization Axis $\boldsymbol{n}_\mathrm{r}(2.0\ \mathrm{sec} \leq t \leq 3.0\ \mathrm{sec})$

Direction of Magnetization Axis $\boldsymbol{n}_\mathrm{r}(3.5\ \mathrm{sec} \leq t \leq 4.5\ \mathrm{sec})$
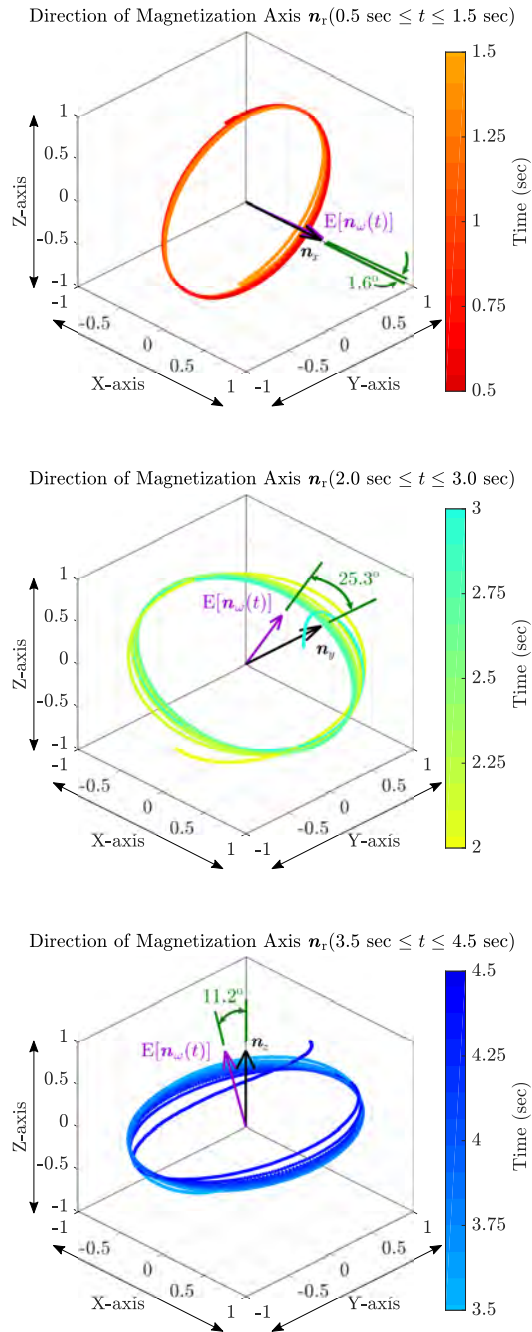
FIGURE 7. *Direction of rotor's magnetization axis during the trapezoidal angular velocity profiles shown in Figure 6.*

Crosstalk was split into two categories: (1) self-crosstalk, a coil's magnetic flux density measured by the Hall effect sensor that coil surrounds and (2) mutual crosstalk, the non-surrounding coils' magnetic flux densities measured by that Hall effect sensor. To reduce complexity, only self-crosstalk was calibrated out as self-crosstalk could only be reduced to the levels of mutual-crosstalk, not beyond. Proper commutation of the coils had 2 effects: (1)

Proper commutation constantly reoriented the rotor such that the rotor's magnetization axis was orthogonal to the control current's rotation axis and (2) decoupled both the rotor's translational and rotational dynamics. As a result, the rotor was successfully rotated about the stator's X-, Y-, and Z-axes despite torque cannot be generated about the rotor's magnetization axis. Lastly, the rotor's rotational dynamics initially resembled that of a free mass only at low frequencies until self-crosstalk was calibrated out.

References

[1] Zhu L, Guo J, Gill E. Review of reaction spheres for spacecraft attitude control. Progress in Aerospace Sciences. 2017 May;91:67–86.

[2] Zhang J, Yuan L, Chen SL, Liang Y, Huang X, Zhang C, et al. A survey on design of reaction spheres and associated speed and orientation measurement technologies. ISA transactions. 2020 April;99:417–431.

[3] Wang J, Jewell GW, Howe D. Analysis, design and control of a novel spherical permanent-magnet actuator. IEE Proceedings - Electric Power Applications. 1998 January;145(1):61–71.

[4] Chabot J. A Spherical Magnetic Dipole Actuator for Spacecraft Attitude Control [Master's Thesis]. Aerospace Engineering Sciences, University of Colorado. Boulder, CO, USA; 2015.

[5] Hamer TT, Noh M, Zhou L, Chabot J, Trumper DL. A Magnetically Suspended, Spherical Permanent Magnetic Dipole Actuator. In: Proceedings of The Thirty-Third Annual Meeting of the American Society for Precision Engineering, Las Vegas, NV, USA. ASPE; 2018. p. 70–75.

[6] Hamer TT, Chabot J, Trumper DL. Sensing And Commutation Of A Spherical Permanent Magnetic Dipole Actuator. In: Proceedings of the Thirty-Fourth Annual Meeting of the American Society for Precision Engineering, Pittsburgh, PA, USA. ASPE; 2019. p. 115–120.

[7] Hamer TT, Chabot J, Trumper DL. Decoupled, Closed-Loop, Multi-DoF Suspension of a Spherical Permanent Magnetic Dipole Actuator. In: Proceedings of the American Society for Precision Engineering 2020 Spring Topical Meeting on Design and Control of Precision Mechatronics Systems, Cambridge, MA, USA. ASPE; 2020. p. 31–36.

MAGNETIC LEVITATED LINEAR SCAN MODULE WITH NANOMETER RESOLUTION

Alexander Goos, Roman Ehrle, Daniel Geissler, Rainer Gloess
Physik Instrumente (PI) GmbH &Co.KG
76228 Karlsruhe, Germany

INTRODUCTION

The paper describes a new magnetic levitation system, stabilized and movable in all 6 degrees of freedom (DOF) for high accurate positioning applications. In the last two decades, a couple of magnetic levitation systems were developed for friction free motion of objects in space (e.g. [1-4]). This magnetic levitation technology works without any mechanical guiding system or joint configuration – the main challenge for high-precision systems in the past century.

Figure 1 shows the new linear magnetic levitating stage with 6 DOF. The movable platform is fully passive without any cable connection and because of this, there is no mechanical friction. All cables are only connected with the stator. This allows the stage to prevent any particle generation in operation, so it is suitable for cleanroom conditions.

Because of gravity force compensation, the stage can levitate nearly powerless with a load of up to a few kilograms. The system is using incremental sensors for providing nanometer resolution.

A Field Programmable Gate Array (FPGA) is used for managing the signals between sensors, amplifiers and the control unit. A state feedback control with I-term and observer is implemented for stabilizing the system.
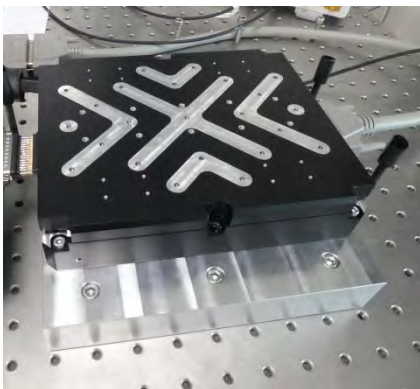
FIGURE 1. Magnetic levitating stage.

SYSTEM CONCEPT

The stage comprises a stator and a movable platform, as shown in Figure 2. All encoders and motors are part of the stator.

The stage uses three types of motors. Four electromagnets generate the lifting force (Z) and also the torques for pitch and roll. The electromagnets are biased with permanent magnets. So by varying the levitation height dependent on the payload, it is possible to levitate nearly powerless.

With Lorentz force motors the stage can do a transversal movement (Y) and rotate around the Z-axis. Lorentz force motors are used, because this type of motor is easy to control due to its linear force characteristic.

A 3-phase linear motor is used combined with a Halbach array to move the platform along the main axis (X).
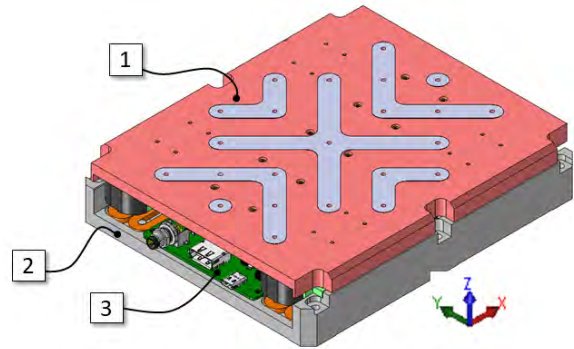
FIGURE 2. Linear magnetic levitation stage comprising:
1) Movable platform
2) Stator
3) Main board

Four optical encoders are placed on each of two sensor boards, so eight encoders are used to sense the position of the movable platform.
After interpolation each sensor has nanometer resolution with a standard deviation of 10 nm.

Although the system is a linear stage, it is controlled in all 6 DOF. So there are a lot of

sensors and amplifiers which have to be read out and driven. Figure 3 shows the electronic architecture.

Two Digital Signal Processors (DSP) located on the main board inside the stage are used for current control. An external master controller is connected to a FPGA via serial bus. The FPGA works as a bridge, which shares the target current values from the master device to the DSP and sends the actual position values from the sensors to the master. For the moment the position loop is closed in the master device, but with this architecture it would be also possible to close the loop within one or both DSP inside the stage without any external Controller.
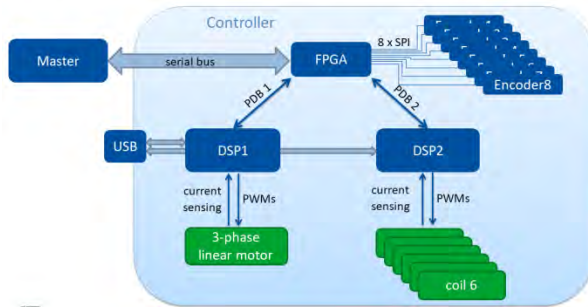
FIGURE 3. Signal path structure of electronics.

All pulse width modulation (PWM) control signals are synchronized to reduce/avoid coupling effects. The architecture also enables parallel position measurement to reduce dead time.

SYSTEM IDENTIFICATION

To stabilize the actuator a MIMO (Multiple Input Multiple Output) state space control is used with additional I-term and Luenberger observer. This control structure is already well known [5].

The control model is simplified with decoupling units in such a way, that the inputs are forces and torques of the Cartesian coordinate system, represented in N and Nm. The outputs of the system are the positions of the Cartesian coordinate system in mm and mrad. This is illustrated in Figure 4.

The stage has both redundant motors and redundant sensors. So the decoupling matrices are not symmetric and there is more than one solution for decoupling the system.
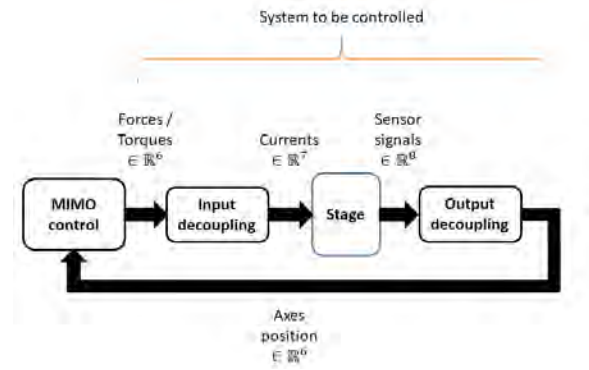
FIGURE 4. Signal path of the control system.

After establishing the differential equations, it is possible to calculate the state feedbacks, the observer parameters and levitate the stage.

For validation of theoretically derived models, black box identification was done.

To do a frequency response measurement it is necessary to close the control loop of the stage.

The system was disturbed actively with broadband noise and to reduce the effect of sensor noise, the results were improved by averaging with Welch's method [6]. Therefor the frequency response was calculated with the cross power spectral densities.

$$S_{xy}(i\omega) = \int_{-\infty}^{\infty} R_{xy}(\tau)e^{-i\omega\tau}d\tau \qquad (1)$$

Figure 5 shows a standard control loop, where "r" is the target value, "d" the disturbance, "y" the output of the system and "n" the sensor noise. The calculation of the frequency response is easier, if the target value "r" is set to zero.
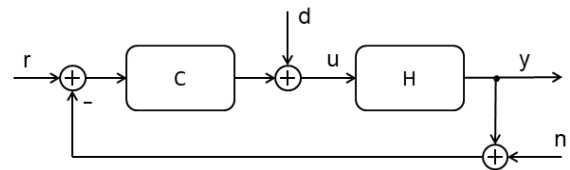
FIGURE 5. Standard control loop.

With r=0 the system input $U(f)$ can be calculated as:

$$U(f) = D(f) \cdot \frac{1}{1 + HC} + N(f) \cdot \frac{-C}{1 + HC} \qquad (2)$$

To get the cross power spectral densities the equation is multiplied with $D^*(f)$.

$$S_{DU} = S_{DD} \cdot \frac{1}{1 + HC} + S_{DN} \cdot \frac{-C}{1 + HC} \qquad (3)$$

S_{DN} can be assumed to zero, because the signals $N(f)$ and $D(f)$ are uncorrelated. So the sensitivity function can be written as:

$$\frac{S_{DU}}{S_{DD}} = \frac{1}{1 + HC} = S(f) \qquad (4)$$

The process sensitivity function can be calculated like the sensitivity function and results to:

$$\frac{S_{DY}}{S_{DD}} = \frac{H}{1 + HC} = PS(f) \qquad (5)$$

The sensitivity $S(f)$ and the process sensitivity $PS(f)$ can be used to calculate the system response $H(f)$ within closed loop.

$$\frac{PS(f)}{S(f)} = \frac{S_{DY} \cdot S_{DD}}{S_{DD} \cdot S_{DU}} = \frac{S_{DY}}{S_{DU}} = H(f) \qquad (6)$$

It should also be mentioned that both sensitivity and process sensitivity in case of MIMO systems are matrices of transfer functions.
So the system model $H(s)$ is a matrix of transfer functions.

A tool was written to calculate the system response $H(f)$ with the measurement data. With this tool it is also possible to fit easily a transfer function $\hat{H}(s)$ to the corresponding frequency response $H(f)$, by adding poles and zeros into a pole-zero graph. An optimization routine changes the position of the poles and zeros using least squares method in such a way, that the model fits to the frequency data. (Figure 6)
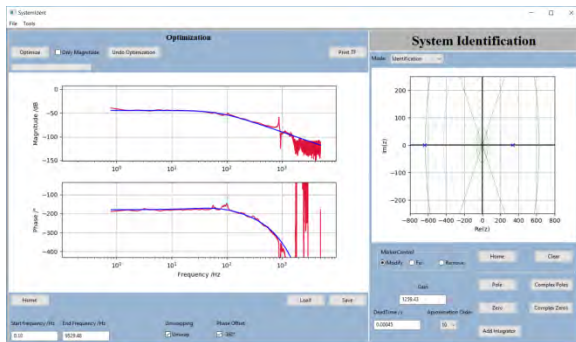
FIGURE 6. System Identification Tool. With this self-written tool it is possible to fit linear models with dead time on measurement data.

Figure 7 shows the pole-zero graph of the system model based on the established differential equations and based on the measurement fits. To prevent large servo calculation times, the model order is reduced to a minimum. So the system is modelled as a single mass system.
As you can see there is a deviation with several influences. This results in a not perfect model, but with system identification that's not a problem at all. On the one hand it is possible to use the fitted model for control synthesis, on the other hand it provides a hint which model part needs more accuracy.
Figure 7 shows three poles in the right half of the pole-zero diagram, which results in an unstable system. To stabilize the system these poles have to be moved to the left half of the diagram.

The goal was to get a closed loop bandwidth of about 500-600 rad/s for all Cartesian axes. So the state feedbacks for the fitted system were calculated via pole placement such that the bandwidth was reached and the controlled system is well damped. The calculation and simulation were done with continuous-time models. This is not very restrictive, because the actual sample frequency of the control loop is 10 kHz. In future the sample frequency will be increased.
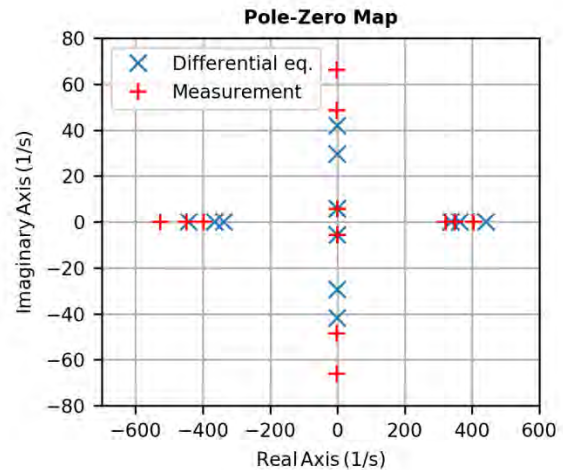
FIGURE 7. Pole-Zero Map of the system model based on differential equations and measured data. Poles are represented with "x" and "+".

To check the closed loop behavior, closed loop frequency response measurements and step response measurements with the real system were done. For example Figure 8 shows a 10 μm closed loop step along the X-axis without

additional I-term. Simulation, based on the fitted system model, and measurement match well, even if the measurement data shows a slightly faster response.
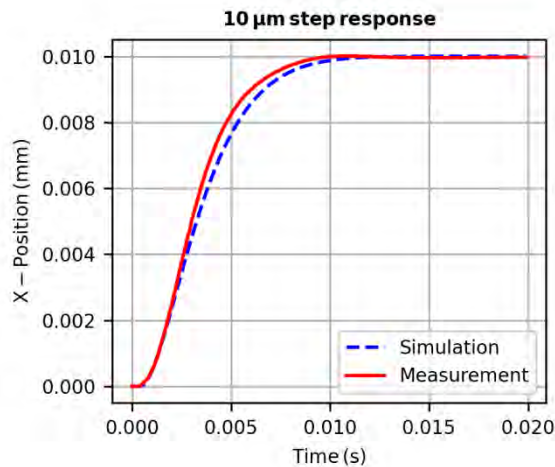
FIGURE 8. 10 µm closed loop step response of state controlled X-Axis without I-term. Simulation vs. Measurement (internal sensors).

To get stationary accuracy a cascaded integrator is implemented. This results in a slower closed loop step response, but with feedforward terms it is possible to compensate this behavior.

POSITION MEASUREMENT
With an external interferometer position measurements were done. The resulting position noise in steady state condition was 5 nm (RMS).

An advantage of magnetic levitated systems compared to mechanical guided systems is the absence of friction. So there are no stick-slip effects at all, which results in a fast transient oscillation without the need of nonlinear control algorithms. This advantage can be seen in Figure 9, which is showing a 100 nm step.

To check the repeatability of the stage, also a step stair with a step width of 100 nm was measured. (Figure 10).
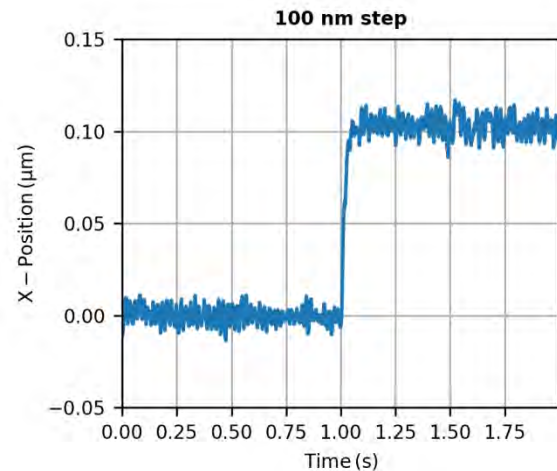
FIGURE 9. 100 nm step (raw external sensor data).
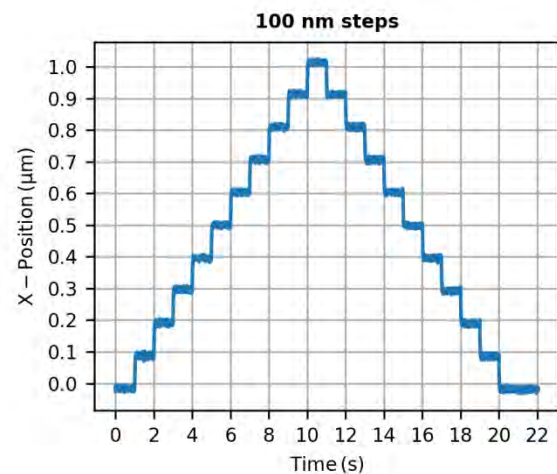
FIGURE 10. Step stair with a step width of 100 nm (raw external sensor data).

SUMMARY
This paper presented an overview of a new linear magnetic levitation stage. It was shown both the black box system identification results and closed loop step response behavior. The closed loop bandwidth is about 500-600 rad/s and was verified by frequency response measurements and step responses.
The resulting position noise in steady state condition was 5 nm (RMS).

REFERENCES
[1] L. Zhou, D. Trumper, Magnetically levitated linear stage for in-vacuum transportation tasks. In: 33 Annual Conference ASPE; 2018. p.1–6.
[2] W.Kim, D. Trumper. High-precision magnetic levitation stage for photo lithography

Precision Eng. 22 2, 1998. p.66-77.

[3]   R.Gloess,   Ch.Mock,   Ch.Rudolf,
      C.Walenda, Ch.Schaeffel, M.Katzschmann,
      H.-U. Mohr. Magnetic Levitation in 6- DOF
      with   Halbach   Array   Configuration.
      ACTUATOR 2010. Bremen.

[4]   R. Gloess. Mag-6D a new mechatronics
      design of a levitation stage with nanometer
      resolution. ASPE Proceedings. Portland
      2016.

[5]   G. F. Franklin, J. D. Powell, A. Emami-
      Naeini. Feedback Control of Dynamic
      Systems. 3rd ed. 1993. p.469-601.

[6]   R. Isermann, M. Muenchhof. Identification
      of Dynamic Systems – An Introduction with
      Applications. 2011. p.51, 95.

VIBRATION MITIGATION ON PRECISION BALL-SCREW FEED-DRIVES THROUGH DATA-DRIVEN TUNING OF TRAJECTORY PRE-FILTERS

Alper Dumanli, Burak Sencer
School of Mechanical, Industrial and Manufacturing Engineering
Oregon State University
Corvallis, Oregon, USA

INTRODUCTION

Their high torque/force transmission ratio and low design costs make ball-screw drives a widely-used choice in design of modern motion systems. Ball-screw drives are used in variety of manufacturing equipment ranging from low cost motion platforms to ultra-precision and high-speed machine tools. Nevertheless, a well-known weakness of ball-screw drives is their structural dynamics as they suffer from various vibration modes, which limit their achievable dynamic stiffness. These lightly damped structural resonances can be excited easily during high-speed motion either by the reference command trajectory or by external disturbances. Excitations originating from disturbance forces can only be rejected by design of feedback controller that inject modal damping to the system [1], [2]. However, excitation due to reference trajectory can be mitigated through careful design of feedforward control [3].

This paper presents a novel 2-step filtering method, which modulates reference trajectories to avoid excitation of ball-screw resonances in a feedforward manner. The filter tuning is achieved fully autonomously, where filter parameters are tuned iteratively by making use of convex optimization and motion data collected in operation. The proposed trajectory pre-filter is presented in Fig. 1. The two trajectory pre-filters; so-called the *Rotary Command Generator (RCG)* and *Closed Loop Dynamics Compensator (CLDC)* are used to modulate the reference trajectory such that the table position follows the desired command position. Their structure is pre-determined but their parameters are tuned automatically through hardware-in-the-loop iterations as explained in the following sections. The RCG pre-filter in Fig. 1 targets the motor side anti-resonance to mitigate table vibrations excited due to frequency spectrum of reference trajectory. The CLDC filter, on the other hand, aims to avoid trajectory induced resonance vibrations and widen the closed-loop tracking bandwidth. Design, tuning and validation of the pre-filters are presented systematically in the following Sections.

MODELING OF BALL-SCREW DYNAMICS

Flexible ball-screw feed drive systems are typically modeled as a lumped-mass a 2DOF system as shown in Fig. 1, and the equation of motion can be written as:

$$m_M \ddot{x}_M = u - b_M \dot{x}_M - c(\dot{x}_M - \dot{x}_T) - k(x_M - x_T)$$
$$m_T \ddot{x}_T = -b_T \dot{x}_T - c(\dot{x}_T - \dot{x}_M) - k(x_T - x_M) \quad (1)$$

where x_M and x_T are motor and table displacements, and m_T and m_M are the table and motor masses. u is the control signal (torque, or current) applied by the motor.
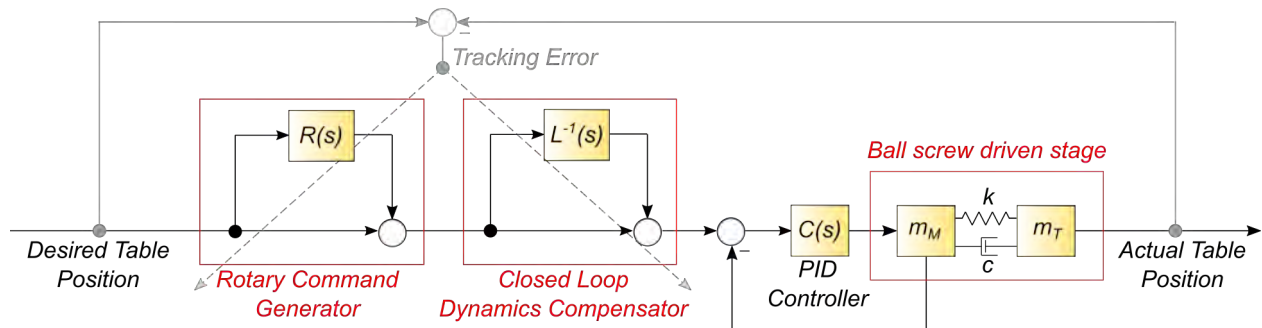
FIGURE 1: Block diagram of the proposed tuning and control strategy, where $L^{-1}(s)$ is the estimated inverse loop transmission transfer function.

k is the equivalent stiffness, which is mainly dictated by ball-screw, nut and support bearing stiffnesses and c is the damping coefficient. b_M and b_T denotes viscous friction coefficients acting on motor and table. In ultra-precision applications, table side friction may be negligible $b_T=0$ by the use of air-bearing supports. Eq. (1) is put in the transfer function (TF) form as:

$$G_M = \frac{X_M}{U} = \frac{m_T s^2 + cs + k}{P}, \quad G_T = \frac{X_T}{U} = \frac{cs + k}{P}$$

$$P = m_M m_T s^4 + \left(m_T b_M + c\left(m_M + m_T\right)\right)s^3 \cdots \quad (2)$$
$$+ \left(b_M c + k\left(m_M + m_T\right)\right)s^2 + b_M k s$$

where G_M and G_T denote motor and table side transfer functions, e.g. collocated and non-collocated transfer dynamics.

Notice that based on where the feedback measurement is taken, transfer dynamics vary. This is illustrated in Fig. 2.

a) Experimental Setup
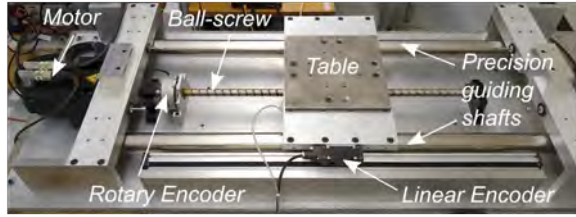
b) Ball-screw Frequency Response Functions
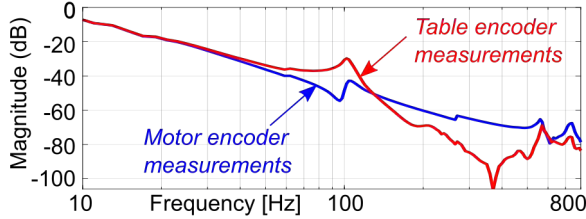
c) Vibration mode
eliminated by RCG
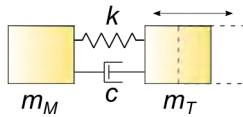
d) Vibration mode
eliminated by CLDC
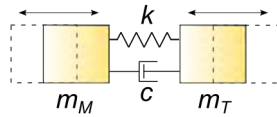
FIGURE 2: Experimental setup (a) and its open loop FRFs (b). Illustration of vibration modes that are cancelled by Rotary Command Generator (RCG, c) and Closed Loop Dynamics Compensator (CLDC, d).

In case of non-collocated control, e.g. when $G_T(s)$ is used, transfer dynamics suffer only from a resonance behavior at which both motor and table vibrate out of phase of phase at

$\omega_n \cong 105$[Hz]. On the other hand, when collocated control scheme is implemented, only motor-side feedback is utilized and G_M represents the plant dynamics. In this case, the system exhibits an additional anti-resonance at $\omega_z \cong 95$[Hz] during which table vibrates w.r.t to the motor.

In practice, majority of ball-screw systems are controlled in a "collocated" fashion where feedback is taken only from the motor side encoder. However, the ultimate positioning goal is still to ensure that the table tracks the reference trajectory precisely. Therefore, the objective of the proposed pre-filter design is to compensate flexible ball-screw dynamics during collocated control operation.

DESIGN OF ROTARY COMMAND GENERATOR (RCG) PRE-FILTER

This section introduces design of the RCG pre-filter R(s). The design principle is to attenuate the anti-resonance by mitigating the vibration of the table w.r.t the motor. Thus, the objective is to essentially cancel 2nd order structural dynamics between motor and table (G_T/G_M) from Eq. (2). Note from Fig. 1 that when RCG is applied, pre-filtered trajectory $1+R(s)$ should invert transfer dynamics between motor and the table by:

$$1 + R(s) \cong \frac{G_M}{G_T} \rightarrow R(s) = \underbrace{\frac{m_T}{k}}_{m_k} s^2 + \underbrace{\frac{c}{k}}_{c_k} s \quad (3)$$

where RCG form follows a 2nd order high-pass filter. m_k and c_k are stiffness-normalized table mass and viscous friction that needs to be identified.

Identification of $R(s)$ filter parameters are realized automatically through convex hardware-in-the loop iterations. The objective is to minimize the discrepancy between uncompensated motor ($\mathbf{x}_{Mu}$) and table displacement ($\mathbf{x}_T$):

$$J_{RCG} = \min_{\theta = [m_k, c_k]} \left(J_{RCG} = \frac{1}{2}\left(\mathbf{x}_T - \mathbf{x}_{Mu}\right)^T \left(\mathbf{x}_T - \mathbf{x}_{Mu}\right) \right) \quad (4)$$

by converting to optimal $\theta = [m_k \ c_k]$. This optimization problem is solved by making use of Newton's second order iterations:

$$\begin{bmatrix} m_k \\ c_k \end{bmatrix}^{n+1} = \begin{bmatrix} m_k \\ c_k \end{bmatrix}^n - \alpha \left(\nabla^2 J_{RCG}\right)^{-1} \left(\nabla J_{RCG}\right) \quad (5)$$

where n is the iteration counter, and α is learning rate, which can be selected within the interval [0, 1] for reliable convergence. Gradient

∇J_{RCG} and Hessian $\nabla^2 J_{RCG}$ must be determined for reliable convergence. In this work they are calculated based on the data collected during basic motion experiments. As shown in Fig. 4.a, the ball-screw system is commanded by a simple back-and-forth motion trajectory, and motion data is collected. The gradient/Hessian are extracted directly from motion data analytically during each iteration where:

$$\nabla J_{RCG} = \left(\nabla\left(\mathbf{x}_T - \mathbf{x}_{Mu}\right)\right)^T \left(\mathbf{x}_T - \mathbf{x}_{Mu}\right)$$

$$\nabla^2 J_{RCG} = \left(\nabla\left(\mathbf{x}_T - \mathbf{x}_{Mu}\right)\right)^T \left(\nabla\left(\mathbf{x}_T - \mathbf{x}_{Mu}\right)\right) \quad (6)$$

$$\text{with:} \quad \nabla = \left[\frac{\partial}{\partial m_k} \quad \frac{\partial}{\partial c_k}\right]^T$$

All the signals in Eq. (6) can be measured easily during a basic motion test. If the system is not equipped with a table side encoder, a low-cost accelerometer can be used to measure x_T. x_{Mu} is the original uncompensated motor position, which need to be recorded only once by the rotary encoder.

Notice that gradients in Eq. (5) are updated based on the collected data at each iteration, n. $\nabla(x_T - x_{Mu})$ can be expressed from closed loop tracking dynamics as:

$$x_T - x_{Mu} = \left(1+R\right)x_R \frac{G_T C}{1+G_M C} - x_R \frac{G_M C}{1+G_M C}$$

$$\nabla\left(x_T - x_{Mu}\right) = \left(\nabla R\right)x_R \frac{G_T C}{1+G_M C} = \left(\nabla R\right)x_{Tu} \quad (7)$$

$$\text{where:} \quad \nabla R = \left[s^2 \quad s\right]^T$$

where C is the feedback controller, and x_R is the original reference displacement command. Eq. (7) reveals that gradients can be estimated from the table acceleration and velocity measured during an uncompensated tracking experiment.

Performance of the RCG pre-filter on compensating table-motor anti-resonance mismatch is shown in Fig. 3.b-c. As seen, table displacement deviates from the uncompensated motor motion without the RCG filter. After 4 iterations, convergence is achieved and mismatch between table and motor motion is completely eliminated.

DESIGN OF THE CLOSED LOOP DYNAMICS COMPENSATOR (CLDC)

Once the RCG is implemented, the table follows uncompensated motor position. This compensates any anti-resonance vibrations. However, the resonance can still be excited by the reference trajectory and induce unwanted vibrations. The objective of the CLDC filters it to modulate the reference trajectory to avoid resonance vibrations while at the same time inverts the closed loop dynamics to widen overall tracking bandwidth.
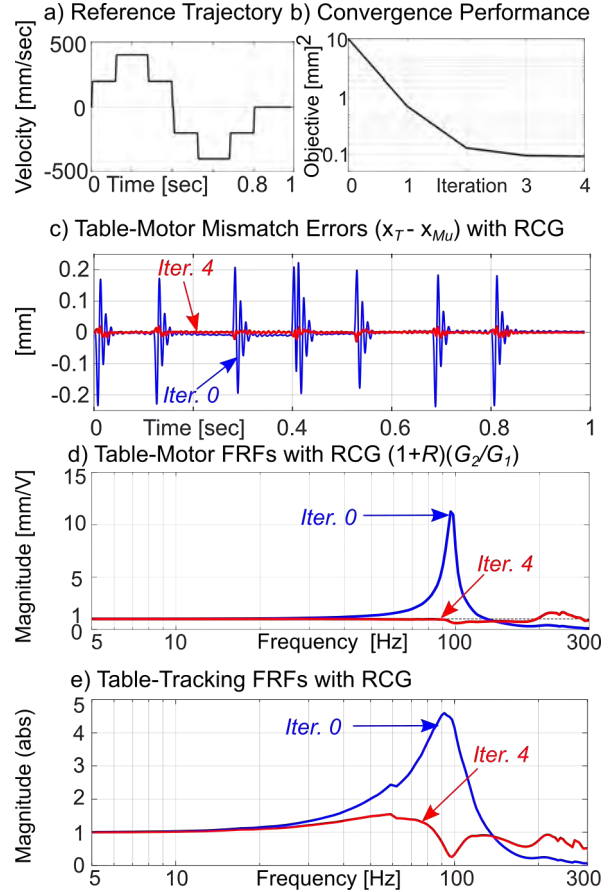
FIGURE 3: Performance of RCG.

In order to achieve this, the CLDC is designed as $G_{CLDC} = T_{Mu}^{-1} = 1 + L^{-1}$ (see Fig. 1), which is to invert the closed loop dynamics between table x_T and reference x_R, $T_T(s)$;

$$\frac{x_T}{x_R} = T_T = \left(1+R\right)T_{Mu}\frac{G_T}{G_M}$$

$$T_{Mu} = \frac{L}{1+L}, \quad L = \left(\frac{K_D s^2 + K_P s + K_I}{s}\right)G_M \quad (8)$$

where K_P, K_I and K_D are the PID controller gains. L is the loop transmission dynamics. T_{Mu} is the uncompensated closed loop dynamics from the reference displacement x_R to actual motor displacement x_M.

Notice that, previous section presented iterative tuning of RCG, i.e. the $R(s)$. Once RCG is

applied, motor and table move together satisfying, $T_T \cong T_{Mu}$. This in order to design the CLDC, T_T can be identified utilizing following two steps:

Step 1: Single-shot Subspace Identification:
Firstly, both numerator and the denominator of motor-side loop transmission $L_M(s)$ is estimated from a basic tracking test by applying state-space identification techniques [4], [5].

Step 2: Machine-in-the-loop Convex Iterations:
Next, numerator of the identified TF (L^{-1}) is fine-tuned through machine-in-the-loop iterations to achieve near-perfect tracking performance.

The procedure for Step 1 is outlined in the following. Firstly, closed loop dynamics identification is applied on the acceleration error dynamics, E_A, rather than conventional position state. This allows better capturing the higher-order dynamics as:

$$E_A = \frac{e}{a_R} = \frac{1}{s^2}\left(1 - T_{Mu}\right)$$

$$= \frac{Ps}{Ps^3 + s^2\left(K_D s^2 + K_P s + K_I\right)\left(m_T s^2 + cs + k\right)} \quad (9)$$

$$= \frac{c_4 s^3 + c_3 s^2 + c_2 s + c_1}{s^5 + \alpha_1 s^4 + \alpha_2 s^3 + \alpha_3 s^2 + \alpha_4 s + \alpha_5}$$

where a_R is the reference acceleration command, and e is the tracking error, i.e. $e = x_R - x$. P is the open loop denominator defined by Eq. (2). To identify the parameters of E_A, ($c_1 \ldots c_4$ and $\alpha_1 \ldots \alpha_5$) the ball-screw stage is moved back-and-forth once. The resulting tracking error is recorded and stored alongside the reference acceleration in the following data matrices:

$$\mathbf{U} = \begin{bmatrix} a_R(0) & a_R(T_s) & \cdots & a_R((j-1)T_s) \\ a_R(T_s) & a_R(2T_s) & \cdots & a_R(jT_s) \\ \vdots & \vdots & \ddots & \vdots \\ a_R((i-1)T_s) & a_R(iT_s) & \cdots & a_R((i+j-2)T_s) \end{bmatrix} \quad (10)$$

$$\mathbf{E} = \begin{bmatrix} e(0) & e(T_s) & \cdots & e((j-1)T_s) \\ e(T_s) & e(2T_s) & \cdots & e(jT_s) \\ \vdots & \vdots & \ddots & \vdots \\ e((i-1)T_s) & e(iT_s) & \cdots & e((i+j-2)T_s) \end{bmatrix} \quad (11)$$

where i and j are measurement sample counters. Utilizing these measurements, E_A in Eq. (9) is written in extended state-space form as:

$$\mathbf{E} = \Gamma \mathbf{X} + \Pi \mathbf{U} + \mathbf{N}$$
$$\mathbf{X} = \begin{bmatrix} \mathbf{x}(0) & \mathbf{x}(T_s) & \cdots & \mathbf{x}((j-1)T_s) \end{bmatrix} \quad (12)$$

where $\mathbf{x}$ is the vector of system states, and $\mathbf{N}$ is the noise data matrix with the same structure as $\mathbf{E}$ and $\mathbf{U}$. Γ is the extended observability matrix, and Π is the input Toeplitz matrix defined as:

$$\Gamma = \begin{bmatrix} \mathbf{C} \\ \mathbf{CA} \\ \vdots \\ \mathbf{CA}^{j-1} \end{bmatrix}, \quad \Pi = \begin{bmatrix} 0 & 0 & \cdots & 0 \\ \mathbf{CB} & 0 & \cdots & 0 \\ \vdots & \vdots & \ddots & \vdots \\ \mathbf{CA}^{j-2}\mathbf{B} & \mathbf{CA}^{j-3}\mathbf{B} & \cdots & 0 \end{bmatrix} \quad (13)$$

where $\mathbf{A}$ is the state transition matrix, $\mathbf{B}$ and $\mathbf{C}$ are input and output matrices of the discrete-time state space representation of Eq. (9).

The goal is to identify the state transition matrix $\mathbf{A}$, which will help identify the coefficients of E_A given in Eq.(9). To achieve this, Γ is identified by adopting the Multi-variable Output-Error State Space (MOESP-type) method [4]. Once, Γ is constructed, it is used to obtain a stable estimation of the state transition matrix $\mathbf{A}$. The following paragraphs outline the mathematical procedures followed for achieving that.

Firstly, the shift invariance property of the extended observability matrix is utilized, and Γ is partitioned into two overlapping sections from Eq. (13) as:

$$\Gamma_1 = \begin{bmatrix} \mathbf{C} \\ \mathbf{CA} \\ \vdots \\ \mathbf{CA}^{j-2} \end{bmatrix}, \quad \Gamma_2 = \begin{bmatrix} \mathbf{CA} \\ \mathbf{CA}^2 \\ \vdots \\ \mathbf{CA}^{j-1} \end{bmatrix}, \quad \text{where: } \Gamma_1 \mathbf{A} = \Gamma_2 \quad (14)$$

The relation given in Eq. (14) is then used to postulate the following optimization problem in order to extract $\mathbf{A}$ matrix as:

$$\min_{\mathbf{A},\mathbf{P}} \left\| \Gamma_1 \mathbf{A} - \Gamma_2 \right\|_F^2, \quad \text{subject to: } \begin{cases} \mathbf{A}^T \mathbf{P} \mathbf{A} - \mathbf{P} \prec 0 \\ \mathbf{P} = \mathbf{P}^T \succ 0 \end{cases} \quad (15)$$

where $\|.\|_F$ denotes the Frobenius norm [5]. The linear matrix inequality (LMI) constraints of Eq. (15) guarantees that $\mathbf{A}$ is stable according to Lyapunov's discrete stability criterion [5], where $\mathbf{P}$ is the Lyapunov matrix. Notice that Eq. (15) poses a non-convex optimization problem, which is difficult to solve. Thus, it is converted into a convex optimization problem as follows.

Firstly, inequality constraints in Eq. (15) are rewritten using their equivalent Schur complement as [6]:

$$\begin{bmatrix} \mathbf{P}^{-1} & \mathbf{A}\mathbf{P}^{-1} \\ \mathbf{P}^{-1}\mathbf{A}^T & \mathbf{P}^{-1} \end{bmatrix} \succ 0 \quad (16)$$

Next, non-linearities in Eq. (16) are circumvented by defining the new variables $\mathbf{R} = \mathbf{A}\mathbf{P}^{-1}$ and $\mathbf{Q} = \mathbf{P}^{-1}$, and Eq. (15) is rewritten as a convex optimization problem:

$$\min_{\mathbf{R},\mathbf{Q}} \left\| \Gamma_1 \mathbf{R} - \Gamma_2 \mathbf{Q} \right\|_F^2, \quad \text{subject to: } \begin{bmatrix} \mathbf{Q} & \mathbf{R} \\ \mathbf{R}^T & \mathbf{Q} \end{bmatrix} \succ \mathbf{0} \quad (17)$$

Eq. (17) poses a convex semi-definite program, and it can be solved efficiently to global optimality. Solution of Eq. (17) provides $\mathbf{R}$ and $\mathbf{Q}$, and $\mathbf{A}$ is easily recovered from: $\mathbf{A} = \mathbf{R}\mathbf{Q}^{-1}$.

Eigenvalues of $\mathbf{A}$ contains the poles of E_A, i.e. poles of closed-loop ball-screw dynamics, T_{Mu} Note that $\mathbf{A}$ is the *discrete-time* state transition matrix, whereas the desired acceleration error dynamics model E_A is written in continuous time (see Eq. (9)). For this reason, $\mathbf{A}$ is converted to its continuous counterpart in controllable canonical form $\mathbf{A}_C$ as:

$$\mathbf{A}_C = \begin{bmatrix} 0 & 1 & 0 & 0 & 0 \\ 0 & 0 & 1 & 0 & 0 \\ 0 & 0 & 0 & 1 & 0 \\ 0 & 0 & 0 & 0 & 1 \\ -\alpha_5 & -\alpha_4 & -\alpha_3 & -\alpha_2 & -\alpha_1 \end{bmatrix} \quad (18)$$

with $\alpha_1 \dots \alpha_5$ are defined as:

$$s^5 + \alpha_1 s^4 + \cdots + \alpha_5 = (s - p_1)(s - p_2) \cdots (s - p_5)$$

$$p_k = \ln\left(eig_k(\mathbf{A})\right)/T_s \quad (19)$$

Utilizing the $\mathbf{A}_C$ matrix, E_A is written in continuous state-space form as:

$$\dot{\mathbf{x}}_C = \mathbf{A}_C \mathbf{x}_C + \mathbf{B}_C a_R, \quad e = \mathbf{C}_C \mathbf{x}_C$$

$$\text{where: } \mathbf{x}_C = \begin{bmatrix} x_C & \dot{x}_C & \ddot{x}_C & \dddot{x}_C & \ddddot{x}_C \end{bmatrix} \quad (20)$$

where $\mathbf{x}_C$ is the vector of continuous states. e and a_R are the tracking error and reference acceleration input given by Eq. (9). Structure of the continuous input matrix $\mathbf{B}_C$ is selected as: $[0,0,0,0,1]^T$, and thus all the zeros of E_A are captured by the continuous output matrix $\mathbf{C}_C = [c_1, c_2, c_3, c_4, c_5]$. This enables us to identify zeros of E_A easily. To identify $\mathbf{C}_C$, continuous estimate of state propagation $\mathbf{x}_C$ is calculated for M samples using Eq. (20), and the following optimization problem is formed:

$$\min_{\mathbf{C}_C} \left\| e - \mathbf{C}_C \mathbf{x}_C \right\|_\infty \text{ subject to: } c_5 = 0 \quad (21)$$

Note that the equality constraint $c_5 = 0$ is imposed to respect the structure of E_A as given in Eq. (9). Eq. (21) is an infinity-norm minimization problem, and it can easily be implemented as a linear program with linear inequality constraints.

It is a convex optimization problem and can be solved efficiently to its global optimum. Finally, E_A is obtained by Eqs. (19) and (21) as:

$$E_A = \frac{c_4 s^3 + c_3 s^2 + c_2 s + c_1}{s^5 + \alpha_1 s^4 + \alpha_2 s^3 + \alpha_3 s^2 + \alpha_4 s + \alpha_5}$$

$$c_1 = b_M k / (m_M m_T), \quad c_2 = \left[b_M c + k(m_M + m_T) \right] / (m_M m_T)$$

$$c_3 = \left[b_M m_T + c(m_M + m_T) \right] / (m_M m_T)$$

$$\alpha_1 = \left[b_M m_T + c(m_M + m_T) + K_D m_T \right] / (m_M m_T) \quad (22)$$

$$\alpha_2 = \left[b_M c + k(m_M + m_T) + K_D c + K_P m_T \right] / (m_M m_T)$$

$$\alpha_3 = \left(b_M k + K_D k + K_P c + K_I m_T \right) / (m_M m_T)$$

$$\alpha_4 = \left(K_P k + K_I c \right) / (m_M m_T), \quad \alpha_5 = K_I k / (m_M m_T)$$

Once E_A is identified, inverse loop transmission function L^{-1} is estimated to be used in the *CLDC* filter as:

$$L^{-1} = 1 \Big/ \left(\frac{1}{E_A s^2} - 1 \right) \quad (23)$$

Estimation of L is demonstrated in Fig. 4. As seen, the proposed identification method captures dynamics of L. This concludes Step 1 of CLDC design.
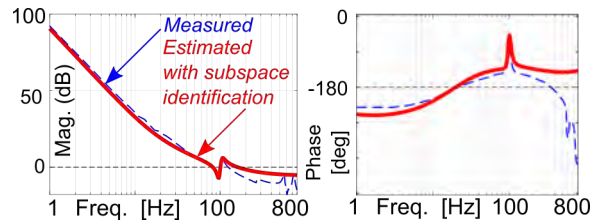
FIGURE 4: Performance of subspace identification.

Step (2) of CLDC design process requires machine-in-the-loop iterations. Notice that L^{-1} identified from step 1 is stable but may suffer from inaccuracy. In step 2, it is augmented with additional Finite Impulse Response (FIR) dynamics by,

$$L_{aug}^{-1} = L^{-1} \left(m_0 + m_1 z^{-1} + m_2 z^{-2} \right) \quad (24)$$

This additional terms help recover phase loss due to low-pass filtering and amplifier delay within the control loop. Parameters $m_0 \dots m_2$ are obtained by data-based tuning through solving the following optimization problem:

$$\min_{m_0, m_1, m_2} \left(J_{CLDC} = \frac{1}{2} \mathbf{e}_T^T \mathbf{e}_T \right) \quad (25)$$

where $\mathbf{e}_T$ is the table tracking error vector with the CLDC. Similar to Eq. (4), Eq. (25) also requires the gradient and Hessian of the

objective function, ∇J_{CLDC} and $\nabla^2 J_{CLDC}$, which can be obtained through the gradient of $\mathbf{e}_T$ as:

$$e_T = x_R - \left(1 + L_{aug}^{-1}\right)\left(1 + R\right)\frac{G_2 C}{1 + G_1 C} x_R$$

$$\nabla e_T = -\nabla L_{aug}^{-1}\underbrace{\left(1 + R\right)\frac{G_2 C}{1 + G_1 C} x_R}_{x_{T,RCG}}$$ (26)

$$\cong -\begin{bmatrix} 1 & z^{-1} & z^{-2} \end{bmatrix}^T x_{T,RCG}$$

$$\nabla J_{CLDC} = \mathbf{e}_T^T \nabla \mathbf{e}_T, \quad \nabla^2 J_{CLDC} = \nabla \mathbf{e}_T^T \nabla \mathbf{e}_T$$

where $x_{T,RCG}$ is the table displacement compensated only by the RCG filter, which can be obtained using only measurement data, without relying on any system model. Therefore, parameters of L_{aug}^{-1} can be obtained in a fully data-driven fashion using Newton's iterations similar to Eq. (5) as:

$$\begin{bmatrix} m_0 \\ m_1 \\ m_2 \end{bmatrix}^{n+1} = \begin{bmatrix} m_0 \\ m_1 \\ m_2 \end{bmatrix}^n - \alpha\left(\nabla^2 J_{CLDC}\right)^{-1}\left(\nabla J_{CLDC}\right)$$ (27)

where n is the iteration counter, and α is the learning rate.

In order to validate the effectiveness of CLDC, steps (1) and (2) are implemented sequentially on the ball-screw motion stage. The reference trajectory given in Fig. 3.a is used. The results are summarized by Fig. 5. As seen in, CLDC, combined with the RCG provides superior command tracking performance compared to conventional rigid-body model-based feedforward (FF) compensator.

CONCLUSIONS

This paper presented a novel trajectory pre-filtering scheme for feed drives suffering from lightly damped structural vibrations, such as ball-screw drives. Presented pre-filter-pack generates rotary commands for the motor so that the table tracks set-points accurately. Closed loop servo lag-induced tracking errors are eliminated, and near-perfect tracking is achieved. The designed pre-filter is tuned automatically through machine in the loop iterations and shown that it can greatly improve accuracy of ball-screw drives.
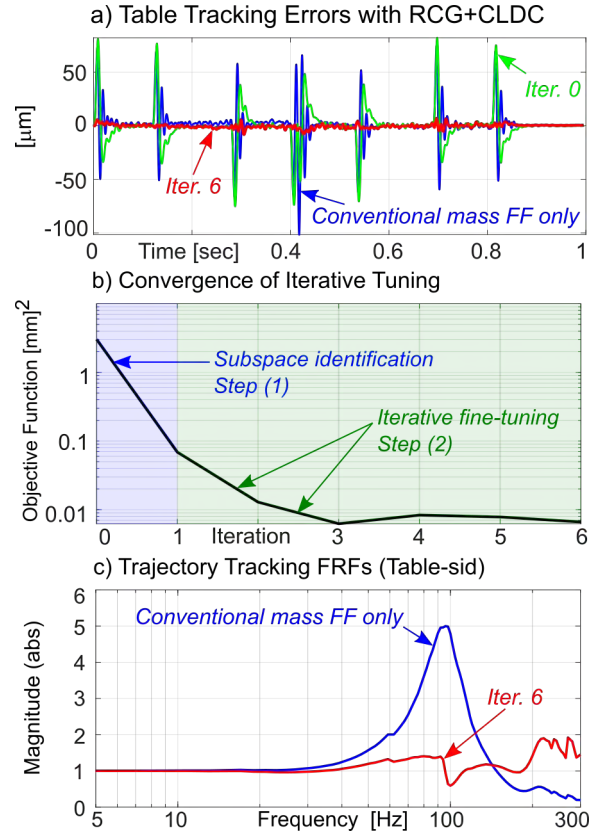
FIGURE 5: Tuning and tracking performance of the CLDC filter.

REFERENCES

[1] Erkorkmaz K, Gordon D. J. 2013. Accurate control of ball screw drives using pole-placement vibration damping and a novel trajectory prefilter. Precision Engineering 37(2):308-322.

[2] Dumanli A, Sencer B. 2018. Optimal high-bandwidth control of ball-screw drives with acceleration and jerk feedback. Precision Engineering 54:254-268.

[3] Blanken L, Boeren F, Bruijnen D, Oomen T. 2017. Batch-to-Batch Rational Feedforward Control: From Iterative Learning to Identification Approaches, With Application to a Wafer Stage. IEEE/ASME Transaction on Mechatronics 22(2):826-837.

[4] Overschee PV, Moor BD. 1995. A Unifying Theorem for Three Subspace System Identification Algorithms. Automatica 31(12):1853-1864.

[5] Miller DN, Callafon RA. 2013. Subspace identification with eigenvalue constraints. Automatica 49:2468-2473.

[6] Boyd S, Vandenberghe K. 2004. Convex Optimization. Cambridge University Press.

COMBINED SERVO ERROR PRE-COMPENSATION AND FEEDRATE OPTIMIZATION USING SEQUENTIAL LINEAR PROGRAMMING

Heejin Kim[1] and Chinedum E. Okwudire[1]
[1]Department of Mechanical Engineering
University of Michigan
Ann Arbor, MI

INTRODUCTION

Precision manufacturing and metrology machines typically use motion stages powered by computer numerical control (CNC) to generate motion commands. Two critical requirements for manufacturing and metrology are productivity and quality, which often involve a trade-off between speed and accuracy of precision motion stages [1]. This trade-off is typically handled, in practice, by maximizing speed so long as a pre-specified accuracy (tolerance) level is not violated.

Major source of inaccuracy in precision motion stages are servo errors caused by commanded motion, i.e., motion-induced servo errors. They are very important in determining the trade-off between speed and accuracy because servo controllers always have limited bandwidth. One way of reducing motion-induced servo errors is through servo error pre-compensation (SEP), i.e., feedforward compensation) [2-6]. On the other hand, in feedrate optimization (FO), tolerance constraints are introduced implicitly by imposing velocity, acceleration and jerk limits [7]. Some works have explicitly added tracking or contouring accuracy constraints to FO [8].
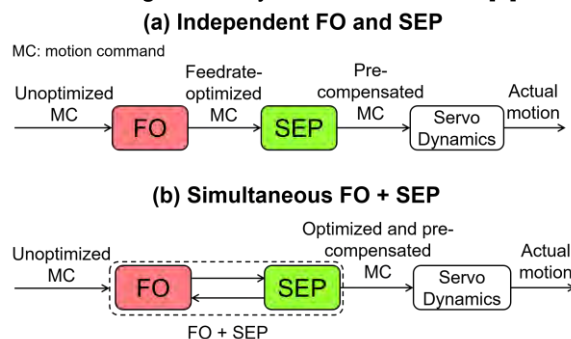
FIGURE 1. Comparison of (a). independent FO and SEP – standard practice – and (b). proposed concept of simultaneous FO and SEP (i.e., FO+SEP).

In practice, SEP and FO are combined by first performing FO and then applying the optimized results to SEP for error minimization, as shown by the one-way arrow between FO and SEP in Fig. 1(a). However, this independent (or sequential) approach is suboptimal. Therefore, FOSEP (i.e., FO combined with SEP) has been proposed in [9] so that FO benefits from the reduction of error provided by SEP in maximizing feedrate. However, in [9], FOSEP was implemented in full-preview using linear programming, meaning that it processed the entire length of a motion command simultaneously. The shortcomings of full-preview FOSEP using linear programming (denoted as Full-FOSEP hereafter) are: 1. Long trajectory leads to high computational load/time, and 2. If the initial guess for linearization and the optimal solution differ significantly, it could lead to inaccurate axis-level performance.

Therefore, this paper proposes two additional concepts which are: 1. The use of limited preview (Lim-FOSEP), adapted from tracking control framework proposed by Duan et al [6], to recursively compute the optimal trajectory; and 2. Sequential linear programming (SLP) in each preview window. Because SLP achieves global convergence when certain step-size conditions are met, each horizon will converge to a local optimum regardless of the initial guess, where linearization error is decreased by each step. It is shown here that, compared to Full-FOSEP [9], applying SLP to Lim-FOSEP reduces linearization error and saves computation time by up to 89.9%.

OVERVIEW OF Full-FOSEP APPROACH USING FILTERED B SPLINES
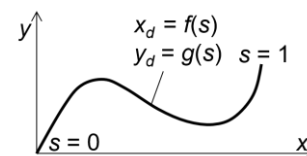
FIGURE 2. Parametric planar curve as function of path variable, s

Consider an arbitrary, curved path in the *x-y* plane with path parameter $s \in [0,1]$ in Fig. 2. Note that s is a function of time t (i.e., $s = s(t)$). Let $x_d = f(s)$ and $y_d = g(s)$ denote a pair of parametric equations in s, representing the x and y components of desired position, respectively. In this paper, $s(t)$ is assumed to be the arclength of the curve traversed at time t, which can be approximated by quintic spline interpolation of x and y [10].

Full-FOSEP adopts time-based linear programming approach for FO from the model predictive contour control framework in [11]. Assume that $s(t)$ is discretized with fixed sampling interval, T_s, and expressed as a vector $s = \{s(0), s(1), \ldots, s(N-1)\}^T$. Then, FO with kinematic constraints F_{max} and A_{max} on feedrate and axis acceleration, respectively, can be formulated as follows:

$$\min_{s} \sum_{k=0}^{N-1} -s(k)$$

$$\text{s.t. } s(k-1) \leq s(k) \leq 1 \; \forall \, k = 1, 2, \ldots, N-1 \quad (1)$$

$$\frac{D[s]}{T_s} \leq F_{max}$$

$$\left| \frac{D^2[\hat{x}_d]}{T_s^2} \right|, \; \left| \frac{D^2[\hat{y}_d]}{T_s^2} \right| \leq A_{max}$$

Here, D denotes a finite difference operator, while F_{max} and A_{max} are vectorized representations of the corresponding kinematic limits. The terms $\hat{x}_d(k)$ and $\hat{y}_d(k)$ are linearized versions of $x_d = f(s)$ and $y_d = g(s)$, which are generally nonlinear in s. At each time step k, they are linearized with linearization points $s^e(k)$ estimated from an initial unoptimized trajectory as:

$$\hat{x}_d(k) = \left. \frac{\partial f(s)}{\partial s} \right|_{s=s^e(k)} \cdot (s(k) - s^e(k)) + f(s^e(k)) \quad (2)$$

$\hat{y}_d(k)$ is obtained by linearizing $g(s)$ in the same manner; $\hat{x}_d$ and $\hat{y}_d$ are vectorized versions of $\hat{x}_d(k)$ and $\hat{y}_d(k)$, respectively, similar to s. This notation is maintained hereinafter.

Linearized desired x-axis position, $\hat{x}_d$, is used to generate modified position command $\hat{x}_{dm}$ using a SEP process represented by C_x. A linear model, $\hat{G}_x$, of the actual servo dynamics, G_x, is used to estimate the x-axis position as $\hat{x}$ and

tracking error as $\hat{e}_x = \hat{x}_d - \hat{x}$. A similar process is followed using C_y and $\hat{G}_y$.

In addition, tracking error limit is imposed as an additional constraint on the time-based linear programming formulation of as:

$$|\hat{e}_x| = \left| (I - \hat{G}_x C_x)\hat{x}_d \right| \leq E_{max} \quad (3)$$

where E_{max} is the vectorized form of the maximum allowable tracking error E_{max}; C_x, $\hat{G}_x$, C_y and $\hat{G}_y$ are matrix (lifted) versions of the corresponding system dynamics; and I is the identity matrix. Same constraint is imposed on $\hat{e}_y$. The implication is that a model of SEP is incorporated into FO, yielding FOSEP. The optimized x_d and y_d from FOSEP are then applied to the actual servo dynamics, G_x and G_y, pre-compensated using C_x and C_y, respectively.

It is worth pointing out that C_x and C_y can be any SEP (feedforward tracking control) method, e.g., [2-6], as long as it is linear. However, among the available SEP methods, the filtered B spline (FBS) approach [5,6] stands out because of its effectiveness and versatility in handling any type of linear system dynamics [5]. Therefore, it is selected for SEP in this paper as in [9].

INCORPORATION OF SLP IN FULL-FOSEP
However, using LP in Full-FOSEP may introduce violations in axis-level constraints on acceleration and tracking error, which depends on the linearization as well as the proximity of the initial guess to the optimal solution.

Therefore, SLP is used in replace of LP by reiterating the LP process using the previous step's optimal solution as the next linearization points. If global convergence condition is met, then regardless of the initial points, the iteration will converge to a locally optimal solution. However, it will require longer computation time that depends on the number of iterations.

LIM-FOSEP USING SLP
To resolve this computation issue, an SLP in Lim-FOSEP is introduced. First, in the optimization in Eq. (1), the full-preview length N is replaced with the limited-preview horizon length N_p as in Eq. (4):

$$\min_{s} \sum_{k}^{k+N_p-1} -s(k) \quad (4)$$

s.t. $s(k-1) \leq s(k) \leq 1 \ \forall k, k+1, ..., k+N_p-1$

$$\frac{D[\boldsymbol{s}]}{T_s} \leq \boldsymbol{F}_{max}$$

$$\left|\frac{D^2[\hat{\boldsymbol{x}}_d]}{T_s^2}\right|, \ \left|\frac{D^2[\hat{\boldsymbol{y}}_d]}{T_s^2}\right| \leq \boldsymbol{A}_{max}$$

At each window, N_c points within the control window are updated and the rest of optimal solution is used as part of the linearization point in the next window. In addition, continuity constraints that ensures adjacent batches meet kinematic and monotonicity constraints are imposed as in Eq. (5):

$$s(k-1) \leq s(k) \leq s(k-1) + F_{max}T_s$$

$$\left|\frac{\hat{x}_d(k) - 2x_d(k-1) + x_d(k-2)}{T_s^2}\right| \leq A_{max}$$

$$\left|\frac{\hat{y}_d(k) - 2y_d(k-1) + y_d(k-2)}{T_s^2}\right| \leq A_{max}$$

$$\left|\frac{\hat{x}_d(k+1) - 2\hat{x}_d(k) + x_d(k-1)}{T_s^2}\right| \leq A_{max}$$

$$\left|\frac{\hat{y}_d(k+1) - 2\hat{y}_d(k) + y_d(k-1)}{T_s^2}\right| \leq A_{max}$$

(5)

Furthermore, the tracking error constraint can be formulated as in Eq. (6). Unlike above kinematic constraints in Eq. (5), the updated points in the past time steps should be considered because the matrix $\boldsymbol{I} - \hat{\boldsymbol{G}}_x\boldsymbol{C}_x$ is, in general, non-diagonal:

$$|\hat{e}_x| = \left|\underbrace{(\boldsymbol{I} - \hat{\boldsymbol{G}}_x\boldsymbol{C}_x)}_{:=\dot{N}_{ex}}\hat{\boldsymbol{x}}_d\right| \leq E_{max}$$

(6)

Here, $\boldsymbol{N}_{ex}$ is further decomposed into $\boldsymbol{N}_{ex,past}$ and $\boldsymbol{N}_{ex,pres}$, where each represent concatenated columns that corresponds to the past $\hat{x}_{d,past}$ and present (current window) points of $\hat{x}_{d,pres}$ respectively, as:

$$\left|[\boldsymbol{N}_{ex,past} \quad \boldsymbol{N}_{ex,pres}]\begin{bmatrix}\hat{\boldsymbol{x}}_{d,past} \\ \hat{\boldsymbol{x}}_{d,pres}\end{bmatrix}\right| \leq E_{max}$$

(7)

$$\therefore -E_{max} - \boldsymbol{N}_{ex,past}\hat{x}_{d,past} \leq \boldsymbol{N}_{ex,pres}\hat{x}_{d,pres}$$
$$\leq E_{max} - \boldsymbol{N}_{ex,past}\hat{x}_{d,past}$$

The Lim-FOSEP optimization formulated in Eq. (4)-(7) are iterated within the same window $t = k$ to $k + N_p - 1$ as SLP until the cost function difference reaches certain tolerance.

BENCHMARKING TO DETERMINE ERROR TOLERANCE

A conservative kinematic trajectory is generated by using trapezoidal feedrate profile with sampling time T_s = 1 ms and applying an S-shaped digital filter of time constant τ = 0.02 s, which generates a profile of feedrate limit F_{max} = 30 mm/s and axis acceleration limit A_{max} = 3 m/s^2, shown in Fig. 3.

For simulation, a linearly-fitted model of x, y dynamics of a biaxial linear-motor-driven XY stage (Aerotech ALS 25010) shown in Fig. 4, denoted as G_x and G_y respectively, are used. As seen in Fig. 3, the conservative profile yields maximum absolute axis tracking error as 159.2 µm, which will be the simulated error tolerance limit for optimization in both Full-FOSEP and Lim-FOSEP.
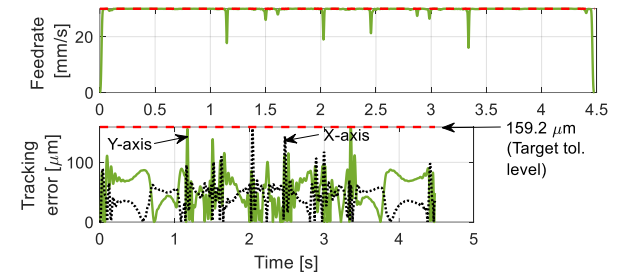
FIGURE 3. (a) Commanded feedrate and (b) simulated tracking error profiles of conservative motion commands

FIGURE 4. Aerotech ALS-25010 with optical linear encoders (resolution = 0.1µm)

SIMULATION RESULTS
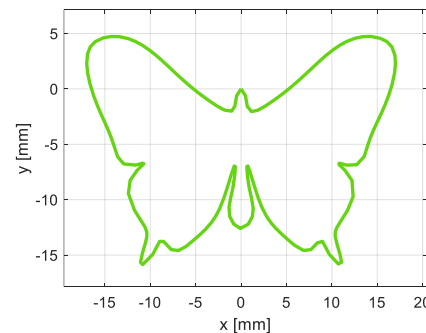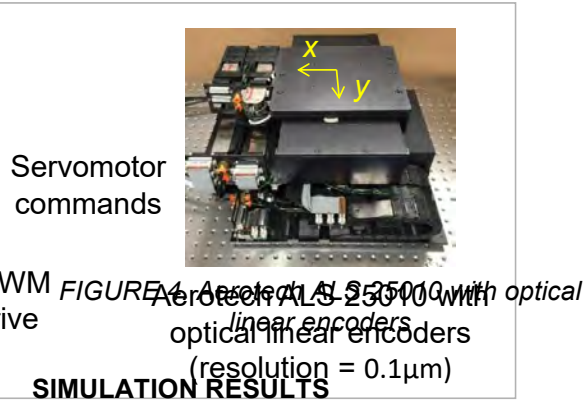
FIGURE 3. Desired path

In Fig. 5, an exemplary butterfly trajectory is shown. Applying Full-FOSEP on this path with aggressive kinematic limits on F_{max} = 80 mm/s, A_{max} = 8 m/s^2, E_{max} = 159.2 µm results in cycle time of 1.69 s and computation time of 34.56 s, along with some violation in axis acceleration, as shown in Fig. 6.
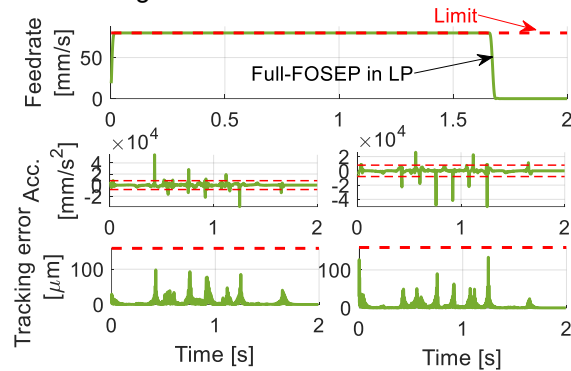
FIGURE 4. Feedrate, acceleration and tracking error profiles of Full-FOSEP approach using LP

However, if SLP is used in place of LP, i.e., the optimization is repeated by using the solution in Fig. 6 as the initial linearization point, after 2 iterations the results appear as Fig. 7, with cycle time of 2.61 s and total computation time of 42.44 s.
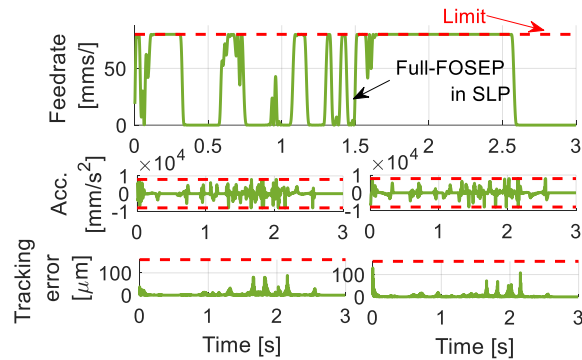
FIGURE 5. Feedrate, acceleration and tracking error profiles of Full-FOSEP approach using SLP

Here, using SLP indeed improves linearization error that is manifested as violations at axis-level acceleration constraints in Fig. 6. However, the computation time is 22.8% longer than using linear programming and the feedrate suffers from high fluctuation.

Therefore, the proposed SLP applied to Lim-FOSEP is used, with limited-preview parameters as N_p = 50 and N_c = 30, B-spline ratio of 10:1 in SEP, of which the results are shown in Fig. 8,

with much lower computation time of 4.30 s and the same cycle time of 1.69 s.
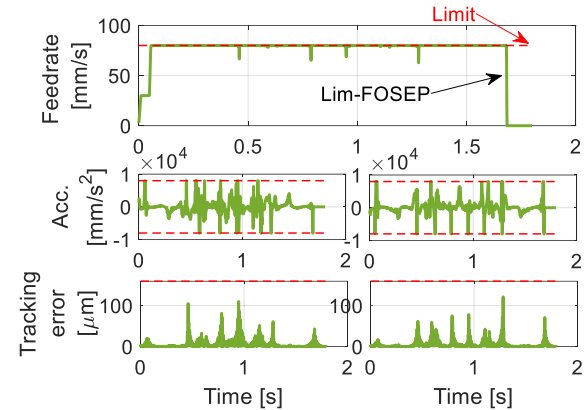
FIGURE 6. Feedrate, axis acceleration, and simulated tracking error profiles of Lim-FOSEP using SLP

CONCLUSIONS

This paper has proposed a concept of Lim-FOSEP using SLP, which incorporates limited-preview framework and sequential linear programming for simultaneous FO and SEP. Simulation executed on a butterfly path with XY stage dynamics showed 89.9% reduction in computation time using the proposed Lim-FOSEP with SLP compared to Full-FOSEP, without unduly sacrificing cycle time. Future work will explore incorporating a kinematic backup solution to Lim-FOSEP to guarantee feasibility regardless of error limit, as well as actuator (e.g., torque) limits in FO to help expand its performance benefits.

ACKNOWLEDGEMENT

REFERENCES

[1] Altintas Y, Verl A, Brecher C, Uriarte L, Prtischow G. Machine Tool Feed Drives. CIRP Annals 2011; 60(2): 779-796.
[2] Tomizuka M. Zero Phase Error Tracking Algorithm for Digital Control. 1987.
[3] Altintas Y, Khoshdarregi MR. Contour Error Control of CNC Machine Tools with Vibration Avoidance. CIRP Annals 2012; 61(1): 335-338.
[4] Yang S, Ghasemi AH, Lu X, Okwudire CE. Pre-Compensation of Servo Contour Error Using a Model Predictive Control

Framework. International Journal of Machine Tools and Manufacture 2015; 98: 50-60.

[5] Okwudire C, Ramani K, Duan M. A Trajectory Optimization Method for Improved Tracking of Motion Commands Using CNC Machines That Experience Unwanted Vibration. CIRP Annals 2016; 65(1): 373-376.

[6] Duan M, Yoon D, Okwudire CE. A Limited-Preview Filtered B-Spline Approach to Tracking Control-With Application to Vibration-Induced Error Compensation of a 3D Printer. Mechatronics 2018; 56: 287-296.

[7] Fan W, Gao XS, Lee CH, Zhang K, Zhang Q. Time-Optimal Interpolation for Five-Axis CNC Machining along Parametric Tool Path Based on Linear Programming. The International Journal of Advanced Manufacturing Technology 2013; 69(5-8): 1373-1388.

[8] Guo J, Zhang Q, Gao XS, Li H. Time Optimal Feedrate Generation with Confined Tracking Error based on Linear Programming. Journal of Systems Science and Complexity 2015; 28(1): 80-95.

[9] Kim H, Okwudire CE. Simultaneous Servo Error Pre-Compensation and Feedrate Optimization With Tolerance Constraints using Linear Programming. The International Journal of Advanced Manufacturing Technology 2020; 109(3): 809-821.

[10] Erkorkmaz K, Altintas Y. Quintic Spline Interpolation With Minimal Feed Fluctuation. ASME Journal of Manufacturing Science and Engineering 2005; 127(2): 339-349.

[11] Lam D, Manzie C, Good MC. Model Predictive Contouring Control for Biaxial Systems. IEEE Transactions on Control Systems Technology 2012; 21(2): 552-559.

OVERSAMPLING AND AVERAGING, NOISE ANALYSIS FOR IMPROVING CONTROL PERFORMANCE

Brij M. Bhushan[1], **Allison Lenhard**[1], **David L. Trumper**[1]
[1]**Department of Mechanical Engineering**
Massachusetts Institute of Technology
Cambridge, MA, United States of America

INTRODUCTION

Systems with feedback motion control are typically limited in bandwidth and control performance by the effect of system parameters which limit the gain of the controller, such as: (1) sensing noise; (2) plant dynamics - dominant behavior near crossover, resonances, and right-half plane zeros; (3) sampling time - phase lag due to zero order hold; and, (4) non-linearities such as amplifier saturation and actuator limits. This paper presents a mechatronic platform for experiential learning where students can learn about such issues.

In a teaching environment, students are taught about all these aspects, but it is more challenging to create cost-effective labs where students get a feel for the constraints which dynamics places on feedback control performance. It is desirable to have a portable, low-cost setup that enables students to learn these principles hands-on, even outside dedicated lab facilities. Such a setup, the FlexLab and LevLab printed circuit board (PCB) has been developed in our lab for this purpose [1], and has been used successfully in teaching the Analysis and Design of Feedback Control Systems (2.14) course at the Massachusetts Institute of Technology (MIT) [2].

We demonstrate a higher control loop performance and management of dynamics and measurement noise on the 2-degree of freedom (DOF) FlexLab T-beam system, achieving a crossover of 100 Hz, with about 40° phase margin in both the bending and twisting directions. This is enabled by: (1) implementing high-speed digital control by leveraging the Field Programmable Gate Array (FPGA) on the NI-myRIO embedded evaluation board by National Instruments (NI), and (2) implementing oversampling and averaging of the sensor measurement signals to reduce sensing noise within the control bandwidth.

This paper describes the experimental setup, plant modeling, sensor noise reduction by oversampling and averaging, and controller design along with its implementation and achieved performance results. The paper also describes noise analysis using spec-
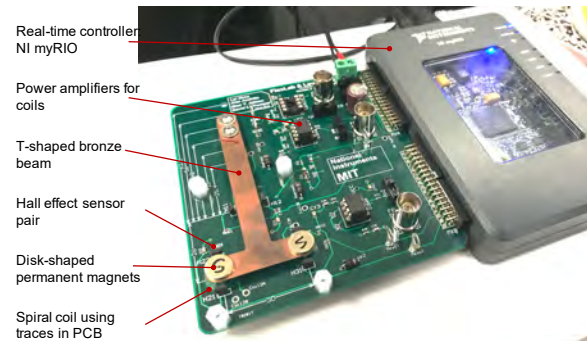
FIGURE 1. *The experimental setup includes a FlexLab PCB and an NI-myRIO. Components of interest are labeled accordingly.*

tral tools such as power spectral density and cumulative power spectrum, which can be used to identify areas for improving the control performance. The approach described in this paper provides a low-cost way to improve control performance on commonly available high-speed micro-controllers that usually have moderately low resolution analog inputs. We also provide links to sample open-source LabVIEW code for implementation using NI hardware.

EXPERIMENTAL SETUP

The experimental setup consists of the FlexLab/LevLab PCB connected to an NI-myRIO real-time controller. Fig. 1 shows the FlexLab experimental setup with key components labeled. The FlexLab configuration is composed of a bronze T-shaped cantilever beam with two permanent magnet (PM) pairs on each end of the T. The stem of the T-beam is bolted to the PCB, while the end of the beam with the PM pairs is the free end above two actuating coils printed as spirals on the PCB.

Fig. 2 shows a block diagram of the setup. The PM pairs mounted at the two ends of the T-beam are used for both sensing and actuation. The PM flux is measured by the Hall sensors which is correlated to the beam position above the coils. The Hall sensor measurement circuit averages and low-pass filters the outputs from the Hall sensor pair, acting as a first-order anti-aliasing filter (AAF) at 20 kHz bandwidth.
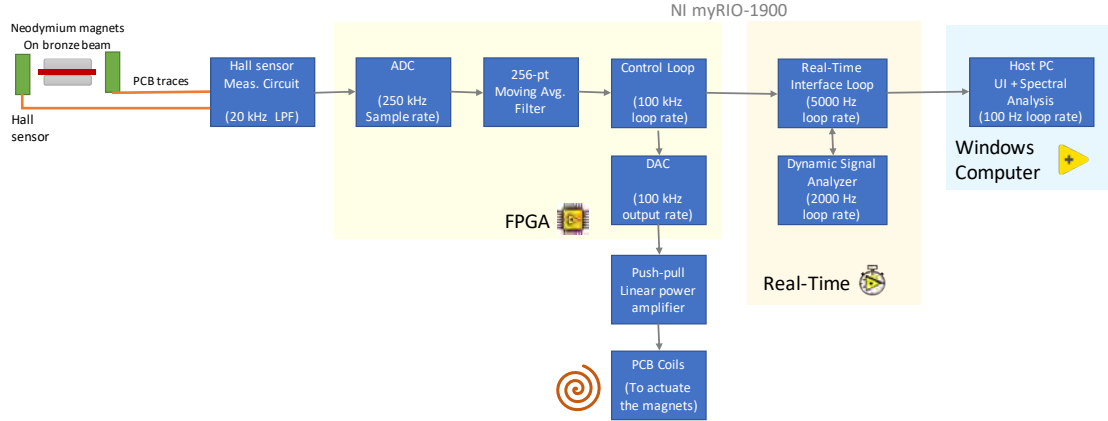
FIGURE 2. *Setup block diagram. Multi-processor architecture enables high speed controller implementation.*

The input-output interface and controller is implemented in FPGA on the myRIO. The Hall sensor signals are read at 250 kHz and low-pass filtered with a 256-pt. moving average (MA) filter. The control loop runs at 100 kHz generating a control effort signal in response to position error. The control effort signal commands the on-board linear power amplifier to drive current through the PCB coils to actuate the magnets. The user interface and dynamic signal analyzer enabling measurement of Bode plots run on the real-time processor, while waveform visualization and spectral analysis execute on the Host-PC.

PLANT MODELING
The T-beam with a pair of PMs located at each end of the T as seen in Fig. 1 can be most simply modeled as a fourth-order dynamical system. The plant modeling for the system is described in [1]. The modeling assumptions and resulting dynamic equations are reproduced here for completeness.

To simplify the modeling of the system, we make the following assumptions: the PMs move in the vertical direction with small displacements relative to their distance from the coils; the power amplifiers driving the actuator coils are linear and have no significant dynamics within position loop bandwidth; the actuator coils have small inductance which has a negligible effect on the circuit dynamics. Resolving the vertical PM measurements coil actuation into a transformed coordinate system of bend and twist makes the first two lumped modes at 11 Hz and 32 Hz independent in each direction.

The dynamic equations resulting from the lumped parameter model with respect to the decoupled bend (z_c) and twist (θ_x) coordinates are as follows. Table 1 defines the modeling parameters used in the following equations:

$$\ddot{z}_c = -\frac{k_b}{2m}z_c - \frac{K_i^2}{mR_c}\dot{z}_c + \frac{g_{amp}K_i}{2mR_c}u_z$$

$$\ddot{\theta}_x = -\frac{k_t}{I}\theta_x - \frac{2K_i^2L^2}{IR_c}\dot{\theta}_x + \frac{g_{amp}K_iL}{IR_c}u_{\theta_x}$$

The moment of inertia I, bending stiffness k_b, and twisting stiffness k_t of the T-beam are defined as

$$I = 2mL^2, \ k_b = \frac{3E}{l_{beam}^3}\frac{wt^3}{12}$$

$$k_t = \frac{G}{l_{beam}}wt^3\left(\frac{1}{3} - 0.21\frac{t}{w}\left(1 - \frac{t^4}{12w^4}\right)\right)$$

To get the state-space model of the system, define $\mathbf{x} = [z_c, \dot{z}_c, \theta_x, \dot{\theta}_x]^T$, $\mathbf{u} = [u_z, u_{\theta_x}]^T$, and $\mathbf{y} = [z_c, \theta_x]^T$, which gives

$$\dot{\mathbf{x}} = \mathbf{Ax} + \mathbf{Bu}$$

$$\mathbf{y} = \mathbf{Cx}$$

where,

$$\mathbf{A} = \begin{bmatrix} 0 & 1 & 0 & 0 \\ -\frac{k_b}{2m} & -\frac{K_i^2}{mR_c} & 0 & 0 \\ 0 & 0 & 0 & 1 \\ 0 & 0 & -\frac{k_t}{I} & -\frac{2K_i^2L^2}{IR_c} \end{bmatrix}$$

$$\mathbf{B} = \begin{bmatrix} 0 & 0 \\ \frac{g_{amp}K_i}{2mR_c} & 0 \\ 0 & 0 \\ 0 & \frac{g_{amp}K_iL}{IR_c} \end{bmatrix} \quad \mathbf{C} = \begin{bmatrix} 1 & 0 & 0 & 0 \\ 0 & 0 & 1 & 0 \end{bmatrix}$$

The coordinate transformation matrix used to get z_c and θ_x from the Hall sensor (sensitivity, S_{Hall}) measurements [V] at each PM is:

$$\begin{bmatrix} z_c \\ \theta_x \end{bmatrix} = S_{Hall}^{-1}\begin{bmatrix} 1/2 & 1/2 \\ -1/2L & 1/2L \end{bmatrix}\begin{bmatrix} V_{H2} \\ V_{H3} \end{bmatrix}$$

| | (a) | | (b) |
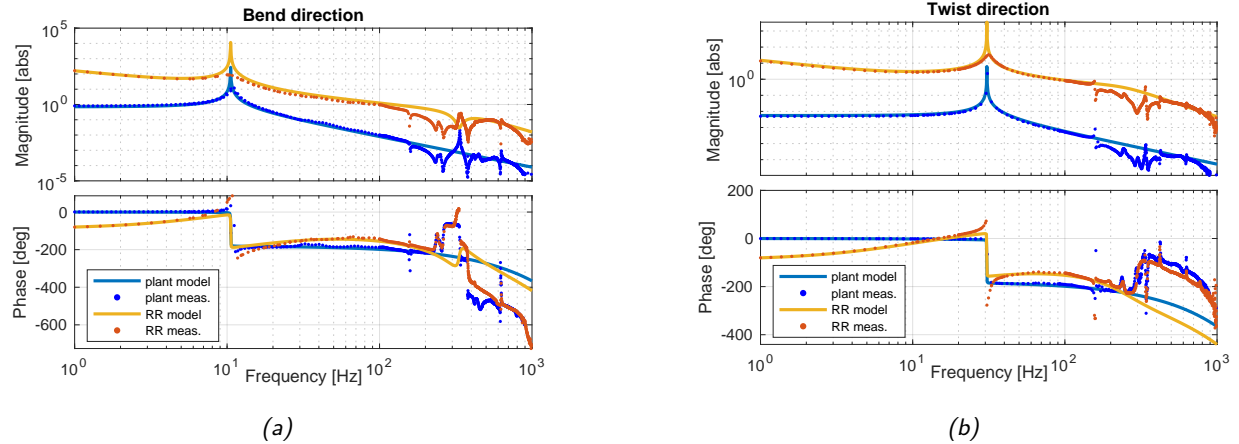
FIGURE 3. Measured and modeled Bode plots of plant and loop return-ratio (RR), of the T-beam system driven in (a) bend, and (b) twist directions. The plant inputs are the decoupled bending and twisting control voltages [V], and the plant outputs are the decoupled bend [mm] and twist [rad] displacements. The units of the plant magnitudes are in mm/V and rad/V for bend and twist respectively and RR magnitudes are dimensionless.
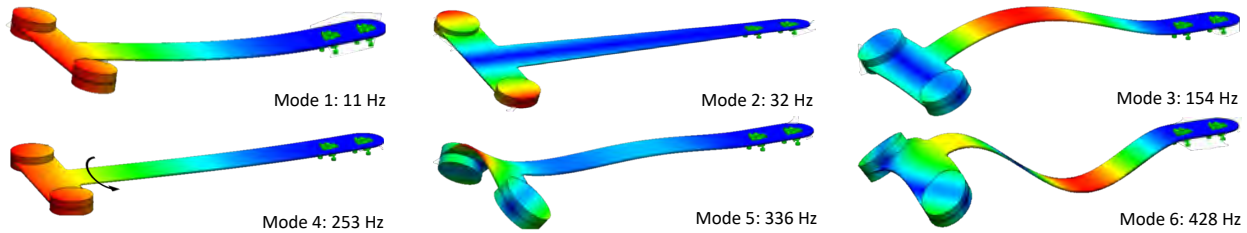
FIGURE 4. First 6 flexible vibration modes of the FlexLab T-beam, as determined by finite element analysis. Color gradients represent maximum total displacement from blue (small displacement) to red (large displacement).

TABLE 1. Modeling Parameters

Description	Parameter	Value	Unit
beam length	l_{beam}	65	mm
beam width	w	9.525	mm
beam thickness	t	0.25	mm
T end length	$2L$	30	mm
elastic modulus	E	110.3	GPa
shear modulus	G	38	GPa
mass of PM pair	m	1.7	g
amplifier gain	g_{amp}	2	V/V
coil resistance	R_c	10.5	Ω
coil force-const.	K_i	0.055	N/A
Hall-sensor sens.	S_{Hall}	1.25	V/mm

.

Fig. 3 shows the modeled and measured plant and return-ratio Bode plots in the bend and twist directions. The fidelity of the model is limited to 100 Hz due to only accounting for the first two lumped flexible modes in the dynamic model. However, there are higher frequency dynamics present in the system,

which are observable in the measured plant bend and twist frequency responses. The next four flexible vibration modes occur at approximately 154 Hz, 253 Hz, 336 Hz, and 428 Hz. These modes are all a combination of bending, twisting, and sideways motion; their respective shapes can be seen in Fig. 4. Since these higher frequency mode shapes do not strictly fall into the bend or twist category, the vibration modes are more complex to model, and not amenable to control from the available inputs. Based on the plant Bode plot measurements, the high frequency modes that are problematic to control loop stability are the 3rd and 5th flexible modes. The Controller Design section discusses the control implications of these higher order modes.

SENSING NOISE REDUCTION

One of the main contributions of this paper is showing how to use an FPGA to implement high-speed oversampling, and thereby extend the control loop bandwidth in the face of sensing noise. In our system, the sensing noise is dominated by analog to digital converter (ADC) quantization. The NI-myRIO has a 12-bit ADC, with a 0–5 V range on the A,B
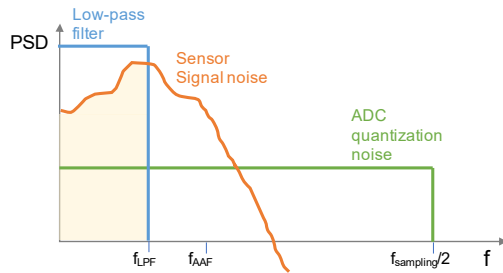
FIGURE 5. *Power spectral density (PSD) of sensor and ADC noise components. Digital low-pass filter cuts off noise density as shown.*

connectors [3]. The corresponding measurement resolution is 1.2 mV per least-significant bit.

Oversampling and averaging [4] helps improve sensing resolution by reducing the effective ADC quantization noise as shown in Fig. 5. The sensor has an approximately white-noise component from 0 to f_{AAF}, the anti-aliasing filter cut-off frequency. This PSD is independent of sampling frequency and depends on many factors such as inherent sensor noise characteristics, wiring, signal conditioning, and AAF. On the other hand, ADC quantization noise has approximately white-noise characteristics from 0 until $f_{sampling}/2$, the sampling Nyquist frequency. This noise has a fixed variance and therefore its PSD magnitude reduces with increasing sampling frequency.

Reduction in quantization noise is achieved by: (1) sampling much faster than the required crossover frequency, which spreads out the quantization noise power over a wider range of frequencies up to the Nyquist frequency ($f_{sampling}/2$), and (2) implementing a low pass filter at a frequency (f_{LPF}) such that only noise power up to f_{LPF} remains. These stages reduce the overall noise variance and thereby improve the apparent measurement resolution. The sensor noise, originally appearing up to the anti-aliasing filter cut-off (f_{AAF}), is also limited by f_{LPF}. All noise sources are assumed to be Gaussian, which is a good approximation for commonly available ADCs in which the quantization non-linearity can be ignored.

FPGA implementation in the NI-myRIO enables 2-channel sampling rates of up to 250 kHz along with 256-pt. MA filters at this data rate. This high speed implementation helps in two ways: (1) by oversampling 256-times faster, we can reduce the ADC quantization noise standard deviation approximately by a factor of 16, which corresponds to an increase in effective number of bits (ENOB) of 4 [5]. Thus, the ADC input behaves as a 16-bit ADC up to a bandwidth of about 1 kHz; (2) achieve higher sensing

resolution while reducing the accompanying phase lag in the control loop. The 256-pt. MA filter is a linear-phase finite impulse response (FIR) filter and has a phase drop reaching about 18° at the desired crossover of 100 Hz. The control loop running at 100 kHz loop rate causes negligible phase drop of 0.18° at 100 Hz due to the zero-order hold (ZOH). On the other hand, if the controller is implemented on the real-time processor in the NI myRIO, the maximum achievable control loop rate is about 2 kHz, which causes a phase drop of about 9° at 100 Hz due to the ZOH. Implementing non-linear phase FIR or Infinite Impulse Response (IIR) filters as the low-pass filter could further help reduce phase lag due to oversampling and averaging. The value from the MA filter is placed in a memory location from which the control-loop reads values at a lower rate of 100 kHz, which is like the decimation step [6].

Fig. 6 shows the measured sensor noise in the bend and twist directions under closed loop control with oversampling and averaging. The noise standard deviation in both directions is about 60 µV, which corresponds to 50 nm and 3.3 µrad (0.2 milli deg) RMS positioning noise in the bend and twist directions respectively. Frequencies where the CPS plot shows a large jump correspond to frequencies with high noise power. For the bend direction, this corresponds to about 45 Hz which is likely from some external source such as floor vibration. For the twist direction, the noise power jumps significantly at about 154 Hz corresponding to the 3rd flexible mode of vibration. In contrast, raw measurements have a noise standard deviation of about 600 µV which corresponds to 500 nm positioning noise in the bend direction. The plant requires a gain of about 100 (combination of proportional gain and lead) from the controller at 100 Hz for crossover at that frequency (Fig. 3). This controller gain would increase the control effort standard deviation to about 60 mV which results in a peak to peak noise amplitude of about 0.6 V. Thus, the control effort due to noise becomes a significant portion of the amplifier range of 5 V making it difficult to crossover at 100 Hz with raw measurements.

CONTROLLER DESIGN

Mechanical resonances arising from the flexible modes limit the achievable crossover frequency. From the measured plant Bode-plots (Fig. 3), it can be seen that the resonance at 336 Hz limits crossover for the bend direction and the resonance at 154 Hz limits the crossover for the twist direction. The 336 Hz resonance in the bend direction is from the 5th flexible mode which is both observable and controllable in the bend direction. The impact of this
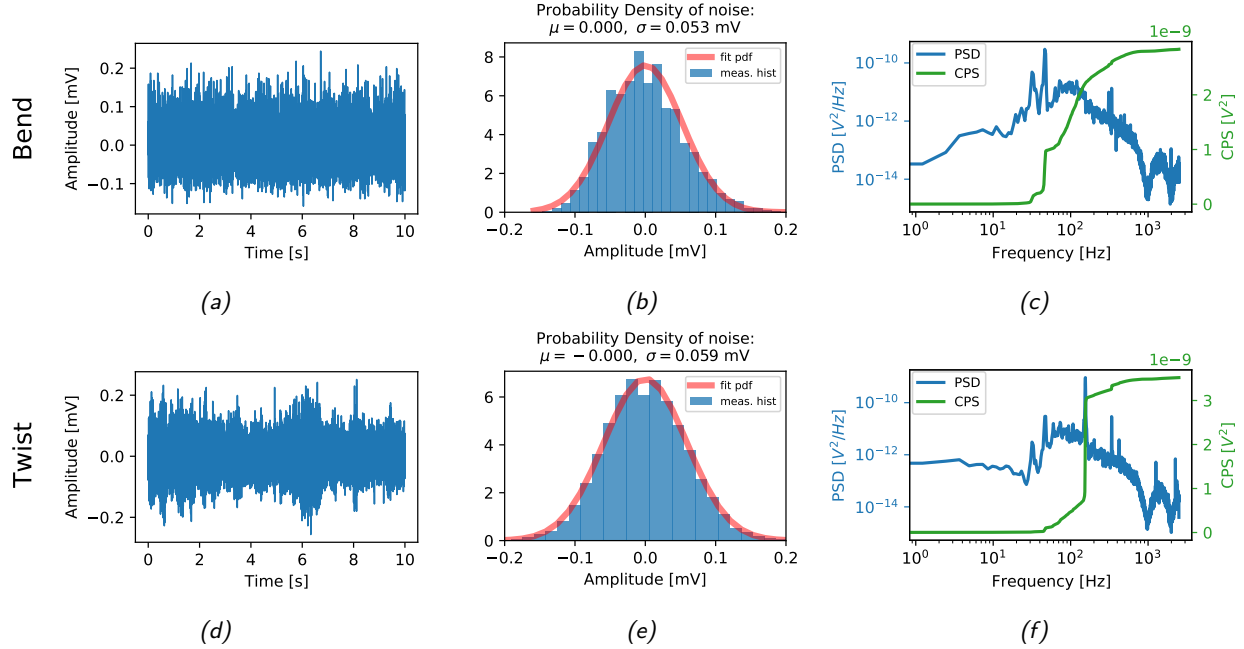
FIGURE 6. Noise measurement of position in closed loop. The top plots (a,b,c) represent the bending direction and the bottom plots (d,e,f) represent the twisting direction. (a,d) time-waveforms of bend and twist directions when reference kept at 0. (b,e) probability density of noise. (c,f) The PSD and CPS of the noise waveform.

mode is mitigated by implementing a notch filter at 336 Hz with a quality factor, Q of 10. The notch filter is of the form:

$$H_{notch}(s) = \frac{\frac{s^2}{\omega_0^2} + 2\zeta_z \frac{s}{\omega_0} + 1}{\frac{s^2}{\omega_0^2} + 2\zeta_p \frac{s}{\omega_0} + 1}$$

with $\omega_0 = 2090$ rad/s, $\zeta_z = 0.025$, and $\zeta_p = 0.25$. The 3rd flexible mode corresponding to 154 Hz resonance, in which the center of the T-beam oscillates vertically, should in principle be unobservable in the twist direction. The coupling of this mode into twist measurements is believed to be due to the small parasitic motions in the twist direction due to misalignment of PMs or other asymmetry of the T-beam mechanism. This same mode should ideally have a zero in the bend direction which is seen as an anti-resonance in the bend-direction Bode plot. This makes the 154 Hz mode observable, but uncontrollable in the rotation direction. A notch filter at 154 Hz would make this mode unobservable, but such a notch filter reduces phase significantly at 100 Hz and is therefore not feasible. Due to the parasitic origin of this mode, the magnitude of resonance is small and this mode was managed by keeping the phase above $-180°$ to keep the loop stable. However, the sensitivity Bode plot of the closed loop in the twist direction is large at 154 Hz and this mode is easily excited by any jerk in the bending direction

that can excite the 3rd vibration mode. The excited oscillation slowly dampens out from energy dissipation in the mounting joints and structural damping in the T-beam.

With the notch filters in place, a standard PID controller with a low pass filter is used in both bend and twist directions. The controllers were designed in continuous time and then mapped into discrete time using pole-zero matching for implementation as difference equations in the FPGA at $T_s = 10\,\mu s$ loop time. The controller is of the form:

$$G_c(s) = K_p \left(1 + \frac{K_i}{s}\right)\left(\frac{\alpha \tau s + 1}{\frac{s^2}{\omega_0^2} + 2\zeta \frac{s}{\omega_0} + 1}\right)$$

with the values of $K_p = 31.25$ V/mm, $K_i = 62$ rad/s, $\alpha = 20$, $\tau = 3.9789 \times 10^{-4}$ s, $\omega_0 = 2285$ rad/s, and $\zeta = 0.707$ for the bend direction. For the twist direction, the values are $K_p = 375$ V/rad, $K_i = 45$ rad/s, $\alpha = 10$, $\tau = 5.6841 \times 10^{-4}$ s, $\omega_0 = 1600$ rad/s, and $\zeta = 0.5$. Fig. 3 shows the measured decoupled loop return ratios using the specified controller parameters. As discussed in the Plant Modeling section, high frequency dynamics are observable in both the bending and twisting directions.

(a)

(b)
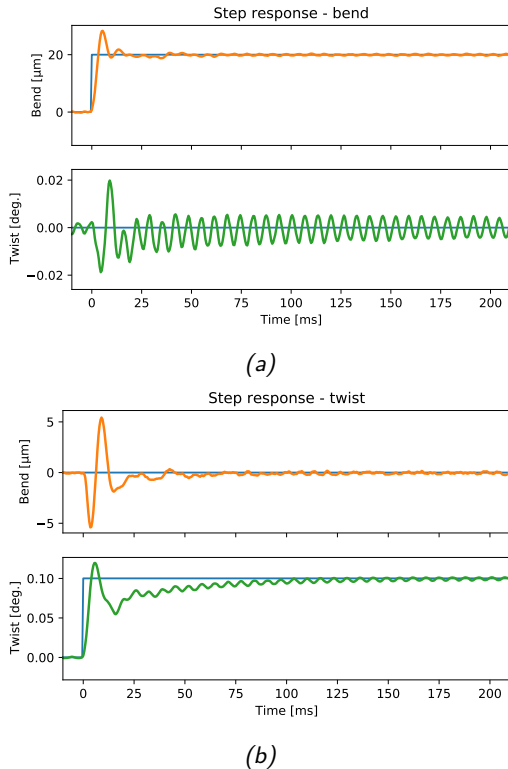
FIGURE 7. Step responses in bend and twist.

RESULTS AND DISCUSSION

With oversampling and averaging, we are able to achieve a crossover frequency of 100 Hz in both the bend and twist directions with a phase margin of about 40° (Fig. 3). Step responses of the system in bend and twist directions is shown in Fig. 7. The step responses are consistent with the crossover and phase margin obtained above. As expected, in the step response for the bending direction, the impulse excites the 3rd flexible vibration mode at 154 Hz that shows up parasitically in the twist direction and rings down very slowly. Note that this mode is visible because of the improved sensing resolution. In the raw measurements, this mode gets masked by the ADC noise. Using the raw ADC measurements we can achieve a maximum crossover frequency of about 50 Hz in the bend direction and 65 Hz in the twist direction with 40° phase margin.

The control bandwidth is severely limited by the resonance at 154 Hz. The performance of the system could be improved by increasing damping of the T-beam or by better alignment of the magnets and the Hall sensors to decrease the magnitude of the resonance. Further, the 3rd flexible mode could in principle be actively damped using the 3rd coil at the center of the long beam - the location at which the beam has large amplitude in this mode (anti-node).

SUMMARY

In this paper, we presented an example of improving the control performance enabled by sensing noise reduction by oversampling and averaging and high-speed control implementation in FPGA. The control was implemented in an NI-myRIO for 2-DOF T-beam control on the Flexlab PCB. We also describe the role of dynamics in achieving desired control performance and the use of spectral noise analysis tools. The approach described in this paper provides a relatively low-cost way to improve the control performance on commonly available high-speed micro-controllers that frequently have low-resolution ADCs.

SOFTWARE

Sample LabVIEW code for implementation of the controller on the FlexLab hardware using NI-myRIO is provided at [7]. The design details of the FlexLab system are open-source and can be found at [8].

REFERENCES

[1] L. Zhou, J. Y. Yoon, A. Andriën, M. I. Nejad, B. T. Allison, and D. L. Trumper, "Flexlab and levlab: A portable control and mechatronics educational system," *IEEE/ASME Trans. on Mechatronics*, vol. 25, no. 1, pp. 305–315, Feb. 2020. DOI: 10.1109/TMECH.2019.2951308.

[2] D. Trumper, in *2.14 Analysis and Design of Feedback Control Systems. Spring 2014*, MIT OpenCourseWare, Cambridge MA, 2014.

[3] *User Guide and Specifications NI myRIO-1900*, 376047C-01, National Instruments Corp., May 2016. [Online]. Available: http://www.ni.com/pdf/manuals/376047c.pdf.

[4] B. Bhushan and D. Trumper, "Low cost, high dynamic range position sensing enabled by oversampling and averaging," in *2020 ASPE Spring Topical Meeting Design and Control of Precision Mechatronic System*, May 2020.

[5] "Improving Adc Resolution By Oversampling and Averaging," pp. 1–20, 2013. [Online]. Available: https://www.silabs.com/Support%20Documents/TechnicalDocs/an118.pdf.

[6] A. V. Oppenheim and R. W. Schafer, *Discrete-Time Signal Processing*, 3rd edition. Pearson Education Limited, 2013, p. 647, ISBN: 978-0131988422.

[7] B. Bhushan, *FlexLab*. [Online]. Available: https://github.com/mbrijbhushan/Flexlab.

[8] L. Zhou, *FlexLab Design Files*. [Online]. Available: https://pmc.mit.edu/projects/project-flexlab-and-levlab.

Improvement of the Reversal Motion of a Numerical Control Moving Table by Frictional Force Compensation

Yusuke Inomata[1], Yoshitaka Morimoto[2], and Akio Hayashi[2]
[1]Graduate Program in Mechanical Engineering
Kanazawa Institute of Technology Graduate School
Ohgigaoka Nonoichi Ishikawa, Japan
[2]Department of Mechanical Engineering
Kanazawa Institute of Technology
Ohgigaoka Nonoichi Ishikawa, Japan

INTRODUCTION

With the spread of numerical control (NC) machine tools, productivity has improved greatly and consistent, high-quality machining has been made possible. An NC machine tool can simultaneously control multiple axes by feed drive mechanisms, and can thus easily be used to create workpieces with a range of desired shapes. Among these mechanisms is the NC moving table, which is often used in the feed drive system for NC machine tools. The NC moving table consists of a linear guide that supports the table, a ball screw that converts rotational motion to linear motion, and a servomotor that controls the overall positioning. It is evident that the motion accuracy of the feed drive mechanism directly affects the machining accuracy, and for NC moving tables in particular, motion errors which reduce accuracy can occur during velocity reversal, such as during circular interpolation motion [1]. The cause of this motion error is often due to the frictional force characteristics generated by the ball screw, nut, or guides during velocity reversal [2]. To further improve the accuracy of these tools, appropriate compensatory methods should be developed in consideration of these frictional force characteristics at velocity reversal.

In the present study, we used a single-axis NC moving table driven by a ball screw mechanism to compensate for the loss of accuracy during reversal motions. The motion measurements are performed using a rotary encoder and a linear encoder, and the drive current value corresponding to the rotational direction force is also measured. The torque loss due to friction is calculated from these measurements, and the dynamic characteristics of the NC moving table are clarified. The reversal motion of the NC moving table is then improved by applying a frictional compensation method based on the measured motion characteristics during velocity reversal.

DRIVING PRINCIPLE OF THE AC SERVOMOTOR AND EXTRACTION OF THE TORQUE COMPONENT CURRENT

Vector control in the AC servomotor

Vector control is employed to manipulate the AC servomotor used in this study [3]. The current flowing in the motor can be expressed as a vector in the rotational direction (torque component) and the radial direction (field component). Hereinafter, these components are represented by subscripts q and d, respectively.

Relational expression between drive current component and torque

The AC servomotor is driven by a three-phase AC UVW. Using vector control, this three-phase AC UVW can be decomposed into two parts, namely, the current in the rotating direction, I_q, corresponding to the torque component, and the current in the radial direction, I_d, corresponding to the field component. Table 1 shows the conversion formula [4]. The torque, T_M, is calculated based on the I_q obtained by vector control as follows:

$$T_M = \sqrt{\frac{3}{2}} P_m \Phi_m I_q = K_t I_q$$

Here, p_m is the number of magnetic poles of the motor, K_t is the torque constant of the motor, and Φ_m is the flux linkage of the winding. Note that T_M and I_q are proportional to one another. Additionally, I_q is corrected based on the difference from the target value, and is then converted back to the UVW component before being input to the servomotor. Therefore, by using I_q for the friction compensation method during velocity reversal, the correction can be performed without being affected by the

interpolation from each control loop or by the control system delay.

TABLE 1. Conversion formulas used in vector control

Three-phase	Two-phase (fixed coordinates)	Two-phase (rotational coordinates)
U	$\alpha = U$	$q = \alpha\cos\theta + \beta\sin\theta$
V	$\beta = (V - W)/\sqrt{3}$	$d = \alpha\sin\theta - \beta\cos\theta$
W		

EXPERIMENTAL DEVICE
NC moving table to be controlled
Figure 1 shows the NC moving table used in this study, and Table 2 shows the details of the table. The AC servomotor is connected to a ball screw through a coupling and a velocity reducer, and the table moves by converting the rotational motion of the servomotor into a linear motion by the ball screw. A velocity reducer is installed in order to improve the minimum positioning accuracy, and the reduction ratio is 50. A semi-closed system is constructed in which the position information of the table is fed back by a rotary encoder with a resolution of 0.122 μm behind the servomotor. A linear encoder with a resolution of 10 nm is attached to the side of the table as an external position detector.
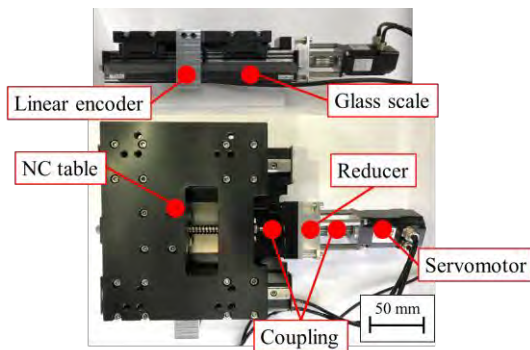
Figure 1. Photograph of the NC moving table

TABLE 2. Specifications of the NC moving table

Item	Value	Unit
Stroke	100	mm
Table size	200×200	mm
Lead length of the ball screw	4	mm
Minimum resolution	9.77	nm
Control method	P-PI control semi-closed	
Motor model number	AKM11FANMN2-00	
Motor peak output power	0.2	kW
Motor continuous output power	0.1	kW
Motor torque constant	0.046	Nm/A
Reduction ratio	50	
Torque constant	0.18165	Nm/V

Experimental system
Figure 2 shows a schematic diagram of the control system used in this study. A field-programmable gate array (FPGA) is installed in a real-time controller. Command values are sent from a personal computer (PC), which is the host computer, to the FPGA controller in the comma separated value (CSV) file format. The transmitted command value is interpolated by the position, velocity, and current loops in the FPGA controller, becomes a target value, is output to the servo amplifier, and is then driven by supplying power to the servomotor. In this system, the drive current calculated by the current loop is output from the FPGA controller to the servo amplifier as a drive voltage, and the servo amplifier then sends a current proportional to this voltage to the servomotor.
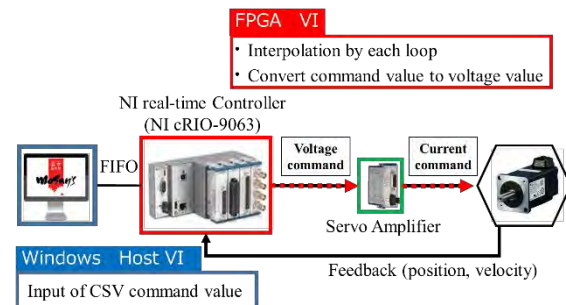
Figure 2. Schematic of the control system

MOTION CHARACTERISTICS OF THE NC MOVING TABLE
Measuring and comparing stationary time
The command value in this experiment drives the table by giving a single-axis component corresponding to a circular interpolation motion with an amplitude of 2.4 mm and a frequency of 0.14 Hz. The table position when the table is driven is measured using the rotary encoder attached to the AC servomotor and the linear encoder attached to the side of the table, and the stationary times during velocity reversal are compared. Figure 3 shows an enlarged view of the velocity reversal data. Based on the measurements for the position command, it was found that there was a stationary time of approximately 10 ms when the velocity was reversed. In the present study, in consideration of the time when the NC moving table is unintentionally stationary due to the influence of friction on the position command, the value obtained by subtracting the stationary time of the position command from the stationary time of each encoder is defined as the actual stationary time. Thus, based on the measurements from

each encoder, a stationary time of 14 ms was confirmed at the table position detected by the rotary encoder, and a stationary time of 28 ms was confirmed at the position detected by the linear encoder. As described above, the cause of this unintended stationary time is due to be the effect of the non-linear friction characteristics of the feed drive system during velocity reversal. In addition, note that the stationary time measured using the linear encoder is longer than that using the rotary encoder. This difference is because the rotary encoder detects the rotation angle of the motor and calculates the table position from the lead angle of the ball screw and the reduction ratio of the reducer, while the linear encoder directly measures the position of the table, and thus, delays due to non-linear elements, such as elastic deformation and backlash occurring in the feed drive system, as well as transmission loss due to coupling and shaft coupling, are added to the time measurement.
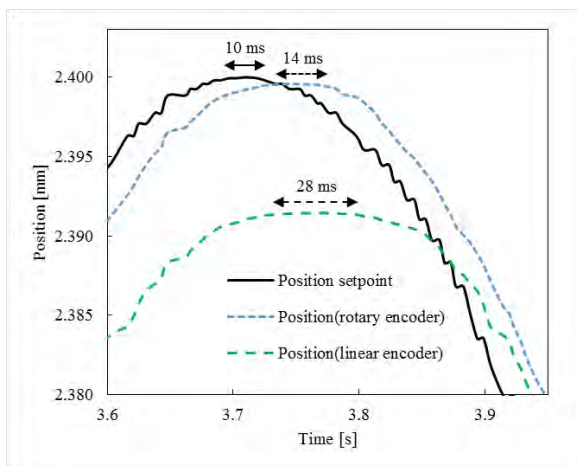
Figure 3. Position of the NC moving table at velocity reversal

Drive voltage measurement

Figure 4 shows the measurement results for the drive voltage, and Fig. 5 shows the measurement results for the T_M converted from the voltage q (torque component) and the table velocity fed back from the rotary encoder. Figures 4 and 5 show that the voltage q and T_M are proportional to one another. As shown in Fig. 5, it is possible to confirm that the table is stationary for 63 ms even though the motor torque is applied. In this interval, the static frictional force generated on the sliding surface is larger than the thrust due to the motor torque, so the table remains stationary.
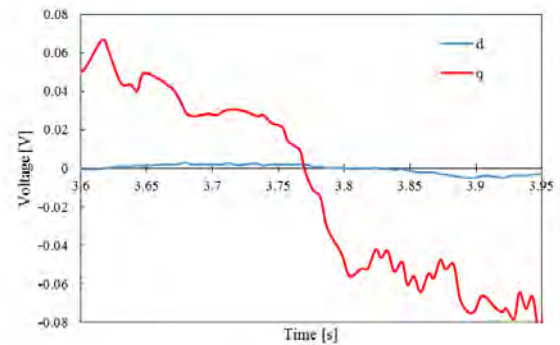
Figure 4. Torque component voltage (q voltage) and radial voltage (d voltage) at velocity reversal
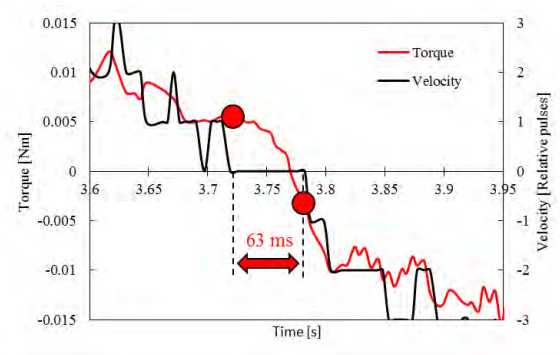
Figure 5. Motor torque and NC moving table velocity at velocity reversal

Friction compensation method at velocity reversal

Figure 5 shows that the table is stationary when the motor torque is within the range of 0.006 Nm to -0.003 Nm. We attempted to shorten the stationary time within this range, and the devised compensation method is shown in Fig. 6. The guiding principle of the devised compensation method is that the stationary section can be quickly exited by rapidly reducing the torque when the torque becomes less than 0.006 Nm, which corresponds to the onset time of the stationary torque. Figure 7 shows the motor torque and table velocity at the time of velocity reversal when the devised frictional compensation method is applied. As shown in Fig. 7, the motor torque reverses from the positive direction to the negative direction more quickly than in the case without the applied compensation, and the reversal motion is also observed to start earlier. Furthermore, the interval in which the table is stationary is 25 ms, which is a lower value compared to the case without the applied compensation. Figure 8 shows a comparison of the position measurement results of the NC moving table

detected by each encoder in the velocity reversal unit with and without compensation. Although the measured value with the rotary encoder in Fig. 8 exceeds the command value of 2.4 mm, it can be observed that the reversal occurs earlier with the compensation applied. On the other hand, the measurement results with the linear encoder do not overshoot this value, while the reversal motion still occurs faster due to the applied compensation. It is thus considered that the motion accuracy is improved by the proposed compensation. Additionally, as shown in Fig. 7, the torque near 3.85 s increases rapidly. Given that there is also a sudden rise in position approximately 3.85 s after the reversal motion measured by each encoder, the rapid change in torque is considered to be due to the original position command being restored by the feedback operation of the program after the end of the compensation signal. That is, after the compensation is completed, the positional command value is rapidly returned to the original value, thus causing the torque to overshoot drastically.
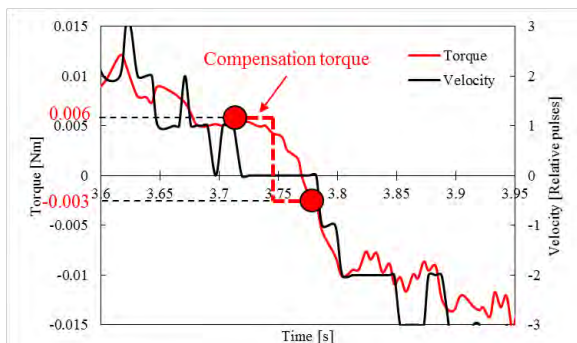
Figure 6. Compensation torque generated by the proposed method
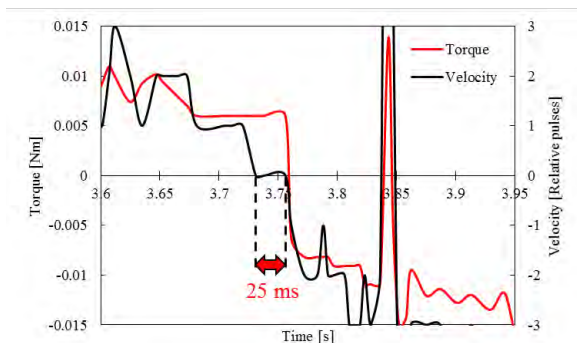
Figure 7. Result of compensation application
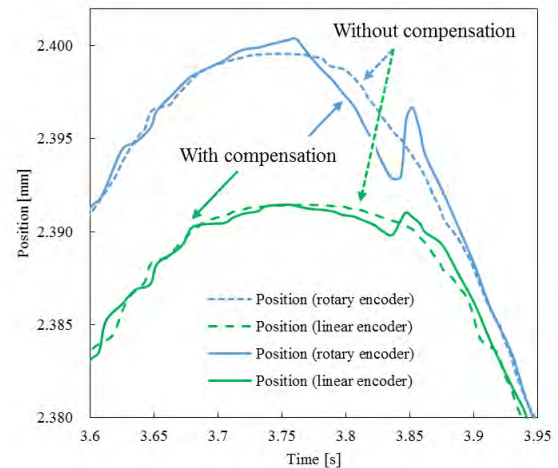
Figure 8. Position measurement results for the NC moving table with and without compensation by each encoder

CONCLUSION

1. Based on the measurement results for the voltages q (torque component) and d (field component) extracted via vector control and the velocity data of the NC moving table, we confirmed that the table was stationary for an interval of time when the velocity was reversed.

2. By applying the devised compensatory method, the reversal motion could be sped up, but the table position thereafter also increased sharply.

3. It was confirmed that it is effective to perform compensation at the time of velocity reversal using the motor drive current value.

REFERENCES

[1] Y. Kakino, Y. Ihara, Y. Nakatsu, A. Shinohara. Study on Motion Accuracy of NC Machine Tools (6th Report) -Generation Mechanism of stick Motion at Circular Interpolation Feed and Its Correction-. Journal of Japan Society for Precision Engineering. 1990; 56: 739-744

[2] R. Sato. NC Machined Surface Simulation Technology Considering Motion Error of NC Machine Tools. Journal of Japan Society for Precision Engineering. 2017; 83: 204-209.

[3] M. Ishizima. Control Circuit Design For Small AC Servo Motor. CQ, 1987; 105-112.

[4] T. Kuboshima. AC Servo Motor Control Method and Application. Modern books, 1993; 36-40.

ROLE OF PRECISION ENGINEERING IN PUSHING THE PERFORMANCE LIMITS OF NANOSCALE ADDITIVE MANUFACTURING

Harnjoo Kim and Sourabh K. Saha
G.W. Woodruff School of Mechanical Engineering
Georgia Institute of Technology
Atlanta, GA 30332, USA

INTRODUCTION

Nanoscale additive manufacturing (AM) based on two-photon lithography (TPL) is a promising technology for fabrication of arbitrarily complex 3D structures with submicron features. The TPL process relies on nonlinear absorption of light in photosensitive polymers to locally generate sub-diffraction features smaller than the focused light spot [1]. TPL has been extensively used in the past to fabricate functional structures such as mechanical and optical metamaterials, miniaturized optics, biological scaffolds, micromachines, and electrochemical interfaces [1]. Although TPL has traditionally been limited to research labs and one-off demonstrations due to its low throughput, the recent demonstration of a high-throughput projection-based TPL technique has expanded the opportunities for its broader adoption in real-world applications [2]. Here, we critically analyze and review the past research in TPL to identify the areas in which performance improvements can be achieved by applying precision engineering principles. We focus on the factors that limit the rate of printing, size of the printed structures, the material variety and complexity in a printed structure, the uniformity of printing, and the affordability of the process.

Figure 1. Schematic of serial scanning TPL and exemplary printed structures.

PROCESS OVERVIEW

In TPL, absorbed light locally cures a photopolymer into cross-linked polymeric features. Printing occurs only when the light "dosage" (i.e., a combination of intensity and exposure time) exceeds a threshold. The 3D structure is developed by dissolving and washing away the uncured photopolymer leaving behind the cured polymer. TPL relies on nonlinear two-photon absorption to achieve sub-diffraction printing on the nanoscale [1]. Due to the nonlinear behavior, the dosage gradient is stronger than the intensity gradient. The printed features are therefore smaller than the focused light spot, thereby leading to sub-diffraction printing.

Since its inception in 1997 [3], TPL has undergone three generations of technology development wherein each transition represents a thousand-fold increase in rate. The most common implementation of TPL involves scanning a focused femtosecond (fs) laser beam in 3D space to generate the 3D structure by printing one volumetric pixel (i.e., "voxel") at a time (Fig. 1). The 1st generation of TPL systems used piezoelectric mechanical stages for this scanning [4] whereas the 2nd generation systems with a thousand times higher throughput used high-speed galvanometric stages [5]. The rest of the serial implementation remained the same. Recent work on femtosecond projection TPL (FP-TPL) has further increased the rate of printing by a thousand times through parallelization [2]. The key difference between this 3rd generation system and the previous systems lies in the light focusing mechanism and the projection process; the rest of the implementation remains the same.

Parallelization in FP-TPL was achieved by projecting a patterned 2D "light sheet" (comprising a million points) that is focused *both in space and time domains*. The light sheet can be patterned into arbitrary 2D patterns through a digital mask in the form of a digital micromirror device (DMD) which is a standard component of
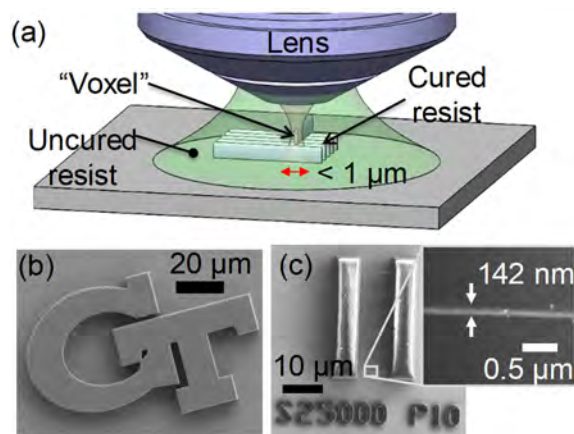
digital projectors (Fig. 2). The broadband nature of the ultrafast laser source and diffraction from the grating-like DMD was harnessed to achieve temporal focusing [2]. In this technique, the fs pulse is progressively shortened as it travels through the photopolymer resist so that the shortest pulse (i.e., highest light intensity) is achieved only at the spatial focal plane. Thus, printing can be spatially restricted in the focal plane without any polymerization above or below it.
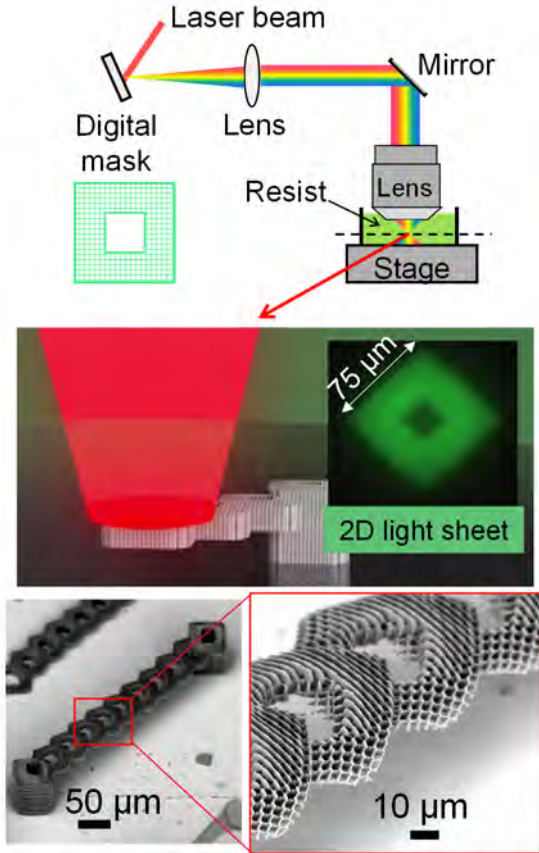
Figure 2. Schematic of parallelized FP-TPL and exemplary printed structures [2].

RATE OF PRINTING
In serial TPL, the rate of printing the 3D structures scales with the volume of the printed material whereas the rate of printing in the parallel FP-TPL technique scales linearly with the height of the structure. The total print-time for the serial (t_s) and parallel (t_p) process are given by:

$$t_s = N_l\left(\frac{L_s}{V} + t_{l,s}\right) \qquad \text{(Eq. 1)}$$

$$t_p = N_l\left(t_e + t_{l,p}\right) \qquad \text{(Eq. 2)}$$

Here, N_l is the number of layers printed, L_s is the total linear path length per layer during serial printing, V is the linear speed of serial printing, $t_{l,s}$ is the step-settle time to move to the next layer during serial printing, t_e is the exposure time per projection during parallel printing, and $t_{l,p}$ is the step-settle time to move to the next layer during parallel printing. Typical numerical values for these parameters are: V=10 mm/s, L_s=10mm $t_{l,s}$ = 20 ms, t_e=5 ms, $t_{l,p}$=15 ms. It is important to note here that Eq. 1 is a lower bound estimate of the print-time for the serial case because it does not account for the time taken to accelerate and decelerate the beam/stage. The contribution from acceleration and deceleration is less than 17% for moderate speeds of 10 mm/s but becomes a significant fraction of the total print-time with increasing speed (up to 50% at 50 mm/s).

The rate of printing a single layer during serial TPL can be increased by increasing the scanning speed and the maximum acceleration and deceleration of the beam scanner. In addition, high-speed scanning will require either open-loop or closed-loop position control to ensure that the beam tracks the desired print locations. At the current scanning speeds of ~10 mm/s, the ratio of time spent on moving the stage from one layer to the next (by 1-2 µm per step) versus the time spent on printing a single layer is 1:50. Therefore, improving the dynamic performance of the vertical motion stage (i.e., Z-stage) will not have a major impact on the printing rate. However, at significantly higher writing speeds, improvements in the step-settle dynamic performance of the Z-stage will be necessary to increase the overall rate of printing.

The rate of printing a 3D structure in the parallelized FP-TPL process can be increased by increasing the area of the 2D projection. The area of projection can be increased by projecting larger images using a larger digital mask and by using oil immersion objective lenses with larger field-of-view (FOV) than commercial off-the-shelf lenses. In addition, the dynamics of the Z-stage has a significant impact on the overall rate. This is because the ratio of time spent on moving the stage from one layer to the next (by 1-2 µm per step) versus the time spent on printing a single layer is 3:1 for FP-TPL. However, reducing the step-settle time ($t_{l,p}$) to less than 10 ms is challenging because it is challenging to achieve scan rates higher than 100 Hz with mechanical motions stages. To overcome this, one may take advantage of focus tunable lenses to optically

scan the focal plane within the photoresist material. In addition, the low weight (< 5 g) of the substrate and small step sizes (1-2 μm) may be leveraged to design high-dynamics mechanical stages suitable for high-speed FP-TPL.

PART SIZE

The width and depth of the printed parts in both serial TPL and FP-TPL are determined by the size of the FOV of the objective lens. Due to the limited FOV of high numerical aperture (NA) immersion lenses (~100 μm diameter), larger parts must be generated by stitching together individual sections corresponding to each FOV [2]. Seamless stitching is challenging due to the accuracy and repeatability limitations of mechanical stages (Fig. 3). For seamless stitching, the X-Y stages must be repeatable to within less than the feature width (~ 100 nm). In addition, the stages must not drift along the perpendicular direction by more than the feature width (~100 nm) while moving over a distance of ~10 mm. This 10^5 dynamic range (range/drift) is challenging to achieve, especially in desktop-scale low-cost motion stages.
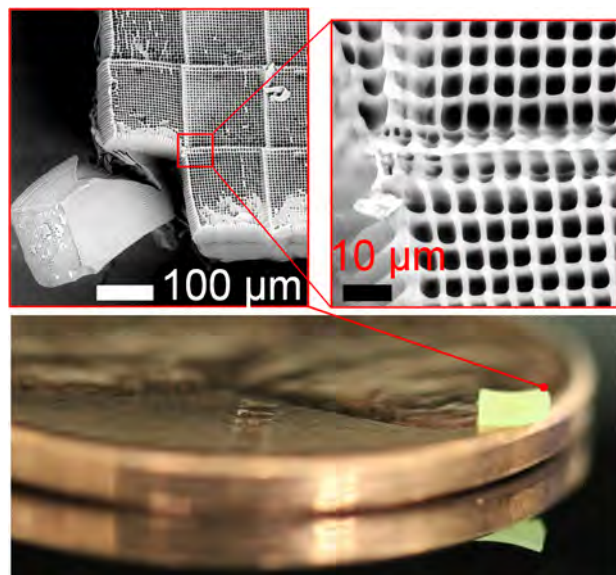
Figure 3. Visible seams due to imprecise motion stages present during printing of a 3D structure by FP-TPL [2].

The height of the printed features is limited by the spherical aberrations induced by a mismatch in the refractive index (RI) of the photoresist and the immersion medium of the objective lens. When present, the defocusing due to spherical aberrations limits the height of the printed structures to less than 100 μm because the beam cannot be sharply focused deeper into the material. Both serial TPL and FP-TPL encounter this limitation. A straightforward workaround for this limitation is to tune the RI of the photoresist to match that of the immersion medium of the lens. However, this approach is not applicable for a vast majority of photoresists wherein tuning of the RI may adversely affect other relevant properties of the photoresist. Another workaround is to modify the lens to hold a thin film of the immersion oil sandwiched between the exit aperture of the lens and a transparent thin glass window (6). This minimizes spherical aberrations by reducing the distance over which the focused beam encounters a medium with a mismatched RI. However, this technique is challenging to implement due to the small working distances of immersion lenses (~ 100 μm) and due to challenges of handling thin and fragile glass windows (~170 μm). Solving this challenge will significantly increase the number of materials that can be used to print mm-scale tall structures with TPL.

MATERIAL COMPLEXITY

There are at least two challenges to printing complex multi-material 3D structures using TPL: (i) printing with different photoresist materials that are compatible with each other and (ii) precisely locating the voxels (i.e., volumetric pixels) that are printed with different materials in relation to each other. The first challenge can be tackled for TPL by printing with materials that have similar underlying chemical reaction mechanisms. For example, using photoresists with acrylate functional groups ensures that strong covalent bonds can form between the materials after printing. The second challenge has recently been solved in microscale projection stereolithography wherein a new photoresist material is pumped into the printing zone while the previous photoresist is displaced out (7). However, this approach is challenging to implement for TPL due to the higher viscosity of the photoresists and the fragile nature of the printed parts. Instead, one should fully develop the parts before printing with a new photoresist. As the substrate must be moved out of the printer for development, this approach requires submicron registration for accurate positioning.

Submicron registration can be achieved in TPL printers by using a combination of passive and active alignment techniques. Passive alignment using kinematic mounts has already been demonstrated for multi-material TPL printing in

the past [8]. However, active alignment is limited by the lack of high-precision motion stages and sensors. Often, optical imaging is the only sensing modality available on TPL printers and it is ineffective for submicron registration at the length scale of the voxels (~100 nm). In addition, it is challenging to build low-cost motion stages with mm-scale range and nm-scale resolution that are necessary to achieve the submicron registrations through active alignment. Solving this challenge will enable printing of complex multi-material structures with precisely located voxels.

UNIFORMITY

The lack of uniformity in serial TPL is driven by two major factors: (i) non-uniform shrinkage of the printed material and (ii) non-uniform printing due to proximity effect. The non-uniformity arising from both these factors can be eliminated by extensively calibrating the process and compensating the printing conditions to account for these effects. This calibration has been performed empirically in the past. Although effective, such calibrations are not generalizable and are therefore not broadly applicable. Broadly generalizable process models (either physics-based or data-driven) would significantly improve process planning for uniform printing.
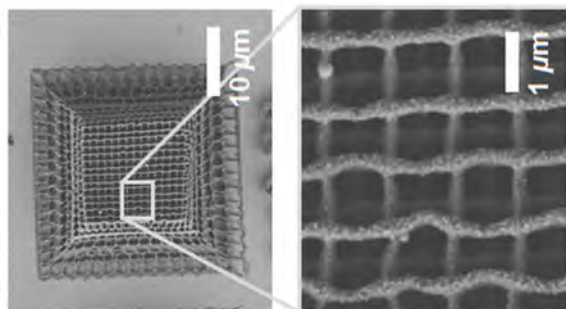
Figure 4. Non-uniform shrinkage in serial TPL [9].
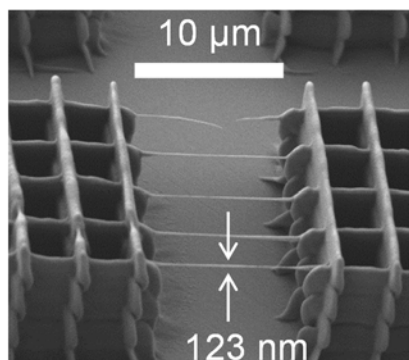
Figure 5. Non-uniform printing of suspended nanowires due to proximity effects in FP-TPL [2].

In addition to the factors present during serial TPL, FP-TPL experiences an additional source of non-uniformity due to the 2D projection mechanism. Any non-uniformity in the intensity distribution of the projected pattern would lead to non-uniform printing. Achieving flat-top intensity fields is challenging as the femtosecond lasers used in this process generate beams with Gaussian spatial intensity distribution. Flat-top intensity fields may be achieved using refractive beam shapers but the performance of such devices is highly sensitive to beam misalignments. The uniformity of FP-TPL printing can be improved by generating beam shapers that are less sensitive to misalignments or by generating active alignment techniques for alignment of beam shaping optics.

AFFORDABILITY

The cost of the TPL printers is driven primarily by the capital cost of the femtosecond (fs) laser and the high-precision motion stages. As high intensities on the order of ~ 1 TW/cm^2 are required for two-photon absorption in common photoresist materials [1], it is unlikely that fs lasers could be replaced with lower-cost lasers. Nevertheless, the cost of the printed structures can be reduced by increasing the printing rate so that more material can be printed during the finite lifetime of each fs laser. With respect to the need for low-cost high-precision stages, TPL presents a niche set of functional requirements that may be satisfied with custom-built motion stages. Specifically, serial TPL requires high-speed and high-dynamics X-Y scanners whereas FP-TPL requires high-dynamics Z-scanners. Both processes have a low load of < 5 g and require stages with ~10 mm travel range with <100 nm resolution and 1-2 μm steps. Low-cost motion stages that satisfy these requirements will significantly broaden the accessibility of TPL for real-world applications.

CONCLUSION

We have reviewed the TPL process and identified how application of precision engineering principles can improve the performance of nanoscale AM. Specifically, we have identified that (i) printing rate and size of the parts can be increased by use of precise and fast motion stages optimized for low-mass loads and cycle times of <10 ms, (ii) the material complexity of a part can be increased through use of a combination of passive and active alignment techniques with submicron repeatability, (iii) uniformity of printing can be improved by active

compensation of process parameters, and (iv) affordability can be improved by generating a new class of low-cost, high-precision, and high dynamic range (range/resolution) positioners and sensors that leverage the low-mass and small step sizes in typical nanoscale AM systems. We expect that these applications of precision engineering principles will transform nanoscale AM into a reliable industry-ready manufacturing technology.

REFERENCES

[1] Jonušauskas L, Juodkazis S, Malinauskas M. Optical 3D printing: bridging the gaps in the mesoscale. Journal of Optics. 2018;20(5):053001.

[2] Saha SK, Wang D, Nguyen VH, Chang Y, Oakdale JS, Chen S-C. Scalable submicrometer additive manufacturing. Science. 2019;366(6461):105-9.

[3] Maruo S, Nakamura O, Kawata S. Three-dimensional microfabrication with two-photon-absorbed photopolymerization. Optics Letters. 1997;22(2):132-4.

[4] Malinauskas M, Žukauskas A, Bičkauskaitė G, Gadonas R, Juodkazis S. Mechanisms of three-dimensional structuring of photo-polymers by tightly focussed femtosecond laser pulses. Optics Express. 2010;18(10):10209-21.

[5] Oakdale JS, Smith RF, Forien JB, Smith WL, Ali SJ, Bayu Aji LB, et al. Direct laser writing of low-density interdigitated foams for plasma drive shaping. Advanced Functional Materials. 2017;27(43):1702425.

[6] Obata K, El-Tamer A, Koch L, Hinze U, Chichkov BN. High-aspect 3D two-photon polymerization structuring with widened objective working range (WOW-2PP). Light: Science & Applications. 2013;2(12):e116-e.

[7] Han D, Yang C, Fang NX, Lee H. Rapid multi-material 3D printing with projection micro-stereolithography using dynamic fluidic control. Additive Manufacturing. 2019;27:606-15.

[8] Saha SK, Uphaus TM, Cuadra JA, Divin C, Ladner IS, Enstrom KG, et al. Kinematic fixtures to enable multi-material printing and rapid non-destructive inspection during two-photon lithography. Precision Engineering. 2018;54:131-7.

[9] Saha SK, Oakdale JS, Cuadra JA, Divin C, Ye J, Forien J-B, et al. Radiopaque resists for two-photon lithography to enable submicron 3D imaging of polymer parts via X-ray computed tomography. ACS Applied Materials & Interfaces. 2018;10(1):1164-72.

CERAMIC TWO-PHOTON PRINTING OF HIGH ASPECT RATIO MICROSTRUCTURES

John Cortes, Magi Mettry, Matthew Worthington, Swetha Chandrasekaran, Robert Panas
Lawrence Livermore National Laboratory (LLNL)
Livermore, CA, USA

INTRODUCTION

The additive manufacturing revolution over the last decade or so has generated novel ways to create increasingly complex three-dimensional geometries from a variety of materials. Though much of the development of additive manufacturing has focused on macro-scale processes, Two-photon Polymerization (2PP) is one of the technologies that has allowed for development of 3D printed microstructures. 2PP processes utilize femtosecond laser pulses with two-photon absorption to generate sub-micrometer features using a wide variety of photon-activated photoresists and resins [1,2]. However, much of this work has focused on printing microstructures from polymers which feature compromised mechanical properties as well as limitations high-temperature environments, which ultimately limit their scope of potential applications.

Recent advances in preceramic monomers, which are often referred to as polymer-derived ceramics (PDCs) have allowed for additive manufacturing of ceramic structures which are much stronger and temperature resistant [3]. These PDCs can then be converted into ceramics by pyrolysis at temperatures over 1000 °C in an inert atmosphere, such as argon or nitrogen gas [4]. This process removes volatile organic species such as water, carbon dioxide and other hydrocarbons, resulting in a final form of silicon oxycarbide, or SiOC. Silicon oxycarbide features low porosity and isotropic shrinkage, which is advantageous for applications that rely on consistent mechanical properties.

In this work, we present the print and characterization of ceramic structures created through 2-photon polymerization (2PP) with sub-micrometer features. More specifically, we characterize the quality of prints featuring aspect ratios as high as 100:1. Lastly, we quantify the amount of shrinkage of these prints before and after pyrolysis.

METHODS

The two-photon printing process was carried out in a NanoScribe GmbH Photonic Professional GT system. A single-side polished silicon chip measuring approximately 1" by 1" was treated by 3-(Trimethoxysilyl)propyl methacrylate (Silane) for 5 minutes at 90 °C to aid with print adhesion. A drop of the custom polymer-derived ceramic (PDC) resin was applied to the polished side of the silane-treated silicon chip. The structures were printed up-side-down using "dip-in laser lithography." The printed structure was then developed by submerging it in a beaker of propylene glycol monomethyl ether acetate (PGMEA) overnight.

After full development, the sample was dried using a critical point drying system. After critical-point-drying, the samples were pyrolyzed in an oven in a nitrogen atmosphere at temperatures of 250° C, 400° C, 600° C and 1000° C, each step for an hour. The sample was then allowed to cool down to room temperature at a rate of 5° C per min. The samples were then characterized using a Phenom XL benchtop scanning electron microscope (SEM).

RESULTS

The structures that we printed feature a base that is 25 µm by 25 µm and is approximately 5 µm tall. The blade structure is shaped in an L-shape to provide vertical rigidity and features lateral dimensions of 15 um by 15 µm. The height of the blade is set at 100 µm with a wall thickness of 1
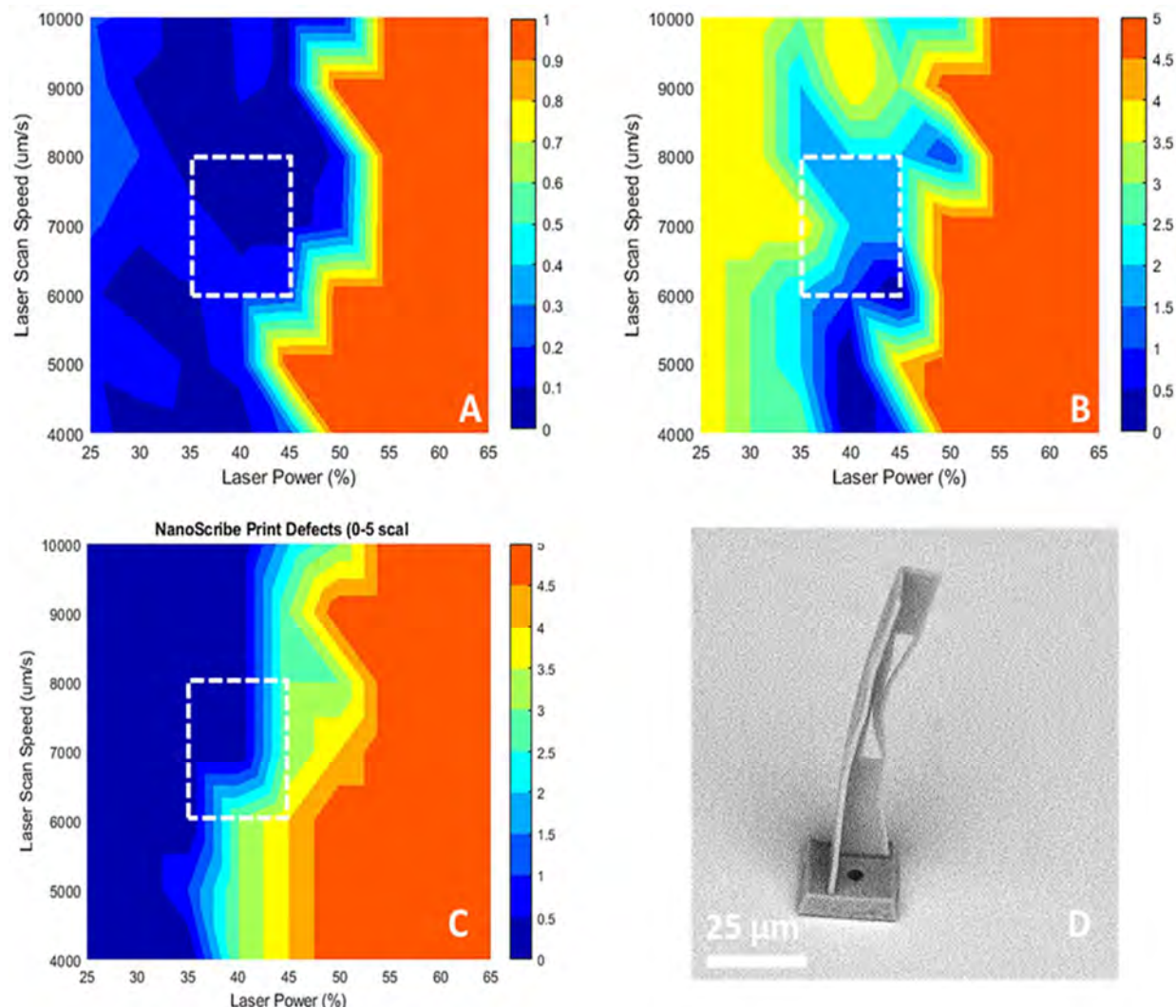
FIGURE 1. Contour characterization plots of the ceramic printing process in terms of A) deviation from designed dimensions, in μm, B) print distortion on a qualitative 0-5 scale (5 is worst), C) print defects on a qualitative 0-5 scale (5 is worst), D) SEM micrograph of one of the high aspect ratio test blades, printed at 40% power and 4,000 μm/s.

μm. Lastly, we included a diagonal 1 μm by 1 μm beam structure at the midpoint (height-wise) of the blade to test our ability to create non-horizontal and non-vertical thin structures. We characterized the quality and performance of the printing process in terms of both qualitative and quantitative methods. On the qualitative side, we measured the deviation of the blades from the designed dimensions using SEM imaging. Figure 1A shows a contour plot of the deviation from 1 μm features in terms of both the print power percentage and the galvanometer scan speed during the print process.

The 1 μm features measured were the thickness of the blades near the base. The least deviation occurs at about 40-45% power and a printing or scan speed of approximately 7,000-8,000 μm/s. We also analyzed these same SEM images for both print distortion and defects on a 0-5 scale, where 0 means no distortion or defects and 5 means that the prints were severely damaged or unrecognizable. Figures 1B and 1C show the qualitative analysis for distortion and defects, respectively. One of the more common types of distortion noticed were holes where the resin was burnt during the print process. Usually, these holes indicate that the power delivered to the
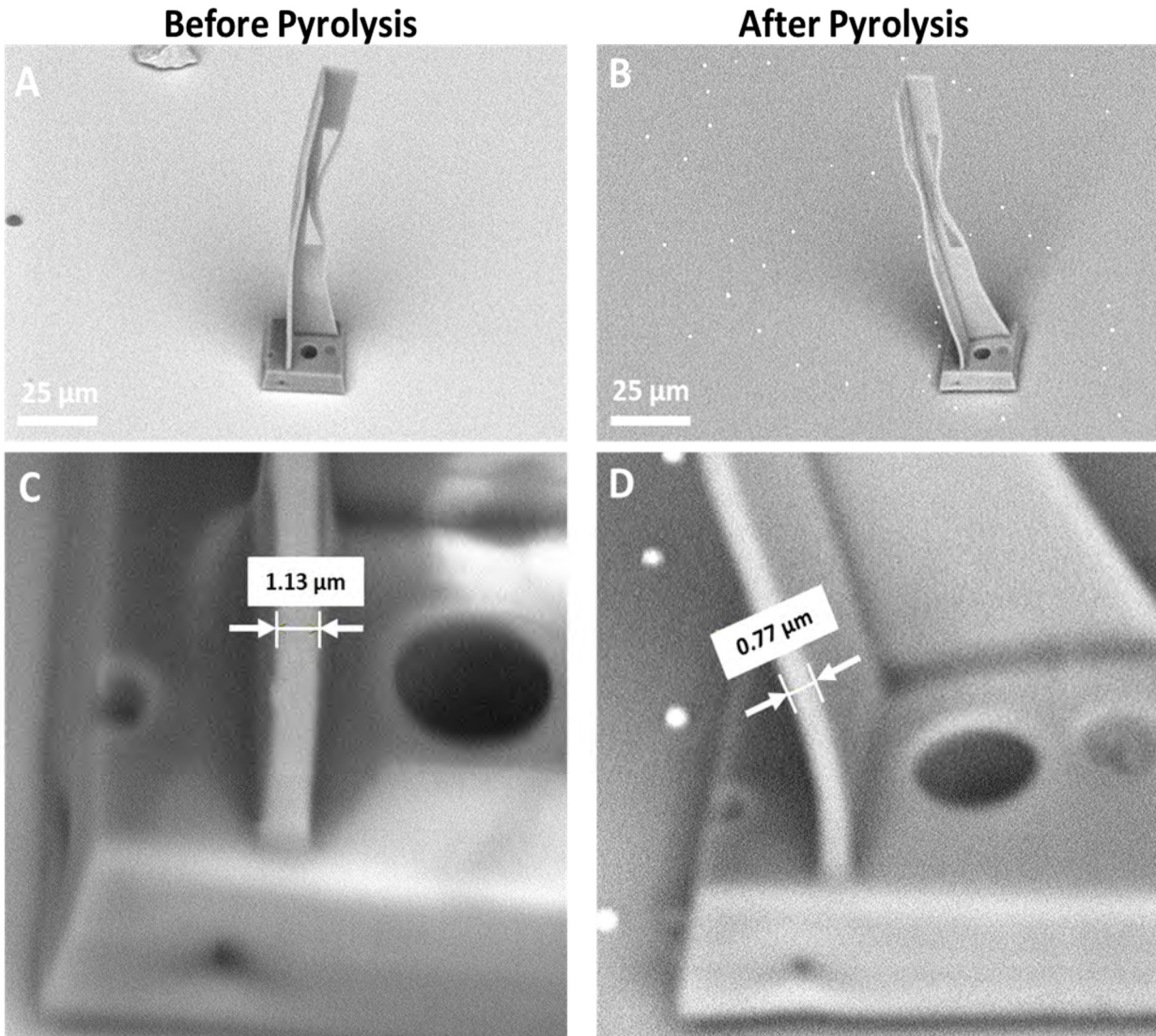
FIGURE 2. SEM pictographs of A) high aspect ratio blade structure before pyrolysis, B) high aspect ratio blade structure after pyrolysis, C) high aspect ratio blade thickness measurement before pyrolysis and D) high aspect ratio blade thickness measurement after pyrolysis.

resin is either too high (>50%) or the scanning speed is too low (under 4,000 µm/s). Figure 1D presents a structure which shows a large hole (about 5 µm in diameter).

Other distortions include structures that were not properly crosslinked due to low power inputs or scan speeds that were too high. These resulting structures were significantly weaker and did not remain vertical during the drying process.

Combining the overall performance based on these three criteria, we found that the optimal printing parameters were 35-45% power and 6,000-8,000 µm/s, which is enclosed in the white dotted line of Figure 1.

However, we found that the prints are less sensitive to variations in printing speed than variations in laser power. For example, structures with acceptable quality were achieved with speeds as low as 4,000 µm/s, as seen in Figure 1D. While characterizing the quality of these prints is useful, the ultimate goal of the project is to characterize the mechanical properties of this novel resin.

One of the major challenges of printing microstructures with a ceramic-based material in the expected shrinkage during post processing. During post-pyrolysis SEM characterization, we found that the samples shrunk uniformly and isotopically by about 30-35%. We determined this by measuring the change in thickness of the vertical wall before and after pyrolysis, as shown in Figure 2.

The beam shown initially had a thickness of about 1.13 μm before pyrolysis. After the high-temperature process, this dimension shrunk to about 0.77 μm, or about 32%. This amount of isotropic shrinkage was typical of what was measured in all other structures. It is important to note that the shrinkage was found to be independent of power and scan speed parameters.

3D printed ceramic flexures at the microscale would be useful in MEMs devices that require complex geometries with low thermal conductivities and consistent mechanical properties. For example, MEMS devices which require actuation (such as the next generation of micromirrors devices) could use ceramic based materials to further expand their range of operational capabilities.

FUTURE WORK

One of the key future components of this study includes mechanical characterization of the material properties of the ceramic materials. This will be crucial for determining the types of applications that are most suitable for these advanced materials.

In addition to this, we are exploring ways for ceramic structures printed through this process to "self-center" during shrinkage. We can accomplish this by intelligently designing anchor to the substrate that ensure that there is no lateral shift in the center point of the structures post pyrolysis. The results of this study will allow micro-device designers accurately predict the final position of PDC-based ceramic structures in relation to a substrate or surrounding device components.

REFERENCES

[1] Sourabh K. Saha, et al. "Scalable Submicrometer Additive Manufacturing." *Science*, vol. 366, no. 6461, 2019, pp. 105–109.

[2] Wei Chu, et al. "Centimeter Height 3D-Printing with Femtosecond Laser Two-Photon Polymerization." *Advanced Materials Technologies*, vol. 3, no. 5, 2018, p. 1700396.

[3] Huachen Cui, et al. "Additive Manufacturing and Size-Dependent Mechanical Properties of Three-Dimensional Microarchitected, High-Temperature Ceramic Metamaterials." *Journal of Materials Research*, vol. 33, no. 3, 2018, pp. 360–371.

[4] Zak C. Eckel, Chaoyin Zhou, John H. Martin, Alan J. Jacobsen, William B. Carter, Tobias A. Schaedler. "Additive Manufacturing of Polymer-Derived Ceramics." *Science*, vol. 351, no. 6268, 2015, pp. 58–62.

TOWARDS 3D PART FABRICATION USING A MICRO-SCALE ADDITIVE MANUFACTURING TOOL

Dipankar Behera[1], Nilabh Roy[1], and Michael A. Cullinan[1]
[1]Department of Mechanical Engineering
The University of Texas Austin
Austin, TX, United States of America

INTRODUCTION

Most of the conventional metal additive manufacturing (AM) processes today are becoming increasingly applicable the aerospace, biomedical and electronics industry because of their ability to handle complex macroscale architectures. However, the commecially available AM tools have resolutions to the order of 100s of microns which is higher to the required feature sizes in several microscale applications. Consequently, there is a gradual shift towards developing metal AM techniques with micron and sub-micron level accuracies to replace multi-step and expensive subtractive manufacturing processes[1].

In a powder fusion processes like SLS, a focused laser beam is applied on selective regions in the layers of particles to produce a sintered 3D part. There are, however, some significant challenges while producing 3D microcomponents like electronic interconnects, precision microtools, and microfluidic arrays etc. Limited laser focus, uneven agglomeration of finer particles and higher susceptibility to oxidation, largely undermine the fidelity of the microscale sintering process.
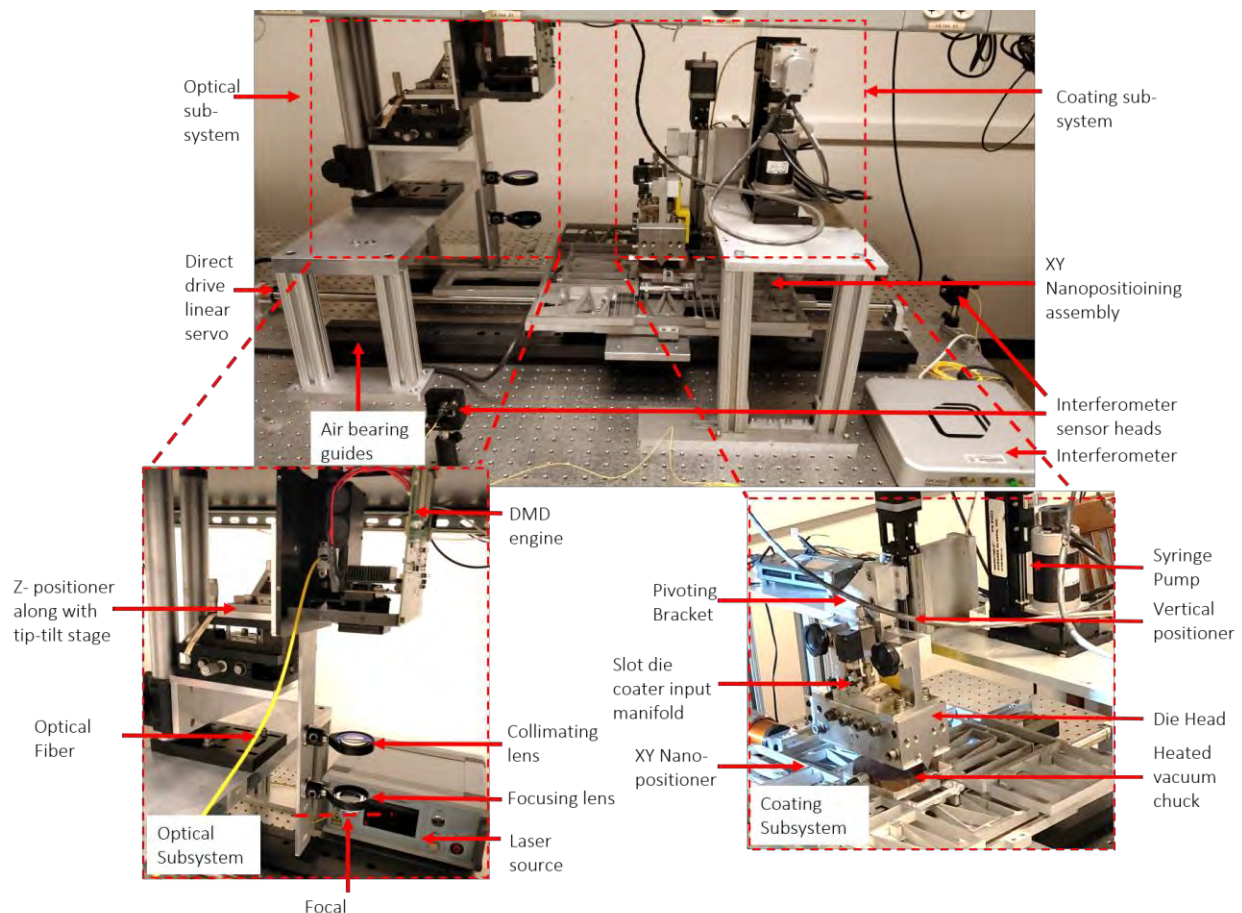
FIGURE 1: Physical Embodiment of the μ-SLS tool showing different subassemblies [2]

Figure 1 shows the physical embodiment of the Microscale Selective Laser Sintering (µ-SLS) system. The current design consists of the following subsytems: micron-level accuracy global translation system, XY-nanopositioning flexure stage, powder-bed dispense system, and the optical sub-system. The sintering process starts with the positioning of the substrate under the dispense system, followed by the translation of the dispensed bed under the optical system for sintering. The process is then repeated to fabricate layer-by-layer 3D parts. A critical auxiliary step includes the alignment of the sample under the dispense and optical subsytems to achieve submicron accuracy and repeatability in the positioning which is achieved by the long-range XY-nanopositioning stage.

SINTERING TEST RESULTS

The current sintering tests are done by horizontally setting up the optical subsystem on an optical table. After the first layer was coated and sintered, the excess ink was removed from the sample using an ultrasonication process. The ultrasonication parameters depend on the amount of ink present on the sample. Then, the samples were annealed for improving the structural and electrical properties.

MULTIPLE LAYER SINTERING

For the initial multilayer sintering experiment, a 500µm circle was sintered. The first layer of the coated substrate (100 µm coating gap) was partially dried to remove excess solvent at 115ºC for 5-7 minutes and then sintered at 50W, 4 seconds exposure duration. The average height of the sintered circle measured using optical profilometry was 2.37µm. Another sample was coated and sintered at the same parameters. The sintered sample was coated again at a 200 µm coating gap and then dried. After the second layer was dispensed on the top of the first layer, the same circular pattern was sintered at an exposure duration of 6 seconds. The average height of the 2 layers was around 5.26 µm. Excess NP ink was removed from both the samples by ultrasonicating them. The bilayer sintered sample was found to be 2.34 times higher than the single layer sample. Figure 3 shows a 3D rendering of the surface topography of single layer and two-layer sintered samples.

The subsequent multiple layer sintering results would include sintering Cu and Ag nanoparticle inks using a higher power laser for shorter exposure durations to avoid heat affected zones
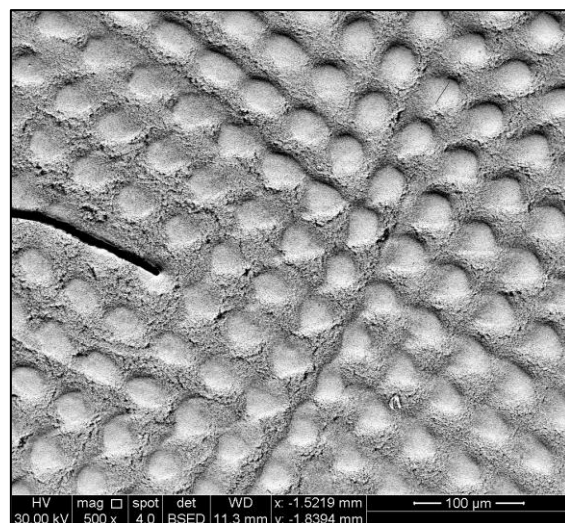
FIGURE 2: Surface topography of 20µm diameter circles with a pitch of 40 µm.
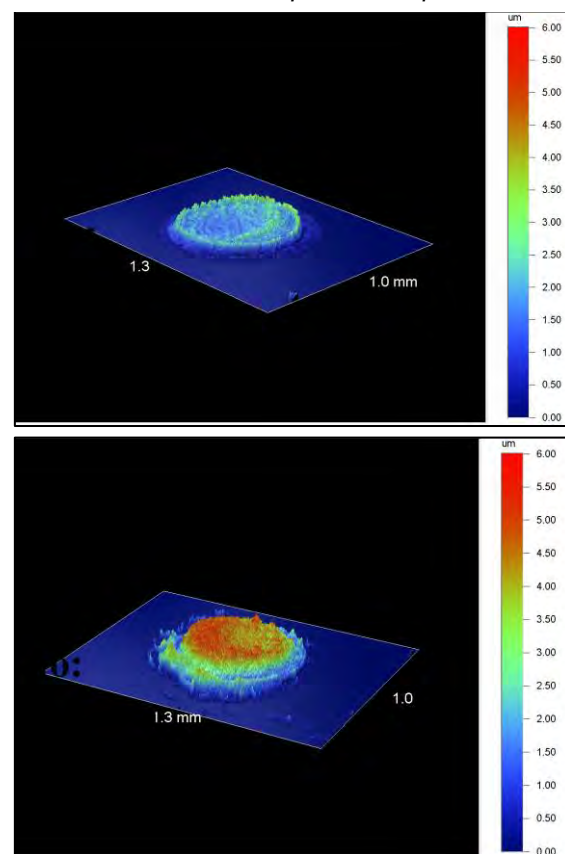
FIGURE 3: 3D rendering of the surface topography of single layer and two-layer sintered samples.

and improve the process throughput. The fabricated parts will then be used to characterize the process on the basis of the repeatabiilty of the print, coating and printing uniformity, overlay errors and the ability to achieve near net shaped features.

REFERENCES

[1]   L. Hirt, A. Reiser, R. Spolenak, and T. Zambelli, "Additive Manufacturing of Metal Structures at the Micrometer Scale," *Adv. Mater.*, vol. 29, no. 17, 2017.

[2]   Roy, N.K., Behera, D., Dibua, O.G. et al. A novel microscale selective laser sintering (μ-SLS) process for the fabrication of microelectronic parts. Microsyst Nanoeng 5, 64 (2019). https://doi.org/10.1038/s41378-019-0116-8

TOTALLY-DECOUPLED OPTICALLY VARIABLE DEVICES FABRICATED BY VIBRATION ASSISTED CUTTING

Jianjian Wang [1], Yaoke Yang [1], and Ping Guo [1*]

[1] Department of Mechanical Engineering, Northwestern University, Evanston, USA

INTRODUCTION

An optically variable device (OVD) is a colored image that utilizes diffractive optical structures to exhibit angle-dependent visual effects. When the OVD is observed from different viewing angles, different pictures will be identified. Since the OVD is not photocopiable or scannable, and cannot be accurately replicated, it is often adopted as a security element for anti-counterfeiting [1].

The principle of OVD mainly relies on the structural coloration, which utilizes micro/nano-structures to tune the reflected spectrum of incident light through interference, such as the grating diffraction of periodic structures in sub-micrometer scale [2]. Compared with pigmented color, structural color is brighter under sunlight, and more tunable through structure regulation. It is also long-lasting and does not fade over time. The most unique feature of diffractive structural color is the angle-dependent iridescent effects, which can be utilized for the fabrication of OVDs.

The precision and efficient surface texturing of micro-structures is a long-standing challenge for the fabrication of OVDs. Recent advances in micro/nanofabrication technologies have enriched the techniques of machining surface structures on various kinds of materials down to the sub-micrometer [3]. Notably, laser-based processes, represented by femtosecond laser structuring [4] and laser interference lithography [5], are attractive for industrial applications due to their high efficiency and flexibility. The current state-of-the-art for wavelength structure texturing technique utilizes laser-induced periodic surface structures (LIPSSs), which result from the nonlinear laser-matter interaction with enhanced surface plasmon. It further improves the process efficiency to overcome the serial writing of individual features with the conventional laser ablation. The generated structure spacing in LIPSS, however, cannot be easily predicted and limited in the adjustable range associated with the laser wavelength. LIPSSs also suffer from low diffraction efficiency due to the semi-random structure distribution.

Ultraprecision diamond machining with the assistance of fast/slow tool servos or multidimensional mechanical vibrations has been adapted for texturing microstructures. Compared with the laser-based processes, ultraprecision diamond machining can cost-effectively fabricate scale-tunable micro-structures with optically qualified surface finish and high form accuracy on free-formed and large-area surfaces. However, diamond surface texturing has the drawbacks of limited tunability of microstructure (replication of tool geometry), which will reduce the decoupling and visual quality of OVD [6]. Hence, how to use diamond surface texturing to fabricate totally decoupled and high-quality OVD is still challenging.

In this study, the elliptical vibration-assisted diamond cutting has been applied to generate 1D grating-type microstructures in the sub-micrometer scale on brass. Based on the directionality of one-dimensional (1D) diffractive gratings, a new strategy to fabricate OVD with totally decoupled encoding on the metallic surface has been demonstrated.

PROCESS PRINCIPLE

The principle of the proposed strategy to fabricate totally decoupled and high-quality OVD with diamond is based on the directionality of 1D gratings. FIGURE 1 illustrates the grating induced diffraction of parallel incident light. As shown in FIGURE 1, the diffraction induced desperation of white light happens in the diffraction plane, which is perpendicular to the orientation of the 1D grating. In general, the incident plane is identical to the diffraction plane, which means the incident

light is also in the principle diffraction plane. However, the diffraction of white light also happens when the incident light is not in the diffraction plane. Under this circumstance, as shown in FIGURE 1, the incident plane has an azimuthal angle ϕ with the diffraction plane.
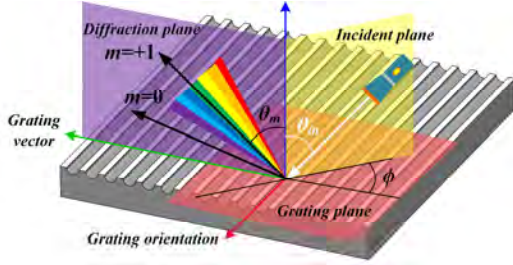
FIGURE 1. Grating diffraction of white light incident from non-principle diffraction plane.

For a general ϕ, the diffraction equation of 1D grating can be described as:

$$m\lambda = d\left(\sin\theta_m - \frac{\sin\theta_{in}\cos^2\phi}{\sqrt{\sin^2\theta_{in}\cos^2\phi + \cos^2\theta_{in}}}\right) \quad (1)$$

where θ_m is the diffraction angle of the mth diffraction order, θ_{in} is the incident angle of light relative to the normal direction of the grating plane. The gratings disperse the white light to provide structural colors through diffraction when the azimuthal angle ϕ meets specific conditions. The intensity of the dispersed white light is related to the azimuthal angle ϕ. In particular, when $\phi=0°$, the intensity of dispersed white light reaches its maximum value. However, when $\phi=90°$, the intensity of diffracted white light drops down to zero, and no dispersion spectrum can be observed [7]. Hence, OVDs with totally decoupled encoding can be realized by taking advantage of the directionality of 1D diffractive grating.

The 1D diffractive gratings are generated through the elliptical vibration-assisted cutting process. As shown in FIGURE 2, with the elliptical vibration, a circular diamond cutter forms an overlapping trajectory, which can create conjunctive scallops on the grooved surface at the rate of vibration frequency, enabling a fast surface texturing method. In elliptical vibration-assisted cutting, each vibration cycle will generate a discrete surface feature. It shows the advantages of high efficiency, low cost, and high material adaptability to utilize elliptical vibration-assisted cutting to fabricate sub-micrometer 1-D diffractive gratings.
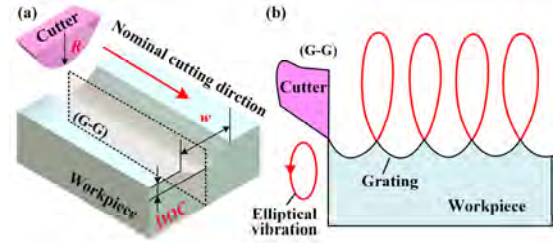
FIGURE 2. (a) illustration of the machined groove using a diamond cutter with a nose radius R. (b) illustration of the grating generation with elliptical vibration-assisted cutting.

The proposed strategy of OVD fabrication using elliptical vibration-assisted diamond cutting can be separated into two steps, as shown in FIGURE 3. At first, an elliptical vibration-assisted diamond cutting method is utilized to texture 1D grating patterns. Due to its unique surface generation mechanism, the direction of created 1D gratings is intrinsically perpendicular to the cutting direction of the diamond cutter, enabling us to control the direction of gratings easily and reliably. By modulating the cutting speed pixel by pixel, a high-resolution structurally colored image (image A) can be replicated on the metallic surface.
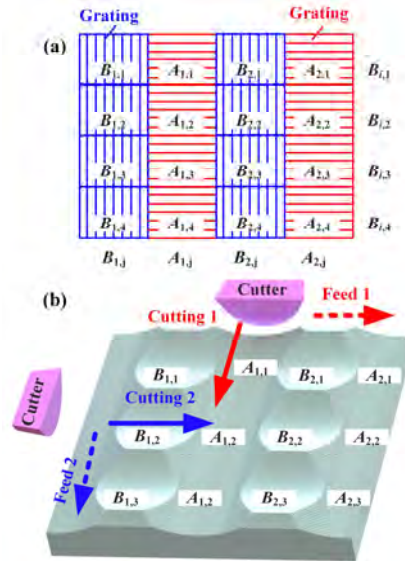
FIGURE 3. Totally decoupled encoding strategy to fabricate OVD. (a) Distribution of gratings with different orientations. (b) Programming of cutting paths.

Then, in the second step, the surface continues to be textured with a cutting direction perpendicular to the first step with a reduced depth-of-cut. In this way, due to the circular nose of the diamond cutter, the surface can be textured

with 1D grating patterns of two orthogonal directions. Also, in the second step, the other image (image B) is encoded on the surface. When the structurally colored surface with 1D grating patterns of two orthogonal directions is observed from different angles, it will show optically variable visual effects, which means we will only see one image in one direction.

EXPERIMENTAL SETUP

The experiments were conducted on an ultra-precision lathe (Nanoform X, Precitech, USA) with the coordinate system definition shown in FIGURE 4(a). It has three linear axes (XYZ axis), which can be used to generate relative servo motions of the tool relative to the workpiece. The main spindle can be used to precisely rotate the workpiece. The brass workpiece, which is pre-turned before texturing to ensure a flat surface, is fixed on the lathe using a vacuum chuck. A 2-D non-resonant vibration cutting tool, which has an operation bandwidth up to 2 kHz with full strokes of 16 µm × 15 µm, is used to perform elliptical vibration cutting. The vibration cutting tool is actuated by two-channel signals from a function signal generator (TG5011A, Aim-TTi, UK), which are amplified by a piezo amplifier (PX200, PiezoDrive, Australia). The designed elliptical trajectory at 2 kHz for surface texturing is shown in FIGURE 4(b).
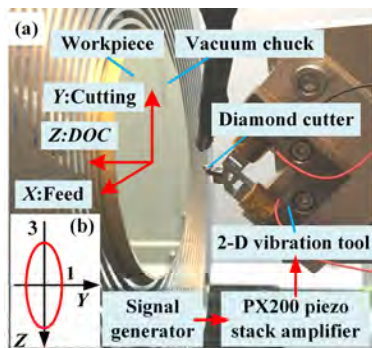
FIGURE 4. (a) Experimental setup; (b) designed elliptical trajectory when f=2 kHz.

The two images to be encoded in the OVD are shown in FIGURE 5, which are the logo of Northwestern University and Northwestern Wildcat respectively. The key process parameters for the image rendering are shown in FIGURE 6, in which the feed for both two images is 125 µm. The depth-of-cut for images *A* and *B* rendering is 4 µm and 1.5 µm respectively, which are different from each other to ensure that the second fabrication step, namely the image B

rendering process, will not wipe out all the information of image A.

FIGURE 5. Two images to be encoded in the optically variable devices. (a) Image A: the logo of Northwestern University. (b) Image B: the logo of Northwestern Wildcat.
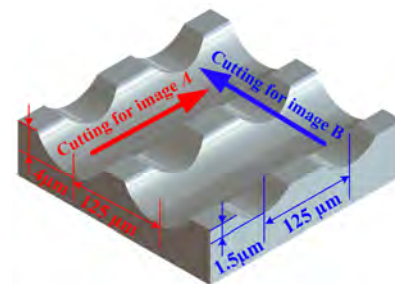
FIGURE 6. Illustration of key processing parameters including the depth-of-cut and feed.

The machined surface with grating-type microstructures was measured using an atomic force microscope (AFM, Bruker Edge, UK). The optical system to observe and record the visual effects of the machined surface is schematically shown in FIGURE 7, in which the incident angle is fixed at 20°, while the azimuthal angle ϕ varies from 0° to 90°.
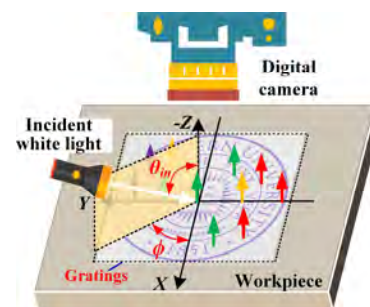
FIGURE 7. Observation method of machined results with varying azimuthal angle ϕ and fixed incident angle θ_{in} of 20°.

RESULTS AND DISCUSSION

The AFM measurement results of the grating 3D morphology and cross-sectional profiles are plotted in FIGURE 8. The grating depth is around 100 nm at the pitch of 1 µm with a relatively

smooth surface finish, which can guarantee the efficient diffraction of white light. The high-speed generation of sub-micrometer gratings is successful (at the rate of two thousand gratings per second), which should be easily extended to the ultrasonic frequency with a resonant-type elliptical vibration tool for even higher process efficiency.
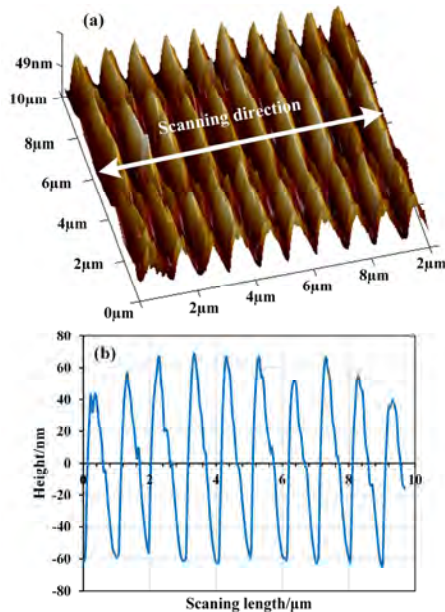
FIGURE 8. Machined results of gratings. (a) 3D morphology. (b) Scanned profile.
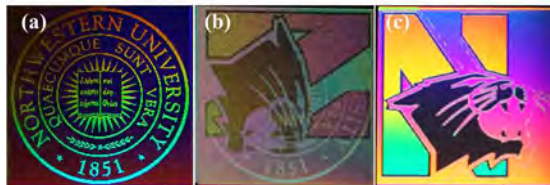
FIGURE 9. Machined results of optically variable devices with azimuthal angle ϕ of (a) 0°, (b) 45° and (c) 90°.

Texturing of diffractive grating for OVD encoding is demonstrated with samples shown in FIGURE 9. As demonstrated in FIGURE 9, when the azimuthal angle ϕ is 45°, the two encoded images cannot be distinguished from each other. However, when the azimuthal angle ϕ is 0°, only image A, namely the logo of Northwestern University can be observed. On the other hand, when the azimuthal angle ϕ is 90°, only image B, namely the logo of Northwestern Wildcat can be observed. Hence, the two encoded images have been decoupled to show high-quality optically variable visual effects.

CONCLUSION

In this study, a strategy to fabricate totally decoupled OVD on the metallic surface has been demonstrated based on the directionality of one-dimensional (1D) diffractive grating. When the surface textured with 1-D grating patterns is illuminated from a direction that is parallel to the direction of gratings, the diffractive efficiency of incident lights will be down to as small as zero. The brass surface has been textured with 1D grating patterns of two orthogonal directions for two different images encoding. When it is observed from different angles, it will show decoupled optically variable visual effects.

ACKNOWLEDGMENTS

REFERENCES

[1]. Leech P W, Lee R A, Davis T J. Printing via hot embossing of optically variable images in thermoplastic acrylic lacquer. Microelectronic Engineering. 2006; 83(10): 1961-1965.

[2]. Sun J, Bhushan B and Tong J. Structural coloration in nature. RSC Advances. 2013; 3(35): 14862.

[3]. Heo Y, Kang H, Lee J S. Lithographically Encrypted Inverse Opals for Anti‐Counterfeiting Applications. Small. 2016; 12(28): 3819-3826.

[4]. Vorobyev A Y, Guo C. Colorizing metals with femtosecond laser pulses. Applied Physics Letters. 2008; 92(4): 041914.

[5]. Wu H, Jiao Y, Zhang C, et al. Large area metal micro-/nano-groove arrays with both structural color and anisotropic wetting fabricated by one-step focused laser interference lithography. Nanoscale. 2019;11(11): 4803-4810.

[6]. Guo P, Yang Y. A novel realization of diffractive optically variable devices using ultrasonic modulation cutting. CIRP Annals, 2019; 68(1): 575-578.

[7]. Jwad T, Penchev P, Nasrollahi V. Laser induced ripples' gratings with angular periodicity for fabrication of diffraction holograms. Applied Surface Science, 2018, 453: 449-456.

DESIGN, FABRICATION, AND SIGNAL PROPAGATION CHARACTERISTICS OF MICRO-MECHANICAL LOGIC ELEMENTS

Frederick Sun, Robert M. Panas, Logan Bekker, Julie A. Mancini, Andrew J. Pascall
Lawrence Livermore National Laboratory
Livermore, California, USA

Amin Farzaneh, Jonathan B. Hopkins
University of California Los Angeles
Los Angeles, California, USA

INTRODUCTION
The purpose of this paper is to present the design and fabrication of several selected basic building blocks of a micromechanical logic circuit. The design in this paper is based on a chain of bi-stable flexure systems, where one bi-stable state represents the digital state of 0 and the other bi-stable state represents 1. The design is the first to demonstrate state-reversible, unidirectional propagation of a digital signalrepresented by a state-switch pulse in a chain of mechanical logic gates, which enables the construction of more complex mechanical logic circuits.

Mechanical computation offers a variety of advantages over traditional semiconductor electronics, such as low energy consumption[2,3], passive data storage and the ability to survive under harsh environment such as extreme heat or high radiation where semiconductors are prone to failure [4]. Recent advancement in 3D micro-additive manufacturing technology have provided fabrication techniques that enables the building of complex micro-structures, and a printed micromechanical logic is presented in this paper.

OVERVIEW
The most fundamental of a mechanical logic circuit is the bi-stable mechanical bit.

A chain of two mechanical bits in their unstressed state connected by a compliant connector is shown in Figure 1. The mechanical bit is fabricated in its unstressed configuration, prior to operation the end tabs will be displaced inwards to cause the transverse cross-pivot flexures to rotate and snap the motion stage into an upward or downward position representing 0 or 1 depending on the user's definition. The prestressing action is called preloading in this paper. After the preload the mechanical bit is in its 0 or 1 state, held in an equilibrium created by the transverse flexures' restoring force and the
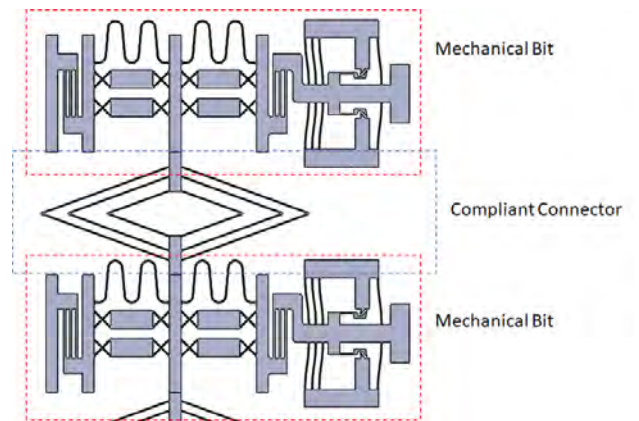
FIGURE 1:. A chain of two mechanical bits in their unstressed state connected by a compliant connector.

axials flexures' restoring force opposing each other.

This setup has two main advantages over the prior iterations where flexure elements themselves buckle: 1) The overall stress across the flexure elements is smaller when compared to forcing the elements to buckle, increasing the life cycle and therefore the practicality of the logic element. 2) The stiffness of the flexures can be easily adjusted such that desirable system characteristics such as input force needed, potential energy stored, equilibrium position, signal propagation energy loss along the chain

and many other parameters can be tune to a desirable value.

To send the 0 or 1 state from one mechanical bit to another and ultimately into a mechanical logic gate, the mechanical bits are connected by compliant connectors. When a mechanical bit on one end of the connector is switched to another state, the connector momentarily stores the incoming kinetic energy as elastic potential energy before passing it to the mechanical bit on the other end. This compliance producing a momentary storage of energy allows the input force to only have to overcome the resistance of one mechanical bit instead of the entire connected chain, thus bounding the amount of energy required to transmit a pulse. The flexures of each successive mechanical bit are tuned to
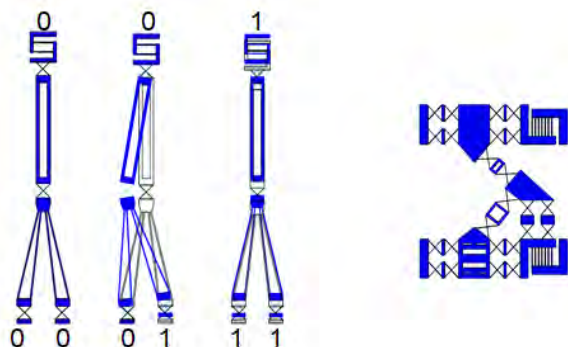
FIGURE 2:. A AND gate in its three different logic states on the left and a NOT gate on the right

be slightly less stiff, thus gradually reducing the amount of stored potential energy in the pulse. This gradual release of potential energy enables the pulse to controllably convert its potential to kinetic energy, allowing it to achieve a steady state propagation velocity independent of initial conditions.

An AND gate and a NOT gate has been designed as shown in figure 2. All basic logic gates can be achieved by connecting a combination of AND gates and NOT gates.

As can be seen in Figure 2, input tabs are located at the bottom of the mechanical AND gate, and output tab located at the top. When both inputs are at the down position, the output remain in the lower position; when only one input is displaced into the up position the bulk of the gate rotates, and the output is not pushed upwards; when both inputs are displaced upwards, the output is pushed up. These motion fulfills the motion requirements of the AND gate.

Also as seen in Figure 2, the NOT gate consists of two 90 degree transmissions, such that an upward motion at one end creates a downward motion in the other end, satifying the NOT gate motion.

An AND and a NOT are a complete set, as together (with a NOT at each port) these can create an OR as well as all other major logic structures.

RESULTS

A software with analytical solutions for the simulations of the signal pulse propagation characteristics is coded using MATLAB. Future designers may utilize the theory behind the software and software itself to quickly calculate favorable deisgn parameters. A table-top sized chain of a mechanical logic device is constructed for testing and validation of said singal pulse propagation. A microscale chain of mechanical logic gates is fabricsted by two-photon lithography with flexure blade thickness of 1 um. Preloading of the microscale chain is achieved by printing the structure on a pre-stressed substrate and releasing the substrate to create the preloading displacement. A mechanical probe is used to physically push the mechanical bit from one bi-stable state to the other.

ACKNOWLEDGEMENTS

REFERENCES

[1] Song, Y., Panas, R.M., Chizari, S., Shaw, L.A., Mancini, J.A., Hopkins, J.B., Pascall, A.J., 2019, "Additively Manufacturable Micro-Mechanical Logic Gates," Nature Communications

[2] C. Monroe, D. M. Meekhof, B. E. King, W. M. Itano, D. J. Wineland, 1995, "Demonstration of a Fundamental Quantum Logic Gate" Phys. Rev. Lett.

[3] R. Landauer, 1988 "Dissipation and noise immunity in computation and communication" Nature

[4] M. R. Werner, W. R. Fahrner, 2001 "Review on materials, microsensors, systems and devices for high-temperature and harsh-environment applications" IEEE Trans. Ind. Electron.

MULTI-FOCUS RANDOM-ACCESS PUMP-PROBE MICROSCOPY BASED ON COMPRESSIVE SENSING

Wanping Lu, Bingxu Chen, and Shih-Chi Chen[*]
Department of Mechanical and Automation Engineering
The Chinese University of Hong Kong
Shatin, N.T., Hong Kong SAR, China
[*]Email: scchen@mae.cuhk.edu.hk

Pump-probe microscopy that combines the temporal resolution of femtosecond spectroscopy and spatial resolution of light microscopy has been extensively used in biomedical imaging and material research. However, the imaging speed is greatly limited by the point-scanning process required by point detectors, e.g., photodiode. Recently, we developed a digital micromirror device (DMD)-based pump-probe microscope that enables the measurements of ultrafast transient absorption processes at arbitrarily selected regions in a 3D specimen [1]. In this paper, we apply compressive sensing (CS) algorithms to the DMD-based pump-probe microscope to increase the imaging speed by a factor of 3 - 5 times. In the experiments, multiple foci are simultaneously generated by modulating the wavefront of a femtosecond laser via binary holography [2] at randomly selected positions in the specimen, where the combined intensity is recorded by a photodetector, followed by 3D image reconstruction via CS algorithms [3]. The multi-focus pump-probe system is designed to have a field of view of $65 \times 130 \times 155 \ \mu m^3$ in the x, y, z axes respectively.

COMPRESSIVE SENSING
Compressive sensing (CS) is a signal processing technique for acquiring and reconstructing sparse signals by using significantly lower data points than those required by the Nyquist rate. In recent years, CS has achieved great success in different fields of signal processing. For example, CS framework has been implemented in the imaging field through single-pixel cameras [4]. In microscopy, several works applied CS to improve the imaging speed by 2-10s times [5]. In a typical CS imaging process, the sample is illuminated by a patterned light, where the signals are collected by a point detector. By illuminating the sample with different designed patterns, images can be computationally reconstructed. 2D and 3D pump-probe imaging by combing CS with multi-focus random-access scanning, which may further improve the imaging performance, has yet to be investigated.

SYSTEM CONFIGURATION
The optical configuration of the DMD-based pump-probe system is presented in Fig. 1, where the laser source is an 80 MHz Ti:Sapphire femtosecond laser (Chameleon Ultra II, Coherent) with a central wavelength of 800 nm and a pulse width of 140 fs. The laser is first divided into two beams by a polarizing beam splitter (PBS) and a half-wave plate. The beam with the most laser energy (3 W) is reflected by the PBS and, subsequently, focused to a β-barium borate (BBO) crystal by lens L1 (f_{L1} = 50 mm) to generate a 400 nm pump beam through second-harmonic generation and, lastly, re-collimated by L2 (f_{L2} = 100 mm). A 750 nm low-pass filter is used to remove the residual 800 nm laser. The pump beam is then modulated at 8.5 kHz by an optical chopper. (Note that the chopper is placed at the focal plane of L3 (f_{L3} = 100 mm) due to its limited aperture.) L3 and L4 (f_{L4} = 200 mm), which form a 4-f system, adjust the size of the pump beam. Lastly, the pump beam is focused to the back aperture of the objective lens (UPLSAPO 40×, N.A. = 0.95, Olympus) by L5 (f_{L5} = 300 mm) to generate a uniform illumination (∅ = 15 μm) to the sample, mounted on a precision xyz stage.

The laser beam that passes through the PBS is used as the probe beam, where its wavefront is modulated by binary holograms displayed on the DMD (DLP 4100, 0.7" XGA, Texas Instruments). Since the DMD simultaneously functions as a programmable binary mask and a grating, a blazed transmission grating (1200 lines/mm) and a 4-f system (f_{L6} = 100 mm, f_{L7} = 250 mm) are included in the light path to compensate for the angular dispersion introduced by the DMD [3]. An iris diaphragm is placed at the conjugate plane of the DMD to spatially select the −1st order diffraction. To improve spatial resolution, the

probe beam is expanded by a 4-f system (f_{L8} = 200 mm, f_{L9} = 200 mm) to fully fill the back aperture of the objective lens. Note that the probe beam is aligned spatially with the pump beam via a dichroic mirror (DM) before the objective lens. The signals reflected from the sample, i.e., intensity modulated probe light, is collected by the same objective lens and directed to a photodiode (818-UV/DB, Newport). A notch filter (800±12 nm) is placed in front of the photodiode to remove the residual pump light. The time delay between the pump and probe pulses is adjusted by a linear translation stage. The signals from the photodiode are first amplified by a current preamplifier (SR570, Stanford Research) and, subsequently, sent to a digital lock-in amplifier (SR850, Stanford Research) for data collection and analysis. A wide-field optical microscope (LED, BS1, BS2, CCD) is built into the pump-probe system to allow easy sample placement before experiments [1].
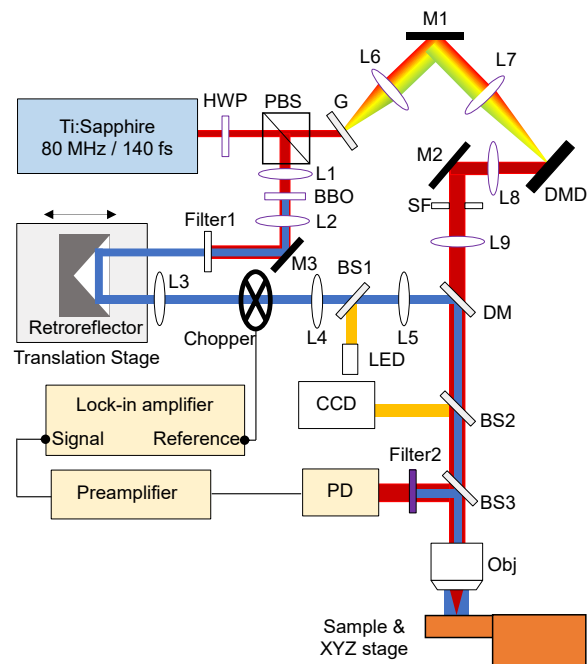
FIGURE 1. Optical configuration of the DMD-based pump-probe microscope system; L1-L9, lenses; M1-M3, high-reflectivity mirrors; BS1-BS3, beam splitters; DM, dichroic mirror.

SINGLE-FOCUS EXPERIMENTS

First, we perform a single-focus imaging experiment to verify the performance of the DMD pump-probe system; the results are used as a reference image to be compared with the multi-focus imaging results. The 2D sample used in the experiment is custom-fabricated through electron-beam lithography, where 150 nm gold films are deposited and patterned on a silicon substrate as a "U" letter. Figure 2A presents a reflectance image of the gold sample by raster-scanning the probe beam via the DMD, where the image contains 70 × 70 pixels with a size of 21 × 21 μm^2.

Next, we perform a transient absorption measurement on the 2D sample with different time delays at the selected points (A and B) on the gold pattern and silicon substrate respectively. Figure 2B and 2C present the measured decay curves of gold and silicon which can be fitted by exponential functions; the estimated decay times for silicon and gold are found to be ~125 ps and ~2000 ps respectively. The large decay time (i.e., 2 ns) of gold is attributed to the transient thermal (phonon-limited) effects; we find the measured values are compatible with typical decay times in the reported studies of transient thermal reflectivity dynamics of metals (1~2 ns) [6-9]. For silicon, the measured decay time (125 ps) matches well with the pump-probe studies of bulk silicon and silicon nanowires (~100 ps) [10,11]. As heat accumulations are negligible on the silicon chip due to its large volume in comparison to the gold film (150 nm). These results confirm our system can perform pump-probe measurement at any point in the DMD work space with good sensitivity and signal-to-noise ratio (SNR).
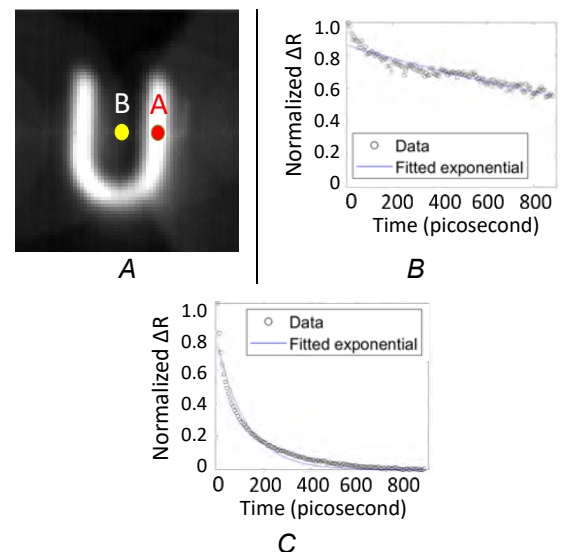
FIGURE 2. A. Reflected image of the custom-made 2D sample (gold pattern on a silicon substrate); B & C. measurements of the transient absorption on gold and silicon respectively with different time delays.

Next, we perform single-focus pump-probe imaging on the 2D sample at different depths to verify the optical cross-sectioning as well as the DMD scanning capabilities. The results are shown in Fig. 3. The top row in Fig. 3 presents the imaging results of the 2D sample, where the XYZ stage moves the sample to z = −10, 0 and 10 μm respectively; from the results one can clearly observe that no signals are recorded when the sample is moved out of the focal region, which verifies the optical cross-sectioning capability. Next, calculated spherical wavefronts are applied to the DMD to compensate the axial movement of the sample at ±10 μm. The results are shown in the bottom row of Fig. 3, where all "U"s are in focus with indistinguishable image quality. From the results, we can confirm the DMD can perform 3D scanning in pump-probe experiments without compromising the image quality.
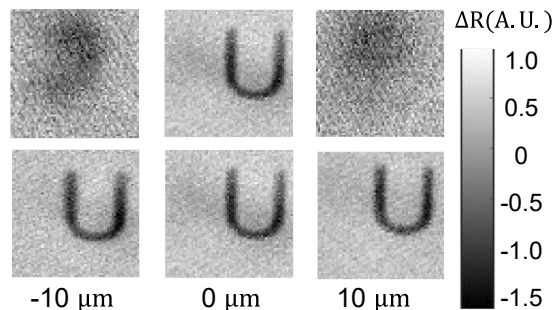
FIGURE 3. 3D transient absorption measurement of the sample positioned at different depths, i.e., −10, 0 and 10 μm (top row). Next, the probe beam is moved to the sample plane via the DMD, resulting in-focus imaging results (bottom row).

SIMULATION OF MULTI-FOCUS SCANNING

In this section, we perform simulated multi-focus pump-probe experiments to identify optimal processing parameters for the CS algorithm, including the sampling ratio and number of foci. We first record a single-focus pump-probe image as a reference image to compare with the multi-focus imaging results. In the following experiments, the size of all images is set to 70 × 70 pixels with a pixel size of 0.3 μm. In the first experiment, we set the sampling ratio to a fixed value, i.e., 30%, and vary the number of scanning foci, i.e., 2, 5 and 10. The results are presented in Fig. 4, where Fig. 4A shows the reference image; Fig. 4B − 4D present the multi-focus imaging results using 2, 5, and 10 foci respectively. To emulate the practical imaging condition, noises are applied to the multi-focus scanning process, where the magnitude of the

white noise is determined based on the differences between the reference images taken at different times; and the corresponding mean squared deviations (MSD). The results are presented in Fig. 4E − 4G corresponding to 2, 5, and 10 laser foci respectively. We use $||x-\bar{x}||_2/||x||_2$ to estimate the errors in each image, where x represents the reference image and $\bar{x}$ represents the reconstructed image. The estimated errors for Fig. 4E − 4G are 20.0%, 19.5% and 19.9% respectively. In Fig. 4B − 4D, one may find that pump-probe images can be reconstructed without observable errors; when noises are included in the simulation, they contribute to ~20% errors independent from the number of laser foci used.

In the second experiment, we vary the sampling ratio, i.e., 5%, 15%, and 30%, and fix the number of scanning foci to four. The results are presented in Fig. 5, where Fig. 5A shows the reference image; Fig. 5B − 5D present the multi-focus imaging results using sampling ratios of 5%, 15%, and 30%, corresponding to errors of *34.0%, 14.0%, and 10.0%,* respectively. Next, noises are applied to the multi-focus scanning process to emulate practical imaging conditions. The results are presented in Fig. 5E − 5G corresponding to sampling ratios of 5%, 15%, and 30%, and errors of 36.3%, 19.8%, 20.0%, respectively. From the results, we can conclude that the sampling ratio is a more important factor to determine the quality of the reconstructed pump-probe image; and a sampling ratio larger than 15% is recommended for reconstructing high quality images.
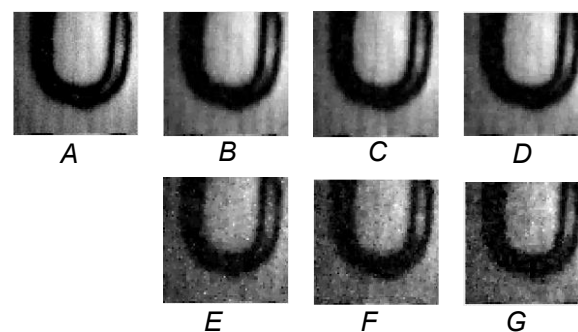
FIGURE 4. Simulated multi-focus pump-probe imaging results using a sampling ratio of 30%. (a) reference image based on single-point raster-scanning; (b) – (d) use of 2, 5, and 10 foci without noises; and (e) – (g) use of 2, 5, and 10 foci with noises, where the relative errors are calculated to be 20.0%, 19.5% and 19.9% respectively. The image size is 21 × 21 μm².

A   B   C   D

E   F   G
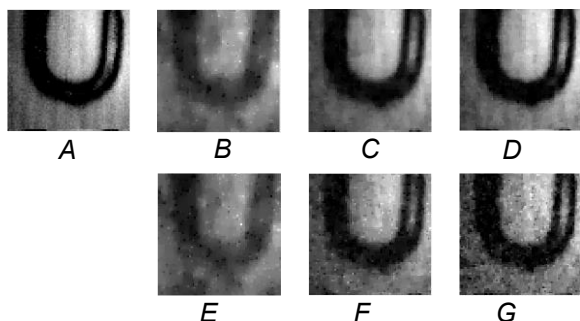
FIGURE 5. Simulated multi-focus pump-probe imaging results with varying sampling ratios using four foci: (a) reference image based on single-point raster-scanning; (b) - (d) sampling ratios of 5%, 15%, and 30% without noises, where the relative errors are calculated to be 34.0%, 14.0%, 10.0%; and (e) - (g) sampling ratios of 5%, 15%, and 30% with noises, where the relative errors are calculated to be 36.3%, 19.8%, 20.0%.

MULTI-FOCUS IMAGING EXPERIMENTS

In this section, we perform pump-probe imaging experiments on the 2D sample to verify the efficacy of the CS algorithm. As the simulation experiments suggest that the image quality is not sensitive to the number of laser foci, we devise the imaging experiments with a fixed number of foci, i.e., four, and vary the sampling ratios from 5% to 40%. The pump-probe imaging results are presented in Fig. 6, where one may observe that as the sampling ratio increases, the image quality improves accordingly and plateaus at around 30%. As the lower the sampling ratio, the higher the imaging speed, i.e., enhancement of imaging speed = 1/sampling ratio, the experimental results suggest that the 30% sampling rate is an optimal processing parameter that strikes a good balance between image quality and speed enhancement. This agrees with our study on applying the CS algorithm to two-photon microscopy, where a 25% sampling ratio and five laser foci yield the optimal imaging results [3].
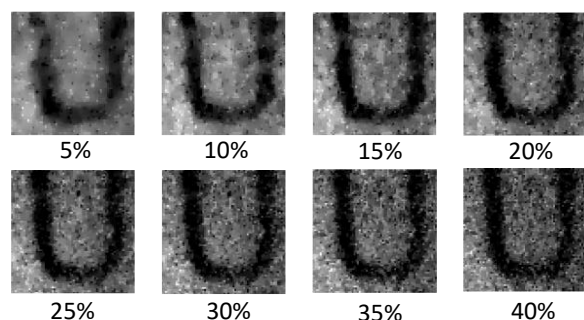
5%   10%   15%   20%

25%   30%   35%   40%

FIGURE 6. Multi-focus pump-probe imaging results based on CS algorithm with four laser foci

and varying sampling ratio, i.e., 5%, 10%, 15%, 20%, 25%, 30%, 35%, and 40%. Each image contains 70 × 70 pixels with a size of 21 × 21 μm².

CONCLUSION

In conclusion, we have demonstrated the use of CS algorithms to a DMD-based pump-probe microscope system to substantially improve the imaging speed by a factor of 3 – 5 times. Important processing parameters, including the number of laser foci as well as sampling ratios, have been investigated via simulation and imaging experiments, where the two results match well. The results indicate that a 30% sampling ratio (i.e., ~3.3 times speed enhancement) in combination with four laser foci can generate pump-probe images of good quality. Although the imaging experiments are limited to 2D samples, the DMD pump-probe system can directly be applied to any 3D samples via the multi-focus random-access scanning algorithm.

ACKNOWLEDGMENT

REFERENCES

[1] Wen C, Feng F, Ren M, Somekh M, Zhao N, Chen S, Spatially-resolved Random-access Pump-probe Microscopy based on Binary Holography, Optics Letters, 44(16): 4083-86, 2019.

[2] Geng Q, Wang D, Chen P, Chen S, Ultrafast Multi-focus 3-D Nano-fabrication based on Two-photon Polymerization, Nature Communications, 10:2179, 2019.

[3] Wen C, Ren M, Feng F, Chen W, Chen S, Compressive Sensing for Fast 3-D and Random-access Two-photon Microscopy, Optics Letters, 44(17): 4343-46, 2019.

[4] Duarte MF, Davenport MA, Takhar D, Laska JN, Sun T, Kelly KF, Baraniuk RG, Single-pixel Imaging via Compressive Sampling, IEEE Signal Process. Mag. 25: 83-91, 2008.

[5] Pavillon N, Smith NI, Compressed Sensing Laser Scanning Microscopy, Opt. Express, 24: 30038-30052, 2016.

[6] Schmidt A J, Chen X, Chen G, Pulse Accumulation, Radial Heat Conduction, and Anisotropic Thermal Conductivity on Pump-probe Transient Thermoreflectance, Review of Scientific Instruments, 79(11): 114902, 2008.

[7] Stevens RJ, Smith AN, Norris PM, Signal Analysis and Characterization of

Experimental Setup for the Transient Thermoreflectance Technique, Review of Scientific Instruments, 77(8): 084901, 2006.

[8] Block A, Liebel M, Yu R, Spector M, Sivan Y, de Abajo FG, van Hulst NF, Tracking Ultrafast Hot-electron Diffusion in Space and Time by Ultrafast Thermomodulation Microscopy, Science Advances, 5(5): eaav8965, 2019.

[9] Smith AN, Hostetler JL, Norris PM, Thermal Boundary Resistance Measurements Using a Transient Thermoreflectance Technique, Microscale Thermophysical Engineering, 4(1): 51-60, 2000.

[10] Gabriel MM, Kirschbrown JR, Christesen JD, et al, Direct Imaging of Free Carrier and Trap Carrier Motion in Silicon Nanowires by Spatially-separated Femtosecond Pump–probe Microscopy, Nano Letters, 13(3): 1336-1340, 2013.

[11] Sabbah AJ, Riffe DM, Femtosecond Pump-probe Reflectivity Study of Silicon Carrier Dynamics, Physical Review B, 66(16): 165217, 2002.
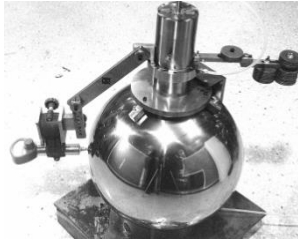
MOONSHOT METROLOGY

Mel Liebers, Henry Arneson
Professional Instruments Company
Hopkins, Minnesota, USA

ABSTRACT

Apollo 11 landed on the moon 51 years ago, the climax of a vast national effort. The path to the moon is complex and the mid-course correction rockets must fire in exact coordination. This was ensured, in part, by an earth borne Spacecraft Simulator Platform to precisely measure the performance of the guidance system. This platform was the approximate size and mass of the three man Command and Service Module, with the ability to rotate 360 degrees and tilt ±30 degrees without friction so that engineers could evaluate the functioning of the system, and also so that astronauts could practice. Working with Honeywell Aeronautics Division, Professional Instruments Company played a key role by producing the spherical air bearing system at the heart of the Simulator. This paper discusses the project from the viewpoint of precision engineering, toolmaking, and metrology.

FIGURE 1. Lead Honeywell engineer, Len Aske demonstrating the frictionless reaction of the 9 ton platform by moving it with a single finger

INTRODUCTION

2019 marked the 50th anniversary of the moon landing, the culmination of a project to outshine the Russians whilst pushing technology forward and inspiring a new generation of scientists and engineers. Successfully steering the Command and Service Module (Figure 2) required precision testing of the stabilization and control systems under low gravity conditions. To

accurately simulate these conditions on earth the system must be able to freely rotate and tilt about its physical center of mass, completely absent of friction and vibration. The system must also be precisely balanced about the central bearing. When these conditions are met, even a simulator the size of the spacecraft, could be moved by the touch of a finger. Only then would it be sensitive enough to qualify the critical control systems for the mission. The only bearing capable of achieving this would be a unique air bearing gimbal.

FIGURE 2. Apollo 11 Command and Service Module during construction. Image credit: NASA

Honeywell had previously made autopilot systems for WW2 aircraft and had recently developed an ultra-precise electrostatically suspended spherical gyro [1] for which Harold Arneson of Professional Instruments (PI)

Company developed advanced lapping and balancing tools [2,3] including a dual-hemisphere "Zeron" sub-μinch air bearing spindle [4]. Precision grinding was becoming a PI specialty, with attention to spindles, wheel selection, truing and balancing and these skills proved invaluable to making this project feasible.

SPACECRAFT SIMULATOR REQUIREMENTS

For the system to work as intended, these requirements must be met:

- Full 360 degree rotation
- +/- 30 degrees of tilt
- Zero friction
- Near-zero self-driving torque
- Lift and lock in any orientation
- Support 9 tons of equipment
- Minimum uncertainty of measurement results

Nine tons is approximately the weight of a loaded school bus and lifting this required a 17 inch ball, as visualized in Figure 3 [6], which shows a cross section detailing the inside of the simulator, which is 13 feet in diameter and 7 feet tall. The form accuracy of the ball was toleranced at 10 μinches in order to minimize any tendency for self-driving torque stemming from non-uniform air flow though the bearing surfaces which would result in uncertainty of the measurement results. The matching cup had a number of orifices, 4 capacitive (cap) probes, and 4 angled anti-rotation nozzles. It was required to be spherical to 20 μinches with a radius .0001 inches smaller than the ball so the air bearing clearance would be tightest at the rim. The nominal air film thickness was designed to be .0005 to .0007 inches. To ensure that the table can be lifted and replaced without damaging the air bearing surfaces, cap probes are imbedded into the cup. The cap probes also provided information for a safety interlock to guard against inadvertent rotation.. The requirement for locking the table in any orientation necessitated a concentric (to the ball) shell and lifting ring, detailed in Figure 3.
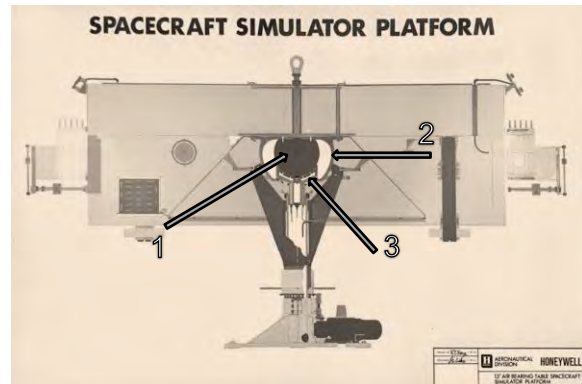
FIGURE 3. Cross section showing the ball [1], the lift-off shell [2], and the cup [3]. Counterweights were used to set the center of mass at the center of the ball. [Ref. 6]

LAPPING THE BALL

Not much is known about the process of lapping the ball. This was kept a tight secret, even to those working at Professional Instruments at the time. The closest approximation of how the ball was lapped can be obtained by inspecting Harold's original patent [3] and how current test balls are lapped at Professional Instruments Company (Figure 4). A cup lap is attached to a universal joint which keeps the lap in contact with the centered ball rotating on a 4B Blockhead while simultaneously oscillating on another Blockhead as a trunnion. Utilizing this set up, sub-μinch level roundness at the equator has been achieved. For Harold, the lapping process was similarly hands-off, but he later reported that despite all efforts at randomization, the procedure required constant attention lest the motion lock into a specific path and create a micro-groove. Harold likened this non-random effect to a type of "strange attractor" as in chaos theory in which an unbidden pattern emerges.

FIGURE 3. Modern set-up for lapping test balls utilizing two 4 inch Blockheads as the trunnion and workhead spindles.

The 640-pound 440C stainless steel ball (shown in its finished state in Figure 4) had been forged, machined and heat treated to 45 Rockwell C. After rough lapping an unanticipated problem arose when a ring of non-metallic inclusions appeared. These regions were relatively soft and tended to undercut, leading to valleys in the surface. The inclusions were a consequence of insufficient stock removal after forging. It was too late in the game to start over, so having consulted with the customer it was elected to proceed by using sub-micron diamond lapping paste to keep the undercut areas no deeper than 20 µinches. Hundreds of hours of attentive work ensued.

FIGURE 4. Underside of the ball after hundreds of hours of lapping. The ring of defects in the center are non-metallic inclusions, a remnant of the forging process. [6]

BALL MEASUREMENT

Harold Arneson demonstrates a roundness measurement along the equator of the ball in Figure 5. Measurements were performed with respect to the axis of rotation of a Zeron spindle [5], the only spindle at the time capable of sub-µinch error motion. A Carl E Johansson Model 510E-10S Mikrokator (Figure 6) was used for final inspection. This was a limited model of a frictionless, flexure-based, half-µinch-per-graduation mechanical displacement indicator, the only indicator at the time precise enough for the measurements of the ball. Although the contact force was very low, its spring rate was not insignificant, meaning that the force at the high end of the scale would be higher than at the low end. Consequently, a full-scale total indicator readout (TIR) reading would influence the structural loop a bit more than if the same out-of-roundness was measured with better centering. This could introduce uncertainty into the measurement of the ball which was on the

order of µinches. This is the reason for building robust indicator holders for precision work. It's also the justification for expending extra effort to center the axis of rotation over the ball.
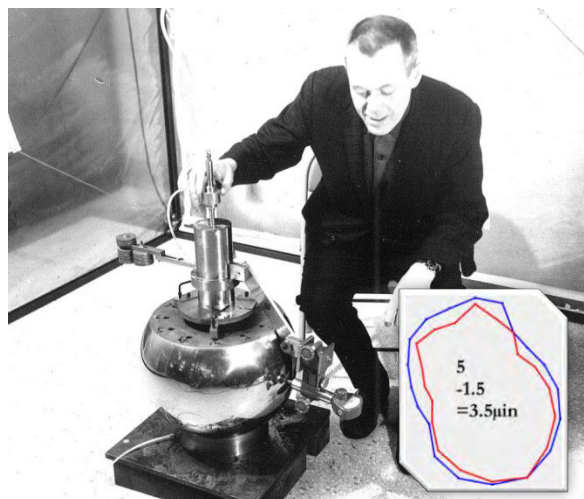
FIGURE 5. Harold Arneson measuring the finished ball using a Zeron spindle. Shown in the lower right are two measurements where the spindle was indexed 90°, showing that the 2 lobe error stayed with the ball.

A ¼ inch radius polished diamond tip functioned as a morphological filter, thus modifying the definition of the measurand (in this case, the ball) as seen by the metrologist. The analog readout was hand-digitized with careful attention to parallax and thermal drift. Displacements were sampled in 10 degree increments and the averages of the two rotations were hand-plotted on polar coordinate graph paper. When combined with the measurements of 6 meridians, the sphericity of the ball was deemed to be "Probably good enough." [5]

FIGURE 6. Half µinch per graduation, 40 µinch full-range Carl E Johansson Model 510E-10S Mikrokator used for the final inspection of the ball.

LAPPING THE CUP

Lapping the cup was another labor intensive process, requiring hundreds of hours of lapping, many measurements and minute adjustments to the lapping parameters and even the lap itself. In Figure 7, the grooved lead lap pivots as the cup rotates. The pivot stroke is adjustable (denoted by 2) so that the cross-hatch angle can be modified for geometry control. The rate of stock removal is controlled by adjusting the effective weight of the lap (denoted by 1). Rough lapping was done with 1000 grit alumina abrasive and sub-micron levigated alumina was used for finish lapping. Diamond lapping compound was not used as it would have embedded in the Monel-metal cup. Figure 8 shows one of the many incremental measurements using a purpose-made gauging set up.
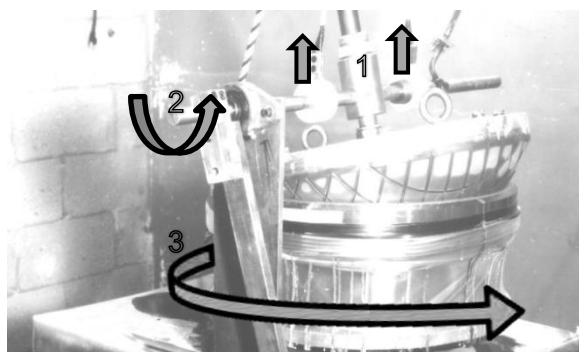
FIGURE 7. Lapping the cup: the grooved lead lap is adjustable for effective weight by lifts (1) while oscillating (2) as the cup rotates (3).

CUP MEASUREMENT

Back then, before cap gages were fully developed, the ball and the cup were measured manually using contact indicators. Form and size deviations are measured with respect to a two-inch 52100 steel bearing ball. The ball was drilled for an air gage feed and re-lapped with tooling developed for test balls. The cup measurements were with Mahr Millimess and Supramess displacement indicators and backed up by an Ames non-contact (but not zero force) air gauge (shown in Figure 8). The fixed-in-place air gauge readout enabled the entire surface to be scanned without the operator needing to move. The structural loop for measuring was short and stiff and the free-swinging indicator enabled fast, stepless evaluation of the entire surface of the cup.

FIGURE 8. Gauging sphericity with Earl Clauson (left) and Ted Arneson (right). For this picture, the thermal insulation was removed from the hand-manipulated gauge. The radius was set with gauge blocks, not shown here. [6]

COMPLETED BEARING MEASUREMENT

The features of the ball and cup were sufficient to generate a functioning air bearing gimbal. Figure 9 shows a demonstration by Ted and Harold Arneson to lead Honeywell engineer, Len Aske of the air bearing ginbal. However, the air bearing still needed to be evaluated to prove that it was sufficient for the simulator. Bearing influence (self-driving torque) needed to be near zero to closely simulate zero gravity conditions and more importantly minimize uncertainty of measurement results.

FIGURE 9. Ted Arneson, Len Aske, and Harold Arneson [left to right] demonstrating the free floating nature of the bearing assembly (the steel rod is for balance) [6].

To evaluate self-driving torque, weights were used to lower its center of inertia as shown in Figure 10. With the anti-rotation nozzles active, residual motion was under one arc-minute over ten minutes, measured by autocollimation.
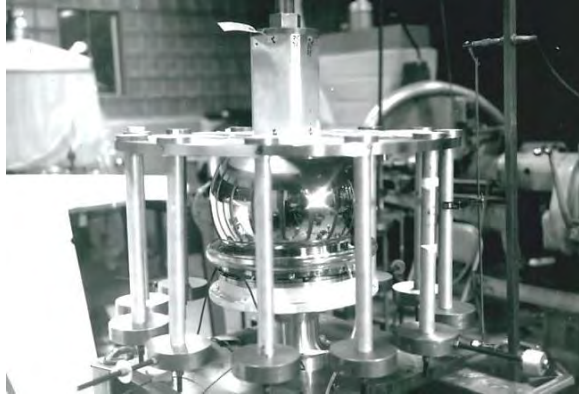
FIGURE 10. Air bearing assembly, composed of the finished ball and cup, arranged for testing self-induced motions [6].

GRINDING ON AN AIR BEARING GIMBAL

The method to ensure concentricity of the lift off shell to the ball was to grind the assembly while floating on the ball-and-cup air bearing itself. Grinding in-assembly meant that the irreplaceable bearing surfaces would be inches away from grinding grits and coolant. To isolate the bearing zone, a bespoke bellows was arranged to bend, rotate, and slide with the assembly. The joint used a rotating and sliding steel ring on a base plate. Positive pressure from the air bearing also helped keep debris out of the sensitive area. The purpose built grinding and bellows set up is shown in Figure 11. This was a white-knuckle job, run by Harold alone, after business hours. The result was a lovely grind job, with zero visible chatter in the surface finish. The concentricity of the shell to the ball was measured to be under .0001 inches.

FIGURE 11. Grinding the 28 inch lift-off shell in assembly. The long lead screw [left] changes the tilt of the spindle, as the shell rotates [6].

RESULTS

The final air bearing assembly shown in Figure 12 met every one of the requirements needed to simulate low gravity conditions on Earth. The system was also robust enough to allow the repeated assembly and disassembly required to perform the many tests and calibrations during the development of the Apollo Command Module Stabilization Control System. The fully assembled simulator was truly a marvel, weighing "more than a fully loaded school bus yet can be moved by a puff of air" [7]. Also visible in Figure 12 is a locking ring that allows the simulator to be locked into any orientation without damage to the air bearing. The simulator table could then be safely disengaged from the air bearing to allow for adjustments to the instrumentation on the simulator. When the simulator is ready for another test, the table is safely lowered back onto the air bearing whilst monitoring the embedded cap probes in the cup to ensure proper engagement of the air films. Without these precautions in place, the 9 ton platform could irreparably damage the painstakingly crafted and sensitive surfaces of the ball and cup.

FIGURE 12. Air bearing assembly mounted on the base of the Simulator platform. The air bearing itself is within the lift off shell. Also visible is the ring used to lock the platform in any orientation by lifting the shell. [6]

The completed air bearing system functioned as designed and was sufficient to carry the load of the Apollo Spacecraft Simulator. This platform enabled the successful proofing of the control system as well as enabling the astronauts to train on the best approximation of zero gravity conditions in a lab. Shown in Figure 13 [6] is the proposed simulator control station. The finished simulator had to be operated in a vacant room to minimize measurement errors caused by stray air currents.
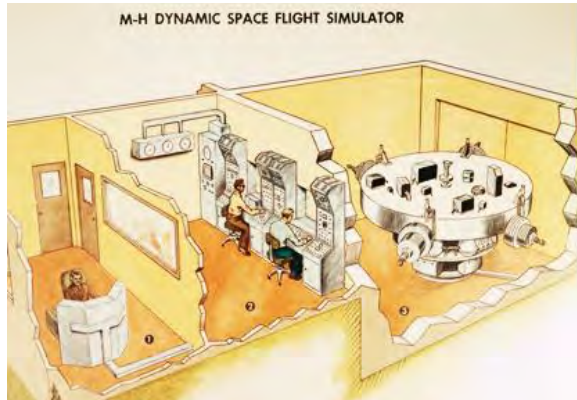
FIGURE 13. Simulator operation required that the room be free from stray air currents so the operators were next door, as were the astronauts-in-training. [6]

One of the developments enabled by this platform was the Stabilization and Control System. This enabled the precise motion control necessary for the successful rendezvous of the Command and Service Module with the Lunar Module. Figure 14 shows a rendering of the spacecraft demonstrating the precise and complex coordination and control required for one crucial aspect of the space mission.
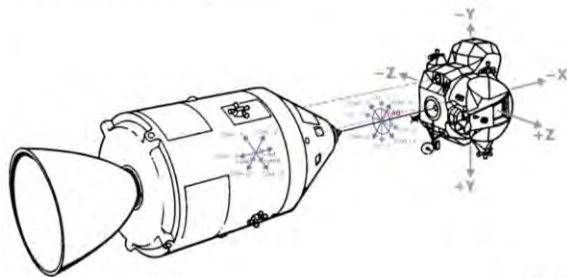
FIGURE 14. The critical rendezvous of the Command and Service Module with the Lunar Excursion Module was made possible through precision toolmaking, metrology, and engineering. Image credit: NASA

CONCLUSION AND FUTURE WORK

Putting a man on the moon and bringing him back alive was an astronomical feat requiring countless pieces to come together and fit perfectly. Manufacturing the air bearing to simulate low gravity conditions was a small but important part of that. Harold and Ted Arneson of Professional Instruments were in a unique position to meet this challenge. This was one of many projects in the early days of Professional Instruments Company that included many other high profile jobs, such as electrostatically levitated gyroscopes for use in submarine navigation. Involvement in this project led to advancements such as the 10 inch Blockhead air bearing spindle, a large air bearing with sub-microinch accuracy and over 800 lbs of load capacity used as a horizon simulator for the same project. This wouldn't be the last time Professional Instruments was involved in high profile space projects. To meet the 2011 deadline for the Mars Curiosity Rover, Professional Instruments was called upon again to meet the precision demands of the critical mobility system components [8]. Spacecraft simulator technologies have since evolved; however, this unique air bearing will remain an integral part of precision toolmaking history that was necessary for beating the Russians to the moon.

REFERENCES

[1] Mackenzie, Donald. Inventing Accuracy
[2] C. Arneson, et al. History of the Blockhead Spindle. Professional Instruments Company. ASPE 2018
[3] Arneson, Harold E. G. Sphere Lapping Apparatus. US 3110987, United States Patent and Trademark Office, Nov. 19, 1963
[4] Mel Liebers, et al. Testing the Earliest Sub-Microinch Spindles. Professional Instruments Company. ASPE 2015
[5] ASME B89.3.4-2010 Axes of Rotation, A-7.7 Variation in Sag Causes One-for-One Roundness Error
[6] Historical Professional Instruments Company documents
[7] Spangler, Robert. Huge Spacecraft Simulation Platform built by Honeywell, Feb. 10, 1964
[8] D. Arneson, et al. Machining and Grinding Critical Components for the Mars Rover, Curiosity. Professional Instruments Company. ASPE 2012

Phase- shifting Strobo-Stereoscopic 3D Imaging of Rotating Milling/Drilling tools

Xiangyu Guo[1] and ChaBum Lee[1]
[1]J. Mike Walker' 66 Department of Mechanical Engineering
Texas A & M University
College Station, Texas, USA

INTRODUCTION

Drilling and milling operations are material removal processes involved in everyday conventional productions, especially in the high-speed metal cutting industry. The proper monitoring of tool information (wear, chattering, deformation, etc.) is essential to guarantee the success of product fabrication. Many methods have been applied to monitor the cutting tool conditions from the information of cutting force, spindle motor current, vibration, as well as acoustic emission originated from the spindle and/or tool [1]. However, those methods are indirect and sensitive to environmental noises.

Here, the in-process imaging technique that can capture the cutting tool information while cutting the metal was investigated. As machinists judge whether a tool is worn-out by the naked eye, utilizing the vision system can directly present the performance of the machine tools. We proposed a phase-shifting strobe-stereoscopic method for three-dimensional (3D) imaging. The schematic illustration is shown in Figure 1. While the stereoscopy algorithm can provide 3D image at specific measurement position, the phase-shifting of the strobe-light allow the whole-view reconstruction of the machine tool.
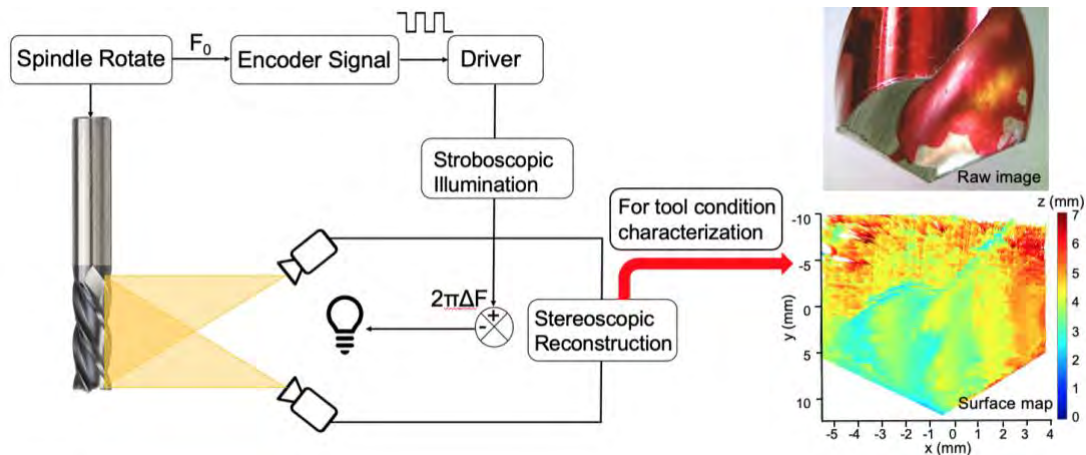
FIGURE 1. Methodology schematic of strobe-stereoscopy 3D imaging for Drilling/Milling tools metrology and inspection.

The illumination system and camera system are synchronized with the spindle motion, the measurement operations are automated and digitalized. The strobo-stereoscopy algorithm can provide 3D image at each location along the circumference of the machine tool. The measurement location is depended on the stroboscopic illumination, so that the phase-shifting of the illumination enables the whole 3D surface characterization around the machine tools. Thus, this proposed method provides the in-process metrology for whole-view 3D reconstruction of the drilling/milling tools for tool condition examination and characterization.

STROBO-STEREOSCOPY SYSTEM
The stroboscopic instrument is typically applied for the measurement of fast-moving objects. The operation principle is as follows: In general, if a

changing phenomenon is periodic in time, when synchronizing the frequency of the light source illumination and the motion of object, the resulting successive identical images are integrated by the eye and (if they occur sufficiently rapidly) merge to show the state of the system frozen or to be stationary [2]. If small differences are added to the frequency, the object appears to be slowly moving or rotating. This slow motion can be working as the source for the phase-shifting; with this phase information, the target can be whole-view 3D reconstructed by 360 degrees. The stereoscopic technique is embedded with two CCD cameras equipped capturing images that are located bilateral symmetrically in regard to the target. The 3D scene is reconstructed by the location information of the same object points from both the left and right images.

Stereo imaging is one of the powerful methods used for measurements of 3D structures and volumes [3]. The basic principle of the stereo method is that when a 3D scene is photographed by a pair of cameras, range information can be recovered from the pair of stereo images. The pair of images is known as a stereoscopic image pair. A range image is one where the matrix of gray levels represents the distances of the points of objects in the scene from the camera [4]. From the computation point of view, if a 3D scene is represented by two different views, the recapture of the depth information is possible when the information therein is combined with knowledge of the sensor geometry (eye or camera location); this process is called stereovision. In addition, stereoscopic displays always convey a very compelling sense of 3D depth, and the most important aspect is providing 3D information, such as orientations and distances, of the objects in the scene [5].

PHASE-SHIFTING PROCESS

The flow chart of the stroboscopic light system for phase shifting process is presented in Figure 2. The stroboscopic control algorithm synchronizes the rotational speed RPM (revolution per minute) with the light blinking frequency and shifts the phase of the light signal from 0 to 360 degree. This phase-shifting scan method by stroboscopic control algorithm is programmed in the LabVIEW environment.
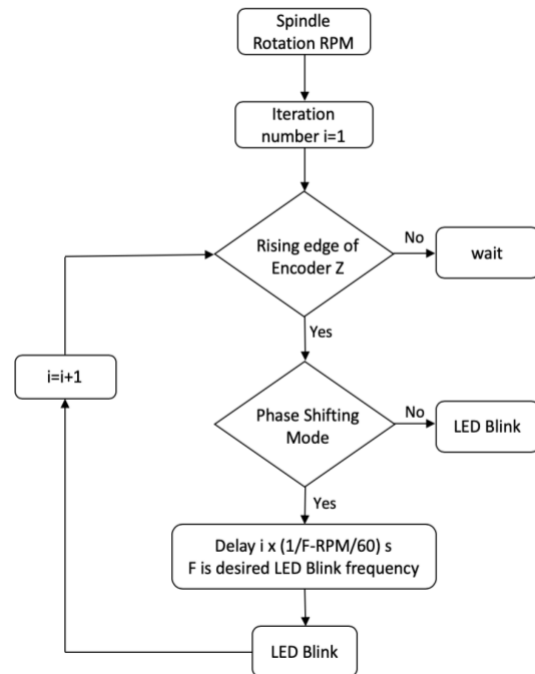
FIGURE 2. Flow chart of stroboscopic motion and light control algorithms.

The rising edge of Encoder Z is used as the signal that whole cycle of rotation is finished. This signal is related to the rotary speed, F is the desired LED blink frequency, the delayed time for the LED blink can be calculated. When F is equal to the spindle rotary frequency, both CCDs gather pictures at the single location of the machine tool, this is also called as phase-locking mode. When F is different from the spindle rotary frequency, a sequence of images was gathered under the phase-shifting process for a whole-view 3D reconstruction, this is called as phase-shifting mode.

EXPERIMENT SETUP

In the proposed system, an air spindle was applied to secure the motion accuracy and drilling/milling speed. As shown in Figure 3, Two CCDs with 10X objective lenses were installed on two linear rails (x and z-direction) with rotary stages to capture the raw picture of a cutting tool bit for further 3D reconstruction. Cross lasers on top of each CCD camera are added to guarantee both cameras focus at the same location of the measurement target.
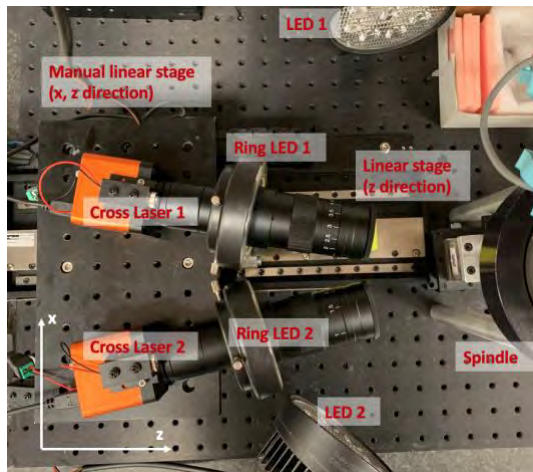
FIGURE 3. Experiment set-up of the proposed method.

WHOLE-VIEW 3D RECONSTRUCTCION

The whole-view 3D image reconstruction process is illustrated in Figure 4. The measurement process in the figure is presented in previous session. Here, we focus on the depth map reconstruction.

The center surface reconstruction is based on the stereoscopic algorithm. Before the depth map is recovered, pre-process for target centering, distortion removal, and brightness adjustment need to be done. Gaussian filter is applied to remove system noises.

For the neighbor surfaces stitching process, we used SIFT (scale-invariant feature transform) to determine the similar characteristics first, as they
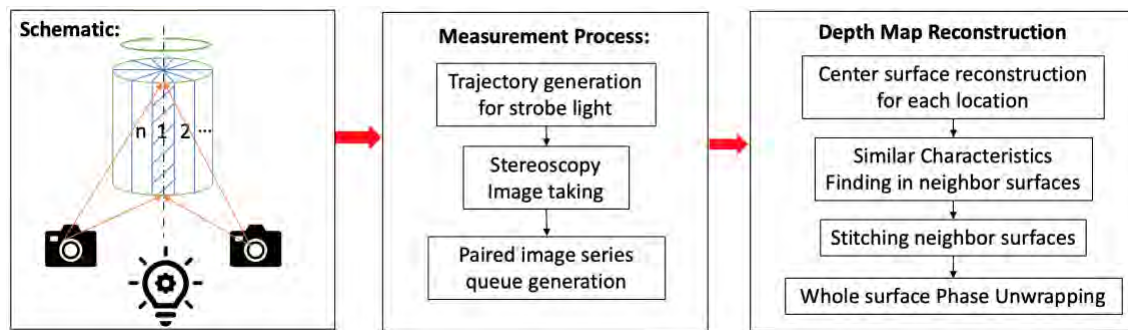
FIGURE 4. Whole view 3D surface building process.

provide reference information. Along with the rotating angle, the panorama surface can be generated. After the stitched panorama surface is generated, a surface phase unwrapping process is applied to match the depth information as well as to remove the stitching errors .

Figure 5 shows an example that the target machine tool bit was taken pictures along the rotation every 45 degrees.
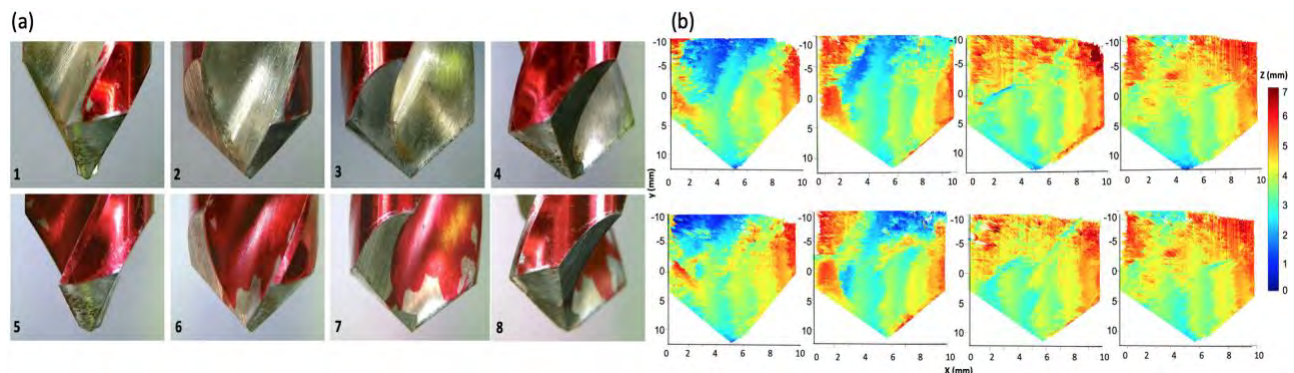
FIGURE 5. (a) raw image from location 1~8, 45 degree per picture along the cycle, and (b) depth maps for images from location 1~8.

Towards the results from Figure 5, the stitched panorama surface for the tool body (a) and the tool bit (b) are presented in Figure 6. A circular mask was applied for Figure 6 (a), as the target area here is the tool bit.
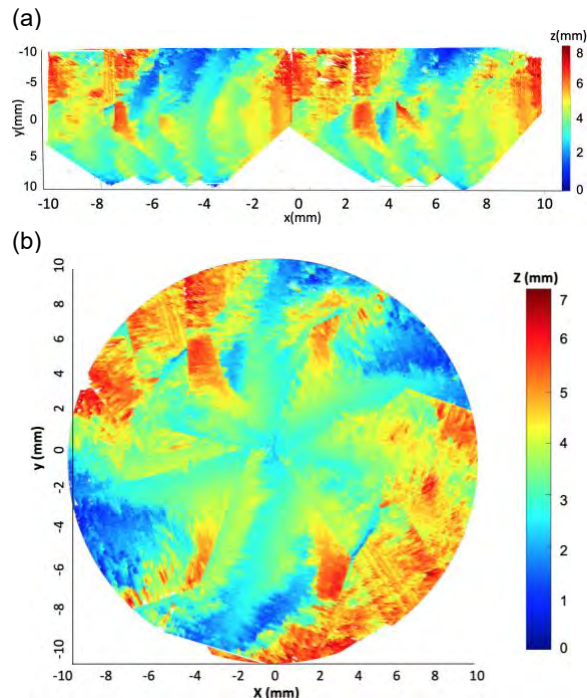
FIGURE 6. stitched panorama surface for tool body (a) and tool bit (b)

The results prove the potential of reconstructing the whole-view machine tool bit in the purposed technique.

FUTURE WORK
For further implementation on this technique, a phase unwrapping technique will be investigated, and a laser scanning process will be added on the system, which can help collect tool edge conditions and dynamic performances. Galvanometer which determine the rotation of the laser source will also be synchronized with spindle motion and illumination system. This combination of strobe-stereoscopy and laser scanning process can improve the 3D image quality, in-process characterization and identification of machine tool dynamic behavior and cutting tool conditions.

CONCLUSION
This paper presents the novel 3D imaging technique for cutting tool condition monitoring by the phase-shifting strobe-stereoscopy. A hardware set-up is introduced, as well as the 3D imaging algorithm. The reconstructed image analysis under different working speeds is discussed, the reconstruction resolution included. The uncertainty of the imaging process and the built-up system are also analyzed. As the input signal is the working speed, no other information from other sources is required. This proposed method can be implemented into machine tool in on-machine or in-process configuration, enhancing machine tool metrology capabilities. Apart from that, this method can supplement the blank for determining the machine tools' performance status, which further ensures the fabrication process.

REFERENCES
[1] Wong, S.Y., Chuah, J.H. & Yap, H.J. Technical data-driven tool condition monitoring challenges for CNC milling: a review. International Journal of Advanced Manufacturing Technology. 2020; 107: 4837–4857.
[2] Plows, G.S. and Nixon W.C. Stroboscopic scanning electron microscopy. Journal of Physics E: Scientific Instruments. 1968; 1:595.
[3] Karthik A., Chandra S., Ramamoorthy B., Das S. 3D tool wear measurement and visualisation using stereo imaging. International Journal of Machine Tools and Manufacture. 1997; 37: 1573-1581.
[4] Niranjan K., Ramamoorthy B. Tool wear evaluation by stereo vision and prediction by artificial neural network, Journal of Materials Processing Technology. 2001; 112: 43-52.
[5] Ng, W.B., Zhang, Y. Stereoscopic imaging and reconstruction of the 3D geometry of flame surfaces. Exp Fluids. 2003; 34: 484 - 493.

SPINDLE METROLOGY FOR A HIGH RESOLUTION X-RAY MICROSCOPE

Byron Knapp[1], Curt Preissner[2], and Dan Oss[1]

[1]Professional Instruments Company
Hopkins, Minnesota, USA

[2]X-Ray Science Division
Argonne National Laboratory
Argonne, Illinois, USA

ABSTRACT
State-of-the-art scanning X-ray microscopy applications require nanometer-level positioning accuracy. Positioning uncertainty complicates data reconstruction with a critical degree-of-freedom being the sample rotational axis. In this work, the metrology of an air bearing spindle used for high resolution X-ray microscopy is demonstrated. The dynamic stiffness and spindle error are measured. The Grejda optimum orientation for minimum error is calculated.

BACKGROUND
The Advanced Photon Source (APS) at Argonne National Laboratory is one of five US national synchrotron radiation light sources. High energy electrons travel around a 1.1 kilometer circumference storage ring and emit synchrotron radiation in wavelengths suitable for imaging features of atoms, molecules, crystals, and cells. The APS is scheduled for an upgrade to increase coherent flux by 100 times enabling further improvements in scanning speed and resolution. In order to fully realize the benefit of increased brightness, a new X-ray microscope called Velociprobe (Figure 1) was built to explore technologies and techniques for fast ptychographic imaging with high spatial resolution [1].

Nanometer-level radial error and nanoradian tilt error motion are desired for the Velociprobe sample rotation. The original crossed-roller bearing, stepper motor driven rotation stage was recently upgraded to an air bearing spindle with direct drive brushless servo motor [2]. The air bearing has a large diameter aperture to accommodate auxiliary equipment.

FIGURE 1. The original Velociprobe designed by scientists and engineers at Argonne National Laboratory [1].

DESIGN
The 10R-606 Blockhead shown in Figure 2 is ideally suited for the Velociprobe sample rotation upgrade. It features high dynamic stiffness with nanometer-level radial and nanoradian-level accuracy. The 154 mm diameter aperture allows the translation stack to be embedded within the bore resulting in a tight structural loop for high bandwidth scanning.

FIGURE 2. The large aperture air bearing spindle Blockhead 10R-606 is ideal for Velociprobe.

A bespoke aluminum lamination motor (Aerotech S-240-43-A) was selected in order to minimize motor influence on spindle accuracy [3]. Sufficient torque was achieved without compromising accuracy using a low harmonic stator winding that features sinusoidal gap flux. A linear amplifier (Aerotech HLe-10-40) minimizes current ripple and radiated electrical noise.

A 32,768 line count, 209 mm diameter encoder (Renishaw RESM) is closely coupled to the motor. The graduation accuracy is ±1 arc second with a grating resolution of 20 µm. The analog output enables the position signal to be highly interpolated (as fine as 0.0006 arc second resolution).
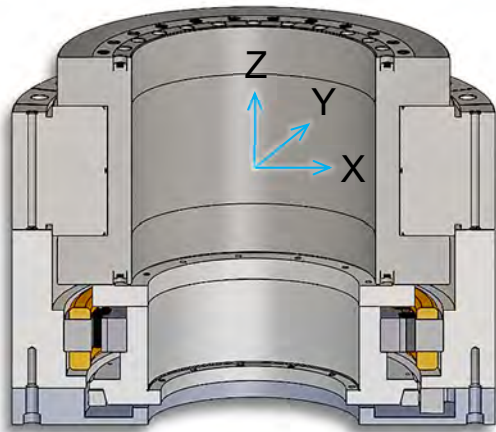
FIGURE 3. Cross section of the motorized spindle assembly with high resolution encoder.

HIGH DYNAMIC STIFFNESS

High-speed scanning with Velociprobe requires a spindle with high dynamic stiffness. A roving hammer experimental modal analysis is used to determine natural frequencies and mode shapes.

FIGURE 4. Experimental modal analysis is used to determine natural frequencies and mode shapes.

The spindle is supported on compliant foam and an impact hammer (Kistler 500 N) is used to excite the structure. The rotor and stator are impacted at 6 locations while an accelerometer (Kister K-Shear 25 g) measures the response. A 24-bit dynamic signal analyzer (Data Physics SignalCalc Ace) records excitation and response to calculate the frequency response functions. Quadrature peak picking is used to extract tilt, bending, and axial mode shapes shown in Figure 5.
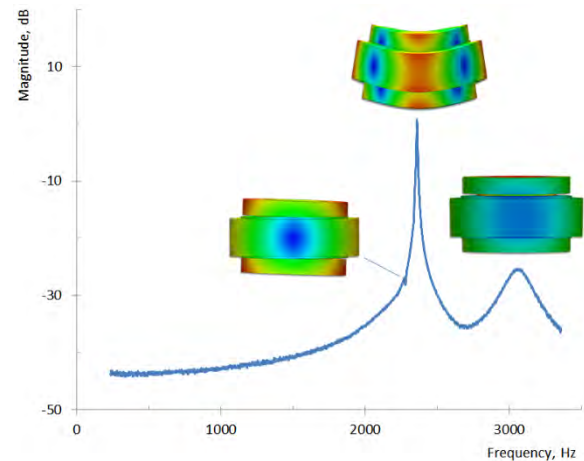
FIGURE 5. Tilt, bending, and axial modes all occur above 2,000 Hz.

PRECISION SPINDLE METROLOGY

The experimental procedures needed to accurately capture error motion of a spindle are described by Marsh [4]. The spindle error motion measurement task is complicated by the fact that spindle errors and artifact out-of-roundness are nearly equal. Therefore, separation techniques must be used to distinguish each error. Whitehouse developed a multiprobe technique which avoids the potential errors introduced when repositioning and reattaching the artifact and probe during reversal [5].
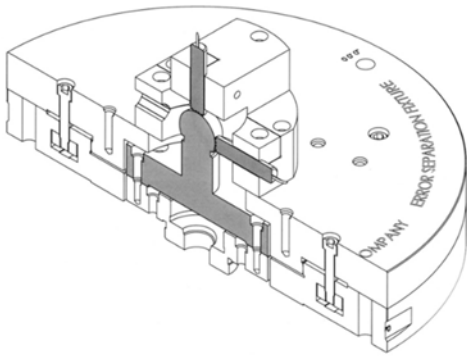
FIGURE 6. Multiprobe error separation tooling.

In this work, an implementation of multiprobe separation is demonstrated using tooling shown in Figure 6. Radial and axial error motion components are obtained for 10 revolutions at 120 RPM. A capacitive sensor (Lion Precision C23-C) targets a 25 mm diameter lapped sphere that is 225 mm from spindle center. The sensor amplifier (Lion Precision CPL190) incorporates a 15 kHz first-order, low-pass analog filter with linear phase response. The data acquisition system (Lion Precision SEA) is triggered by the divided encoder signal (32x divider providing 1,024 points per revolution). The spindle metrology setup is shown in Figure 7.
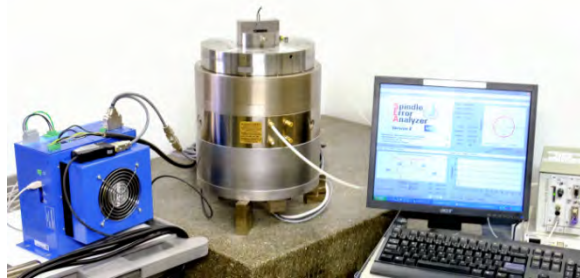
FIGURE 7. Test setup for precision spindle metrology. Measurement location is 225 mm from spindle center.

Bespoke tooling is used to position a single sensor to three angular orientations chosen to minimize harmonic distortion through 225 Undulations Per Revolution (UPR). Then the target out-of-roundness is removed leaving the X direction radial error $\Delta X_1(\theta)$ shown in Figure 8. The tooling also enables measurement of the $\Delta Y_1(\theta)$ component by repeating the separation with each measurement shifted 90° as shown in Figure 9. A low-pass digital filter with a 150 UPR cut-off is applied to the results.
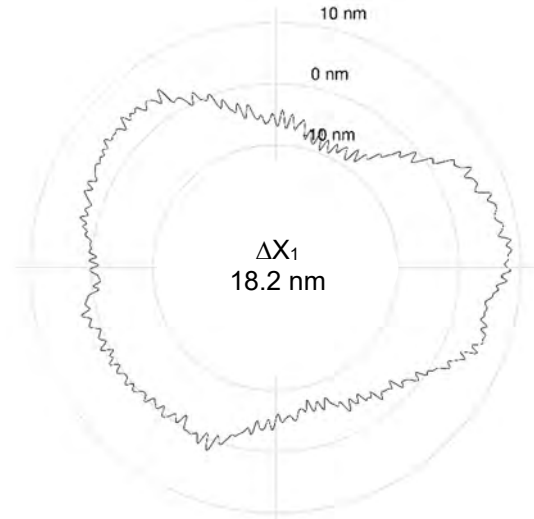
FIGURE 8. X direction radial error is 18.2 nm at a height 225 mm from spindle center.
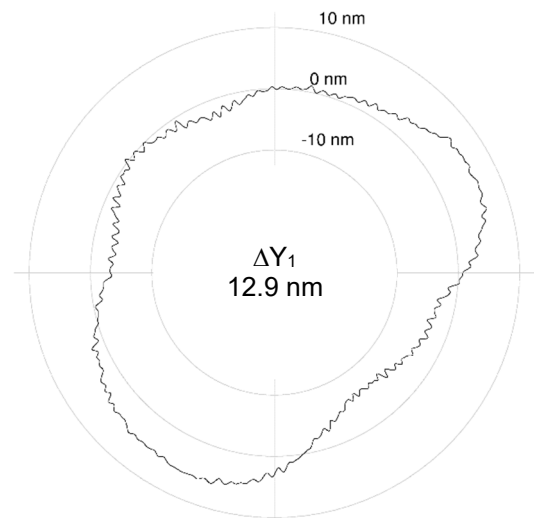
FIGURE 9. Y direction radial error is 12.9 nm at a height 225 mm from spindle center.

Orthogonal error components $\Delta X_1(\theta)$ and $\Delta Y_1(\theta)$ are used to map the error as a function of orientation angle as was demonstrated by Grejda [6]. The error map shown in Figure 10 reveals spindle stator orientations for minimum and maximum radial error. Radial error of the original Velociprobe crossed-roller stage was about 2 μm which means the 10R-606 at a height of 225 mm is an improvement of more than two orders of magnitude.
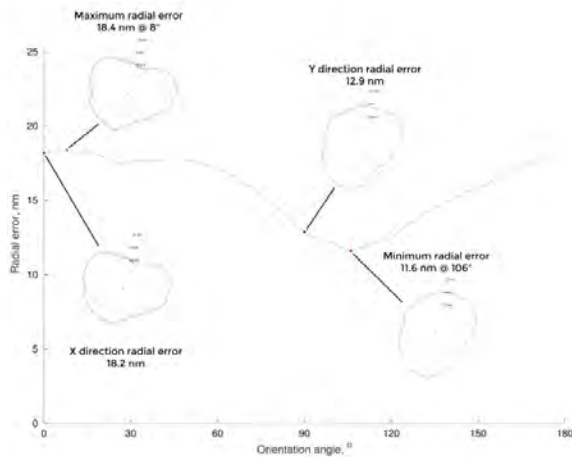
FIGURE 10. Mapping radial error of the spindle at a height of 225 mm. The minimum error is 11.6 nm at 106° orientation angle.

Axial error measurement does not require error separation but misalignment of the probe will cause erroneous measurement of apparent fundamental axial error. Therefore probe alignment is ensured during assembly of the tooling.
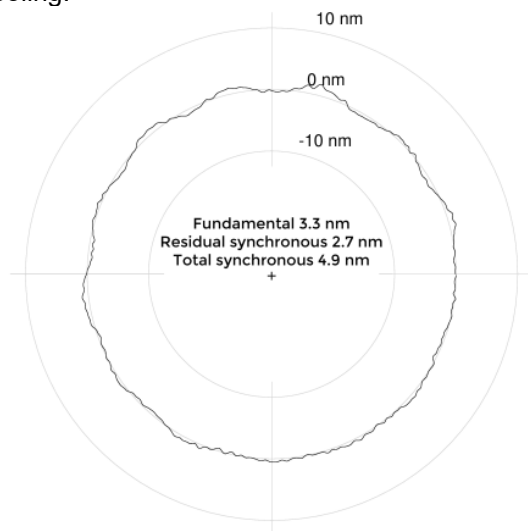
FIGURE 11. Axial error motion with 3.3 nm fundamental, 2.7 nm residual, and 4.9 nm total synchronous.

A second set of radial measurements at a known distance from the first set is required to calculate the tilt error motion. The measurements are informally referred to as "low ball" and "high ball" which are shown in Figure 12. The high ball setup is 375 mm from the center of the spindle (150 mm higher than the low ball measurement). Using multiprobe separation again, the synchronous spindle error components $\Delta X_2(\theta)$ and $\Delta Y_2(\theta)$ are found. Using $\Delta X_1(\theta)$ from Figure 8 and $\Delta X_2(\theta)$ in Figure 13, the X direction component of tilt error $\alpha_X(\theta)$ is calculated and shown in Figure 14.
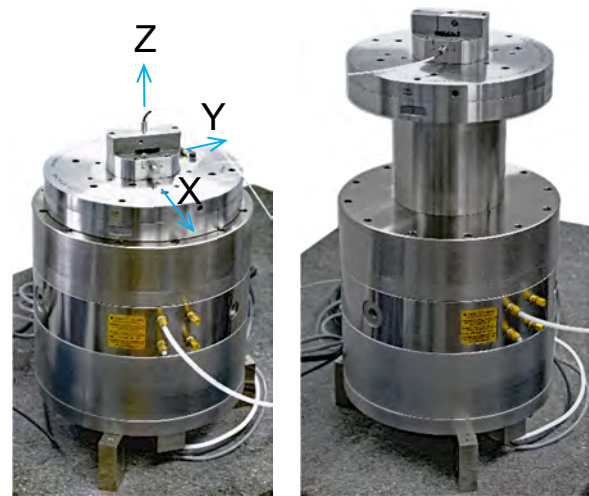
FIGURE 12. Low ball and high ball measurements are required to calculate tilt error. Low ball height is 225 mm from spindle center and high ball is 375 mm.
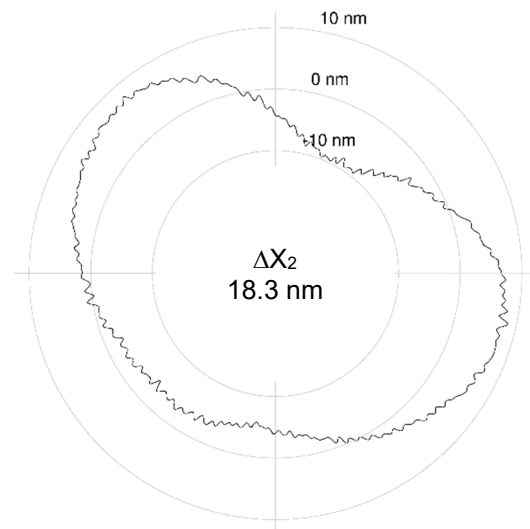
FIGURE 13. X direction radial error is 18.3 nm at a height 375 mm from spindle center.
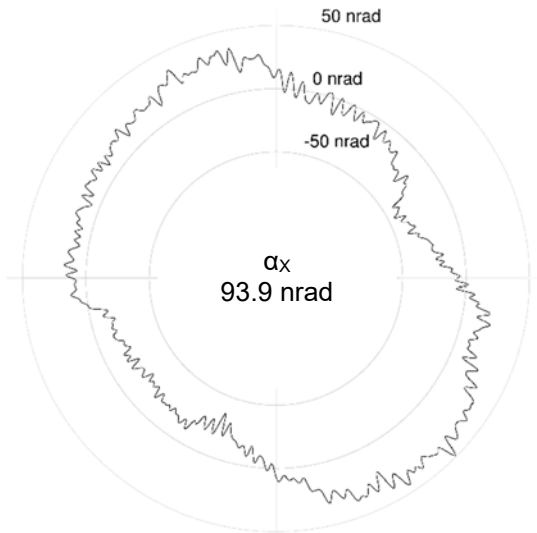
FIGURE 14. X direction tilt error calculated from low and high ball measurements is 93.9 nrad.

The tilt error map is found using $\alpha_X(\theta)$ and $\alpha_Y(\theta)$ and the result is shown in Figure 15. The maximum error is 97.7 nanoradians whilst the minimum is 71.9 nanoradians.
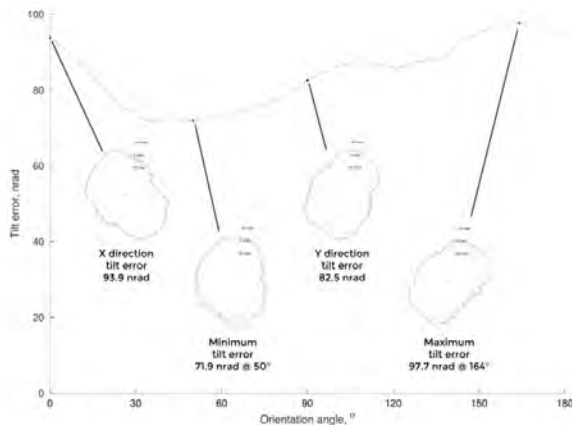
FIGURE 15. Tilt error map shows a maximum of 97.7 nrad and minimum of 71.9 nrad.

CONCLUSIONS

A nanometer-level air bearing spindle was designed and tested for use in a high speed, high resolution scanning X-ray microscope. Grejda optimization is used to create an error map as a function of orientation angle. The optimum orientation angles provide a 37% improvement in radial error and a 26% improvement in tilt error simply by correctly positioning the spindle stator during installation. For example, if the spindle stator is oriented with X-ray beam aligned to the Y direction, the radial error is 12.9 nm with a tilt error of 82.5 nrad. This represents an improvement of more than 150 times compared to the previous rotary stage resulting in improved projection alignment and 3D reconstruction quality. These results highlight the importance of spindle orientation for fixed sensitive direction precision manufacturing and metrology applications.

REFERENCES

[1] Deng J et al. 2019 The Velociprobe: An ultrafast hard x-ray nanoprobe for high-resolution ptychographic imaging. Rev. Sci. Instrum. 90, 083701.

[2] Deng J et al. 2019 Instrumentation and method developments of x-ray ptychography at the Advanced Photon Source. Proc. SPIE 11112, X-Ray Nanoimaging: Instruments and Methods IV, 111120E.

[3] Arneson H 2019 Motorization of a large aperture air bearing for use in a new X-ray microscope. Proc. ASPE Annual Meeting. Pittsburgh, PA.

[4] Marsh E 2010 Precision Spindle Metrology, Second Edition. (Lancaster, PA: Destech Publications, Inc.)

[5] Whitehouse D 1976 Some Theoretical Aspects of Error Separation Techniques in Surface Metrology. J. of Phys. E: Sci. Inst. 9:531-536

[6] Grejda RD 2002 Use and calibration of ultraprecision axes of rotation with nanometer level metrology (University Park, PA: The Pennsylvania State University)

PERFORMANCE EVALUATION OF X-RAY COMPUTED TOMOGRAPHY INSTRUMENTS: SENSITIVITY TO DETECTOR AND STAGE ERRORS- TRENDS FOR DIFFERENT MAGNIFICATIONS

Prashanth Jaganmohan[1,2], Bala Muralikrishnan[1], Meghan Shilling[1] and Edward P. Morse[2]
[1]Sensor Science Division
National Institute of Standards and Technology
Gaithersburg, MD, USA
[2]Center for Precision Metrology, Department of Mechanical Engineering
University of North Carolina at Charlotte
Charlotte, NC, USA

INTRODUCTION

In recent times, industrial metrology has been experiencing a steady increase in the use of X-Ray Computed Tomography (XCT) as a means for inspection, primarily when dealing with complex parts that would be time consuming to measure by traditional inspection procedures, or parts with internal features that simply cannot be accessed or measured by contact-based methods. This increasing demand brings forth the need for development of standardized test procedures to evaluate the performance of XCT instruments and support claims of metrological traceability. To meet these needs, the International Organization for Standardization (ISO), the American Society of Mechanical Engineers (ASME), and ASTM International have been working independently to develop performance evaluation standards for XCT systems. Current drafts of these standards recommend testing at different measurement volumes (i.e., at different stage and detector positions), but do not provide specific guidance as to where these measurement volumes are to be located or all of the test positions within these volumes [1-2]. Part of the reason for the lack of such specific information could be the cumbersome task of testing all conditions experimentally or through extensive radiographic simulations. The work described in this paper overcomes the difficulty of such an unrealistic workload of simulations since a significantly faster simulation method is used.

One of the main goals associated with the development of performance evaluation standards is to design test procedures that are sensitive to all or as many known error sources

as possible. Thus, it becomes imperative to identify all significant error sources, understand their influence on dimensional measurements and accordingly make recommendations on methods to capture them. Several error sources in XCT systems have been identified and discussed in the VDI/VDE 2630-1.2 [3]. The National Institute of Standards and Technology (NIST) has conducted studies [4-5] on the effect of one particular type of error source, namely uncorrected geometry errors in cone-beam XCT systems. In that work, the sensitivities of sphere center-to-center distance errors and sphere form errors to various geometrical error sources were explored for one position of the detector and the rotation stage. Based on results obtained by a NIST-developed rapid simulation method, i.e., the single point ray tracing method (which was validated against more traditional radiograph-based reconstruction method), sphere center-to-center distance error sensitivities and form error sensitivities of spheres were reported.

The present work is an extension of the research in [4-5] by repeating the simulations at several combinations of the source-stage (also known as source-object) and source-detector distances. For a given error source under consideration, the combination of these distances at which the highest sensitivities can be obtained, is first identified. Such a combination of distances establishes the geometric magnification, given by the ratio of the source-detector distance to the source-stage distance. This combination also establishes the dimensions of the measurement volume for a given XCT instrument. Within such a measurement volume, the measurement line (i.e., the position and orientation of a center-to-center distance segment in the measurement

volume) that produces the maximum center-to-center distance error (and therefore, the highest sensitivity) for a given magnitude of the considered error source is identified. This process is repeated for all error sources studied here. Therefore, for every error source, the source-stage distance, source-detector distance, and the line of highest sensitivity in the corresponding measurement volume are determined here.

SIMULATION SETUP

All simulations in the present work are carried out in MATLAB (R2018b)[1]. The simulated reference object consists of a set of 125 spheres distributed into five horizontal planes. Each plane consists of one centrally located sphere, 16 spheres arranged in an outer circle, and eight spheres arranged in an inner circle whose radius is half the radius of the outer circle, as shown in Figure 1. This is the same arrangement described in [4]. Note that in Figure 1, the positions of the source and detector are to scale, but the size of the detector is not. The coordinate system is centered at the source, with axis directions as shown in Figure 1. Detailed descriptions on how these axes are defined to establish the coordinate system can be found in [4]. While the object was of a single fixed size in the study conducted earlier [4-5], here, the diameter and height of the overall cylindrical shape are a function of the source-stage and source-detector distances. That is, the simulated object is scaled for each combination of source-stage and source-detector distance pair so as to fill 98% of the area of a 250 mm x 250 mm detector. Such scaling is done to obtain the largest magnitudes of distance errors possible for each combination of stage and detector positions. The diameters of the spheres are also scaled accordingly (varying from 3.40 mm at the smallest measurement volume to 18.68 mm at the largest measurement volume) while making sure their projected images still fit on the detector.

---

[1] Certain commercial equipment, instruments, or materials are identified in this paper to foster understanding. Such identification does not imply recommendation or endorsement by the National Institute of Standards and Technology, nor does it imply that the materials or equipment identified are necessarily the best available for the purpose.
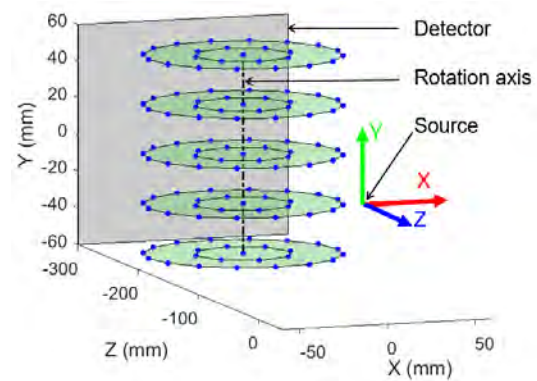
FIGURE 1. *Reference object containing 125 spheres chosen for simulation.*

The geometric error sources associated with the detector include errors in location along the three mutually perpendicular axes, and errors in angular position about the same axes. These are shown in Figure 2. Errors associated with the stage include a location error along the Z axis (connecting the source and rotation axis), and error motions of the stage, which includes encoder scale, axial, radial, and wobble errors. All the error motions of the stage are assumed to have harmonic components and therefore are represented as sine and cosine functions of the rotation stage indexing angle. Harmonics of orders one through ten are included in this study. The error sources associated with the stage are shown in Figure 3. Detailed descriptions of these error sources and the coordinate system in which these error souces are defined, can be found in Ferrucci et al. [6-7] and NIST studies [4-5].

METHODOLOGY

The methodology used for the simulations consists of the single point ray tracing method introduced in [4]. This method has been proven to be a faster and more practical alternative to the full X-ray CT tomographic reconstruction methods for estimating the effects of geometric errors using sphere-based artifacts. In the single point ray tracing method, only the centers of the spheres are projected on to the detector using a known set of parameters describing the geometric errors of the system. A locus representing the motion of each projected center on the detector is obtained by determining the projection for each angular position of the stage until a full revolution is complete. The loci obtained are used in a back-projection algorithm to estimate the location of each sphere through a least-squares minimization. The reconstructed
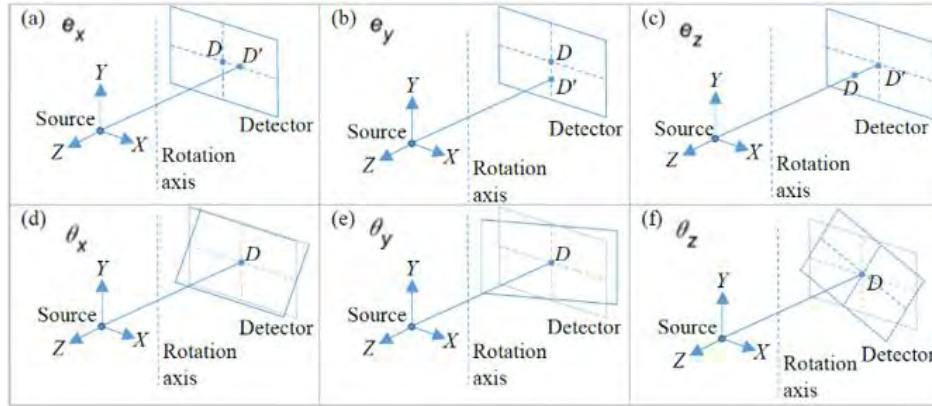
FIGURE 2. Geometrical error sources associated with the detector. (a) Detector location error parallel to X axis. (b) Detector location error parallel to Y axis. (c) Detector location error along the Z axis. (d) Detector rotation error about an axis parallel to X axis. (e) Detector rotation error about an axis parallel to Y axis. (f) Detector rotation error about the Z axis.

FIGURE 3. Geometrical error sources associated with the stage. (a) Error in the location of the rotation axis along Z. (b) Axial error motion. (c) Radial error motion components along X and Z. (d) The X component of the wobble error. (e) The Z component of the wobble error. (f) Error in the angular position of the stage.

sphere centers obtained in this way allow the calculation of the center-to-center distances for each pair of the 125 sphere centers. Circles comprising discrete points are drawn normal to each ray from the source to the detector with their centers located on the previously identified least-squares centers. The points lying on the outer surface of the resulting point cloud are considered for form error calculation.

When analyzing the effect of a particular error source, its actual value is fed into the forward projection, for example, the actual pitch angle error of the detector is considered in order to generate the simulated sphere centers for each angular position. However, the back-projection, or reconstruction algorithm, assumes an ideal geometry, i.e., the absence of that geometric error. In this example, this would mean the ideal pose of the detector, i.e., zero pitch. This discrepancy between actual and assumed parameters defines the magnitude of simulated geometry errors and results in sphere center-to-center distance errors and sphere form errors. In this way, the effect of all geometry errors including detector errors and stage errors on the center-to-center distance errors and form errors of the spheres on the reference object are studied. To understand the effect of magnification, such simulation studies are performed at several positions of the stage and detector throughout the working volume.

For each error source under consideration, the pair of spheres that produced the highest center-to-center distance error is identified for the combination of source-stage and source-detector distances identified in [4]. The line joining the previously identified pair of spheres constitutes the line of highest sensitivity, i.e. center-to-center distance error (in mm) per mm or degree of geometric error, and is tracked across all combinations of the stage and detector positions.

The stage is positioned at varying distances (d) from the source, starting from 200 mm and increasing in steps of 100 mm up to a maximum of 1100 mm. For each chosen position of the stage, the source-detector distance (D) is varied from d+100 mm to 1200 mm, in steps of 100 mm.

RESULTS AND DISCUSSION

For all the error sources under consideration, the highest distance error sensitivity is observed to occur at one of two configurations. In the first configuration, the detector is positioned as close to the source as possible, and the stage is then positioned as close to the detector as possible. For the simulations conducted, this corresponds to a source-stage distance (d) of 200 mm and a source-detector distance (D) of 300 mm.

The second configuration that tends to produce the highest distance sensitivity is where the stage is positioned as far from the source as possible and the detector is then positioned as close to the stage as possible. Here, this configuration corresponds to d=1100 mm and D=1200 mm. In traditional XCT systems, this second configuration usually corresponds to the largest measurement volume possible for a given instrument.

The solid lines shown in Figure 4 indicate the lines that produced that highest distance error sensitivity for the six detector errors and the Z location error of the rotation axis. In cases where multiple lines are shown for a single error source, it simply indicates that all the highlighted lines are equivalent in capturing the highest sensitivity shown. The values of d and D at which this highest sensitivity is observed are also mentioned in each case.

Figures 5 through 8 show similar illustrations of sensitive lines for the error motions of the stage. These errors are represented by sine and cosine components of orders 1 to 10. However, the magnitudes of sensitivities corresponding to fifth order and higher harmonics are found to be negligible. Therefore, the sensitive lines for the first four orders are shown here. Further, only the cosine components of the error sources are shown. The sensitive lines for the sine components are observed to have similar orientations but rotated by 90 degrees about the rotation axis.
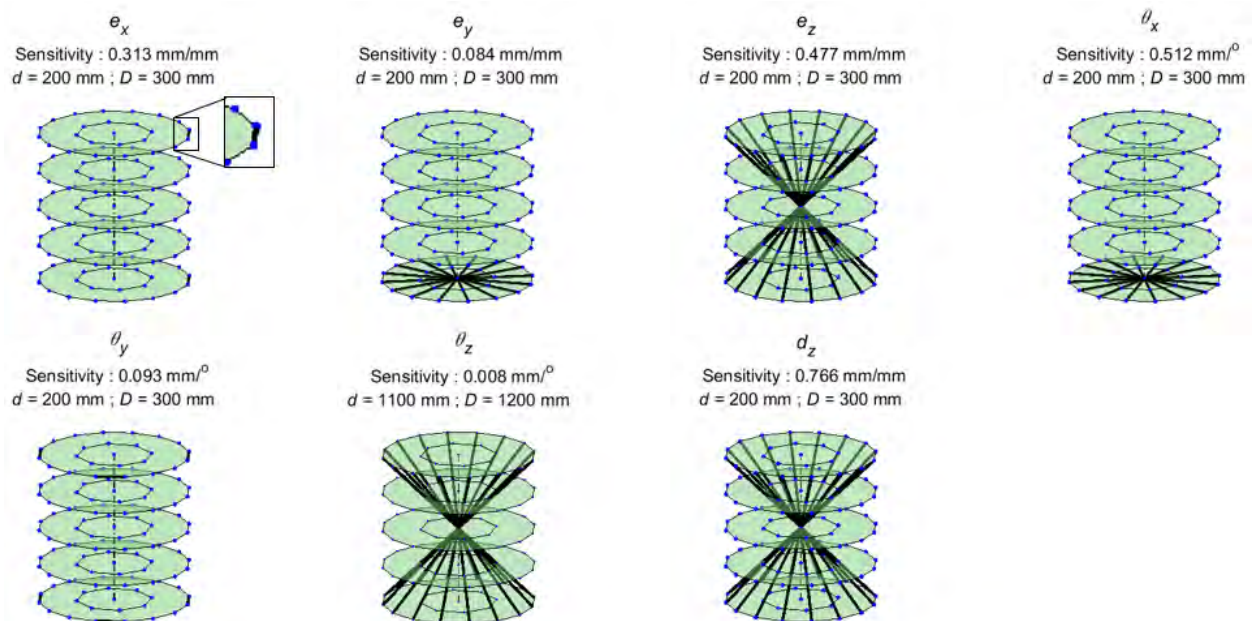
FIGURE 4. Sensitive lines for detector errors and Z location error of rotation axis.
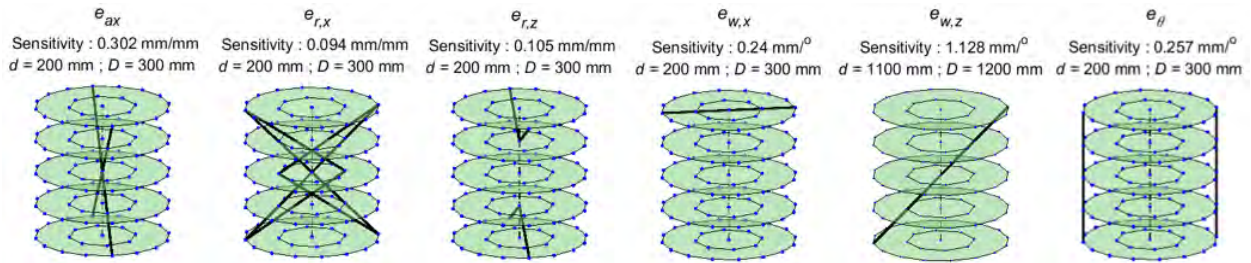
FIGURE 5. Sensitive lines for first order cosine components of stage error motions
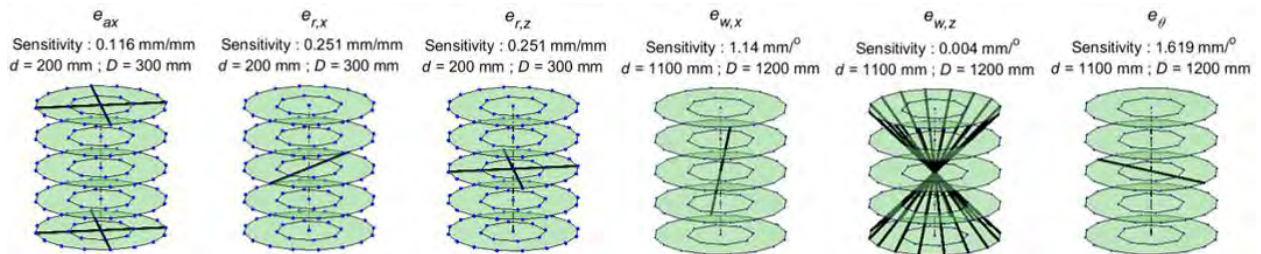
FIGURE 6. Sensitive lines for second order cosine components of stage error motions
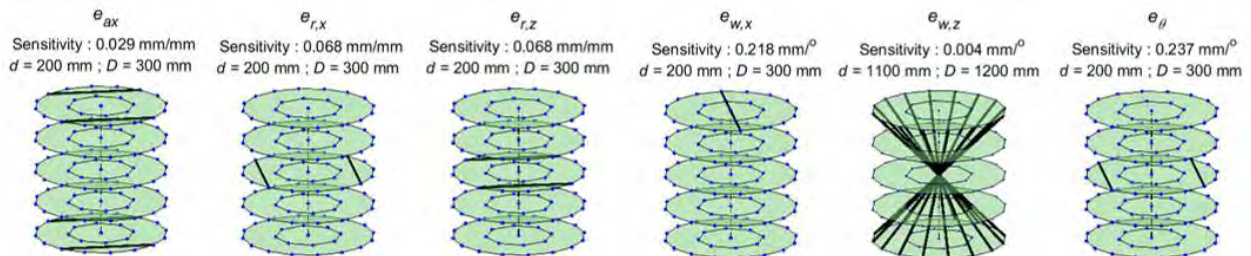
FIGURE 7. Sensitive lines for third order cosine components of stage error motions
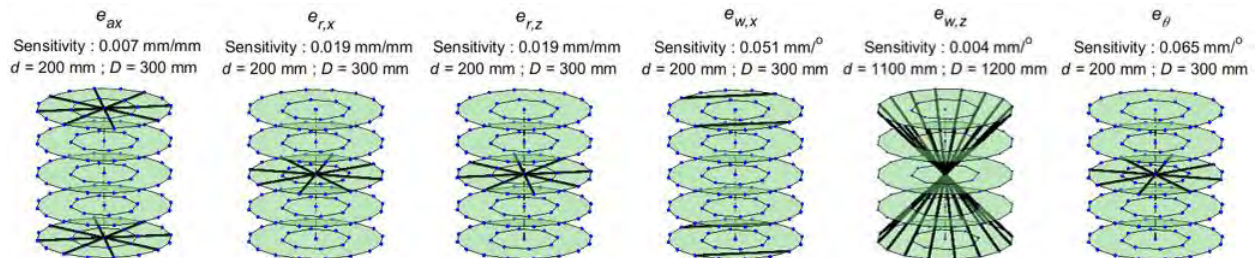
FIGURE 8. Sensitive lines for fourth order cosine components of stage error motions

CONCLUSIONS

Simulations have been conducted on a set of 125 spheres distributed throughout the measurement volume. Such simulations have been repeated for various positions of the stage and detector. The pair of spheres that produced the largest error per unit magnitude of a given geometric error source have been identified. This pair defines the line of highest sensitivity for that error source, i.e., this line defines the position and orientation in the measurement volume that is most sensitive to the given error source. Some key takeaways are:

- All error sources have their maximum center-to-center distance error sensitivity occurring at one of two configurations, one with the detector as

close as possible to source and stage as close as possible to detector, and the other with the stage as far as possible from the source and the detector as close as possible to the stage. Notice that in both cases, i.e., whether the stage is as close to the source or the stage as far away from the source, the magnification is the lowest possible.

- Most of the sensitive lines identified are body diagonals, vertical lines and diametrical lines at various horizontal levels, but it is interesting to note that some other 'uncommon' lines were also identified- such as some horizontal lines that are not diametrical or otherwise intuitive.

Future work could include extension of such a study to other error sources not included here. Further, studies can be conducted on designing suitable artifacts and making recommendations on a minimum set of test positions and measurement lines by which all known error sources can be captured to a satisfactory degree. In addition, experimental validation of these results by measurements on a physical artifact are also envisioned.

REFERENCES

[1] Draft ISO/CD 10360-11 - Geometrical product specifications (GPS) — Acceptance and reverification tests for coordinate measuring machines (CMM) — Part 11: CMMs using the principle of computed tomography (CT)

[2] Draft ASME B89.4.23 - X-Ray Computed Tomography (CT) Performance Evaluation Standard.

[3] VDI/VDE 2630 -1.2: Computed tomography in dimensional measurement; Influencing variables on measurement results and recommendations for computed tomography dimensional measurements.

[4] Muralikrishnan B, Shilling M, Phillips S, Ren W, Lee V, Kim F. X-ray Computed Tomography Instrument Performance Evaluation, Part I: Sensitivity to Detector Geometry Errors. Journal of Research of the National Institute of Standards and Technology. 2019; 124:124014 1-16.

[5] Muralikrishnan B, Shilling M, Phillips S, Ren W, Lee V, Kim F. X-ray Computed Tomography Instrument Performance Evaluation, Part II: Sensitivity to Rotation Stage Errors. Journal of Research of the National Institute of Standards and Technology. 2019; 124:124015 1-13.

[6] Ferrucci M, Ametova E, Probst G, Craeghs T, Dewulf W. Sensitivity of CT dimensional measurements to rotation stage errors. Proceedings of the 8th Conference on Industrial Computed Tomography (Wels, Austria), 2018.

[7] Ferrucci M, Ametova E, Carmignato S, Dewulf W. Evaluating the effects of detector angular misalignments on simulated computed tomography data. Precision Engineering, 2016; 45 230-241.

DEVELOPMENT OF A NEW STANDARD FOR THE PERFORMANCE EVALUATION OF SINGLE AXIS LINEAR POSITIONING SYSTEMS

Gregory W. Vogl[1], Ronnie R. Fesperman[2], Stephen Ludwick[3], Richard W. Klopp[4], Axel Grabowski[5], Justin Lebel[6], Jimmie A. Miller[7], Nathan L. Brown[8], Eric Belski[3], Nicholas Duncan[3], and C. William Hennessey[8]

[1]National Institute of Standards and Technology (NIST), Gaithersburg, MD, USA
[2]Corning Inc., Newton, NC, USA
[3]Aerotech Inc., Pittsburgh, PA, USA
[4]Exponent Inc., Menlo Park, CA, USA
[5]Physik Instrumente (PI) GmbH & Co. KG, Karlsruhe, Germany
[6]Renishaw Inc., West Dundee, IL, USA
[7]University of North Carolina at Charlotte (UNCC), Charlotte, NC, USA
[8]ALIO Industries Inc., Arvada, CO, USA

INTRODUCTION

Linear positioning systems are utilized in wide-ranging manufacturing applications from machine tools to high-precision applications such as semiconductors and photovoltaics. New linear positioning systems exist with ranges of motion as long as several centimeters and positioning resolutions as low as on the order of a nanometer. The ability to meet high-precision manufacturing tolerances requires accurate knowledge of the positioning performance of these systems, yet a dedicated standard for evaluating the performance of single axis linear positioning systems does not exist. In contrast, performance standards have been used to measure the performance of single axis linear positioning systems within machine tools.

Yet use of these standards to measure high-precision systems with off-the-shelf instrumentation and test methods can be difficult, because the performance of the high-precision class of positioning systems can approach the measurement uncertainty [1]. Due to increasing demands on performance and new applications and needs, many manufacturers and users have developed their own internal methods and standards for characterizing these systems. Performance specifications based on these different methods and terminology has led to certain customer confusion. Hence, a new standard is needed with specific measurement methods for single axis linear positioning systems to address these challenges.

Towards this end, a new standard is being created by members from industry, academia, and government in coordination with the B5 Standards Committee of the American Society of Mechanical Engineers (ASME), the Standards Developing Organization [2, 3]. The intended use of the tests described within this standard are acceptance testing of new/reconditioned systems and verification of the performance of systems already in operation.

This document focuses on the new methods under consideration for inclusion in the new standard for performance evaluation of single axis linear positioning systems.

SCOPE OF NEW STANDARD

The primary goal of the standard is for it to be used by both manufacturers and users as the main standard to guide them in characterizing the performance of their single axis linear positioning systems. As such, the new standard will describe the following for single axis linear positioning systems:

- A methodology for specifying and testing the performance of systems with travels ranging from micrometers to meters and with potentially high relative positioning performance compared to standard machine tools.
- Existing test methods and instrumentation described in machine tool standards [4-6] and new methods and instrumentation for single axis linear positioning systems.

- Unified terminology and the treatment of environmental effects and measurement uncertainty to enable performance comparisons between systems.

NEW TEST METHODS

In order for the new standard to be as useful as possible, a variety of new methods are under consideration for inclusion in the new standard. These methods attempt to "fill in the gaps" for performance evaluation of single axis linear positioning systems. Some of the additional tests being considered for inclusion are described in the following subsections.

Coordinate System Referenced Measurement

A positioning system consists of a carriage, a base, guideways and bearings (five degrees of fixed constraint), actuator(s) (effecting one degree of variable positioning constraint), physical actuator interface(s), position feedback sensor(s) and intelligent electronics [7], an electromagnetic force controller, and a program with a user interface. All of these influence how the carriage moves with respect to the base not just quasi-statically as prevalently characterized but also dynamically [8] as a function of time, temperature, environment, acceleration, velocity, payload, controller parameters, etc. Additionally, every point associated with the carriage has a unique path with respect to the base as the carriage is translated, as seen in FIGURE 1.
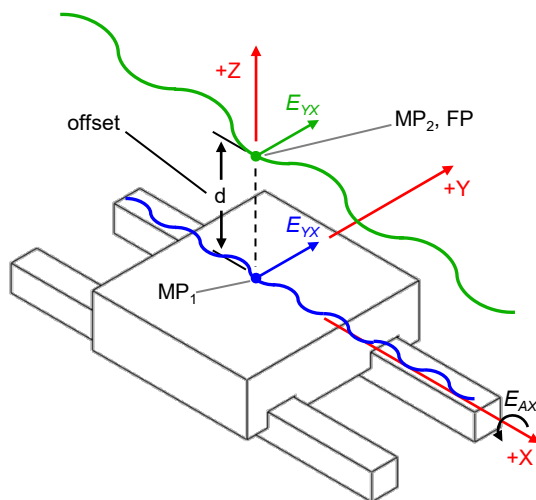
FIGURE 1. *Illustration comparing the motion of two distinct measurement points (MP) fixed with respect to the carriage of a linear positioning system. The functional point (FP) is where a particular manufacturing process would occur.*

The measurements for one point do not directly characterize another point. However, by establishing well-defined coordinate systems for the carriage (moving element, csM), and the base (fixed element, csF), the motion of any point of interest can be calculated from the measurement of the linear path of a single point if the relative orientations of the carriages are also determined and the positions of the points are well defined in the csM or csF coordinate frames. The provided mathematical calculations for these enable motion calculations for an application's functional point even if it is not the measurement point for characterization. This also facilitates error budgeting, error simulation [9], and uncertainty determination.

Incremental Step

Many industrial applications require positioning systems to repeatably make small incremental movements. As a result, vendors provide specifications for the smallest increment of motion their devices are capable of achieving. Most vendors refer to this performance capability as the minimum incremental motion (MIM), while others use terms such as minimum achievable positioning increment, minimum achievable incremental movement, least incremental step, minimum step size, and the like. Note that these terms are not used to specify the resolution in measuring the position of a system, but instead describe the smallest increment of motion a device is capable of consistently delivering.

Currently, no standard test method exists for quantifying the smallest (or minimum) incremental step (or movement) that a positioning system can achieve. ASME B5.54-2005 outlines a Least Increment Test, where small steps (see FIGURE 2) are performed to illustrate a machine tool's ability to make small incremental moves [4]. However, a quantitative treatment of what constitutes the smallest positioning increment is missing.
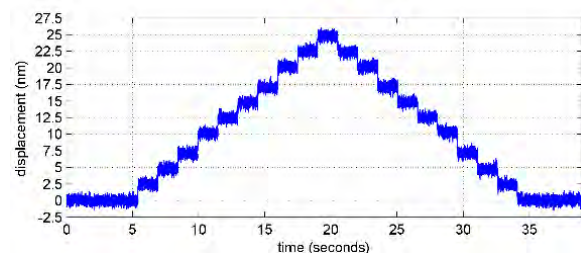
FIGURE 2. *Example displacement plot for an Incremental Step Test.*

This new standard will describe a new Incremental Step Test and provide procedures for calculating MIM values for both unidirectional and bidirectional movements. In addition to MIM, a procedure for calculating the Incremental Step Reversal Error will be described. Accurate calculation of these performance values also requires the introduction of two additional and new test procedures: 1) In-Position Jitter and 2) Move and Settle.

In-Position Jitter

The in-position jitter refers to a measure of the amount of residual motion that occurs in a positioning system when the system is nominally at rest. When provided today, this number is often specified as simply a peak-to-peak or perhaps root mean square value. However, the procedures used to arrive at this value are at best inconsistent, and at worst undocumented. In many cases the jitter of the positioning system approaches the jitter of the available sensors. The measurement of in-position jitter is heavily influenced by a number of test conditions, each of which are elaborated upon in the draft standard. It is the objective of this section to introduce techniques for the measurement of in-position jitter so that the measures are both relevant to the product being manufactured or process being performed and are applied consistently. Doing so requires establishing guidelines for the measurement setup, the data acquisition system, and the subsequent data processing.

The *measurement setup* includes the sensor used in performing the measurement, the position of that sensor in the structure of the positioning system, the metrology loop, and the state of the servo system. The preferred configuration uses an independent sensor located so as to measure the motion at the functional point of the positioning system relative to the machine base via the metrology loop. As the sensor output is influenced by all motion occurring anywhere within the metrology loop, it is critical that any fixturing used in locating the sensor be well-documented and designed and located to not unduly influence the measurement. Included in the measurement setup is the documentation of the state of the closed loop controller (likely enabled) and the state of any mechanical brakes in the system. Also included in the measurement setup is the definition of the amount of time that has passed since any commanded move has occurred to allow time for transient dynamics to settle, as well as documentation of any vibration isolation systems in place. An inferior configuration for measuring in-position jitter uses the same internal sensor that is also used as the feedback device in the servo loop. These measurements are generally much more convenient, but do not clearly capture dynamic motion of the machine structure. It is also important to know and document the sensor characteristics, including but not limited to its resolution, frequency response bandwidth, measurement quantization levels, and any inherent spatial or temporal frequency characteristics.

The *data acquisition system* saves the real-time electrical signals from the sensor into a form that can subsequently be archived and post-processed. Salient details of the data acquisition system include the sample rate (usually time-based, but can also be triggered by position or other variable), the resolution of any analog-to-digital convertors, the presence or absence of any analog or digital filtering, the length of the data sets being collected, and the number of repeated experiments. The goal is to reduce the influence of the data acquisition system on the measurand. In general, it is best to collect samples as fast as possible and for as long as possible pending practical and economic limits to the testing. At a minimum the data acquisition should gather samples substantially faster than any known frequency component in the measurand in order to reduce the likelihood of aliasing, and for a long-enough time to adequately reflect the time scale of the process in operation.

The *data processing* algorithms convert the previously-captured position data into concise metrics. Of key importance is the documentation of the time over which the jitter is to be measured, and the presence or absence of any detrending or digital filtering that could be applied to, for example, attempt to separate the effects of low-frequency thermal drift from higher-frequency vibration. In the absence of other agreements, the standard recommends a record length of one second, no filtering of the data, and processing to report both a peak-to-peak value (the difference between the maximum and minimum values over a record) and a standard deviation with uncertainty bounds on both. Particular applications may benefit from processing and reviewing the data sets in the frequency domain and using the tools of Fourier transforms and

power spectral densities to isolate the motion that occurs in a particular range of frequencies. The particulars of those techniques are not planned to be included in the first release of the draft standard.

Move and Settle

To analyze and determine the MIM values, two temporal variables to perform a commanded step must be measured and defined: the move-and-settle time, t_{ms}, and the average time, t_{ave}. As such, the new move and settle test quantifies the time required for a servo-controlled axis to move a particular distance and settle to a pre-defined position error tolerance. An illustration of these two temporal variables is shown in FIGURE 3.
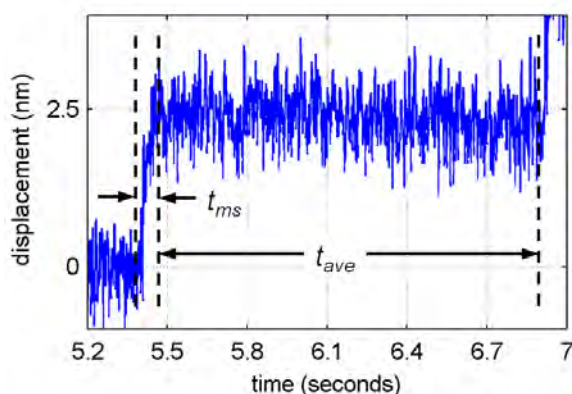
FIGURE 3. Illustration of the move-and-settle time, t_{ms}, and the average time, t_{ave}.

Static positioning

Test procedures for measuring the static positioning repeatability and accuracy of machine tools are already described in public standards like the ASME B5.54 (2005) [4] and ISO 230-2 (2014) [10]. Since these procedures were originally developed for large machines like milling centers, and not for higher-precision positioning systems used in the most demanding applications, the new standard will modify and extend these measurement procedures.

One example is adoption of an improved measurement sequence. Prior standards typically have required that target positions used to calculate accuracy and repeatability, for example, be approached bidirectionally. In the new standard, target positions were added that can only be approached unidirectionally at the end of the travel range. This enables one to describe for the first time a calculation method for the so-called linearity of a system. This specification value is quite common in the world

of short-stroke piezoelectric-based positioning systems, but has up to now never been described in a consensus standard. These additional target positions also allow determination of the complete stroke of a system in a defined procedure.

The draft standard for the first time describes correction methods to be applied prior to evaluating data for positioning system performance. For example, many users of high precision positioning systems request the accuracy or the positioning error with respect to a dataset that has been corrected for any underlying linear component of the deviation, so that only the higher-order errors are used in the evaluation. The new standard currently adopts a similar philosophy for correcting the Abbé error with respect to a functional plane prior to evaluating, e.g., accuracy or positioning error. Prior standards typically require only that the Abbé offset distance of the measurement point be recorded in the test report. In the proposed standard, a method is described where both the positional and angular deviations are measured and the positional deviation is corrected for the Abbé error and calculated back to a defined functional plane.
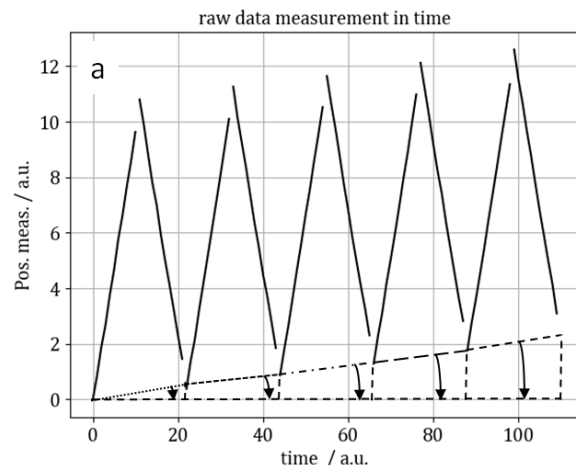
FIGURE 4. Visualization of the drift correction.

The proposed standard also includes methods for basic thermal correction. For the high-precision systems under consideration, it is often impractical if not impossible to stabilize environmental conditions sufficiently to forego correction, especially in industrial series production. This is true for short stroke high precision positioning systems with overall accuracies in the one-digit nanometer range, in

which thermal variations of only a few millikelvins during the measurement may obscure and corrupt the results. To address this issue, a basic thermal correction method is described, as illustrated in FIGURE 4, that is based on an assumption that thermal drift occurs on a significantly longer timescale that any single measurement traverse of the system, and therefore that the drift appears as an underlying linear variation over the timescale of one sweep through the positioning system's travel range.

Point Repeatability

Existing standards ASME B5.54 (2005) [4] and ISO 230-2 (2014) [10] define test methods to characterize an axis repeatability through single degree of freedom (DOF) tests focused on machine tool architecture and precision levels. Individual tests are required to quantify axial, horizontal straightness, and vertical straightness (or flatness) components of repeatability. The ASME B5.54 standard also includes procedures for using a three sensor nest to test for tool changer unidirectional repeatability. The purpose of the new Point Repeatability test methodology is to combine and expand this prior art into a test methodology that can capture bidirectional repeatability errors in three degrees of freedom with a single efficient system level test.

As seen in FIGURE 5, the standard defines a test that can be easily adjusted to match myriad end user applications, that captures all errors at nanometer level sensitivity, that captures Abbé error influence on linear repeatability, and that is compatible with many test equipment options. This methodology utilizes the multi-sensor nest concept from ASME B5.54 but updates terminology with a focus on characterization in three-dimensional space, specification of bidirectional testing, and coverage of both fixed-sensitive and moving-sensitive functional points (or testing locations).

The industry norm is to specify repeatability of a motion system as the axial repeatability, neglecting straightness and flatness repeatability errors. Furthermore, on multi-axis systems the repeatability is typically defined as only the individual axis axial repeatability error components. This industry norm correlates with the definition in prior standards where "repeatability is defined on a per-axis basis [4]." However, many applications are operating at a precision level where off-axis (straightness and flatness) repeatability errors cannot be neglected,

especially at the nanometer precision level. On an XYZ system this would require nine single DOF tests to fully characterize all three axes' repeatability errors. This is inefficient and there is no industry consensus on how to sum repeatability errors for multi-axis motion systems.
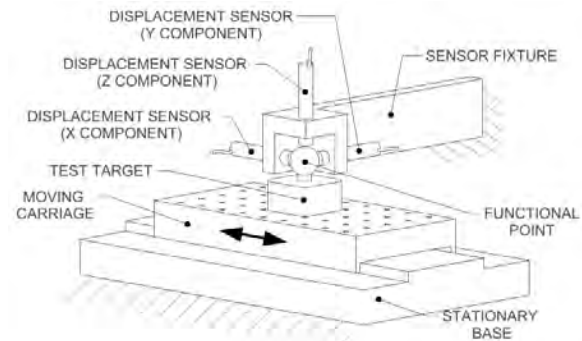
FIGURE 5. A three sensor nest is used to collect the X, Y, and Z components in a single Point Repeatability test of a linear positioning system.

This new single axis Point Repeatability test methodology is also intended to potentially lay the groundwork for a future multi-axis test that could be used to quantify all repeatability errors of all axes, as a system, in a single efficient test. The focus of the terminology and methodology defines Point Repeatability as a three-dimensional test and a "per system" test compared to prior art which is focused on a "per axis" test.

For six degree of freedom (6DOF) measurements, the linear displacement, straightness, and angular errors are traditionally measured independently and with different instrumentation. While this does allow for full characterization of a linear axis, this method also introduces potential local errors such as machine/axis bending that can cause separate measurements to become unrelated or "contaminated." Extended time is also needed to set up different instruments, subjecting the different data sets to being influenced by environmental changes and leading to potential non-repeatability between measurements.

Future extension of this section would include measuring all six degrees of freedom simultaneously. The method of testing six degrees of freedom simultaneously involves using a 6DOF instrument coupled with the linear axis stage under test. This method is likely to prove more useful on larger stages than on

micro/nano stages due to the size of the instrumentation and/or weight limitations of the linear axis.

Benefits would include having all measurements related to a single effective point or line in the work volume along the axis and reduced need to transform data sets to a common spatial location. Reduced set up and measurement time leads to a reduction in thermal and environmental effects. Repeatability between measurements of different types is improved as the state of the axis and environment is identical for all measurements recorded at each point of the test at the same moment in time.

CONCLUSIONS

A new standard for the performance evaluation of single axis linear positioning systems is in development. The standard builds upon previous standards via the addition of new test methods for incremental step, point repeatability, in-position jitter, constant-velocity evaluation, dynamic performance, and servo characterization, among others. The primary goal of the standard is for it to be used by both manufacturers and users as the main standard to guide them in characterizing the performance of their single axis linear positioning systems. Another goal of the standard is for it to serve as a strong foundation to be improved upon for future versions, in order to keep up with technological changes and customer needs. Currently, the new test methods are being evaluated and improved upon by various contributors. A final draft of the new standard is planned to be submitted to ASME by December 2020.

REFERENCES

[1] Fesperman Jr. RR, Donmez, MA, Moylan, SP. Ultra-Precision Linear Motion Metrology of a Commerically Available Linear Translation Stage. The American Society for Precision Engineering (ASPE) Twenty-sixth Annual Meeting. 2011; 52: p. 81-4.
[2] Fesperman R, Brown, N, Elliott, K, Ellis, J, Grabowski, A, Ludwick, S, et al. Methods for Performance Evaluation of Single Axis Positioning Systems: A New Standard. The American Society for Precision Engineering (ASPE) Twenty-eighth Annual Meeting. 2013; 56: p. 498-503.
[3] ASME B5 Standards Committee. B5 Machine Tools - Components, Elements, Performance, and Equipment 2020. Available from: https://cstools.asme.org/csconnect/CommitteePages.cfm?Committee=C12000000.
[4] American Society of Mechanical Engineers (ASME). B5.54-2005, Methods for Performance Evaluation of Computer Numerically Controlled Machining Centers. 2005.
[5] American Society of Mechanical Engineers (ASME). B5.57-2012, Methods for Performance Evaluation of Computer Numerically Controlled Lathes and Turning Centers. 2013.
[6] International Organization for Standardization (ISO). ISO 230-1:2012, Test code for machine tools — Part 1: Geometric accuracy of machines operating under no-load or quasi-static conditions. 2012.
[7] Miller J. Scope of Metrology Systems. The American Society for Precision Engineering (ASPE) Thirty-first Annual Meeting. 2016.
[8] Miller J, Hocken, R, Ramanan, V, Feng, Q. Foundation for Dynamic Metrology of Machine Tools. The American Society for Precision Engineering (ASPE) Fourteenth Annual Meeting. 1999.
[9] Fesperman RR, Moylan, SP, Vogl, GW, Donmez, MA. Reconfigurable data driven virtual machine tool: geometric error modeling and evaluation. CIRP Journal of Manufacturing Science and Technology. 2015;10:120-30.
[10] International Organization for Standardization (ISO). ISO 230-2:2014, Test code for machine tools — Part 2: Determination of accuracy and repeatability of positioning of numerically controlled axes. 2014.

FLATNESS MEASUREMENT OF LARGE SURFACES APPLYING IMPROVED SEQUENTIAL THREE-POINT METHOD

Shunya Yamada, Yutaka Uda, Shoichi Shimada
Division of Mechanical and Control Engineering
Osaka Electro-Communication University
Neyagawa, Osaka, Japan

BACKGROUND

The most widely used technique for highly precise flatness measurement is optical interferometry. However, for the evaluation of large plane, it is difficult to prepare large reference plane. Three-dimensional measuring machine is also the promising equipment for that purpose. However it is difficult to use in machining process at the factory site.

In this paper, a flatness measuring technique using improved sequential three-point method combining with a data stitching algorithm. The technique is a simple and convenient method for on-machine flatness measurement of large plane. Another advantage of the technique is that free-form surfaces can also be evaluated.

SURFACE SHAPE MEASURMENT USING IMPROVED SEQUENTIAL THREE-POINT METHOD [1][2]

Figure 1 shows the principle of sequential three-point method. The I-shaped sensor head, on which three displacement sensors F (front), C (center) and R (rear) are fixed in a line at equal spaces of d, is scanned along a straight line (x-axis) on the specimen surface to be measured. The surface shape profile of the specimen and the output signals of the front, center and rear sensors are expressed by $g(x)$ and S_F, S_C, and S_R, respectively. e_z and e_θ are the translational and rotational error motions of the sensor head, respectively. The surface shape profile of the specimen $g(x)$ is numerically calculated using the discontinuous displacement date obtained at every space of d as described in Eq. (1). ΔS_F and ΔS_R are the differences between output signals of the front and center sensors and between the center and rear sensors, respectively. The error motions e_z and e_θ are numerically eliminated.

$$g(x_n) = G_0 + (n-1)\Delta G_0$$
$$+ \sum_{i=0}^{n-1}(n-i)\{\Delta S_F(x_i) - \Delta S_R(x_i)\} \quad (1)$$

When the three sensors have different zero positions as shown in Figure 2, the zero position error α cannot be eliminated. A large quadratic error component $n(n-1)\alpha/2$ is superimposed on shape profile as shown in Eq. (2), where n is the total number of measuring point.

$$g(x_n) = G_0 + (n-1)\Delta G_0$$
$$+ \sum_{i=0}^{n-1}(n-i)\{\Delta S_F(x_i) - \Delta S_R(x_i)\} + \frac{n(n-1)}{2}\alpha \quad (2)$$
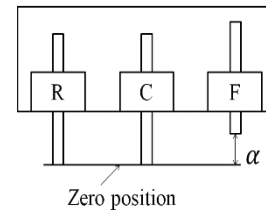
Figure 2 *Zero position error between sensors*

In Eq. (2), G_0 and ΔG_0 are the surface height at x_0 and the difference in height between x_0 and x_1 respectively. These are unknown parameters.
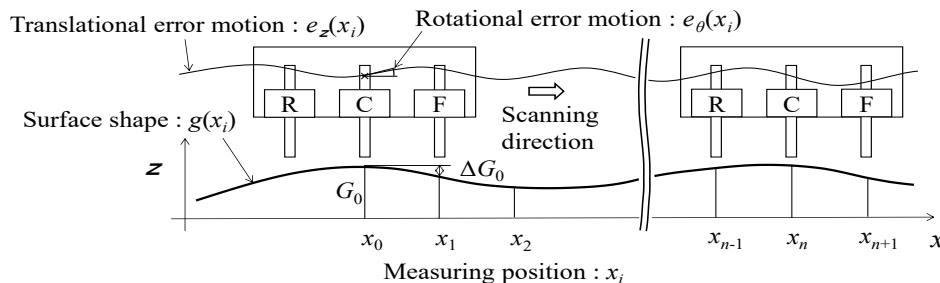
Figure 1 Principle of sequential three-point method

However, in straightness measurement, these values are considered to be zero because the straightness is defined as the deviation from the straight line connected between the measured points on specimen surface at x_0 and x_1.

The zero position error α can be numerically compensated using the difference in inclination angles of the sensor head between at starting point x_0 and finishing point x_n of scanning operation measured by an inclination sensor mounted on the sensor head. [1]

2-D FLATNESS MEASUREMENT BY BIAXIAL IMPROVED SEQUENTIAL TREE-POINT METHOD

Figure 3 shows the configuration drawing of biaxial improved sequential tree-point method. Five displacement sensors are mounted on the L-shaped sensor head which is the combination of two I-shaped sensor heads as shown in Figure 3(a). Figure 3(b) and 3(c) are the front views of the sensor head from y axis and x axis, respectively. The sensor R_0 is common one to two I-shaped sensor heads for measuring the surface profiles in x and y directions. In 2-D flatness measurement, the L-shaped sensor head is scanned in x and y directions on the grid lines perpendicularly intersecting each other on a specimen plane. The same displacement dataset are collected by the use of I-shaped sensor head shown in Figure 1 by rotating it 90 degrees in the interval between the scanning in x and y directions. However, in this work, the L-shaped sensor head is used to avoid an alignment error to scanning line occurring in rotation of the sensor head. Another advantage of the L-shaped sensor head is convenience to install on machine tool for on-machine measurement in machining process, because the rotational mechanism is not necessary.

When the sensor head is scanned in x direction, output signals from the three-point sensors set Fx, Cx and Ro are S_{Fx}, S_{Cx} and S_{R0}, respectively as expressed in Eqs. (3) to (5). The output signals from the sensors Ro, Cy and Fy are S_{R0}, S_{Cy} and S_{Fy}, respectively as expressed in Eq. (5) to (7) when the sensor head is scanned in x direction.

$$S_{Fx}(x_i, y_j) = g_x(x_{i+2}, y_j) + e_z(x_i, y_j) + 2de_{\theta x}(x_i, y_j) \quad (3)$$

$$S_{Cx}(x_i, y_j) = g_x(x_{i+1}, y_j) + e_z(x_i, y_j) + de_{\theta x}(x_i, y_j) \quad (4)$$

$$S_{Ro}(x_i, y_j) = g_o(x_i, y_j) + e_z(x_i, y_j) \quad (5)$$

$$S_{Cy}(x_i, y_j) = g_y(x_i, y_{j+1}) + e_z(x_i, y_j) + de_{\theta y}(x_i, y_j) \quad (6)$$

$$S_{Fy}(x_i, y_j) = g_y(x_i, y_{j+2}) + e_z(x_i, y_j) + 2de_{\theta y}(x_i, y_j) \quad (7)$$

In Eqs. (3) to (7), d, e_z, $e_{\theta x}$ and $e_{\theta y}$ are the distance between adjoining sensors, translational error motion of the sensor head in z direction and rotational error motions around x and y axes. Eliminating the error motions by the numerical treatment same as that used in uniaxial improved three-point method [ ], surface profiles along the grid line are obtained as expressed by Eqs. (8) and (9), where α and β are the zero position errors of three-point sensor sets for scanning in x and y direction, respectively.

$$g_x(x_n, y_j) = G_{0x} + n\Delta G_{0x} + \sum_{i=1}^{n}(n-i)\{\Delta S_{Fx}(x_i, y_j) - \Delta S_{Ro}(x_i, y_j)\} + \frac{n(n-1)\alpha}{2} \quad (8)$$

$$g_y(x_n, y_j) = G_{0y} + n\Delta G_{0y} + \sum_{i=1}^{n}(n-i)\{\Delta S_{Fy}(x_i, y_j) - \Delta S_{Ro}(x_i, y_j)\} + \frac{n(n-1)\beta}{2} \quad (9)$$

COMPENSATION OF ZERO POSITION ERROR

The rotational error motions $e_{\theta x}$ and $e_{\theta y}$ around x and y axes at measuring point (x_i, y_j) are
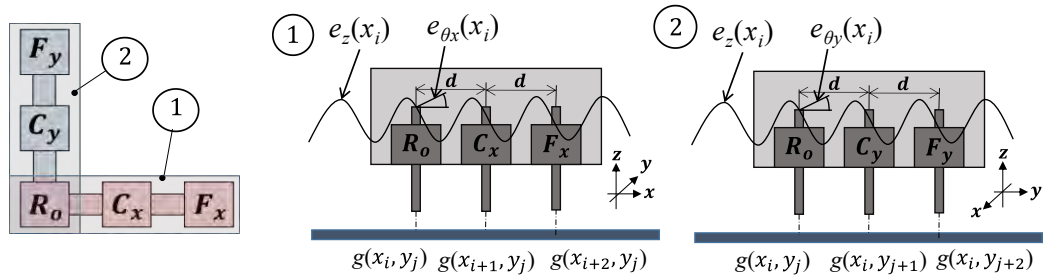
(a) Top views   (b) front views from y axis   (c) front views from x axis

Figure 3 L-shaped sensor head combining two I-shaped sensor heads

calculated from the differential output signals as expressed in Eq. (10) and (11).

$$de_{\theta x}(x_i, y_j) = [S_{Fx}(x_i, y_j) - S_{Cx}(x_i, y_j)]$$
$$- g_x(x_{i+1}, y_j) + g_x(x_i, y_j) + (i-1)\alpha \quad (10)$$
$$de_{\theta y}(x_i, y_j) = [S_{Fy}(x_i, y_j) - S_{Cy}(x_i, y_j)]$$
$$- g_y(x_i, y_{j+1}) + g_y(x_i, y_j) + (i-1)\beta \quad (11)$$

The zero position errors α and β of the three-point sensor sets for scanning in x and y direction can be calculated using Eqs. (12) and (13), respectively.

$$\alpha = [\Delta de_{\theta x}(x_n, y_j) - \Delta de_{\theta x2}(x_n, y_j)]/n \quad (12)$$
$$\beta = [\Delta de_{\theta y}(x_i, y_n) - \Delta de_{\theta y2}(x_j, y_n)]/n \quad (13)$$

Where $\Delta de_{\theta x}(x_n, y_j)$ is the difference in inclination angles of sensor head between at starting point x_0 and finishing point x_n in scanning along the grid line $y=y_j$ calculated using Eq. (12). $\Delta de_{\theta y}(x_i, y_n)$ is that between y_0 and y_n along the grid line $x=x_i$. On the other hand, $\Delta de_{\theta x2}(x_n, y_j)$ and $\Delta de_{\theta y2}(x_j, y_n)$ are the differences in inclination angles between same points as those of calculated ones measured by an inclination sensor mounted on the sensor head.

The straight line connecting the starting and finishing points of measurement is still superimposed on surface shape profile after eliminating the quadratic component due to zero point error.

2-D FLATNESS EVALUATION BY DATA STITCHING

Here, the 2-D flatness of the specimen surface is defined as the fluctuation in surface shape from an arbitrary base plane. The 2-D surface shape profile is obtained by a stitching technique based on the least squares method.

As shown in Figure 4, the common base plane CBP$_X$ for every surface shape profiles along the grid lines in x-direction is defined by replacing the G_0 and ΔG_0 of the profiles to the identical value obtained by least squares method. By the same procedure as that describe above, the common base plane CBP$_Y$ for every surface shape profiles along the grid lines y-direction. These two planes have different inclination. Therefore, the inclination of one plane is made coincide with that of other one by tilting and shifting to z-direction. Furthermore, z-coordinate of surface profile at individual grid points are composed by the weighted average of two profile data depending on the magnitude of deviation in x and y direction.
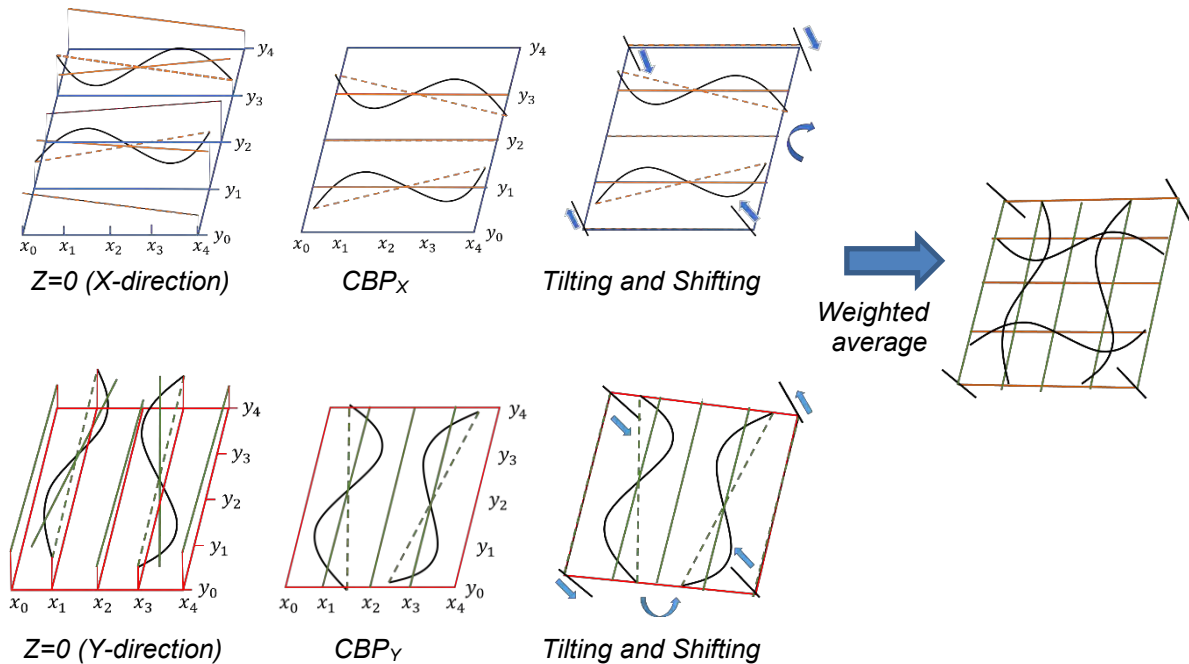
Figure 4 Data stitching procedure

MEASURING EXPERIMENT

To certify the validity of the method described above, a measuring experiment was carried out. The aluminum plate was used as the specimen. The length, width and thickness are 270mm, 260mm and 35mm, respectively. On the specimen surface, a 2-D sinusoidal unevenness is produced by a machining center. The wavelength and amplitude of the unevenness in both of x and y axes are 200mm and 0.25mm, respectively.

2-D surface profile was measured using the L-shaped sensor head along the biaxial grid lines perpendicularly intersecting each other. Five displacement sensors are mounted on the sensor head. The grid spacing is 20mm. The result after stitching is shown in Figure 5 comparing with that measured by 3-D measuring machine. The coincidence ratio between the both surface profiles was 91%. The result shows that the biaxial improved sequential three-point method combined with the stitching algorithm of the measured data proposed is useful for an on-machine flatness evaluation method of large plane.

SUMMARY

A useful flatness measuring technique using biaxial improved sequential three-point method combining with a data stitching algorithm is proposed. The coincidence ratio with the actual surface shape is 91%. The technique is a simple and convenient method for on-machine flatness measurement of large plane.

The technique can be improved to evaluate free-form surfaces profile.

REFERENCES

[1] Obi, M., Furukawa, S. : A study of the measuring for straightness using a sequential point method, 1991, Trans. JSME, C-57, 542, 3197-3201.

[2] Tamagawa, T., Uda, Y., Shimada, S., Imura, R. : Development of surface shape measuring machine of large optics by sequential three-point method, 2014, Proc. Japan Society for Precision Engineering 2014 Autumn Meeting, 823-824. (in Japanese)

[3] Natsume Y., Tamagawa, T., Uda, Y., Shimada, S., Imura, R. : Surface Shape Measurment of Large Curved Surface Applying Improved Sequential Three-Point Method, 2016 Proc.31-ASPE Autumn Meeting, 351-354
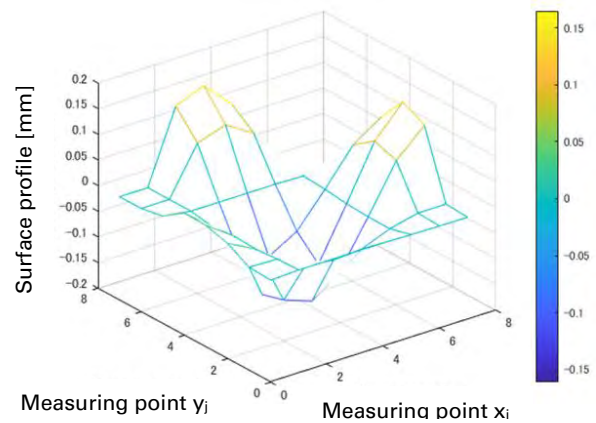
(a) Measured by the L-shaped sensor head
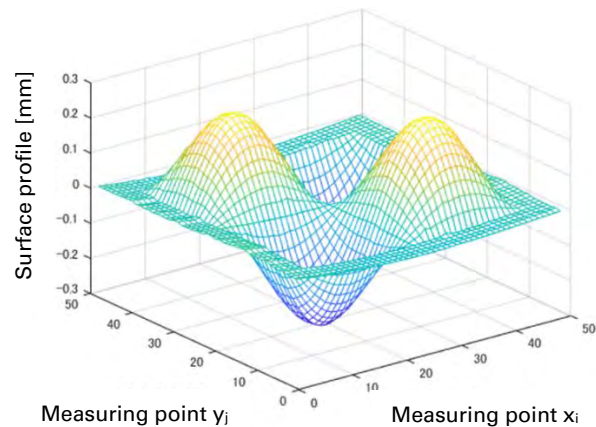
(b) Measured by 3-D measuring machine

Figure 5 3-D surface profiles measured by the method proposed comparing with that by commercial measuring machine

SUCCESS AND FAILURE IN FRICTION IDENTIFICATION, SIMULATION, AND COMPENSATION FOR PRECISION MOTION STAGES

Eric Belski, Nicholas Duncan, and Stephen Ludwick
Mechatronic Research Group
Aerotech, Inc.
Pittsburgh, Pennsylvania

INTRODUCTION

Friction is important to consider when working with high-performance, precision motion systems. When left unchecked, it can contribute to increased move and settle times, increased tracking errors, and decreased constant velocity stability. Especially troublesome are the nonlinear components of friction that appear at very low velocities. There are multiple ways to model these nonlinear components and each comes with their own limitations [1].

This work examines and implements, both in simulation and practice, the ElastoPlastic friction model [2] and uses the identification methods proposed in [3]. This particular model is useful in that it only has a model order of one and is comprised of parameters that can be identified with two relatively simple experiments. The model attempts to capture the macro and micro characteristics of friction by way of a composite, two part model. The macro scale friction parameters are identified with one experiment that is largely based on the Stribeck curve while the micro scale friction parameters are identified in a separate experiment that characterizes spring-like behavior.

IDENTIFICATION

In this work, the PRO190LM linear stage [4] powered by an Ndrive HLe amplifier [5], both produced by Aerotech, Inc., will be considered the system under test. Before the ElastoPlastic friction model can be put into practice, the parameters that comprise the model must be identified for the system under test.

Micro Regime Identification

The micro motion friction regime behavior is characterized by Equation 1, which is proposed in [2] and condensed in [3]

$$\dot{z} = \dot{x}(1 - \alpha(z, \dot{x})\frac{z}{z_{ss}(\dot{x})}) \qquad (1)$$

where $\dot{z}$ is the bristle's displacement velocity (in reference to the Dahl friction model), $\dot{x}$ is the macroscopic stage velocity, $\alpha(z, \dot{x})$ is a piecewise function defining the transition from purely elastic motion to purely plastic motion, z the average bristle displacement, and $z_{ss}(\dot{x})$ which represents the Stribeck-curve that will define friction during macro level motion. These variables then contribute to the frictional force through the relationship presented in Equation 2

$$F_f = \sigma_0 z + \sigma_1 \dot{z} + \sigma_2 \dot{x}, \qquad \sigma_0, \sigma_1, \sigma_2 > 0 \qquad (2)$$

where F_f is the frictional force acting upon the linear stage, σ_0 is the spring rate of the bristle like behavior at low velocities, σ_1 represents damping for the tangential compliance of the model, and σ_2 represents the viscous friction of the system [2].

The parameters that require identification for the micro regime are σ_0, σ_1, and z_{ba}. z_{ba} is a parameter that is used in the piecewise function for $\alpha(z, \dot{x})$ to identify when the transition from purely elastic motion to purely plastic motion occurs [2]. z_{ba} represents, for a specific stage, the amount of displacement that a stage can be subjected to and still return to its original starting place. σ_0 and z_{ba} can be isolated by applying a small amount of force to a stage for a short duration before reducing the current back to zero while measuring the position of the stage. This test is repeated with incrementally more force until the stage achieves sliding regime motion. One step of this experiment is presented in Figure 1.

From each step, the parameters x_{max}, z, and F_{max} are recorded (see Figure 1 for details). Once all steps have been measured and their individual parameters extracted, the plots in Figures 2 and 3 are produced. From these two figures the variables σ_0 and z_{ba} are extracted. z_{ba}
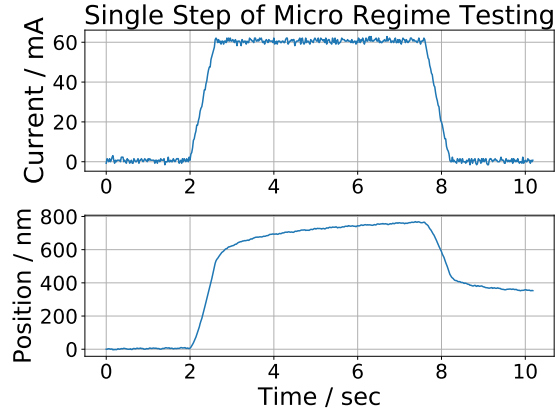
FIGURE 1. A single step from the micro regime experiment on the PRO190LM stage. The maximum displacement recorded in each step is labeled as x_{max} (roughly 800 nm in this figure) while the distance the stage returns after the current is commanded to zero is considered z (roughly 400 nm in this figure). Additionally the maximum applied force is recorded for each step. Given a force constant of 26.67 $\frac{N}{A}$, about 1.6 N of force is recorded as F_{max}. Multiple steps are measured with increasing levels of force.

is the value of z at which the slope on Figure 2 transitions from 1 $\frac{\mu m}{\mu m}$ to a slope of less than 1, which indicates that the maximum displacement of the stage exceeds the distance that the stage will return after a force input is removed. For the stage under test, z_{ba} is about 7 μm. Similarly σ_0 is the average slope of Figure 3 which represents the compliance of the "bristles" in the Dahl model [2].

The final variable to determine for the micro regime is σ_1 which can be calculated by Equation 3 presented in [3]

$$\sigma_1 = 2\zeta\sqrt{\sigma_0 m} - \sigma_2 \qquad (3)$$

where ζ is assumed to be 1 due to high levels of damping in the system, m is the moving mass of the stage, and σ_2 represents the viscous friction the stage experiences in macro level motion [3]. While the value of σ_2 will be calculated in the macro regime section, the value of σ_1 for this stage works out to be $4,196\frac{N}{m/s}$.

Macro Regime Identification

There is a separate test necessary to identify the macro level parameters, which include σ_2 and the
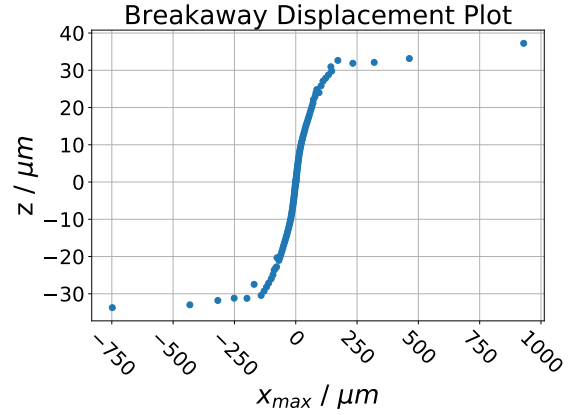
FIGURE 2. A graph of hysteretic displacement vs. maximum displacement for all points from the micro regime friction testing on the PRO190LM stage. The z value at which the slope, for both positive and negative velocity moves, deviates from unity is the point at which the "breakaway" occurs. In this plot it may be considered to be 7 μm.

Stribeck curve parameters shown in Equation 4

$$z_{ss}(\dot{x}) = \frac{F_{stribeck}}{\sigma_0} = \frac{sig(z)}{\sigma_0}(F_C + (F_S - F_C)e^{-(\frac{\dot{x}}{v_s})^2})$$

$$(4)$$

where $z_{ss}(\dot{x})$ is a contributing factor to the micro regime friction estimate in Equation 1, $sig(z)$ is defined as $sig(z < 0) = -1$ and $sig(z \geq 0) = +1$, F_C represents Coulomb-Friction, F_S represents stiction, and v_s represents the form factor of the Stribeck curve [3]. F_C, F_S, and v_s are identified through a series of experiments where the stage is commanded at a constant velocity, under closed loop control, and the necessary force required to achieve this constant velocity is recorded. Multiple different velocities, usually in a logarithmic step size, are measured and the force required for each velocity is plotted to form the so called Stribeck curve as seen in Figure 4. There are differences in the Stribeck curve parameters between positive and negative velocities that not negligible. Therefore for accurate compensation and simulation, parameters for both cases must be identified and used.

Now that a methodology for identifying both the micro and macro regime friction parameters has been established, the next step is to implement a simulation of friction to more accurately predict

Bristle Spring Constant Plot

$\sigma_0 = 0.989$
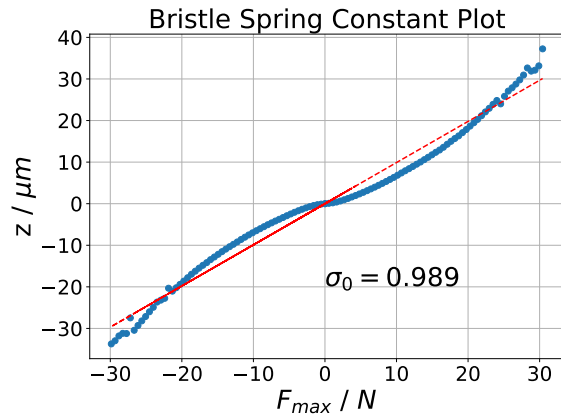
FIGURE 3. A plot of hysteretic displacement vs. maximum force applied for all points from the micro regime friction testing on the PRO190LM stage. The average slope represents the compliance of the bristle like behavior at low velocities and contributes to the micro regime friction approximation in Equation 1. In this plot the slope is approximately 0.989.

stage dynamics and performance.

SIMULATION

A golden goose for motion control companies would be a tool that accurately predicts stage performance for a customer without needing actual hardware. Unfortunately there are many factors that make this a difficult task. Friction for example makes it difficult to predict positioning error, especially on multi-axis systems, at periods of low velocities, or zero velocity crossings. A first step in accurately predicting friction is to match simulations of stage motion profiles with measured data from a physical stage under test.

MATLAB Simulink was used to develop a simulation of the form seen in Figure 5. The plant model is a parametric state space model that was fit to a frequency response taken from the PRO190LM under test. The state space model form was useful to prevent numerical issues within MATLAB, especially if the plant model is of large order. Current noise and feedback noise (input and output noise respectively) were added into the model to help to accurately simulate the behavior of a stage at rest. These values were estimated based on specifications of the feedback device and the motor amplifier and controller. The servo control loop is a realization of the control architecture on the Aerotech A3200 HLe. Lastly, the friction model acts as a feedback loop around the plant

Stribeck Curve

Negative Velocity
$F_c = 17.875$
$F_s = 27.593$
$v_s = 0.014$
$\sigma_2 = 30.874$

Positive Velocity
$F_c = 16.984$
$F_s = 26.584$
$v_s = 0.013$
$\sigma_2 = 23.269$
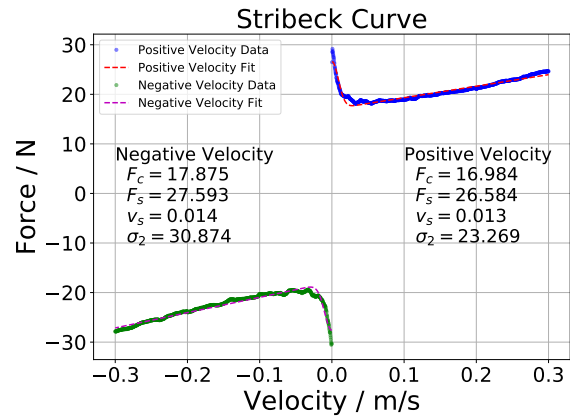
FIGURE 4. A plot of both positive and negative Stribeck curves measured on the PRO190LM stage. Parameters are fit to each curve, as in Equation 4 using a non-linear fitting algorithm, and used to estimate friction in the macro motion regime.
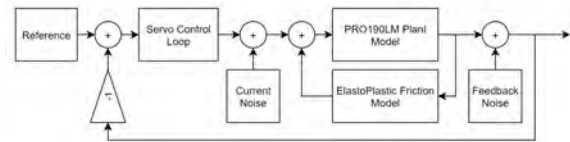
FIGURE 5. The architecture of the Simulink model used to simulate stage performance and estimate the influence of friction.

model. The position and velocity of the stage influence the frictional forces that need to be fed back into the plant as a disturbance. The friction model is a series of Simulink subsystems that require the parameters (listed in the Identification Section) of the ElastoPlastic model to be set for the specific stage under test. Once these parameters are identified, a position and velocity can be input to the model and a frictional force is output for each time step.

With the Simulink model developed, an arbitrary profile is now designed on a physical stage and the reference command along with the positioning feedback and actuator current are measured and stored. The reference command from the physical stage will become the input to the Simulink model while the positioning feedback will be compared to the simulated version of this quantity. Subplot 1 in Figure 6 illustrates an example of a motion profile commanded to the PRO190LM.
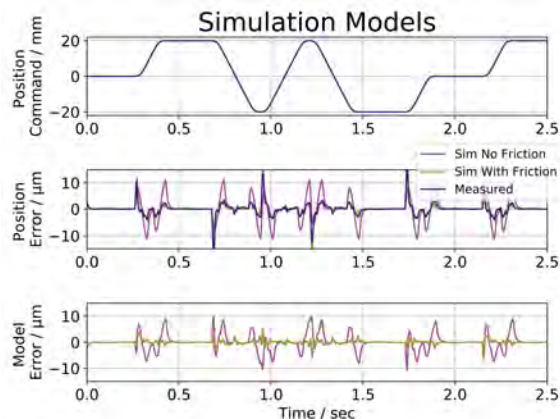
FIGURE 6. *The first subplot shows the motion profile commanded to the stage under test. The second subplot compares the measured and simulated position errors. The "Sim No Friction" trace is a simulation run that does not include the ElastoPlastic friction model. Similarly the third subplot shows the difference in simulated position error from the measured value. It is clear that the simulation model which includes the ElastoPlastic friction model (Sim With Friction) predicts the positioning error more accurately than the simulation model without friction.*

In order to determine the benefit of including a friction model when predicting stage performance, the simulation including the ElastoPlastic model is compared against a model that only contains the parametric model of the plant. Each model receives the position command from the physical stage as an input and the simulated position feedback and error are measured and collected. In Figure 6, subplots 2 and 3 show the effectiveness of including a friction model, specifically the ElastoPlastic model, in a performance estimation simulation. The model with friction exhibits a maximum disagreement from measured results of $6.3\,\mu$m with an average disagreement of $2.5\,\mu$m or less. While the model without friction exhibits a maximum disagreement from measured results of $10.5\,\mu$m and average disagreement of $5.5\,\mu$m or less. By adding a friction model to the simulation, the accuracy of the simulation increases by about a factor of two in direction reversals and zero velocity crossings.

COMPENSATION

Logically, the next step after simulation is implementation in the form of a real time compensation algorithm. The friction model approximates the frictional force acting on the stage and feeds forward the motor current necessary to overcome said frictional force.

Using Aerotech's AeroBasic programming language and Motion Composer application, a real time version of the frictional model is implemented. The identified parameters listed previously in this paper are applied to this implementation of the friction model. The model operates at the servo rate of the system, 8 kHz, and calculates a new frictional force acting upon the stage for every time step. Figure 7 shows a motion profile commanded on the PRO190LM where the position error of the stage was measured with and without the friction model active. Clearly the positioning error with the model active is poorer performing.
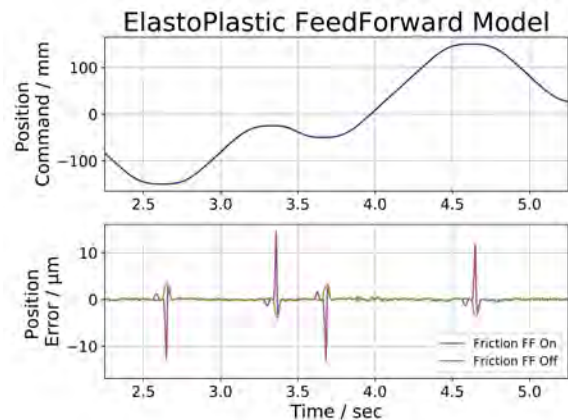
FIGURE 7. *The measured position error on a PRO190LM with and without a friction compensation feedforward model. The friction model is introducing additional position error and does not effectively predict frictional forces.*

The cause of the model error is unknown at this point, however the expectation was that a similar improvement as shown in simulation would have been realized. Some of the error introduced by the model could be due to latency in updating the model. The time from when the position and velocity of the stage are measured until the model is updated and sends current to the actuator is on the order of a few milli-seconds. This latency could explain the large spike in position error near the zero velocity crossings, Figure 7. Additionally friction depends on the amount of grease on the bearings at a given time, where the stage is located within its travel, environmental conditions, and when the stage was last moved, among other things. Which is just a lengthy way of stating that the identified parameters for the stage could have

changed or been incorrectly identified. Further study and experimentation is necessary to determine the source of error for this implementation of the friction model.

DISCUSSION

Reviewing the identification methods shown in [3] has provided an effective method for identifying the parameters of the ElastoPlastic friction model. The increased accuracy this model provides when estimating stage positioning error via simulation may prove to be useful. Streamlining the identification of friction parameters and developing simulations for more stage types will be necessary to determine the efficacy of this process, however the hope is that it will allow stage errors to be predicted early on in a customer's design process. The lack of success in the implementation of the friction compensation model on the PRO190LM stage is rather interesting. Further investigation may reveal a requirement of faster model update rates, more accurate identification of friction parameters, or perhaps the need to re-identify parameters every so often.

In summary, this work identifies the friction parameters of the ElastoPlastic model for a given linear stage, demonstrates how the friction model can improve simulation models, and examines the results of implementing the ElastoPlastic friction model as a compensation model on a digital controller. The results presented here attempt to replicate and build upon those presented in [3]. Any questions, comments, or feedback are welcomed by the authors in order to better understand and compensate for friction.

REFERENCES

[1] T Mathis, Adam Ray Brink, and D Dane Quinn. Implementation and comparison of advanced friction representations within finite element models. Technical report, Sandia National Lab.(SNL-NM), Albuquerque, NM (United States), 2018.

[2] Pierre Dupont, Brian Armstrong, and Vincent Hayward. Elasto-plastic friction model: contact compliance and stiction. In Proceedings of the 2000 American Control Conference. ACC (IEEECat. No. 00CH36334), volume 2, pages 1072–1077. IEEE, 2000.

[3] Alexander Keck, Jan Zimmermann, and Oliver Sawodny. Friction parameter identification and compensation using the elastoplastic friction model. Mechatronics, 47:168–182, 2017.

[4] https://www.aerotech.com/product-catalog/stages/linear-stage/pro190lm.aspx

[5] https://www.aerotech.com/product-catalog/drives-and-drive-racks/ndrive-hle.aspx

MAGNETIC LEVITATION FINE STAGE
WITH PITCHING MOMENT AND GRAVITY COMPENSATION SYSTEM

Motohiro Takahashi, Hironori Ogawa, and Takashi Saegusa
Research and Development Group,
Hitachi, Ltd., Hitachinaka, Ibaraki, Japan

INTRODUCTION
This paper describes the development of a magnetic levitation (maglev) fine stage with a pitching moment compensation system that also works as a gravity compensator.

Some maglev positioning technologies have been developed for various industries [1-5] and are expected to achieve nanometer-scale positioning accuracy. However, supporting gravity is often a problem because the gravity compensation sometimes requires a coil cooling system including movable piping or a water jacket. Another problem is magnetic leakage because it limits the application of the maglev stage. The motors should be installed using the appropriate distance from the table to reduce the magnetic density. This increases the pitching moment caused during fast movements.

We previously proposed a maglev stage system that has a unique motor structure fusing gravity compensation and pitching moment compensation [6].

In this paper, the basic characteristics of the proposed gravity and pitching moment compensation system are evaluated through driving experiments, and its efficiency demonstrated.

STRUCTURE AND Z-ASSIST SYSTEM
To achieve high cost-effectiveness while maintaining high positioning accuracy, we adopt a coarse-fine structure for the XY stage.

Figure 1 shows the overall structure of the developed coarse-fine stage system. A six-degrees-of-freedom (6DOF) maglev fine stage was installed as a fine stage on the coarse XY-stage. This fine stage has a system to compensate for the pitching moment and gravity of levitated mass (particularly a 12-kg top-table).

(a) Coarse-fine XY-stage

(b) Bottom view of fine maglev stage
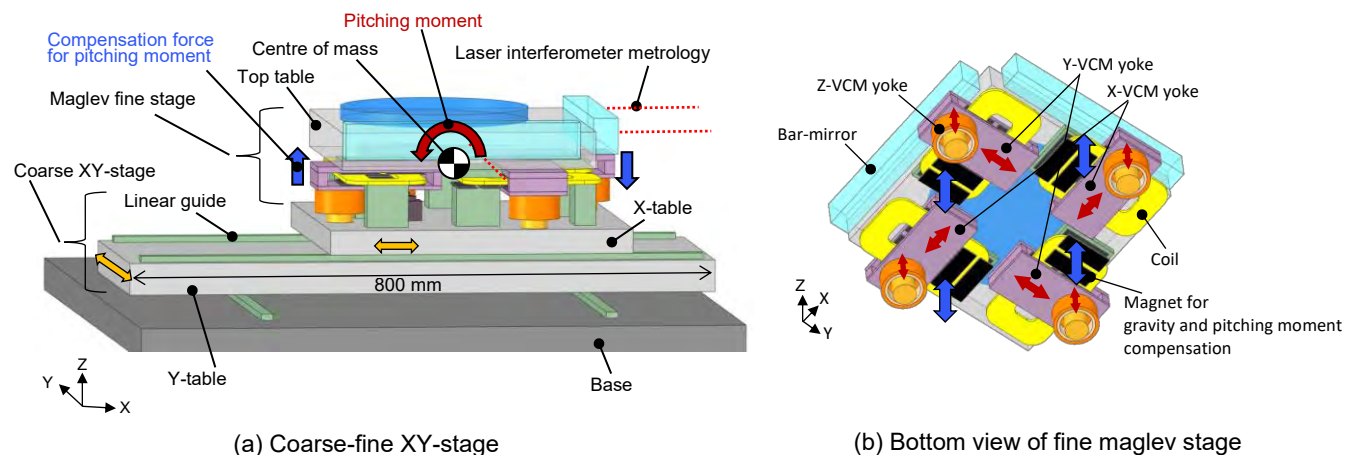
FIGURE 1. Overview of structure of developed coarse-fine stage system.
Fine maglev stage has pitching moment and gravity compensation system.
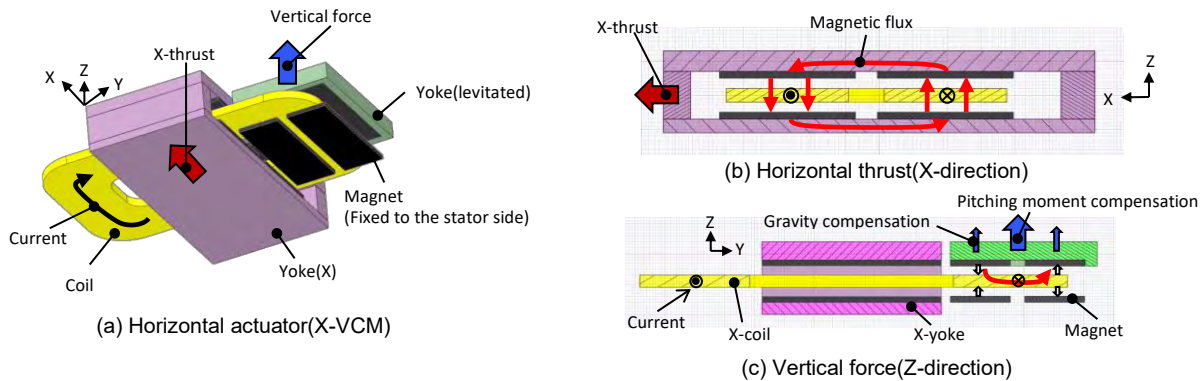
FIGURE 2. Compensation system of gravity and pitching moment integrated with horizontal actuator.

Figure 2 shows a schematic diagram of an actuator incorporating the pitching moment compensation system. As shown in (a), the coil current flows through the X-VCM with a magnetic yoke at the coil end. Moreover, as shown in (b), a thrust in the X-direction is obtained. At the same time, as in (c), the magnetic circuit formed by the yoke at the end of the coil produces a thrust in the Z-direction. This force is used to compensate for the pitching moment that occurs on the table during stage acceleration and deceleration.

The pitching moment increases in proportion to the horizontal acceleration, i.e., the horizontal thrust, and this Z-direction thrust is also generated in proportion to the horizontal thrust, so moment is automatically compensated for

without the need for special control. A magnet is arranged to face the yoke at the end of the coil, and magnetic repulsive forces causes it to levitate. The gravity of the table is also compensated for.

DETAILED DESIGN OF MAGLEV STAGE

Figure 3 shows the configuration of the developed maglev stage, and its basic specifications are listed in Table 1. The moving mass is larger due to the top table for the 386-mm-long bar mirror and the VCM yoke with the magnetic circuit closed. The positioning control is performed using a bar mirror and laser interferometer, and a planar scale is mounted on the table to evaluate the positioning accuracy of the sample.
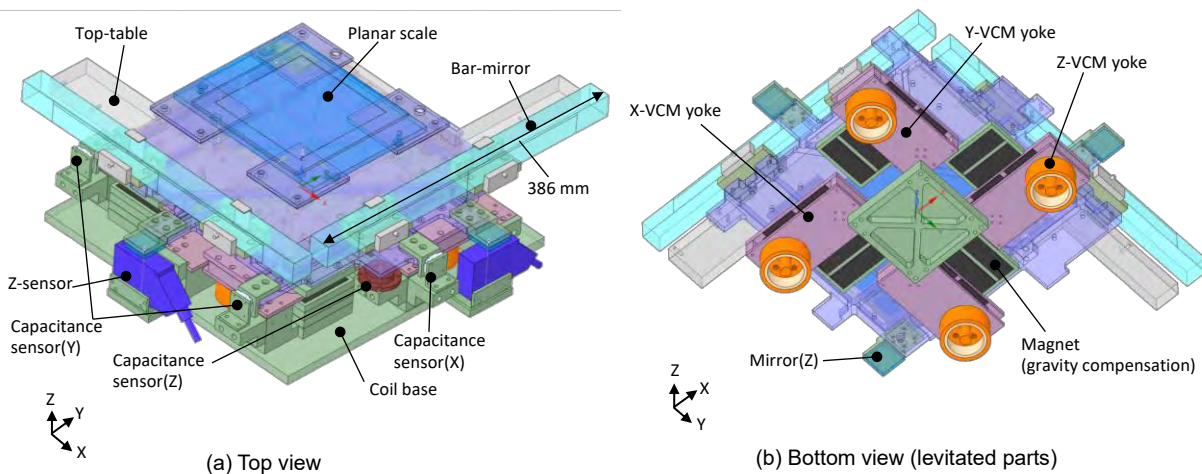
FIGURE 3. Configuration of 6DOF fine stage with maglev mechanism.

TABLE 1. Target specifications.

Levitation mass		12.0 kg
Total mass of fine stage		25.0 kg
Dimensions		400×400×100 mm
Strokes	XY	±3 mm (±200 mm with course XY stage)
	Z	±2 mm
Max. Acc.	XY	9.8 m/s²
	Z	9.8 m/s²
Sampling frequency		10 kHz
Resonance frequency		>600 Hz
Bandwidth		300 Hz

The appearance of the developed maglev stage is shown in Figure 4. Laser interferometers for measuring displacements in the X, Y, and θz directions were fixed to the side walls surrounding the stage.

Figure 5 shows the main resonant modes of the levitated part and stator part of the maglev stage. The levitated part has a resonant mode of a table bending shape at 620 Hz, and the stator part has a torsional natural vibration mode at 262 Hz.

The vibration of the stator side is thought to be damped by levitation, but the extent of the effect will be investigated in the future. As for the stator part, we will leave a degree of freedom in the design for further study of the gravity compensation mechanism. The mass is increased due to the mass of the device being increased. After the shape of this area has been determined, weight can be further reduced to improve the natural frequency.
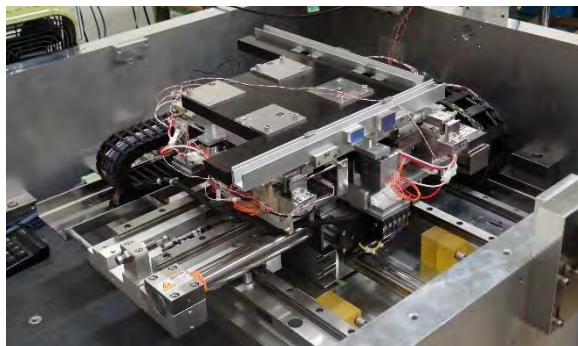
FIGURE 4. Appearance of the developed stage system which consists of maglev fine stage with pitching moment compensator.
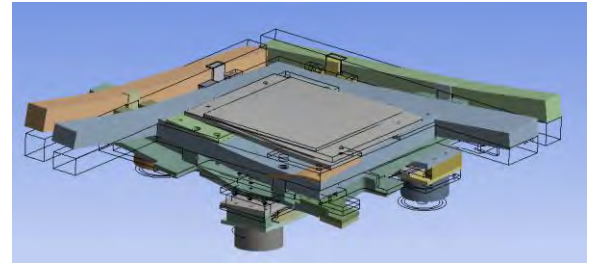
(a) Levitated part bending mode: 620Hz
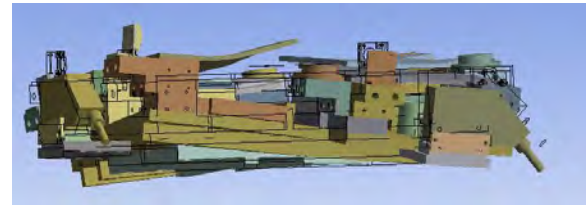
(b) Stator part torsion mode: 262Hz

FIGURE 5. Resonance mode of maglev stage.

CONTROL SYSTEM

Figure 6 shows a block diagram of the coarse and fine motion control system of the stage.

The 2DOF control system for the coarse XY stage and the 6DOF control system for the fine movement maglev stage are decoupled and combined.
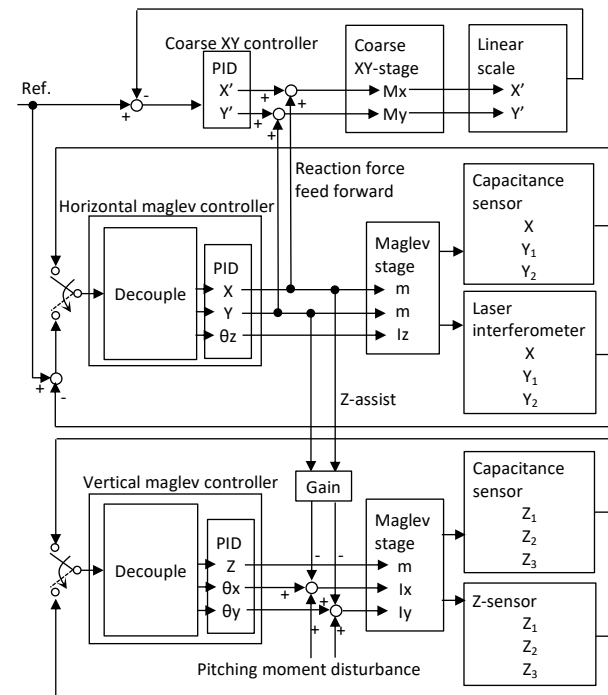
FIGURE 6. Controller for coarse-fine drive and switching of position sensors.

The control system for the developed maglev stage consists of two control loops: a capacitance sensor for initial levitation, which aligns the optical axis of the laser, and a laser interferometer and a Z-sensor for control in the final levitation state.

In addition, the control of the levitating side is divided into two control loops: one for position control in the horizontal plane, and the other for control outside the horizontal plane. This is because the stroke in the direction of the table tilt is small to prevent the laser beam axis from deviating. This configuration is made possible by the small inter-axial interference. This reduces the load on the control operations and enables a fast sampling cycle of 10 kHz.

Figure 7 shows the frequency response characteristics of the maglev stage.
The black and red lines show the characteristics from the motor thrust to the displacement of the capacitance sensor and of the laser interferometer, respectively.
The laser interferometer has a high resolution and therefore low phase noise up to several hundred Hz.

A Bode diagram of the closed-loop characteristics of the maglev stage is shown in Figure 8. The black line shows the characteristics with the identified transfer function based on the measured characteristics, and the red line shows the closed-loop characteristics with the ideal characteristics with the resonances up to 300 Hz removed from those characteristics.

The gain of the proportional–integral–derivative (PID) controller in each case was adjusted with the stability evaluation using the Nyquist diagram shown in Figure 9. In the observed frequency response, there are some small peaks around 200 Hz, and the bandwidth is limited by these resonances.

These resonances were found to possibly be limited by the effect of the twisting resonance mode on the stator side, which was also observed in the vibration mode analysis, and the local mode of the small parts, which was not fully reproduced in the analytical model. We will investigate the cause of the resonance peak and take measures to reduce the peak in the future.

(a) X-axis

(b) Y-axis

FIGURE 7. Frequency response of maglev stage.
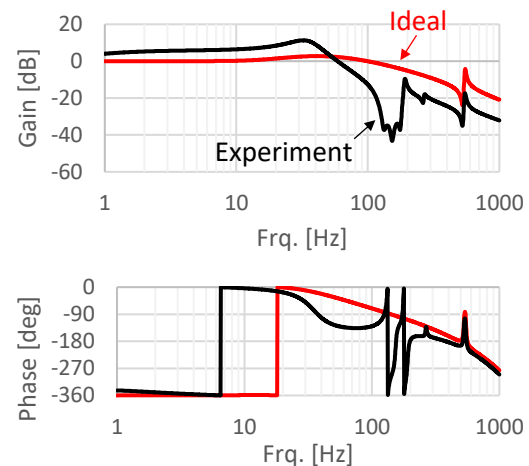
FIGURE 8. Bode diagram of closed loop.
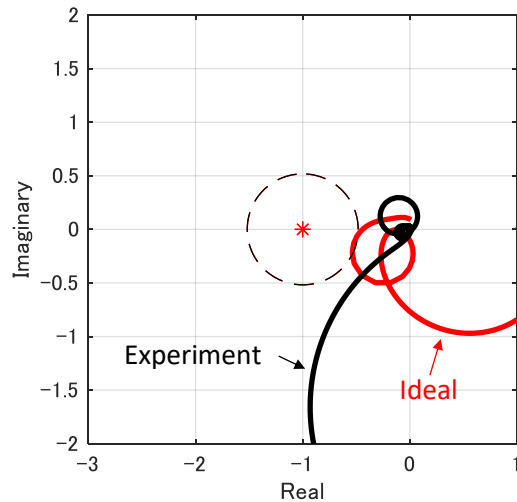
FIGURE 9. Comparison of Nyquist plot.

EVALUATION

In order to evaluate the effectiveness of the proposed pitching moment compensation mechanism, the inter-axis interference in the frequency response of the maglev stage was evaluated.

Figure 10(a) shows a comparison of the frequency response in the X direction and the response of the pitching in the θy direction from the motor thrust in the X axis. The response of the pitching was compared with the response in the X direction as a displacement in the Z direction at the sensor position. The pitching moment compensation mechanism reduces the inter-axis interference, i.e., the response in the θy direction. Similarly, Figure 10(b) shows the inter-axis interference in the Y direction. Since the pitching

(a) X-axis (from X-thrust)

(b) Y-axis (from Y-thrust)
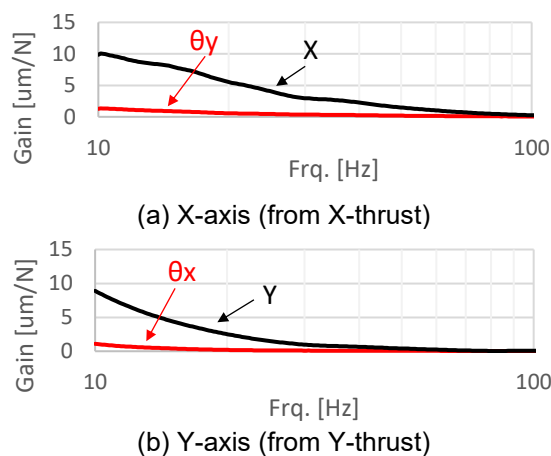
FIGURE 10. Interaxial interference in the frequency response.

moment is compensated, the response in the θx direction is reduced.

In the maglev stage of this report, the motor is located at the bottom of the stage and extra pitching is likely to occur, but this is suppressed by the moment compensation mechanism. In conclusion, the effectiveness of the proposed pitching moment compensation mechanism is confirmed.

Figure 11 shows static vibrations under positional control using the capacitance sensors. Figure 12

(a) X-axis

(b) Y-axis
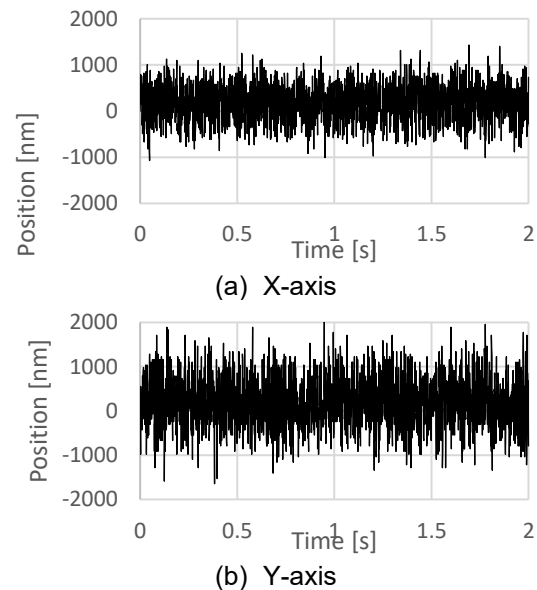
FIGURE 11. Static vibration controlled with capacitance sensors.

(a) X-axis

(b) Y-axis
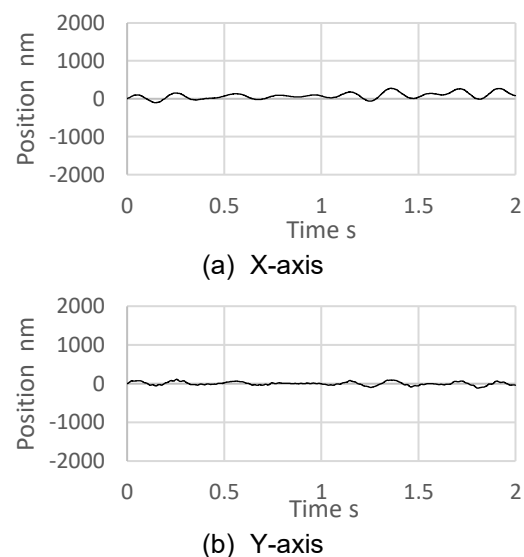
FIGURE 12. Static vibration controlled with laser interferometers.

shows static vibrations under positional control using the laser interferometers only in the horizontal plane. In the control using the laser interferometer, the amplitude is small due to high gain by low noise.

In the future, we plan to further reduce vibration by combining control with the Z-sensors.

CONCLUSION

We developed a maglev stage with a system to compensate for pitching moment and gravity integrated that has horizontal actuators. We demonstrated that the developed maglev system has nanometer scale positioning capability under the newly designed 6DOF control system with interferometers.

FUTURE WORK

We plan to evaluate the static vibration under vertical positioning control with a Z-sensor (vertical interferometer) instead of a Z-capacitance sensor. In addition, the resonance peak will be reduced while improving the detailed structure. By evaluating the dynamic characteristics, the effectiveness of pitching moment compensation during high speed movement will be determined.

REFERENCES

[1] Zhou L, Trumper D. Finite element model for pre-magnetized linear hysteresis motors. In: 33th Annual Conference of American Society of Precision Engineering. ASPE; 2019, pg. 121-126.

[2] Butler H, Simons W. Position control in lithographic equipment. Proceedings ASPE 2013 Spring Topical Meeting on Precision Control for Advanced Manufacturing Systems. 2013, pg. 7-12.

[3] Laro, D. Through the Wall, MIKRONIEK, No.1, 2013, pg. 31-35.

[4] Shinshi T. A linear table system using repulsive forces of permanent magnets (Static stiffness of levitated table and its stabilization using two-axis control). JSME. 2001, 67(653): pg. 232-239.

[5] Takahashi M, Ogawa H, Kato T. Development of compact maglev stage system for nanometer-scale positioning. In: 34th Annual conference of American Society of Precision Engineering. 2019, 352-357.

[6] Takahashi M, Ogawa H. Development of a novel maglev stage system with z-assist actuation mechanism. In: euspen's 20th International conference & exhibition. 2020.

Milling force measurement using a low-cost, constrained-motion dynamometer

Michael Gomez[1,2] and Tony Schmitz[1,2]
[1]Mechanical, Aerospace, and Biomedical Engineering
University of Tennessee, Knoxville
Knoxville, TN 37996, USA
[2]Energy and Transportation Science Division
Oak Ridge National Laboratory
Oak Ridge, TN 37830, USA

INTRODUCTION

The ability to measure and model cutting forces enables improved understanding of machining processes. Piezoelectric-based dynamometers currently provide the most common solution for cutting force measurement. However, the structural dynamics must be considered when operating with tooth passing frequencies near the dynamometer's multiple natural frequencies, where amplification of the local spectral content reduces accuracy. To mitigate this effect, prior research efforts have focused on two approaches. The first involves new dynamometer designs [1-9]. The second implements post-processing to remove the effect of the dynamometer's electro-mechanical "filtering" of the machining forces [10-13]. Despite these advancements, the widespread implementation of in situ cutting force measurement generally remains limited by cost and complexity.

In this paper, the design and testing of a low-cost dynamometer for milling force measurement is presented. The dynamometer design is based on constrained-motion/flexure-based kinematics. The ideally SDOF structure is excited by the cutting force to produce small amplitude displacement, which is measured using a low-cost optical interrupter (i.e., a knife edge that partially interrupts the beam in an emitter-detector pair). The force is calculated from the measured displacement using the dynamometer's FRF. This structural deconvolution is carried out by filtering the frequency domain displacement using the inverted SDOF FRF for the constrained-motion dynamometer.

STRUCTURAL DECONVOLUTION

There are five primary steps to obtaining the machining force using the constrained-motion dynamometer (CMD) [14]. These are summarized here:

1. Measure the ideally SDOF FRF for the CMD structure. In this study, the FRF was obtained using impact testing, where an instrumented hammer is used to excite the structure and the response is measured using a linear response sensor, such as a low-mass accelerometer. Ideally, the dynamometer should be mounted to the machine tool table since clamping (boundary) conditions can affect the dynamic response. Also, the test sample (to be machined) should be attached to the dynamometer because its mass affects the dynamometer's natural frequency.

2. Machine the sample using the desired axial depth of cut, radial depth of cut, feed per tooth, and spindle speed for the selected endmill-holder combination. During material removal, measure the dynamometer motion using the optical interrupter. Because the interrupter infers motion from the voltage generated by the optical detector, a calibration step is required to relate the voltage to displacement. This is typically a nonlinear relationship that can be approximated as linear over a limited displacement range (small fraction of a millimeter). In the linear case, a single calibration coefficient is used for the voltage to displacement conversion.

3. Convert the time domain displacement to the frequency domain using the discrete Fourier transform (DFT). Due to the nature of the

DFT, it is preferred to remove the transients at the cut entry and exit. The short-time Fourier transform is also an acceptable option.

4. Convert the frequency domain displacement to force using the inverted CMD FRF; see Eq. 1, where F is force, X is displacement, ω is frequency. In practice, a low pass digital filter is convolved with the inverted FRF. This is because the inverted FRF magnitude grows with increasing frequency and would otherwise amplify any high frequency noise in the displacement signal. The filter cutoff frequency is set above the dynamometer's natural frequency.

5. Once the frequency domain force is known, convert it to the time domain using the inverse DFT. The time domain force signal is then available for traditional analysis techniques, such as fitting to extract cutting force coefficients [15] or magnitude tracking to evaluate tool wear.

$$F(\omega)= [X/F\,(\omega)]^{-1} \cdot X(\omega) \qquad (1)$$

DYNAMOMETER DESIGN

A monolithic, constrained-motion dynamometer was designed and constructed to measure milling forces. The design included a moving platform for workpiece mounting and four leaf-type flexure elements in an H-bar arrangement. The flexure elements guide the moving platform in the compliant direction resulting in SDOF, approximately linear motion. The emitter-detector was mounted on the base while a knife edge was attached to the moving platform (Fig. 1). The dynamometer was machined from 6061-T6 aluminium with an elastic modulus, E, of 69 GPa and a yield strength, σ_y, of 276 MPa. For the design to remain elastic, the maximum acceptable stress was selected to be $0.6\sigma_y$; as a result, the limiting stress, σ_{max}, is 160 MPa [16]. The corresponding maximum allowable displacement is:

$$\delta_{max} = \sigma_{max} \cdot L^2/3Et \approx 50 \ \mu m, \qquad (2)$$

where the leaf dimensions are provided in Table 1. Given δ_{max}, the dynamometer force range is ±1500 N.
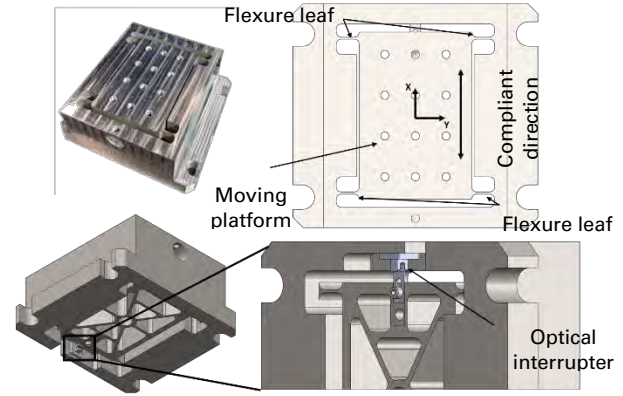
FIGURE 1. Constrained-motion dynamometer design.

TABLE 1. Flexure leaf geometry for the CMD.

Length, L (mm)	Width, b (mm)	Thickness, t (mm)
9	44.5	1.2

The optical interrupter performance was quantified using a linear air bearing positioning stage (Aerotech ABL 10100-LT). The stage had a manufacturer-specified positioning uncertainty of ±0.2 µm and resolution of 0.5 nm. The knife edge was positioned outside the emitter-detector (ROHM RPI-0352E) range and moved towards the sensor until the full range was exceeded. It was observed that the optical interrupter had a resolution of less than 1 µm with a nonlinear range of 700 µm and a linear range of 170 µm. For the linear range, the displacement sensitivity was 80 µm/V.

RESULTS

Machining trials were completed on a Haas TM-1 three-axis computer numerically controlled (CNC) milling machine. The dynamometer was mounted on the machine table with the compliant direction aligned parallel to the machine's x direction. A 6061-T6 Al workpiece (0.565 kg) was mounted on the moving platform. With this setup, x and y direction force measurement is possible with no change in dynamometer orientation. To measure x force, the feed direction is x. To measure y force, the feed direction is y. The experimental setup is detailed in Fig. 2. The cutting parameters provided in Table 2 were used for milling trials completed on both the CMD and commercial dynamometer (Kistler 9257B) for comparison.
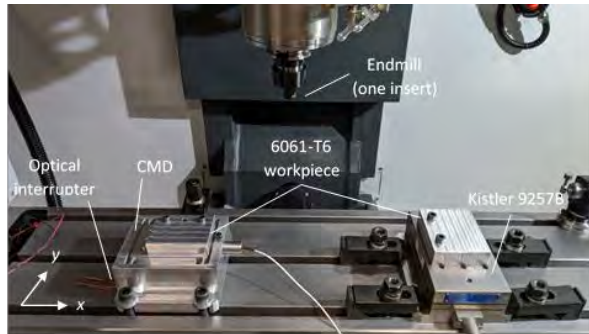
FIGURE 2. Experimental setup showing the CMD, commercial dynamometer (Kistler 9257B), endmill, and workpieces.

TABLE 2. Tool description and cutting parameters for milling trials.

Diameter (mm)	Teeth	Material
19.05	1	PVD coated micro-grain carbide
Cutting parameters for down milling tests		
Spindle speed, Ω (rpm)	1000, 2000, 3000, 4000, 5000, 6000	
Feed per tooth (mm)	0.1	
Axial depth (mm)	3	
Radial depth (mm)	1.91 (10% radial immersion)	

Impact testing results for the dynamometer are displayed in Fig. 3. For the compliant (x) direction, the natural frequency is 794 Hz, the stiffness is 2.6×10^7 N/m, and the viscous damping ratio is 0.0053 for the SDOF mode. Fig. 4 displays the inverse filter used to determine the force. A third-order Butterworth low pass filter (800 Hz cutoff frequency) was convolved with the inverted x direction FRF to avoid amplifying high frequency noise.

.
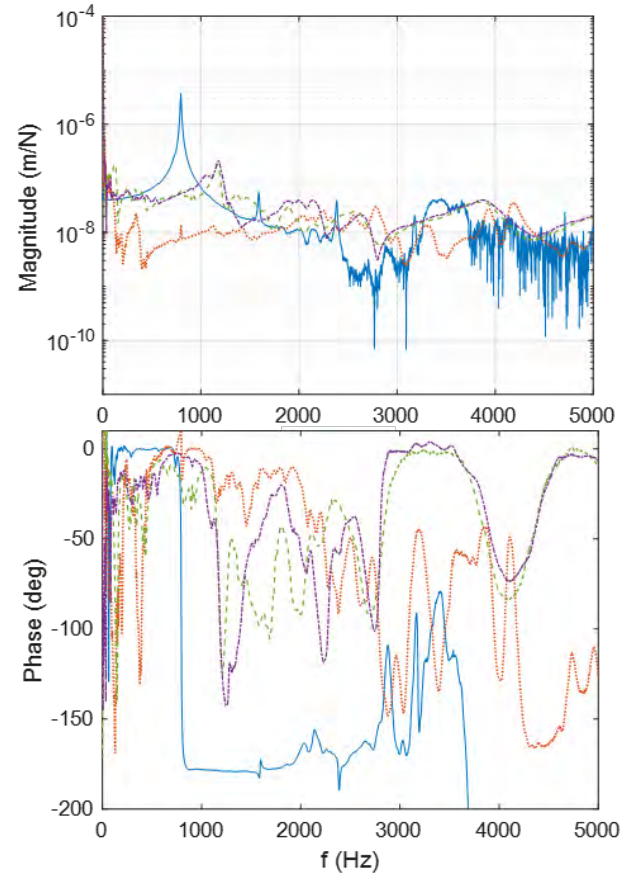
FIGURE 3. Semi-logarithmic magnitude (top) and phase (bottom) components of the CMD and tool FRFs.
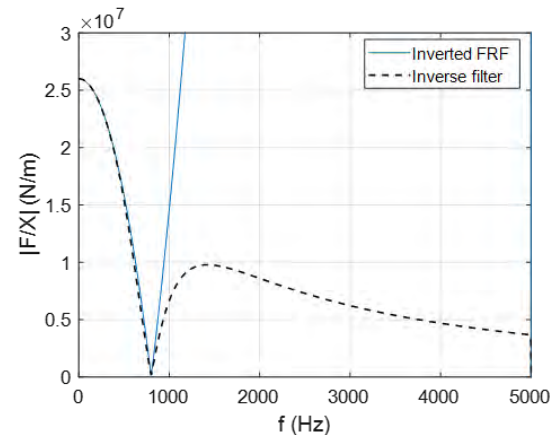
FIGURE 4. Inverted FRF and inverse filter used to determine force from measured displacement.

For each test in Table 2, the displacement was measured using the optical interrupter. Structural deconvolution was then completed to determine the force using the Fig. 4 inverse filter. Force measurements were also completed using a Kistler 9257B dynamometer for comparison. Figures 5-6 presents a comparison of the CMD

and Kistler force measurements. Good agreement is observed in Fig. 5 due to the sufficiently low spindle speed and, consequently, tooth passing frequency (16.7 Hz).

At the increased spindle speed in Fig. 6 (6000 rpm, 100 Hz), however, the Kistler force because the dynamometer is itself a dynamic system and its response can be excited by the tooth passing frequency and harmonics.
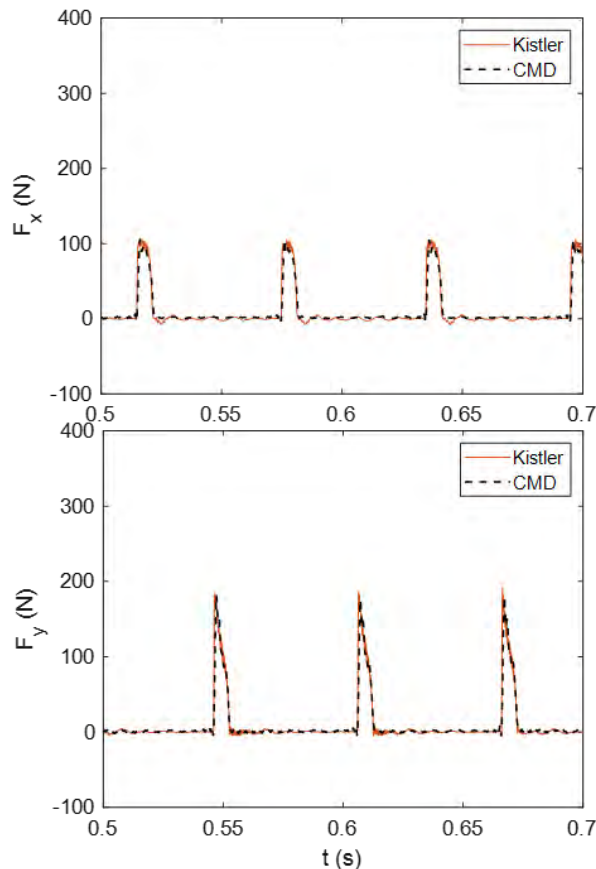
FIGURE 5. Comparison of x and y direction cutting force signals for CMD (black dashed line) and Kistler 9257B (red solid line) for a spindle speed of 1000 rpm.
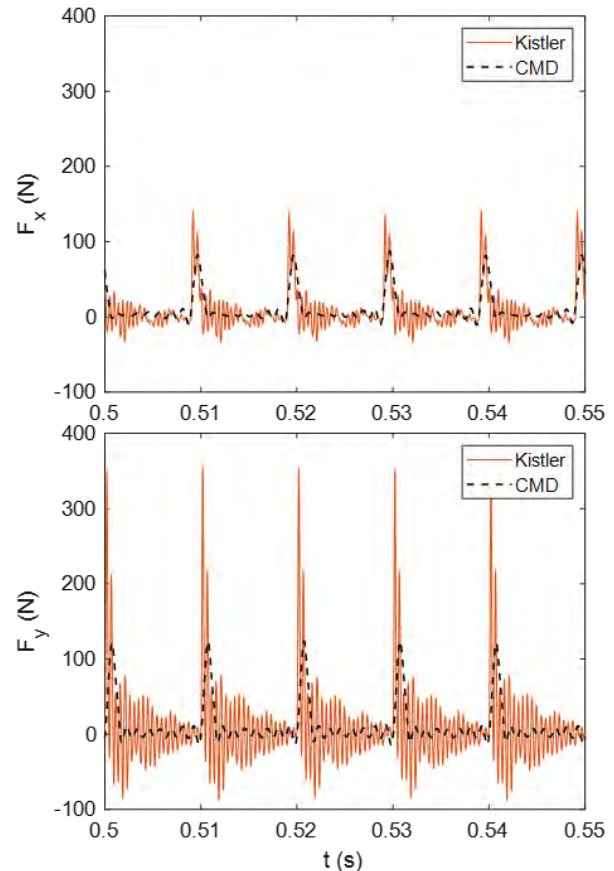
FIGURE 6. Comparison of x and y direction cutting force signals for CMD (black dashed line) and Kistler 9257B (red solid line) for a spindle speed of 6000 rpm.
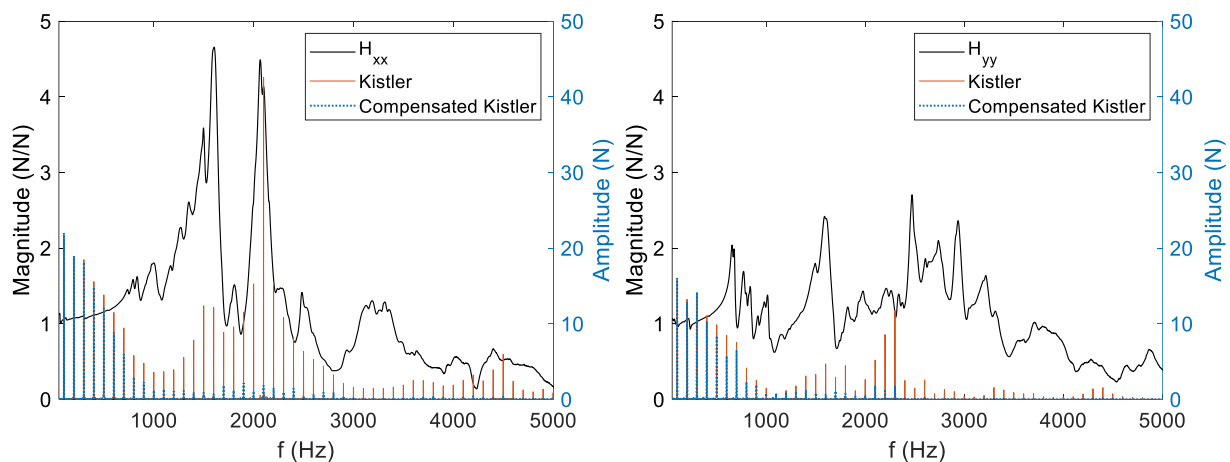
FIGURE 7. Kistler 9257B force-to-force transmissibility FRF magnitudes for the x (left) and y (right) directions (black solid line) and force frequency content: measured (red solid) and compensated (blue dashed).

The measured force-to-force transmissibility FRFs for the dynamometer's x (H_{xx}) and y (H_{yy}) directionsare shown in Fig. 7. Multiple modes are observed starting at approximately 700 Hz. The frequency content of the measured force has the expected peaks at the tooth passing frequency (100 Hz) and its harmonics. However, harmonics between 1000 Hz and 3000 Hz are artificially amplified by the dynamometer's vibration modes. To compensate for this amplification, the filtering technique described by Korkmaz et al. [12] was applied. The 1500 Hz cutoff frequency for the lowpass filter was selected such that the magnitude response of the final, inverse FRF filter is near unity at the limit of the dynamometer bandwidth, 5000 Hz. The filtered frequency content is displayed in Fig. 7, where the amplification has been effectively removed. Figure 8 demonstrates good agreement between the compensated Kistler 9257B and CMD time domain cutting force results.
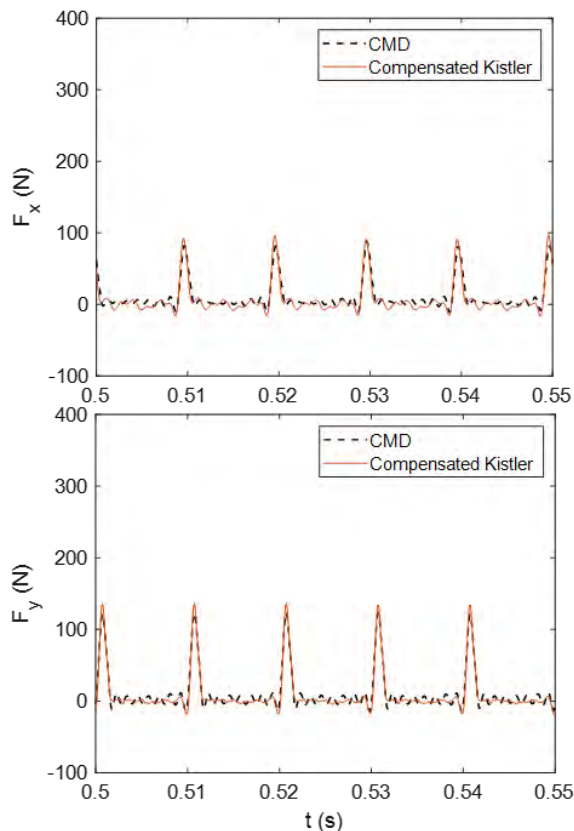
FIGURE 8. Cutting force for compensated Kistler 9257B (red solid line) and CMD (black dashed) at a spindle speed of 6000 rpm for the x and y direction forces.

To further compare the two dynamometers, the steady-state, peak values for the time domain x and y direction forces were recorded over 150 revolutions at each spindle speed. The mean values and 95% confidence intervals are presented in Fig. 9. The overlapping error bars between the CMD and compensated Kistler 9257B values demonstrate statistical agreement and validate the new low-cost CMD performance.
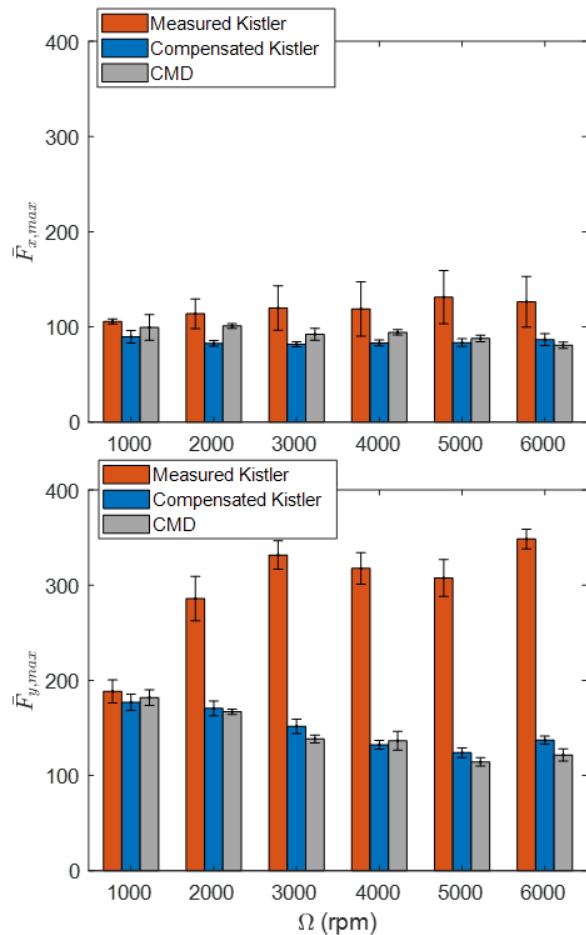
FIGURE 9. Mean peak x-direction force for the: CMD (gray), Kistler (red), and Kistler compensated (blue). Error bars indicate two standard deviations.

CONCLUSIONS
Cutting force measurement is an effective method for monitoring machining performance. The force signal can be used to optimize machine tool usage by in-process tool wear evaluation and chatter detection, for example. However, current commercially available solutions are costly and often require frequency domain signal processing to obtain accurate results.

This paper described an alternative low-cost constrained-motion dynamometer for in-process milling force measurement. The dynamometer was a monolithic design with constrained-motion of a moving platform defined by four leaf-type flexure elements arranged in the traditional H-bar configuration. An optical interrupter (fixed emitter-detector pair with a moving knife edge to partially interrupt the beam) was used to measure the moving platform's motion during milling. The cutting force was calculated from the measured displacement using the dynamometer's frequency response function (FRF). A structural deconvolution procedure was followed to filter the frequency domain displacement using the inverted dynamometer FRF and calculate the time domain force. The sensor selection, monolithic constrained-motion design, and companion structural deconvolution technique provides a low-cost, high fidelity cutting force dynamometer for use in both production and research environments.

REFERENCES
[1] Santochi, M., Dini, G., Tantussi, G. and Beghini, M., 1997, A sensor-integrated tool for cutting force monitoring, CIRP Annals, 46/1: 49-52.

[2] Burton, D., Duncan, G.S., Ziegert, J., Schmitz, T., 2004, High frequency, low force dynamometer for micro-milling force measurement, Proceedings of the 19th American Society for Precision Engineering Annual Meeting, 221-224.

[3] Yaldiz, S., Unsacar, F., Haci, S., Isik, H., 2007, Design, development and testing of a four-component milling dynamometer for the measurement of cutting force and torque, Mechanical Systems and Signal Processing, 21, 1499-1511.

[4] Byrne, G. and O'Donnell, G.E., 2007, An integrated force sensor solution for process monitoring of drilling operations, CIRP Annals, 56/1: 89-92.

[5] Transchel, R. Stirnimann, J., Blattner, M., Bill, B., Thiel, R., Kuster, F., Wegener, K, 2012, Effective dynamometer for measuring high dynamic process force signals in micro machining operations, Procedia CIRP, 1, 558-562.

[6] Gu, G.M., Shin, Y.K., Son, J. and Kim, J., 2012, Design and characterization of a photo-sensor based force measurement unit (FMU), Sensors and Actuators A: Physical, 182: 49-56.

[7] Totis, G., Adams, O., Sortino, M., Veselovac, D. Klocke, F., 2014, Development of an innovative plate dynamometer for advanced milling and drilling applications, Measurement, 49, 164-181.

[8] Ettrichratz, M., Drossel, W., Gebhardt, S., Bucht, A., Kranz, B., Schneider, J., 2018, Performance of a new piezoceramic thick film sensor for measurement and control of cutting forces during milling, CIRP Annals, 67/1, 45-48.

[9] Bleicher, F., Schörghofer, P., Habersohn, C., 2018, In-process control with a sensory tool holder to avoid chatter, Journal of Machine Engineering, 18.

[10] Altintas Y., and Park S.S., 2004, Dynamic compensation of spindle-integrated force sensors, CIRP Annals, 53/1, 305-308.

[11] Castro, L.R., Vieville, P., Lipinski, P., 2006, Correction of dynamic effects on force measurements made with piezoelectric dynamometers, International Journal of Machine Tools & Manufacture, 46, 1707-1715.

[12] Korkmaz, E., Gozen, B.A., Bediz, B., Ozdoganlar, O.B., 2015, High-frequency compensation of dynamic distortions in micromachining force measurements, Procedia Manufacturing, 1, 534-545.

[13] Scippa, A., Sallese, L., Grossi, N., Campatelli, G., 2015, Improved dynamic compensation for accurate cutting force measurements in milling applications, Mechanical Systems and Signal Processing, 54-55, 314-324.

[14] Gomez, M.F., Schmitz, T., 2019, Displacement-based dynamometer for milling force measurement, Procedia Manufacturing, 34, 867-875.

[15] Rubeo, M., Schmitz, T., 2016, Mechanistic force model coefficients: A comparison of linear regression and nonlinear optimization, Precision Engineering, 45: 311-321.

[16] Smith, S.T., 2000, Flexures: Elements of Elastic Mechanisms, CRC Press, Boca Raton, FL.

PORTABLE MICROSCOPE SYSTEM FOR REAL-TIME AEROSOL MEASUREMENT

Songyun GU, Bingxu CHEN, Chenyang WEN and Shih-Chi CHEN
Department of Mechanical and Automation Engineering
The Chinese University of Hong Kong
Shatin, N.T., Hong Kong SAR, China

In this paper, we present the design of a portable microscope system (PMS) as well as the characterization and use of this system for (1) real-time aerosol measurement for endoscopy operations; and (2) characterizing performance, i.e., filtration efficiency, of different face masks, including medical masks and home-made face masks. The PMS system can measure the aerosol particle size, concentration, and velocity at a rate of 35 frames per second (fps); when pairing with a 5x objective lens, the minimal detectable aerosol size is ~ 500 nm with a field of view of 1 mm^2.

INTRODUCTION

During the coronavirus pandemic in 2020, N95 and medical masks become rare sources even in hospitals. In Hong Kong, many common surgical procedures at public hospitals have been called off temporarily due to the lack of N95 masks. As such, there is an urgent need to determine whether certain common procedures, e.g., upper gastrointestinal (GI) endoscopy, are aerosol generating procedures. If not, these procedures may be resumed with reduced protection.

Aerosols are fine solid particles or liquid droplets suspended in air, which can easily enter lungs or cardiovascular systems [1], leading to the transmission of novel coronavirus and various diseases. Aerosols also present risks for various surgical procedures [2]. As such, a compact and high-speed solution for aerosol detection becomes important. With requests from the Prince of Wales Hospital (PWH), we have custom-developed a low-cost PMS to monitor the aerosol generation in different common procedures; and to investigate the protection power of different classes of face masks.

PRINCIPLE OF AEROSOL IMAGING

In our design, the aerosol flow is back-illuminated as shown in Fig. 1; after background subtraction, the aerosol particle information, including size, concentration and velocity, can be extracted from the calculated shadowgraphs. To accurately monitor the traveling aerosols in air, a light emitting diode (LED) is used as the light source, where the light is condensed to provide high illuminance. During the measurement, the images are acquired frame by frame with a shutter time on the scale of several microseconds; although the shutter time is short, the signal-to-noise ratio (SNR) can be maintained appropriately by adjusting the LED intensity. Out-of-focus aerosol particles can be determined by evaluating their edge blurriness level; and only particles within the depth-of-focus will be used for the analyses [3].

SYSTEM CONFIGURATION

Figure 1 presents the optical design of the PMS. The backlight illumination system consists of a white LED (maximum power: 3W) and a condenser. The detection field is isolated in a transparent chamber between the illumination system and the long working distance objective lens (MY10X-823, Mitutoyo). A high-speed complementary metal–oxide–semiconductor (CMOS) camera (CM3-U3-13Y3M-CS, FILR) is used for image acquisition and is in conjugation with the focal plane of the objective lens. The images are acquired and analyzed by a custom-developed MATLAB program. All optical components are mounted on an optical breadboard (350 × 150 mm^2), and sealed within an acrylic box, as illustrated in Fig. 2, making it compact and portable. As shown in Fig. 1, a suction system can be connected to the detection chamber of the PMS for controlling the flow rate.
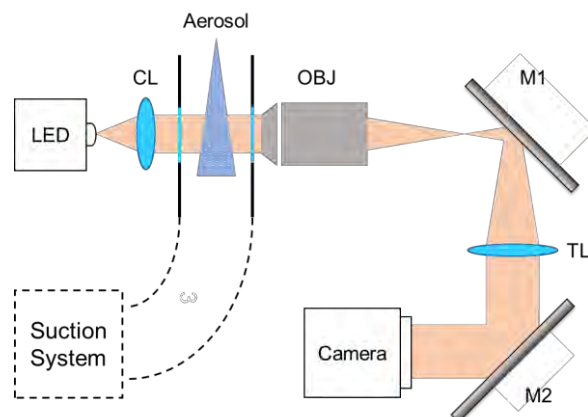
FIGURE 1. Optical configuration of the PMS; CL: condenser lens, TL: tube lens; M1, M2: mirrors.
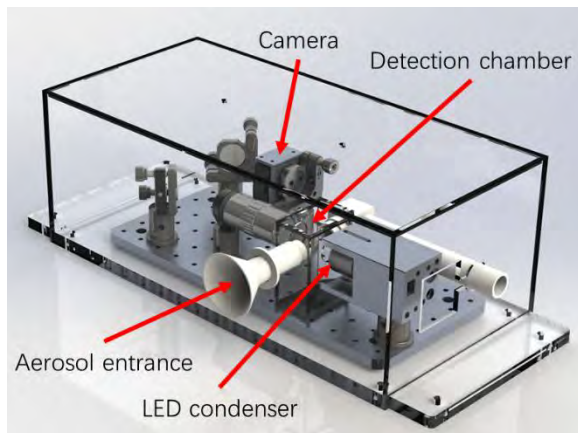
FIGURE 2. CAD model of the PMS, with all optical components mounted to an optical breadboard and sealed in an acrylic box.

Figure 3 presents the aerosol measurement workflow. First, the image background and noises are recorded. Next, the CMOS camera acquires images when the air flow passes through the detection chamber at the same illumination condition; the recorded images are then transferred to the buffer of the "producer-consumer real-time streaming loop" as shown in Fig. 3, which sequentially analyzes each acquired image. The depth information, flow rate, and concentration of the detected aerosols are extracted from the image after background subtraction, where the depth is calculated by the autocorrelation of aerosol particles and the calibrated edge blurriness. Note that the output frame rate is determined by system computing power. In our system, the frame rate is ~35 fps (CPU: Inter Core i7-8700; RAM: 32GB; 2666 MHz ddr4).
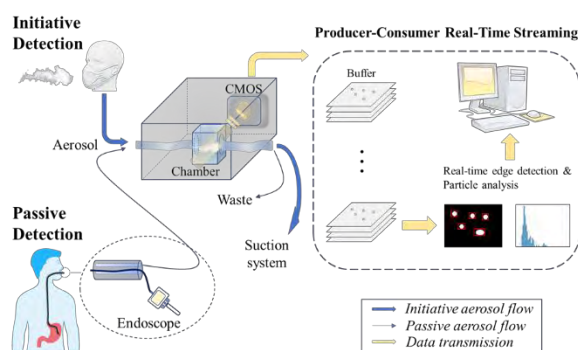
FIGURE 3. Workflow of the aerosol measurement procedure.

SYSTEM CALIBRATION

Figure 4 shows the detection volume and its position in reference to the objective lens. To ensure the flow rate and concentration of aerosol particles can be accurately estimated, we need to determine the number of the total aerosol particles that fall in the volume of analysis. Although for plane illumination, images of all

particles are projected to the CMOS camera, their distances (i.e., Δz) to the objective focal plane can be estimated by analyzing the edge intensity profile of each particle. This is important as particles far away from the focal plane not only have blurry edges but also low intensities that are close to the background noise level and must be excluded from the analysis.

We used a resolution target to characterize the edge profile variation as the target shifts away from the focal plane. The measured intensity profiles are plotted as a function of z over the range of ±2 mm, as shown in Fig. 5. Based on this result, we can exclude all aerosol particles outside a specific distance from the focal plane by comparing the autocorrelation results between the aerosol particle intensity profiles and the reference intensity profiles in Fig. 5. As such, the depth of each aerosol particle is determined by selecting the corresponding depth whose autocorrelation curve gives the highest value. From our experimental observation, aerosol particles that are 2 mm away from the focal plane would have intensity level close to the background noises. Accordingly, we confine our analyses to particles whose distances are less than ±1 mm from the focal plane.

FIGURE 4. Detection volume of the PMS. The focal plane of the objective lens is located at the center plane of the detection chamber (z = 20 mm).
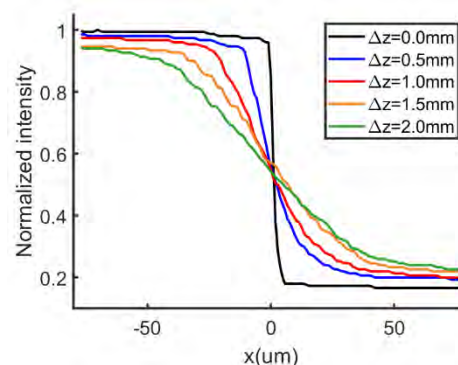
FIGURE 5. Edge Intensity profiles of a resolution target (1951 USAF Resolution Target, Edmund Optics) measured at different depths. The

resolution target is placed in the x-y plane; and Δz refers to the distance between the edge and the focal plane of the PMS.

Figure 6 presents a typical image recorded from the experiments, where one may observe particles are of different sizes, intensities and edge profiles. Based on their edge profiles, aerosol particles outside the volume of analysis (i.e., ±1mm) are excluded by the method described above. Considering the detection chamber has a width of 20 mm and assuming the velocity profiles are uniform in the z-direction, the volume flow rate (Q) can be estimated by multiplying the average velocity (V) to the ratio of 20 mm/2 mm, i.e., $Q = V \times 10$ (m³/s).
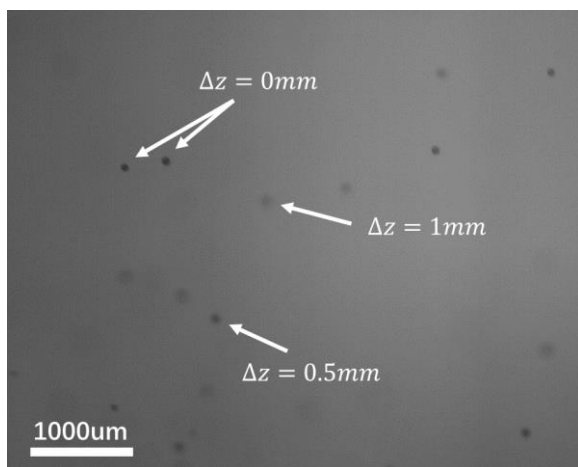
FIGURE 6. A sample image of aerosol particles, which contains particles from different depths. The depth of each particle is determined by the comparison of autocorrelation curves.

EXPERIMENTS
In the experiments, the PMS is used to characterize the (1) filtration efficiency of different face masks; and (2) aerosol generation for an endoscopy procedure on a pig stomach. (The license for the clinical trial on human subjects is being pursued.)

Figure 7 presents a phantom experiment to measure the filtration rate of different masks at different flow rates to emulate different breathing conditions (e.g., normal breathing vs. sneezing), where the flow rate is controlled by the suction system. In the experiment, the aerosols are generated by a humidifier positioned nearby the silicone model head that wears two different masks, i.e., medical mask and homemade face mask (made by folding a cotton towel). The air flow carrying the aerosols travels to the PMS detection chamber after passing through the mask at designed flow rates. The test results of particle distribution are presented in Fig. 7B, where the middle and bottom rows present

measurements from the medical masks (mask1) and homemade (mask2) with low (1.8 × 10⁻⁴ m³/s) and high (7.2× 10⁻⁴ m³/s) flow rates respectively. The flow rates are selected based on reported human breathing flow rates, i.e., 1 × 10⁻⁴ m³/s – 2 × 10⁻⁴ m³/s, where the low and high air flow rates correspond to 1 and 4 times the human breathing flow rates. The results surprisingly show that the homemade facemask has better protection power at low flow rates; this may be attributed to its better conformation to the model head, which minimizes leaks from the sides of typical medical masks. At high flow rates, the average velocity of the aerosol particles passing the medical mask is approximately twice than that of the homemade mask, as shown in Fig. 7C. The results indicate the medical mask has better protection for high speed aerosols, e.g., aerosol generated during coughing. The result shows the importance to always (1) have protections, e.g., homemade masks, when professional gears are unavailable; and (2) to wear face masks correctly in order to minimize leakage.
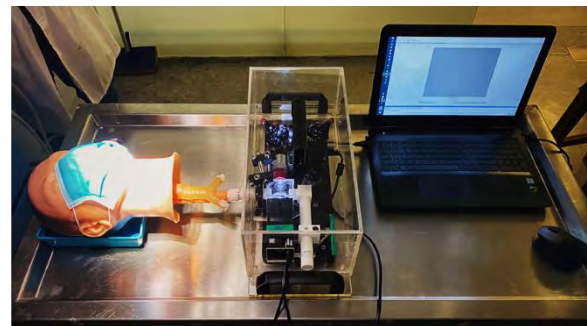
A
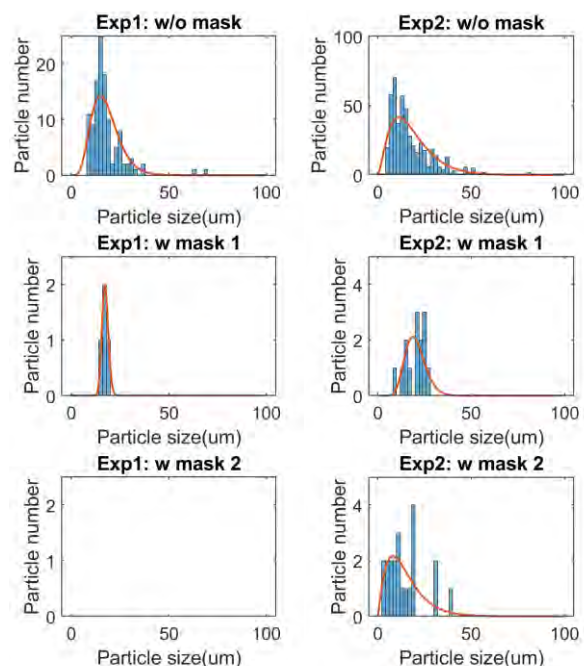
B
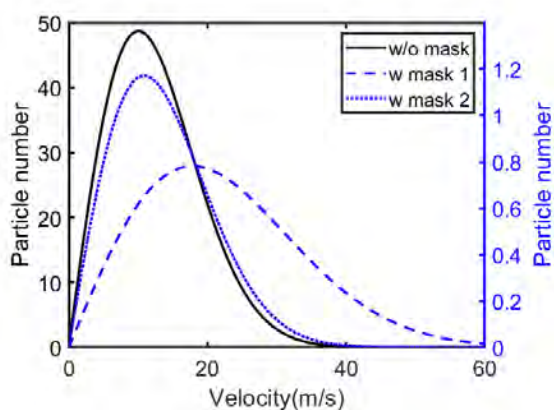
C

FIGURE 7. Face mask filtration test: A. Experiment setup; B. top row: measurement without masks; middle & bottom rows: measured filtration rates of medical and homemade masks under low (Exp1: left column) and high (Exp2: right column) flow rates respectively; and C. Velocity distribution of aerosol particles in Exp2; The number of particles reported in B and C are counted over a duration of 0.3s.

In the second experiment, we measured the possible aerosol generations for endoscopy procedures on a pig stomach, as shown in Fig. 8. Generally, upper GI endoscopic procedures are considered an aerosol generation process [4, 5]. As the human clinical trial license is still in pursuit, we first conducted an experiment on a pig stomach to emulate the real endoscope or surgical procedures. As shown in Fig. 8, in the experiment the PMS is connected to the endoscope system via a 3D printed Y connector. During the experiment, water and air are continuously injected into the pig stomach, which is a common practice in endoscopy.
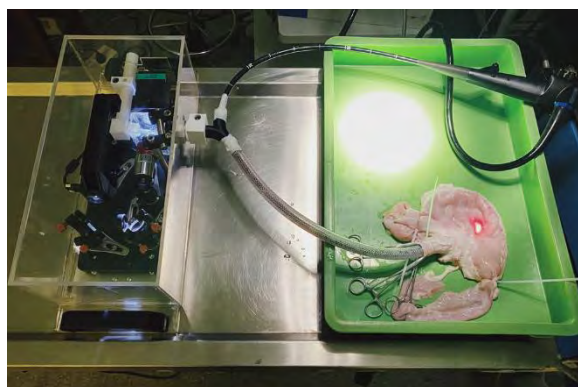
FIGURE 8. Aerosol measurement on a pig stomach that emulates a real endoscopic procedure.

Our results show no evidence of aerosol generation during the experiment. The water and air pumped into the stomach by the endoscope

system do not form detectable aerosol particles even at maximum endoscope pump pressure. As such, the reported aerosol generation during endoscopy procedures may be attributed to other reasons, e.g., coughing or retching. Comparing with other surgical procedures, the upper GI endoscopy presents more risks of transmission of diseases due to the close contact with patients and respiratory droplets.

CONCLUSION
We have presented the design and characterization of a PMS as well as the related image processing algorithm for real-time high-speed aerosol measurement. Based on the PMS, experiments have been devised and performed to investigate the effectiveness of different face masks and medical procedures, i.e., upper GI endoscopy, that may induce aerosols for disease transmission. The results show the PMS can detect any particles larger than 500 nm at a speed of 35 fps, which is superior to existing commercially available aerosol detection systems in terms of speed, resolution, versatility, and cost. In the future, the PMS will continue to be used for monitoring and studying medical operations at PWH in Hong Kong as well as to investigate the performances of different face masks, providing safety guidelines for both the medical professionals and general public. As the PMS can detect any micron to submicron scale particles, it may find applications in other fields, e.g., detection of construction dust.

ACKNOWLEDGMENT

REFERENCES
[1] Yin B, Chan CK, Liu S, Hong H, Wong SH, Lee LK, Ho LW, Zhang L, Leung KC, Choi PC, Bian L. Intrapulmonary Cellular-Level Distribution of Inhaled Nanoparticles with Defined Functional Groups and Its Correlations with Protein Corona and Inflammatory Response. ACS Nano. 2019;13(12):14048-14069.

[2] Workman AD, Welling DB, Carter BS, Curry WT, Holbrook EH, Gray ST, Scangas GA, Bleier BS. Endonasal Instrumentation and Aerosolization Risk in the Era of COVID–19: Simulation, Literature Review, and Proposed Mitigation Strategies. International Forum of Allergy & Rhinology 2020.

[3] Minov SV, Cointault F, Vangeyte J, Pieters JG, Nuyttens D. Spray Droplet Characterization from a Single Nozzle by High Speed Image Analysis Using an In-

focus Droplet Criterion. Sensors. 2016;16(2):218.

[4] Ang TL. Gastrointestinal Endoscopy During COVID−19 Pandemic. Journal of Gastroenterology and Hepatology. 2020;35(5):701-702.

[5] Soetikno R, Teoh AY, Kaltenbach T, Lau JY, Asokkumar R, Cabral-Prodigalidad P, Shergill A. Considerations in Performing Endoscopy During the COVID-19 Pandemic. Gastrointestinal Endoscopy. 2020.

UNCERTAINTY EVALUATION BY MONTE CARLO METHOD ON THE EFFECTIVE TOOL LENGTH IN A PRECISION MACHINE TOOL

Nicholas Horvath[1] and Michael Gomez[1]
[1] Energy and Transportation Science Division
Oak Ridge National Laboratory[1]
Oak Ridge, TN, USA

INTRODUCTION

Measurements and compensation techniques for positional uncertainties in machine tools are critical to create components in high precision applications. These uncertainties arise from error sources such as: kinematic errors, static or dynamic displacements, thermally induced motions, control or toolpath errors, and work holding errors. However, as described in previous works by Venugopal and Barash [1], Bryan [2], Weck et al. [3], and more recently Mayr et al. [4], thermal deformations are responsible for up to 75% of the error motions on a machine tool.

A principle contributor of tool center point location errors is thermally induced deformations caused by bearing friction in the spindle. Foundational work by Spur et al. [5] provided a strategy for thermal error reduction: attenuate, mitigate, and compensate. With the advent of high-speed spindles and high-speed milling, reduction of thermal deformation in spindles became an even greater focus [6]–[8]. The reduction strategies included using advanced ceramics such as silicon nitride for ball bearings to reduce friction, using bearing oil-air flow and mixture combinations, and using thermo-mechanical models such as FEM/FDM simulations for predictive compensation [9].

Another method for thermal error reduction is active compensation using continuous feedback. Much of this work has been implemented by using a neural network and machine learning techniques. Described earlier by Weck [3], neural networks and real time compensation have been at the forefront of compensation techniques due

to advancements in computational efficiency [10]-[12]. Neural network and machine learning techniques rely on extensive sensor packages, good modelling capabilities, inexpensive computing power, and long-term data collection [13]. As noted by Bryan [2], using software to correct for poor mechanical design is not the best solution. Therefore, a comprehensive understanding of the cumulative error sources and design choices are critical to achieve high precision motion in machine tools

However, even though the research findings for general error motions and thermal effects are expansive, the uncertainty associated with setting the tool length – and subsequently the tool tip location – is less often described in detail. Machine tool manufacturers and operators use a variety of metrology instruments or techniques to locate the tip of the cutting tool in the global coordinate system of the machine after all static error methods are applied. Tool tip locating strategies include: touching off the workpiece using a mechanical tool height gauge, using an off-machine tool setting station, or laser-based optical reference beams. While each of these measurements has an uncertainty associated with it, there has yet to be a thorough discussion of the fundamental measurand.

General purpose tool length setters are readily available by most resellers with claims of 5 μm accuracy and repeatability. While the measurment apparatus may have the stated accuracy, simply assuming the tool length measurement uncertainty is within that accuracy limit may result in erroronous components. The stated accuracy and resolution of a tool setter is

on the order of, or better than, the stated accuracy of most machine tools. However, this cannot be assumed to be the main contributor to the uncertainty in tool length measurement. This manuscript is intended to evaluate the uncertainty and contributing sources of the effective tool length in a CNC machine tool. Where possible, experiments were performed to quantify the contributions to the uncertainty. The quantification of the uncertainty does not include the volumetric position uncertainty in the work space of the machine, but rather the intial measurement for a static tool compensation. Because most general precision machine tools can generate surface contours on the order of 10 μm, the target uncertainty for this measurand was set to 5 μm.

Tool length compensation methods and instruments

Tool length setters refer to instruments used to measure the effective length of a tool relative to the gauge line in the spindle. We shall now discuss some of the options and intrinsic contributions to the uncertainty in the measurand.

Mechanical touch off gauges

One of the least expensive, lower precision, and versatile measurement tools is a plunge type micrometer. This tool comprises a precision ground cylindrical bore and plunger that is paired with a drop-style indicator. To quantify the tool length for compensation, the plunger is driven into the bore until the face of the plunger is coplanar with the ground top surface of the bore. The top surface is defined as some value, which is assumed to be the distance between the tool tip and the work piece. Some intrinsic error sources are the uncertainty in the gauge height of the tool, friction in the bore, micrometer gears, dial markings, and parallelism between the top and bottom face. Often the tool is held by the operator which can induce change in size due to temperature, or simply a Type-B uncertainty from user error.

Other mechanical measurement devices are also found off the machine. These systems include a height gauge paired with a ground taper to hold the tool holder. This techinque uses a reference artifact to locate the height gauge relative to the taper. The tool and tool holder are placed in the taper and a comparision measurement is taken.

An assumption with this technique is that the taper is perfect on both the measurement tool and the tool holder, therefore constraining the location of the gauge line on the tool holder. This assumption results in a contribution to the uncertainty of the effective tool length since the tapers are not perfect. Secondly, once the tool is installed in the spindle, the tolerance on the taper is different and a significant preload is applied.

Optical touch trigger setter

Similarly to the plunge-type gages, the optical touch trigger setter, this instrument requires the tool to come into contact with a probe or gauge. Instead of a μm, the tool uses optical transmission to a receiver. The tool will come into contact with the probe, which will trigger a electrical pulse from a small displacement. The pulse will turn on an LED which transmits an infra-red light to the receiver. The measurement of tool length is independent of the signal transmission, rather the instrument is calibrated with an artifact to establish a reference for the trigger point. These instruments have a better resolution and repeatablity than the mechanical style indicators, with manufacturers claiming 1.00 μm 2σ repeatability.

The sources of uncertainty now include the uncertainty in the length of the reference artifact, the reproducability of the tool change, thermal contributions, and machine positioning and resolution. Because the measurement instrument's stated accuracy is on the order of the machine tool resolution, uncertainty contributions from the machine tool start to dominate the ability to quantify the effective tool length.

Non-contact laser trigger setter

A recent development in tool setters is a laser-based system that uses either red or blue light. This instrument detects the tool length as the tool tip breaks the beam path. The instrument comprises a source end, which projects a collimated beam to a photodetector in the receiving end. Manufacturers have different and proprietary techniques for collimation control and compensation due to enviromental conditions. This style of instrument claims an order of magnitude better repeatablity and resolution from the optical touch probes.
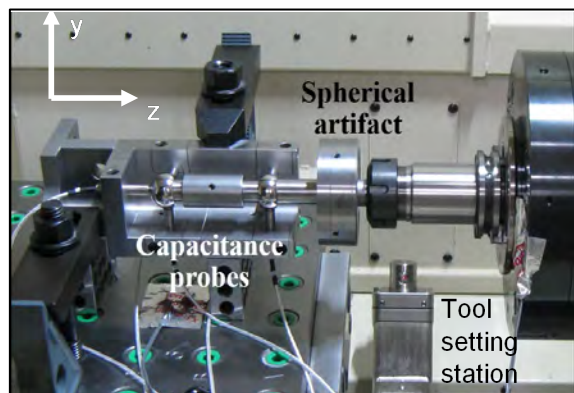
FIGURE 1. Metrology setup for axial spindle displacement showing the capacitance probe nest, ball bar, and optical tool setting station

EXPERIMENTAL EQUIPEMENT

Our experiments to quantify tool length bias and uncertainty were performed on a horizontal machining center with an optical tool setting station installed on the table, Fig. 1. The tool setting station is calibrated with a high precision calibration artifact that is comprised of a specified overall length from the gauge line and end boss diameter. From this, the uncertainty is traceable to the stated uncertainty on the calibration report.

To quantify other uncertainty sources, a calibrated Lion Precision capacitance probe nest with 10 nm resolution was used along with 7 surface mounted thermistors to measure temperature changes during experiments.

UNCERTAINTY INPUT SOURCES

To help quantify the uncertainty in the tool length measurement an Ishikawa diagram was developed. This diagram is a visual representation of the categories of input sources and the specific contributing factors. Some categories and contributing factors were easily approximated to be orders of magnitude less than the target uncertainty and therefore not investigated further. Here we discuss some of the contributing factors that are readily quantified by direct measurement and analysis.

Temperature induced spindle growth

Understanding how the power dissipation from the spindle motor in the form of heat changes the position of the tool tip by axial growth or contraction must be quantified. Unlike traditional manual tool presetters, the laser system performs the measurement with the spindle running. This allows for a dynamic measurement coupled with the measurement of the effective diameter of a multi-flute cutting tool.

Two experiments were performed to quantify the change in length of the spindle due to temperature. The first was a direct measurement of the axial change from a cold, stopped position in order to assess whether a convergence of position change was achieved over time. The second was at the measurement speed of 5k RPM, over time to quantify axial tool tip position stability over a set duration. Each of these measurements was performed with a capacitance probe nest and a double ball bar. During these measurements, any angular change of the spindle that would create a cosine error bias (foreshortening effect) was also quantified, however the angular change resulted in two orders of magnitude less error than the target uncertainty and was omitted from the analysis.

The first measurement from an overnight soak out and cold start up resulted in a convergence to approximately 3 µm of axial growth over a 60 min period. An additional measurement was then performed from a warm condition to assess stability. The stability of the axial growth was less than 1 µm over 60 min. Two results were extracted, an initial bias that is readily compensated by performing a warm-up cycle for 10 min and an even-sided normal distribution of the stability with a standard deviation of 0.2 µm. Contrary to the initial assumption, the growth of the spindle with the initial bias removed is a relatively small contribution to the uncertainty of the effective tool length. However, this particular spindle design enables this low uncertainty source, with extensive engineering in rejection of the waste heat from the power dissipation from both continuous flowing chilled oil, oil-air, and arrangement of the bearings. This uncertainty source may be a significant contribution to the overall uncertainty on other machine tools and in that case should be addressed and quantified.

Axial position and tool change repeatability

An assumed large contribution to the uncertainty is due to the finite repeatability in positioning the table along the z-axis. The axial positioning repeatability was quantified by moving the calibration artifact to the tool change position and

then repositioning the table to a commanded location along the *z*-axis. This relative position was measured using a capacitance probe mounted on the table. However, the successive measurements, once analyzed, exhibited a significant drift over time, with a slope of 0.4 μm per minute. This drift was caused by the expansion of the lead screw during the measurement. This particular machine has a rotary encoder rather than a linear scale; therefore, thermal expansion of the lead screw will result in a pitch change not identified by the rotary encoder. The machine utilizes core cooled ball screws; thus, the bias was readily addressed by running the base coolant on the machine during the experiments. A subsequent set of measurements were performed with the coolant running.

The measurements with the coolant running contained residual drift but was reduced to 30 nm per minute of continuous measurement. Because of the nature of rapid repeated measurements and full range of travel of the *z*-axis required during the measurement, a least squares line with the reported slope was removed. This bias would not be a significant contribution to uncertainty during operation because the *z*-axis is often the least traversed axis during manufacturing and a series of rapid measurements are not traditionally performed. The residual data, after the least squares line was removed, was fit with a normal distribution centered near zero with a standard deviation of approximately 0.5 μm.

Typically, CNC machines use multiple tools; therefore, the taper connection after a tool change must be quantified. Factors influencing the taper connection and repeatability of the tool change are numerous and include the uncertainty in: the diameter of the gauge line on the tool holder and spindle taper, friction, drawbar force, taper angle, and temperature. While this list is expansive, and generally directly measurable, it is impractical to attempt to quantify each term individually. Instead, these factors were combined and analyzed as a distribution by repeat measurements of tool changes. This was performed by first quantifying the positioning repeatability of the table.

To quantify the tool change repeatability, similar measurements were made, however a tool
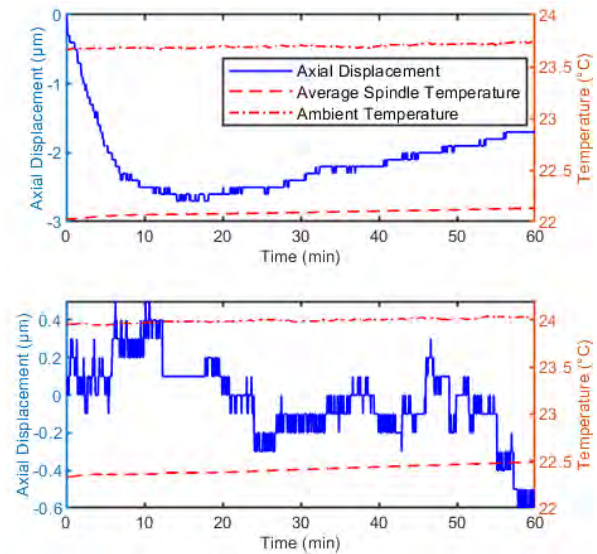
FIGURE 2. Axial spindle displacement showing an initial bias (Top), followed by a stability measurement (Bottom)

change was performed to an arbitrary tool and then back to the calibration artifact. The tool was repositioned to the capacitance gauge and the relative position measurement was taken. With the positioning axis repeatability already quantified by a distribution, this data could be subtracted from the newly acquired data to reveal the tool change contribution. During the analysis the tool change data overlapped with the positioning data, meaning the tool change was in the noise of the positioning repeatability. This result is displayed in Fig. 3. Therefore, this data set was combined with the previous set and a new distribution was formed, again centered around zero with a standard deviation of 0.5 μm.

Laser system repeatability
A similar measurement as the previous section was performed to determine the laser system repeatability. In this case, the laser tool setting system was used rather than the capacitance probe without a tool change. It is assumed that the measurement data collected is a combination of the positioning repeatability of the table, repeatability of the laser system, and some environmental noise. The data set collected showed minimal drift since the position measurement using the laser system took more time than the measurements performed with the capacitance probe, thus allowing for the lead screw to reach a thermally stable condition. This also confirms the assumption that the lead screw
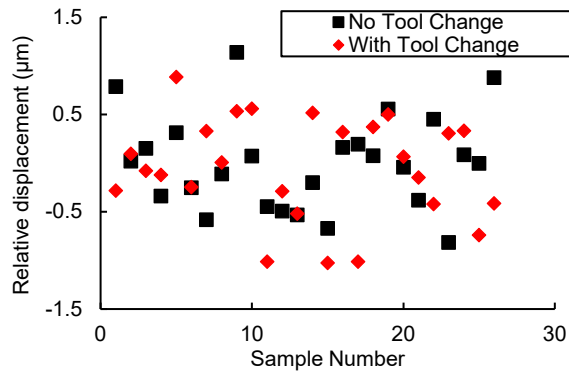
FIGURE 3. Quantification of the linear axis position repeatability and combined factors of tool change repeatability.

growth was the leading cause of the slope in the previous dataset. The laser setting system data was collected, and the positioning distribution was removed from the set. A normal distribution resulted from the laser repeatability centered near zero a with a standard deviation of approximately 70 nm. This is a factor of 2 larger than the stated repeatability of the system by the manufacturer.

Calibration artifact length and temperature
The calibration artifact used during the experiment was made from steel and came with a calibration report. However, the report had no stated uncertainty of the length which is a significant contribution to the effective tool length. From experience, a Type-B uncertainty assumption was made that a well-made artifact was within a uniform distribution with limits of 3 µm. An assumption was also made that the reported length was measured at 20°C. Therefore, to remove bias, the temperature of the artifact was measured. The uncertainty from the temperature using thermistors was estimated to be a uniform distribution with limits of 0.01°C. These distributions were added to the list of uncertainty contribution inputs to be sampled during the Monte Carlo analysis.

Beam angular alignment
Another bias that had to be accounted for during the measurements was the angular alignment of the beam. For tooling other than ball type with center point setting, this angular error creates a bias error in length that is a function of the diameter of the tool. The angular alignment in the sensitive direction was quantified to be

approximately -0.4 mrad, resulting in a bias with the 20 mm diameter artifact of 3.8 µm. This misalignment bias if not accounted for would result in the most significant contribution to uncertainty in the effective tool length. The alignment is easily quantified by probing along the beam with minimal axial movements. However, the angular error measurement is comprised of the positioning uncertainty and environmental noise. This was considered in the reported value, but the uncertainty in position and noise over this distance was orders of magnitude less than the measured value.

Environmental noise
Environmental noise is present in all the measurements performed but not directly quantified. In this case, a normal distribution was created and centered about zero with a standard deviation of 1 µm. Because of the long beam path, this Type-B assumption accounts for some of the nondeterministic laser errors such as beam bending, refractive index variance in the beam path, and noise in the photodetector.

MEASURAND AND UNCERTAINTY EVALUATION
The measurand of interest is the effective tool length, which is length of the tool installed in the CNC, rather than the best estimate of the length of the tool. Because each tool is of different length, an important aspect of the measurand is the uncertainty in the effective tool length and the associated biases encountered during tool setup. The measurand equation is shown as Eqn. 1

$$L_{eff} = L_{best\ est} \pm \sum \delta L \qquad (1)$$

where L_{eff} is the tool length installed in the machine tool and δL are the individual uncertainty sources. The best estimate for the tool is not required in this analysis, thus we focus on the analysis of the uncertainty contributions.

Here, the input source distributions were used in a Monte Carlo simulation; where, at each iteration the input sources take a discrete sample from the respective distribution. Each input term was then summed and stored in a combined distribution, which was fit with a normal distribution. The resulting standard deviation is the uncertainty of the measurand. Fig. 4 shows the distribution from
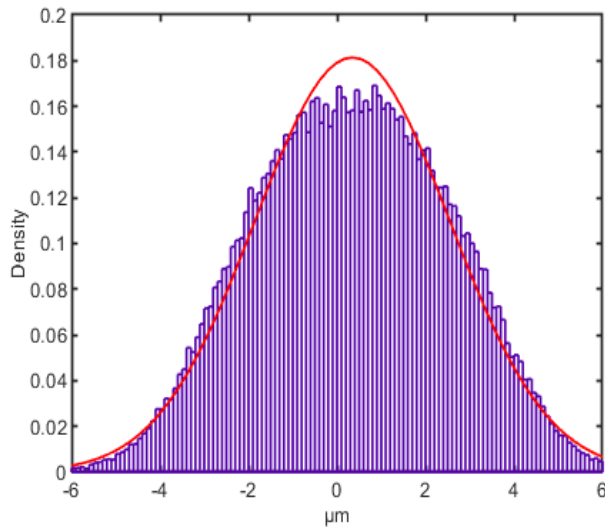
FIGURE 4. Combined distribution of uncertainty input sources after a Monte Carlo simulation with 10,000 iterations.

the Monte Carlo analysis, with the reported distribution being center near zero with a standard deviation of 2.4 µm. Including a coverage factor of 2, the expanded uncertainty of the measurand becomes 4.8 µm, with all identified biases corrected.

CONCLUSION

This paper discussed the uncertainty associated with setting the tool length with a high precision tool setting station in a CNC machine. The target uncertainty initially was set to 5 µm once all biases were corrected. The work shows an uncertainty of the effective tool length was nearly equal to the initial assumption, but it required a systematic approach to setting the tool. Disregarding the biases discussed result in a sufficiently larger uncertainty in tool tip location relative to the gauge line.

ACKNOWLEDGEMENTS

REFERENCES

[1] R. Venupal and M. Barash, "Thermal effects on the accuracy of numerically controlled machine tools," *CIRP Ann-Manuf. Techn.* 35(1)255–258, 1986.

[2] J. Bryan, "International Status of Thermal Error Research (1990)," *CIRP Ann. - Manuf. Techn.* 39(2) 645–656, 1990.

[3] M. Weck, P. Mckeown, R. Bonse, and U. Herbst, "Reduction and compensation of thermal errors in machine tools," *CIRP Ann. - Manuf. Techn.* 44(2) 589–598, 1995.

[4] J. Mayr *et al.*, "Thermal issues in machine tools," *CIRP Ann. - Manuf. Techn.* 61(2) 771–791, 2012

[5] G. Spur, E. Hoffmann, K. Benzinger, and H. Nymoen, "Thermal behaviour optimization of machine tools," *CIRP Ann. - Manuf. Techn.* 37(1) 401–405, 1988.

[6] H. Aramaki, Y. Shoda, Y. Morishita, and T. Sawamoto, "The performance of ball bearings with silicon nitride ceramic balls in high speed spindles for machine tools," *J. Tribol.*, vol. 110, 693–698, 1988.

[7] J. Jedrzejewski, J. Kaczmarek, Z. Kowal, and Z. Winiarski, "Numerical optimization of thermal behaviour of machine tools," *CIRP Ann. - Manuf. Techn.* 39(1) 379–382, 1990.

[8] Y. Li, W. Zhao, S. Lan, J. Ni, W. Wu, and B. Lu, "A review on spindle thermal error compensation in machine tools," *Int. J. Mach. Tools Manuf.*, vol. 95, 20–38, 2015

[9] T. Holkup, H. Cao, P. Kolá, Y. Altintas, J. Zeleny, and Z. Zeleny, "Thermo-mechanical model of spindles," *CIRP Ann. - Manuf. Techn.* 59(2):365–368, 2010

[10] P. Schellekens *et al.*, "Design for Precision: Current Status and Trends," *CIRP Ann. - Manuf. Techn.* 47(2):557–586, 1998.

[11] R. Ramesh, M. A. Mannan, and A. N. Poo, "Error compensation in machine tools- a review. Part II: Thermal errors," *Int. J. Mach. Tools Manuf.*, vol. 40, no. 9, 1257–1284, 2000

[12] F. Li, T. Li, Y. Jiang, H. Wang, and K. F. Ehmann, "Explicit error modeling of dynamic thermal errors of heavy machine tool frames caused by ambient temperature fluctuations," *J. Manuf. Process.*, vol. 48, 320–338, 2019

[13] H. J. Pahk and S. W. Lee, "Thermal Error Measurement and Real Time Compensation System for the CNC Machine Tools Incorporating the Spindle Thermal Error and the Feed Axis Thermal Error," *Int. J. Adv. Manuf. Technol.*, vol. 20, pp. 487–494, 2002.

Optical Gear Inspection Using a Triangulation Sensor and an Areal Evaluation

Abolfazl Hosseinpour[a], Yue Peng[a], Gert Goch[a], Kang Ni[a], and Anke Guenther[b]

[a] **University of North Carolina at Charlotte, Charlotte, North Carolina, USA**
[b] **ETH Zurich (Eidgenoessisch Technische Hochschule), Switzerland**

INTRODUCTION

Precision gears are widely used in automotive industry and wind energy applications. Gears play a major role in the quality of transmission systems in terms of generated noise, vibration, transmission capacity, lifetime, and weight. Manufacturing precision gears requires precision metrology to control the gear geometry in size and shape. So far, the classical gear measurement is based on a tactile measurement of two lines per flank, which is widely used to assess gear parameters. Because standard gear measurement is limited to four gear teeth, a line-oriented classical measurement of a cylindrical automotive gear can be performed within a few minutes period; however, it cannot represent the entire gear flank. Furthermore, modern gears have more and more sophisticated flank modifications to improve functional properties of the gearbox. Yet these geometrically structured modifications might not be captured by the line-oriented evaluation. To address these deficiencies, a new area-oriented evaluation approach was presented by Goch et al. [1]. The new method, however, requires a large number of measured gear flank points, which is time-consuming when using tactile measurement. All of these challenges including partial measurement and evaluation of a gear, tactile measurement time, and sophisticated flank modifications highlight the pressing need for an appropriate optical measurement in gear metrology.

Today, some new optical devices are commercially available and able to scan dense point clouds on each gear flank in a reasonable time. The instrument used for this investigation is equipped with light section triangulation sensor. However, there have always been some serious concerns in optical measurements of commercial gears, such as:

- Evaluation time
- Acceptance in automotive industry
- Multiple light reflection in the root area of gear flank
- Form deviation

Due to the physics of laser optical measurement, speckles and other scattered light phenomena are inevitable in optical inspection. This light deflection can lead to large form deviations when using triangulation sensors. Large form deviations that increase measurement uncertainty have always been a serious challenge, when the evaluation results of optical inspection are to be compared with reference results, i.e. obtained by tactile measurement. Moreover, the detection and correction or avoidance of multiple light reflection are vitally important because they can lead to wrong flank surface points determined by the optical instrument. Also, comprehensive areal inspections need to be consistent with current classical line-oriented inspections within a few microns range to be accepted by the automotive industry. This needs more investigations and therefore more simulations and measurements which are addressed in this work.

In this paper the above-mentioned issues are addressed using data of some commercial gears measured by an optical instrument equipped with a light section triangulation sensor. Beside some suggested methods to reduce form deviation and multiple light reflections, the new areal evaluation method is improved by adding some complex gear modifications. Then the improved evaluation method is implemented to practically compare the evaluation results of optical areal measurements with the results of tactile areal measurements, performed with a Leitz PMM-F. Both types of measurements refer to the same set of commercial gears.

FORM DEVIATION

Since the triangulation principle based on laser light source is used to measure a gear flank surface, there might occur some speckles and other scattered light phenomena on the sensor camera as a result of the deflected laser section line. Those phenomena might cause some inaccurate peak position detection in the current evaluation method. The peak shift in sensor x-y direction leads to a deviation in the evaluated distance, approximately perpendicular to the gear flank's surface in the third direction. This is considered as the reason for the obtained form deviation parameter values, which are not plausible in physical or technical terms, since the measured gear has finished surfaces with a form deviation in the single digit micrometer range (e.g. 3-5 μm). The objective of the performed research work was to develop a mathematical approach improving the detection of the ridge line, which is the line in x-y domain with the highest intensity as illustrated in the contour plot in Figure 1 as a dashed line. Each scanned ridge line is transferred to actual XYZ coordinates and combining all the consecutive ridge lines will later form the entire surface. Some alternative mathematical approaches are going to be considered for the instrument to detect the peak position even more accurately.

MULTIPLE LIGHT REFLECTION

When applying a triangulation sensor, the surface is detected based on scattered light intensity on the sensor camera. If there occurs a multiple light reflection due to shiny surfaces or small curvature radii, e.g. root area of the flank, a wrong surface is detected where actually that surface does not exist as shown in Figure 2.
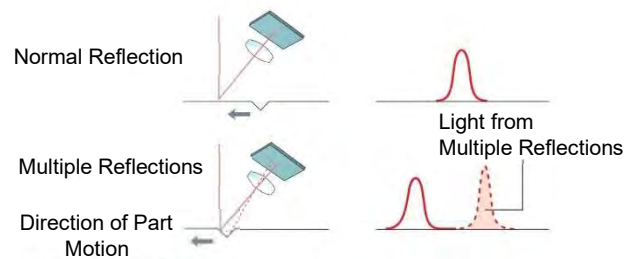
FIGURE 2. Multiple light reflection [2]

To eliminate the undesired reflected light on the sensor plane during a gear flank surface scan, there are manual parameters control the desired evaluation area called generation area. Only scattered light captured inside this area would later form one small portion of the scanned surface. Adjusting this desired area so that firstly it covers the entire ridge line and secondly it eliminates undesired light reflection while it is wide enough for the small predicted movement of the ridge line over a flank scan, the majority of the multiple light reflection can be avoided. Figure 3 shows how the generation area concept eliminates the undesired multiple light reflection in the root area of the gear flank.

Additionally, the instrument used for this study has 6 moving axes including three rotational and three translational axes. After adjusting the flank position so that the ridge line is at the center of the sensor plane, there are some setting parameters that can be changed to adjust the light intensity throughout the ridge line.

FIGURE 1. The intensity of the sensor data vs the ridge line in triangulation sensor [2, 3]
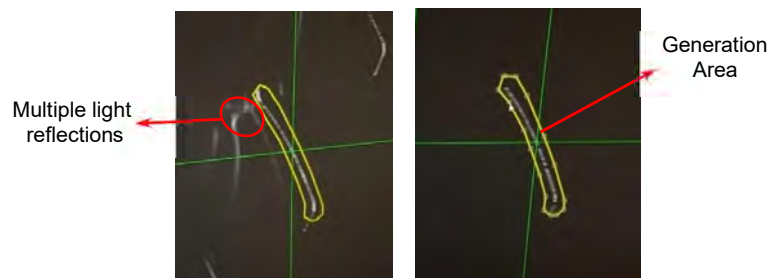
FIGURE 3. Generation area and multiple light reflections

By adjusting two rotational axes, A and B (tilt head axis and rotary table axis), a more or less uniform intensity, in which the maximum intensity does not vary significantly over the line, can be achieved. This can also play an important role in reducing too high intensities, especially at the tip and root area, thereby reducing the multiple light reflections.

ACCEPTANCE IN AUTOMOTIVE INDUSTRY

Optical sensors are adopted in gear measurement for the advantages of high-density data sampling and short cycle time, while the evaluations of geometric parameters are still based on standardized line-oriented algorithms dominantly. Areal evaluations with extended modification and deviation parameters [1] enable three-dimensional representation of surface features and holistic assessments of the entire gear. The areal parameters characterize features that are currently used in industrial inspections, such as profile and helix slope and pitch deviations. In addition, complex surface features, such as triangular relief modifications and waviness, which require measurements of multiple lines with tactile sensors and extensive data analysis with line-oriented algorithms, are more comprehensively sampled by optical sensors and precisely represented by areal parameters.

Table 1 shows a comparison of evaluation results of an automotive gear sample from three different instruments with both line- and area-oriented evaluations. The three evaluations are presented in a random sequence as A, B, and C, which are based on, respectively: 1. tactile measurements with line-oriented evaluations from a commercial software; 2. tactile measurements with areal evaluations; and 3. optical measurements with areal evaluations. 6 deviation parameters are evaluated in each case.

For the slope, crowning, and single pitch deviations, the maximum difference across the three cases is 3.1 µm, while the measurement uncertainty of these parameters in the given experimental condition is typically not less than 3 µm. Therefore, the optical measurements and areal evaluations offers effective results which are comparable to the standard methods. The range of difference for twist is 3.9 µm. In the line-oriented evaluation, the average of profile and helix twists is listed as the holistic twist, which is sensitive to the measurement diameter of the profiles.

TABLE 1. Comparison of evaluation results from three experiments with different instruments and evaluation methods (numbers are in µm)

| PARAMETERS	EVALUATIONS		
	A	B	C
PROFILE SLOPE DEVIATION	-1.4	0.8	-2.0
PROFILE CROWNING	4.3	5.7	7.2
HELIX SLOPE DEVIATION	-1.1	-2.2	0.9
HELIX CROWNING	9.0	9.0	9.4
TWIST	24.4	20.5	21.6
SINGLE PITCH DEVIATION	1.1	2.0	2.2

Figure 4 illustrates the evaluation of a gear flank with tip and root triangular relief modifications. The point cloud consists of the plumb line distances from the sampled points to the nominal three-dimensional gear model. The center (non-modified) region and the triangular relief regions are approximated, respectively. The amount of measured root triangular relief (symbolized by f_{CEfC}^{A}) is defined to be the maximum distance between the center plane and the root triangular relief plane in the plumb line direction within the evaluation range (at the profile control diameter). The transition line is computed at the intersection of the center and the relief planes. Thus, the length of the relief and alignment of the transition area could be evaluated. Similarly, the measured tip triangular relief f_{CEaC}^{A} is defined.
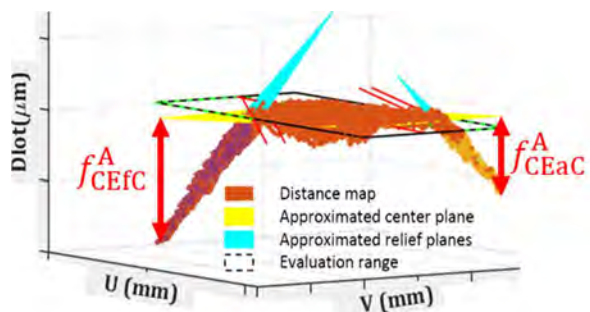
FIGURE 4. Areal evaluations of gear flank with triangular relief modification

EVALUATION TIME

Some efforts have been made to reduce the measurement time and evaluation time. So far,

the evaluation starts after all the gear flanks are measured. An alternative approach is to evaluate the gear parameters flank by flank. After one flank measurement is finished and parallel to the measurement of the next flank, the previously captured flank data is evaluated. This can reduce the evaluation time significantly. Another proposed alternative is to partially measure the flanks around a target flank by adjusting the generation area appropriately as shown in Figure 5.
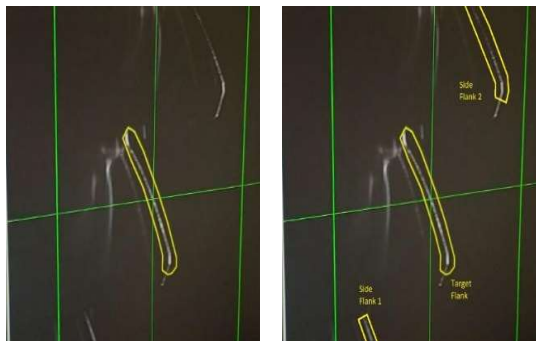
FIGURE 5. Partial measurement of side flanks

CONCLUSION AND FUTURE WORK

Fast optical measurement coupled with areal evaluation method provides a substantial data for gear inspection to meet the pressing need to fast holistic evaluation of commercial gears, especially in today's automotive industry where the main manufacturing processes of mid-size automotive gears take short time period. Developing new methods to remove the current obstacles in optical inspection when using triangulation sensors, in terms of reduction in large form deviation, elimination of multiple light reflections, and improvement in evaluation time, improve the quality of manufactured gears by reducing measurement uncertainty while simultaneously save the production time. Comparing the evaluation results of tactile measurements with line-oriented evaluations, tactile measurements with areal evaluations, and optical measurements with areal evaluations, the maximum difference among the results is within the measurement uncertainty. Therefore, the results verify the effectiveness of the adopted laser triangulation sensor, areal parameters, and algorithms. There are still more open research opportunities on the measurement uncertainty, filtering of the sensor signal, the development of peak detection algorithm, and the improvement of the evaluation process.

REFERENCES
[1]   F. Gert Goch, Kang Ni, Yue Peng, Anke Guenther, "Future gear metrology based on areal measurements and improved holistic evaluations" 2017 CIRP Annals - Manufacturing Technology 66: pg 469–474.
[2]   Cincinnati Automation, laser Measurement Product Brochure, Yumpu, 2020. Accessed on Jul. 9, 2020. [Online]. Available: https://www.yumpu.com/en/document/read/11746393/laser-measurement-product-brochure-cincinnati-automation
[3]   Vision Spectra, A 3D Triangulation Vision System, Photonics, May 15, 2017. Accessed on Jul. 10, 2020. [Online]. Available: https://www.photonics.com/Articles/Configuring_a_3D_Triangulation_Vision_System/a62061

CURVED-EDGE DISPLACEMENT SENSOR FOR SPINDLE DYNAMIC IDENTIFICATION

Seungjoo Lee[1], Jungsub Kim[1], ChaBum Lee[1], and Gregory W. Vogl[2]
[1]J. Mike Walker '66 Department of Mechanical Engineering
Texas A&M University
College station, TX, USA
[2]Production of Systems Group
National Institute of Standards and Technology
Gaithersburg, MD, USA

INTRODUCTION
Spindle plays the most important role on machine tools due to the fact that it determines the productivity and efficiency of the machine [1]. Therefore, the technological demands on the spindle toward high accuracy and efficiency have been significantly highlighted recently. Along with the development of the spindle technology, the significance of monitoring, diagnosing, and predicting spindle conditions including its dynamic behavior has also been emphasized because identification of the spindle dynamics such as runout measurement, stiffness and damping effects may provide useful information of tool life, tool integrity and quality of the part such as shape and surface roughness [1]. Furthermore, monitoring the spindle dynamic condition can prevent unexpected tool failure and reduce the downtime of the machines.

Conventionally, capacitive sensors (CS) are used for identification of the spindle dynamic due to its high bandwidth and inhomogeneity from the material [2]. Numbers of CS are mounted on the rotating shaft in the direction of x, y and z in order to measure the conditions of the spindle. The CS, however, are calibrated with the flat surfaces which may cause measurement error while obtaining the information of cylindrical target because different behavior may occur between a flat and curved surface [3]. Possible errors when monitoring the spindle condition using CS may be noise issue in case of interference between CS and non-linearity of displacement measurements due to the curved surface.

The spindle dynamic identification technologies other than using CS are widely studied. Slatter investigated the monitoring spindle condition using giant magneto-resistive and found out that the system is capable of measuring displacements with a resolution of better than 0.5 μm with high repeatability [4]. Postel studied a method to estimate the cutting forces at the milling tool using vibration sensor and found out that displacement estimations were within 80% [5]. Lee at al. proposed a novel dimensional sensing methodology for a curved surface using lasers based on curved edge diffraction [3]. Lee at al. compared with conventional CS and 0.017% discrepancy in full range was observed.

In this study, Curved-Edge Sensor (CES) based on the curved edge diffraction was developed to observe the spindle identification. The CES was compared with CS in terms of runout measurement and impact test. In addition, CES was compared with 3-axis force sensor to monitor the force implied while cutting the part.

CURVED-EDGE SENSOR
In the study, an alternative measurement sensor, CES was used for curved surface methodology. Due to the limitation of understanding of curved edge diffraction that it is difficult to define an illumination of the edge by different wavefronts, the CES was investigated through experimental approach. The figure 1 shows the schematics of the CES. It is consists of 4 avalanche photodetectors (APD), prisms and the laser diodes. The laser light is incident on the curved surface of the spindle shaft with a radius R, and then transmitted wave, reflected wave, edge diffracted wave and the edge excited waves are detected by four APDs. Signals of X and Y axis will be measured by APD 3 & 4 and APD 1 & 2 respectively. The powers of laser diodes are both 870 μW and the polarizations of APDs for X and Y axis were proceeded in order to incident same power. The incident power from the prism was 210 μW and

200 μW for X axis APDs and 150 μW and 155 μW for Y axis APDs. Low pass filter of 15 KHz were implied for all APDs. The sensor output of X and Y axis are expressed as,

$$V_{out,x} = k_3 V_3 - k_4 V_4 \qquad (1)$$

$$V_{out,y} = k_1 V_1 - k_2 V_2 \qquad (2)$$

Where, $V_{out,x}$ and $V_{out,y}$ are the calibrated measurement of CES X and Y axis respectively, k values are the gain factors compared by the sensitivities of each APDs measured and values of V are the actual signal outputs of APDs. The APDs used in this experiment have the active diameter of 500 μm. The CES was designed to measure the spindle shaft diameter of 12.7 mm. The developed sensor was then mounted inside the spindle as shown in figure 2.
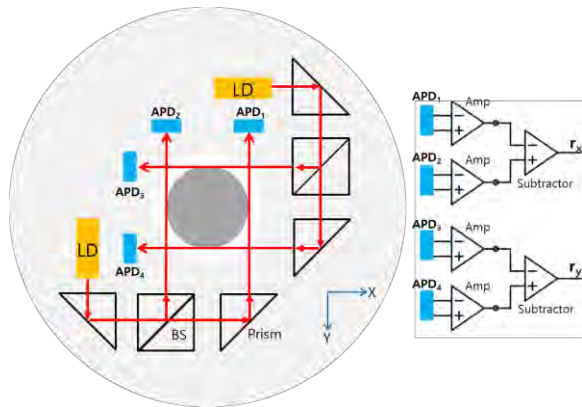
FIGURE 1. Schematics of CES and amplifier
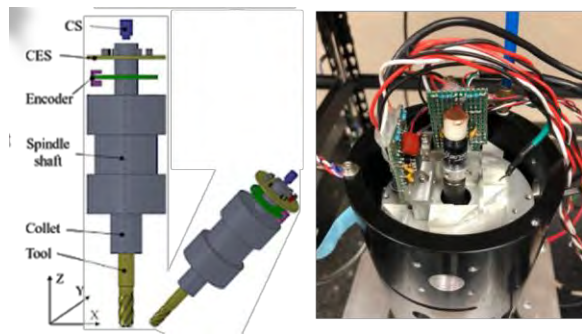
FIGURE 2. Schematic and the picture of spindle system with CES

CALIBRATION
The calibration test was carried out using CS and CES simultaneously. The calibration data of two CS were obtained in prior to determine the CES displacement measurement in respect to

signal outputs. The measured displacements of X and Y axis using CS were used as reference. The sensitivities of two CS were 13.8 mV/um and 10.7 mV/um, respectively, with the range within 500 um.

The diameter 12.7 mm rod, which has the equivalent diameter to the shaft of the experiment spindle system, was implemented on the manual XY stage and installed at the center of the CES to determine the calibration measurement of CES. Two CS were also aligned along X and Y axis of CES. Then the rod was moved manually in x and y direction and signals of CES and CS have been monitored through NI LabView with the sampling frequency of 10 kHz. The figure 3 shows the calibration data of CES. With four signals of APDs, the amplifier was developed with the low pass filter with cutoff frequency of 15 kHz to determine the CES sensitivity of X and Y axis. The CES sensitivity of the X and Y direction obtained were 0.502 mV/um and 0.503 mV/um respectively with the standard error of 1.0% and 1.2% respectively, within the output range of ±10V.
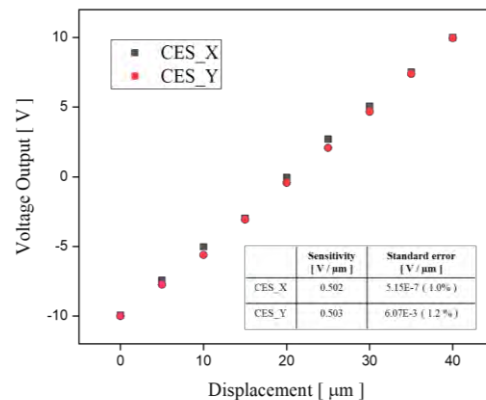
FIGURE 3. CES calibration of X and Y axis

The CES resolution along the X and Y axis was measured. While the air bearing spindle was in stationary, the CES data was collected for 10 second. The CES resolution was estimated approximately 20nm peak-to-peak.

STIFFNESS TEST
The stiffness represents a ratio of applying force and displacement. The air-bearing spindle was used to measure the stiffness by CES. As shown in figure 3, CES was calibrated with CS. Figure 5 shows the CES displacement results in terms of force applied. Both displacement of the CES was measured at the top plane (see figure 2) of the spindle. The force was implied at the

tool tip in order to identify the displacement change with the force. The 3 x 3 stiffness matrix of the spindle was achieved as,

$$\begin{bmatrix} k_{xx} & k_{xy} & k_{xz} \\ k_{yx} & k_{yy} & k_{yz} \\ k_{zx} & k_{zy} & k_{zz} \end{bmatrix} = \begin{bmatrix} 0.213 & 0.012 & 0 \\ 0.011 & 0.210 & 0 \\ 0 & 0 & 0.083 \end{bmatrix} \quad (3)$$
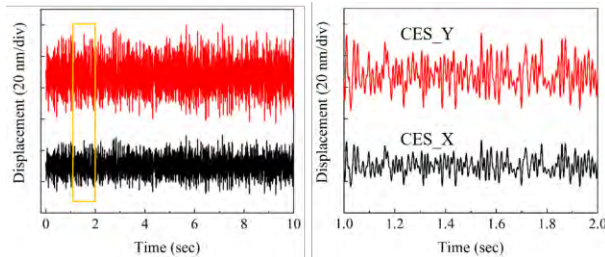
Figure 4. CES resolution test results
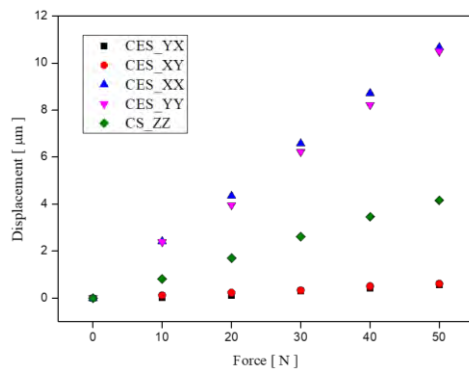
FIGURE 5. Displacement results of CS and CES according to the force applied.

IMPACT TEST

The dynamic characteristics of the spindle were also determined by the DSA test using CS and CES. The magnitude and phase plots of the spindle system with two different sensors are shown in figure 6. The experiments were carried out using the Agilent 35670A Dynamic Signal Analyzer. CES and CS were implemented at the same position of the shaft. The first peak obtained by CES and CS both showed at 42 Hz which showed a good agreement.

RUNOUT MEASUREMENT

For runout measurement experiment, air spindle was used to test the dynamic behaviors of CES and CS. The experiments were carried out in different speeds varying from 500 to 3500 rpm. The radial runout measurements of the spindle using CS and CES were compared at identical XY axis position. The data were obtained using NI LabVIEW data acquisition board.

The figure 7 shows the comparison of CS and CES runout experiment at spindle speed of 1200 rpm and 2520 rpm. The overall tendency of the runout measurements for both speed showed similar results with a slight difference in the measurement values due to different characteristics of CES and CS. For 1200 rpms, CES and CS had variation of approximately 4 µm. The difference in the measurement value may be caused by the different behaviors between flat and curved surface of the surface. The CES, on the other hand, lasers were positioned incident to the curved surface of shaft which could detect the radial runout of the shaft in regardless of the shape of the target surface and solely dependent on the calibration results based on curved edge diffraction. For other rotation speeds, both CES and capacitive showed a good agreement with the displacement and the runout shape as well.

At the speed of 2520 rpm at which the spindle rotated at its natural frequency (42 Hz). CES and CS showed similar tendency that the Lissajous pattern showed oval shape with the displacement of approximately 6 µm in X-direction and 4 µm in Y-direction.
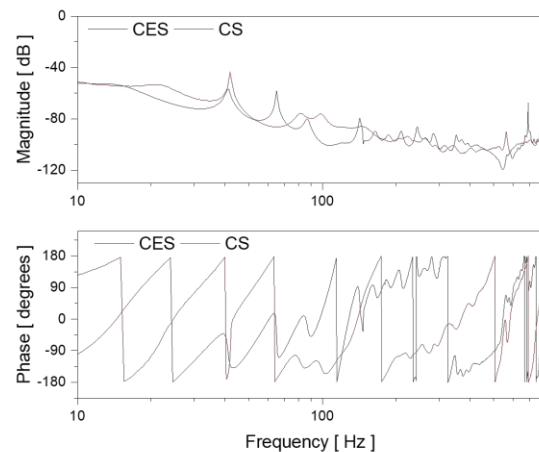
Figure 6. Impact Test comparison between CS and CES

CUTTING EXPERIMENT

To test CES for cutting force measurement, the cutting experiment was built, and the data (CES output x stiffness matrix) could be compared with the 3-axis force sensor results.

Figure 8 shows the picture of the cutting experiment. The force changes in terms of CES displacement changes during the cutting process were compared with the force sensor which was mounted within the cutting part. We

are going to machine the parts under various cutting conditions, and then, two results obtained by CES and 3-axis force sensor will be compared in terms of resolution, dynamic characteristics, noise, etc. to see if the CES can be used for cutting force measurement.
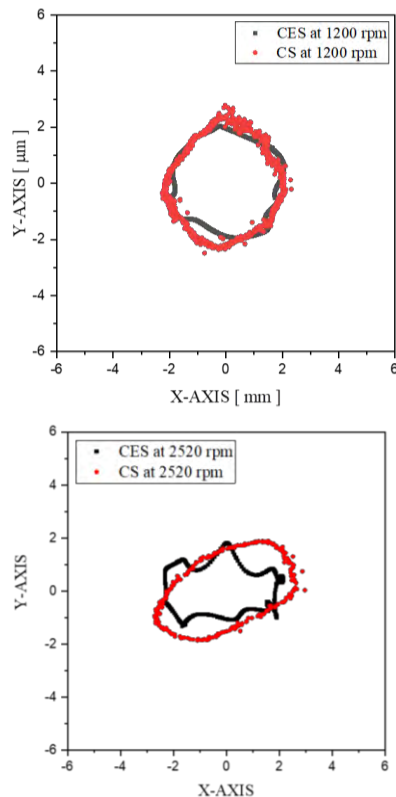
Figure 7. Runout measurement comparison using CS and CES at 1200 rpm (top) and 2520 rpm (bottom)
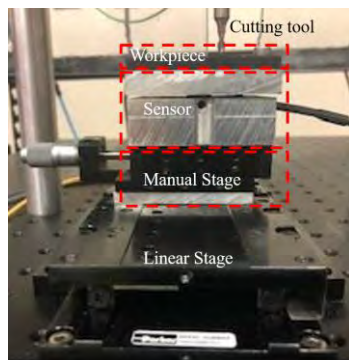
FIGURE 8. Picture of the cutting experiment

CONCLUSION

In the study, CES was developed to observe the spindle static and dynamic behavior. The dynamic characteristics of CES were compared conventional sensors to verify its high potential to the alternative spindle monitoring sensor due to its capability of identifying spindle dynamics and low cost. The results of the experiments are as follows.

1)The X and Y axis sensitivities of CES were found to be 0.502 and 0503 V/um with the standard error of 1.2% and 1.0% respectively in 40 um range. Also, dynamic behaviors of the sensor showed good agreement with the conventional sensor.

2) Using the CES, the dynamic characteristics of the spindle were determined. It was found from the runout measurement and impact test that the tendency showed a good agreement with that obtained by the CS.

3) The dynamic characteristics during the machining process will be characterized by CES and be validated by the conventional force sensor.

REFERENCES

[1] Kim, J., Zhao, S., Kim, G. H., & Lee, S. K. (2013). Rolling bearing-suspended spindle run-out control using repetitive control and adaptive feedforward cancellation. Inter feedforward cancellation. International journal of Precision engineering and Manufacturing, 14(12), 2171-2178

[2] Marsh, E. R. (2010). Precision spindle metrology. DEStech Publications, Inc.

[3] Lee, C., Mahajan, S. M., Zhao, R., & Jeon, S. (2016). A curved edge diffraction-utilized displacement sensor for spindle metrology. Reivew of Scientific Instruments, 87(7), 075113.

[4] Slatter, R., Holland, L., & Abele, E. (2016). Magnetoresistive sensors for the condition monitoring of high-frequency spindles. Procedia CIRP, 46(1), 177-180.

[5] Postel, M., Aslan, D., Wegener, K., & Altintas, Y. (2019). Monitoring of vibrations and cutting forces with spindle mounted vibration sensors. *CIRP Annals*, *68*(1), 413-416.

ACKNOWLEGEMENT

HIGH-PRECISION METROLOGY WITH HIGH-RESOLUTION COMPUTED TOMOGRAPHY USING 3D X-RAY MICROSCOPES

Herminso Villarraga-Gómez[1], Naomi Kotwal[2], Victor Ninov[2], Lars Omlor[3], Abhinav Mishra[2], Bruce Johnson[2], Robert Zarnetta[4], Daniel Weiß[4], Wolfgang Kimmig[4], Martin Krenkel[4], and Christoph Graf vom Hagen[2]

[1]Carl Zeiss Industrial Metrology, LLC, Wixom, MI, USA
[2]Carl Zeiss X-ray Microscopy, Inc., Pleasanton, CA, USA
[3]Carl Zeiss, Inc., White Plains, NY, USA
[4]Carl Zeiss Industrielle Messtechnik GmbH, Oberkochen, Germany

The use of industrial X-ray computed tomography (CT) for dimensional metrology has become an important aspect of modern quality control [1, 2, 3]. The CT technique presently contributes to geometric dimensioning and tolerancing of mechanical parts (and other device components) for technology and manufacturing companies. It is used as a tool for nondestructive dimensional quality control in various industries, such as automotive, aerospace, electronics assembly and packaging, medical devices, injection molding, casting, and additive manufacturing. However, even under optimal measurement conditions, the technologies for CT dimensional metrology have traditionally been limited to spatial resolutions no better than 3–10 µm. This leads to several challenges for measuring samples of small dimensions (with volumes in the order of a few mm^3)—e.g., low signal-to-noise ratio in the CT data, and limited detection of contrast changes and spatial details. To overcome these challenges, the authors of this paper have developed a package—a solution consisting of hardware and software—for performing high-precision metrology using the high-resolution capabilities of ZEISS Xradia Versa 3D X-ray microscopes (XRM, or sub-micron CT systems), which can attain spatial resolutions better than 1 µm (e.g., 0.5 µm with the Versa 620 model). This new package, Metrology Extension (MTX) for Xradia Versa, includes a workflow designed to adjust and calibrate the XRM system to perform metrology tasks. Once the MTX calibration workflow is executed, the system can be used to measure small volumes, in the order of (5 mm)^3 or less, with high dimensional accuracy.

The main purpose of this paper is to present, evaluate, and analyze, the experimental results of several measurement tests to verify the metrological performance of several XRM systems after calibration (and pre-setting of the instrument's work zone) with MTX. In addition, examples of industrial measurement applications that use the MTX workflow are presented.
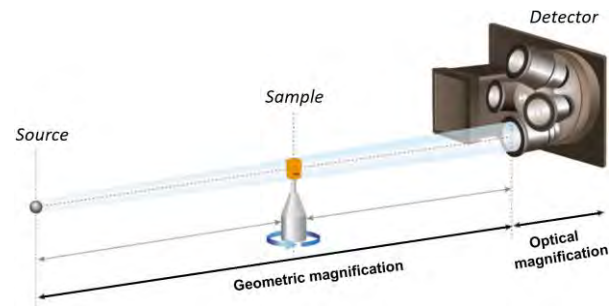
FIGURE 1. Two-stage magnification architecture of the ZEISS Xradia Versa 3D X-ray microscopes. The combination of both geometric and optical magnification enables high-resolution capabilities.

VERIFYING MEASUREMENT ACCURACY

The only reference document with procedures for testing dimensional CT systems is the guideline VDI/VDE 2630-1.3 [4], which was released as the first framework for acceptance testing of X-ray CT systems. In accordance with that guideline, a (multi-sphere) length standard was developed—at Carl Zeiss Industrielle Messtechnik GmbH [5]—for verifying the accuracy of the CT dimensional measurements on small objects that fit in a 5 mm field-of-view (FOV). This length standard consists of 22 identical ruby spheres of 300 µm diameter, and a roundness (form error) that is consistent with the Anti-Friction Bearing Manufacturers Association (AFBMA) criteria for Grade 5 ball or better (tolerances specified by deviations of ±0.13 µm of the combined diameter and roundness of the spheres), attached to a supporting structure made of fused silica (with coefficient of thermal expansion $\alpha \approx 0.55$ µm·m^{-1}·°C^{-1}). See Figure 2 inset or Ref [5]. The spatial arrangement of the spheres enables a distinctive number of different lengths (at least 5 different distances), in a total of 7 different spatial directions, to implement the acceptance test suggested in the VDI/VDE 2630-1.3 guideline. The test evaluation for CT systems typically includes comparisons between the length measurements obtained from CT data and other more accurate and precise reference measurements such as those acquired from a

tactile coordinate measurement machine (CMM). In this work, the reference measurements for the various sphere distances on the multi-sphere standard, measured between the sphere centers, were carried out by the Federal Institute of Metrology METAS, at Switzerland, with an ultra-precise CMM dedicated for calibrating small size objects in 3D (METAS µCMM [6]). The reported uncertainty for the reference measurements, stated as the combined uncertainty multiplied by a coverage factor k = 2, is

$$U_{ref}(k = 2) = 0.138 \text{ µm.} \quad (1)$$

This is the associated expanded uncertainty for the reference measurements, for a confidence level of 95.45 %, which was estimated following the guidelines of the Guide to the Expression of Uncertainty in Measurement (GUM) [7].
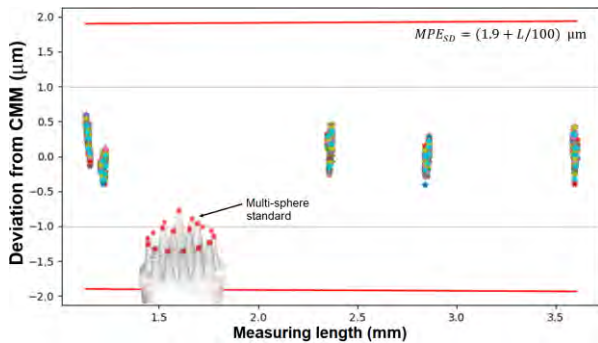
FIGURE 2. Deviations of CT (XRM) dimensional data (from reference data obtained from tactile CMM) for center-to-center length measurements on a multi-sphere standard (of 22 ruby spheres of 300 µm diameter). Data points of different colors represent different test runs.

The evaluation of metrological performance of the Xradia Versa systems (for length measurements), after execution of the MTX calibration, can be assessed by plotting deviations between CT data and CMM references, as shown in Figure 2. After determining the sphere centers with the Gauss (or least-squares) best-fit method, a total of 35 different center-to-center length measurements were evaluated on the multi-sphere standard. As seen from Figure 2, the deviations of CT dimensional measurements (from reference CMM data) are confined to a range between ±0.7 µm. This range is well within a conservative specification of MPE (Maximum Permissible Error), for center-to-center sphere distance (SD), of

$$MPE_{SD} = (1.9 + L/100) \text{ µm,} \quad (2)$$

with L measured in mm. The results shown in Figure 2 provide a proof of accuracy for the metrological capabilities of ZEISS Xradia Versa (at FOV = 5 mm) with the added MTX workflow, enabling high-precision metrology performance over small scale volumes (in the order of 125 mm³ or less).

REPEATABILITY AND REPRODUCIBILITY
To verify the measurement repeatability of Versa XRM, after the MTX workflow is applied, 30 different scans of the multi-sphere standard were performed with three different systems (i.e., 90 scans total). Figure 3 shows the results of dimensional data for one of the largest center-to-center length measurement (~3.605 mm) in the multi-sphere standard. The repeatability standard deviations of the results, assessed per measuring system are $S_1 = 0.08$ µm, $S_2 = 0.06$ µm, and $S_3 = 0.11$ µm; and the reproducibility standard deviation across the three systems is $S_R = 0.36$ µm. From these measures, the deviations between measurements performed on the same feature of length, repeated through 90 different scans, are in the range of ±0.48 µm. The results shown in Figure 3 serve as a proof of repeatability and reproducibility for dimensional measurements with Versa XRM.
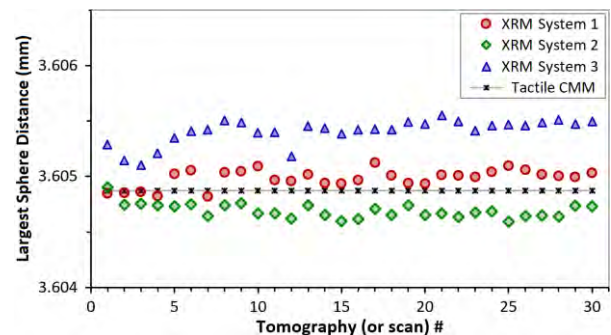
FIGURE 3. Dimensional data for the largest center-to-center sphere distance, in the multi-sphere standard, when the same length measurement is repeated throughout 90 different scans (from three different XRM systems).

INDUSTRIAL METROLOGY APPLICATIONS
Due to its unique capability for the nondestructive assessment of part geometries not accessible to traditional tactile or optical CMMs, e.g., internal cavities and difficult-to-reach or 'hidden' features, the number of industrial applications for X-ray CT in the field of dimensional metrology has been

increasing in the last couple of decades [1, 8]. This section presents examples of dimensional measurement use cases on small industrial devices (a smartphone camera lens module, the tip of a fuel injector nozzle, and a plastic injection-molded connector) performed with XRM systems and assisted by the execution of the MTX workflow.

Smartphone Camera Lens Assembly

In the assembled state of smartphone camera lens modules, the assessment of geometrical properties of the lenses such as thickness of annular wedges, centration interlock diameters, gaps between wedges, lens-to-lens tilt, apex heights and centration, etc., require a non-contact and nondestructive method for measurement. These measurements are important for functional inspection of camera lens modules, and the enhancement of manufacturing designs and processes, to enable the production of versatile cameras to improve the cell phone image quality. Figure 4 shows the 3D image of a smartphone camera lens assembly reconstructed from XRM data. Since the largest dimension of interest in the assembly is around 4.4 mm, a cylindrical region of about 5 mm diameter was scanned from the full camera lens module. Before the acquisition of the CT data, the MTX workflow was applied to verify the measurement accuracy of the measuring system, so that the dimensional measurements extracted from the virtual reconstruction of the camera lens module are accurate. Figure 4 shows examples of typical dimensions of interest in the camera lens in its assembled state.

FIGURE 4. *Dimensional measurement of a smartphone camera lens module, in its assembled state, using 3D CT data reconstruction.*

Tip of a Fuel Injector Nozzle

To facilitate an efficient spray of fuel in internal combustion engines (and uphold lower emissions requirements), fuel injectors use high injection pressures with small nozzle orifices. Since variability of geometric features of the injector nozzle, such as inlet corner sharpness and orifice diameters, can have influence on the internal flow and spray of fuel in combustion engines, manufacturing deviations from nominal nozzle design are typically measured for dimensional quality control. In this case, to measure the smaller nozzle orifices in the fuel injector nozzle (features difficult-to-reach with measuring systems using tactile or optical probes), CT is uniquely suited for dimensional measurement. Figure 5 shows the clipped/semi-transparent view of CT data reconstructed for the tip of a fuel injector nozzle. The size of the region of interest, the tip portion of the fuel injector, is revealed by the dimensions shown in the image (~2.4 mm for the largest diameter). Since the region of interest fits in a volume of less than $(5 \text{ mm})^3$, the MTX workflow was executed, before scanning the tip of the fuel injector, for verification of measurement accuracy of the XRM system. Then, the dimensional check of the small nozzle orifices was performed.

FIGURE 5. *Clipped and transparent view of the CT reconstruction of the tip of a fuel injector nozzle showing measurement of internal cavities.*

It is worth noting, in Figure 5, that the blue spots in the image reveal the presence of voids inside the injector nozzle walls. This is an additional advantage of measurement inspections based on voxel (volumetric) data, so added to the reconstruction of all internal and external surfaces of a mechanical workpiece, material testing can

be performed in the same CT data set. In this case, the high-resolution capabilities of the ZEISS Xradia Versa system used for CT scanning permitted the visualization of the porosity present in the inside the injector nozzle.

Plastic Injection-molded Connector

For the inspection of both internal and external structures in small plastic injection-molded parts, X-ray CT can be better suited for geometrical measurement as compared to contact or vision-based inspection techniques. Non-contact measurement is important to avoid distortions of easy-to-deform or flexible components. In injection-molded workpieces, dimensional measurements assist the determination of the deviations in manufactured parts as compared to the nominal geometry specified in the original computer-aided-design (CAD) models of the part. This is important for product development, quality assurance of part's functional features, and structural integrity assessment of industrial manufactured components and assembled devices. Figure 6 shows the example of a small plastic connector, reconstructed from CT data, featuring dimensional measurements. Again, since the largest length measurement of the connector is about 4 mm, this sample fits well within a volume of less than $(5 \text{ mm})^3$. Therefore, the MTX workflow was used before X-ray scanning the sample for verification of measurement accuracy of the XRM system. Then, the CT data shown in Figure 6 was acquired for dimensional measurements.
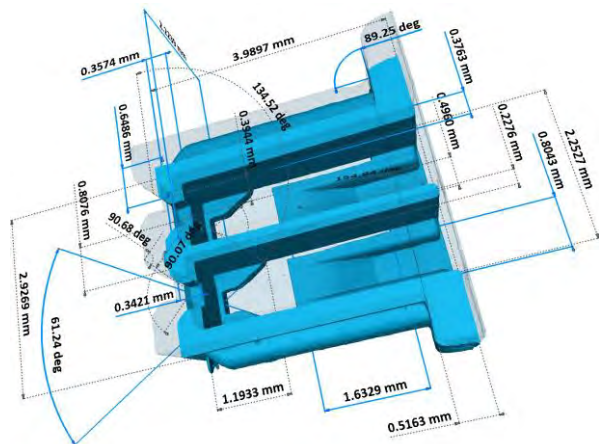

FIGURE 6. Clipped and semi-transparent view of of a small plastic connector, reconstructed from CT data, featuring dimensional measurements.

CONCLUSIONS

After implementation of the MTX workflow (for dimensional metrology) in several high-resolution X-ray CT systems (XRM), the metrological performance of such systems was evaluated. The main results show that XRM systems can perform high-precision dimensional measurements in small scale volumes (in the order of $(5 \text{ mm})^3$ or less), providing measurement accuracies comparable to those offered by tactile CMM (with deviations within the range of ±0.95 µm), while also preserving high-resolution characteristics of the CT voxel data—a unique feature that is useful for other types of nondestructive quality control using the same data. In this paper, three application examples illustrate the unique capability, and further potential, of the MTX workflow for dimensional measurements on small industrial devices.

REFERENCES

[1] H. Villarraga-Gómez, E. L. Herazo and S. T. Smith, "X-ray computed tomography: from medical imaging to dimensional metrology," *Precision Engineering,* vol. 60, pp. 544-569, 2019.

[2] H. Villarraga-Gómez, C. Lee and S. T. Smith, "Dimensional metrology with X-ray CT: A comparison with CMM measurements on internal features and compliant structures," *Precision Engineering,* vol. 51, pp. 291-307, 2018.

[3] A. Buratti, J. Bredemann, M. Pavan, R. Schmitt and S. Carmignato, "Applications of CT for Dimensional Metrology," in *In Industrial X-Ray Computed Tomography (Eds: Carmignato S., Dewulf W., and Leach R.)*, Cham, Switzerland, Springer, 2018, pp. 333-369.

[4] VDI/VDE 2630-1.3, Computed Tomography in Dimensional Measurement - Guideline for the application of DIN EN ISO 10360 for coordinate measuring machines with CT sensors, Berlin (Germany): Beuth Verlag GmbH, 2011.

[5] D. Weiß, W. Kimmig, R. Lonardoni, M. Ilzhöfer, M. Krenkel and C. Kuhn, "Verifying the measurement accuracy for X-ray cone-beam CT scans of objects smaller than 5 mm diameter," in *iCT 2019—9th Conference on Industrial Computed Tomography*, Padova, Italy, 2019.

[6] A. Küng, F. Meli and R. Thalmann, "Ultraprecision micro-CMM using a low force 3D touch probe," *Measurement Science and*

Technology, vol. 18, pp. 319-327, 2007.

[7] ISO/IEC Guide 98-3, Uncertainty of measurement — Part 3: Guide to the expression of uncertainty in measurement (GUM:1995), Geneva (Switzerland): ISO copyright office, 2008.

[8] L. De Chiffre, S. Carmignato, J. P. Kruth, R. Schmitt and A. Weckenmann, "Industrial applications of computed tomography," *CIRP Annals - Manufacturing Technology,* vol. 63, no. 2, pp. 655-677, 2014.

THE ROLE OF VISUALIZATION AND ERROR CORRECTION IN VERY LARGE AREA, TIP-BASED TOPOGRAPHY MEASUREMENT

Liam G. Connolly[1], Eva Natinsky[1], Niyaz Khusnatdinzov[2], Chris Jones[2], Makoto Mizuno[2], Mario Meissl[2], Jin Choi[2], Dwayne LeBrake[2], and Michael Cullinan[1]
[1]Walker Department of Mechanical Engineering
The University of Texas at Austin, Austin, TX, USA
[2]Canon Nanotechnologies, Inc, Austin, TX, USA

INTRODUCTION

With technical advances in tip-based measurement tools and increasing market pressures in the ever-advancing semiconductor industry, both the capabilities and need for nm-scale topography measurement over mm (wafer) scale distances have come to a confluence. Unlike optical-based measurement methods such as laser profilometry or white light interferometry where correction for prefabricated, potentially unknown, thin film stacks with disparate optical properties is required, tip-based measurement can occur without any *a-priori* pattern or fabrication knowledge [1], [2]. In addition, intermittent contact "tapping mode" atomic force microscopy (AFM) techniques allow for long scanning periods without significant tip wear or damage to the measured sample [3]–[5]. In this operational mode, the AFM tip height is regulated in a closed loop manner in order to lock-in to an amplitude or phase peak in the oscillating cantilever signal. As the tip is scanned, the relative Z motion of the AFM tip positioner from the point of engagement is used to determine the topography of the sample beneath the AFM tip.

In traditional applications, the scale of this tip scanning typically results in square image with side dimensions of 128, 256 or 512 pixels, or roughly 10^5 to 10^6 individual measurement sites [6]–[8]. However, while these square AFM scans can provide valuable information for various relevant, sub-diffraction critical dimensions like step height, line edge roughness, and feature pitch, it does little to elucidate the overall sample topology for full die or full wafer measurement. As such, there has been a push to develop new, high-speed atomic force profilers (AFPs) [9]–[15] which are able to scan over larger distances to measure topography profiles on a length scale relevant to die-to-die and wafer-to-wafer correction methods used in modern nanofabrication.

APPARATEUS

The methods described in this work were developed to enhance the measurement capability of a commercially available, AFM-based, 300 mm wafer measurement tool. This tool, which is outlined in Fig. 1, consists of a piezo-based stage mounted to a granite gantry structure which positions a self-contained AFM head in the X, Y, and Z directions in a closed loop
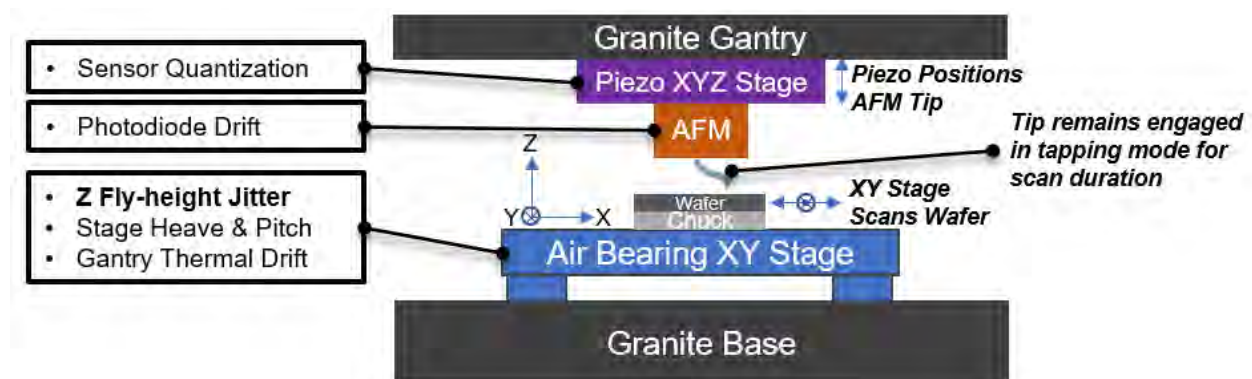

FIGURE 1: Cartoon Outline of Instrument Mechatronic Setup with major sources of error (boxes) and operational details (italics) highlighted.

fashion with capacitance probe feedback sensors and a maximum range of ~100 µm in each axis. Below it, a wafer is positioned by a commercial, air bearing based XY stage with a range > 300 mm.

While the tool can be used in a more traditional sense, where the air bearing stage moves the wafer and parks such that the AFM-Piezo-Stage system is above the region of interest, and the piezo raster scans the AFM tip across its 100 µm x 100 µm range. Of greater interest, however, is the tool's long-range profiling capability. In this mode of operation, the piezo stage still actuates the tip height control loop, but the air bearing stage is scanned at ~1 mm/s while the tip is still engaged. This scanning is typically defined by two principal, and ideally orthogonal, directions: slow- and fast-scan. In fast scan, or profiling direction, the data spacing can range from nm to µm scale, while the slow scan direction typically has data spacing on the µm to mm scale. A depiction of the scan path with respect to the desired scan area can be seen in Fig. 2.

With this relatively unique capability comes a significant difficulty -- as overall data density can easily exceed 10^6 discrete measurements per mm^2, a typical data set could exceed 10^9 points. Two central challenges must be considered before precise conclusions may be drawn about sample topography: (1) how to efficiently visualization scan data in a lossless manner, and (2) how to compensate for the most significant sources of scan error.

DATA VISUALIZATION STRATEGY
A typical fast-scan length of ~30 mm at high-density data collection settings could contain ~1,250,000 data points, and assuming a maximum pixel density which can be perceived by the average human of 300 pixels per inch (PPI), a lossless, full-field visualization for such a scan would require a monitor screen greater than 100 m wide – an obvious impossibility. At the same time, if viewed at full fidelity in a piece-wise fashion on a standard, 4K (3840 px x 2160 px) computer monitor, it would take an operator reviewing over 300 individual, zoomed in subsections to cover the entire scan profile of a single die. As both options are wildly impractical, a different approach is taken.
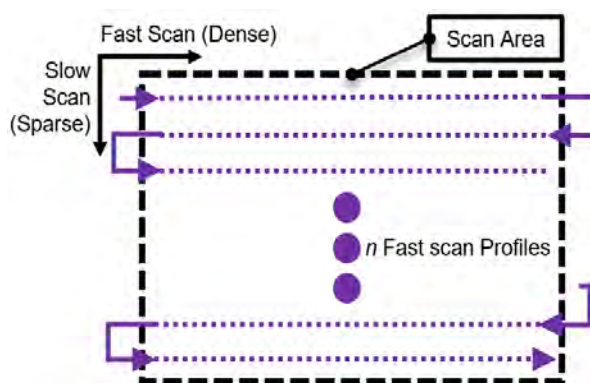

FIGURE 2: Schematic of Tip-based Profiling Procedure.

Ideally, an operator could zoom in to and inspect areas of interest across a 26 mm x 33 mm die, while also being able to visualize and inspect the die as a whole to the best ability of the pixel density of the screen used – essentially down sampling the data to match the binning of the display. Assuming even a relatively short duration (i.e. coarse in slow-scan) die mapping scan with 500 µm slow-scan spacing and 25 nm fast-scan data spacing, this relatively low-density scan easily exceeds 67,000,000 data points. Rendering all the data points at once with a CPU-based routine would be extremely time consuming even with the highest performance hardware available.

Thus, an Open Graphics Library (OpenGL) based, GPU accelerated approach is taken. The high number of parallel compute cores and high memory bandwidth allow for real time manipulation – panning, changing orientation, and zooming in and out – of > 120 million data points in a seamless fashion with the hardware used (Intel Xeon Gold 6254, NVIDIA Quadro RTX 5000) [16]. At full zoom, the individual quantization levels of the Z height capacitance sensor are visible (< 500 pm), and while zooming out the entire die is also visible (26 mm x 33 mm). A screen shot of this OpenGL, 3D point cloud visualization is shown in Fig. 3 where scan data is taken across a bare, silicon wafer [17], [18].
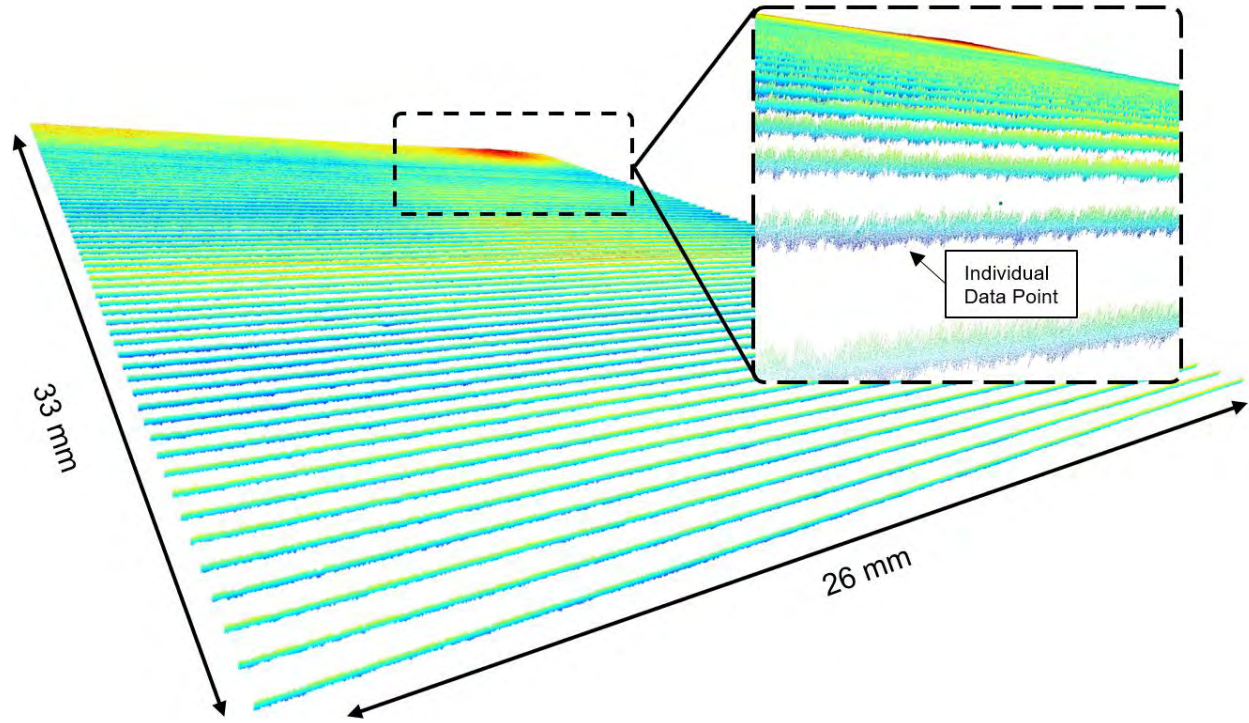
FIGURE 3: OpenGL-based, GPU accelerated data visualization showing scan area overview (~66 million points) and a zoomed in detail where individual data points are visible (dashed box).

DENOISING BY PIECEWISE POLYNOMIAL BASED FITTING AND REFINEMENT

Furthermore, apart from visualization challenges and the classical sources of error in tip-based measurement such as cantilever measurement photodiode sensitivity drift and piezo stage sensor quantization error, the air bearing stage mechanical system which scans the sample beneath the measurement tip is much more susceptible to various sources of error compared to classical atomic force microscopes solely with µm-range piezoelectric scanners. These errors include thermal drift over the potential hour- and day-scale scanning times, and the various motions of the air-bearing based positioning stage relative to the measurement tip. As such, separation of the real sample topography from this polluted data is of critical importance to leveraging this measurement capability for the development of novel nanomanufacturing processes.

While thermal effects can be mitigated by increasing the slow-scan data spacing to thereby reduce overall scanning time, the most significant source of error which must first be corrected is the

$$S(t) = \sum_{i=0}^{m-p-1} N_{i,p}(t)P_i \ (1)$$

$$Z = \{\zeta\}_0^m = (\ \zeta_0 = \zeta_1 = \cdots \zeta_p < \ \zeta_{p+1} \leq \zeta_{p+2} \leq \ldots \leq \zeta_{m-p-1} \leq \zeta_{m-p} = \zeta_{m-p+1} = \cdots = \zeta_m)\ (2)$$

$$N_{i,0}(t) = \begin{cases} 1 \text{ if } \zeta_i \leq t\ < \zeta_{i+1} \ (3) \\ 0 \end{cases}$$

$$N_{i,j}(t) = \frac{t - \zeta_i}{\zeta_{i+j} - \zeta_i} N_{i,j-1}(t) + \frac{\zeta_{i+j+1} - t}{\zeta_{i+j+1} - \zeta_i} N_{i+1,j-1}(t) \ (4)$$

air bearing fly height jitter – seen in the data as a ±~20 nm band of noise in the topography data.

To accomplish this, a piecewise polynomial, specifically a non-uniform basis spline (NURBS), fitting approach was chosen to fit the noisy point cloud data. This fitting technique uses a b-spline, represented by $S(t)$ in Eq. 1 where P_i is the *i'th* control point and $N_{i,p}(t)$ the *i'th, p* degree basis function. This basis function is defined based on a monotonic vector *Z*, or the knot vector, and defined in Eq. (2). The basis function is then defined as the recursive series shown in Eq. (3) and (4) [17], [18]. By controlling the placement and number of knot vectors, control points can be added to the NURBS control polygon, shown in Fig. 4 in black along with a cubic NURBS curve which is separated into its three constituent polynomial curves by color – red and blue. As can be seen, the repeated knots at the beginning and end of the curve force the first and last curve points to be coincident with the first and last control point. By altering the XY location of each control point (i.e. the "pull" on the NURBS curve by each control point), and the knot vector itself to selectively add or remove control points, a

NURBS curve can be fit to a given data set by generating control points based on a least squares based minimization of NURBS curve error to the point cloud data.

In order to drive an accurate fit, an iterative algorithm is developed to refine the NURBS curve where error is high, typically around sharp features such as high-density lines and spaces. Here an initial, fixed length, uniform knot vector is generated, and a thusly fixed degree of freedom curve is fit to each fast scan profile with an initial least squares error minimization. Curve fit error is then pooled from the point cloud data, peaks in this curve error are identified, and knots are added to the knot vector sampled from random distribution centered at the peak of the error and with a standard deviation proportional to initial pixel lateral spacing. Control points corresponding to this new, refined knot vector are then once again calculated from a least squares minimization of error to the point cloud and the process repeated until an error based stopping tolerance is reached. A flowchart representation of this NURBS refinement algorithm is shown in Fig. 5.
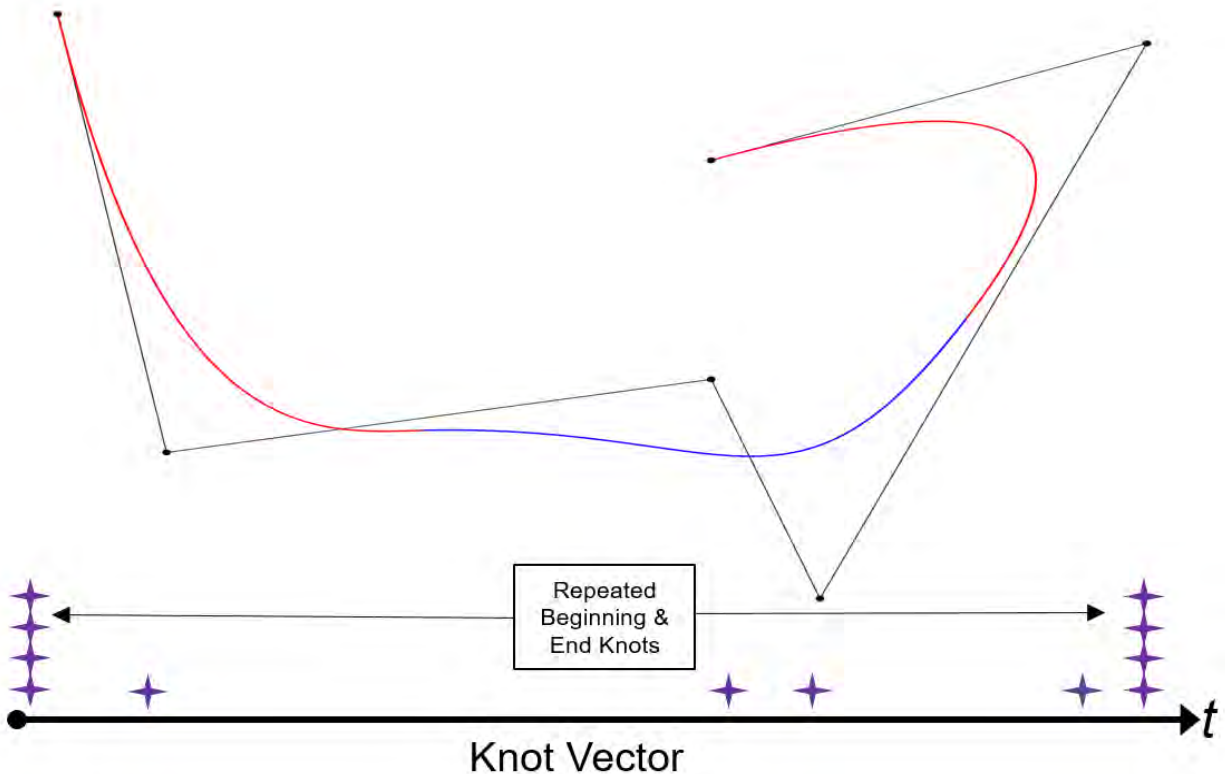

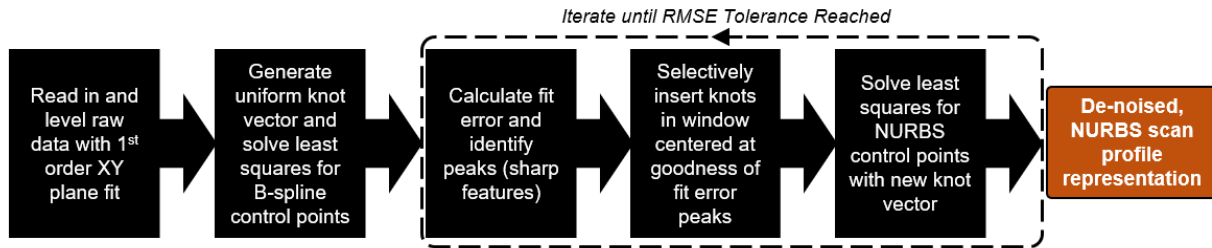*FIGURE 4: Basic outline of a basis spline curve with control polygon and knot vector highlighted*

FIGURE 5: Flowchart of NURBS fitting and refinement algorithm

CONCLUSION AND FUTURE WORK

This paper has posited a framework to begin the process of meaningful visualization and denoising of very large area, tip-based topography measurements with mm-scale fast scan lengths on a silicon wafer. Future efforts will center on the generation of known, ground truth test artifacts and synthetic, noise pollution of these ground truth artifacts in order to test the efficacy of the proposed fitting algorithm, and further algorithm development to optimize fitting control knobs such as error tolerance, minimize computation time, and ensure knot insertion window and knot vector optimality.

REFERENCES

[1]   G. Binnig, C. F. Quate, and Ch. Gerber, "Atomic Force Microscope," *Phys. Rev. Lett.*, vol. 56, no. 9, pp. 930–933, Mar. 1986, doi: 10.1103/PhysRevLett.56.930.

[2]   Zygo, "Optical Profiler Basics," 2019. https://www.zygo.com/?/met/profilers/opticalprofilersabout.htm.

[3]   R. García, "Dynamic atomic force microscopy methods," *Surface Science Reports*, vol. 47, no. 6–8, pp. 197–301, Sep. 2002, doi: 10.1016/S0167-5729(02)00077-8.

[4]   A. D. Mazzeo, A. J. Stein, D. L. Trumper, and R. J. Hocken, "Atomic force microscope for accurate dimensional metrology," *Precision Engineering*, vol. 33, no. 2, pp. 135–149, Apr. 2009, doi: 10.1016/j.precisioneng.2008.04.007.

[5]   N. Sarkar, G. Lee, and R. R. Mansour, "CMOS-MEMS dynamic FM atomic force microscope," *2013 Transducers and Eurosensors XXVII: The 17th International Conference on Solid-State Sensors, Actuators and Microsystems, TRANSDUCERS and EUROSENSORS 2013*, pp. 916–919, 2013, doi: 10.1109/Transducers.2013.6626917.

[6]   S. Zhao and Q. Yang, "A stitching method for AFM based large scale scanning with high resolution," *IFAC Proceedings Volumes (IFAC-PapersOnline)*, vol. 19, pp. 2697–2702, 2014.

[7]   I. Misumi, S. Gonda, T. Kurosawa, and K. Takamasu, "Uncertainty in pitch measurements of one-dimensional grating standards using a nanometrological atomic force microscope," *Measurement Science and Technology*, vol. 14, no. 4, pp. 463–471, 2003, doi: 10.1088/0957-0233/14/4/309.

[8]   N. Sarkar, D. Strathearn, G. Lee, M. Olfat, and R. R. Mansour, "A 0.25mm3 Atomic Force Microscope on-a-chip," in *2015 28th IEEE International Conference on Micro Electro Mechanical Systems (MEMS)*, Jan. 2015, pp. 732–735, doi: 10.1109/MEMSYS.2015.7051062.

[9]   S. V. v Sreenivasan, "Nanoimprint lithography steppers for volume fabrication of leading-edge semiconductor integrated circuits," *Microsystems & Nanoengineering*, vol. 3, no. April, p. 17075, 2017, doi: 10.1038/micronano.2017.75.

[10]   P. Ajay and S. v. Sreenivasan, "Nano - Precision Systems for Overlay in Advanced Lithography Processes," 2019, pp. 1–11.

[11]   C. Wagner and N. Harned, "EUV lithography: Lithography gets extreme,"

Nature Photonics, 2010, doi:
10.1038/nphoton.2009.251.

[12]   A. Cherala *et al.*, "Addressing
nanoimprint lithography mix and match
overlay using drop pattern
compensation," vol. 11324, no. May, p.
10, 2020, doi: 10.1117/12.2552023.

[13]   A. Cherala *et al.*, "Topography and
flatness induced overlay distortion
correction using resist drop pattern
compensation in nanoimprint lithography
systems," vol. 10958, no. May, p. 11,
2019, doi: 10.1117/12.2515146.

[14]   N. MURASATO and T. Arai, "Progress
in nanoimprint wafer and mask systems
for high volume semiconductor
manufacturing," vol. 10807, no. May, p.
16, 2018, doi: 10.1117/12.2326865.

[15]   Corp. Bruker, "Bruker AFMs for
Semiconductor Metrology," 2019.
https://www.bruker.com/products/semico
nductor-metrology/automated-afm.html.

[16]   Q.-Y. Zhou, J. Park, and V. Koltun,
"Open3D: A Modern Library for 3D Data
Processing," *CoRR*, vol. abs/1801.0,
2018, [Online]. Available:
http://arxiv.org/abs/1801.09847.

[17]   V. T. Dung and T. Tjahjowidodo, "A
direct method to solve optimal knots of
Bspline curves: An application for non-
uniform B-spline curves fitting," *PLoS
ONE*, vol. 12, no. 3, pp. 1–24, 2017, doi:
10.1371/journal.pone.0173857.

[18]   L. Piegl and W. Tiller, "The NURBS
book, 2nd edition," *Springer-Verlag*.
1997.

FEEDBACK SENSING AND DYNAMIC OPERATION OF THE LIGHTFIELD DIRECTING ARRAY

Robert M. Panas[1], Princess Corral[1], Steve Hunter[1], Phillip Paul[1], Jeff Scott[2], Miguel Piedrahita[2]
[1] Lawrence Livermore National Laboratory
Livermore, California, USA
[2] 219 Design
Mountain View, California, USA

INTRODUCTION

We have developed an analog circuit to carry out simultaneous sensing and actuation on the electrostatic capacitors driving the lightfield directing array (LDA). The LDA is a high-bandwidth, large-range and high precision micromirror array which is capable of analog, closed-loop control in three degrees of freedom (DOFs)—tip, tilt, and piston. The combination of range, speed and capability for feedback control through exact constraint place the potential capabilities for the system well outside the present state-of-the-art [1]. Such a system could enable advances in a range of fields including laser communications, lidar, displays and optical manufacturing equipment.

This work focuses on the development and testing of the feedback sensing capability enabled by the sense/actuate circuit, with preliminary results of the closed loop performance metrics.
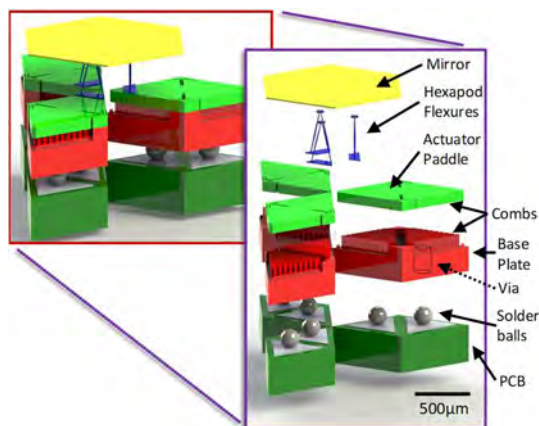

FIGURE 1: LDA MEMS Micromirror Array, showing a single cell with the three driving paddles below the single hexagonal mirror (left). Exploded view of the unit cell layered architecture (right).

OVERVIEW

The combined system contains several elements, all of which contribute to the feedback and control design, this includes the LDA, the drive circuit, the sense circuit and the feedback algorithm.

The LDA MEMS device is shown in Figure 1. This structure uses three symmetrically distributed paddles, each driven with two electrostatic comb drive actuators, which can only generate an attractive force. The mobile paddle is grounded, while the mechanically grounded side of the electrostatic combs are set to the drive voltage. A vertical force and thus a rotation-inducing moment can be generated on each paddle in either direction by using one of the electrostatic comb drives. Each paddle is constrained to only one degree of freedom (a rotation) by a carefully designed set of flexures near the center of the paddle. The mirror location is exactly constrained by the rotation of the three paddles. The three vertical transmissions for the three paddles set the height of the mirror at three places, determining the mirror tip, tilt and piston degrees-of-freedom. The capacitance of the electrostatic combs varies with the angle of overlap, between an expected value of around 0.1pF at equilibrium to approximately 1-1.5pF at maximum overlap. The capacitance of the disengaged comb drive decays rom 0.1pF towards 0. This capacitance signal is used to determine orientation.

The drive circuit utilizes high voltage amplifiers to simultaneously boost function generated sinusoids up to 200V and combine the drive (up to 40kHz) and excitation signals (4MHz). The high voltage drive signal provides the potential that is needed to pull the electrostatic combs down towards the wafer, thus changing the capacitance of the combs. As the paddles are actuated by the drive signal, the capacitance on the electrostatic combs change in response, which is then measured by the change in

amplitude of the excitation signal. The sense circuit then isolates and magnifies the changing excitation signal to measure and characterize the changing comb capacitance.

The sense circuit draws on previous efforts to monitor capacitance in MEMS devices [2] and uses a drive modulator, high-side sense resistor, high pass filter, demodulator and low pass filter all in sequence. The drive signal rejection is accomplished through two approaches. The first is the use of a differential measurement across the sense resistor to nominally remove the high voltage. The second is the use of filters to exploit the frequency sparation between the drive signal (up to 40kHz) and the sense modulation (4MHz).

A differential op-amp approach is used to initially isolate the differential voltage across the sense resistor. This provides some level of sense signal isolation, however more will be needed to cleanly observe the sensor reading. The differential op-amp circuit is shown in Fig. 1 below.
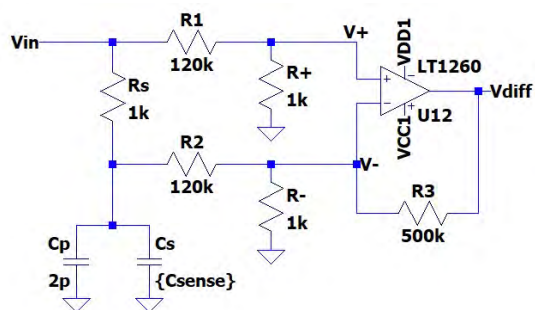
FIGURE 1. Schematic of differential op amp.

High pass filters were designed to pass through the sense modulation while heavily attenuating the drive modulation. These are used to boost the high frequency 4MHz voltage signal coming out from across the sense resistor as well as attenuate the low frequency signals due to the high voltage actuation op-amp. The high pass filter circuit is shown in Fig 2. below
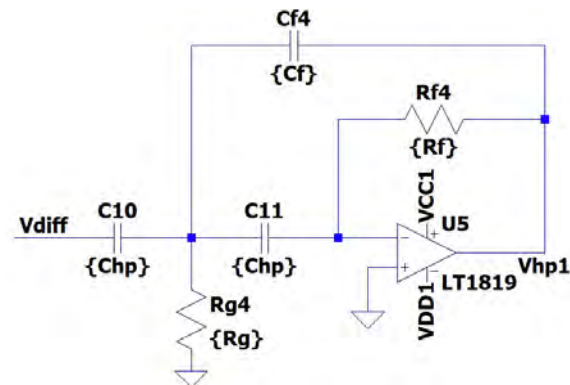

FIGURE 2. Schematic of high pass filters.

The frequency response of the high pass filters are shown in Fig. 3 below and account for the majority of the sense signal isolation. Per filter, there is 70dB of isolation between the excitation and drive frequencies, with a max gain of 23dB at the excitation frequency.
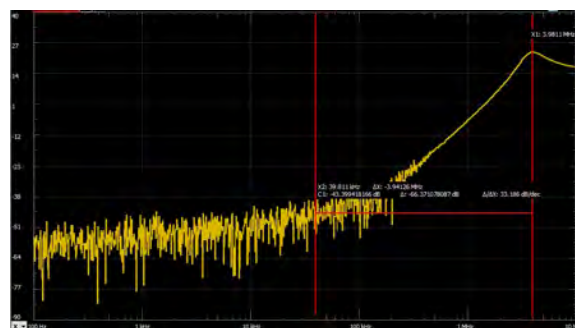

FIGURE 3. High pass filter frequency response

The sense modulation contains information about capacitance stored in the signal amplitude. The amplitude of the sense modulation is extracted with a half-wave rectifier placed after the high-pass filters. The rectifier circuit is shown in Fig. 4 below.
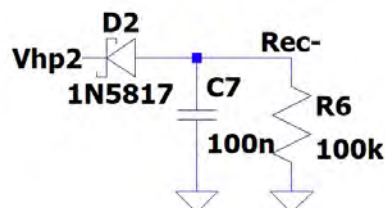

FIGURE 4. Rectifier circuit

A low pass filter is located at the output of the peak-detect circuit to suppress all signal outside of the sensing bandwidth. A critically damped

second order filter is used to quickly attenuate high frequency signal out of the sensor. The low pass filter circuit is shown in Fig. 5 below.
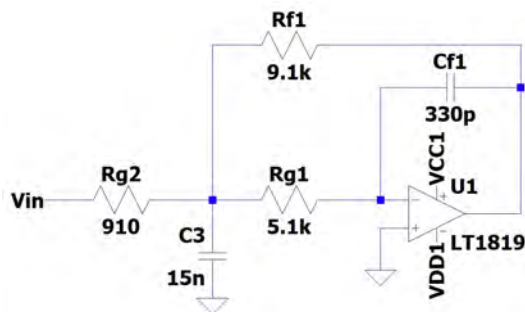

FIGURE 5. Low pass filter circuit

RESULTS

The sense capability of the circuit and MEMS device is quantified through several metrics. First is the sensitivity to changing capacitance. The second is the ability to reject variations purely in drive voltage. The third is the noise in the output measurement. The fourth is the sensor bandwidth. These metrics provide a rough picture of the feedback capability provided by the sense/actuate board.

The sensitivity to capacitance was initially measured by attaching capacitors of known value to the circuit and mapping the output voltage change, as shown in Figure 3 below. RF tuning capacitors within 0.1pF to 1.5pF were used to measure the sensitivity of the sense circuit. Data was gathered over two different rectifier methods to prove repeatability and consistency. The output response to input capacitance changes are linearly related.
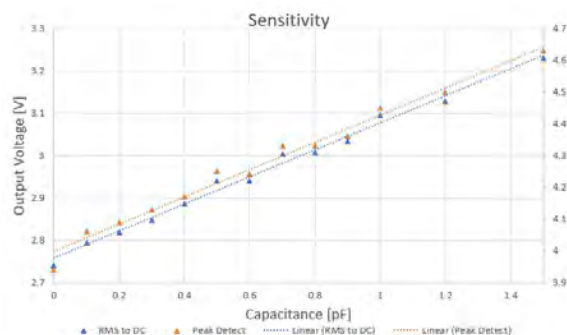

FIGURE 3: Capacitance sensitivity.

The drive voltage rejection ratio, circuit output noise, and dynamic range are to be measured by spectral analysis while maintaining a constant capacitance. We expect to be able to present these full results at the annual conference.

ACKNOWLEDGEMENTS

REFERENCES

[1] Song, Y., Panas, R. M., & Hopkins, J. B. A review of micromirror arrays. Precision Engineering. In Press (2017).

[2] Hung, A.C.L., Lai, H.Y.H., Fu, S.G., and Lu., M.S., An electrostatically driven 2D micro-scanning mirror with capacitive sensing for projection display. Sensors and Actuators A: Physical, 222, 122-129. (2015)

Design and Fabrication of Connected Chains of Mechanical Logic Bits

Frederick Sun[1], Logan Bekker[1], Robert M. Panas[1], Andrew J. Pascall[1], Amin Farzaneh[2], and Jonathan B. Hopkins[2]
[1]Lawrence Livermore National Laboratory (LLNL), Livermore, CA, USA
[2]Department of Mechanical and Aerospace Engineering, University of California Los Angeles, Los Angeles, CA, USA

INTRODUCTION
In this paper, the authors demonstrate the design and fabricated pieces of several mechanical logic bits connected in a chain like fashion in a tabletop demonstration and in micro-scale. The connected mechanical logic bits transmit their logic state from one logic bit to the next, thereby propagating a mechanical signal along the serial chain of mechanical bits similar to an electrical signal passing down a wire. The ability to transmit logic states between mechanical bits allows separate mechanical logic elements to function with one another, enabling computation being carried out by a mechanical logic circuit.

Mechanical logic computation offers several advantages over their traditional semiconductor counterparts in specialized scenarios. Mechanical logic elements based on force and displacements are insensitive to radiation, moisture, and can survive higher temperatures where semiconductors are prone to failure, By storing the energy needed for operation in the form of elastic potential energy within the elements before deployment, mechanical logic circuits have low energy consumptions and lay dormant for a prolonged period without a power source. In applications such as smart sensors in hazardous environment or when constant maintenance is unfeasible, devices utilizing micro-mechanical logical computation provide a promising solution.

DESIGN OF A CHAIN OF MECHANICAL LOGIC BITS
The mechanical logic chain in this paper comprises of two components: mechanical logic bits and compliant connectors joining them, as shown in figure 1. The mechanical bits are bi-stable micro-flexures that indicate their logic state of 0 and 1 with their two stable equilibrium states, after fabrication they are compressed and forced into one of their bi-stable states. Each mechanical bit in the chain is of different stiffness, ordered from the stiffest to the most compliant, gradually lowering along the chain. An input force or displacement is fed into the stiffest mechanical bit within the chain, switching the logic state of the mechanical bit. The switched mechanical bit then compresses or stretches its adjacent compliant connector, momentarily storing the energy of the input pulse in the form of elastic potential energy, such that the input does not need to overcome the stiffness of the mechanical gates combined all at once, then switching the subsequent mechanical bit with said energy. With a gradually lowering flexure stiffnesses, each mechanical bit will have enough energy to overcome the energy barrier of the subsequent gates.
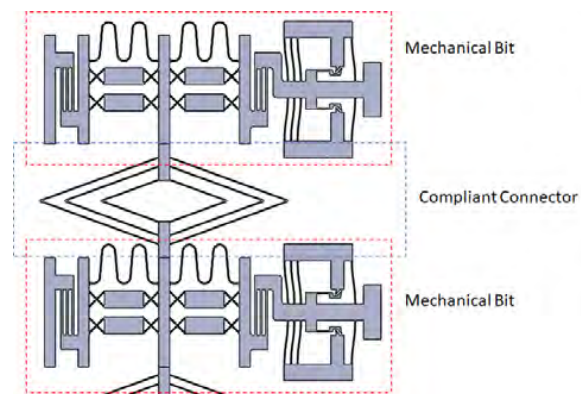

Figure 1. Two connected mechanical logic bits

FABRICATION OF MICRO-MECAHNICAL BITS
A chain of micro-mechanical bits is constructed with two-photon polymerization, and a tabletop-scale gate chain is constructed as a proof-of-concept for the mechanical pulse propagation.

DAMPING CHARACTERISTICS OF FLUIDIC PRESSURE-FED MECHANISM IN DYNAMIC SYSTEMS AND CONTROL

Heebum Chun[1], Jungsub Kim[1], Hyo-Young Kim[2], and ChaBum Lee[1]
[1]J. Mike Walker '66 Department of Mechanical Engineering
Texas A&M University
College station, TX, USA
[2]Manufacturing System R&D Group
Korea Institute of Industrial Technology
Cheonan-si, Chungnam-do, 31056, South Korea

ABSTRACT
This paper represents a fundamentally new approach that enables in-process control of the damping parameters of dynamic systems by using a fluidic pressure-fed mechanism (FPFM). The various fluids (air, water, oil) under adjustable pressure conditions can be filled in the internal structures of nanopositioning system fabricated by metal (Stainless Steel) additive manufacturing process. The damping characteristics according to the fluids and their pressure levels was experimentally studied through free vibration tests, forced vibration tests, open-loop response tests, and closed-loop response tests. The relationships between damping characteristics and fluidic pressure-fed conditions were characterized. As a result, the FPFM has the following characteristics: (1) water-filled condition showed the highest damping increasing, (2) damping decreases as the pressure level increases, and (3) existence of fluid and pressure inside fluidic channel does not influence the motion quality when FPFM is in positioning controlled. The outcomes of this study will potentially provide utilization in noise and vibration control applications for high precision dynamic systems.

INTRODUCTION
The speed and resolution of many machines, such as scanning probe microscopy [1-3], nanofabrication [4], precision optics [5] and aerospace systems [6], are limited by the presence of lightly damped mechanical resonances. Since conventional damping methods, such as viscoelastic damping or tuned-mass absorbers, are bulky and may not work well in low-frequency ranges, the shock absorbers and electromagnetic dampers are often used in many practical applications. Such damping systems require additional hardware (e.g., springs, pneumatic/hydraulic cylinders or electromagnetic coils) and periodic maintenance because of friction, wear or pre-load change.

Electromagnetic damping works for contactless magnetic force, and is environmentally friendly since there is no need of using oils, thus avoiding friction and wear issues, increasing reliability. Nevertheless, critical issues remain, such as system ageing, reduction of external electromagnetic interferences, and frequency tuning. Recently, an active damping control utilizes a sensor and feedback control loop as an alternative method to artificially adjust the damping ratio of the dynamic system such as positive position feedback (PPF) [7], polynomial based control [8], shunt control [9-11], resonant control [12], force feedback [13-16], and integral resonance control [17-20]. It is not an overstatement to say that active damping control is solely a matter of easily programmable and reliable software and precision feedback sensors. Those software and sensors are often expensive and require periodic maintenance. Thus a technological gap exists in weightless, maintenance-free active damping control devices available for micro- and nano-scale motion systems.

In this study, damping-controllable structures and mechanism are monolithically imbedded in the linear motion system for a simple, efficient and inexpensive damping control. The proposed FPFM is driven by the pneumatic or hydraulic pressure control in the fluidic channels created inside of the compliant mechanisms enabling to in-situ tune the dynamic characteristics (stiffness and damping) of the dynamic systems.

FLUIDIC PRESSURE-FED MECHANISM
In the study, the double compound-type flexure mechanism with the internal fluidic channels (2.5 mm × 2.5 mm) was designed as shown in Figure 1, and was fabricated by metal (Stainless Steel) additive manufacturing. The piezoelectric actuator (5 mm × 5 mm × 10 mm) can be placed, and the rectangular fluidic channels have bilateral symmetry. Pressure gauges are placed at the inlet and outlet of the fluidic channels, so

the pressure level (pressure difference) in the internal fluidic channels can be monitored.
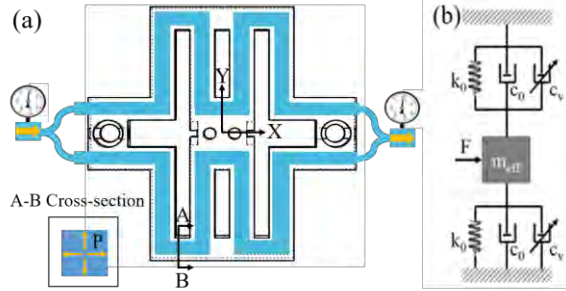

FIGURE 1. Compliant mechanism with integrated FPFM (a) and dynamic model (b)

In this study, considering the pressure-fed medium (air, water, and oil) and their pressure levels, the fluidic channel's geometric effects, the dynamic model of the FPFM can be newly developed and will be implemented in the closed-loop control system available for compliant mechanism as shown in Figure 1. The c_0 and c_v are damping parameters of the compliant mechanism and PFM, k_0 is the stiffness of the compliant mechanism, and m_{eff} is the effective mass of the system.

EXPERIMENTS

The experiment for the damping characterization was set up as shown in Figure 2. The piezoelectric actuator was placed to cause the motion of nanopositioning system and the capacitive sensor (CS) was placed to measure the displacement for free-vibration, frequency response, open-loop, and closed-loop response tests according to fluid types and corresponding pressure levels.
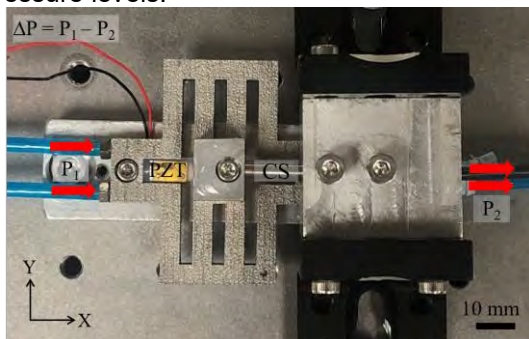

Figure 2. Experiment setup for damping characterization

In this study, six different cases of damping characterizations were evaluated and compared that are ambient, pneumatic air pressure (80 psi), water-filled, hydraulic water pressure (80 psi), oil-filled, and hydraulic oil pressure (80 psi) conditions.

Frequency response
The frequency responses of FPFM were acquired by hammering tests to characterize the damping variances fluid types and corresponding pressure levels. Dynamic signal analyzer (DSA, Agilent 35670a) was used to gather displacement (CS, bandwidth ~10 kHz) and excitation force (PCB 086C03) inputs and to plot the frequency response curve as shown in Figure 3.
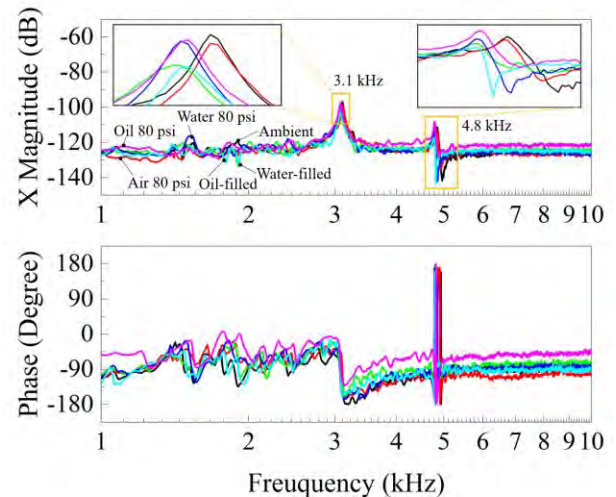

Figure 3. Frequency response curve of FPFM under various media and pressure conditions

The fundamental resonance frequency was found out to be approximately 3.1 kHz, and the second-mode (torsional vibration) was approximately at 4.8 kHz. This result showed that according to fluid types and pneumatic/hydraulic pressure condition conditions existed in the fluidic channels, the resonance peaks can remarkably shift towards to left in both cases of the first and second mode of resonance and the amplitude of the peak can change due to the increase in damping. Interestingly, the water-filled case, denoted as a green line in the bode plot, showed the highest damping on FPFM by looking at the stance width. Based on the frequency response curve, the Q-factors were able to obtain which can compare the disparities of damping of the dynamic system under varying conditions. As a result, the water-filled case showed the smallest Q-factor which tells the highest damping ratio followed by oil-filled, hydraulic oil pressure (80 psi), hydraulic water pressure (80 psi), compressed air pressure (80 psi), and ambient as shown in Figure 4. Hence, it was validated

that the existence of fluid types and pneumatic/hydraulic pressure inside of fluidic channels can change the damping, and can affect dynamic characteristics of dynamic system.
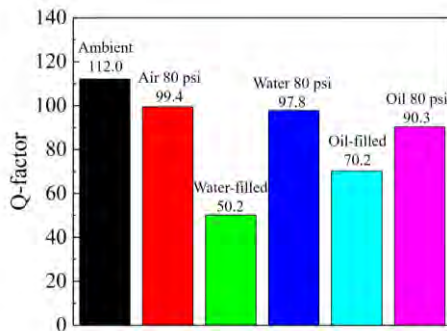

Figure 4. Calculated Q-factor based on the bode plot

Free-vibration test

Free-vibration test was performed to characterize the effects of existing fluid and pressure conditions inside fluidic channels on damping. The CS was used to collect the displacement data while the shuttle part of FPFM was freely excited. The oscillations occurred due to the excitation was able to assess. Five trials were completed for each different condition to achieve the repeatability. Based on the free-vibration test result as shown in Figure 5a, envelope curves shown in 5b were extracted by using Hilbert transformation to evaluate the damping ratio. When evaluating the envelope curve, the first 30 milliseconds of oscillation information result were used to show the optimal damping comparison with varying conditions.
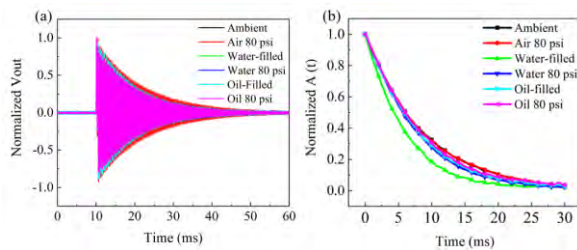

FIGURE 5. Normalized free-vibration result (a) and corresponding envelope curve (b)

From the drawn envelope curves, as similar to the frequency response result from the previous analysis, the water-filled condition showed the radical exponential decaying curve which implies the highest damping ratio. Damping coefficients with respect to varying conditions were able to calculate by taking the coefficient of exponential function with the natural frequency that could be

obtained from the free-vibration oscillation. Figure 6 shows the calculated damping ratio of each varying conditions. As same as the Q-factor calculation, the calculated damping coefficient indicated that it is highest when an internal fluidic channel of FPFM filled with water. On the other hand, the channel filled with oil and applied the pneumatic/hydraulic pressure, it also showed some increase in damping; however, the result was comparably smaller than the water condition. This was thought due to the higher density of water. Moreover, although pressure applied conditions showed damping increasing, applying compressed pressure of 80 psi rather makes the system to be rather rigid. Therefore, the pressure conditions had comparably less effect than natural media filled conditions and damping was decreased as pressure increasing.
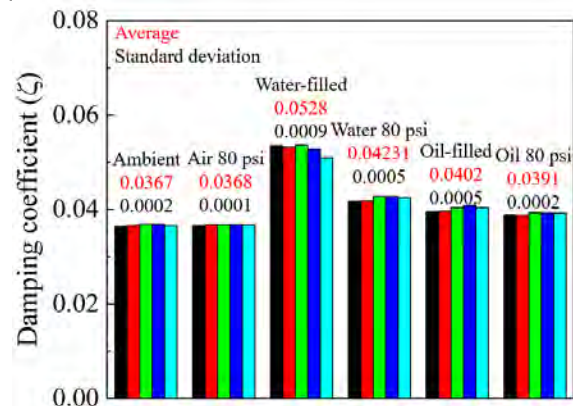

Figure 6. Calculated damping coefficient based on the envelope curve

Open loop motion

The motion of FPFM were evaluated after implementing the piezoelectric (PZT) actuator. The step input was given to PZT actuator to observe any difference motion behavior when different conditions (Ambient, pneumatic air pressure (80 psi), water-filled, hydraulic water pressure (80 psi), oil-filled, and hydraulic oil pressure (80 psi)) were employed. In this experiment, open-loop motion was tested.

Figure 7 shows the result of open-loop responses that convey some distinctions in rising time and the amplitude of oscillation when varying conditions were applied. However, it was hard to draw a conclusion that this discrepancy occurred due to different fluidic conditions because there exist some uncertainties from PZT actuator and environment. Hence, the proper method is required for solely comparing the damping on FPFM and is still under investigation.
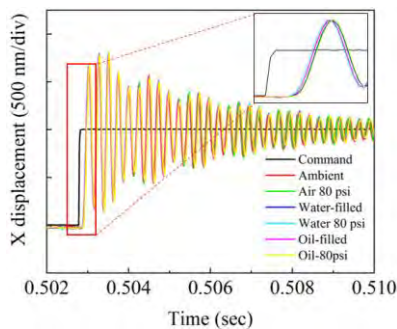
Figure 7. Result of step response when rising

Closed loop motion

Closed-loop positioning control of FPFM was performed by utilizing the simple analog proportional-integral feedback controller. The gain was tuned at the ambient condition with the step input. Similarly as previously performed experiments, effects of six varying conditions on damping were compared as well as the overall performance of FPFM. As a result, the existence of different media and pneumatic/hydraulic pressure did not show significant disparities when the stage is in a controlled condition. Currently, the sine-sweeping method that includes the resonance frequency will be investigated whether the FPFM changes damping and affects positioning characteristics, overcoming the limitation of the resonance vibration of the nanopositioning system.
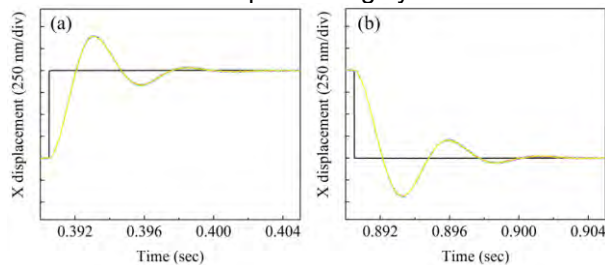

Figure 8. Feedback controlled motion: forward (a) and backward (b)

CONCLUSION

Here the new approach of in-process control of the damping parameters with the FPFM was proposed and was preliminarily investigated. Damping was characterized by acquiring a frequency response, free-vibration test, open-loop, and closed-loop response under varying fluids-filled and pneumatic/hydraulic pressure conditions. As a result, the existence of fluids and pressure inside the fluidic channel can increase damping. However, in the case of pressurized conditions, though it slightly increases the damping, the damping may decrease compared with the fluid-filled condition. Furthermore, the motion of FPFM showed a stable response even when the fluids and pressure are filled in the internal channel. Another approach to characterize the damping better should be considered. As a result, the FPFM could be implemented in dynamic systems and enhance the motion quality of the nanopositioning system in terms of operating speed, resolution, and stable motion in a low-cost, convenient, and effective way.

REFERENCES
[1] N. Jalili and K. Laxminarayana, "A review of atomic force microscopy imaging systems: application to molecular metrology and biological sciences," Mechatronics, vol. 14, no. 8, pp. 907–945, October 2004.

[2] A. J. Fleming, B. J. Kenton, and K. K. Leang, "Bridging the gap between conventional and video-speed scanning probe microscopes," Ultramicroscopy, vol. 110, no. 9, pp. 1205–1214, August 2010.

[3] K. K. Leang and A. J. Fleming, "High-speed serial-kinematic AFM scanner: design and drive considerations," Asian Journal of Control, vol. 11, no. 2, pp. 144–153, March 2009.

[4] A. Ferreira and C. Mavroidis, "Virtual reality and haptics for nanorobotics," IEEE Robotics and Automation Magazine, vol. 13, no. 3, pp. 78–92, September 2006.

[5] L. Vaillon and C. Philippe, "Passive and active microvibration control for very high pointing accuracy space systems," Smart Materials and Structures, vol. 8, no. 6, December 1999.

[6] V. Giurgiutiu, "Review of smart-materials actuation solutions for aeroelastic and vibration control," Journal of Intelligent Material Systems and Structures, vol. 11, pp. 525–544, July 2000.

[7] J. L. Fanson and T. K. Caughey, "Positive position feedback control for large space structures," AIAA Journal, vol. 28, no. 4, pp. 717–724, 1990.

[8] *S. S. Aphale, B. Bhikkaji, and S. O. R.* Moheimani, "Minimizing scanning errors in piezoelectric stack-actuated nanopositioning

platforms," IEEE Transactions on Nanotechnology, vol. 7, no. 1, pp. 79– 90, January 2008.

[9] A. J. Fleming and S. O. R. Moheimani, "Sensorless vibration suppression and scan compensation for piezoelectric tube nanopositioners," IEEE Transactions on Control Systems Technology, vol. 14, no. 1, pp. 33–44, January 2006.

[10] A. J. Fleming, S. Behrens, and S. O. R. Moheimani, "Optimization and implementation of multi-mode piezoelectric shunt damping systems," IEEE/ASME Transactions on Mechatronics, vol. 7, no. 1, pp. 87–94, March 2002.

[13] A. A. Eielsen and A. J. Fleming, "Passive shunt damping of a piezoelectric stack nanopositioner," in Proc. American Control Conference, Baltimore, MD, June 2010, pp. 4963–4968.

[11] A. Sebastian, A. Pantazi, S. O. R. Moheimani, H. Pozidis, and E. Eleftheriou, "A self servo writing scheme for a MEMS storage device with sub-nanometer precision," in Proc. IFAC World Congress, Seoul, Korea, July 2008, pp. 9241–9247.

[12] A. Preumont, J. P. Dufour, and C. Malekian, "Active damping by a local force feedback with piezoelectric actuators." AIAA Journal of Guidance and Control, vol. 15, no. 2, 1992.

[13] A. Preumont, Mechatronics, Dynamics of electromechanical and piezoelectric systems. Dordrecht, The Netherlands: Springer, 2006.

[14] A. J. Fleming, "Nanopositioning system with force feedback for highperformance tracking and vibration control," IEEE Transactions on Mechatronics, vol. 15, no. 3, pp. 433–447, June 2010.

[15] A. J. Fleming and K. K. Leang, "Integrated strain and force feedback for high performance control of piezoelectric actuators," Sensors and Actuators A, vol. 161, no. 1-2, pp. 256–265, June 2010.

[16] S. S. Aphale, A. J. Fleming, and S. O. R. Moheimani, "Integral resonant control of collocated smart structures," IOP Smart materials and Structures, vol. 16, pp. 439–446, April 2007.

[17] B. Bhikkaji and S. O. R. Moheimani, "Integral resonant control of a piezoelectric tube actuator for fast nanoscale positioning," IEEE/ASME Transactions on Mechatronics, vol. 13, no. 5, pp. 530–537, October 2008.

[18] A. J. Fleming, S. S. Aphale, and S. O. R. Moheimani, "A new method for robust damping and tracking control of scanning probe microscope positioning stages," IEEE Transactions on Nanotechnology, vol. 9, no. 4, pp. 438–448, September 2010.

[19] I. R. Petersen and A. Lanzon, "Feedback control of negative-imaginary systems," Control Systems, IEEE, vol. 30, no. 5, pp. 54 –72, oct. 2010.

[20] I. R. Petersen and A. Lanzon, "Feedback control of negative-imaginary systems," Control Systems, IEEE, vol. 30, no. 5, pp. 54 –72, oct. 2010.

Basic study of temperature prediction model for machine tools

Hozumi Kanabe[1], Shumpei Ikushima[2], Jumpei Kusuyama[2]
and Yohichi Nakao[2]
[1] Graduate School of Mechanical Engineering
Kanagawa University
Yokohama, Kanagawa, JAPAN
[2] Department of Mechanical Engineering
Kanagawa University
Yokohama, Kanagawa, JAPAN

INTRODUCTION

One of the most significant causes that decrease the machining accuracies of machine tools is a thermal deformation of machine tools attributed to temperature change of its main components. The influences of thermal deformations cause up to 75% of machining errors [1]. In recent years, speeding up of each moving unit, multi-axis, and multi-tasking operations of machine tools are progressing, because the demands for high-mix low volume production of industrial products is increasing. Along with it, the heat quantity and the number of heat sources of entire machine tools are increasing [2]. Therefore, it is necessary to establish a sophisticated design method for machine tools in which the thermal characteristics of machine tools are fully considered so that thermally stable machine tools can be developed. However, the thermal characteristics of machine tools are still poorly understood. This is because a thermal phenomenon of the machine tool extremely is complicated. For instance, a complex correlation between several heat sources and three kinds of heat transfer forms, namely the conductive heat transfer, the convective heat transfer and the radiative heat transfer exists.

To clarify the thermal characteristics of machine tools, it is necessary to identify various thermal parameters, such as heat quantity, contact thermal resistance, heat transfer coefficient, and radiation coefficient for each part. Therefore, the establishment of measuring and calculation methods of thermal parameters is extremely important for evaluating the thermal parameters individually. For example, even if the heat transfer coefficient of machine tools is only considered, it is difficult to determine correct value by the conventional empirical formulas because the flow field around machine tools is extremely complicated and changeable. Currently, several studies have been reported regarding the heat transfer coefficient of machine tools [3,4]. However, few studies have been reported on the influence of radiative heat transfer and the heat transfer coefficient of machine tools that evaluated experimentally.

Therefore, this study aims to establish a temperature prediction model and a measuring method of thermal parameters for machine tools, but not limited for machine tools. These are useful for clarifying thermal characteristics of existing machine tools and for establishing the effective design method based on the understanding of the thermal characteristics of machine tools.

In this paper, the temperature prediction model and the measuring method of thermal parameters are proposed. A novel measuring method of the convective heat transfer and the radiative heat transfer is proposed as well. In the proposed method, the convective heat transfer and the radiative heat transfer can be measured simultaneously. In addition, the thermal phenomena due to two kinds of simplified heat transfer forms, namely the convective heat transfer and the radiative heat transfer are discussed. Finally, the prediction accuracy of the proposed temperature prediction model is evaluated by comparing the predictions to the measurement results using a simplified machine tool component.

TEMPERATURE PREDICTION MODEL

In the proposed temperature prediction model, the complicated thermal phenomenon of machine tools is considered comprehensively by defining the lumped parameter model or the thermal volumetric spaces [5] in which the temperature in the defined control volumes is constant. The

proposed model cannot predict the temperature distribution in machine tool components. However, global thermal behavior is sufficiently deduced.

The general formula of the temperature prediction model can be expressed by Eq. (1) as follows:

$$mc\frac{dT}{dt} = P - Q_p - Q_c - Q_r, \tag{1}$$

where m is the mass of the components considered, c the specific heat, T the temperature, t the time, P the heating quantity, Q_p the heat conduction quantity to other components through contact surfaces, Q_c the convective heat transfer quantity, and Q_r the radiative heat transfer quantity.

The temperatures of each component can be calculated concurrently by formularizing the simultaneous differential equation like Eq. (1). To use the model for actual machine tool design and temperature prediction, it is necessary to identify various thermal parameters, such as the heating quantity, contact thermal resistance, heat transfer coefficient and radiation coefficient for the components.

MEASURING METHOD OF THERMAL PARAMETERS
This paper focuses on the thermal phenomena due to two kinds of simplified heat transfer forms, namely the convective heat transfer and the radiative heat transfer. Then, heat transfer coefficients due to airflow and radiation coefficient between the components are estimated.

The convective heat transfer can be given by Newton's law of cooling as follows:

$$Q_c = hA\ (T_s - T_\infty), \tag{2}$$

where Q_c is the convective heat transfer quantity, h the heat transfer coefficient, T_s the surface temperature of the object, T_∞ the fluid temperature, and A the contact surface area.
The radiative heat transfer between two surfaces (surface 1 and surface 2 as presented in Fig. 1) can be given by Eq. (3).

$$Q_r = f\sigma A_1\ (T_1^4 - T_2^4) \tag{3}$$

where Q_r is the radiative heat transfer quantity, f the radiation coefficient, T_1 and T_2 the surface temperatures, σ the Stefan–Boltzmann constant, and A_1 the surface area of surface 1.
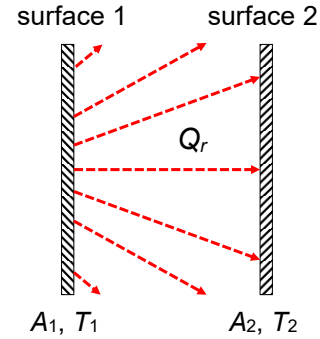

FIGURE 1. Explanatory drawing of radiative heat transfer between two surfaces

If the convective heat transfer and the radiative heat transfer are only considered, the heat flux can be expressed as follows:

$$q_{all} = q_c + q_r, \tag{4}$$

where q_{all} is the total amount of the heat flux, q_c ($=Q_c/A$) the convective heat flux, and q_r ($=Q_r/A_1$) the radiative heat flux.

Accordingly, the convective heat flux q_c can be calculated if q_{all} and q_r can be evaluated separately. To measure q_{all} and q_r, we propose to use two kinds of heat flux sensors. Among the sensors, the sensor A can measure q_{all}. In contrast, the sensor B detects only q_r. Thus, the convective heat flux can be introduced by the difference between measurement results of the two sensors, as based on Eq. (4). Finally, the h can be calculated by measuring temperatures T_s and T_∞ as given Eq. (2) and the f can be calculated by measuring temperatures T_1 and T_2 as given Eq. (3).

EXPERIMENTS
The measuring method and the temperature prediction model were applied to the simplified machine tool component. Figure 2 shows a schematic view of experimental equipment using a motor that was used to simulate a machine tool spindle. The motor was installed in the test section in the wind tunnel and the heat flux sensors A (50×50 mm^2) and heat flux sensors B (50×50 mm^2) were bonded using the grease on each surface of motor to measure heat flux. The sensor A can measure the total amount of heat flux q_{all} by the temperature difference between top and back of the sensor surfaces. In contrast,

the sensor B can measure radiative heat flux q_r because the reflector is set at regular intervals on the surface of the sensor, only radiative heat generates temperature difference in the sensor. The temperatures of motor surfaces and air flow were measured with resistance temperature detectors (RTD). The motor rotational speed was 3000 min^{-1}, it was used as a typical machine tool component. The experiment was carried out in the air flow condition in which the flowrate of air was approximately 3 m/s at the center of test section. The heat transfer coefficients and the radiation coefficients were calculated from the experimental results, and the temperature prediction model was formularized about the motor and the test section.
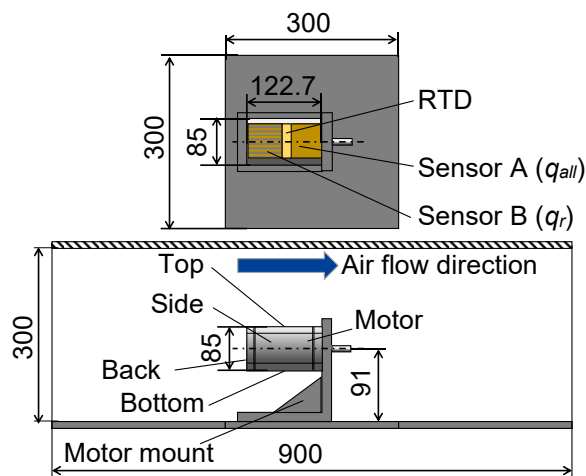
FIGURE 2. Schematic view of experimental equipment of motor

RESULTS
Measuring thermal parameters
The measurement results of temperature, heat fluxes and thermal parameters are shown in Fig. 3, Fig. 4, and Fig. 5, respectively. The averaged heat transfer coefficients and radiation coefficients were introduced by substituting the experimental data into Eq. (2), Eq. (3) and Eq. (4). The introduced average value of heat transfer coefficients and radiation coefficients are summarized in Table 1.

From Fig. 3, the results of temperature are in agreement at the top and side surfaces. From Fig. 4, the results of heat fluxes are in agreement at the top and side surfaces as well, because of the similarity of flow field and radiation conditions by experimental equipment layout.
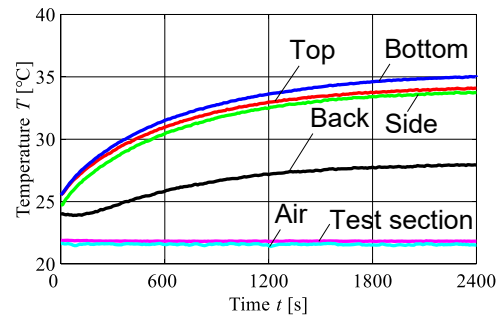

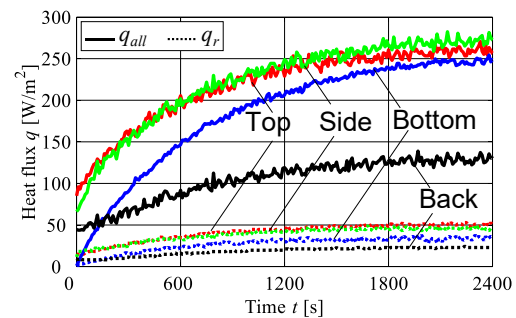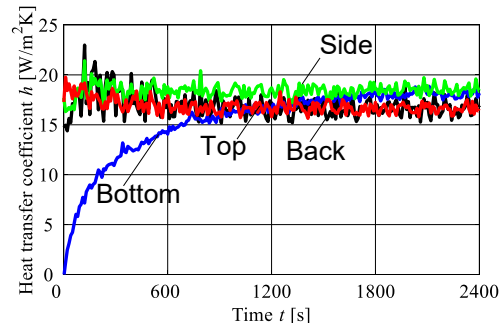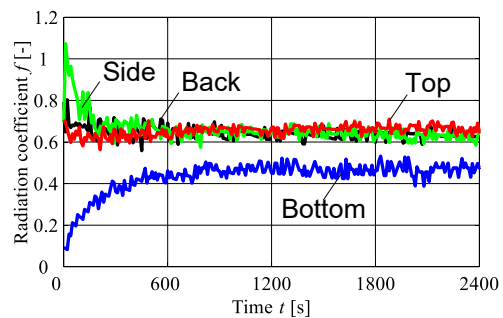FIGURE 3. Experimental results of temperature measurement

FIGURE 4. Experimental results of heat flux

(a) Heat transfer coefficient

(b) Radiation coefficient

FIGURE 5. Experimental results of thermal parameters

TABLE 1. Experimental results of thermal parameters

	Top	Bottom	Side	Back
h [W/m^{2}K]	16.9	15.5	18.4	16.9
f [-]	0.66	0.44	0.66	0.65

Figure 3 indicates that the motor temperature at the bottom surface is higher than other surfaces. In contrast, the heat flux q_{all} at the bottom surface is lower than that at the top and side surfaces as presented in Fig. 4. It is presumed that the amount of air flow at the bottom side of the motor is lower than that at the other surfaces due to the influence of the motor mount as presented in Fig. 2. As a result, the total amount of the heat flux at the bottom surface reduces, meaning a decrease in the cooling effects by the air flow. In addition to the influence of the air flow on the total amount of the heat flux at the bottom surface, the heat flux q_r due to the radiation affects the characteristics as well. From Fig. 4, the heat flux q_r at the bottom surface of the motor was lower than that at the top and side surfaces, mainly due to the low emissivity of counterface of motor mount surface. In general, the emissivity of metal surface tends to be low. Accordingly, the heat flux q_r at the bottom surface of the motor reduces. This also affects the decrease in the cooling effect at the bottom surface. All the characteristics of the heat fluxes affect the temperature increase trend of the bottom surface of the motor.

At the back surface of the motor, the air flow field and the radiation conditions must be very different from other surfaces. As a result, the heat flux q_{all} and q_r are low and the temperature rise is also small. However, the results of the heat transfer coefficient h and the radiation coefficient f as summarized in Table 1 and presented in Fig. 5 are almost the same as the top and side surfaces. It seems to happen occasionally, but further investigation will be needed.

The heat transfer quantity of each surface that is calculated by multiplying q_{all} in the steady state by the area of each surface are shown in Table 2. As expected from the motor structure, the heat transfer quantity at the top, side and bottom surfaces are identical to each other. In contrast, the heat transfer quantity at the back surface is lower than that at other surfaces.

From these results, the proposed measuring technique is effective to investigate the thermal characteristics of the machine tool or machine tool components.

TABLE 2. Heat transfer quantity of each surface

	Top	Bottom	Side	Back
q_{all} [W/m^2]	260	250	270	130
Heat transfer quantity [W]	2.7	2.6	2.8	0.9

Temperature prediction model

Main specifications such as mass, specific heat, and heating quantity used for temperature prediction are shown in Table 3. The experimental results and the temperature prediction by the introduced model using the deduced averaged heat transfer coefficient and radiation coefficient are compared in Fig. 6. The values of heat transfer coefficient (h=17.2 W/m^{2}K), radiation coefficient (f=0.61) are used for the prediction using the introduced model.

From Fig. 6, the temperatures are in agreement, it is thus confirmed that the proposed temperature prediction model is capable of representing the thermal characteristics of the motor and surrounding test section.

Furthermore, the time constants presenting transient thermal characteristics of the system were also investigated experimentally and using the temperature prediction model. The time constant of the temperature prediction model can be expressed as follows:

$$\tau = \frac{mc}{hA + 4f\sigma A_1 T^3},\tag{5}$$

where τ is the time constant, T the initial temperature of the considered component. As presented in Eq. (5), the time constant τ can be deduced using the heat transfer coefficient and the radiation coefficient. Namely, the heat transfer coefficient h and the radiation coefficient f heavily affect the time constant of thermal system. As the heat transfer coefficient h and the radiation coefficient f were measured using the proposed measuring method. Thus, the validity of the proposed method is evaluated in terms of the time constants obtained experimentally and via model prediction.

The time constant obtained by the experiment was 618 s. In contrast, the temperature prediction model introduces the time constant is 630 s. As a result, the difference in the time constant is 12 s and the relative error is only as small as 2 %.

Accordingly, it is concluded that the proposed measuring method of heat transfer coefficient and radiation coefficient is valid in terms of the consideration about the time constants. The results confirmed the validity of the measuring method and the temperature prediction model as well.

TABLE 3. Main specifications of components

	Motor	Test section
Mass m [kg]	3.1	4.86
Specific heat c [J/kgK]	207.4	1470
Area A [m^2]	0.05	0.81
Heating quantity P [W]	12	-
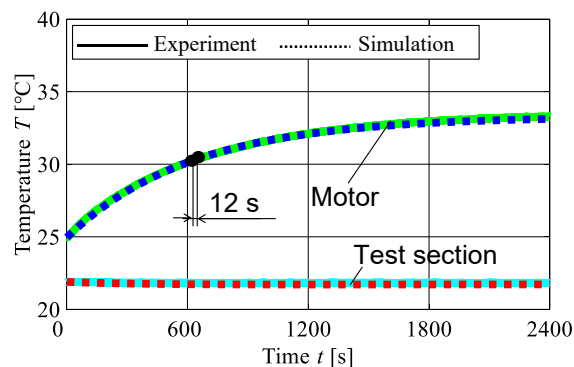
FIGURE 6. Comparison of prediction model and experimental result

CONCLUSIONS
In this report, the measuring method of thermal parameters and the temperature prediction model were proposed and applied for simplified machine tool components. The results confirmed the validity of measuring method and the temperature prediction model that was applied to the simplified machine tool component such as a spindle. Especially, the measuring method of thermal parameters can be expected to use other purposes such as online thermal condition monitoring of machine tools by confirming a response to change flowrate, heating quantity, and heat transfer field during measurement.

In the future work, further experiments that low flowrate condition and the small temperature difference between the surfaces of an object and air flow will be conducted, and the versatility of the temperature prediction model and the measuring method of thermal parameters will be verified. Further investigations regarding the measuring method of thermal parameters and formularized method of the temperature prediction model for actual machine tool system will be carried out.

REFERENCES
[1] J. Mayr., et al. Thermal issues in machine tools. CIRP Annals - Manufacturing Technology. 2012; 61: 771-791.
[2] S. Shimizu. Multi-tasking Machine Realizing High Productive and Accurate Machining: Present State and Evolution in Future. Journal of the Japan Society of Precision Engineering. 2008; 74: 325-328. (in Japanese)
[3] J. Glaenzel., et al. Efficient quantification of free and forced convection via the decoupling of thermo-mechanical and thremo-fluidic simulations of machine tools. Journal of Machine Engineering. 2018; 18: 41-53.
[4] P. Kohút, et al. Experimental Identification of Convective Heat Transfer in Machine Tools. WCE. 2011; 3: 6 - 8.
[5] Y. Ito, T. Matsumura. Theory and Practice in Machining Systems. Springer. 2017.

Experimental investigation on effect of shaft-bore cooling structure on thermal stability against heat generation due to aerostatic bearings

Shumon Wakiya[1], Satsuki Yamazaki[1], Jumpei Kusuyama[2]
Dmytro Fedorynenko[3] and Yohichi Nakao[2]
[1]Graduate School of Mechanical Engineering
Kanagawa University
Yokohama, Kanagawa, JAPAN
[2]Department of Mechanical Engineering
Kanagawa University
Yokohama, Kanagawa, JAPAN
[3]Department of Mechanical and Aerospace Engineering
Tohoku University
Sendai, Miyagi, JAPAN

INSTRUCTIONS

In recent years, it is required that high machining accuracy to produce magnetic disk substrate and micro lens array die for wafer-scale camera and other precision parts. Many of them are produced using die manufacturing using dies with micro structural surfaces. In order to realize such machining, an importance of ultra-precision machine tools for machining the dies increases more than before. In the machining of micro structural surfaces using micro milling cutter, a high rotational speed and rotational accuracy of the machine tool spindle are indispensable.

In the machining application, spindles equipped with aerostatic bearings are most commonly used[1]. However, in the range of the higher rotational speed such as over, for instance, 100,000 min^{-1}, influence of heat generation that attributed to air viscosity cannot be neglected. In general, this problem is underestimated. However, thermal deformation of the spindle shaft due to heat generation is one of the main factors that degrade machining accuracy. For this reason, the thermal deformation cannot be neglected in the ultra-precision machining[2, 3].

On this account, it is indispensable to study thermal characteristics including spindle cooling to suppress thermal deformation and temperature change of the spindle, and to design optimum spindle structure. Especially, direct cooling of spindle-shaft in which thermal deformation directly affects the machining

accuracy, is more effective than that of other machine tool components[4]. In general, a spindle of the many machine tools such as machining centers, is equipped with both or either of two type cooling structures in the spindle casing and/or spindle-shaft. However, few studies of small diameter aerostatic bearing spindle (~ φ20 mm) for ultra-precision milling that equipped with shaft-bore cooling structure have appeared.

Therefore, in the previous study [5], the high rotational speed spindle equipped with shaft-bore water cooling structure and aerostatic bearings has been developed. This spindle is equipped with a built-in motor to realize the ultra-high rotational speed (the rated rotational speed: 100,000 min^{-1}). In this spindle, it is necessary to consider not only the heat generation at the built-in motor but also the heat generation at the aerostatic bearings in order to design thermally stable spindle. In our previous studies, we have designed and developed the spindle with aerostatic bearings and built-in motor equipped with shaft-bore water cooling structure in its rotating small diameter shaft.

In this paper, the thermal stability of the designed spindle is investigated via simulation studies. Specifically, the studies present a desirable cooling performance improvement can be appeared due to the increase in the spindle rotation.

STRUCTURE OF AEROSTATIC SPINDLE

Figure 1 shows the basic structure of the high-speed aerostatic spindle that has been developed in our previous studies[6]. A feature of this spindle is that two different kinds of fluid, one is air for a pressure media to the bearings, another is water as a cooling media are supplied. The shaft-bore cooling structure adopts a special double cylinder structure so that the cooling water can be supplied in and drained from the rotating shaft that is supported by aerostatic bearings without direct contacts with other components. Furthermore, the spindle has a built-in motor to realize the ultra-high rotational speed, high rotational accuracy and miniaturization of the spindle size.
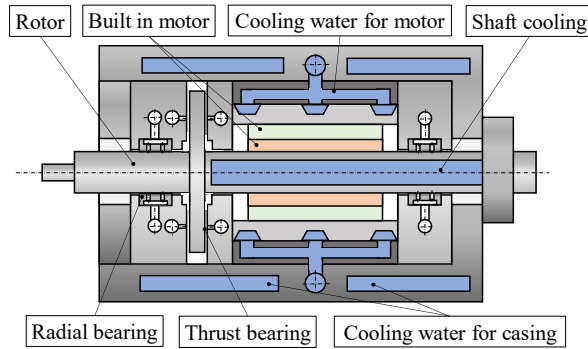
FIGURE 1.   Structure of aerostatic spindle [6]

HEAT SOURCES OF SPINDLE

Main heat sources of the developed spindle are attributed to the power loss of built-in motor P_{mo} and the power loss P_a owing to the air viscosity when the spindle is rotated. These power losses cause to rise the temperature of spindle and air flow for the bearings. Each power losses are given as follows.

Power Loss of Built-in Motor

The power loss of built-in motor P_{mo} is given by Eq. (1),

$$P_{mo} = P_{mo\_o}(1-\eta) \qquad (1)$$

where P_{mo_o} is the rated power of the built-in motor, and η is the motor efficiency.

The power loss of built-in motor P_{mo} divides into constant ratios, the power loss of rotor part P_{mo_ro} and the power loss of stator part P_{mo_st}. If the ratio of the rotor part is given by x, the power loss of the rotor part P_{mo_ro} and the power loss of the stator part P_{mo_st} are given by Eq. (2) and Eq. (3).

$$P_{mo\_ro} = xP_{mo} \qquad (2)$$

$$P_{mo\_st} = (1-x)P_{mo} \qquad (3)$$

Power Loss due to Viscous Friction of Air

When the spindle rotor rotates, the spindle rotation increases the power loss due to the air viscosity of air flow through the bearing gaps. As is well known, the air is widely used for pressure media of hydrostatic bearings, because air viscosity is very low. However, the power losses of bearings increase in proportion to the square of the spindle rotational speed. The power losses of radial bearing and thrust bearing are given by Eq. (4), Eq. (5),

$$P_{th} = \frac{\pi\mu(R_o^4 - R_i^4)}{h_{th}}\omega^2 \qquad (4)$$

$$P_{ra} = \frac{2\pi\mu R_{ra}^3 L_{ra}}{h_{ra}}\omega^2 \qquad (5)$$

where the bearing gap of the thrust bearing is h_{th}, the bearing gap of the radial bearing h_{ra}, the outer radius of axial bearing R_o, the inner radius of axial bearing R_i, the radius of the radial bearing R_{ra}, the length of the radial bearing L_{ra}, the viscosity of air μ_a, and the angular speed of spindle speed ω, respectively. Therefore, in the range of ultra-higher rotational speed as this spindle where the rated speed is 100,000 min^{-1}, the heat generation due to the air viscosity is remarkable. Consequently, the total power loss P_a due to air viscosity is given by Eq. (6)

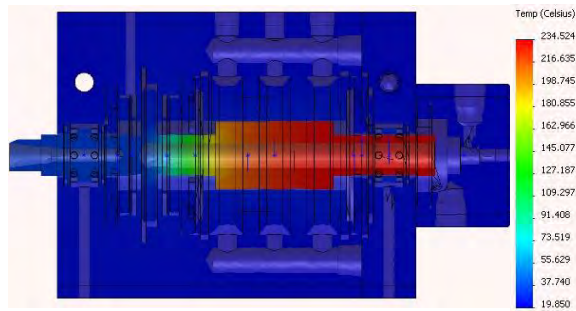$$P_a = P_{ra} + P_{th} \qquad (6)$$

THERMAL STABILITY OF SPINDLE

The thermal stability of the spindle is investigated by the finite-element method. Initial conditions for the analysis were defined as temperatures of all components: 20 °C, the rotational speed: 100,000 min^{-1} and flowrate of air and cooling water: 2 L/min, respectively. Figure 2 shows temperature distribution of the spindle in a steady state condition. Temperature scale in Fig. 2(a) is from 19.850 to 234.524 °C, that in Fig. 2(b) is from 19.850 to 33.220 °C.
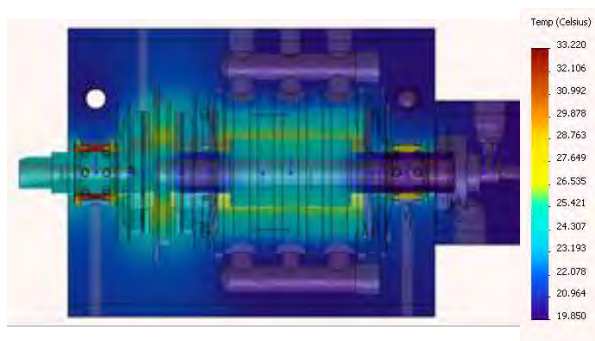
Figure 2 shows that the shaft-bore cooling structure achieves excellent cooling performance. However, the cooling effect cannot be fully obtained in the left end region of the shaft since

no shaft-bore cooling structure is designed in the part as depicted in Fig. 1. In the actual cutting, thermal deformation of the left side of shaft from the thrust bearing mainly affects machining accuracy. Accordingly, the influence of flowrate and temperature of cooling water on thermal deformation is investigated via simulation as well. Here the material of the shaft is stainless 304 (X5CrNi18-10), and the length of the left part is 41 mm.

Figure 3 shows the influence of flowrate and temperature of cooling water on thermal deformation. The simulation result shows the thermal deformation can be controlled by choosing the optimum flowrate and temperature of cooling water, even the shaft-bore cooling structure is not designed in the end part of the shaft. Specifically, no displacement of the end surface of shaft due to the thermal deformation can be obtained by the ideal cooling conditions: temperature of cooling water 16 °C, water flowrate 8.7 L/min or temperature of cooling water 14 °C, water flowrate 5 L/min.
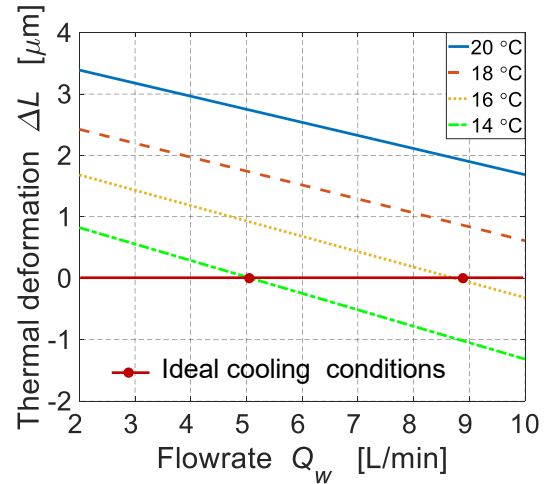
FIGURE 3. Thermal deformation of rotor by controlling temperature and flowrate of cooling water

Cooling performance under spindle rotation

As stated above, the excellence of the shaft-bore cooling in terms of the thermal stability of the spindle is reconfirmed by the simulation studies. However, the influence of the cooling water flow in the narrow bore in the shaft during spindle rotation has not been considered in the simulations. It is however natural to consider that the cooling water flow in the narrow bore inside the rotating spindle shaft affects thermal characteristics in terms of the heat generation due to the influence of water viscosity. This effect can increase spindle temperature.

In contrast, a heat transfer coefficient between the cooling water flow and the inner surfaces of the rotating spindle shaft can be increased with increase in the rotational speed, improving thermal stability of the spindle. Accordingly, it is considered how these effects affect resulting thermal characteristics is very interesting issue. Cooling performance considering the influence of flow of cooling water under the shaft rotating conditions is thus described in this section.

In the simulation considering water flow in the shaft bore, a temperature distribution of rotor is simulated using the finite-element method. The simulation conditions are the temperatures of rotor: 20 °C, the rotational speed: 0 min^{-1}, 100,000 min^{-1} and flowrate of cooling water for shaft-bore cooling: 2 L/min, respectively.

Figure 4 shows temperature distribution of rotor in the steady state. It should be noted that high rotational speed condition shows smaller temperature rise than no-spindle rotation condition. Specifically, the highest values of the


(a) Without shaft bore cooling

(b) With shaft bore cooling

FIGURE 2. Simulation results of temperature distribution

temperature rise are 41.23 °C (0 min^{-1}) and 27.03 °C (100,000 min^{-1}). It necessary to examine a reason for suppressing temperature rise by rotational speed condition.

To clarify the reason, a heat transfer coefficient between the inner surfaces of the shaft-bore and the cooling water is evaluated by the simulations, as well. In the simulations, the influence of the cooling water flowrate and rotational speed on the heat transfer coefficients is studied. The range of cooling water flowrate is 2~35 L/min, and the rotational speed is 0~100,000 min^{-1}. Figure 5 shows the influence of flowrate and rotational speed on heat transfer coefficient. In Fig. 5, the heat transfer coefficient clearly increases with the increase of water flowrate, as expected. In addition, it is noteworthy that the heat transfer coefficient obviously increases with the increase of the spindle speed. The increase of the heat transfer coefficient due to the increase of the spindle speed can be made by the change in the water flow path and the increase of the relative speed between the inner surfaces of the rotating shaft and cooling water. These effects contribute to suppress temperature rise as depicted by Fig. 3.

In fact, the increase of the spindle speed increases heat generation that is negative effect in terms of the thermal stability. However, the presented characteristics of the increase in the heat transfer coefficient due to increase of the spindle speed is a notable effect in terms of the thermal stability of the high-speed spindle.
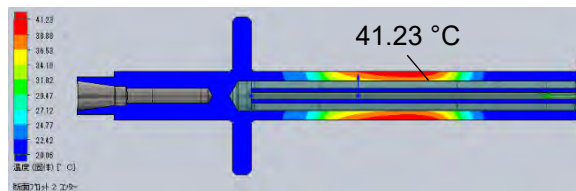
(a) Rotational speed : 0 min^{-1}
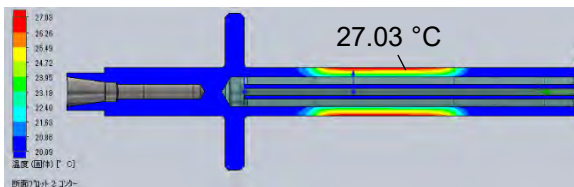
(b) Rotational speed : 100,000 min^{-1}

FIGURE 4. Temperature distribution of rotor
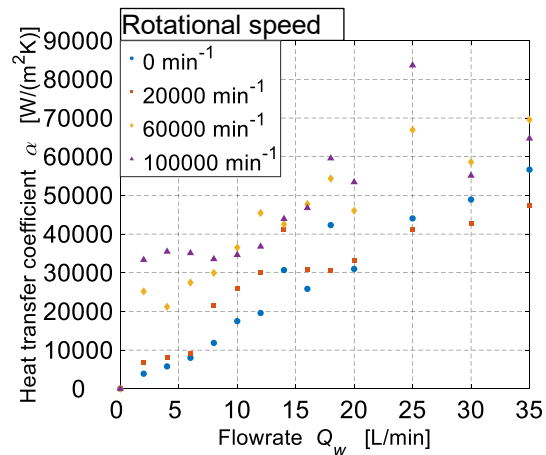
FIGURE 5. Influence of spindle speed and flowrate on heat transfer coefficient

CONCLUSIONS

In this paper, we discussed the temperature variation and cooling characteristics of developed high-speed aerostatic spindle equipped with shaft-bore water cooling structure by the simulations. As a result, the shaft-bore cooling shows an extremely high-cooling performance. In particular, the simulation studies verified that increasing the rotational speed can improve cooling performance to suppress temperature rise of the rotor that directly affects the machining accuracy. The simulation studies verified that the heat transfer coefficient obviously increases with the increase of the spindle speed. Consequently, it is effective to suppress thermal deformation of high speed spindle by designing the optimum shaft-bore cooling structure and choosing cooling conditions.

In the future work, the thermal characteristics of the developed spindle will be investigated experimentally, and the experimental results will be compared with the simulation results.

REFERENCES

[1] Ryuichi Kawakami. Development of Air Spindles for Ultra Precision Machining. Fujikoshi Technical report, Vol. 50, No. 2. 1994; 58-70(in Japanese).

[2] Toshimichi Moriwaki, Eiji Shamoto. Analysis of thermal deformation of an Ultraprecision Air Spindle System. Annals of the CIRP, Vol. 47, No. 1. 1998;315-319.

[3] T. Holkup, H. Cao, P. Kolar, Y. Altintas, J. Zeleny. Thermo-mechanical model of spindles. Annals of the CIRP, Vol. 59, No. 1. 2010;365-368.

[4]   Yuuki   Tamura,   Hiroshi   Sawano, HayatoYohioka,   Hidenori   Shinno.   A Thermally stable aerostatic spindle system equipped wish self-cooling function. Journal of Advanced Mechanical Design, Systems, and Manufacturing, Vol. 8, No. 6. 2014.

[5]   Satsuki Yamazaki, Dmytro Fedorynenko, Yohichi Nakao. Fundamental design study on high-speed aerostatic spindle with water-cooling function. American Society for Precision Engineering the 33rd Annual Meeting. 2018.

[6]   Shumon Wakiya, Satsuki Yamazaki, Jumpei Kusuyama, Dmytro Fedorynenko, Yohichi Nakao. Fundamental analysis on thermal characteristics of high-speed aerostatic spindle. American Society for Precision Engineering the 34th Annual Meeting. 2019.

Design of an air bearing slide for high dynamic response

Christopher Arneson
Professional Instruments Company
Hopkins, Minnesota, USA

ABSTRACT

To manufacture a 140mm linear axis with a natural frequency above 1kHz a hollow box slide with compound compensation was designed. This box shuttle floats on air supplied to 16 separate pads which use a combination of orifice restriction and groove compensation. Properly implemented, the combination of these two restrictor types with tight clearances (6-8 µm air films) yields high load capacity and stiffness.
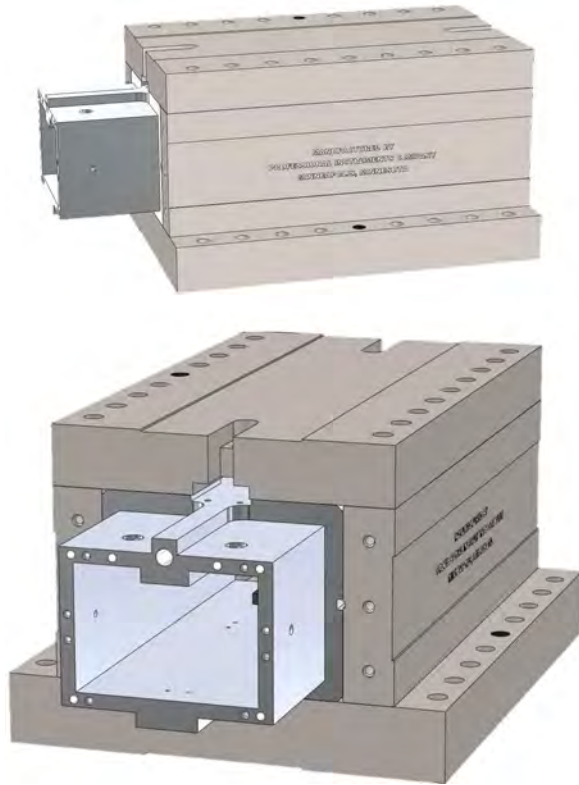
Figure 1. Schematic view of air bearing slide.

INTRODUCTION

Stiffness is a key property to achieve high precision and high dynamic response. Dynamic errors are reduced by increasing the stiffness of the air films resulting in higher natural frequency. The natural frequency dictates the performance of the system with respect to suppression of errors from applied forces. [1]

FEATURES

- 140 mm travel
- Heidenhain LIP-382 with 128 nm signal period
- Zeodur scale at substrate height
- Linear motor forces through center of mass
- Hollow shuttle design to minimize moving mass
- Translating pad design to minimize mass centerline shifts
- High stiffness compound compensation air bearing
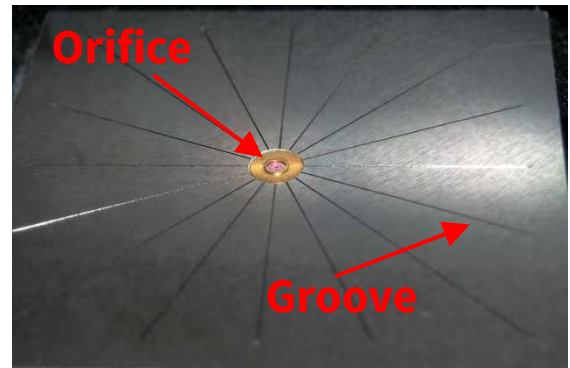
Figure 2. Pad design using compound compensation; orifice restricting and groove compensation.

DESIGN

To design an air bearing slide with high dynamic response, several precision engineering principles are considered and establish how air and power are supplied to the assembly [2]. Air is supplied to a hollow box linear slide through the translating shuttle rather than the stationary box structure via compound compensation, a combination of orifice restriction and groove compensation. Supplying the air to the shuttle eliminates pitch errors caused by mass centerline

changes. Properly implemented, the combination of these two restrictor types with tight clearances (6-8 µm air films) yields high load capacity and stiffness, resulting in a natural frequency above 1kHz.
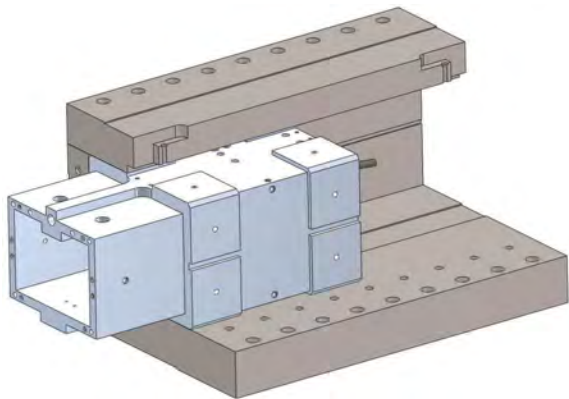

Figure 3. Cross-sectional view showing the pad configuration.

A slight disadvantage to this technique is air lines must be included in the slide umbilical connection. The linear motor is mounted so that the actuation force passes through the center of gravity of the shuttle. This reduces moment loads on the shuttle over the travel. Abbé offset is minimized by locating the linear scale at the same height as the working surface. Flexures are used to mount the scale to allow for structural bi-material expansion rate differentials from a single epoxy point located near the center of the scale center. Dynamic errors are minimized by maximizing the stiffness and natural frequency of the air films and their support structures. Other errors are minimized by precision manufacturing and adherence to precision engineering design principles.

Figure 4. Scale at substrate height for minimal Abbé offset.

Static test results estimate the normal load capacity of the slide to be 1,500 N at 0.6 MPa inlet air pressure. The estimated normal static stiffness is 200 N/µm and the tilt stiffness is 1.2 Nm/µrad at 0.6 MPa inlet air pressure. These values are approximately linear with inlet air pressure.

DYNAMICS

A modal analysis was performed to determine the dynamic response of the slide. An impact hammer (Kistler 2 mV/N) was used to excite the structure and an accelerometer (Kistler 100 mV/g) is used to measure the response (Hewlett-Packard Dynamic Signal Analyzer 35670A).

Figure 5. Impact hammer, accelerometer, and Hewlett-Packard Dynamic Signal Analyzer.

Figure 6. Setup showing impact grid for dynamics testing.
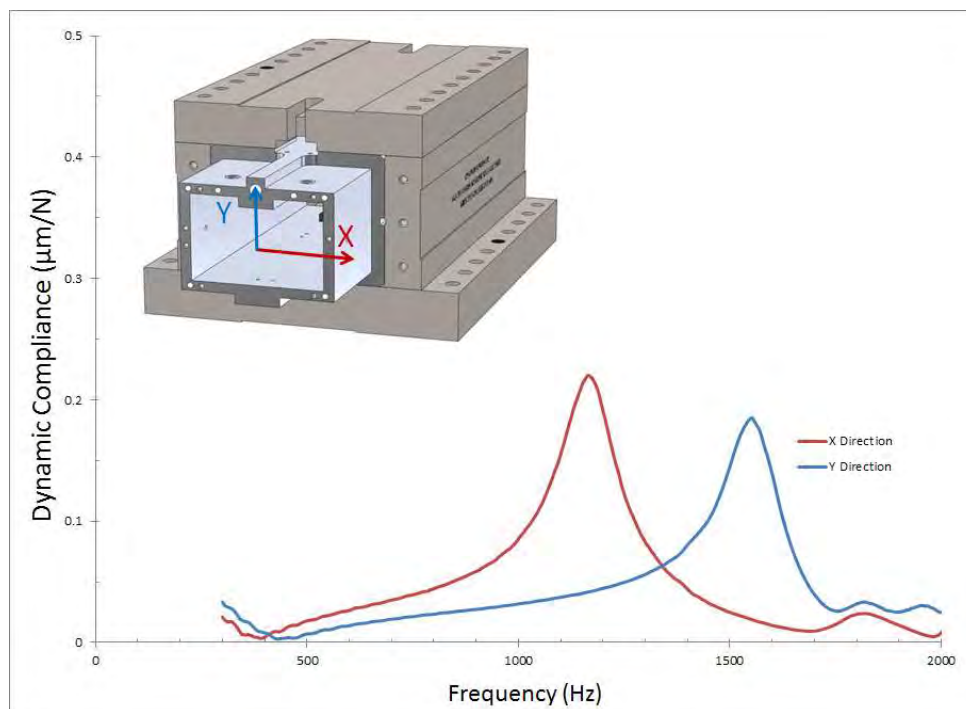
Figure7. Dynamic response of the linear slide is used to determine the first natural frequency. Then inlet air pressure was 0.55 MPa (80 PSI) for this test

With an inlet pressure of 0.55 MPa (80 PSI), the first mode in the horizontal direction occurs at 1,170 Hz and the first mode in the vertical direction is 1,550 Hz.

CONCLUSION

Dynamic errors are minimized by maximizing the stiffness and natural frequency of the air films and their support structures. Other errors are minimized by precision manufacturing and adherence to precision engineering design principles. The result is an air bearing slide with outstanding dynamic performance.

REFERENCES

[1] Munnig Schmidt R, Schitter G, Rankers A, van Eijk J. The Design of High Performance Mechatronics. Delft University Press. The Netherlands: 2014

[2] Knapp B, Oss D, Arneson D, Sheridan T. Positioning System for Optical Disc Mastering. Proceedings of the ASPE. 25th Annual Meeting. Atlanta, Georgia: 2010.

EFFECT OF AIR PRESSURE VARIATION ON 4R BLOCKHEAD AIR BEARING SPINDLE PERFORMANCE

Samuel O. Arneson, David A. Arneson, Daniel D. Oss, Melvin J. Liebers
Professional Instruments Company
Hopkins, Minnesota, USA

ABSTRACT
Professional Instruments Company provides a spindle load and stiffness specification at an inlet pressure of 100 psi for the 4R Blockhead air bearing spindle. This pressure is suitable for most applications; however the 4R Blockhead can operate successfully over a wide range of inlet pressures. Depending on the specific use, the inlet pressure can be changed to optimize the performance in a given application. For example, raising the air pressure increases the load capacity and stiffness but also increases the load on the air compressor and air drying systems. This paper will analyze the performance of a 4R Blockhead spindle at inlet pressures from 75 psi to 150 psi.

FIGURE 1. Professional Instruments 4R Blockhead air bearing spindle

BACKGROUND
The first Blockhead air bearing was produced in 1965 as a universal spindle for precision rotary motion. The combination of high stiffness and accuracy, reasonable load capacity, and compact form factor makes it ideal for a variety of applications. These applications include ultra-precision machining and measurement platforms, such as the one shown in Figure 2.

For machining purposes, generally, the load capacities of the spindle are more important. Whereas, a metrology application may need less load capacity and instead require lower noise from the spindle. By changing the inlet pressure it is possible to change some characteristics of the Blockhead to better suit the application.
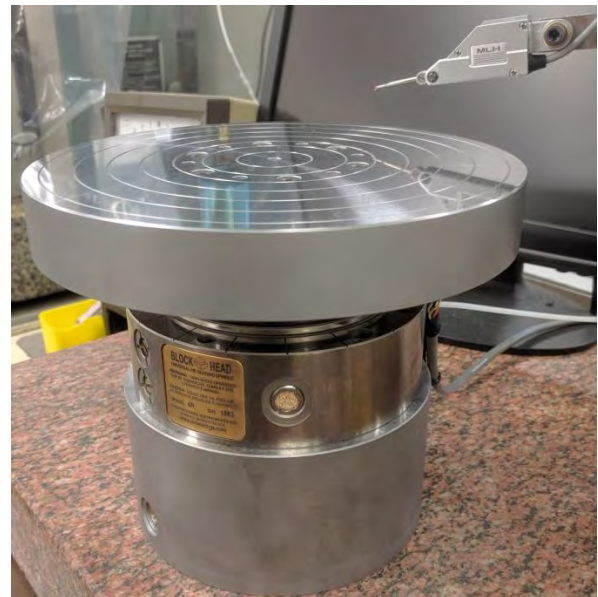
FIGURE 2. In house roundness tester using a 4R Blockhead spindle

AIR REQUIREMENTS OF AIR BEARINGS
This paper will discuss variation from the 100 psi specification Professional Instruments recommends for general use. However, it should be understood that proper air handling and spindle maintenance procedures are still critical, regardless of inlet air pressure. This includes having a sufficient air cleaning and drying system to ensure no outside contaminants or moisture enter into the spindle.

TESTED SPINDLE CHARACTERISTICS

Four spindle characteristics were tested at inlet pressures from 75 to 150 psi.

1. Ultimate load capacities (Axial, Tilt, and Radial)
2. Stiffness
3. Error motion (radial and axial)
4. Air consumption

These four metrics are the characteristics most affected by changes to the inlet air pressure.

LOAD CAPACITY

The ultimate load capacity of the 4R Blockhead increases linearly with the inlet pressure across the range of 75 psi to 150 psi (figure 3). It should be noted that ultimate load capacity is the where contact between the stator and rotor occurs, and the working load capacity is recommended to be half of this value.
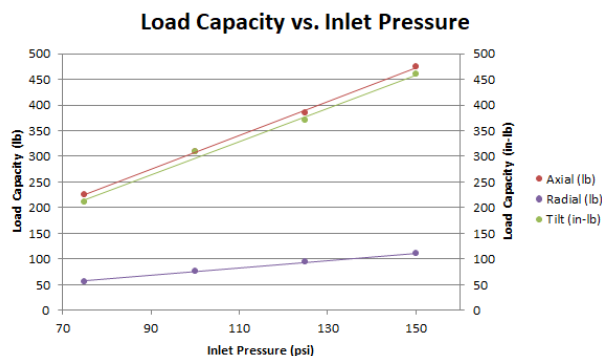
FIGURE 3. *Load capacity vs. inlet pressure*

STIFFNESS

The stiffness of the 4R Blockhead increases with the inlet pressure, however at higher inlet pressures the relative gains are lower (figure 4). These are the static stiffness values, the dynamic stiffness of the 4R Blockhead has been explored previously [1].
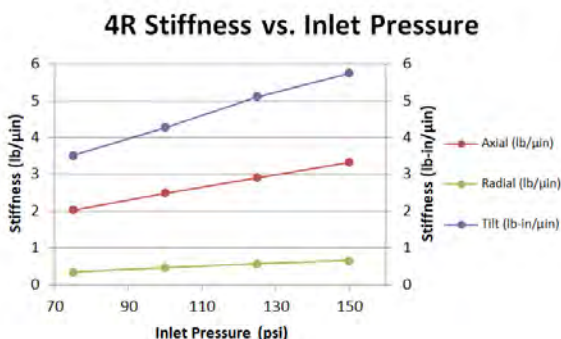
FIGURE 4. *4R stiffness vs. inlet pressure*

ERROR MOTION

Error motion testing of the 4R Blockhead was performed using a motorized Professional Instruments ISO 5.5 air bearing spindle as a drive (figure 5). This was for efficiency, due to the fact that every ISO 5.5 is error motion tested whereas the 4R Blockheads are not and are regularly sold without motorization. This testing setup has been documented previously [2]. The error motion tests highlighted in this paper are from S/N 7154, however all 4R Blockheads are specified to better than 25 nm total error motion in both the radial and axial directions.
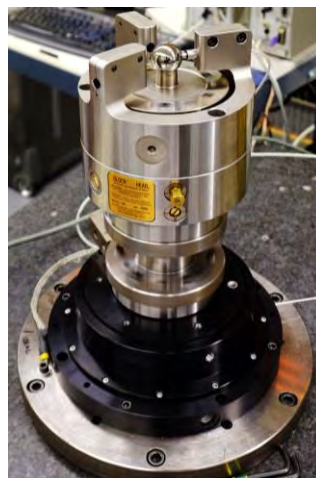
FIGURE 5. *Error motion testing setup of an unmotorized 4R Blockhead driven by an ISO 5.5 spindle which also provides the angular information*

Increasing the air pressure to the spindle has negligible impact on the error motion of the 4R Blockhead (figures 6 and 7). Typical fluctuations across the pressure range are on the order of a few nanometers and can vary between spindles rather than following a deterministic trend.
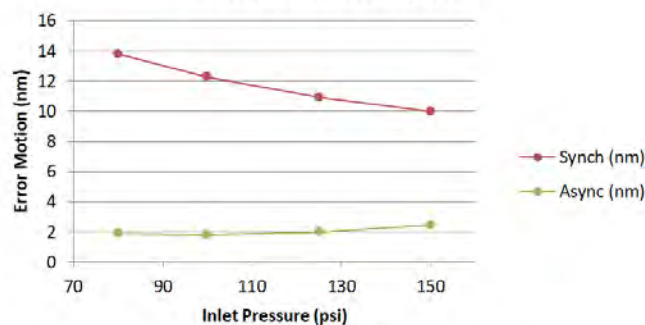

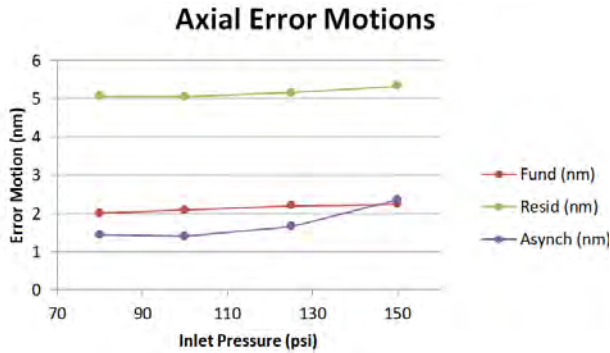FIGURE 6. *Radial error motions S/N 7154*

FIGURE 7. Axial error motions S/N 7154

AIR CONSUMPTION

While running spindles at higher air pressure may be desirable for some applications, the cost is not trivial. The flow rate of air through the Blockhead increases non-linearly with higher inlet pressure (figure 8). Depending on the number of spindles in use and other environmental factors (temperature, humidity, etc.), running the Blockhead at higher pressures can put additional stress onto the air compressor and air drying systems [3]. For less robust air compression systems it may be better to operate at lower inlet pressure to lower the likelihood of crashing due to wet air. The tradeoff is that lower inlet pressure will result in lower load capacities, so additional care must be taken to avoid crashing due to overloading the air bearing.

Professional Instruments utilizes 100+ Blockheads in the main facility and the compressor system consumes ~170 CFM during working hours with the inlet pressure being set to 120 psi on most spindles. At night the compressor is set to 40psi and the compressor only consumes ~50 CFM. Air bearing spindles should be pressurized at all times to prevent contamination entering the air films and corrosion from occurring, especially in wet or humid environments such as grinding with coolant.
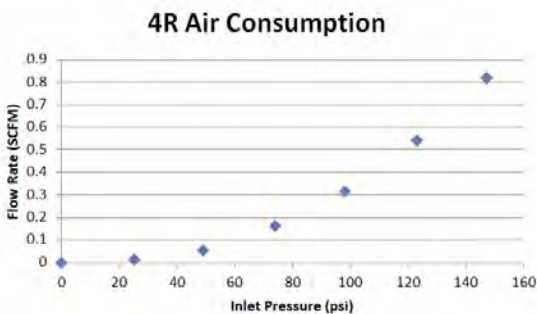
FIGURE 8. 4R air consumption vs. inlet pressure

PNEUMATIC HAMMER

Pneumatic hammer is a problem that occurs in some air bearings [4] and is cause for concern when operating at higher air pressures. However, the Blockhead air bearing design nearly eliminates the problem of pneumatic hammer because the Blockhead design has no upstream restriction [5]. This quality is present in the entire line of Blockhead air bearing spindles, not just the 4R. As a result of this design, the upper limit of the inlet pressure to a Blockhead is bounded by the air supply line ratings and associated air pressure hardware rather than the Blockhead itself. Professional Instruments has used the 4R Blockhead with inlet pressure of up to 200 psi without issue, although there can be small increases in asynchronous error motions.

CONCLUSION

The 4R Blockhead air bearing spindle was designed to be a universal tool for rotary motion and has been used in many different and unique applications. The versatility of the spindle allows for a wide range of operating pressures depending on the requirements of the application. Higher pressures improve the load capacity and stiffness of the 4R Blockhead at the cost of necessitating more robust air compression systems.

REFERENCES

1. B. Knapp et al. Modeling dynamic stiffness of an air bearing spindle using FRFs. Professional Instruments. ASPE 2019.
2. C. Arneson et al. Error motion testing of an unmotorized 4R Blockhead air bearing spindle. Professional Instruments. ASPE 2019.
3. S. Arneson et al. Compressed air system for ultra-precision air bearing spindles. Professional Instruments. ASPE 2018.
4. R. Bassani et al. Pneumatic stability of the integral aerostatic bearing: comparison with other types of bearing. TRIBOLOGY international Vol 22 No 6 December 89.
5. Arneson HEG. 1969 US Patent No. 3472565

MACHINING CHARACTERISTICS OF ROCK BY WIRE-SAWING IN VACUUM AT HIGH CUTTING-LOAD

Katsushi Furutani[1], Haruki Okamura[1], Tatsuaki Okada[2],
Kazuto Saiki[3], and Hiroyuki Ohue[4]
[1]Department of Advanced Science and Technology
Toyota Technological Institute
Tempaku-ku, Nagoya 468-8511 Japan
[2]Institute of Space and Astronautical Science
Japan Aeronautical Exploration Agency
Chuo-ku, Sagamihara 252-5210 Japan
[3]Graduate School of Science
Osaka University
Toyonaka, Osaka 560-0043 Japan
[4]Research and Development Division
Tokusen Kogyo Co., Ltd.
Ono, Hyogo 675-1361 Japan

INTRODUCTION

Since *in-situ* observation of rock samples is required in future lunar and planetary explorations, machining techniques for them will be demanded as a preprocess. Slicing the rock samples is preferable to observe their interior [1]. Because coolant cannot be used in vacuum, a tool life will be shorten. It is expected for a saw wire to keep cutting performance by successive supply of cutting edges. Nickel fixing abrasives adhered on a rock sample in vacuum and the abrasives slipped on the adhered nickel so that the rock was hardly cut [2]. According to experiments and simulation on the temperature rise during machining, and friction tests, it was found that the nickel was not oxidized in vacuum and it is too tough to be removed at a small cutting load [3][4]. A solution to overcome the slip on the adhered nickel may be to increase the cutting load.

This paper describes design of a prototype of a wire-sawing machine to apply a high cutting load and its performance.

PRELIMINARY EXPERIMENTS

In order to investigate effects of the cutting load, rock samples were cut with a simple machine composed of a slider-crank mechanism. Figure 1 shows a structure of the cutting machine which consists of a stepping motor, a saw wire strung on a slider of a linear guide and a lever for mounting a sample. Table 1 shows specifications of the cutting machine. The cutting load was
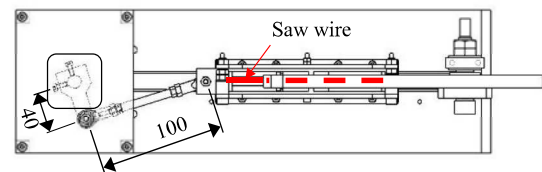
(a) Top view.
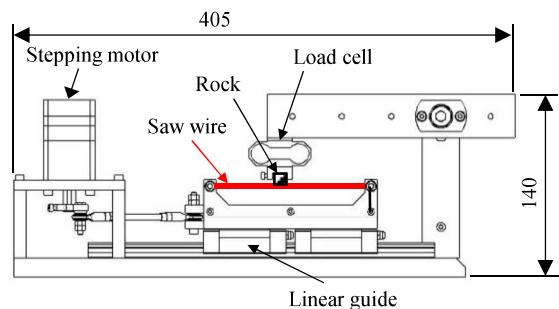
(b) Front view.
FIGURE 1. Slider-crank type cutting machine for preliminary test.

TABLE 1. Specifications of cutting machine for preliminary experiments.

Dimensions	405 mm × 110 mm × 140 mm
Length of saw wire	130 mm
Stroke	80 mm

TABLE 2. Cutting conditions in preliminary test.

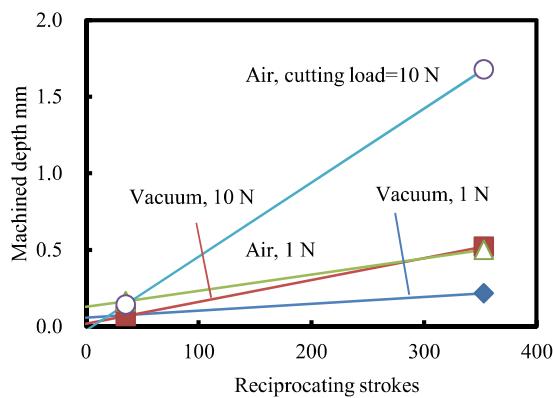| Saw wire	Exposed diamond abrasive
Period of reciprocating motion	1.7 s (96 mm/s)
Machining time	60, 600 s
Cutting load	1.3, 10 N
Ambient pressure	10^{-3}, 10^5 Pa
Specimen	Basalt mined in Shizuoka, Japan (10 mm x 15 mm x 8 mm)

FIGURE 2. Machined depth in preliminary test.

applied to the sample with the dead weight of the lever.

Table 2 shows machining conditions for the preliminary experiments. The saw wire with exposed abrasives was reciprocated 35 or 350 strokes in air or vacuum. The cutting load was at 1 and 10 N. The sample was basalt blocks with dimensions of 10 mm × 15 mm × 8 mm. Figure 2 shows machined depth by measuring an optical microscope. Although the ratio of the depth by 350 reciprocations to that by 35 reciprocations at 1 N in vacuum was 2.9, one at 10 N in air was 7.6. Consequently, the increase of the cutting load retained the performance even if nickel adhered on the surface of the rock sample.

DESIGN OF WIRE-SAWING MACHINE FOR HIGH CUTTING LOAD
In the previous machine [2], the tension of a saw wire could not be increased because of a low stiffness of a leveling arm. The common requirements for a prototype to apply a high cutting load are as follows: applying a cutting load
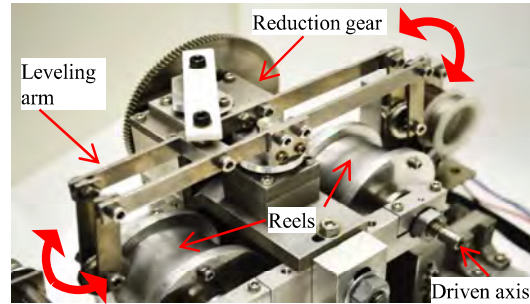
(a) Leveling arm in previous machine.
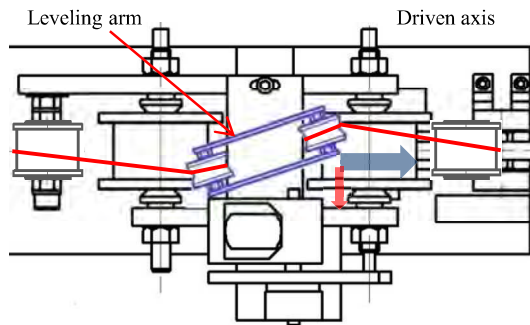
(b) Short leveling arm.
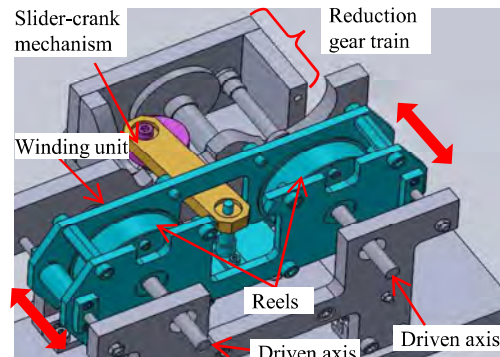
(c) Winding unit of proposed machine.
FIGURE 3. Structure of wire-sawing machines.

up to 50 N, using a long saw wire to extend the duty cycle, and winding and unwinding the long saw wire with two reels.

In the conventional cutting machine shown in Figure 3 (a), the leveling arm was thin and long. In case of use of the previous machine, the cutting load is simply increased. This arm is inappropriate because a large force applied at the end of the arm will twist it.

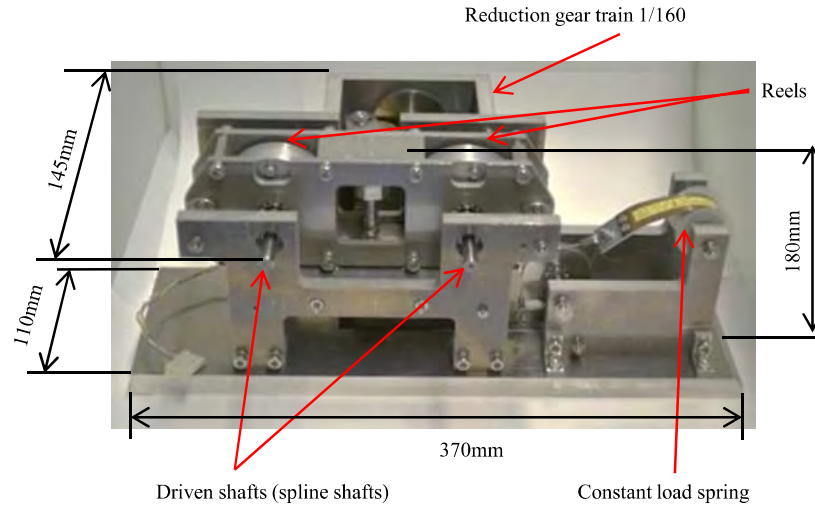Figure 3 (b) shows a path of the saw wire leveled with a half-length arm. A pair of additional pulleys

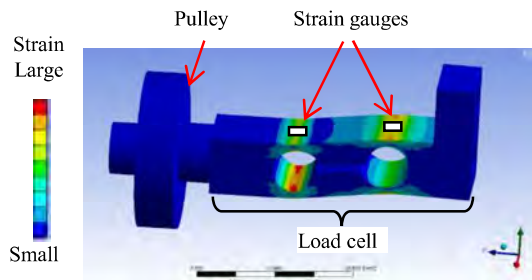FIGURE 4. Wire-sawing machine to apply high cutting load.

FIGURE 5. First vibration mode of load cell.

TABLE 3. Specifications of wire-sawing machine

Dimensions	370 mm x 145 mm x 180 mm
Maximum length of saw wire	24.1 m
Saw wire feeding speed	0.26 m/s
Tension of saw wire	10-50 N
Structural materials	Aluminum alloy, stainless steel

was arranged on the outer side of the reels. Although the arm swings larger than that in the conventional machine, the arm deforms less because of a small moment by the tension of the saw wire. The flanges of the pulleys will damage the saw wire, and the saw wire will skid on the pulleys.

Figure 3 (c) shows a proposed machine in which the reels slide as a unit. The reels driven with ball spline shafts are embedded in a frame. This structure prevents damage of the saw wire due to skidding.

On comparison among them, the last one was built as shown in Figure 4. It consists of two reels, a swing device, a sample holder mounted on a lever and a rotary encoder. Table 3 shows the specifications of the developed machine. The reel unit was shifted with the slider-crank mechanism by reducing the revolution of the reels to 1/160. The structural materials are mainly aluminum

alloy for the housing and 304-stainless steel for bearings. The applicable tension is up to 50 N. Although the movable part is heavier than the short arm, the inertial force is small because the shifting speed is slow. Each reel is driven with a stepping motor to control the tension and feeding speed simultaneously. One of four pulleys is mounted at the end of a load cell shown in Figure 5. The first mode of its natural frequencies is 1074 Hz.

EXPERIMENTS
Table 4 shows machining conditions using the developed machine. The cutting performance was investigated in both air and vacuum of 10^{-3} Pa. The cutting load was increased from 0.9 N to 7.7 N to investigate its effects. The other conditions such as the feeding speed and the tension of the saw wire are the same in all experiments. Since nickel adhered at a cutting load of 0.9 N in the previous experiments, it was

TABLE 4. Machining conditions using developed machine.

Wire speed	0.1 m/s
Tension of saw wire	50 N
Length at constant speed	5 m
Cutting load	0.9, 7..7 N
Number of reciprocation	2, 5, 10, 20
Saw wire	Ni-coated saw wire
Pressure	Air, vacuum (10^{-3} Pa)
Specimen	Basalt (Shizuoka, Japan)

FIGURE 6. Relationship between machined depth and cutting load.
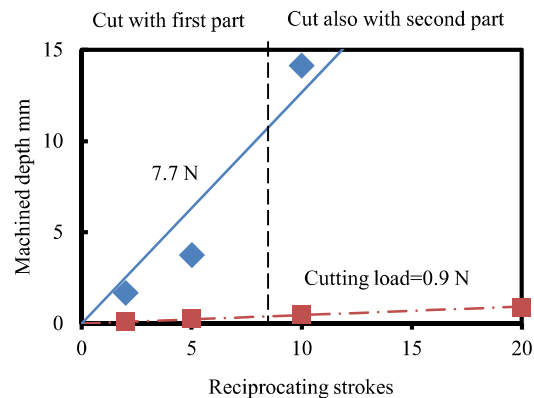
FIGURE 7. Relationship between machined depth in vacuum and reciprocating strokes.

set as the smallest cutting load in later experiments. Since nickel was removed with the progress of machining, another 5-m part of the same saw wire was used over 10 reciprocations.

Figure 6 shows the relationship between the machined depth after 2 reciprocations and cutting load. The machined depth was linearly increased with an increase of the cutting load even in vacuum. The machined depth in vacuum was 43-46% of ones in air. Figure 7 shows the relationship between the machined depth in vacuum and number of reciprocations. The machined depth was linearly increased also with an increase of the reciprocations under a high cutting load. Because the saw wire was switched after 10 reciprocations at a cutting load of 7.7 N, the machined depth at 10 reciprocations in air was increased from the predicted one.

CONCLUSIONS
In this paper, the prototype of a wire-sawing machine to apply a high cutting load was built, and its performance was investigated. The machined depth under a high cutting load was increased with an increase of reciprocations even in vacuum. For a future work, more data will be measured under various cutting load. The authors wish to thank Mr. T. Yoshinaga of Toyota Technological Institute for his helpful cooperation.

REFERENCES
[1] Schwendeman JR, Dreyer CB, Steele JPH. Design Considerations for Development of a Wire-Based Rock Cutting Mechanism for Space Exploration, Transactions of ASME, Journal of Mechanical Design. 2010; 132: 111010.
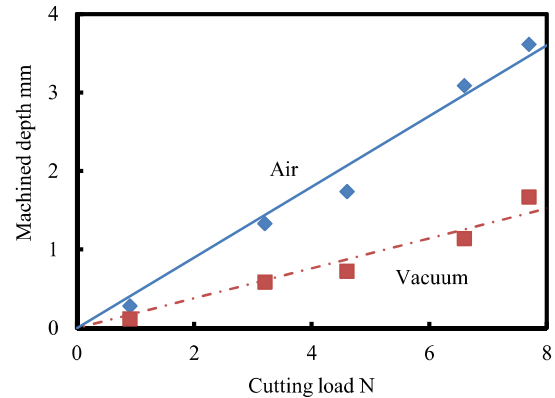
[2] Furutani K, Fukunaga S, Okada T, Saiki K, Ohue H. Effect of Vacuum on Wire-sawing as Preliminary Experiment to Lunar Exploration. Proceedings of 2011 Annual Meeting of American Society for Precision Engineering, Denver, CO. 2011; 349-352.

[3] Furutani K, Inukai R, Takano T, Okada T, Saiki K, Ohue H. Estimation of Saw Wire Temperature during Machining of Rock in Vacuum. Proceedings of 2018 Annual Meeting of American Society for Precision Engineering, Las Vegas, NV. 2018; 273-276.

[4] Furutani K, Inukai R, Takano T, Okada T, Saiki K, Ohue H. Experimental Analysis of Nickel Adhesion Process during Wire-sawing of Rock in Vacuum by Friction Test, Proceedings of 2019 Annual Meeting of American Society for Precision Engineering, Pittsburgh, PA. 2019; 431-434.

COMPARISON OF MANUFACTURING METHODS FOR TURBINE BLADE FIR-TREE ROOTS

Ozan Can OZANER[1,2]
[1]Technology Development
TUSAS Engine Industries, Inc.
Eskisehir, Turkey
[2]Department of Manufacturing Engineering
Gazi University
Ankara, Turkey

INTRODUCTION

Gas turbines can examine component groups names as well as working temperature such as cold section parts and hot sections parts. Turbine blades are located in hot section, so they are suffered from various type of loads like dynamic forces. This situation causes the use of connecters. There are most of type of connecters, but the most common is fir tree geometry [1]. Even if turbines blades are produced by casting or forging, connecters of turbine blades to turbine disk must be produced by manufacturing methods. There are most type of manufacturing methods such as wire electrical discharge machining and creep feed grinding. Nevertheless, both processes have disadvantages due to their nature.

In aviation industries, creep feed grinding is preferred by most of companies [2]. Creep feed grinding wheel enters the part about ten times more passes than conventional grinding systems and feed rate is about one in ten, compared to conventional grinding [3]. In literature, there are some research papers about creep feed grinding, most of them are focused on temperature distribution. Although, temperature distribution is studied for creep feed grinding, it was not studied enough for continuous creep feed grinding [4].Process parameter optimization of creep feed grinding is so hard because this process has plenty of parameters such as feed rate, wheel speed and depth of cut. Most of parameters effect to material of parts. For fir tree geometry, it is desired that the properties of the material do not change, while producing with narrow tolerances. In literature, feed rate is most important parameter for phase transformation [5]. Moreover, temperature on top of surface of part and wheel speed are linear proportional. As a result of most studies, it is obtained that depth of cut is very important parameter for the temperature on the part [4]. Therefore, all parameters must be examined in terms of parts.

Wire electrical discharge machining is another common process type for using fir tree manufacturing. However, this process working with the principle of erosion so quite high temperatures are occurred on the top surface of part. Therefore, wire electrical discharge machining has significantly disadvantages. Nevertheless, it is studied to produce the necessary slots with wire electrical discharge machining for the turbine discs [6]. In literature, it is understood that wire electrical discharge machining has many parameters like pulse on, pulse off and voltage. However, it was observed that it causes damage to mechanical strengths because of recast layer and heat affected zone by these parameters [7]. Nonetheless, pulse on, pulse off and voltage parameters are crucial parameters for surface roughness, profile accuracy and hardness [8][9]. On the other hand, studies on discharge energy in wire electrical discharge machining show that these are the most basic parameters [9]. In addition, it is observed that there are difficulties in the production of parts as fir tree, in achieving profile tolerances in transitive radius regions [10]. Therefore, wire electrical discharge machining parameters must be studied for specific parts like creep feed grinding.

The two processes are not compared to each other for producing fir tree geometry with using additively manufactured Inconel 939 materials. In this study, based on the own parameters of the processes, and disadvantages and advantages of the processes are discussed.

MATERIALS AND METHODS

In this study, two different production methods are compared with using Taguchi analysis considering on recast layer, heat affected zone thickness, surface roughness and profile accuracy. Table 1 shows the parameters selected for wire electrical discharge machining and the experimental set created as type of L9 Taguchi analysis. Table 2 shows the parameters

TABLE 1. Experimental Results of Wire Electrical Discharge Machining

Sample No	Pulse On (µs)	Pulse Off (µs)	Voltage (V)	Recast Thickness X (µm)	Recast Thickness Y (µm)	Recast Thickness Z (µm)	Heat Affected Zone Thickness Y (µm)
1	0,1	1	40	3,73	2,62	3,95	54,80
2	0,1	3	80	1,90	1,81	1,90	64,72
3	0,1	9	120	1,88	2,86	2,97	51,30
4	0,6	1	80	3,10	3,11	5,73	46,50
5	0,6	3	120	3,04	3,31	3,73	42,67
6	0,6	9	40	3,83	2,64	4,01	52,34
7	0,9	1	120	4,25	3,94	5,59	21,83
8	0,9	3	40	3,11	4,00	4,41	35,23
9	0,9	9	80	4,07	3,44	4,25	27,63

TABLE 2. Experimental Results of Creep Feed Grinding

Sample No	CFG Type	Feed Rate (mm/min)	Depth of Cut (µm)	Wheel Speed (m/s)	Recast Thickness Y (µm)	Heat Affected Zone Y (µm)	Heat Affected Zone Z Thickness (µm)
1	Continuous	300	50	15	2,54	31,50	56,42
2	Continuous	300	200	25	1,76	34,52	54,53
3	Continuous	300	600	35	1,43	36,72	59,26
4	Continuous	400	50	15	3,32	21,80	30,21
5	Continuous	400	200	25	3,56	26,87	34,57
6	Continuous	400	600	35	1,87	29,57	40,76
7	Continuous	500	50	15	6,76	14,00	28,00
8	Continuous	500	200	25	6,20	16,67	32,41
9	Continuous	500	600	35	4,12	15,68	29,70
10	Non-Dressing	300	50	15	2,17	29,84	36,76
11	Non-Dressing	300	200	25	1,30	29,27	34,85
12	Non-Dressing	300	600	35	1,13	28,78	34,74
13	Non-Dressing	400	50	15	3,87	15,97	23,56
14	Non-Dressing	400	200	25	3,20	16,63	29,82
15	Non-Dressing	400	600	35	1,54	14,80	22,71
16	Non-Dressing	500	50	15	5,67	15,51	27,22
17	Non-Dressing	500	200	25	6,57	16,70	29,50
18	Non-Dressing	500	600	35	3,60	15,00	29,00

selected for creep feed grinding and the experimental set created as type of L18 Taguchi analysis. In this way, continuous and without continuous creep feed grinding can be compared with each other.

There are 3 important geometric features for the fir tree geometry. In order to make comparisons according to regions, they are examined by separating from each other. For comparisons, the geometry and selected areas shown in Figure 1 are used. The regions are indicated by X-Outer radius in fir tree, Y-Contact refer to the flat areas that come into contact with turbine disc during operation, and the areas are indicated by Z-Inner radius.

In order to compare the processes, Inconel 939 materials are produced by additive manufacturing method. Details of the Inconel

939 used are given in Table 3. For trials, prisms of 125x40x40mm dimensions were produced. The produced samples are heat treated at 1160°C for 4 hours and 850°C for 16 hours. Since wire electrical discharge machining and creep feed grinding are separated from each other as thermoelectrically and mechanically,

different number of experiments have been carried out on the same samples in two processes. Thanks to the working flexibility are offered by wire electrical discharge machining, 6 different trials can be done in a single sample. Experiments on W-EDM are done with Thermo Tex copper wire 0.30mm diameter at Agie Charmilles CUT300Sp. Samples produced for CFG are carried out by performing a single experiment in a single sample to allow the wheel to reach the sample and at the same time

prevent nozzle from hitting the fixtures. Experiments on CFG are done with Tyrolit Strato Ultra wheels at Blohm Profimat 607 Mc. The wheel properties are given in Table 4. Surface roughness measurements are checked with MarSurf LD 26. However, instead of radii, flat areas Y-Contact are preferred for the accuracy of measurements. Also, it is more important to compare the parts that come into contact in working conditions. The surfaces are scanned by laser and the accuracy of produced profiles are examined. Finally, parts for recast layer and heat affected zone thickness measurements are etched with Schanz and measurement are done with using a microscope.

RESULTS AND DISCUSSIONS

In this study, recast layer, heat affected zone thickness, surface roughness and dimensional accuracy are examined with fir tree geometry produced by two different processes. The results obtained in two processes are shown in Table 1 and Table 2. Comparisons are made on a process basis for the locations shown in Figure 1. As can be seen from Table 1 and Table 2, the two processes show different results in different areas.

Y-Contact Area

Y contact is one of the most important regions of fir tree geometry. Since, it is the location that comes into contact with the turbine disc after assembly and is exposed to the heaviest loads like dynamic centrifugal forces. Therefore, this section profile tolerances are the narrowest. For this reason, in this area, recast layer and heat affected zone formations are generally kept to a minimum.

Wire Electrical Discharge Machining

It is observed that the parameters examined for field Y are quite effective for recast layer and heat affected zone thickness. As seen in Figure 2a, pulse on has a very serious effect for recast layer formation. As the pulse on value increases, recast layer thickness also increases. This situation is related to the increase of pulse on value, the direct increase of the heat input transferred to the part. This confirms the discharge energy in Equation 1. Briefly, as pulse on increases, discharge energy increases. In this way, as the heat energy transfers to the unit area increases, it increases at the maximum temperature that occurs on the part. In Equation 1, V is voltage, I is current, t_{on} is pulse on time and t_{off} is pulse off time.

As is known, the phase change temperature of the material must be exceeded for recast layer

TABLE 3. The Nominal Chemical Composition of Inconel 939 in wt%[11]

Cr	Co	C	Fe	W	Mo	Nb	Ta	Ti	Al	Zr	B	Ni
22.5	19.0	0.15	-	2.0	-	1.0	1.4	3.7	1.9	0.1	0.01	Bal.

TABLE 4. Wheel Details

Abrasive Type	A	Aluminum Oxide
Grain Size	602	Super Finish / Very Fine
Grade	G	Soft
Type of bond	V	Vitrified

$$E_e = \int_0^{t_e} V_e(t)I_e(t)dt = V_eI_et_{on}\frac{1}{t_{on}+t_{off}}$$

Eq 1.[12]

formation. Therefore, if the presence of other factors such as flushing are ignored, the recast layer thickness is expected to increase with increasing temperature value. On the other hand, pulse off value appears as a divider in Equation 1. Thus, as pulse off increases, discharge energy decreases. Test results confirm this situation. In addition, according to the main working principle of wire electrical discharge machining, the molten material is removed from the main material with the upper and lower head of W-EDM, thus recast layer formation can be prevented. With the increase of pulse off time, sufficient time is given for flushing, which is one of the reasons for the decrease of recast layer thickness with increase of pulse off time in this study.

For voltage parameter, a general trend like other parameters could not be obtained. When the Equation 1 is examined, it is seen that there is an increase in voltage value and an increase in discharge energy. Therefore, the increase in recast layer thickness between 80 to 120 voltage values in Figure 2a makes sense. However, the decrease between 40 and 80 voltage values loses, its meaning against the equation shown. Although discharge energy increases in this interval, it can be interpreted as the meting material re-filling the craters formed as shown in Figure 2b and increasing the thickness of recast layer.

The samples shown in Figures 3a and 3b are processed with 80 voltage. As can be seen from these processed samples, craters are occurred and are filled with recast layer. Continuous recast layer values are measured throughout the study like figure 3a. Maximum recast layer thickness are not evaluated as in Figure 3a, but maximum recast layer thickness is shown by Figure 3b with using crater region. For figures 3a and 3b, the areas shown in the original pictures in the upper line are shown by enlarging in them

in the lower line. Therefore, the recast layer thickness appears to decrease in the range specified for voltage which is between 40 to 80. Considering that the values other than the voltage in Equation 1 are kept constant, as the voltage value increases, the discharge energy is increased, therefore high temperatures occur on the surface of the part. However, if the critical temperature is not reached, a decrease in recast layer thickness may occur. A similar situation is seen in the previous study [13].

Formation of heat affected zone shows similar trend with generation of recast layer. For pulse on, it had a much more serious effect on heat affected zone than recast layer in the range of 0,1-0,6 μs. The thickness difference for the heat affected zone formed for the 0.1, 0.6 and 1.2 states are shown in Figure 4. In Figure 4, the pulse on affect are shown respectively, the figures shown on the left are enlarged images of the original images to the right. This can be related to discharge radius shown in Equation 2. In Equation 2, K is contact which is calculated from first hit of radius, I is current and t_{on} is pulse on time.

$$R_{plasma} = KI^m t_{on}^n \qquad \text{Eq 2.[12]}$$

As can be seen in Equation 2, pulse on value and discharge radius are directly proportional. In other words, if the pulse on time is increased, maximum distance is increased so temperature distribution can be extended. Therefore, the slope in Figure 2b shown for pulse on appears in an increasing direction with heat affected zone thickness.

Pulse off time does not have a serious effect on the formation of heat affected zone, because it can be associated with the requirements for the formation of heat affected zone. It is known that it is the period to be passed in the cooling process for the formation of heat affected zone after high temperature. Since pulse off does not meet these requirements, it is quite normal to see it ineffective.

The increase of voltage values and heat affected zone is a controversial issue, it is related by Equation 1, as the voltage value increases, the temperature increases due to discharge energy. Generally, heat affected zone thickness increases as the temperature increases as the voltage increases. This situation is observed when the voltage value is increased from 40 to 80V. However, when the voltage is increased from 80 to 120V, the heat affected zone thickness value drops. The reason for this can be considered as not being able to catch the
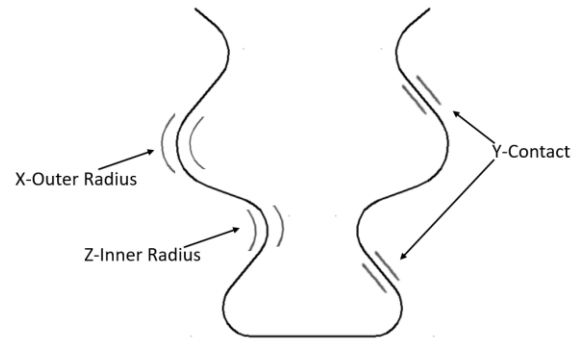
FIGURE 1. Geometric Features on Fir Tree
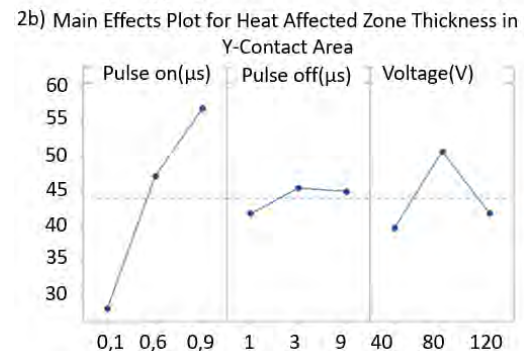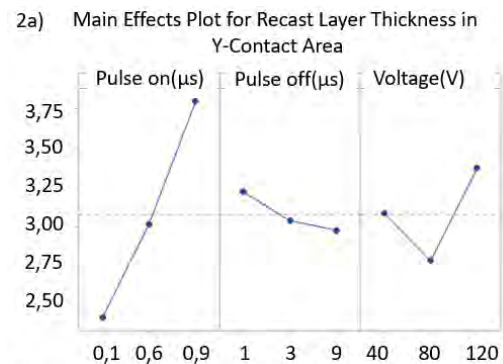
FIGURE 2. Main Effects Plots for Wire EDM
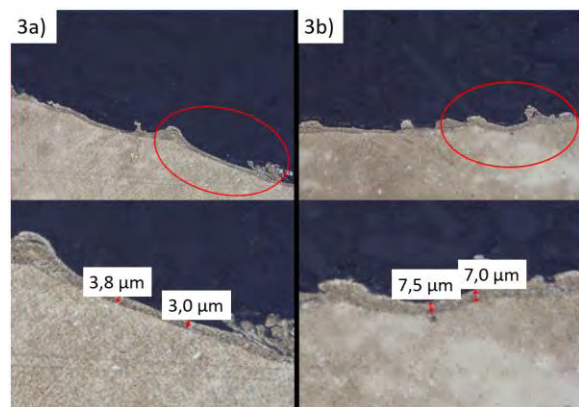
FIGURE 3. Continuous Recast Layer and Crater Formation

critical temperature values required for the formation of heat affected zone. However, this situation should be studied separately.

For profile accuracy, a general problem wire lagging is occurred in wire electrical discharge machining. Working NC code makes progress in the cutting direction by calculating at certain intervals. However, when moving from the area is indicated by Y to the Z area, the wire that has to travel on the radius due to the delay in the calculation continued straight cutting in the Y direction. This led to a deviation from the mean, 20-micron profile in trials. In wire electrical discharge machining, the feed rate of wire increases with increase in the voltage value. Wire lagging can be prevented by decreasing voltage value. However, this situation could not be determined in the experimental set prepared, it will be studied in future work.

Creep Feed Grinding

While examining the Y region, experiments are carried out with feed rate, depth of cut and wheel speed parameters in both type since the creep feed grinding is divided in to 2 types which are continuous and without continuous.

First of all, each of the selected parameters has serious effects on recast layer formation, as shown in Figure 5a. The parameter that has the most serious effect emerges as the feed rate, as it increases recast layer thickness increases significantly. This is because total heat flux is directly proportional to feed rate, as shown in Equation 4. In Equation 4, qt is total heat flux, F_t is grinding force, v_s is wheel speed, a_p is contact length, d_b is contact depth.

$$q_t = \frac{F_t v_s}{\sqrt{a_p d_e b}}$$

Eq 4.[4]

Another parameter that is effective on recast layer generation is depth of cut. As seen in Figure 5a, the general trend is the decrease of recast layer thickness with the increase of depth of cut value. When Figure 5a is examined carefully, there is a serious difference between the slope seen between 0.05 and 0.2mm, and the slope between 0.2 and 0.6mm. This reason for this can be related to the heat input removed by chips. As can be seen from Equation 5, heat flux on the chip is directly connected to the contact area of between wheel and part. In Equation 5, q_{ch} is chip heat flux. Also, total heat flux depends on heat flux of chip, as shown in Equation 6. Equation 6, q_w is workpiece heat flux, q_f is fluid heat flux. Consequently, as depth of cut increases, decreases in total heat flux. In
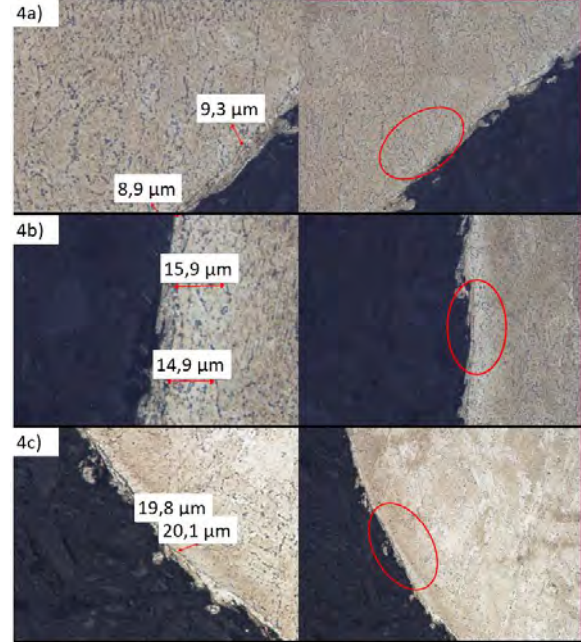
FIGURE 4. Heat Affected Zone Thickness with Different Pulse on Values

other words, as depth of cut increases, decreases heat flux of part. Therefore, it is an expected result that the recast layer thickness decreases. The difference in the slopes are caused by the extraction which is relater contact areas shown in Equation 5.

$$q_{ch} = \rho c T_m \frac{a_p v_w}{\sqrt{a_p d_e}}$$

Eq 5.[3]

$$q_t = q_w + q_s + q_f + q_{ch}$$

Eq 6.[3]

Wheel speed appears to have a very strong effect for recast layer formation. In continuous creep feed grinding, dressing and wheel system works like conventional cylindrical grinding. In this case, an increase in recast layer is expected due to the increase in rotational speed of wheel and the increase in temperature. However, this can be avoided with the high-pressure coolant used in creep feed grinding machines. In addition, since the porosity amounts of the wheels used in machining are quite high compared to the wheels used in conventional grinding systems, cooling becomes more effective. Therefore, it is quite normal that wheel speed has no serious effect.

It is observed that creep feed grinding, whether dressing systems are used continuously or not, have an effect on recast layer thickness. It is quite normal that the recast layer thickness is higher due to the use of continuous dressing and the loading of additional heat input the total system.

In the Y region, even if the continuous system does not have much effect on recast layer formation, it has a serious effect on heat affected zone formation. The reason for this is the addition of heat flux from dressing to the Equation 6. Since the added extra heat flux causes high temperature, it causes heat affected zone formation.

In both continuous and without continuous, although the recast layer thickness increases with increasing feed rate, heat affected zone thickness decreases. The reason for this is related to the time exposed to heat. Since the time exposed to the heat decreases, there is not enough time for heat affected zone to form.

Increasing wheel speed has a negative effect for heat affected zone thickness, even if it does not have a serious effect on recast layer thickness.

Profile accuracy in area Y shows similar results for continuous and without continuous dressing. In this study, dressing amounts are not studied. However, if the dressing amount is studied, it is obvious that the two different processes produce different profile accuracy.

X-OUTER RADIUS AND Z-INNER RADIUS

X and Z regions are one of the areas where loads are most common, even if they do not directly form a contact surface in turbine blade root production. Therefore, even if there are many different connection types, fir tree geometry is most preferred for turbine blade roots. The studies for the Y area are done in the same way, in the X and Z areas.

Wire Electrical Discharge Machining

As a result of the studies with wire electrical discharge machining for X and Z areas, it shows similar results with Y area as for the pulse on and voltage for recast layer thickness as shown in Figure 2a. However, for pulse off, it does not show a similar result to the that in the Y area. The reason for this is that even if pulse off increases, it is not sufficient for flushing with the shrinking cutting areas like inner radius, and the molten material settles into the metal again and increases the amount of recast layer thickness. The effect of flushing is mostly seen in the Z field. When compared with the Y area, the recast layer thickness is 1.2 microns more, while it is 1 micron more than X area. X is the area where flushing is most effective since it is outside the cutting area. However, in this study, continuous recast layer thickness is evaluated. In addition, the maximum recast layer thickness
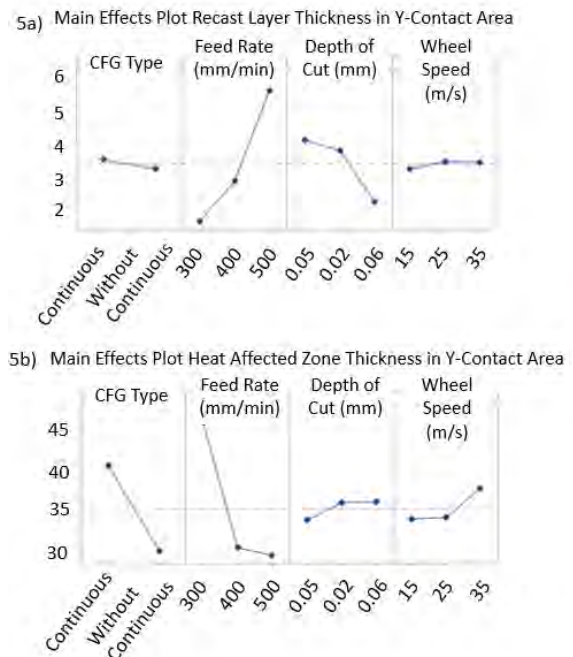
FIGURE 5. CFG Parameter Effects on Recast and Heat Affected Zone Thickness
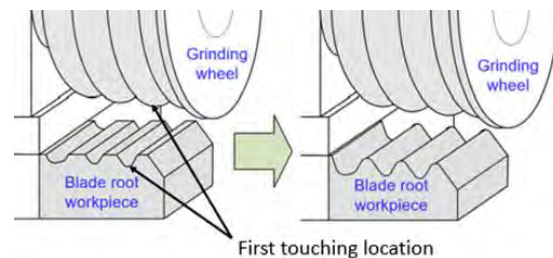
FIGURE 6. CFG Demonstration [4]

is compared. When the maximum conditions are compared, an average of 6 microns thickness differ in the inner radius regions compared to the other fields. This situation is shown in Figure 3a and 3b. In this study, flushing rate in upper and lower heads are not directly examined. However, in the future studies can be performed by detecting optimal parameters of flushing.

As a result of the studies, the thickness of heat affected zone in inner and outer radiuses are like Y area's heat affected zone thickness.

As a result of the examinations carried out, it is found that wire lagging has a great effect on inner and outer radius. In case of a decrease in voltage value, it is seen that the target profile was approached. However, the profile is produced in positive direction in inner radius and profile in negative direction in the outer radius. With the decrease of voltage, the amount of

error decrease because feed rate value decreases at the same time.

Creep Feed Grinding
The analyzed parameters show a similar effect to recast layer and heat affected zone thickness in the inner and outer areas as in the Y area. In areas inner and outer, recast layer occurs much less than Y area, but for inner area, the thickness of heat affected zone increase significantly. The reasons are using formed wheels, the area with the most time remaining in contact with the piece is the inner radius. In other words, as shown in Figure 6, the inner radius is the only contact surface that remains in contact until machining start and end. It is an expected result that the heat affected zone thickness is increased because it is exposed to the heat much longer.

In continuous creep feed grinding systems, Z areas are generally produced minus profile. The reason for this can be wheel that is constantly dressing has more sharp inserts and negative effects on profile accuracy. On the other hand, it is observed that the profile remained in positive direction in without continuous creep feed grinding because clogging causes inserts can no longer function. Especially in depth of cut value of 0.2 and above, serious distortions is occurred in the positive direction.

On the other hand, there is no difference for the two processes for the outer radius because the X area is at the outermost point, and the part profile is formed without the inserts being affected.

CONCLUSION
As a result of the experiments and reviews;
- It is found that time of producing fir tree with creep feed grinding is on average 4 times faster than processing with wire electrical discharge machining.
- Creep feed grinding consumable costs are found to be 2 times higher for a single fir tree geometry than wire electrical discharge machining. Also, CFG is significantly higher for initial investment costs than W-EDM.
- In general, CFG should be selected for low recast thickness value in all selected ones.
- Although there is no significant difference between the two processes for the low heat affected thickness in Y-Connected area, W-EDM for the Z-Inner Radius is quite better compared to the CFG.

- CFG is slightly better, although the two processes show similar results for the surface roughness.
- CFG shows much better result across all selected areas for profile accuracy.
- Optimization is required in the parameters studied for the production of parts with the use of CFG. In addition, optimization of material removal rate of dressing is essential for dimensional accuracy.
- A better profile accuracy can be obtained by lowering the voltage value for machining with W-EDM, but there is a need for specific optimization for the fir tree models as the recast layer thickness increases with decreasing voltage.

REFERENCES
[1] Helmut G. Naumann . Steam turbine blade design options: how to specify or upgrade., Proceedings of the 11th Turbomachinery Symposium ed. Texas A&M University. Turbomachinery Laboratories: ; 1982.
[2] Rolls Royce The Jet Engine. John Wiley & Sons.; 2015
[3] Malkin S, Guo C. Thermal Analysis of Grinding. CIRP Annals. 2007;56(2):760-782.
[4] Miao Q, Li H, Ding W. On the temperature field in the creep feed grinding of turbine blade root: Simulation and experiments. International Journal of Heat and Mass Transfer. 2020;147:118957.
[5] Duscha M, Eser A, Klocke F, Broeckmann C, Wegner H, Bezold A. Modeling and Simulation of Phase Transformation during Grinding. Advanced Materials Research. 2011;223:743-753.
[6] Welling D. Results of Surface Integrity and Fatigue Study of Wire-EDM Compared to Broaching and Grinding for Demanding Jet Engine Components Made of Inconel 718. Procedia CIRP. 2014;13:339-344.
[7] Xavior M A, p A. Fatigue life and Fracture Morphology of Inconel 718 machined by spark EDM process. Procedia Manufacturing. 2019;30:292-299.
[8] Li L, Guo Y, Wei X, Li W. Surface Integrity Characteristics in Wire-EDM of Inconel 718 at Different Discharge Energy. Procedia CIRP. 2013;6:220-225.
[9] Subrahmanyam M, Nancharaiah T. Optimization of process parameters in wire-cut EDM of Inconel 625 using Taguchi's approach. Materials Today: Proceedings. 2020;23:642-646.

[10] Mohapatra K, Satpathy M, Sahoo S. Comparison of optimization techniques for MRR and surface roughness in wire EDM process for gear cutting. International Journal of Industrial Engineering Computations. 2017;:251-262.

[11] Kitteringham G. High Temperature Alloys for Gas Turbines and Other Applications 1986. High Temperature Technology. 1987;5(1):52-54.

[12] Singh H. Experimental study of distribution of energy during EDM process for utilization in thermal models. International Journal of Heat and Mass Transfer. 2012;55(19-20):5053-5064.

CAPTURED POWDER DAMPING IN ADDITIVE MANUFACTURING

Tony Schmitz[1,2], Emma Betters[1,2], and Justin West[1,2]
[1]Mechanical, Aerospace, and Biomedical Engineering
University of Tennessee, Knoxville
Knoxville, TN 37996, USA
[2]Energy and Transportation Science Division
Oak Ridge National Laboratory
Oak Ridge, TN 37830, USA

INTRODUCTION[1]

Additive manufacturing has been embraced as a disruptive technology for new production capabilities and strategies across multiple industries. Examples of its value include reduced part count in assemblies, maintenance and repair, and innovative structural designs [1]. Metal additive can be generally categorized by the feed material: powder or wire. Powder-based technologies include powder feed and powder bed. The layered melting or sintering of metal powder offers a unique opportunity for increased damping of printed components.

The dynamics of structures can be described by modal analysis, where the eigenvalues (or natural frequencies) and eigenvectors (or mode shapes) are used to define the vibration behavior. For any location on a structure, the frequency response function, or FRF, can be measured and the natural frequency, stiffness, and damping can be extracted for each mode [2]. Generally, it is desired to maximize the stiffness and damping to reduce the vibration magnitude due to external dynamic forces.

In this research, metal powder is intentionally retained within powder bed fusion structures to achieve increased damping. This internal, captured powder serves as an energy dissipation mechanism during vibration of the surrounding solid body. This work builds on seminal research by Scott-Emuakpor et al. [3-7]. This group first used laser powder bed fusion to produce components that contain internal geometries packed with powder trapped during layer-by-layer powder spreading and fusion. The application domain is integrally bladed rotors, where the monolithic design does not offer the airfoil-to-disk frictional energy dissipation for assembled designs. They studied damping for high strain-long duration tests and evaluated the endurance, repeatability, and recovery of the damping provided by unfused powder pockets in beam geometries. This research also adds to the prior work on particle dampers, which dissipate external energy within a constrained particle bed through collisions between the particles and container walls and collisions, sliding friction, and rolling friction between the individual particles [8].
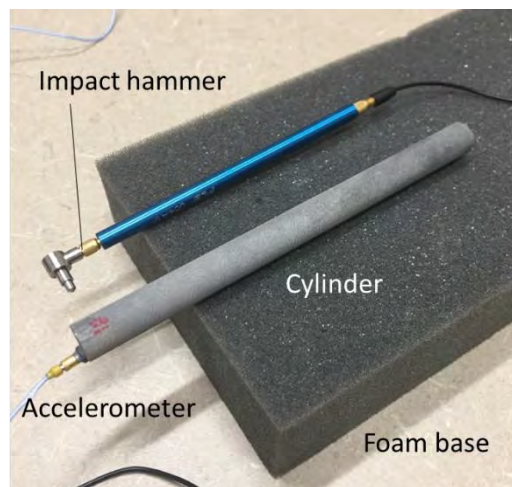
FIGURE 1: Impact testing setup for FRF measurement.

EXPERIMENTAL APPROACH

To demonstrate the potential for increased damping through captured powder, aluminum cylinders were designed and printed in a powder

bed Concept Laser M2. Ingots of an aluminum-based alloy were produced by Eck Industries and atomized and sieved to a 20-63 μm size distribution (spherical shape) by Connecticut Engineering Associates Corporation. The nominally 10.3 mm diameter by 129.5 mm long cylinders were printed in a vertical orientation and then separated from the horizontal build plate using wire EDM. Solid and hollow filled geometries with different internal diameters were selected.

Modal testing was carried out by placing the cylinders on a soft foam base. This approximated free-free boundary conditions and eliminated the complication associated with providing a repeatable fixed boundary condition for cantilever testing. Impact testing was completed using a small impact hammer (PCB model 086E80), low-mass accelerometer (PCB model 352C23), and MLI's MetalMax TXF software. The measurement setup is shown in Fig. 1.
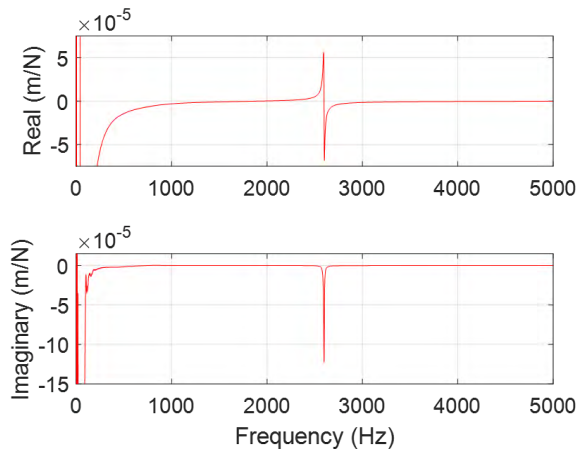
FIGURE 2: FRF for solid cross-section cylinder. (Top) Real part. (Bottom) Imaginary part.

The FRF for a 10.25 mm diameter, 129.4 mm long solid cross-section cylinder is displayed in Fig. 2. It is observed that the solid cylinder is lowly damped with a single bending mode at 2598 Hz. The large roll-off in the real part of the FRF at low frequencies is due to the free-free boundary conditions (i.e., rigid body modes). While the results are not included here for brevity, hollow cylinder (no powder fill) measurements were also completed and similar damping behavior to the solid cylinder was observed.

The FRF for a 10.29 mm outer diameter, 129.4 mm long hollow cross-section cylinder is

displayed in Fig. 3, where the inner diameter is 4.9 mm (the design value was 5.1 mm). The same scale as Fig. 2 is shown; the bending mode is now at 2791 Hz. This inner diameter was estimated from a computed tomography (CT) scan of the cylinder since both ends were solid to contain the captured powder. Also, the powder fill for the internal volume was measured to be 97%. example results are presented in Fig. 4. From Fig. 3 it is observed that the captured powder increases the damping substantially based on the significant magnitude reduction (approximately an order of magnitude). The natural frequency also increases, primarily because the powder density is less than the solidified metal density.
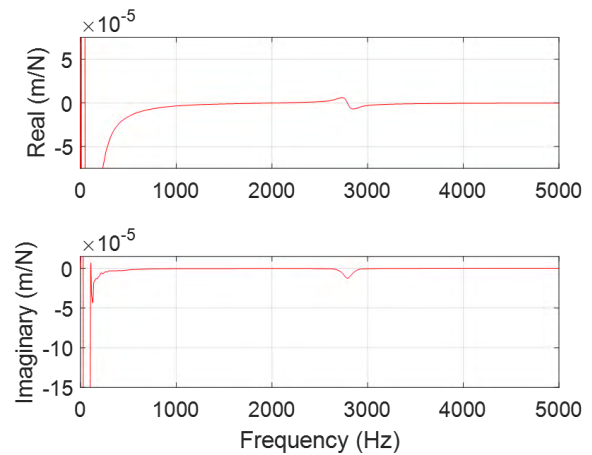
FIGURE 3: FRF for hollow cross-section cylinder with captured powder (4.9 mm inner diameter).
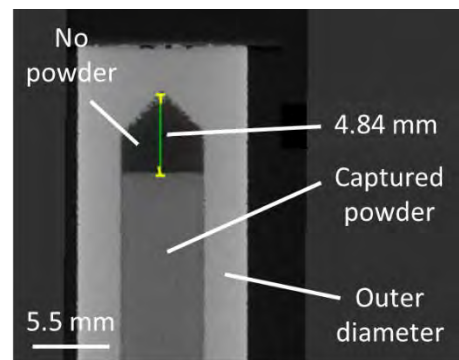
FIGURE 4: Example measurement result for 4.9 mm inner diameter cylinder. The density difference between the sintered outer diameter (light) and captured powder (dark) is identified by the image gray scale.

The FRF for a 10.30 mm outer diameter, 129.3 mm long hollow cross-section cylinder is displayed in Fig. 5, where the inner diameter is 9.0 mm (the design value was 9.1 mm) and the powder fill for the internal volume was measured to be 93%. The same scale as Fig. 2 is again shown; the bending mode is now at 2605 Hz. It is observed that the additional volume of captured powder due to the larger inner diameter further increases the damping. The natural frequency decreases due to the reduced wall thickness and associated stiffness.
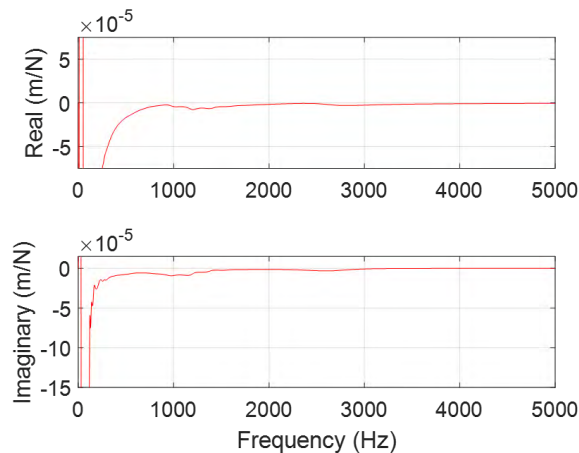
FIGURE 5: FRF for hollow cross-section cylinder with captured powder (9.0 mm inner diameter).
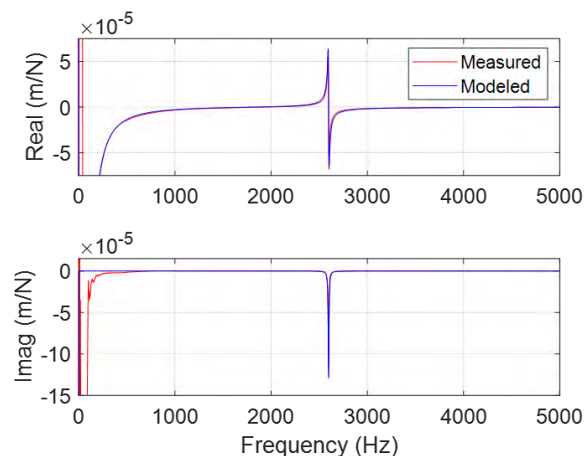
FIGURE 6: Measured and modeled FRF for solid cross-section cylinder.

MODELING

In order to extract damping values from the Fig. 2, 3, and 5 results, receptance coupling

substructure analysis, or RCSA, was implemented to model the beams. In this approach, constant cross-sections are modeled using Timoshenko beam theory and then their receptances (or FRFs) are coupled to predict the assembly dynamics. Use of the Timoshenko beam model for the individual sections enabled structural damping to be incorporated as the complex modulus, $E' = E(1 + i\eta)$, where E is the elastic modulus and η is the dimensionless structural damping factor. The details of the RCSA procedure are provided in [2] and are not repeated here.

Initially, the 10.25 mm outer diameter, 129.4 mm long solid cross-section cylinder was modeled, where the density was determined from mass measurement and the cylinder dimensions, and the elastic modulus and damping factor were treated as fitting parameters. The modulus was used to match the measured natural frequency and the damping factor was used to match magnitude. The RCSA model prediction is compared to the measurement in Fig. 6. The free-free model parameters are provided in Table 1.

TABLE 1: RCSA model parameters for solid cross-section cylinder.

Model parameter	Value
Outer diameter (mm)	10.25
Length (mm)	129.4
Elastic modulus (GPa)	63.2
Density (kg/m^3)	2693.5
Damping factor (-)	0.004

FIGURE 7: RCSA model for hollow cylinders. Five separate sections were rigidly coupled to predict the direct assembly receptance at the left end.

Next, the two hollow cylinders were modeled. The cross-sections are identified in Fig. 7 and the RCSA parameters are listed in Tables 2 (4.9 mm inner diameter) and 3 (9.0 mm inner diameter). Note that sections 2-4 were powder filled and the powder elastic modulus was assumed to be zero (no bending resistance). A comparison between the measured and modeled FRFs for the 4.9 mm inner diameter cylinder is displayed in Fig. 8.
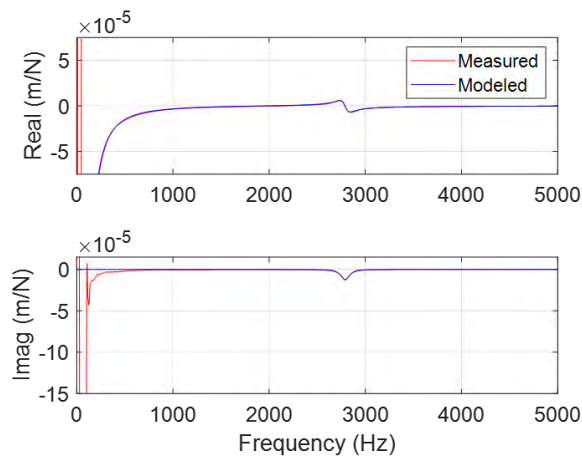
FIGURE 8: Measured and modeled FRF for hollow cross-section cylinder with captured powder (4.9 mm inner diameter).

TABLE 2: RCSA model parameters for hollow cross-section cylinder (4.9 mm inner diameter).

Model para-meter	Section				
	1	2	3	4	5
Outer dia. (mm)	10.29	10.29	10.29	10.29	10.29
Inner dia. (mm)	0	1.225	3.675	4.9	0
Length (mm)	3.2	1.35	1.35	118.9	4.55
Outer modul. (GPa)	69.55	69.55	69.55	69.55	69.55
Inner modul. (GPa)	69.55	0	0	0	69.55
Outer density (kg/m^3)	2670.3	2670.3	2670.3	2670.3	2670.3
Inner density (kg/m^3)	2670.3	1338.7	1338.7	1338.7	2670.3
Damping factor (-)	0.004	0.039	0.039	0.039	0.004

RESULTS AND DISCUSSION
Figures 2, 3, and 5 demonstrate the additional energy dissipation provided by the captured powder. Tables 1-3 list the structural damping factors for the three cylinders. To provide a visual comparison, Figs. 9 and 10 plot the damping factors as a function of internal diameter and cross-sectional area. Fitting functions are also included. For diameter, the fourth-order fit is given by Eq. 1, where d is the inner diameter. For area, the second-order fit is given by Eq. 2, where A is the inner cross-sectional area. Both support the trend that increased powder volume provides increased energy loss and structural damping.

$$\eta = 0.004 + 5 \times 10^{-5}d^4 \tag{1}$$

$$\eta = 0.004 + 8 \times 10^{-5}A^2 \tag{2}$$

TABLE 3: RCSA model parameters for hollow cross-section cylinder (9.0 mm inner diameter).

Model para-meter	Section				
	1	2	3	4	5
Outer dia. (mm)	10.3	10.3	10.3	10.3	10.3
Inner dia. (mm)	0	2.25	6.75	9.0	0
Length (mm)	1.3	2.15	2.15	120.9	2.8
Outer modul. (GPa)	69	69	69	69	69
Inner modul. (GPa)	69	0	0	0	69
Outer density (kg/m^3)	2670.3	2670.3	2670.3	2670.3	2670.3
Inner density (kg/m^3)	2670.3	1366.8	1366.8	1366.8	2670.3
Damping factor (-)	0.004	0.33	0.33	0.33	0.004

CONCLUSIONS
This paper reported measurements and models for the increased damping provided by retention of metal powder within additively manufactured structures. Solid and hollow aluminum cylinders were fabricated in a powder bed Concept Laser M2 printer where the internal, captured powder in the hollow cylinders provided increased energy dissipation when acted on by external forces.
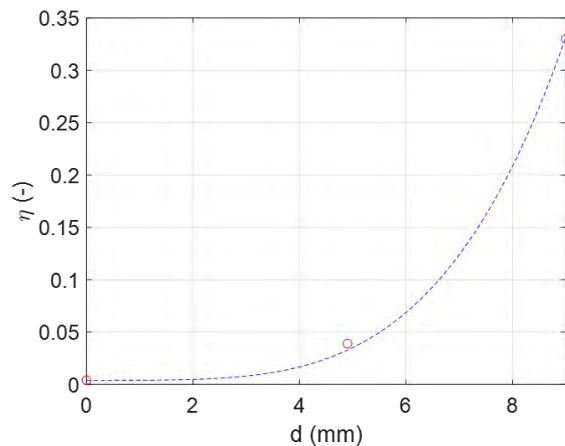
FIGURE 9: Damping factor data (circles) and fit (dashed line) versus inner diameter.
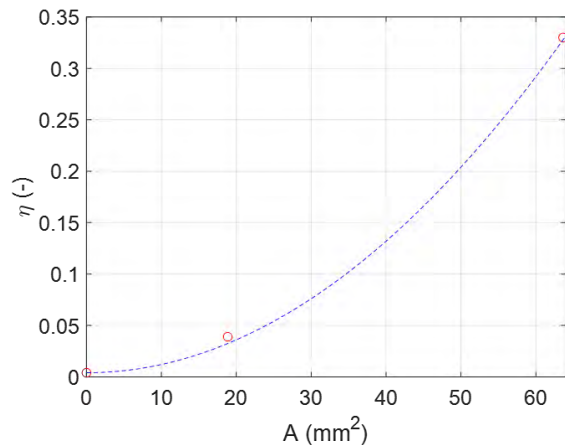
FIGURE 10: Damping factor data and fit versus inner cross-sectional area.

Free-free boundary condition impact testing was competed to compare the frequency response functions for three cylinder geometries: one solid cross-section and two hollow cross-sections with 4.9 mm and 9.0 mm inner diameters. It was observed that the frequency response function magnitude decreased with larger powder volumes, which indicated increased damping. The damping increase was quantified using a structural damping model. Timoshenko beam models of the cylinders' constant cross-sections were defined and rigidly joined using receptance coupling substructure analysis to predict the assembly dynamics. The dimensionless damping factor was considered a fitting parameter so its variation with cross-sectional geometry could be determined. It was observed that the damping

factor increased with the fourth power of inner diameter and second power of inner cross-sectional area.

REFERENCES
[1] Frazier, W.E., 2014. Metal Additive Manufacturing: A Review. Journal of Materials Engineering and Performance, 23(6), pp.1917-1928.
[2] Schmitz, T.L. and Smith, K.S., 2011. Mechanical Vibrations: Modeling and Measurement. Springer Science & Business Media.
[3] Scott-Emuakpor, O., George, T., Runyon, B., Holycross, C., Langley, B., Sheridan, L., O'Hara, R., Johnson, P. and Beck, J., 2018, June. Investigating Damping Performance of Laser Powder Bed Fused Components with Unique Internal Structures. In ASME Turbo Expo 2018: Turbomachinery Technical Conference and Exposition. American Society of Mechanical Engineers Digital Collection.
[4] Scott-Emuakpor, O.E., George, T., Beck, J., Runyon, B.D., O'Hara, R., Holycross, C. and Sheridan, L., 2019. Inherent Damping Sustainability Study on Additively Manufactured Nickel-Based Alloys for Critical Part. In AIAA Scitech 2019 Forum (p. 0410).
[5] Scott-Emuakpor, O., George, T., Runyon, B., Sheridan, L., Holycross, C. and O'Hara, R., 2019, June. Assessing Manufacturing Repeatability of Inherently Damped Nickel Alloy Components via Forced-Response Testing. In Turbo Expo: Power for Land, Sea, and Air (Vol. 58677, p. V006T24A010). American Society of Mechanical Engineers.
[6] Scott-Emuakpor, O., George, T., Runyon, B., Langley, B., Sheridan, L., Holycross, C., O'Hara, R. and Johnson, P., 2019. Forced-Response Verification of the Inherent

Damping in Additive Manufactured Specimens. In Mechanics of Additive and Advanced Manufacturing, Volume 8 (pp. 81-86). Springer, Cham.

[7] Scott-Emuakpor, O.E., Beck, J., Runyon, B. and George, T., 2020. Multi-Factor Model for Improving the Design of Damping in Additively Manufactured Components. In AIAA Scitech 2020 Forum (p. 1631).

[8] Gagnon, L., Morandini, M. and Ghiringhelli, G.L., 2019. A Review of Particle Damping Modeling and Testing. Journal of Sound and Vibration, p.114865.

STABILITY ANALYSIS WITH UNCERTAINTY FOR TWIST DRILLING

Tony Schmitz[1,2], Michael Gomez[1,2], Andrew Honeycutt[2], Jaydeep Karandikar[2],
Jongyoup Shim[3], Seung-Kook Ro[3], and Jooho Hwang[3]
[1]Mechanical, Aerospace, and Biomedical Engineering
University of Tennessee, Knoxville
Knoxville, TN 37996, USA
[2]Energy and Transportation Science Division
Oak Ridge National Laboratory
Oak Ridge, TN 37830, USA
[3]Advanced Manufacturing Systems Research Division
Korea Institute of Machinery & Materials
Yuseong-gu, Daejeon 34103, Korea

INTRODUCTION[1]

Hole making is an important machining activity for the aerospace, automotive, ship building, and biomedical industries, to name a few. The associated materials of interest are metal alloys, reinforced composites, polymers, bone, and others [1-5]. Mechanical techniques include twist drilling, vibration assisted twist drilling, ultrasonic machining, and rotary ultrasonic machining [1]. Among these, twist drilling is the most prevalent technique with process parameters that include spindle speed, feed rate, drill diameter and geometry, drill material, drill coating, work material, pilot hole diameter, and coolant/lubricant application method and amount.

One limitation to hole quality, drill life, and material removal rate in twist drilling is chatter, a self-excited vibration caused by regeneration of waviness, or the overcutting of the previously machined surface with a spindle speed-dependent time delay [6]. In milling, regeneration of waviness causes chip thickness variation due to lateral bending of the end mill and other vibration modes that give deflection perpendicular to the tool axis (i.e., the feed direction in peripheral end milling) [7-8]. In drilling, on the other hand, regeneration occurs due to vibrations in the axial (feed) direction. Axial deflection of the twist drill during material removal causes chip thickness variation which, in turn, can lead to self-excited vibration depending on the combination of spindle speed and chip width

(i.e., the difference between the twist drill diameter and pilot hole diameter, if applicable). A primary mechanism for this axial vibration is torsional-axial coupling due to the drill geometry. The helical drill shape leads to beam twist (about the axis) when an axial force is applied and, conversely, an axial deflection when a torque is applied [9].

While prior modeling efforts differ in approach and solution technique, they each treat the drilling process as deterministic. However, it is well-understood that the inputs to these models, as well as the analyses themselves, are uncertain. To enable a predictive capability, it is essential to consider these uncertainties and subsequently provide uncertain (probabilistic) model outputs. The contribution of this paper is to present the first uncertainty analysis for drilling stability using the frequency-domain model presented in [6] to identify the relationships between uncertainties in the measured inputs and output (i.e., the stability map). Due to the nonlinear nature of the stability model, Monte Carlo simulation is implemented to complete the uncertainty propagation. Experiments are also performed to compare with predictions and stability limit uncertainty bounds.

The paper is organized as follows. First, as a convenience to the reader, the twist drilling stability algorithm described in [6] is detailed. Second, the Monte Carlo uncertainty analysis is

---

described. Third, experimental results are presented. Finally, conclusions are discussed.

FREQUENCY-DOMAIN STABILITY ANALYSIS

Axial feed of a twist drill into the workpiece causes the chip thickness to increase. The thrust force (aligned with the drill axis, z) required to shear away this chip is:

$$F_z = -C_2 bh, \qquad (1)$$

where C_2 depends on the drill geometry and work material, h is the chip thickness and b is the chip width (i.e., the difference between the twist drill diameter and the pilot hole diameter, if applicable). The associated torque is:

$$M_z = -C_1 bh R_{av}, \qquad (2)$$

where C_1 also depends on the drill geometry and work material and R_{av} is the average radius of the force. With vibration in the axial direction, the chip thickness varies and its instantaneous value depends on the mean (commanded) value, the current vibration, and the previous cutting edge vibration at the same drill rotational angle:

$$h = h_{av} + z - z(t - \tau), \qquad (3)$$

where h_{av} is the feed per cutting edge (or flute, two flutes total for twist drills) and τ is the time delay between flutes. This time delay serves as the mechanism for regenerative chatter. Although the twist drill is stiff in the z (axial) direction, its geometry leads to coupling between the torsional and axial vibration modes. As noted, an axial force causes the beam to twist and a torque causes it to change length.

The second-order, time delay differential equation of motion for the drilling process can be written as:

$$M\ddot{u} + C\dot{u} + Ku = F, \qquad (4)$$

where u is the generalized coordinate that includes translations in the x, y, and z directions and rotations, θ, about the z axis:

$$u = \begin{bmatrix} x_1 & x_2 & \cdots & x_N & y_1 & y_2 & \cdots & y_N \\ z_1 & z_2 & \cdots & z_N & \theta_1 & \theta_2 & \cdots & \theta_N \end{bmatrix}^T. \qquad (5)$$

and the subscripts indicate the axial location (N is the tip). Returning to Eq. 4, F is the generalized force:

$$F = \begin{bmatrix} F_{x1} & F_{x2} & \cdots & F_{xN} & F_{y1} & F_{y2} & \cdots & F_{yN} \\ F_{z1} & F_{z2} & \cdots & F_{zN} & M_{z1} & M_{z2} & \cdots & M_{zN} \end{bmatrix}^T. \qquad (6)$$

In Eq. 6, F_x and F_y are the unbalanced forces in the x and y directions and the other entries were defined in Eqs. 1 and 2. To convert from physical to modal parameters using modal analysis, the mode shapes are required. Let ψ_n be a vibration mode (mode number n) that can contain contributions from bending, torsion, and axial deformations of the twist drill.

$$\psi_n = \begin{bmatrix} q_{1n} & q_{2n} & \cdots & q_{Nn} & r_{1n} & r_{2n} & \cdots & r_{Nn} \\ s_{1n} & s_{2n} & \cdots & 1 & \alpha_{1n} & \alpha_{2n} & \cdots & \alpha_{Nn} \end{bmatrix}^T. \qquad (7)$$

$$u = \psi_n p. \qquad (8)$$

Substitution of Eq. 8 into Eq. 4 yields:

$$M\psi_n \ddot{p} + C\psi_n \dot{p} + K\psi_n p = F. \qquad (9)$$

Pre-multiplying both sides by ψ_n^T gives:

$$\psi_n^T M\psi_n \ddot{p} + \psi_n^T C\psi_n \dot{p} + \psi_n^T K\psi_n p = \psi_n^T F. \qquad (10)$$

Considering excitation at the twist drill tip only, Eq. 6 simplifies to:

$$F = \begin{bmatrix} 0 & 0 & \cdots & F_{xN} & 0 & 0 & \cdots & F_{yN} \\ 0 & 0 & \cdots & F_{zN} & 0 & 0 & \cdots & M_{zN} \end{bmatrix}^T. \qquad (11)$$

Applying the orthogonality of eigenvectors and assuming proportional damping [34], the equation of motion in modal coordinates is:

$$M_q \ddot{q} + C_q \dot{q} + K_q q = \psi_n^T F. \qquad (12)$$

Considering only the torsional-axial contributions to Eq. 7, the mode shape simplifies to:

$$\psi_n = \begin{bmatrix} 0 & 0 & \cdots & 0 & 0 & 0 & \cdots & 0 \\ 0 & 0 & \cdots & 1 & \alpha_{1n} & \alpha_{2n} & \cdots & \alpha_{Nn} \end{bmatrix}^T \qquad (13)$$

In this case, the generalized modal force vector simplifies to:

$$\psi_n^T F = F_{zN} + \alpha_{Nn} M_{zN}, \qquad (14)$$

where α_{Nn} serves as a coupling parameter that relates the torque to the torsional-axial vibration mode. The simplified mode shape in Eq. 13

enables the chip thickness equation (Eq. 3) to be written in modal coordinates by direct substitution:

$$h = h_{av} + q - q(t - \tau). \tag{15}$$

Substituting Eqs. 1 and 2 in Eq. 14 yields:

$$F_{zN} + \alpha_{Nn}M_{zN} = -C_2 bh - \alpha_{Nn}C_1 bhR_{av}. \tag{16}$$

Rewriting Eq. 16 gives:

$$F_{zN} + \alpha_{Nn}M_{zN} = -(C_2 + \alpha_{Nn}C_1 R_{av})bh = -\left(\frac{C_1}{C_2} + \alpha_{Nn}C_1 R_{av}\right)C_1 bh. \tag{17}$$

Substituting $\beta = \frac{C_1}{C_2}$ and inserting the chip thickness from Eq. 15 yields:

$$F_{zN} + \alpha_{Nn}M_{zN} = -\beta C_1 b\left(h_{av} + q - q(t - \tau)\right). \tag{18}$$

Considering only the time-varying component of Eq. 18, the new equation of motion is:

$$M_q\ddot{q} + C_q\dot{q} + K_q q = -\beta C_1 b\left(q - q(t - \tau)\right). \tag{19}$$

Converting Eq. 19 to the frequency domain using the Fourier transform, the result is:

$$Q(\omega)\left(-M_q\omega^2 + i\omega C_q + K_q\right) = -\beta C_1 bQ(\omega)(1 - e^{-i\omega_c \tau}), \tag{20}$$

where ω_c is the chatter frequency. Substituting the torsional-axial mode receptance, $H_n(\omega) = \left(-M_q\omega^2 + i\omega C_q + K_q\right)^{-1}$, in Eq. 20 gives:

$$Q(\omega) = -\beta C_1 H_n(\omega)bQ(\omega)(1 - e^{-i\omega_c \tau}). \tag{21}$$

Moving all terms to the left hand side of Eq. 21 and factoring yields:

$$Q(\omega)\left(1 + \beta C_1 H_n(\omega)b(1 - e^{-i\omega_c \tau})\right) = 0. \tag{22}$$

The (τ, b) pairs that define the stability limit satisfy the characteristic equation:

$$1 + \beta C_1 H_n(\omega)b(1 - e^{-i\omega_c \tau}) = 0. \tag{23}$$

The torsional-axial mode receptance is complex-valued, i.e., $H_n(\omega) = \mathrm{Re}(H_n) + i\mathrm{Im}(H_n)$. Additionally, the Euler identity can be used to rewrite the exponential term, $e^{-i\omega_c \tau} = \cos \omega_c \tau - i \sin \omega_c \tau$. Substituting both in Eq. 23 gives:

$$1 + \beta C_1\left(\mathrm{Re}(H_n) + i\mathrm{Im}(H_n)\right)b(1 - \cos \omega_c \tau + i \sin \omega_c \tau) = 0. \tag{24}$$

Expanding Eq. 24 results in:

$$1 + \beta C_1 b\big((\mathrm{Re}(H_n) - \mathrm{Re}(H_n) \cos \omega_c \tau + i\mathrm{Re}(H_n) \sin \omega_c \tau) + i(\mathrm{Im}(H_n) - \mathrm{Im}(H_n) \cos \omega_c \tau + i\mathrm{Im}(H_n) \sin \omega_c \tau)\big) = 0. \tag{25}$$

Both the real and imaginary parts of Eq. 25 must equate to zero. The real part is:

$$1 + \beta C_1 b(\mathrm{Re}(H_n) - \mathrm{Re}(H_n) \cos \omega_c \tau - \mathrm{Im}(H_n) \sin \omega_c \tau) = 0. \tag{26}$$

The imaginary part of Eq. 25 is:

$$\beta C_1 b(\mathrm{Re}(H_n) \sin \omega_c \tau + \mathrm{Im}(H_n) - \mathrm{Im}(H_n) \cos \omega_c \tau) = 0. \tag{27}$$

Rewriting Eq. 27 gives:

$$\frac{\mathrm{Im}(H_n)}{\mathrm{Re}(H_n)} = \frac{-\sin \omega_c \tau}{1 - \cos \omega_c \tau} = \tan \phi, \tag{28}$$

which relates the chatter frequency and the time delay. Also, from the receptance definition, the ratio of the imaginary part to the real part is the tangent of the phase, ϕ. Returning to Eq. 26 and solving for the limiting chip width, b_{lim}:

$$b_{lim} = \frac{-1}{\beta C_1(\mathrm{Re}(H_n)(1 - \cos \omega_c \tau) - \mathrm{Im}(H_n) \sin \omega_c \tau)}. \tag{29}$$

Rewriting the denominator gives:

$$b_{lim} = \frac{-1}{\beta C_1 \mathrm{Re}(H_n)\left((1 - \cos \omega_c \tau) - \frac{\mathrm{Im}(H_n)}{\mathrm{Re}(H_n)} \sin \omega_c \tau\right)}. \tag{30}$$

Substituting Eq. 28 into Eq. 30 gives:

$$b_{lim} = \frac{-1}{\beta C_1 \mathrm{Re}(H_n)\left((1 - \cos \omega_c \tau) + \frac{\sin \omega_c \tau}{1 - \cos \omega_c \tau} \sin \omega_c \tau\right)}. \tag{31}$$

Equation 31 simplifies to:

$$b_{lim} = \frac{-1}{2\beta C_1 \mathrm{Re}(H_n)}. \tag{32}$$

Because β is negative, only the positive portion of the frequency-dependent $\mathrm{Re}(H_n)$ is considered (i.e., $\mathrm{Re}(H_n) > 0$) in order to obtain positive limiting chip width values. Returning to Eq. 28, the sine and cosine terms can be rewritten using the

double angle trigonometric formulas provided in Eqs. 33 and 34.

$$\sin \omega_c \tau = 2 \sin \frac{\omega_c \tau}{2} \cos \frac{\omega_c \tau}{2} \tag{33}$$

$$\cos \omega_c \tau = \cos^2 \frac{\omega_c \tau}{2} - \sin^2 \frac{\omega_c \tau}{2} \tag{34}$$

Substituting these formulas in Eq. 28 yields:

$$\frac{\text{Im}(H_n)}{\text{Re}(H_n)} = \frac{-2 \sin \frac{\omega_c \tau}{2} \cos \frac{\omega_c \tau}{2}}{1 - \cos^2 \frac{\omega_c \tau}{2} + \sin^2 \frac{\omega_c \tau}{2}} = \frac{-2 \sin \frac{\omega_c \tau}{2} \cos \frac{\omega_c \tau}{2}}{2 \sin^2 \frac{\omega_c \tau}{2}} =$$
$$\frac{-\cos \frac{\omega_c \tau}{2}}{\sin \frac{\omega_c \tau}{2}} = \cot \frac{-\omega_c \tau}{2}. \tag{35}$$

The final expression from Eq. 35 can be written as:

$$\tan \left(\frac{\pi}{2} + \frac{\omega_c \tau}{2} \pm l\pi \right). \tag{36}$$

Equating Eq. 36 to the right hand side of Eq. 28 gives:

$$\frac{\pi}{2} + \frac{\omega_c \tau}{2} \pm l\pi = \phi. \tag{37}$$

Solving Eq. 37 for $\omega_c \tau$ results in:

$$\omega_c \tau = 2\phi - \pi \mp 2l\pi. \tag{38}$$

Because twist drills have two flutes, the spindle speed (in rpm) is written as:

$$\Omega = \frac{60}{2\tau} = \frac{60}{2} \frac{\omega_c}{2\phi - \pi \mp 2l\pi} = \frac{60\omega_c}{4\phi - 2\pi \mp 4l\pi} = \frac{60\omega_c}{4\phi + 2\pi(2l-1)}, \tag{39}$$

where l = 1, 2, 3, … is the integer number of oscillations in the surface profile between cutting edges (at the bottom of the drilled hole) and the negative values for $\mp 4l\pi$ were selected to obtain positive spindle speeds. The stability map is finally obtained by plotting the spindle speed (Eq. 39) versus the limiting chip width (Eq. 32) for l = 1, 2, 3, …. The stability limit is determined from the smallest b_{lim} value at each spindle speed considering all stability lobes simultaneously.

MONTE CARLO SIMULATION

The primary steps for Monte Carlo simulation are: 1) define the inputs and their probability distributions; 2) randomly select a value for each input from the probability distributions; 3) perform a deterministic computation using the inputs to find the output(s); and 4) aggregate the results after many repetitions for a statistical analysis. In this study, the inputs were selected to be: the

modal stiffness, k, modal damping ratio, ζ, and natural frequency, f_n, for the torsional-axial vibration mode of the twist drill when clamped in the holder and spindle; and the torque coefficient C_1. For the remaining parameters, it was assumed that $C_2 = \frac{C_1}{3}$ and $\alpha_{Nn} R_{av} = -3.2$. For the former, this means that the tangential force component is three times larger than the axial force component. For the latter, the negative sign indicates that the twist drill extends as it unwinds and that the torsional deflection is 3.2 times the axial deflection at the drill tip. Both assumptions follow the analysis from [6].

Mean values for the uncertain inputs, {k, ζ, f_n, C_1}, were selected based on testing. Standard deviations were chosen using testing, experience, and process knowledge; a normal distribution was assumed for each input. Additional details are provided in Section 4. The output was the stability map, which identifies the stability boundary as a function of spindle speed. The algorithm described in Section 2 was used to generate this map over multiple iterations with inputs randomly sampled from the pre-defined normal distributions. The speed-dependent variation in the collection of output stability boundaries was then analyzed to determine the associated confidence intervals.

RESULTS
The experimental setup included:
- 9.525 mm diameter, 135 deg split point, 152.4 mm long, high-speed steel (cobalt oxide coating) twist drill with a 116 mm extension
- collet holder with CAT-40 spindle interface
- Haas TM-1P CNC machining center
- 6061-T6 aluminum workpiece
- Kistler 9257B cutting force dynamometer.

The workpiece was bolted to the dynamometer, which was mounted on the machine table, to enable thrust (z) force measurement during drilling trials.

Separate drilling tests were completed for a range of feed per tooth values to define C_1 = 2.69×10^8 N/m^2 as described in [6]. For these tests, it is important to understand that the drill geometry varies with radial position along the cutting edge. In this study, blind hole stability was evaluated, so blind holes were selected to determine C_1.

However, to generalize predictions, pilot hole drilling should also be completed. Because the force model coefficients changes with pilot hole diameter, a mean value can be selected. However, this increases uncertainty.

Frequency response functions, or FRFs, were measured by impact testing, where a small hammer (PCB model 086E80) was used to excite the drill tip and an accelerometer (PCB model 352C23) was used to measure the vibration response; both time-domain signals were collected and converted to the frequency-domain using MLI's MetalMax TXF software. To identify the required torsional-axial mode, three measurements were performed. First, the FRF in the axial direction, where the accelerometer was mounted at the drill tip with its sensitive direction aligned (as much as possible) with the drill axis. The hammer was used to tap the drill adjacent to the accelerometer in the axial direction. Due to the angled lips and small surface area, the tap direction was not perfectly aligned with the drill axis, nor perfectly consistent.

Due to the imperfect alignment of both the hammer and accelerometer with the drill axis, the drill's bending modes (in the lateral direction) were also excited. To distinguish between the torsional-axial and bending modes, two additional measurement setups were used. For the lateral direction FRF measurements, the drill was impacted on the margin perpendicular to the drill axis and nominally on its centerline. The accelerometer was attached on the opposite margin (directly across from the hammer strike), where the accelerometer measurement axis was colinear with the force vector (again, with some alignment uncertainty) to ideally excite only bending modes.

For the torsion measurements, the drill was excited at the outer edge of the cutting lip to intentionally cause rotation about the drill axis. The accelerometer was placed on the outer edge of the cutting lip with its measurement axis parallel to, but offset from, the force vector and pointing in the opposite direction. This setup inherently excites both bending and torsional modes. The three measurement results are superimposed in Fig. 1. It is seen that the lateral FRF primarily excites the first bending mode with a natural frequency of 500 Hz; however, a second mode at 535 Hz is also observed. The torsion FRF, on the other hand, primarily excites the torsional response at 535 Hz although the 500 Hz

bending mode is still seen with a smaller magnitude. The axial FRF shows both modes, but it is now possible to isolate the peak at 535 Hz as the torsional-axial mode to be used for the stability analysis. The mode is inverted due to the accelerometer orientation/strike direction and relationship between axial and torsional deflection. A modal fit provided the following values: $k = 6 \times 10^7$ N/m, $\zeta = 0.005$, and $f_n = 540$ Hz (note that the measurement was compensated for the accelerometer mass, so the modeled natural frequency is higher than the measured natural frequency in Fig. 1 [35]).
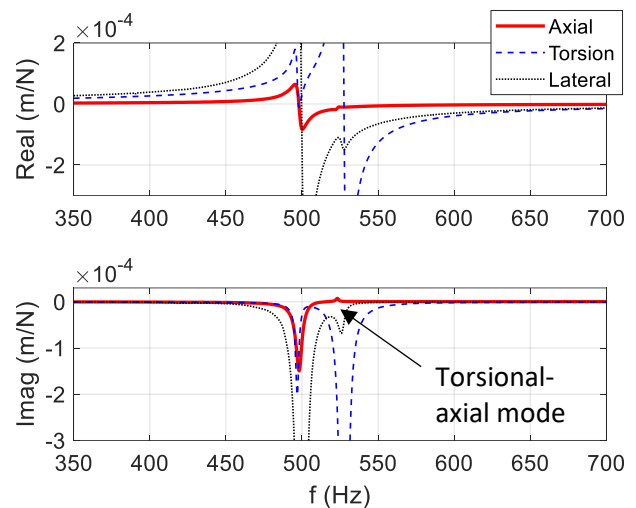
FIGURE 1: FRF measurement results.
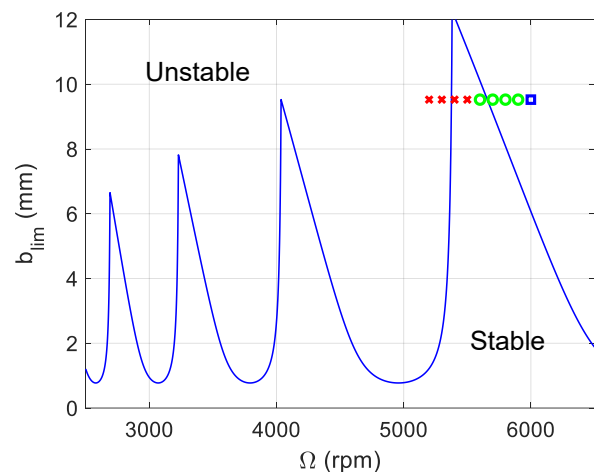
FIGURE 2: Drilling stability map with experimental results, where an × represents an unstable (chatter) result, a circle is for a stable result, and a square indicates marginal stability.

Drilling experiments were completed at spindle speeds from 5200 rpm to 6000 rpm in 100 rpm increments. A 3.175 mm diameter center drill was used to set each hole location prior to drilling and avoid bending vibrations during the hole entry transient. No pilot hole was used so the chip width was equal to the 9.525 mm drill diameter at steady-state. The feed per flute was 0.152 mm in all cases. The stability map and test results are displayed in Fig. 2. The corresponding chatter frequency, f_c, versus spindle speed plot is provided in Fig. 3. The flute passing frequency line (equal to the product of the spindle speed and number of flutes, 2) is also included to identify the stable cuts, where no chatter frequency was present.
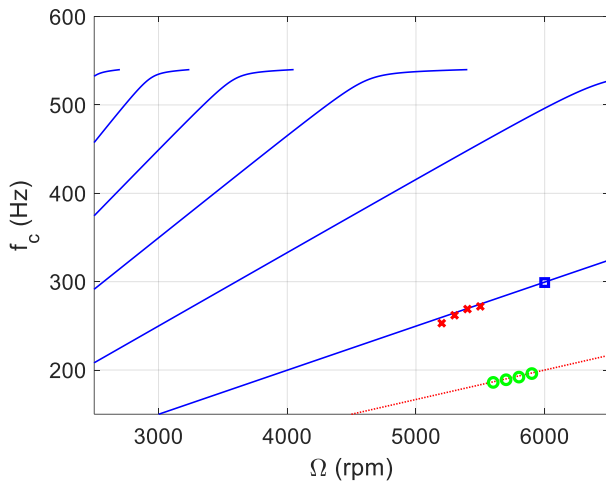
FIGURE 3: Chatter frequency variation with spindle speed (solid lines). Experimental results are included, as well as the flute passing frequency (dotted line).

The Monte Carlo simulation was next completed using the input mean and standard deviation values listed in Table 1. The standard deviation is presented as a percent of the mean value in each case. These percentages were selected based on the authors' experiences with the input parameter measurements. For example, in the axial direct FRF measurement, it is challenging to apply the force and measure the response in the drill's axial direction. Therefore, large uncertainty percentages were assigned to the modal stiffness and damping for the fit to the torsional-axis mode. A much smaller percent was applied to the natural frequency, however, because it is not as sensitive to the measurement location or direction. The C_1 uncertainty was based on axial force uncertainty and hole-to-hole variation for

the blind hole calibration tests. This number would be increased to incorporate variation in C_1 with pilot hole diameter if the model was evaluated at these other b_{lim} values.

TABLE 1: Monte Carlo simulation input mean and standard deviation values.

	Mean	Standard deviation
k	6×10^7 N/m	20%
f_n	540 Hz	1%
ζ	0.005	20%
C_1	2.69×10^8 N/m^2	10%
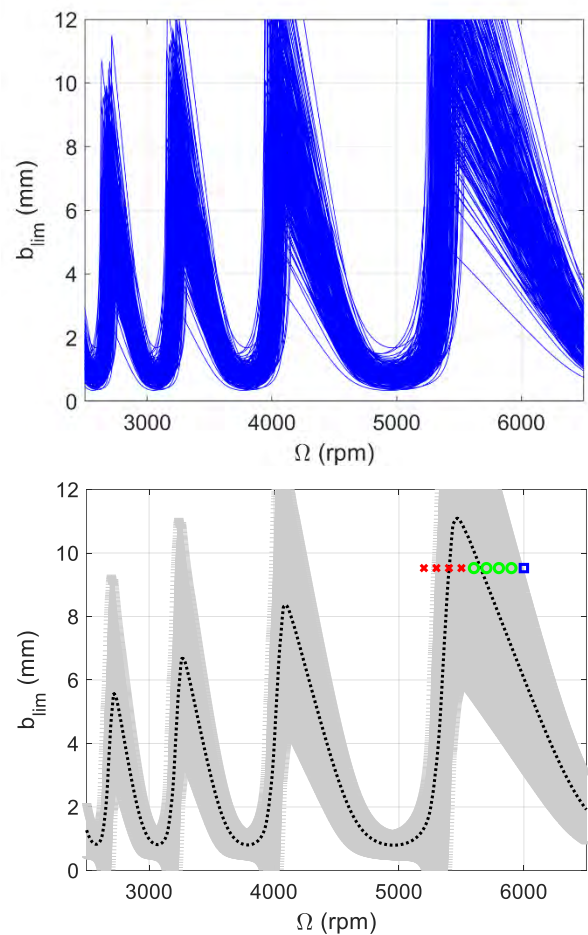
FIGURE 4: Monte Carlo simulations results when varying all four inputs. (Top) 250 stability boundaries obtained by randomly sampling the four inputs from normal distributions. (Bottom) Mean and 95% confidence intervals. Experimental results are included for visual comparison.

Monte Carlo simulation results are displayed in Fig. 4. The top panel shows 250 stability boundaries determined by randomly sampling from independent normal distributions defined by the mean and standard deviation values in Table 1. The four inputs were uncorrelated and generated using the Matlab randn function. Note that C_2 also varied, but was correlated to C_1 since it was calculated using $C_2 = \frac{C_1}{3}$. The bottom panel in Fig. 4 shows the mean and 95% confidence intervals (plus/minus two standard deviations with symmetric error bars) for the stability boundary when varying all four inputs simultaneously. The experimental results are also included. It is seen that all stable cuts are captured within the uncertain boundary; further, the marginal result and two of the four unstable results are outside the boundary.

CONCLUSIONS
In this paper, an uncertainty evaluation for drilling stability was presented using a deterministic frequency-domain drilling stability model. Monte Carlo simulation was used to propagate measurement uncertainties in the model inputs to the output, where the inputs included the modal stiffness, damping ratio, and natural frequency for the torsional-axial vibration mode from the twist drill-holder-spindle axial frequency response function; and the mechanistic coefficients that relate the torque and thrust force to chip area for the selected drill-workpiece material combination. The stability model was used to generate multiple stability maps by randomly sampling from the input distributions. After many iterations, the mean stability boundary and its 95% confidence intervals were determined.

Experimental results for blind hole drilling were presented. It was seen that the deterministic stability boundary obtained from mean input values was qualitatively correct, but shifted in spindle speed. When incorporating the input uncertainties to identify the 95% confidence intervals, all stable results (100%) were captured within the stable zone and the majority of unstable results (3 out of 5) were excluded. Practically, the frequency-domain drilling stability model offers a useful tool for pre-process drilling parameter selection, but conservative choices must be made due to the input uncertainties. The use of Monte Carlo simulation enables the uncertainty in the predicted stability boundary to be evaluated so that improved confidence can be achieved for parameter selection.

REFERENCES
[1] Zhang, P.F., Churi, N.J., Pei, Z.J. and Treadwell, C., 2008. Mechanical drilling processes for titanium alloys: A literature review. Machining Science and Technology, 12(4), pp.417-444.
[2] Liu, D., Tang, Y. and Cong, W.L., 2012. A review of mechanical drilling for composite laminates. Composite structures, 94(4), pp.1265-1279.
[3] Abrão, A.M., Faria, P.E., Rubio, J.C., Reis, P. and Davim, J.P., 2007. Drilling of fiber reinforced plastics: A review. Journal of Materials Processing Technology, 186(1-3), pp.1-7.
[4] Pandey, R.K. and Panda, S.S., 2013. Drilling of bone: A comprehensive review. Journal of Clinical Orthopaedics and Trauma, 4(1), pp.15-30.
[5] Xu, J., Mkaddem, A. and El Mansori, M., 2016. Recent advances in drilling hybrid FRP/Ti composite: A state-of-the-art review. Composite Structures, 135, pp.316-338.
[6] Bayly, P.V., Metzler, S.A., Schaut, A.J. and Young, K.A., 2001. Theory of torsional chatter in twist drills: Model, stability analysis and composition to test. Journal of Manufacturing Science and Engineering, 123(4), pp.552-561.
[7] Altıntaş, Y., 2000. Manufacturing Automation. Cambridge: The Press Syndicate of the University of Cambridge.
[8] Schmitz, T. and Smith, K.S., 2019. Machining Dynamics: Frequency Response to Improved Productivity, Second Edition, New York: Springer.
[9] Hodges, D. H., 1980. Torsion of pretwisted beam due to axial loading. ASME Journal of Applied Mechanics, 47, pp.393-397.

INVESTIGATION OF TOOL PROTECTIVE EFFECT AND SURFACE DETERIORATION RESULTING FROM BUTILT-UP LAYER FORMATION IN MICRO SCALE MACHINING OF INCONEL 718

Xiaoqi SONG[1], Yukio TAKAHASHI[1], Weiming HE[2] and Tohru IHARA[1]
[1] Department of Precision Mechanics,
Chuo University,
Tokyo, 112-8551, Japan
[2] School of Mechanical Engineering,
University of Shanghai for Science and Technology,
Shanghai, 200093, China

INTRODUCTION

Micro cutting is a flexible and efficient machining technology for producing functional, high quality at reasonably low cost and has the ability to machining a variety of engineering materials [1-2]. The built-up layer (BUL)/Built-up edge (BUE) is a commonly observed phenomenon in metal macro scale cutting and it has significant influences on the cutting process such as cutting temperature, chip formation, surface quality, and tool wear [3-7]. And the BUE formation has also been observed in micro milling/micro cutting of titanium alloy Ti-6Al-4V [8-10], stainless steel 316L [11], and duplex stainless steel UNS S2205 [12]. It was confirmed that cutting conditions affect the size of the BUE, and BUE can protect the cutting tool from flank and crater wear and affect surface roughness in micro cutting of Ti-6Al-4V [9]. Nickel alloy Inconel 718 has good mechanical properties and chemical stability, which has been commonly used in many industries such as aircraft engine parts, pressure vessels, and so on. However, the influences of BUL/BUE on the micro scale cutting of Inconel 718 has not been studied in detail.

In our previous study, Song et al. confirmed that not BUE but BUL occurs on the tool rake face in macro scale cutting of Inconel 718, and it has the tool protective effect and has few influences on the cutting process such as the cutting forces and surface roughness [13]. Because the uncut chip thickness in micro scale cutting is comparable in size to the edge radius of cutting tool, resulting in a large negative rake angle and the elastic-plastic deformation of workpiece material [1-2], the BUL formation in micro scale cutting may differ from its formation in macro scale cutting. Therefore, the study of BUL formation in micro scale machining of Inconel 718 has remained an important subject. The aim of this study is to synthetically investigate the BUL formation and its influence on the tool wear, cutting forces and surface deterioration in micro scale machining of Inconel 718. Attempts are made to explain and correlate the tool wear formation and surface roughness with the cutting parameters (cutting speed, uncut chip thickness) and the BUL formation. The protective effect of BUL in micro scale cutting is also discussed.

EXPERIMENTAL PROCEDURE
Workpiece And Cutting Tools

In this study, a commercial grade Inconel 718 with aging treatment was used as workpiece. All workpieces were of length 200 mm and were cut from the same bar (its diameter is 45 mm). The material properties and chemical composition of Inconel 718 are listed in **Table 1** and **Table 2,** respectively. The Vickers hardness and actual average grain size obtained are also presented in Table 1, and the microstructure of the Inconel 718 used is shown in **Fig.1**.

Uncoated cemented carbide inserts without chip breaker (rake angle 0° and flank angle 11°, TPGN 160304, Tungaloy) were used as cutting tool for

TABLE 1. Material properties of Inconel 718 at room temperature.

Yield point (MPa)	1280
Tensile strength (MPa)	1455
Elongation (%)	21
Reduction of area (%)	46
Vickers hardness (HV0.1/10)	531
Average grain size (μm)	33

TABLE 2. Chemical composition of Inconel 718 (%).

Ni	C	Mn	Si	Cr
53.07	0.03	0.04	0.04	18.57
Co	Mo	Nb+Ta	Ti	Al
0.09	3.05	5.28	0.94	0.58
Cu	Fe	Nb	Other	
0.03	18.2	5.28	Bal	

all the tests. The inserts were set on a tool holder having a seating surface with rake angle 5°, flank angle 6° (CTGPR2020K3, Tungaloy). Therefore, the actual rake angle and flank angle after mounting are 5° and 6°, respectively. As the tool cutting edge angle κr is 91°, the uncut chip thickness tu can be calculated as $tu = f * sin(91°) \approx f$ and the uncut chip width b can be calculated as $b = w/sin(91°) \approx w$ in turning, where f is the feed rate and w is the depth of cut. The edge radius of cutting tool re was measured by a laser confocal microscopy (LCM, OLS 4100, Olympus), as shown in **Fig.2**. Ten measurements were carried out and the mean cutting tool edge radius re is 2.5 μm.

Experimental Set-up
A CNC lathe machine (MULTUS B200, Okuma) was used to conduct micro cutting experiments. Depth of cut ($w = 1\,mm$) was kept constant. Cutting speed (V) and feed rate (f) were the input variable. **Table 3** shows the cutting parameters. Cutting forces were measured by a 3-component piezoelectric dynamometer (9129A, Kistler). The machined surface was measured by LCM. The surface roughness parameters used in this study are arithmetical mean surface roughness value (Ra) and mean maximum height of the profile (Rz), which are generally used in the industry.
To study the BUL formation and to measure tool wear, the tools after cutting were examined using a scanning electron microscope (SEM, Quanta 250, FEI) and LCM. And the maximum height of BUL above tool rake face *h1*, contact length between BUL and cutting tool *L*, and maximum depth of crater wear below tool rake face *h2* were measured by LCM, as shown in **Fig.3**.

RESULTS AND DISCUSSION
Investigation Of BUL Formation During Micro Scale Cutting
In our previous study, it was confirmed that BUL can form on the tool rake face and function as a protective layer by separating the tool surface from the chip during cutting Inconel 718 with feed rate 0.1 m/min [13]. In this part, the BUL formation in micro scale cutting was firstly investigated.
The variations of maximum height of BUL above tool rake face *h1*, contact length between BUL and cutting tool *L*, and maximum depth of crater wear below tool rake face *h2* with the ratio of uncut chip thickness to cutting tool edge radius tu/re under different cutting speeds after cutting 60 s are shown in Fig.3. It can be seen that as tu/re increases up to 2, the stable BUL above rake face can be clearly observed (**Fig.4**) and an
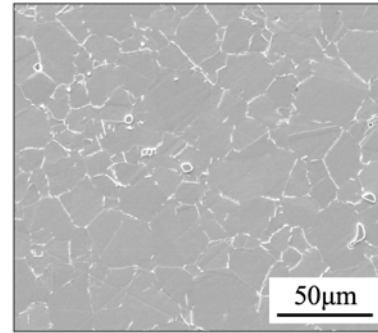
FIGURE 1. Microstructure of Inconel 718.

TABLE 3. Cutting parameters.

Tool	TPGN160304, K10
Cutting speed V (m/min)	10, 30, 50, 70, 90
Feed rate f (mm/rev)	0.001, 0.002, 0.005, 0.01, 0.02, 0.05, 0.1, 0.2
Depth of cut w (mm)	1.0
Cutting time t (s)	60
Rake angle α (°)	5
Flank angle γ (°)	6
Nose radius r (mm)	0.4
Wedge angle β (°)	60
Cutting edge angle κr (°)	91
Cutting fluid	Dry
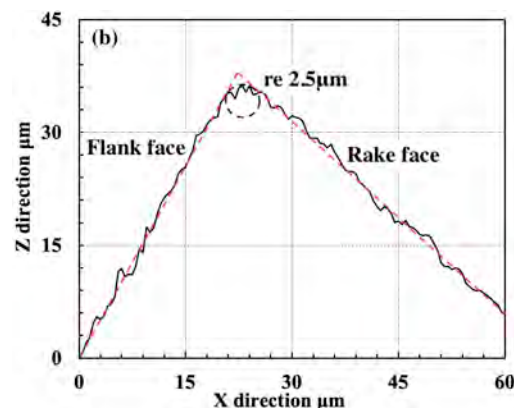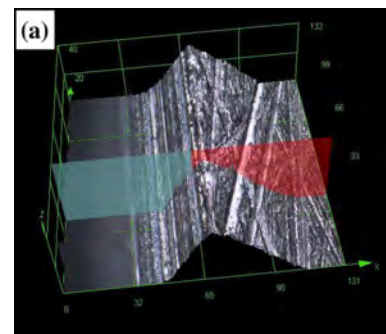
FIGURE 2. Cutting tool edge radius measurement by LCM.
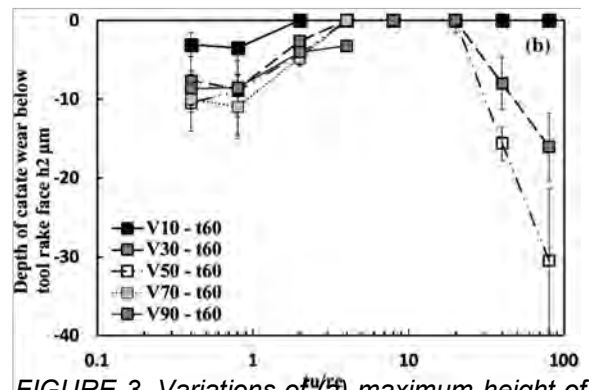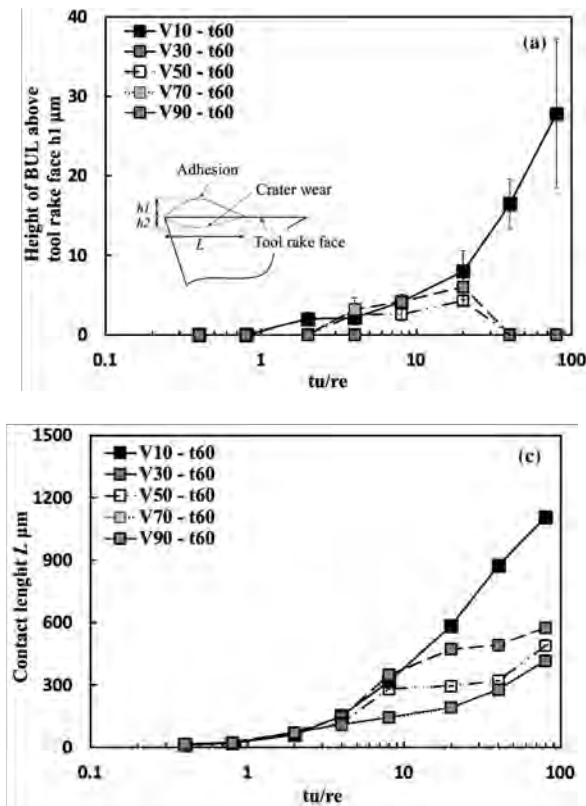
FIGURE 3. Variations of (a) maximum height of BUL above tool rake face h1, (b) contact length between BUL and cutting tool L, and (c) maximum depth of crater wear below tool rake face h2 with the ratio of uncut chip thickness to cutting tool edge radius tu/re under different cutting speeds after cutting 60 s.
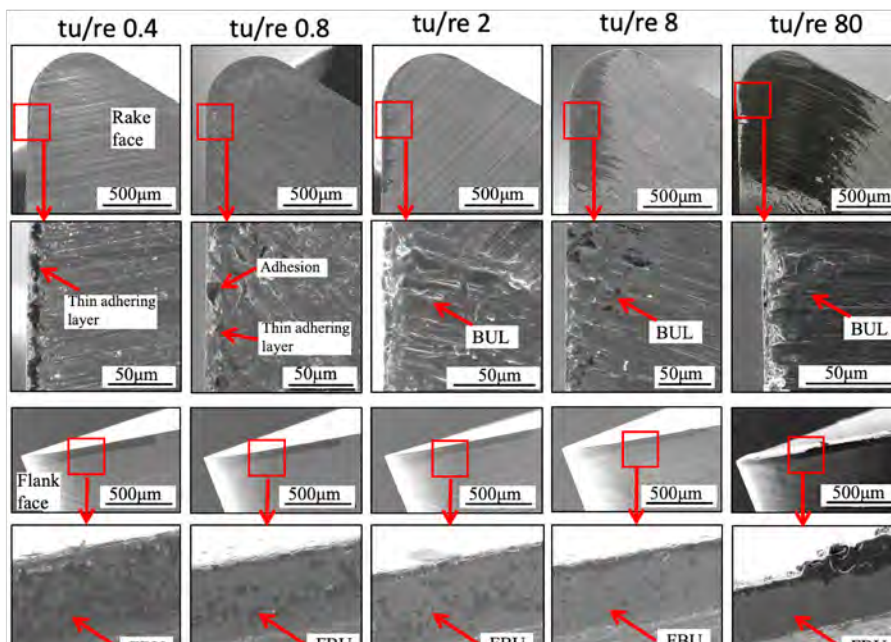
FIGURE 4. SEM images of cutting tool under different tu/re at cutting speed 10 m/min after cutting 60 s.

increase of height of BUL above tool rake face h1 can also be observed as tu/re increases at cutting speed 10 m/min. However, the stable BUL above rake face can only be formed for tu/re 4, 8, and 20 at cutting speed 30 and 50 m/min, and

for tu/re 4 at cutting speed 70 m/min. By the comparison of the SEM images of cutting tool in Fig.4, it can be seen that the thin adhering layer or adhesion (its height is less than 1µm), which cannot be regarded as BUL, forms on the tool

rake face near the cutting edge for tu/re 0.4 and 0.8 at cutting speed 10 m/min. Comparing the variation of *h2* with *h1* in Fig.3(a) and Fig.3(b), it can also be found that no crate wear occurs on the tool rake face when the stable BUL forms. This phenomenon can be explained as a result of the protective effect of BUL. The larger crate wear at the higher cutting speed V and the larger feed rate f may relate to the increase of cutting temperature and sliding velocity at the tool and chip interface. As shown in Fig.3(c), it can be seen that the length of BUL L increases as tu/re increases. This result illustrates that tu/re can significantly affect not only the height of BUL h1 but also the length of BUL L.

On the other hand, as shown in Fig.4, it can be observed that in all cases the entire worn tool flank face is covered by the thin adhering layer, identified as flank built-up (FBU). And FBU seems easier to form on the flank face for the smaller tu/re at different cutting speeds.

Protective Effect of BUL During Micro Scale Cutting

In order to study the protective effect of BUL, not only the crate wear (Fig.3(b)) but also the tool flank wear after cutting 60 s was measured.

The variation of width of flank wear with tu/re under different cutting speeds after cutting 60 s is shown in **Fig.5**. At cutting speed 10 and 30 m/min, the width of flank wear decreases as tu/re increases. At cutting speed 50 m/min, the width of flank wear decreases with increasing tu/re from 0.4 to 8, but increases with increasing tu/re from 8 to 80. At cutting speed 70 and 90 m/min, the cutting tool features high flank wear and a reduced tool life. This phenomenon relates to the higher cutting temperature and the higher sliding velocity at the tool and chip interface, and the tool and workpiece interface generated by the higher cutting speed and larger feed rate, which reduce the hardness and wear resistance of cutting tool, accelerating tool wear formation. Comparing the width of flank wear with the height of BUL, it can be concluded that there seems to be a correlation between the tool flank wear and the height of BUL as shown in **Fig.6**. The higher BUL can reduce the tool flank wear. However, in this study, as the uncut chip thickness is in microscale and smaller than the average grain size of Inconel 718 (Table 1), the influence of size effect [1] on the tool flank wear should not be ignored.

Figure 7 shows the variation of specific cutting energy $kc\ (= Fc/wtu)$ with tu/re, where Fc is the principal cutting force. It can be seen that kc
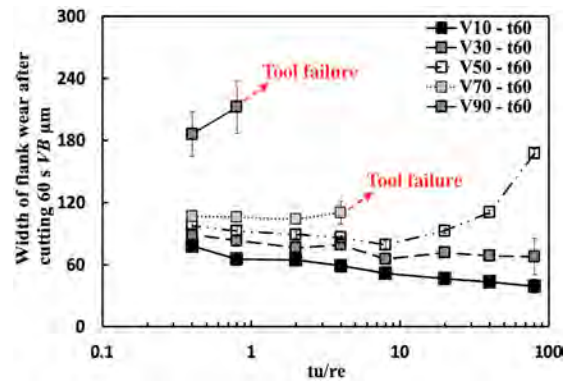
FIGURE 5. Variations of width of flank wear after cutting 60 s with tu/re.
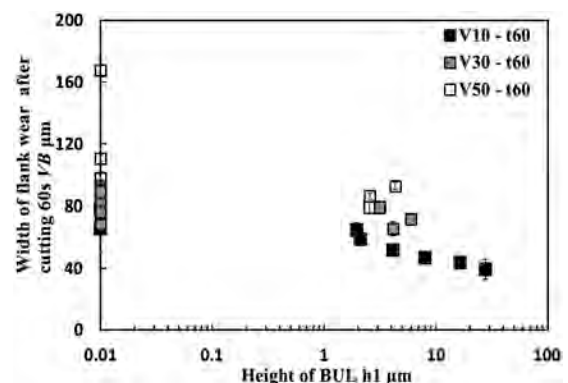
FIGURE 6. Relation between width of flank wear after cutting 60 s and height of BUL h1.
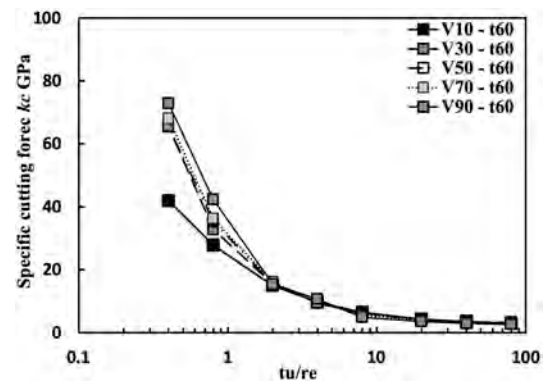
FIGURE 7. Variations of specific cutting energy with tu/re.

increases rapidly as tu/re decreases, and it can reach above 30 GPa when tu/re is below 1. This means that when the uncut chip thickness is smaller than cutting edge radius and the rake angle becomes negative when tu/re is below 1, the workpiece is difficult to be removed and the ploughing of machined material accelerates flank wear formation (Fig.5). Meanwhile, it can also be seen that kc trends toward a constant level (about 3 GPa) as tu/re increases above 8. The

relation between flank wear and specific cutting energy is shown in **Fig.8**. It can be seen that the width of flank wear has a decreasing trend as kc decreases and it decreases quickly when kc is below 10 GPa at cutting speed 10 and 30 m/min. This indicates that kc has few influences on the flank wear formation when kc is below 10 GPa or tu/re increases above 8. Because the cutting tool edge radius re is much smaller than the uncut chip thickness tu when tu/re increases above 8, re has almost no influence the tool flank wear formation. Generally, it is well known that the flank wear (or flank wear rate) increases as cutting speed or feed rate increases in cutting of Inconel 718 [14]. However, there is no increasing trend for flank wear for larger feed rate at cutting speed 10 and 30 m/min as shown in Fig.5. Feed rate f (or tu) also doesn't have much influences on the tool flank wear formation. From these results, it can be said that the stable BUL has the protective effect and can reduce the tool flank wear formation at cutting speed 10 and 30 m/min.

Influences of BUL and FBU On Surface Roughness During Micro Scale Cutting

BUL/FBU is produced by the deformed workpiece accumulating on the tool surface. As shown in Fig.4, BUL and FBU become the actual cutting edge and lead to change the contact conditions at the tool and chip interface and the tool and workpiece interface during cutting, which would affect chip formation mechanism, tool wear formation, and further influence the generated surface quality. Therefore, it is quite important to investigate the influences of BUL and FBU on the surface roughness in micro scale cutting.

To evaluate the influences of BUL and FBU on the surface roughness, the surface roughness Ra and Rz were measured during the micro cutting tests under different cutting conditions. Surface roughness Ra and Rz along the feed direction after cutting 60 s are depicted in dependence on the tu/re in **Fig. 9**, while the machined surface morphology at cutting speed 30 m/min is shown in **Fig.10**. It can be seen that surface roughness Ra and Rz decrease as tu/re decreases, and they tend toward a constant level 0.35 μm for Ra and 2.5 μm for Rz when tu/re decreases up to 8 for all cutting speeds investigated. Comparing the surface roughness Ra and Rz with the machined surface morphology for $tu/re \geq 8$ (Fig.10), it can be observed that the cutting marks for tu/re 80 are deeper and the peak spacings are larger than them for tu/re 8. The decrease of surface roughness Ra and Rz can be attributed to the
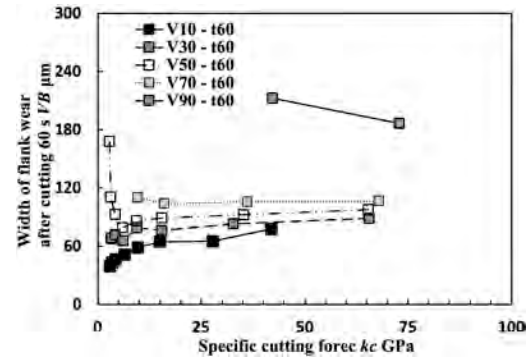
FIGURE 8. Relation between width of flank wear after cutting 60 s and specific cutting energy.
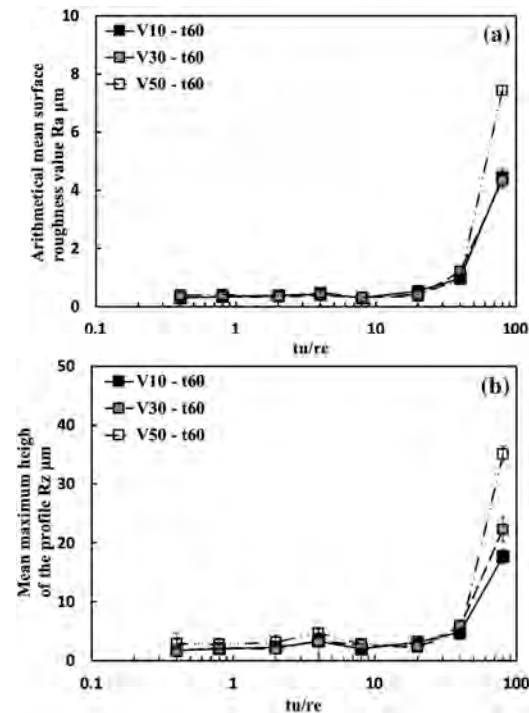
FIGURE 9. Surface roughness analysis along the feed direction after cutting 60 s for different tu/re at cutting speed 10, 30, and 50 mm/min.

decrease of feed rate f, as the theoretical surface roughness can be given approximately by $Ra \approx 0.0321 f^2/r, Rz \approx f^2/8r$ [15]. For $tu/re < 8$, the feed rate f has few influences on the surface roughness Ra and Rz. By comparison of the specific cutting energy kc in Fig.7, it can be observed that the larger specific cutting force kc for the smaller tu/re, which will increase the ploughing effect, has few influences on the surface roughness Ra and Rz. This indicates that compared with roughness due to the tool wear and cutting edge, roughness due to the plastic sider flow could significantly contribute to the overall surface roughness in micro scale cutting
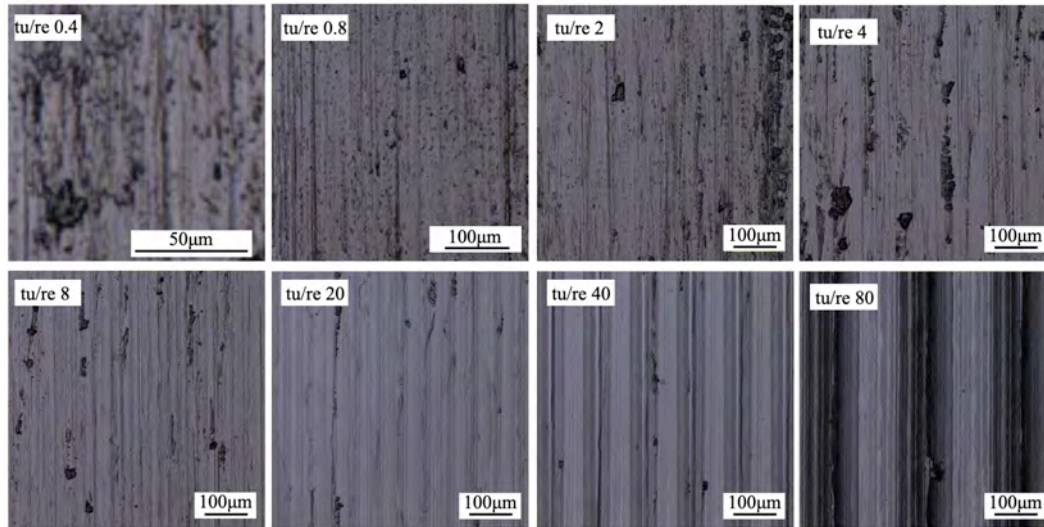
FIGURE 10. Machined surface morphology at cutting speed 30 m/min after cutting 60 s for different tu/re.

of Inconel 718 in this study. Comparing the height of BUL $h1$ in Fig.3(a) and surface roughness Ra and Rz in Fig.9, it can also be concluded that BUL has few influences on the surface roughness Ra and Rz in micro scale cutting of Inconel 718.

On the other hand, as shown in Fig.10, it can be observed that the formation of adhesion material, plastic deformation and burr occur easily on the machined surface when tu/re decreases from 4 to 0.4. Meanwhile, FBU seems easier to form on the entire worn tool flank face at the smaller tu/re as discussed above. These results indicate that there may be a close relationship between FBU and surface quality.

CONCLUSIONS

The following conclusions can be drawn:

1. The stable BUL can occur on the tool rake face when the uncut chip thickness tu is equal or larger than the cutting tool edge radius re ($tu/re \geq 1$) at low cutting speed in micro cutting of Inconel 718.

2. The ratio of uncut chip thickness to cutting tool edge radius tu/re can significantly affect the height and length of BUL.

3. The stable BUL has tool protective effect and it can protect the cutting tool from the crater wear and flank wear. The size effect analysis indicates that the tool wear forms easily when the specific cutting energy increases at low cutting speed. And cutting temperature plays a very important role in tool wear formation at the higher cutting speed and larger feed rate.

4. From the surface roughness analysis, it can be concluded that BUL has few influences on the surface roughness. And there may be a close relationship between FBU and surface

quality. However, further investigations shall be undertaken to finally clarify the influences of BUL/FBU on the surface quality.

REFERENCES

[1] O'hara, J. and Fang, F., Int. J. Extrem. Manuf., 1, 3 (2019), 032003.

[2] Shunmugam, M. S., J. Institu. Eng. (India): Series C, 97, (2016), 223-241.

[3] Trent, E.M. and Wright, P.K., Metal Cutting, 4th Edition, Butterworth-Heinemann, 2000.

[4] Shaw, M.C., Metal Cutting Principles, 2nd Edition, Oxford University Press, 2005.

[5] Tomac N., Tønnessen K., Rasch F.O. and Mikac T., AMST'05 Adv. Manu. Sys. Tech., 486, (2005), 183.

[6] Kümmel J. et al.: Wear, 311, 1-2, (2014) 21.

[7] Song X. et al.: Int. J. Autom. Tech., 13, 1, (2019) 13.

[8] Thepsonthi, T. and Özel, T., J. Mater. Proc. Tech., 221, (2015), 128–145.

[9] Oliaei, S. N. B. and Karpat, Y., Precis. Eng., 49, (2017), 305-315.

[10] Oliaei, S. N. B. and Karpat, Y., Jou. Mater. Proc. Tech., 235, (2016), 28-40.

[11] Kovvuri, V., Wang, Z., Araujo, A., Bukka-patnam, S., and Hung, W. N. P., Proceed-ings of the ASME IMECE2015, (2015).

[12] Santos, A. G., da Silva, M. B., and Jackson, M. J., Wear, 414-415, (2018), 109-117.

[13] Song, X., Takahashi, Y., Ihara, T., J. Jpn. Soc. Precis. Eng., 85, 10 (2019),856–65.

[14] Thakur, D. G., Ramamoorthy, B. and Vijayaraghavan, L., Mater. Des., 30, (2009), 1718-1725.

[15] He, C. L., Zong, W. J. and Zhang, J. J., Int. J. Mach. Tools Manuf., 129, (2019), 15-26.

POLISHING OF EPOXY RESIN SURFACE OF CFRP MIRROR FOR SPACE TELESCOPES

Takahito Igawa[1], Hideo Takino[2], Shin Utsunomiya[3]
[1] Department of Mechanical Science and Engineering, Graduate School of Engineering, Chiba Institute of Technology, Narashino, Chiba, Japan.
[2] Department of Mechanical Engineering, Faculty of Engineering, Chiba Institute of Technology, Narashino, Chiba, Japan.
[3]National Astronomical Observatory of Japan, Mitaka, Tokyo, Japan.

INTRODUCTION

Mirrors used in a space telescope should be large to increase their optical resolution. However, it is difficult to use low-expansion glass or SiC as the mirror material for such large mirrors because of the restriction of loading weight. Thus, carbon-fiber-reinforced-plastic (CFRP) for mirrors has attracted attention because it is a light low-thermal-expansion as well as high-stiffness material.

The fabrication process of a CFRP mirror, in which epoxy resin is applied on its surface, has already been proposed [1]. Figure 1 shows this fabrication process of the CFRP mirror. The reason for the application of epoxy resin is that the surface cannot be used as a mirror owing to the exposed carbon fibers on the surface. Previous studies showed that high-precision polishing of an epoxy resin surface is required to achieve a smooth and highly accurate mirror surface [1, 2]. To polish the surface to a high quality, it is necessary to determine the polishing characteristics of epoxy resin. However, unlike acrylic resin, which is a general optical material, there are few studies of the polishing characteristics of epoxy resin.

Thus, in this study, we polished test pieces of CFRP mirrors coated with epoxy resin and acrylic resin in the same batch under various conditions to accurately compare their removal rates. In the experiment, removal rates were calculated by measuring the changes in the height of test pieces. Suede and foamed polyurethane were used as the materials of the polishing pad. Alumina and SiC grains were used as abrasives. The grain size of both abrasives was 3 µm. We found that the removal rate for epoxy resin was lower than that for acrylic resin under every polishing condition. Moreover, polishing using SiC abrasive slurry with a foamed polyurethane pad showed the highest removal rate.

We also evaluated the surface roughnesses of the epoxy resin workpiece before and after polishing. Surface roughness was measured using an interferometric three-dimensional optical surface profiler. The roughness of the initial surface of epoxy resin was 10.76 nm RMS. We confirmed that the combination of alumina abrasive slurry and a suede pad provided the target surface roughness of 5 nm RMS; the roughness of the resultant surface was 4.75 nm RMS.
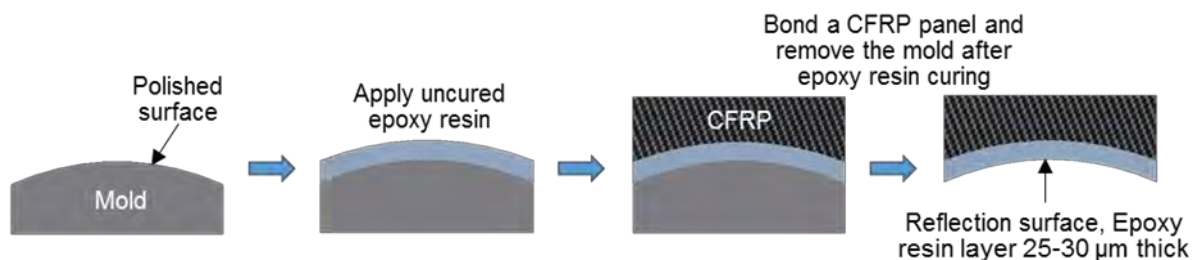
FIGURE 1.   Process of molding reflecting surface using epoxy resin.
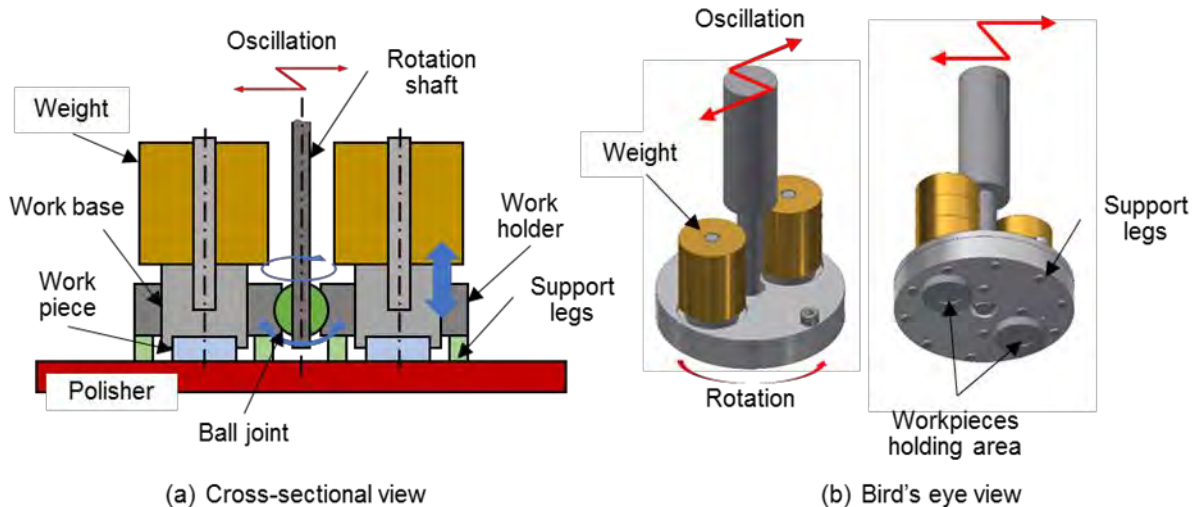
FIGURE 2.   Schematic view of the holding structure for workpieces developed in this study.

(a) Cross-sectional view

(b) Bird's eye view

EXPERIMETAL DEVICE

An Oscar-type polishing machine was constructed and used in experiments. This polishing machine consists of two parts, an oscillating shaft and a rotating shaft. A workpiece or a polishing plate is mounted on the swinging shaft or rotating shaft. Then, by the relative motion of the two parts in contact with each other, the polishing process is carried out. In this study, the oscillating shaft is the workpiece side and the rotating shaft is the polishing plate.

Figure 2 shows a schematic view of the holding structure for workpieces attached to the aforementioned polishing machine. As shown in the figure, this holding structure allows the weight to act independently on two workpieces. The two workpieces are attached to work bases 1 and 2, which move freely only in the vertical direction inside the work holder; the work holder rotates around the rotation axis driven by the frictional force between the polishing pad and work pieces. This work holder is connected to the rotation axis by a ball joint so that the polishing surface of the workpiece is in parallel contact with the polishing pad. This holding structure enables workpieces made of different materials to be polished in the same batch.

EXPERIMENTAL METHODS

Simultaneous polishing of epoxy and acrylic resin workpieces was performed using the fabricated holding structure for workpieces, and the difference in removal rate between the workpieces

was measured. The workpieces used in this experiment were an acrylic resin disk of 10 mm diameter cut from a plate and a CFRP disk coated with epoxy resin by the replication method. Figure 3 shows the dimensions of the workpiece.
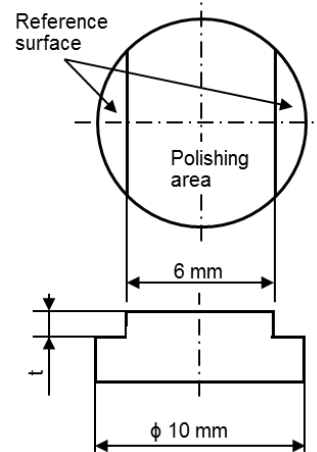
FIGURE 2.   Schematic view of the holding structure for workpieces developed in this study.

Table 1 shows the polishing conditions. Polishing for 5 minutes and measurement of the shapes of polished surfaces (cross-sectional surface profile) were repeated 4 times. The cross-sectional surface profile was measured using a noncontact, laser-probe type three-dimensional measuring device (Mitaka Kohki Co., Ltd., NH-3). The reference surface for shape measurement is the surface at a depth of t from the polishing area.

TABLE 1. Polishing conditions.

Polishing load	1.29 N		
Polisher	Suede		Polyurethane
Polishing liquid	• Almina suspension (Baikalox 3.0CR, average particle size: 3 µm) • Concentration: 10%	• Almina abrasive (average particle size: 3 µm) with tap water. • Concentration : 11%	• SiC abrasive (average particle size: 3 µm) with tap water. • Concentration : 11%

Cross-sectional measurements were performed on a section with a length of 9 mm crossing the edges of reference surfaces and passing through the center of the workpiece. The measurement pitch was set to 9 µm. The removal rate was calculated from the amount of change in the cross-sectional surface profile.

EXPERIMENTAL RESULTS

Figure 4 shows cross-sectional profiles of surfaces polished with alumina suspension as an example of the cross-sectional shape measurement. The figure shows the cross-sectional surface profiles of epoxy and acrylic resins at the initial stage and after polishing for 20 minutes. This indicates that the amount of epoxy resin removed is smaller than that of acrylic resin.

Figure 5 shows the relationship between the amount removed and polishing time for epoxy resin and acrylic resin after polishing with alumina suspension. This figure shows that the amount removed from workpieces increases in proportion to the polishing time. Therefore, it was decided to calculate the removal rates for each workpiece from the inclination of the approximate lines of polishing time and amount removed by the least-squares method. As a result, the removal rate was found to be 0.127 µm/min for epoxy resin and 1.41 µm/min for acrylic resin. Thus, the removal rate of epoxy resin is 92.8% lower than

FIGURE 4. Cross-sectional surface profiles of acrylic resin (a) and epoxy resin (b) before and after polishing with alumina suspension.
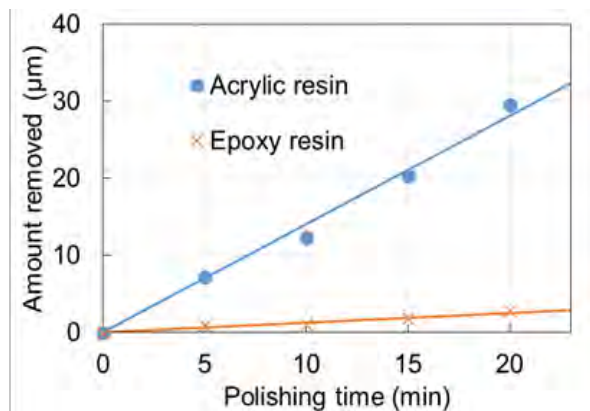
FIGURE 5. Relationship between amount removed and polishing time for epoxy resin and acrylic resin after polishing with alumina suspension.
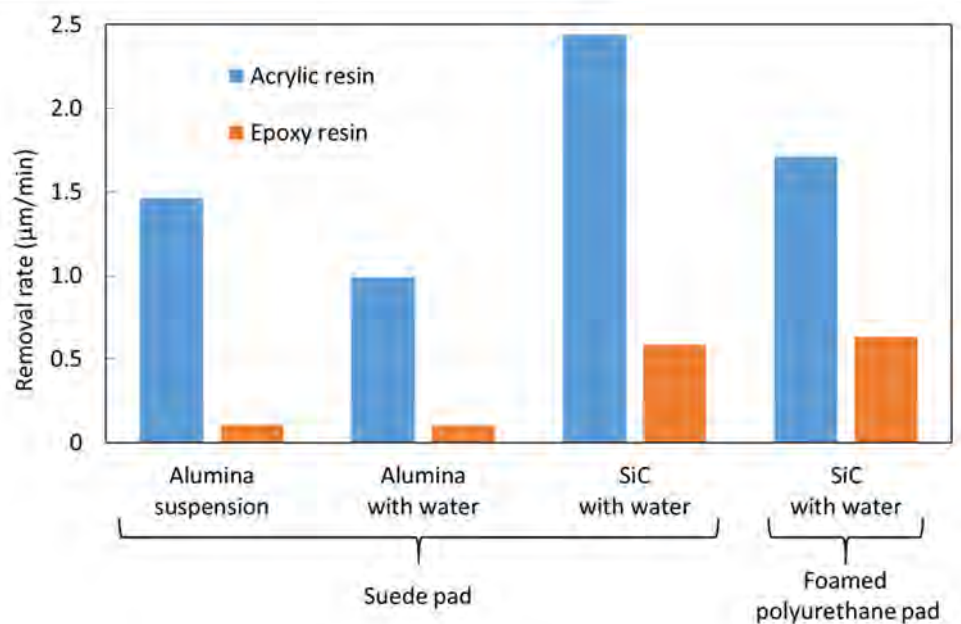
FIGURE 6.   Removal rates of epoxy and acrylic resins under various conditions.

that of acrylic resin.

In the same way, removal rates in the case of using other abrasive materials and polishing pads were also calculated. Figure 6 shows the removal rates of epoxy and acrylic resins under various conditions. Under all conditions, removal rates of epoxy resin were found to be significantly lower than that of acrylic resin. This figure shows that

(a) Acrylic resin
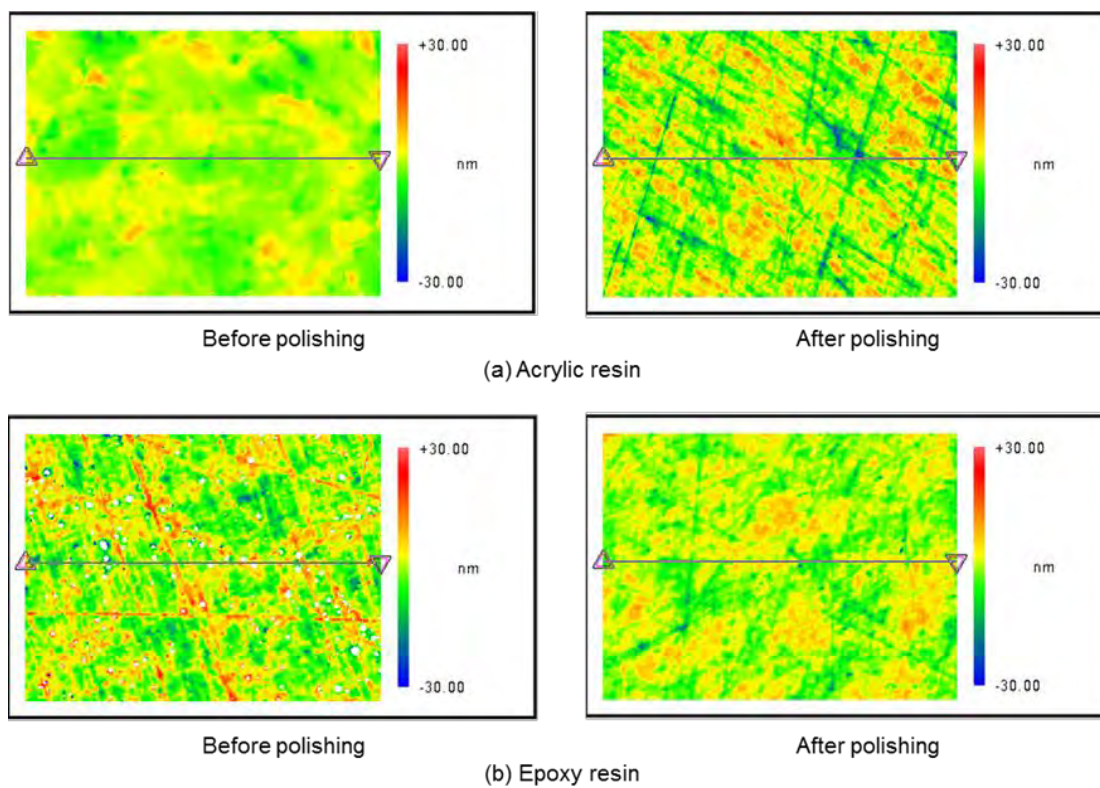
(b) Epoxy resin

FIGURE 7.   Surface topographies of acrylic resin (a) and epoxy resin (b) before and after polishing. Measuring area: 143 µm x 107 µm.

the difference in removal rate between epoxy and acrylic resins was the smallest (63.1%) when SiC abrasive and a foamed polyurethane pad were used.

ROUGHNESS MEASUREMENT

The purpose of this study is to investigate the removal rate, but it is also important to evaluate the surface roughness of the polished surface, assuming the epoxy resin is to be used as an optical surface. Therefore, the surface topographies and surface roughness of workpieces polished with the alumina suspension and a suede pad were measured using an interferometric three-dimensional optical surface profiler (ZYGO, NewView™).

Figure 7 shows the surface topographies of acrylic resin and epoxy resin workpieces before and after polishing. Figure 7(a) shows that scratch marks appear on the surface of the acrylic resin workpiece after polishing. Figure 7(b) shows numerous ridges in the shape of lines on the surface of the epoxy resin workpiece before polishing. This is thought to be caused by scratches on the surface of the mold used to form the epoxy resin surface. As shown in Figure 7(b), these ridges were removed by polishing.

Figure 8 shows the changes in the surface roughness (RMS) of the acrylic and epoxy resin workpieces determined from the results of the surface profile measurements shown in Figure 7. This figure shows that the surface roughness of the acrylic resin workpiece increases, possibly

because of the scratches observed in Figure 7. On the other hand, the surface roughness of the epoxy resin workpiece decreases to 4.76 nm RMS. This satisfied the target surface roughness of 5 nm RMS. In this study, it was found that the target surface roughness could be achieved with the appropriate polishing method.

CONCLUSIONS

High-precision polishing of epoxy resin, which is a reflective surface material, is required for the realization of CFRP mirrors. For this purpose, it is necessary to clarify the polishing characteristics of epoxy resin. Therefore, in this study, simultaneous polishing of epoxy and acrylic resin workpieces under various conditions was performed, and in removal rates were compared. As a result, we found the following.

1. The removal rate of epoxy resin was significantly lower than that of acrylic resin.

2. The combination of SiC abrasives and a foamed polyurethane pad resulted in the highest removal rate of epoxy resin and the smallest difference between epoxy resin and acrylic resin.

REFERENCES
[1] Kamiya T, Utsunomiya S, Shimizu R. Development of High-precision CFRP Mirrors for Space Telescopes. Proceedings of 56th Space Sciences and Technology Conference. 2012; JSASS-2012-4288.
[2] Utsunomiya S, Kamiya T, Shimizu R. Development of CFRP Mirrors for Space Telescopes: Study on optical polishing. Proceedings of the Materials and processing conference. 2012; DOI: 10.1299/jsmemp.20 12.20.813-1_.
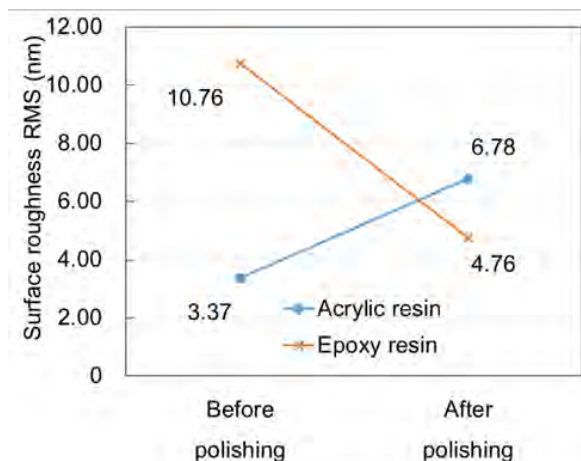
FIGURE 8. Surface roughnesses of acrylic resin and epoxy resin before and after polishing.

EFFECTS OF SURFACE ROUGHNESS ON FATIGUE LIFE OF STAINLESS-STEEL AISI 304 PARTS FINISHED BY TURNING

Hideo Takino and Takashi Ogata
Department of Mechanical Engineering, Faculty of Engineering
Chiba Institute of Technology
Narashino, Chiba, Japan

INTRODUCTION

AISI 304 is a common stainless steel used in household articles, building components, chemical plants, and mechanical parts used in high-temperature and high-pressure environments. In the general production process for mechanical parts made of AISI 304, their surfaces are finished by machining, such as turning and milling. Surface characteristics, such as surface roughness and the depth and hardness of work-hardened layers, of the machined parts affect their fatigue life. Thus, it is important to understand the effects of surface characteristics on fatigue life to efficiently produce mechanical parts made of AISI 304 with high fatigue strength. However, few studies have been carried out to investigate the effects of surface roughness generated by turning on the fatigue life of machined parts made of AISI 304 [1-3].

In this study, to investigate the effects of surface roughness on the fatigue life of turned parts made of AISI 304, we performed the fatigue test of specimens with various surface roughnesses under a pulsating tension condition.

PREPARATION OF SPECIMENS

The specimens for the fatigue test were dumbbell-shaped with a length of 200 mm and a diameter of 6 mm at the center. Cylindrical rods formed by cold drawing were used as the blanks of the specimens. The blanks were turned by changing the feed rate to produce specimens with various surface roughnesses. We also prepared specimens with smooth surfaces by polishing the turned surfaces.

The surface roughnesses of the specimens we prepared were 2.04, 1.14, 0.63, and 0.11 μm Ra; the last one was obtained by polishing. The surface roughness was measured using a surface-measuring instrument with a laser probe.

The work-hardened layers of the specimens were measured by the Vickers hardness test,

and the results showed that all specimens had almost the same depth and hardness of their work-hardened layers. The work-hardened layer existed from the outer surface to a depth of approximately 100 μm in every specimen. The Vickers hardness at the position of 10 μm from the outer surface was approximately 300, and that of the portion without a work-hardened layer was 200.

Figure 1 shows examples of the surface roughnesses of the specimens. The surface
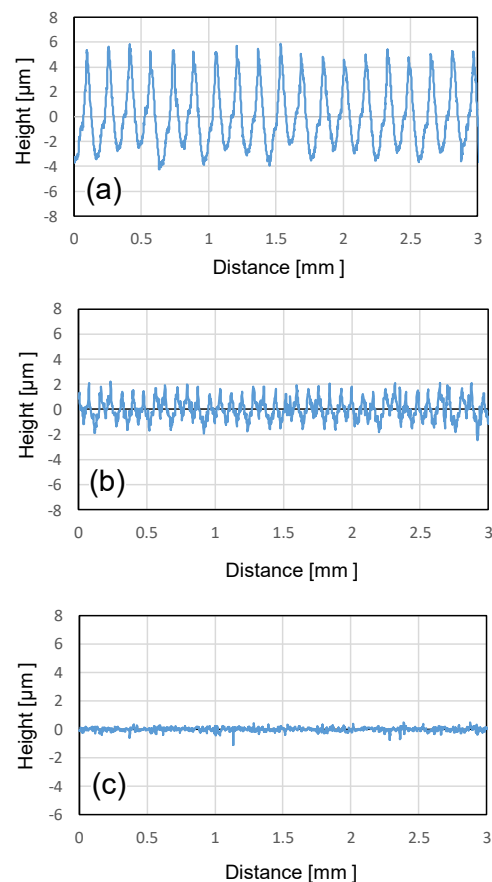
FIGURE 1. Examples of surface roughnesses of specimens.

roughness shown in Fig. 1(a) was the largest, 2.04 µm Ra. A specimen with a surface roughness larger than that shown in Fig. 1(a) was difficult to turn because of the fracturing of the turning tool. Figure 1(b) shows a surface roughness of 0.63 µm Ra. Figure 1(c) shows the roughness of 0.11 µm Ra of a polished surface.

FATIGUE TEST OF SPECIMENS WITH VARIOUS SURFACE ROUGHNESSES

The fatigue test was conducted under a pulsating tension condition with stress amplitudes of 200 and 250 MPa. The frequency of the stress was 15 Hz. The test was terminated when the number of stress cycles reached 1×10^6.

Figure 2 shows the results of the fatigue test, which revealed the relationship between the number of stress cycles, i.e., fatigue life, and the stress amplitude for the specimens with various surface roughnesses. In Fig. 2, the arrows represent unbroken specimens by a fatigue life of 1×10^6. As shown in Fig. 2, it is obvious that polishing prolongs the fatigue life. The fatigue

life of the turned specimens is shorter than that of the polished specimens, and every turned specimen was broken before the fatigue life reached 1×10^6. However, the fatigue life is independent of the surface roughness, although it is generally known that surface roughness affects the fatigue life.

FATIGUE TEST OF GROOVED SPECIMENS

The fatigue life decreases with increasing depth of a groove existing on a surface. Therefore, we investigated the effect of a microgroove on the fatigue life of specimens made of AISI 304.

We produced specimens with a groove at the center. The groove was machined around the specimen, the depth of which ranged from 2 to 35 µm. Figure 3 shows an example of the profile of a groove. In this study, the depth of a groove is defined as the distance between the bottom of the groove and the top of pile-ups on both sides of the groove. The pile-ups are plastically generated owing to the machining of the groove, and are also generated on the turned surfaces.
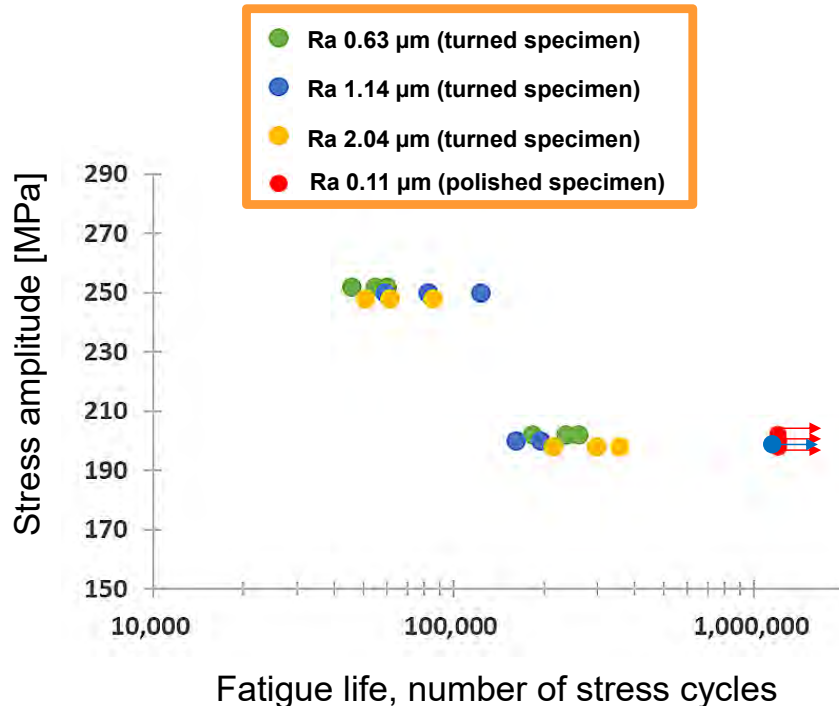
FIGURE 2. Relationship between fatigue life and stress amplitude for specimens with various surface roughnesses.
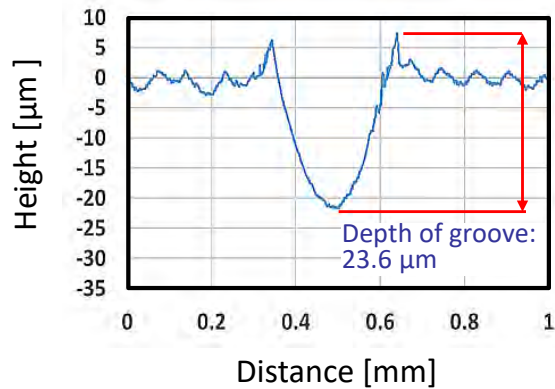
FIGURE 3. *Example of the profile of a groove.*

The fatigue test of the grooved specimens was performed under a stress amplitude of 200 MPa. The observation of the fractured specimens showed that the fracture occurred at the groove in each specimen. Figure 4 shows the results of the fatigue test, revealing the relationship between the depth of the groove and the fatigue life. As shown in Fig. 4, the fatigue life tends to increase with decreasing depth of the groove. The variation of the fatigue life seems to become large with deceasing depth of the groove.

The results of the fatigue test for the grooved specimens raises the question, why is the fatigue life of the turned specimens independent of surface roughness? Therefore, we decided to replot the results of the fatigue test for the turned specimens in Fig. 4. For this purpose, we assumed the peak-to-valley surface roughness to be the depth of the groove. Figure 5 shows the replotted results of the fatigue tests for the turned specimens. As shown in Fig. 5, the results for the turned specimens are plotted around the correlation line for the grooved specimens. Moreover, the plots for the turned specimens are included within the distribution of the results for the grooved specimens. Thus, the
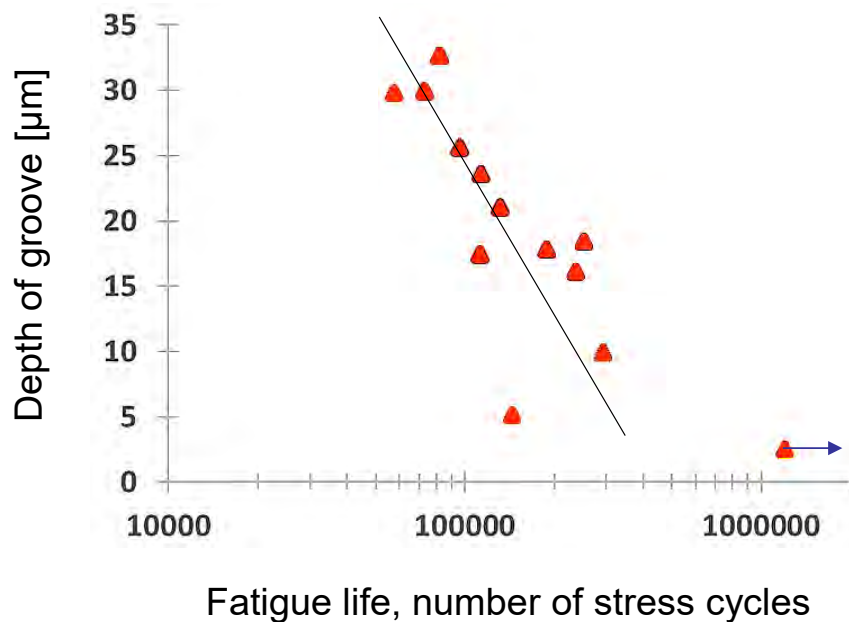
FIGURE 4. *Relationship between fatigue life and depth of groove.*
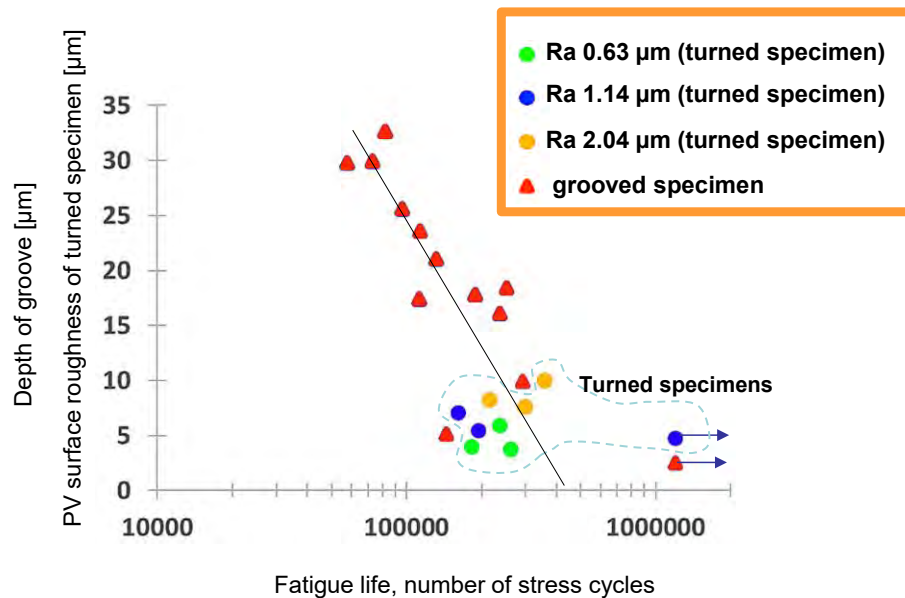
FIGURE 5. Relationship between fatigue life and depth of groove and the peak-to-valley surface roughness of turned specimen

results for the turned specimens do not contradict those for the grooved specimens. Although the difference between the surface roughnesses shown in Figs. 1(a) and 1(b) appears to be large, such a difference did not result in a significant difference in fatigue life.

CONCLUSIONS

To investigate the effects of surface roughness on the fatigue life of turned parts made of AISI 304, the fatigue test of the specimens with various surface roughnesses under a pulsating tension condition was performed. The surface roughnesses of the turned specimens ranged from 2.04 to 0.63 μm Ra, which are approximately the maximum and minimum roughness values for the surfaces of machined parts finished under conventional turning conditions. The fatigue test of the turned specimens reveals that the difference between surface roughnesses does not result in a difference in the fatigue life. The fatigue test of the grooved specimens revealed that the fatigue life increases with decreasing depth of the groove. Considering the results for the grooved specimens, a significantly rough surface probably results in the reduced fatigue life; however, such a rough surface is hardly produced by a general turning process.

REFERENCES
[1] Takeuchi E, Matsuoka S, Nishijima S, Kimura M. Fatigue Strength Properties at Room Temperature for SUS 304 Steels, Transactions of the JSME Series A, 1985; 51: 967-974, (in Japanese).
[2] Murakami Y, Tsutusmi K, Fujishima M. Quantitative Evaluation of Effect of Surface Roughness on Fatigue Strength, Transactions of the JSME Series A. 1996; 62: 1124-1131, (in Japanese).
[3] Hasunuma S, Noro R, Aso S, Ogawa T. The effect of machined surface layer on low cycle fatigue strength of austenitic stainless steel. Transactions of the JSME. 2016; 82: 16-00183, (in Japanese).

COMPARISON OF DYNAMIC STIFFNESS IN TOMBSTONE MATERIALS

Emma D. Betters[1,2], Justin West[1,2], and Tony L. Schmitz[1,2]
[1]Manufacturing Demonstration Facility
Oak Ridge National Laboratory, Oak Ridge, TN
[2]Department of Mechanical, Aerospace, and Biomedical Engineering
University of Tennessee, Knoxville, TN

ABSTRACT
The pre-process selection of stable cutting conditions in milling requires knowledge of the structural dynamics. An important metric for describing the dynamic response of a system is the dynamic stiffness, or product of modal stiffness and damping ratio for each vibration mode, for both the cutting tool (as reflected at the tool point) and workholding setup. A common workholding method in horizontal machining centers is a tombstone. Traditionally, these tombstones are cast iron or steel weldments; however, there are potential dynamic stiffness and cost benefits to the use of different materials. In this work, impact testing was used to measure the frequency response functions for cast iron, aluminum, steel, epoxy-mineral, and concrete tombstones. Improved dynamic characteristics were observed in the epoxy-mineral and concrete tombstones when compared to traditional cast iron.

Keywords: Dynamic stiffness, damping, workholding

INTRODUCTION
Tombstones are fixturing blocks that generally have between two and eight surfaces used for mounting parts to be machined on a horizontal milling machine. Often, they are used in production environments to fixture and machine many parts on each surface. They enable shops to increase their capacity and implement automation. The stiffness and damping characteristics of the tombstone directly impact the quality of components that can be manufactured and the productivity of the machine tool. Traditionally, tombstones are either cast iron or a steel weldment and can be solid or hollow, where steel tombstones offered higher stiffness with low damping and cast iron provides slightly more damping and less stiffness. A useful way capture both the stiffness and damping characteristics is dynamic stiffness, or the product of the stiffness and damping. Maximizing the dynamic stiffness in a tombstone increases the maximum metal removal rate and productivity of the setup [1].

A material with the potential to provide greatly increased damping is concrete. Concrete has been used by machine tool manufacturers as a damping material or as the primary base material for decades. For example, Studer began using a polymer concrete as the base for their grinding machines as early as 1971 [2]. Hardinge Inc. has a patent for the use of polymer concrete to decrease the influence of machine tool vibration on part accuracy and increase in thermal stability of composite or cast-iron lathe bases [3]. As with the machine base, the tombstone is part of the structural loop connecting the workpiece and spindle. Increasing the damping of the tombstone should result in an improvement in material removal.

In this paper, results are presented for frequency response function measurements, and the corresponding damping ratios, of five different tombstone materials including cast iron, welded steel, aluminum, epoxy-mineral, and a contractor grade, fiber-reinforced concrete mix. Comparisons are made between the material-dependent damping values.

SETUP AND EXPERIMENTATION
To evaluate the variation in dynamic response of potential workholding materials, frequency response function measurements of commercially-available cast iron (hollow), welded steel (hollow), aluminum (hollow), and epoxy-mineral (solid) tombstones (see Fig. 1) were compared to a concrete tombstone (solid) with nominally the same dimensions (508 mm × 203 mm × 711 mm, or 20" × 8" × 28") manufactured at Oak Ridge National Laboratory. The concrete tombstone was cast in an additively manufactured polymer composite mold produced using the Big Area Additive Manufacturing (BAAM) system. A 48 MPa (7 ksi) compressive strength concrete mix with 0.0375% fiber fill by mass and a maximum aggregate size of

19.1 mm (0.75") was used. The pour was allowed to cure for 35 days prior to testing.
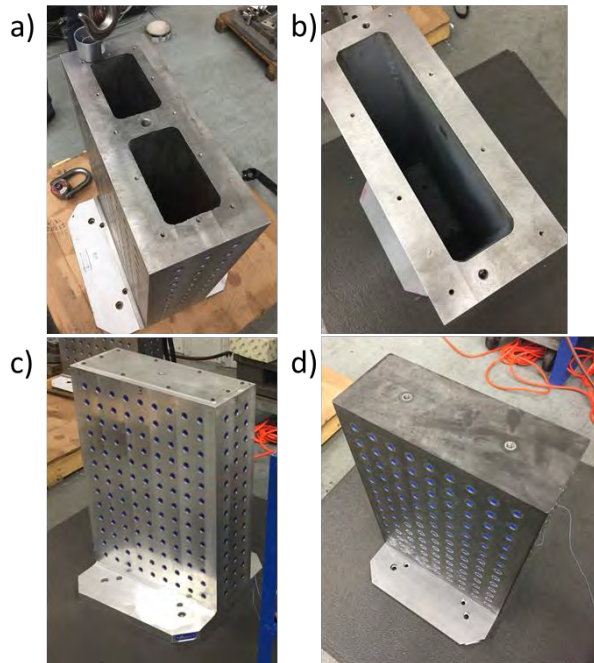
FIGURE 1. a) Hollow cast iron tombstone (no top cap)
b) Hollow steel tombstone (no top cap, no center rib)
c) Hollow aluminum tombstone (with top cap)
d) Solid epoxy-mineral tombstone.
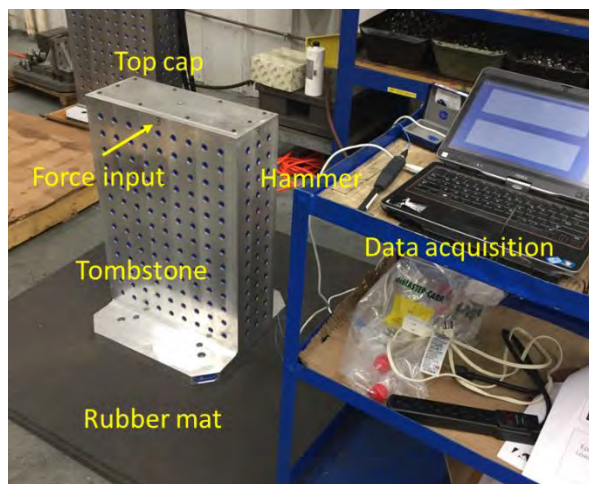
FIGURE 2. Experimental setup for frequency response function measurement.

The frequency response functions were measured by impact testing, where an instrumented modal hammer is used to excite the structure and low mass accelerometer is used to measure the vibration response. Measurements were completed on all tombstones in a free-free condition, where the boundary condition was approximated by setting the tombstones on a soft rubber mat. The direct frequency response function was measured at the top center of each tombstone; see Fig. 2. For the aluminum, steel, and cast iron tombstones, testing was completed with no top cap. For the concrete tombstone, a section of the mold was removed from the concrete on either side, as shown in Fig. 3, so that the measurement was not influenced by the interface between the cured concrete and polymer mold.

The three most flexible modes were used to evaluate the dynamic response for each tombstone. The natural frequency and damping ratio for the three modes were extracted from the frequency response function by peak picking. The results are provided in Table 1 [4].

FIGURE 3. Section of mold removed to allow for direct measurement on concrete.

RESULTS AND DISCUSSION

The measured frequency response functions for each of the five tombstones are displayed in Figs. 5-9.Only the magnitude is shown for brevity; note that the scales are identical for direct visual comparison. As seen in Fig. 1b, the welded steel tombstone did not have an internal rib. The absence of this stiffening feature accounts for the additional modes observed in Fig. 7. The large response magnitude at low frequencies observed in each figure is due to rigid body modes associated with the free-free boundary condition.
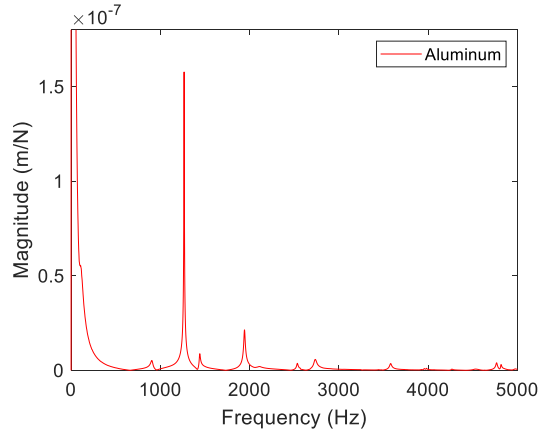
FIGURE 4. Frequency response function for aluminum tombstone with no cap in free-free condition.
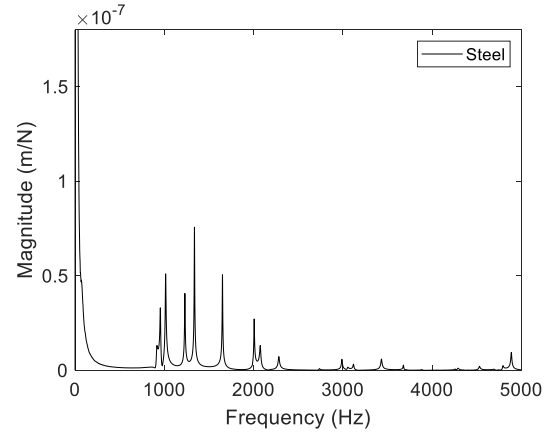
FIGURE 6. Frequency response function for welded steel tombstone with no cap in free-free condition.
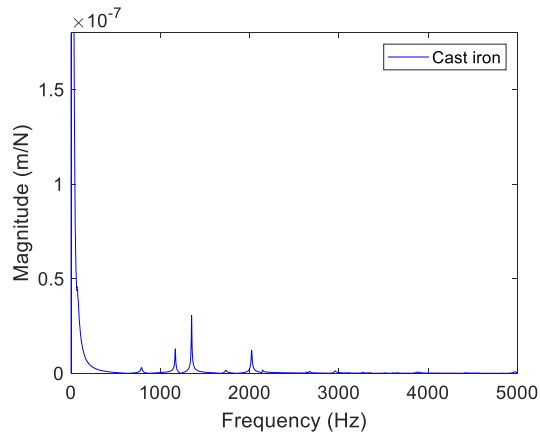
FIGURE 5. Frequency response function for cast iron tombstone with no cap in free-free condition.
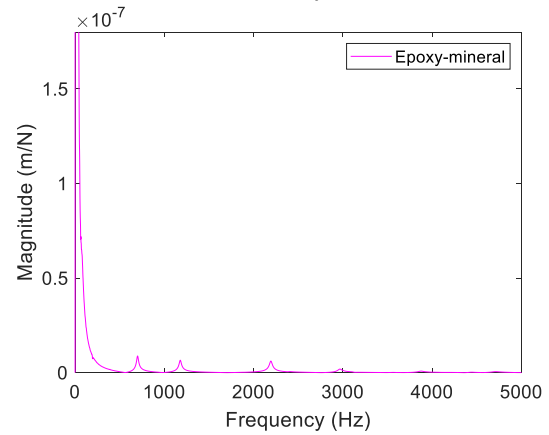
FIGURE 7. Frequency response function for epoxy-mineral tombstone in free-free condition.

Table 1: Modal parameters for three most flexible modes.

Mode	Modal parameter	Cast iron	Steel	Aluminum	Epoxy	Concrete
1	Natural frequency, Hz	1167.7	1229.9	1266.4	699.7	1477.9
	Damping ratio, %	0.33	0.26	0.19	1.48	1.30
2	Natural frequency, Hz	1350.0	1651.4	1441.8	1177.2	2541.3
	Damping ratio, %	0.23	0.16	0.40	1.06	0.59
3	Natural frequency, Hz	2022.6	2075.2	1943.8	2192.5	2918.4
	Damping ratio, %	0.25	0.3	0.41	0.73	1.04
Avg	Damping ratio, %	0.27	0.24	0.33	1.09	0.98
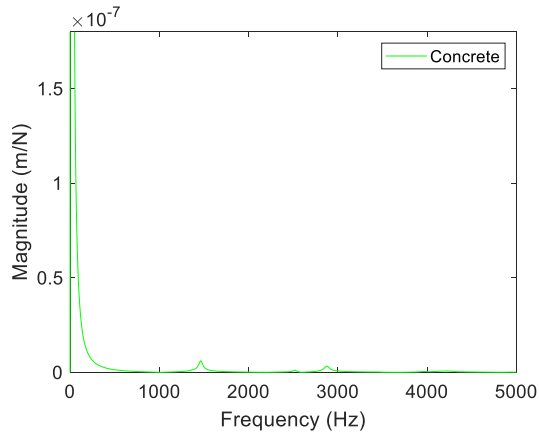
FIGURE 8. Frequency response function for concrete tombstone in free-free condition.

The frequency response function magnitude for the aluminum tombstone shown in Fig. 4 is much larger than other tested materials. this indicates a lower dynamic stiffness and decreased machining performance in comparison. The magnitudes for the concrete and epoxy-mineral tombstones are similar, as displayed in Fig. 10, indicating a similar dynamic stiffness.

The damping ratios for the three most flexible modes for each material are listed in Table 1. The average damping ratio for the epoxy-mineral tombstone is the largest, followed closely by the concrete. This suggests that a contractor grade concrete has material properties which could enable it to function as a viable and improved workholding material versus traditional cast iron. Additionally, its cost is much less than the epoxy-mineral material.
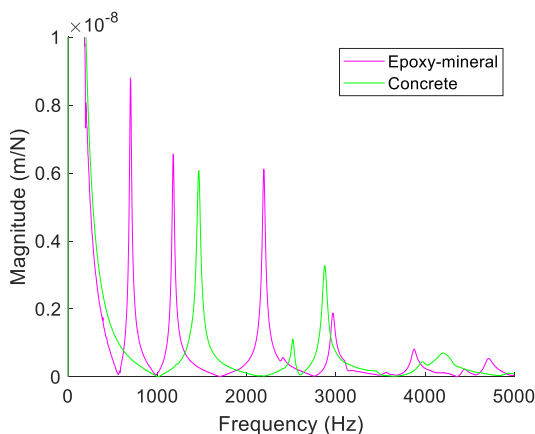
FIGURE 9. Comparison of epoxy-mineral and concrete tombstone frequency responses

It has been demonstrated that the structural properties of concrete change throughout its lifetime [5]. While this study is a relatively new effort, measurements have been taken at several stages of the cure, and dynamic changes have been observed. Further analysis and discussion will be presented in follow-on studies.

CONCLUSIONS

The optimized cutting parameters in a milling or turning application are a function of the structural dynamics of both the tool/spindle and workpiece/workholding combinations. While cast iron or steel weldments have been the traditional choices for tombstone materials, manufacturers also provide aluminum options, which offer a weight advantage and is often used as a sacrificial surface, and epoxy-mineral tombstones, which boast improved damping, but at increased cost. Both increased stiffness and damping enable higher material removal rates.

In this study, it was shown that an epoxy-mineral tombstone provided significantly higher damping than steel weldment and aluminum tombstones. However, comparable damping was measured between tombstones with a similar geometry made from epoxy-mineral and a contractor grade, fiber-reinforced concrete (48 MPa/7 ksi compressive strength). This offers the potential for a similarly high performing workholding system at a fraction of the material price. The improvement in damping also demonstrates the capability of concrete construction for use in machine tools as an alternative to castings and traditional manufacturing methods.

Future work will focus on the changing dynamic parameters of concrete as it continues to cure over time, and the implementation of low-cost concrete construction for machine tools and their components.

REFERENCES
[1] Schmitz, T. and Smith, K.S., 2019, *Machining Dynamics: Frequency Response to Improved Productivity*. New York, NY: Springer.
[2] "Our History: Fritz Studer AG." STUDER, 6 Aug. 2020, www.studer.com/en/fritz-studer-ag/news-topics/history/.
[3] T. Sheehan, "Reduced vibration lathe" U.S. Patent 20010042424A1, issued August 4, 1998

[4] Schmitz, T. and Smith, K.S., 2012, *Mechanical Vibrations: Modeling and Measurement*. New York, NY: Springer.

[5] Hop, T., 1991, The effect of degree of prestressing and age of concrete beams on frequency and damping of their free vibration. Materials and Structures 24, 210–220 https://doi.org/10.1007/BF02472987.

Authors Index

Authors Index

*No abstract included

*No abstract included

*No abstract included